Volcanisme alcalin à l'initiation de la rupture continentale Rift Est Africain, Nord Tanzanie, bassin de Manyara

Céline Baudouin

Collège Doctoral Languedoc-Roussillon

THÈSE

Pour obtenir le grade de

Docteur

Délivré par Université de Montpellier

Préparée au sein de l'école doctorale Gaïa
Et de l'unité de recherche Géosciences Montpellier

Spécialité : Géosciences

Présentée par Céline BAUDOUIN

Volcanisme alcalin à l'initiation de la rupture continentale

Rift Est Africain, Nord Tanzanie, bassin de Manyara

Soutenue le 25 novembre 2016 devant le jury composé de

Jacques DEVERCHERE, PR, UBO, Brest	Examinateur
Tahar HAMMOUDA, MCF, LMV, Clermont-Ferrand	Rapporteur
Dmitri IONOV, PR, GM, Montpellier	Examinateur
Nicole METRICH, DR, IPGP, Paris	Rapporteur
Fleurice PARAT, MCF, GM, Montpellier	Directrice
Christel TIBERI, CR, GM, Montpellier	Co-directrice

UNIVERSITÉ MONTPELLIER

GÉOSCIENCES MONTPELLIER
ÉCOLE DOCTORALE GAÏA

THÈSE

présentée par

Céline BAUDOUIN

le 25 novembre 2016

en vue de l'obtention du

Doctorat de l'Université de Montpellier

Spécialité : Physique et Chimie de la Terre

Volcanisme alcalin à l'initiation de la rupture continentale

Rift Est Africain, Nord Tanzanie, bassin de Manyara

Volcan Hanang

JURY

DEVERCHERE Jacques	Professeur (Univ.de Bretagne occidentale, Domaines océaniques)	Examinateur
HAMMOUDA Tahar	Maitre de conférences (Laboratoire Magmas et Volcans)	Rapporteur
IONOV Dmitri	Professeur (Géosciences Montpellier)	Examinateur
METRICH Nicole	Directrice de recherche (IPGP, Institut de physique du globe de Paris)	Rapporteur
PARAT Fleurice	Maitre de conférences (Géosciences Montpellier)	Directrice
TIBERI Christel	Chargée de recherche (Géosciences Montpellier)	Co-directrice

Remerciements

Je remercie les membres de mon jury, Tahar Hammouda, Nicole Métrich, Dmitri Ionov et Jacques Déverchère pour avoir accepté d'évaluer mon travail.

Je tiens en particulier à dire un grand merci à Fleurice. Merci de m'avoir proposé ce sujet et de m'avoir fait confiance tout au long de ces années. Merci de m'avoir initiée aux inclusions carbonatées et aux apatites, ce n'était pas de tout repos ! Merci pour ces nombreuses discussions fructueuses et ces samedi matins en conditions oxydantes… Le thé tanzanien sans thé me restera toujours en mémoire !

Merci à Christel pour les bons moments que nous avons passés sur le terrain, et pour m'avoir fait découvrir les « aléas » de la sismologie pendant les missions de terrain. Et pour compléter l'équipe des « Tanzanian girls », je tiens à remercier Sophie et Stéphanie pour leur gentillesse et leur grain de folie. Ce travail n'aurait pu exister sans l'aide de très nombreuses personnes en Tanzanie. Je tiens à exprimer ma gratitude aux personnes impliquées dans ce projet à l'université de Dar es Salaam et au Nelson Mandela institute (Arusha). Je tiens à remercier plus particulièrement Majura Songo et Fredrik Mangasini pour l'aide qu'ils m'ont offerte lors de mes 2 missions de terrain.

Ce projet n'aurait pas été possible sans le laboratoire Géosciences et l'équipe Manteau Interfaces qui m'ont accueillis. Merci aux membres de l'équipe, et plus particulièrement, à Sylvie et Olivier pour leur expertise respective. Le travail que j'ai effectué pendant ma thèse n'aurait été possible sans les compétences de nombreuses personnes d'ici et d'ailleurs : Christophe Nevado, Doriane Delmas, Bernard Boyer, Olivier Brugier, Chantal Douchet, Thierry Michel, Moulay Tahar Sougrati. Je remercie Manuel Munoz pour son aide précieuse au synchrotron.

Merci à Carole pour son soutien et pour avoir essayé de m'initier à l'ironie, travail de longue haleine, « lui on ne comprend ni c'qui dit, ni c'qui fait... C'est rare! ». Merci à Julie pour sa bonne humeur et ses fameuses tartes. Merci les filles pour les fous rires dans le bureau et les bons moments passés aux soirées 'mojitos-guacamole'. Merci aussi pour vos relectures et vos conseils « et pis il y a toujours une proportion de secoués dans tous les métiers de toute façon ». Je tiens à remercier mes collègues de couloir pour avoir su conserver cette bonne ambiance au fil des années, merci donc à Cristiane, Camille, Carlotta, Sofia, Julien, et Hicham. Merci également à tous les autres thésards de GM et d'ailleurs.

Merci à mes profs de SVT du lycée du Vigan qui m'ont donné envie de faire de la géologie, il y a presque 10 ans maintenant. Je tiens également à remercier Jean-Marie Dautria alias Dodo qui a su me faire apprécier la pétrologie magmatique.

Enfin, je souhaite dire un grand merci à ma famille, ma mère, mon père, Quentin, Yannick et les autres pour avoir toujours été présents, pour m'avoir encouragée et soutenue. Merci pour les week-ends détente et les bons repas.

Volcanisme alcalin à l'initiation de la rupture continentale

Exemple du Rift Est Africain : Nord Tanzanie, bassin de Manyara

Céline BAUDOUIN*

Le rift Est africain (REA) est une frontière de plaque en extension qui présente plusieurs stades d'extension, de l'initiation du rift dans la lithosphère cratonique (Tanzanie) jusqu'à l'accrétion océanique en Afar. Au nord de la Tanzanie, le magmatisme et des processus tectoniques sont impliquées dans la rupture continentale. Cette étude est centrée sur le bassin de Manyara dans la partie méridionale de branche Est du REA. Le volcanisme hyperalcalin récent (< 1,5 Ma) associé à un essaim sismique dans la croûte inférieure (20 – 40 km), caractérise la zone de l'initiation de la rupture continentale.

Les néphélinites à mélilite (Labait et Kwaraha) sont des laves primaires composées d'olivines et de clinopyroxènes (cpx). La modélisation géochimique des éléments en trace suggère que ces magmas primaires résultent d'un degré de fusion partielle ≤ 1 % à partir d'une péridotite à grenat et phlogopite. Ces magmas proviennent d'une profondeur > 120 km. Les minéraux ont cristallisés à 1250°C et 1000 MPa à partir d'un magma pauvre en eau (0,1 et 0,5 pds % H_2O). La calciocarbonatite et les néphélinites différenciées sont issues des néphélinites à mélilite par cristallisation fractionnée et processus d'immiscibilité. Les néphélinites du Hanang sont riches en éléments alcalins (9,5 – 12,1 pds % Na_2O+K_2O) et en silice (44,2 – 46,7 pds% SiO_2) et sont composés de cpx, grenat, néphéline, titanite et apatite. La zonation complexe dans les cpx (par exemple, changement brusque de Mg#, Nb/Ta, et H_2O) implique une différenciation magmatique en système ouvert avec immiscibilité de liquide carbonaté et silicaté ainsi qu'un remplissage de la chambre magmatique avec des liquides primaires. La faible teneur en eau des cpx (3 – 25 ppm H_2O) indique la présence d'un magma pauvre en eau (0,3 pds % H_2O) lors de la cristallisation des cpx à des conditions crustales (340 – 640 MPa et 1050 – 1100 °C). L'étude des inclusions vitreuses dans les néphélines de Hanang permet de contraindre l'évolution magmatique tardive des néphélinites et le comportement des éléments volatils (CO_2, H_2O, S, F, Cl) lors du stockage et de la remontée du magma. Les inclusions vitreuses sont composées d'un verre trachytique, d'une phase carbonatée et d'une bulle de rétraction. Le verre trachytique contient du CO_2 (0,43 pds % CO_2, analyses SIMS), du soufre (0,21 à 0,92 pds% S), du chlore (0,28 – 0,84 pds % Cl) et très peu d'H_2O (< 0,1 pds % H_2O, analyses Raman). Le processus d'immiscibilité conduisant à la formation du carbonate se produit dans un système fermé pendant l'ascension rapide du magma à ~500 MPa. La phase carbonatée est un carbonate anhydre et riche en Ca-Na-K-S (33 pds % CaO, 20 pds % Na_2O, 3 pds % K_2O, et 3 pds % S). Le liquide pré-immiscible a une composition phonolitique avec 6 ± 1,5 pds % CO_2 à une pression de 700 MPa. Une étude préliminaire des inclusions par spectroscopie XANES et des roches par spectroscopie Mössbauer a permis de déterminer que les laves de Manyara se sont formées à conditions oxydantes (~ ΔFMQ +1,5). Le volcanisme alcalin à l'initiation de la rupture continentale est caractérisé par des magmas riches en CO_2 et pauvres en H_2O issus d'une source profonde 120 km à partir de faible taux de fusion.

L'association des données géochimiques, géophysiques et tectoniques a permis de mettre en évidence des interactions entre le magmatisme, les structures héritées et la sismicité au nord de la Tanzanie. Dans le bassin de Manyara, la présence de magmas alcalins riches en CO_2 associée à de faibles volumes de lave en surface suggèreraient que le piégeage et la percolation de ces magmas en profondeur serait un déclencheur potentiel d'un essaim sismique profond.

Mots clefs : rift, néphélinite, carbonatite, éléments volatils, inclusions vitreuses, fusion partielle, immiscibilité, conditions redox

*Géosciences Montpellier, Université Montpellier, Place E. Bataillon, 34095 Montpellier.

Alkaline volcanism associated with early stage of rifting

East African Rift: North Tanzania, Manyara Basin

Céline BAUDOUIN*

East African Rift (EAR) exposes different stages of extension, from early stage rifting in cratonic lithosphere (Tanzania) to oceanic accretion in Afar (Ethiopia). In north Tanzania, both magmatic and tectonic processes are involved in lithospheric break-up. This study focuses on Manyara basin in the southernmost rift system of the east branch of EAR. The recent hyperalkaline volcanism (< 1.5 Ma) is associated here with seismic swarm in the lower crust (20 – 40 km) and represents the earliest stage of rifting.

Melilite nephelinites (Labait and Kwaraha) are primary lavas mainly composed of olivine and clinopyroxene (cpx). Geochemical modelling from trace elements suggests that these primary magmas result from a low degree of partial melting < 1 % from a CO_2-garnet-phlogopite-bearing peridotite. These magmas have an asthenospheric mantle source and partial melting occurred at depth > 120 km. The minerals crystallized at 1250°C and 1000 MPa (30 km) from magma with a low H_2O content (0.1 and 0.5 wt% H_2O). The calciocarbonatite and evolved nephelinites derived from melilite nephelinites by fractional crystallization and immiscibility processes. Hanang nephelinites are silica- and alkaline-rich lavas (44.2 – 46.7 wt % SiO_2, 9.5 –12.1 wt % Na_2O+K_2O, respectively) composed by cpx, Ti-garnet, nepheline, apatite and titanite. Complex zonation of cpx (e.g. abrupt change of Mg#, Nb/Ta, and H_2O) and trace element patterns of nephelinites record magmatic differentiation involving open system with carbonate-rich silicate immiscibility and melilitite melt replenishment. The low H_2O content of cpx (3 – 25 ppm wt. H_2O) indicates that at least 0.3 wt % H_2O was present at depth during carbonate-rich nephelinite crystallization at 340 – 640 MPa and 1050 – 1100 °C. Hosted-nepheline melt inclusions record the late magmatic evolution of nephelinites during magma storage and ascent. Melt inclusions are composed of silicate trachytic glass, carbonate phase and shrinkage bubble resulting from immiscibility during ascent. Trachytic glass contains high content in CO_2 (0.43 wt %, SIMS analyses), sulfur (0.21 – 0.92 wt % S), chlorine (0.28 –0.84 wt % Cl) and H_2O low content (< 0.1 wt %, Raman analyses). Immiscibility process leading to the formation of carbonate occurs in a closed system during rapid magma ascent at ~500 MPa. The carbonate phase is a Ca-Na-K-S-rich and anhydrous carbonate (33 wt % CaO, 20 wt % Na_2O, 3 wt % K_2O, and 3 wt % S). The pre-immiscible liquid has a phonolitic composition with 6 ± 1.5 wt % CO_2 at 700 MPa. Study of iron (Fe^{3+}/Fe^{2+}) and sulfur (S^{6+}/S^{2-}) speciation in melt inclusions, minerals (XANES spectroscopy) and whole rocks (Mössbauer spectroscopy) indicates that nephelinite from Manyara Basin evolved at oxidized conditions (~ ΔFMQ +1.5). Alkaline volcanism associated with early stage of rifting is characterized by CO_2-rich and H_2O-poor magmas from at least 120 km below the rift escarpment resulting from low degree of partial melting. Association of geochemical, geophysical and tectonic results allows to highlight interplays between magmatism, inherited tectonic structures and seismicity in northern Tanzania. In Manyara basin, the presence of CO_2-rich magmas and small amount of volcanic rocks may indicate that the storage and percolation of these magmas at depth is a potential trigger for deep seismic swarms.

Key words: rift, nephelinite, carbonatite, volatile elements, melt inclusions, partial melting, immiscibility, oxidation state

*Géosciences Montpellier, Université Montpellier, Place E. Bataillon, 34095

Table des Matières

Chapitre I. Introduction

L'introduction de cette thèse est constituée d'un état de l'art (I) sur la genèse des magmas alcalins et des carbonatites dans les rifts ainsi que (II) sur les éléments volatils et les conditions redox dans les magmas. Cette introduction se conclue par une présentation (III) de la zone d'étude au sein du rift Est africain et (IV) des objectifs de cette thèse.

I.I Magmas intracontinentaux et rift

I.I.1 Modèles de rift, rôle du magmatisme

Les rifts continentaux sont les zones de déformation en extension visibles à la surface de la Terre. On observe des rifts aux caractéristiques distinctes : étroits ou larges, magmatiques ou amagmatiques, symétriques ou asymétriques, actifs, fossiles ou avortés. La rupture continentale (rifting) est influencée par le volume de magma, la rhéologie de la croûte/manteau lithosphérique, et de l'héritage structural (Tommasi et Vauchez 2001).

Il y a 2 modèles principaux (Fig.I.1) pour la formation des rifts : le rift « passif » et le rift « actif ». Le rift passif est dû à des contraintes extensives aux limites de plaque, ayant pour conséquence une remontée de l'asthénosphère par décompression adiabatique (McKenzie 1978, Huisman et al. 2001).

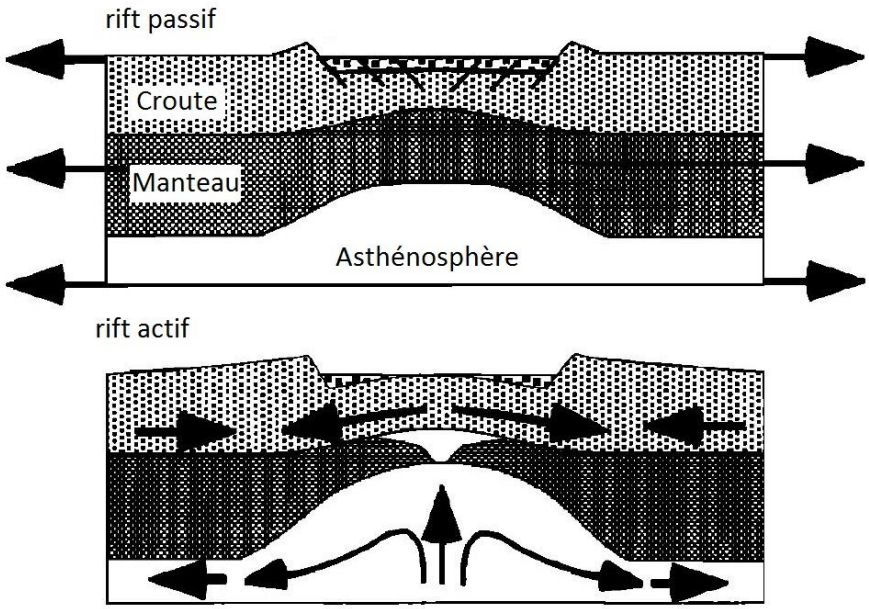

Fig.I.1 *Schéma des 2 modèles de rift (passif vs actif) (d'après Huisman et al. 2001)*

Le rift actif est dû à l'impact d'un panache à la base de la lithosphère induisant un déséquilibre thermique (érosion de la lithosphère) et donc une compensation isostatique (McKenzie 1978). Les 2 modèles impliquent une remontée de l'asthénosphère et donc un amincissement lithosphérique. L'activité du rift peut être magmatique et/ou tectonique. La part d'accommodation de la déformation par le magmatisme et la relation directe entre l'activité volcanique et tectonique sont mal connues. De récentes études sur l'effet de l'intrusion de dyke sur la sismicité (Calais et al. 2008, Wright et al. 2006) suggèrent que l'occurrence de ce phénomène diminue la résistance de la lithosphère (augmentation de la chaleur). Les intrusions magmatiques (dykes) seraient des initiateurs potentiels de l'extension d'une lithosphère continentale (Buck 2006).

I.I.2 Genèse des magmas alcalins

Les laves alcalines sont essentiellement présentes dans les zones de volcanisme intraplaque : îles océaniques, volcanisme intracontinental et les rifts continentaux. Le magmatisme alcalin est lié à l'existence d'un point chaud et est interprété comme le produit de faible taux de fusion partielle à grande profondeur (Green et Ringwood 1967, Kushiro 1968). Ces laves peuvent être issues de la fusion de péridotite (Green 1973), d'une partie de croûte océanique recyclée (Hofmann 1986), de la fusion de péridotite (± pyroxénite) en présence de CO_2 (Eggler et Holloway 1977, Dasgupta et al. 2007, Baasner et al. 2016) ou encore de la fusion d'un manteau métasomatisé (Halliday et al. 1995, Paslick et al. 1995).

Les différentes hypothèses sur l'origine des laves alcalines ont été contraintes par des études expérimentales. Ces études (Green et Falloon 1998, Herzberg et O'Hara 1998, Foley et al. 2009, 2012) ont permis de délimiter la température et la pression de formation des différentes laves alcalines. La fusion de péridotite (± H_2O et CO_2) va produire pour une température de 1300 °C : (1) des basanites à 60 – 70 km (facies à spinelle), (2) des néphélinites à 90 km (facies à grenat) (3) des mélilitites à 100 km (4) et des kimberlites à 160 km (Fig.I.2).

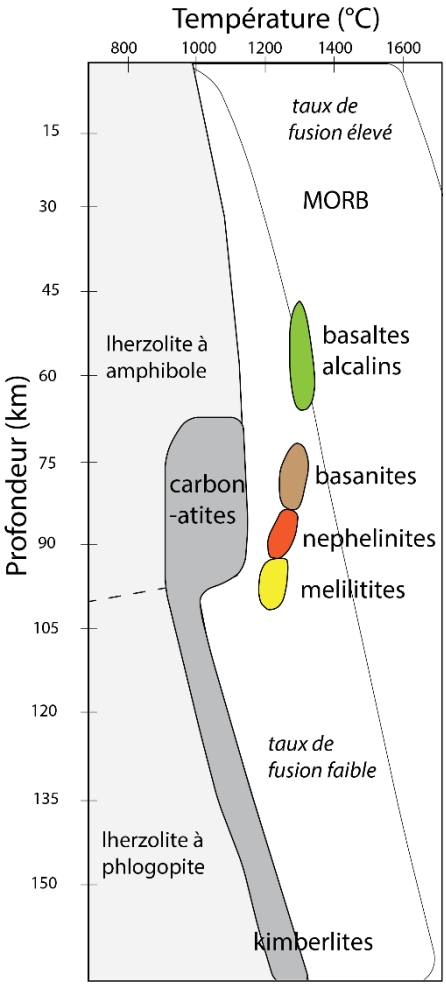

Fig.I.2 *Température et pression de formation des différentes laves alcalines (d'après Foley et al. 2012).*

Les magmas qui ont de très faible taux de fusion partielle (< 1 %) ont des concentrations en CO_2 supérieures à celles en H_2O (Fig.I.3). De plus récentes études ont été réalisées afin de déterminer l'effet de l'H_2O et surtout du CO_2 entre 3 et 6 GPa (Dasgupta et al. 2013, Kessel et al. 2015, Green 2015), qui peuvent diminuer de manière importante la température de fusion. La présence d'éléments volatils (H_2O et CO_2) dans la péridotite est essentielle pour la formation de magmas néphélinitiques à kimberlitiques (Bultitude et Green 1971, Brey et Green 1977). Le taux de fusion est calculé à partir de modélisation de fusion partielle et des comportements des éléments. Les basaltes alcalins et les basanites ont de faible taux de fusion (< 5 %, Edgar 1987) et plus faible pour les néphélinites (2 – 4 %) et les melilitites (1 %) (Green 1970).

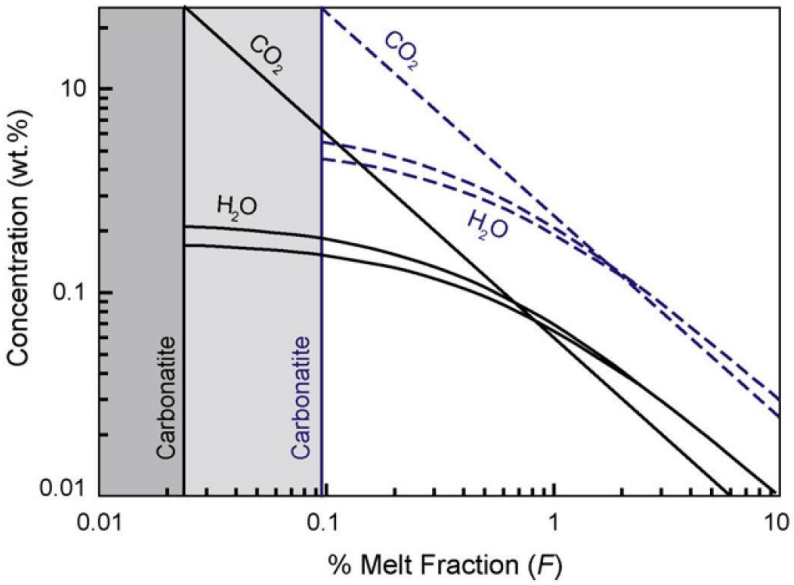

Fig.I.3 *Concentration calculée en CO_2 et H_2O en fonction du degré de fusion partielle d'une péridotite (Hirschmann 2010, Fig.2). Les courbes pleines représentent la source des MORB et les courbes en pointillés la source des OIB.*

La présence de minéraux hydratés, telles que l'amphibole et la phlogopite dans le manteau source est reflétée dans les magmas primaires dans les rapports Rb/Sr et Ba/Rb (Furman et Graham 1999, LaTourette et al. 1995). La présence de phlogopite est évoquée lorsque le rapport Rb/Sr est élevé et Ba/Rb est faible. Certains rapports d'éléments en trace sont sensibles au métasomatisme carbonaté présent dans le manteau, tels Nb/Ta, Zr/Hf et Ti/Eu (Rudnick et al. 1993). Le comportement des éléments volatils durant la fusion partielle est lié à leur mode de stockage dans les roches mantelliques. L'eau est principalement stockée dans les minéraux hydratés tels que l'amphibole et la phlogopite (Green 2015) et dans les minéraux silicatés 'anhydres' (Demouchy et Bolfan-Casanova 2016). Le carbone peut prendre plusieurs forme dans le manteau (Hazen et al. 2013) : du carbone réduit (graphite et diamant), des phases carbonates (dolomite, magnésite) ou bien du CO_2 présent dans les inclusions fluides.

Les laves présentes en domaine intracontinental font partie de la série alcaline (des basanites aux phonolites) jusqu'à des laves très sous-saturées en silice (e.g. néphélinites, mélilitites). Les laves présentent dans le rift Est africain (base de donnée Georoc) ont des compositions différentes du Nord (Ethiopie) vers le Sud (Tanzanie). En Ethiopie, les laves évoluent des basaltes jusqu'à des rhyolites (Fig.I.4).

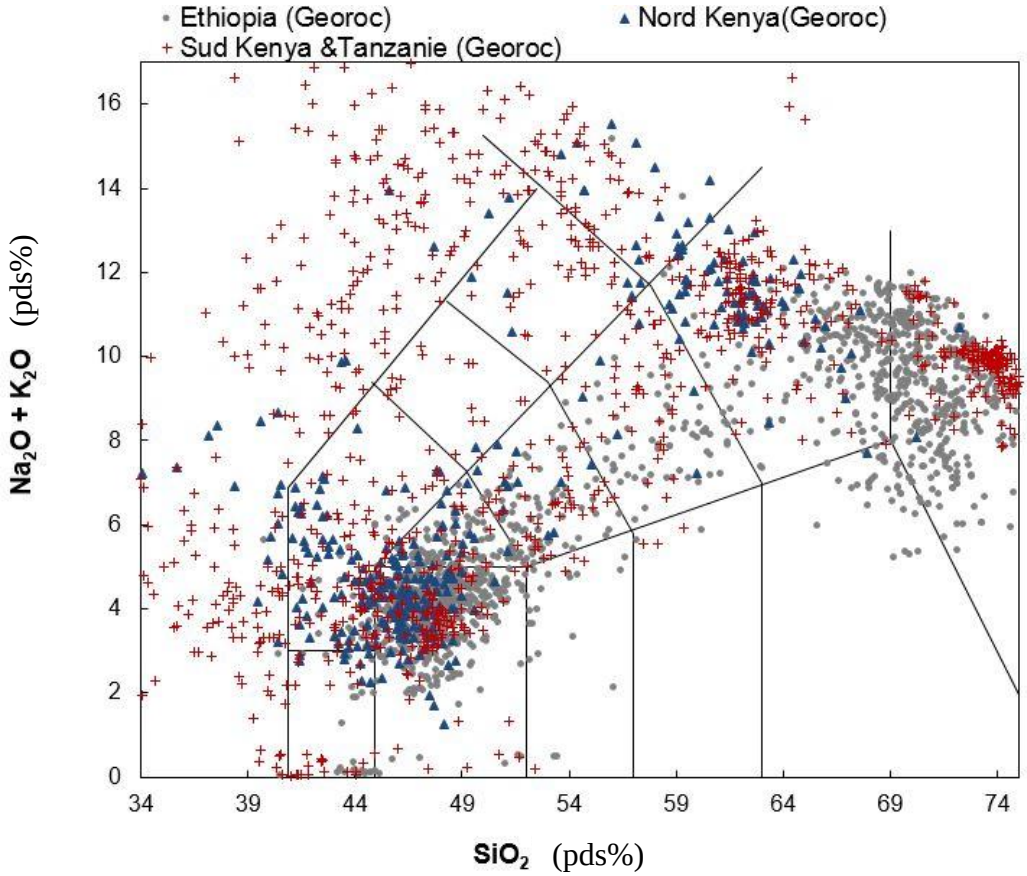

Fig.I.4 *TAS des laves du rift Est africain (base de donnée GEOROC)*

En comparaison, les laves au nord du Kenya sont davantage sous saturées en silice, on retrouve des basanites, trachytes et des phonolites. Enfin les laves du sud du Kenya et du Nord de la Tanzanie sont également composées de néphélinites et de phonolites hyperalcalines. Parmi les laves hyperalcalines près du craton tanzanien, les laves de la branche Ouest (Virunga) sont plus riches en potassium que celles de la branche Est (sud Kenya-Tanzanie ; Furman 2007, Foley et al. 2012). Plus le système de rupture continentale est immature, et plus les laves sont sous-saturées en silice et riche en alcalins.

I.I.3 Genèse des carbonatites

Les carbonatites (> 30 % CO_2) sont divisées en plusieurs types : calciocarbonatite (e.g. Kaiserstuhl, Tamazert), ferrocarbonatite (e.g. Homa Mountain, Kenya), magnesiocarbonatite (Cap vert, Rufunsa (Zambia)) et natrocarbonatite (Oldoinyo Lengai). Les natrocarbonatites du Oldoinyo Lengai sont uniques au monde de part leur teneur exceptionnelle en Na_2O et K_2O (Dawson 1962). Les carbonatites sont généralement des laves riches en terres rares légères (LREE), Sr, Ba et P (review Jones et al. 2013). Les carbonatites sont localisées en domaine intracontinental, dont la moitié des occurrences sur le continent africain. Pour les carbonatites d'origine magmatique, 76 % d'entre elles sont associées à des laves silicatées (Woolley et

Kjarsgaard 2008). Les carbonatites sont associées, par ordre d'occurrence, à des néphélinites, des phonolites, des trachytes, des mélilitites, des kimberlites et des basanites (Woolley et Kjarsgaard 2008).

Il y a 3 hypothèses pour expliquer l'origine des carbonatites : la carbonatite est (1) un liquide résiduel d'une néphélinite ou d'une mélilitite riche en CO_2 (Gittins et Jago 1998), (2) un liquide immiscible à partir d'un liquide silicaté saturé en CO_2 (e.g. Freestone et Hamilton 1980, Baker et Wyllie 1990, Brooker et Kjarsgaard 2011) (Fig.I.5), (3) un liquide primaire mantellique à partir de la fusion partielle d'une péridotite enrichie en CO_2 (Gudfinnsson et Presnall 2005, Dasgupta et Hirschmann 2006) (review Jones et al. 2013) (Fig.I.6).

La cristallisation fractionnée à partir d'un liquide néphélinite ou d'une mélilitite riche en CO_2 peut être à l'origine de la formation de carbonatite (Gittins et Jago 1998). La cristallisation d'olivine a pour conséquence d'augmenter la teneur en CO_2 et en alcalins du liquide résiduel et permet la coexistence de 2 liquides (immiscibilité) (Kjarsgaard 1998).

Le processus d'immiscibilité entre un liquide silicaté et carbonaté est un processus qui a été étudié à travers de nombreuses expériences (Freestone et Hamilton 1980, Baker et Wyllie 1990, Lee et Wyllie 1997, Church et Jones 1995, Brooker et Kjarsgaard 2011). Ces expériences ont été réalisées à des profondeurs allant de 0.1 à 6 GPa avec des compositions simplifiées (i.e. SiO_2-Na_2O-Al_2O_3-CaO + CO_2) pour définir les conditions à lesquelles les 2 liquides coexistent (Fig.I.5). L'une des motivations de ces études expérimentales est d'expliquer la formation de complexe volcanique qui associe des lavas alcalines et des carbonatites (Le Bas 1987).

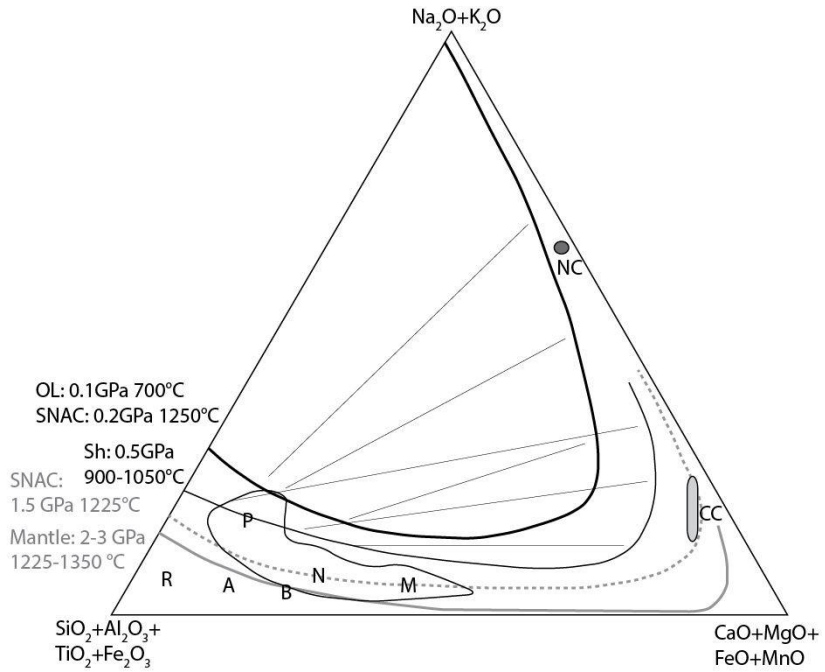

Fig.I.5 *Diagramme ternaire des liquides silicatés et carbonatés. R : rhyolites, N : néphélinites, M : mélilitites, A : andésites, B : basaltes, P : phonolites NC : natrocarbonatite, CC : calciocarbonatite. (d'après Brooker et Kjaargaard 2011)*

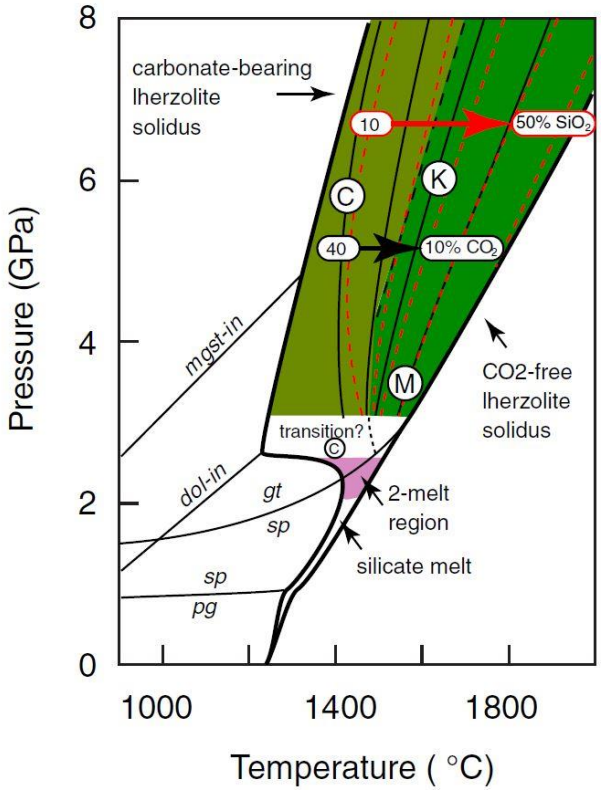

Fig.I.6 *Conditions de formation des carbonatites dans le manteau à partir de la fusion partielle d'une lherzolite à CO_2 (Hammouda et Keshav 2015). C : carbonatite, K : kimberlite, M : mélilitite*

La fusion d'une lherzolite à des pressions > 2.5 GPa peut être à l'origine des carbonatites (i.e. Gudfinnsson et Presnall 2005, Dasgupta et Hirschmann 2006). La fusion de péridotite + CO_2 a pour résultat une Mg-Ca carbonatite alors que la grande majorité des carbonatites naturelles sont des Ca-carbonatites. Les expériences de fusion d'une éclogite + CO_2 permettent de se rapprocher des Ca-carbonatites (Hammouda 2003).

Les coefficients de partage des éléments en trace lors du processus d'immiscibilité entre un liquide carbonaté et silicaté ont été déterminés dans quelques études récentes (Veksler et al. 1998, 2012, Martin et al. 2013, Fig.I.7).

Les éléments compatibles dans les liquides carbonatés sont principalement les LILE (de l'anglais « *large-ion lithophile elements* », e.g. Rb, Ba, Sr) ainsi que les REE pour des liquides hydratés et potassiques (Martin et al. 2013). Les éléments qui sont très incompatibles dans le liquide carbonaté sont le silicium, l'aluminium et les HFSE (de l'anglais « *high field strength elements», e.g. Zr, Hf, Nb, Ta).* Ta et Hf sont plus incompatibles que Nb et Zr respectivement (Veksler et al. 2012), ce qui a pour effet d'augmenter les rapports Nb/Ta et Zr/Hf dans le liquide silicaté qui coexiste avec le liquide carbonaté (Fig.I.7) (Veksler et al. 2012, Rudnick et al. 2013).

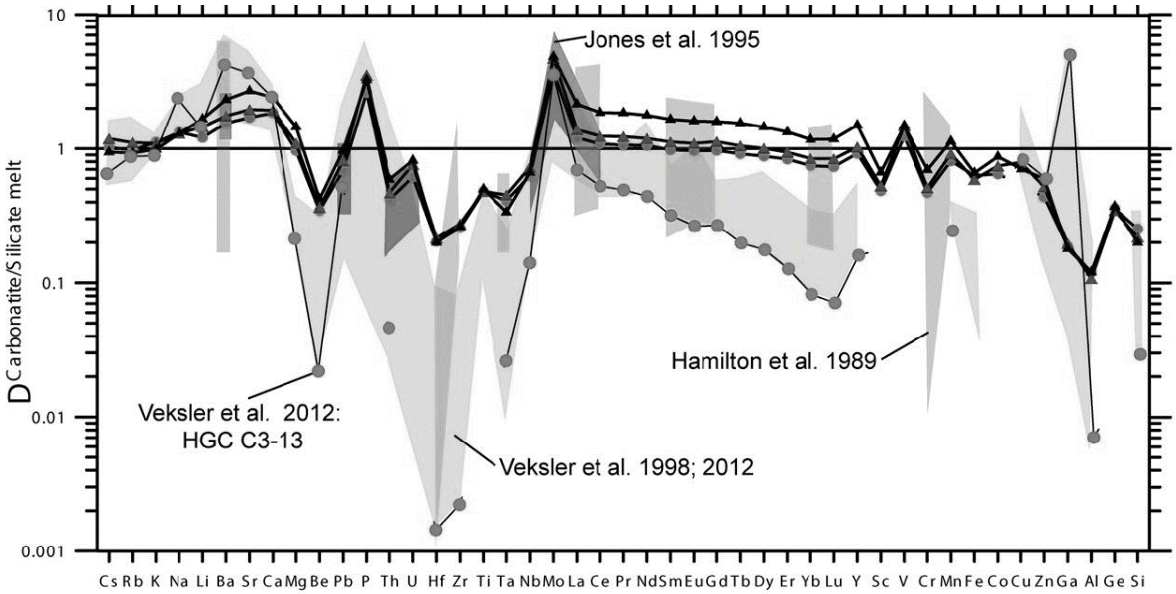

Fig.I.7 *Coefficient de partage des éléments entre un liquide carbonaté et silicaté (Martin et al. 2013)*

I.II Eléments volatils et conditions redox

I.II.1 Eléments volatils dans les magmas

Les éléments volatils (H_2O, CO_2, S, Cl, F) sont dissous dans les magmas. Cette section a pour but d'introduire l'abondance, la solubilité, et le dégazage des éléments volatils dans les magmas et en particulier dans les magmas alcalins. H_2O et CO_2 sont les composants volatils les plus abondants sur Terre avec des concentrations de plusieurs centaines de ppm au sein du manteau terrestre (Aubaud et al. 2005, Cartigny et al. 2008, Dasgupta et Hirschmann 2010). L'abondance des éléments volatils dans les magmas varie en fonction de la concentration initiale de la source ainsi que de solubilité de chacun de ces éléments qui diffère selon la pression, la température, la composition et les conditions redox (review dans Baker et Alletti 2012).

H_2O est le composant volatil dont la solubilité a été le plus étudiée (i.e. Holloway et Blank 1994, Behrens et al. 2001, Baker et Alletti 2012). À des pressions lithosphériques, la solubilité de l'H_2O dans les magmas basaltiques peut atteindre jusqu'à 14 %, et diminue progressivement jusqu'à la surface (< 4 % à 100 MPa) (Fig.I.8, Dixon et Stolper 1995).

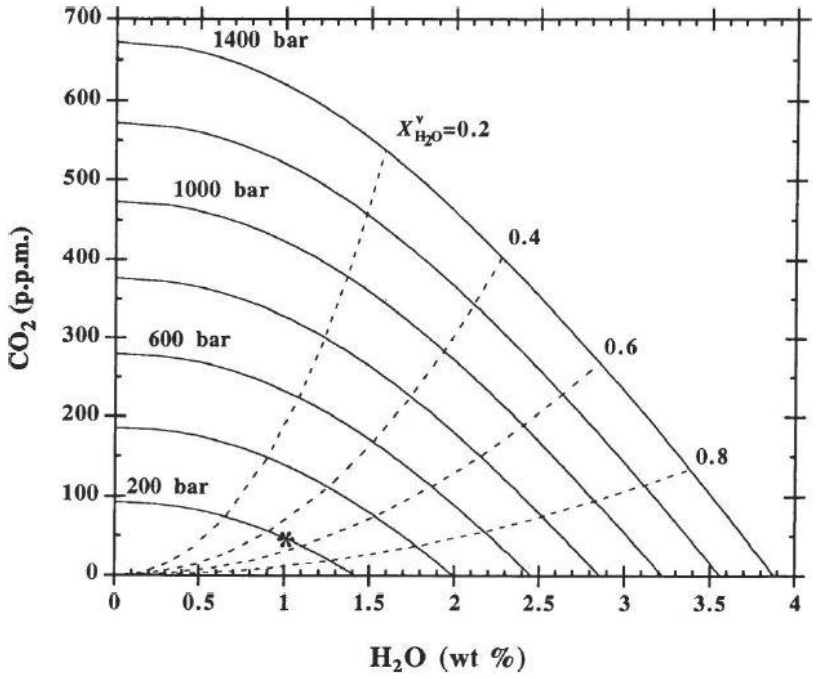

Fig.I.8 *Corrélation inverse de la solubilité du CO_2 et H_2O dans les basaltes à 1200 °C et entre 200 et 1400 bar (Dixon et Stolper 1995, Fig.1)*

Le dioxyde de carbone a une solubilité plus faible que l'eau d'un ou deux ordres de grandeur pour les magmas de la série tholéitique. La solubilité en CO_2 pour les mélilitites à 3 GPa est de l'ordre de 11 pds% (Mysen et al. 1976, Brey et Green 1976, Brooker et al. 2001). Des expériences avec des mixtures CO_2-H_2O ont été menées, les magmas avec de forte concentration en H_2O ont une faible solubilité en CO_2 (Dixon et Stolper 1995, Papale 1997, Fig.1.8). Seules quelques études ont été réalisées pour définir la solubilité de H_2O et CO_2 des magmas hyperalcalins à des pressions crustales (e.g. Morizet et al. 2014, Moussallam et al. 2015, 2016; Shishkina et al. 2014).

La solubilité du soufre est d'environ 0,25 pds % pour des magmas basaltiques (200 MPa et ΔQFM (quartz, fayalite, magnétite), Moune et al. 2009). La solubilité du soufre est dépendante de la composition (e.g. FeO) et de la fugacité en oxygène (Scaillet et McDonald 2006, Jugo 2009, Jugo et al. 2010), et donc de sa spéciation (S^{6+}/S^{2-}). La solubilité du soufre dans les magmas d'arc est de 1 pds % à ΔQFM+1 à ΔQFM+3 (Wallace et Edmonds 2011, Fig.I.9).

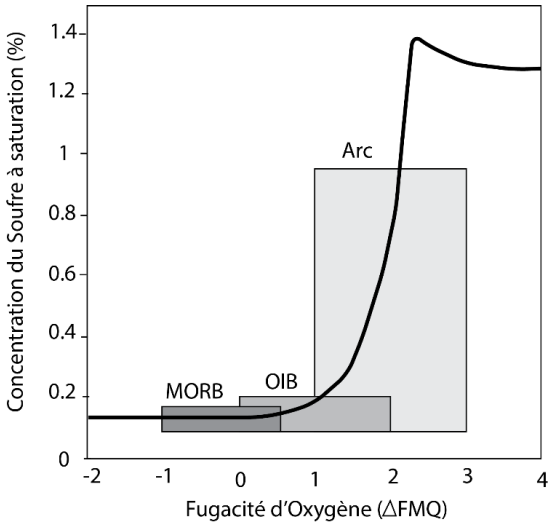

Fig.I.9 *Solubilité du soufre dans les MORB, OIB et les laves d'arc (d'après Jugo et al. 2010)*

La solubilité du chlore dans les magmas est élevée dans les liquides basaltiques (2,5 pds %, Webster et al. 1999) et andésitiques (2,1 – 2,8 pds %, Webster et al. 1999, Botcharnikov et al. 2007). La solubilité du Cl diminue drastiquement lorsque les magmas contiennent 5 – 6 % H_2O (Webster et al. 1999). La solubilité des magmas granitiques (0,3 pds %) et phonolitiques (0,94 pds %) a également été déterminée (Signorelli et Carroll 2000, Webster et al. 2014). La solubilité du fluor pour des magmas granitiques est de 2 pds % (Webster et Holloway 1990) et de 0,7 pds % pour les magmas phonolitiques (Webster et al. 2014).

La solubilité des éléments volatils pour les systèmes alcalins a été étudiée pour les phonotéphrites (Behrens et al. 2009, Vetere et al. 2014), les phonolites (Caroll et Blank 1997, Brooker et al. 2001), ainsi que les laves pauvres en silice (kimberlite, melilitite ; Moussallam et al. 2015 et néphélinite; Shishkina et al. 2014). La composition chimique et donc le nombre d'oxygène non-pontant à un tétraèdre (NBO/T de l'anglais « *non-bridging oxygens per tetrahedral* ») a un effet important sur la solubilité, notamment pour celle du CO_2 (Brooker et al. 2001, Morizet et al. 2014). Les éléments chimiques qui influent sur la solubilité du CO_2 sont les alcalins (Morizet et al. 2015, Shishkina et al. 2014) et la proportion CaO/MgO (Brooker et al. 2001).

La concentration des éléments volatils dans les échantillons naturels est estimée à partir de l'étude des inclusions vitreuses. Les inclusions vitreuses sont des liquides silicatés piégés par les minéraux lors de leur croissance. Ces inclusions permettent de reconstituer l'évolution du magma et ses teneurs en éléments volatils (Métrich et al. 2004). La formation des inclusions vitreuses est directement liée aux mécanismes de croissance cristalline (Faure et Schiano, 2005), et favorisée par la présence d'irrégularités à la surface du minéral. Les inclusions et leur minéral-hôte ont alors une relation co-génétique. Les inclusions vitreuses piégées à haute température et haute pression sont conservées sous forme de verre et les échanges avec le minéral hôte sont faibles si le taux de refroidissement est rapide (Schiano 2003, Métrich et Wallace 2008). La composition des inclusions peut cependant être affectée par la diffusion des éléments volatils dissous vers une bulle formée par contraction de

l'inclusion (bulle de rétraction) durant la décompression (Anderson et Brown 1993). Les inclusions préservées à l'état vitreux et peu affectées par les processus postérieurs (cristallisation de minéraux fils) à leur piégeage permettent de connaitre la composition du magma et de sa teneur en composants volatils (H_2O, CO_2, S, Cl, et F). Lors de la décompression (remontée du magma), une partie de l'inclusion peut former un globule immiscible (i.e. liquide riche en soufre, liquide carbonaté). Les concentrations en éléments volatils peuvent être modifiées après le piégeage, notamment par la diffusion de ces éléments vers le minéral hôte (Bucholz et al. 2013).

Les inclusions vitreuses, qui sont sans aucun doute des outils très puissants pour contraindre les conditions éruptives sont néanmoins rares, et donc leur faible abondance implique que tous les systèmes volcaniques ne peuvent pas être caractérisés. Les éléments volatils (F, S, Cl) peuvent également être étudiés à travers les minéraux accessoires (apatite, sodalite) afin de contraindre leurs rôles lors de la genèse et la différenciation des magmas ainsi que leurs conditions éruptives (e.g. Baudouin et Parat 2015, Annexe A).

Les concentrations des magmas en éléments volatils varient selon le contexte géodynamique et le type de source. En effet, les magmas des rides océaniques, les MORB, (source : manteau appauvri) ont des concentrations plus faibles en éléments volatils que les magmas d'arc (source : coin du manteau, enrichi en H_2O) (review dans Métrich et Wallace 2008, Oppenheimer 2003, table 1). Les magmas intraplaques, les OIB, (i.e. Hawaï) ont des concentrations en éléments volatils intermédiaires entre les MORB et magmas d'arc (Dixon et al. 1995, review dans Oppenheimer 2003).

Table 1 : Eléments volatils dans les MORB, OIB et les laves d'arc

	H_2O	CO_2	S	Cl	F
MORB	<0.5 %	50-400 ppm	800-1500 ppm	20-50 ppm	100-600 ppm
OIB	<1 %	2000-6500 ppm	3000 ppm	100 ppm	100-600 ppm
Arc	4-6 %	<2000 ppm	1000-3000 ppm	1500 ppm	500 ppm

Plus spécifiquement, le volcanisme 'carbonatitique' (i.e. Oldoinyo Lengai, Kaiserstuhl), riche en carbone, est présent en domaine intraplaque continental. Des études sur les inclusions vitreuses ont été réalisées dans le but de contraindre les concentrations en éléments volatils des magmas présents en domaine intracontinental, et plus particulièrement au niveau du rift est africain (e.g. Hudgins et al. 2015, Guzmics et al. 2012) (Table 2).

Table 2 : Eléments volatils dans les laves du rift Est Africain

	H_2O	CO_2	S	Cl	F
Virunga[1]	2.50	1.00	0.40	0.20	0.40
Nyamuragira[2]	1.40	0.20	0.24	0.10	0.22
Erta Ale[3]	-	-	0.12	0.07	0.08
Sadiman[4]	-	-	0.25	0.78	1.80
Kerimasi[5]	-	*	0.70	0.02	0.20
Oldoinyo Lengai[6]	0.1-0.55	*	1.20	0.70	2.20
Oldoinyo Lengai[7]	0.9-8.4	2.7-8.7 *	1.00	0.60	1.00
Rungwe[8]	2.20	-	0.08	0.25	0.12

[1]Hudgins et al. (2015), [2]Head et al. (2011), [3]De Moor et al. (2013b), [4]Zaitsev et al. (2012), [5]Guzmics et al. (2012), [6]Sharygin et al. (2012) éruption 1917, [7]De Moor et al. (2013a) éruption 2007, [8]Fontjin et al. (2013). * présence d'une phase carbonatée dans les inclusions vitreuses.

Les magmas du rift est africain contiennent sensiblement plus d'éléments volatils que les magmas de type OIB : 0,1 – 8,4 pds % H_2O, 0,2 – 8,7 pds % CO_2, 0,1 – 1,2 pds% S, 0,1 – 0,7 pds % Cl et 0,1 – 2,2 pds % F (Table 2).

Les éléments volatils ont des comportements différents lors de la remontée du magma et du dégazage (review dans Oppenheimer 2003). Le dégazage volcanique se produit par l'exsolution des éléments volatils et la formation de bulles de gaz. Les différences de solubilité des éléments volatils, dépendant de la pression, entrainent des exsolutions qui ne produisent pas en même temps (Holloway et Blank 1994). Le CO_2 est le premier volatil a former des bulles en profondeur, y compris à des profondeurs mantelliques (Giggenbach 1996). L'H_2O va s'exsolver après le CO_2. Les éléments volatils les plus affectés par le dégazage sont: C, H, S, et dans une moindre mesure le Cl, et le F (Oppenheimer 2003). Certains rapports de concentrations en éléments volatils comme Cl/S permettent de retracer l'histoire du dégazage (e.g. Spilliaert et al. 2006).

I.II.2 Magmas, éléments volatils et propriétés physiques

Les propriétés physiques des magmas dépendent de plusieurs paramètres : composition chimique, température, masse volumique et teneur en éléments volatils. Les éléments volatils ont un effet non négligeable sur les propriétés physiques des liquides et des processus éruptifs.

Table 3 : Eléments volatils dans les laves du rift Est Africain

	Carbonatite	Kimberlite	Mélilitite	Basalte
Viscosité (Pa s)	5-36 10^{-3}	0.1	1.5	30-50
Masse volumique (kg/m^3)	2050-2200	2690-3190	2808-3055	2600-3570
Conductivité électrique (S/m)	50-200	30-80	-	0.3-50

Voir Hammouda et Keshav 2015 pour les références complètes

La viscosité peut varier de plusieurs ordres de grandeur selon le type de magma. La viscosité d'un magma (Table 3) peut dépendre de plusieurs paramètres comme la composition chimique (Neuville et Richet 1991 ; Giordano et al. 2006), la teneur en H_2O (Whittington et al 2000) et en CO_2, la température (Levesque 1999) ainsi que la proportion en gaz et en cristaux. La viscosité de magma riche en CO_2 (i.e. carbonatite) est très faible (10^{-3} Pa.s).

La présence d'une fraction liquide dans le manteau augmente considérablement la conductivité électrique dans le milieu notamment si les magmas contiennent de l'H_2O et/ou du CO_2 (Sifré et al. 2014) (Fig.I.10). Des mesures de magnétotelluriques permettent de mesurer la conductivité électrique dans la lithosphère et la présence de fluide peut expliquer des fortes valeurs de conductivité (Gaillard 2004, Pommier et Le-Trong 2011).

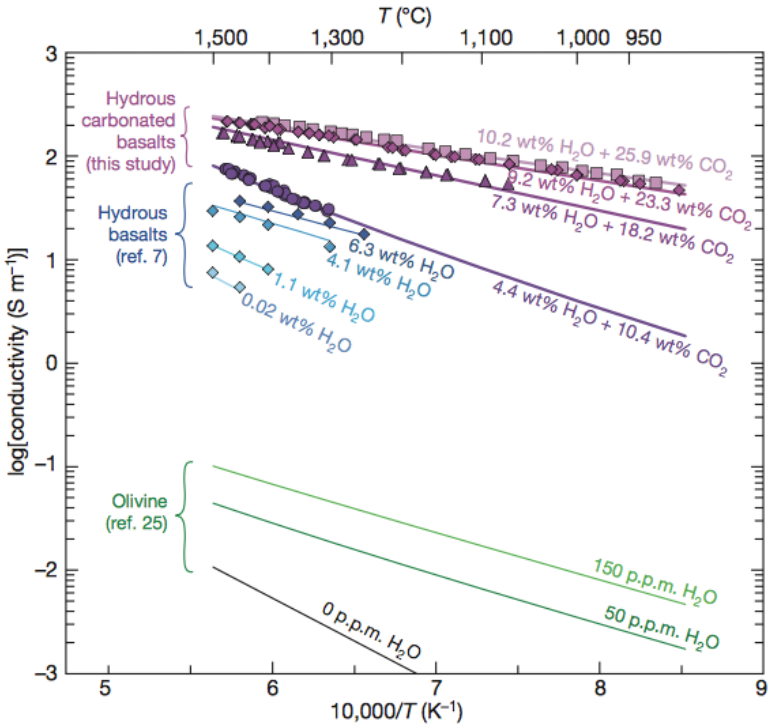

Fig.I.10 *Conductivité électrique dans l'olivine, des basaltes hydratés et carbonatés (Sifre et al. 2014).*

La méthode gravimétrique met en évidence les anomalies de densité (anomalie de Bouguer en mGals). Il est important de noter que des magmas alcalins qui percolent dans la croûte auront une densité équivalente à la roche encaissante. Alors que les carbonatites qui ont une densité faible (d = 2,2) correspondraient à une anomalie négative dans la croûte (d = 2,8).

La présence de fluide va augmenter le rapport des vitesses des ondes P (km/s) et S (Vp/Vs). La présence de fluide a été suggérée par l'interprétation de tomographie sismique (Shelly et al. 2006). La tomographie locale permet d'imager la lithosphère avec une bonne résolution et de pouvoir interpréter des anomalies kilométriques liées à une anomalie thermique, à une différence de composition ou à la présence de fluide.

La présence de fluide va avoir une influence conjointe sur la conductivité électrique et le rapport de vitesse sismique Vp/Vs. La thèse de Matthieu Plasman (AnR CoLiBrEA, Université de Bretagne occidentale) a pour but d'approfondir les problèmes d'inversion

conjointe entre plusieurs méthodes géophysiques (magnétotelluriques, sismologiques, gravimétriques) (chapitre VI) appliquées au nord de la Tanzanie.

I.II.3 Conditions redox

Les conditions redox sont l'un des paramètres qui peut limiter la stabilité d'un minéral. Par exemple, la fayalite ($Fe_2^{2+}SiO_4$) se déstabilise en magnétite ($Fe^{2+}Fe_2^{3+}O_4$) et quartz (SiO_2) lorsque les conditions deviennent plus oxydantes. Le domaine de stabilité d'une phase ou d'un assemblage minéralogique est limité par une courbe tampon (i.e. réaction ΔQFM) dans un diagramme T-fO_2 pour une pression constante. Pour comparer les conditions redox des roches, elles sont généralement exprimées en fonction Δlog fO_2 c'est à dire ΔQFM ou de NNO (Ni-NiO), qui sont des valeurs proches des roches terrestres.

La prédominance d'un état d'oxydation du fer (Fe^{3+} ou Fe^{2+}) ou du soufre (S^{6+} ou S^{2-}) reflète les conditions redox (liée à la fugacité en oxygène) au moment de la formation de la roche (Fig.I.11) (Carmichael 1991, Carmichael et Ghiorso 1990, Carroll et Rutherford 1988).

Les conditions de fO_2 des magmas basaltiques peuvent être déterminées par plusieurs méthodes. Sack et al. (1980) et Kress et Carmichael (1991) ont déterminés une équation empirique ($\ln X_{Fe_2O_3}/X_{FeO} = a \times \ln fO_2 + b/T + c + \sum d_i x_i$) qui permet de calculer les fractions de Fe^{3+} et Fe^{2+} à partir de la composition du verre basaltique, de la fO_2 et de la température. Ghiorso et Sack (1991) ont défini un calcul de thermodynamique permettant de déterminer la fO_2 d'un magma où coexistent 2 oxydes de Ti-Fe (i.e. ilménite et magnétite).

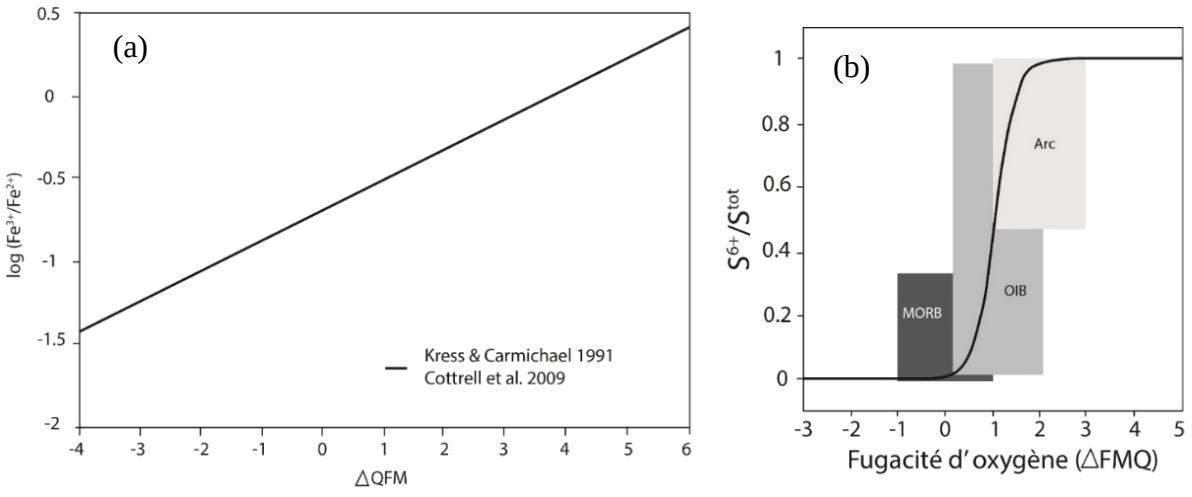

Fig.I.11 *Relation entre la fugacité en oxygène et (a) l'état d'oxydation du fer défini par Kress & Carmichael (1991) et (b) la spéciation du soufre (Jugo et al. 2010)*

Pour définir le ratio Fe^{3+}/Fe^{tot} d'une roche la spectroscopie Mössbauer (Mysen et al. 1985) est la méthode la plus courante. La spectroscopie Mössbauer est basée sur l'absorption de rayons gamma par les noyaux atomiques (Fe) avec des spectres d'absorptions distincts pour le Fe^{3+} et le Fe^{2+}.

On peut également utiliser la spectroscopie XANES (de l'anglais, « X-ray Absorption Near Edge Structure ») pour déterminer l'état redox du fer dans les roches. La méthode XANES est *in situ* avec une résolution à 1 µm. Elle peut être employée sur des verres (e.g. Cottrell et al. 2009) ou sur des minéraux (Wilke et al. 2001). La méthode XANES permet d'analyser des matériaux pauvres en Fe ou S (1 pds %), avec des temps d'analyses faibles (< 1 h), alors qu'il faut 1 semaine avec la méthode Mössbauer (McCammon et al. 1998, Cottrell et al. 2009).

Les calibrations disponibles sont applicables pour les MORB (e.g. Cottrell et al. 2009, 2011, Wilke et al. 2005, Knipping et al. 2015), les rhyolites (Cottrell et al. 2009 ; Métrich et al. 2006), les andésites (Grocke et al. 2016), les téphriphonolites (Moussallam et al. 2014) et les phonolites (Giuli et al. 2011).

Les 2 méthodes les plus utilisées pour définir la spéciation de soufre ($S^{6+}/\Sigma S$) sont l'analyse des spectres : (1) d'émission des rayons-X (microsonde électronique, spectre WDS) (Carroll et Rutherford 1988) et (2) d'absorption des rayons-X (XANES). Avec l'utilisation de standards appropriés, la méthode XANES est la plus précise (Paris et al. 2001, Jugo et al. 2010, Wilke et al. 2011). La méthode WDS a tendance à surestimer le S^{6+} (Jugo et al. 2010).

Différentes gammes de fO_2 ont été définies pour les magmas et les roches du manteau (Jugo et al. 2010, Carroll et Rutherford 1988, Balhaus 1993, Parkinson et Arculus 1999, Carmichael 1991). Les laves dans les conditions les plus réduites sont les MORB (ΔQFM-1 à ΔQFM+1) et les plus d'oxydantes sont les laves d'arc (ΔQFM+1 à ΔQFM+3). Les basaltes des iles océaniques ont des conditions intermédiaires (ΔQFM à ΔQFM+2). Les roches mantelliques du coin du manteau (zone de subduction) ont des conditions légèrement oxydantes (proche ΔQFM+1) (Frost et McCammon 2008). Les laves naturelles formées dans les conditions les plus oxydantes (ΔQFM+3 à ΔQFM+5) sont les lamprophyres.

En associant l'état d'oxydation du fer et du soufre, on peut établir de façon plus précise les conditions d'oxydation des verres (Fig.I.12). Les laves du rift est africain se forment dans des conditions oxydantes (Table 4).

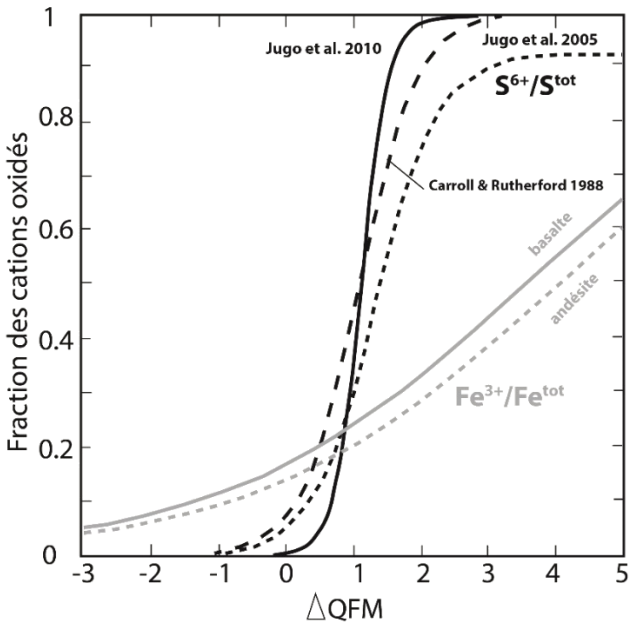

Fig.I.12 *Rapports S^{6+}/S^{tot} et Fe^{3+}/Fe^{tot} en fonction de la fugacité en oxygène (exprimé en fonction de QFM)*

Table 4 : Conditions redox les laves du rift Est Africain

Rift Est Africain	Type	Conditions redox	Méthode	Référence
Ethiopie	basalte	NNO -0.7	Xanes Fe, S inclusions de verre	de Moor et al. 2013
branche ouest	basanite	NNO -1	Fe Ti oxybaromètre	Hudgins et al. 2015
branche ouest	mafurite	NNO +1	olivine -spinel-opx oxybaromètre	Murav'eva & Senin 2009
Kenya	trachyte	NNO -1	Experimental	Scaillet & Macdonald 2006
Kenya	trachyte	NNO to NNO-2	application QUILF	Ren et al. 2006
Sadiman	néphélinite	>>FMQ	calcul thermodynamique	Zaitsev et al. 2012
Rungwe	trachyte	NNO+0.25+0.45	Fe Ti oxybaromètre	Fontjin et al. 2013
Autres rifts				
Erebus	basanite, phonolite	NNO -1 +1	Xanes Fe, S inclusions de verre	Moussallam et al. 2014
Islande	rhyolite	NNO-1.5 (off) +0.5 (axis)	Fe Ti oxybaromètre	Schattel et al. 2014

I.III Cadre géologique de l'étude

I.III.1 Rift Est-Africain

Le rift est-africain (REA) est une frontière de plaque en extension. Ce rift présente plusieurs stades d'extension, de l'initiation du rift en Tanzanie jusqu'à l'accrétion océanique en Afar. Le REA sépare 2 plaques tectoniques majeures : la plaque Nubie à l'ouest et la plaque Somalie à l'est (Fig.I.13). Le taux d'extension varie entre 6,5 mm/an dans la dépression de l'Afar jusqu'à 1,5 mm/an dans le golfe du Mozambique (Stamps et al. 2008). L'origine du rifting et du volcanisme dans le REA est toujours débattue. Les différents modèles suggèrent la présence d'un ou deux points chauds lié(s) au superpanache sous l'Afrique du Sud (Ebinger et Sleep 1998, Nyblade et al. 2000, Pik et al. 2006). Il y a une anomalie négative importante de la vitesse des ondes P à l'aplomb de la DNT (Fig.I.14).

Le volcanisme le plus ancien (40 – 45 Ma) se situe dans le rift éthiopien central, suivit d'un volcanisme massif qui s'est produit en Afar à 30 Ma associé à la mise en place de failles normales (29 Ma, review dans Chorowicz 2005). Le REA est constitué de 2 parties qui sont localisées dans la ceinture orogénique protozoïque et autour du craton tanzanien (> 2,5 Ga). La branche E (Est) s'étend de la Tanzanie jusqu'au nord du Kenya et la branche O (Ouest) se localise du Congo jusqu'au golfe du Mozambique. Dans la branche E, le volcanisme a commencé il y a 30 Ma dans le nord du Kenya, 15 Ma dans la partie centrale du Kenya et 8 Ma pour le nord de la Tanzanie (Mana et al. 2015). Dans la branche O, les laves ont été datées autour du lac Kivu à 12 Ma et du lac Rukwa à 8 Ma. De plus, les séismes M > 4 sont très fréquents dans les 2 branches du rift.

La proximité ou non d'un panache explique les différences entre les branches O et E du rift africain (amagmatique et magmatique, respectivement) (Koptev et al. 2015). Le volume important de magma dans le REA (branche E) est propice à des évènements de 'dyking' présents dans les rifts magmatiques (Calais et al. 2008, Wright et al. 2006).

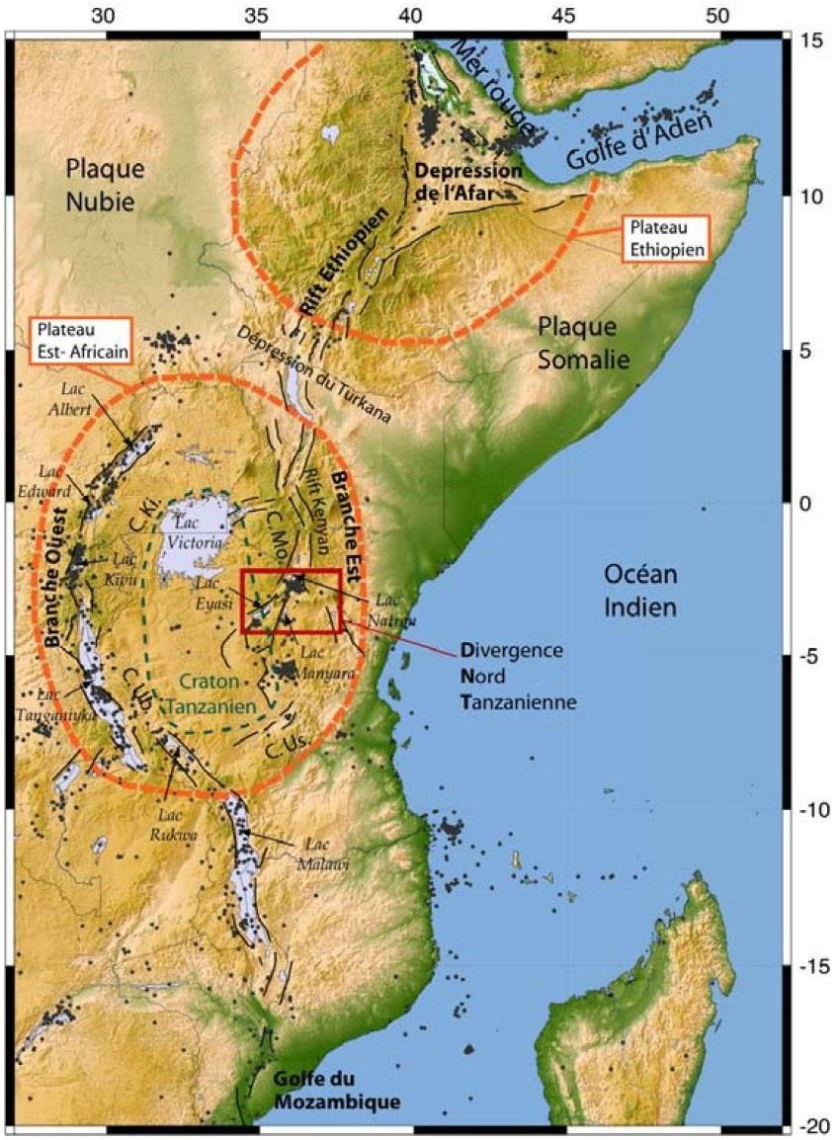

Fig.I.13 *Carte structurale simplifiée du rift est-africain (REA) (Albaric 2009). La sismicité (M > 4) est représentée par des points noirs. Les plateaux Ethiopien et est-africain sont délimités par des*

pointillés orange. L'extrémité sud de la branche E du REA correspond à la divergence nord-tanzanienne (DNT) (carré rouge). Ki., Mo., Ub., et Us., sont respectivement les ceintures (C.) protérozoïques Kibaran, Mozambique, Ubendian et Usagaran, accrétées aux marges du craton archéen tanzanien (délimité par des pointillés verts)

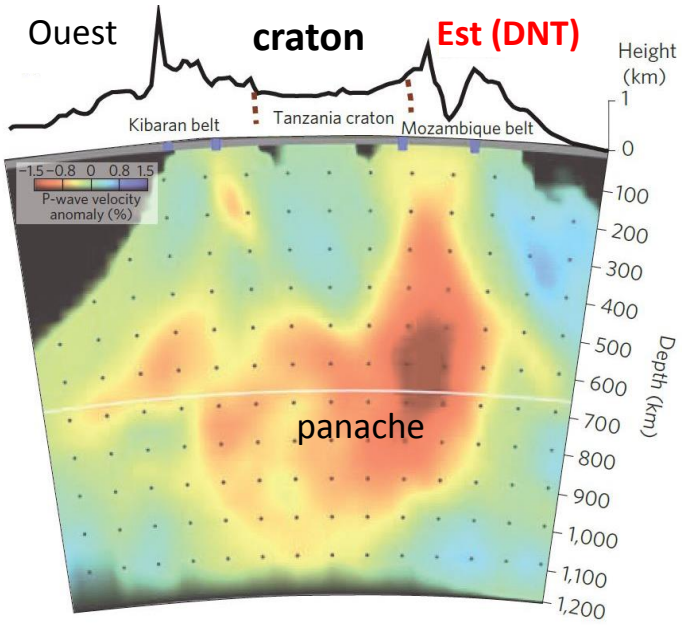

Fig.I.14 *Coupe jusqu'à 1200 km représentant les anomalies de vitesse des ondes P au niveau des branches Est et Ouest du REA (Adams et al. 2012).*

I.III.2 Divergence nord tanzanienne

Dans la branche E, les principales structures tectoniques et volcaniques changent drastiquement entre le Kenya et le nord de la Tanzanie. Au Kenya, la vallée axiale du rift (rift de Gregory) est étroite (50 km) alors qu'au nord de la Tanzanie le rift s'étend sur plus de 200 km pour former la divergence nord-tanzanienne (DNT). Au sud de la DNT, le rift se divise en 3 parties : Eyasi, Manyara-Balangida, et Pangani. Les bassins Eyasi et Manyara-Balangida sont des demi-grabens de 200 – 300 km de long pour 50 – 100 km de large et d'une profondeur inférieure à 3 km. Ces deux systèmes de failles normales sont séparés par les blocs basculés du plateau Mbulu (Fig.I.15). La phase principale de l'activité volcanique de la DNT s'est produite entre 2,5 et 1 Ma (Le Gall et al. 2008, Mana et al. 2015) et le paroxysme de l'activité tectonique s'est produit avant 1,2 Ma (Foster et al. 1997). La DNT a une activité sismique intense avec quelques séismes de magnitude élevé pour un rift (i.e. 1964 : M = 6,3 ; 2007 : M = 5,9).

La DNT est constituée de 2 axes : l'axe nord-sud et l'axe est-ouest.

L'axe E-O a de nombreux complexes volcaniques tels que le Ngorongoro, l'Essimingor, le Mt Meru et le Kilimandjaro. Le Ngorongoro et le Kilimandjaro sont composés de basanite, de trachybasalte et de trachyte (Dawson 2008, Nonnotte 2007), alors que l'Essimingor est constitué de nephelinite et de phonolite (Mana et al. 2012).

L'axe N-S est constitué de 2 bassins : le bassin de Natron au nord et le bassin de Manyara-Balangida au sud. Le bassin Natron est caractérisé par la présence de volcans carbonatitiques (Oldoinyo Lengai et Kerimasi) (Fig.I.15). L'Oldoinyo Lengai est le seul volcan actif de la DNT, le Kerimasi était actif entre 0,6 - 0,32 Ma (Mana et al. 2015). Les volcans dans l'axe N-S ont des laves d'avantages sous saturées en silice (i.e. néphélinite) que les volcans dans l'axe E-O. Les principales structures tectoniques et volcaniques sont détaillées dans la section suivante (I.III.3 zone d'étude).

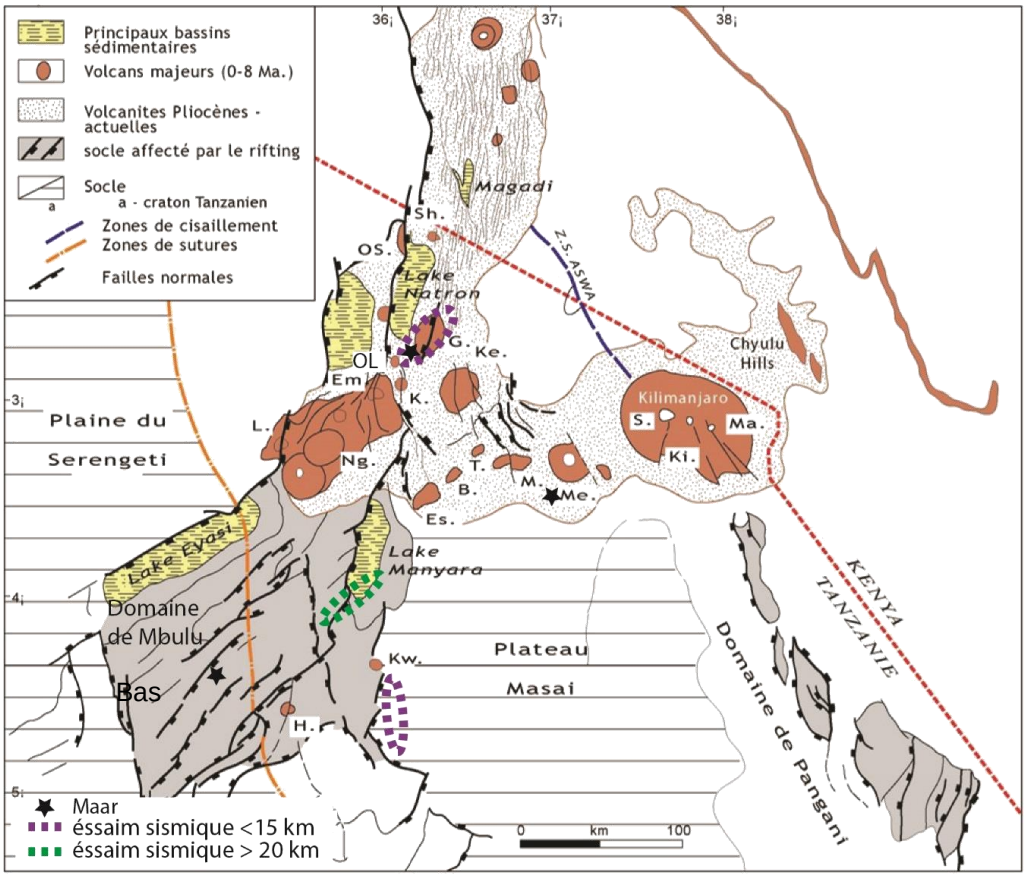

Fig.1.15 *Schéma structural du rift sud-Kenyan et de la divergence nord-tanzanienne (Nonnotte 2007). B. Burko, Bas. Basotu, Em. Empakai, Es. Essimingor, G. Gelai, H. Hanang, K. Kerimasi, Ke. Ketumbeine, Ki. Kibo, Kw. Kwaraha, L. Lemagrut, M. Monduli, Ma. Mawenzi, Me. Meru, Ng. Ngorongoro, OL. Oldoinyo Lengai, OS. OlDonyo Sambu, S. Shira, Sh. Shombole, T. Tarosero.*

La sismicité de la DNT se concentre en 2 essaims dans l'axe N-S du rift (Fig.I.15, Fig.I.16). Le premier essaim se situe au sud du Lac Natron, proche des volcans Oldoinyo Lengai et Gelai. La sismicité de cet essaim est liée à l'activité volcanique des volcans Oldoinyo Lengai et Gelai, et donc à la propagation des dykes en profondeur (Calais et al. 2008). Une récente étude (Lee et al. 2016) menée dans le bassin Magadi-Natron (sud-Kenya) a permis de montrer la coexistence d'une sismicité profonde (15 – 30 km) et l'émission importante de CO_2.

Le deuxième essaim (Fig.I.15, Fig.I.16) se situe au sud du lac Manyara, et est particulier de par l'occurrence de séismes dans la croûte inférieure (20 – 34 km, Nyblade et

Langston 1995). L'origine de cette sismicité pourrait être liée à la circulation de fluide en profondeur (Albaric et al. 2010, 2014). L'étude de cette sismicité est l'un des objectifs de l'AnR Colibrea (études géophysiques). La zone d'étude de cette thèse se situe dans le bassin de Manyara-Balangida.

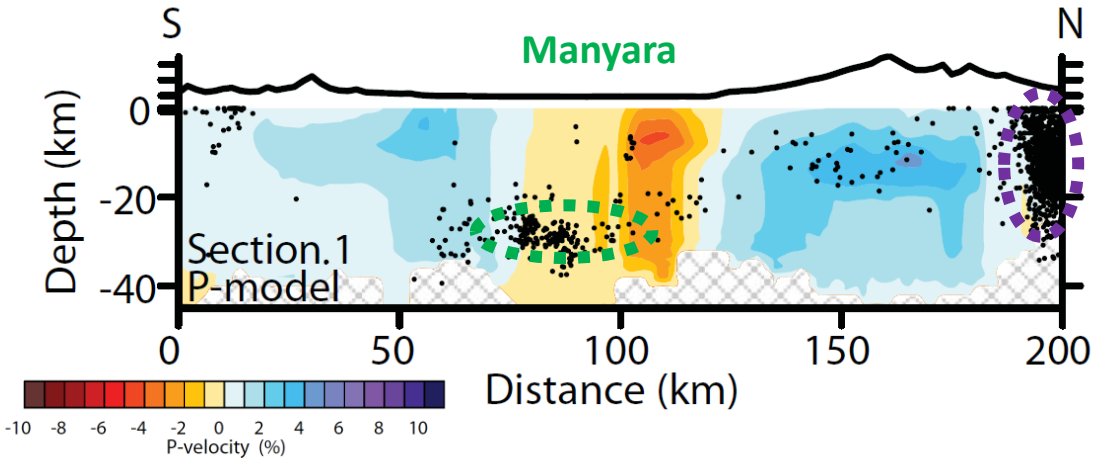

Fig.1.16 *Coupe Nord-Sud de la croute de la DNT représentant les anomalies de vitesse des ondes P et la localisation des 2 essaims sismiques (violet= Natron, vert=Manyara) (Albaric et al. 2014).*

I.III.3 Zone d'étude : bassin de Manyara-Balangida

Le bassin de Manyara-Balangida est la zone la plus au sud de la branche E du REA et correspond à la zone d'initiation du rift continental. Le bassin de Manyara-Balangida est délimité par des failles normales du plateau Mbulu et du bloc Masai composés de roches précambriennes cratoniques (Le Gall et al. 2008). Les failles de Manyara (N20°E) et de Balangida (N50°E) forment l'escarpement du rift. Le bassin de Manyara est faiblement magmatique, seuls quelques volcans sont présents à la surface tels que le Hanang, le Labait et le Kwaraha (Fig.I.15). Une série de maars et de cratères explosifs près de Basotu ont été identifiés sur le plateau de Mbulu. Ces 30 cratères sont alignés avec les failles normales et sont composés essentiellement de tufs carbonatés (Downie et Wilkinson 1962) et de fragments de roches cratoniques.

Le volcan Hanang (4°27'S 35°24'E) se situe au sud du bassin de Manyara, à la bordure de l'escarpement du rift et du craton tanzanien. L'épaisseur de la lithosphère sous le Hanang est estimée à 140 km (Craig et al. 2011). Le Hanang s'est mis en place sur un socle composé de roches granitiques précambriennes (Thomas 1966). Ce volcan est composé d'agglomérats, de tufs néphélinitiques, de tufs carbonatés et de néphélinites. Les coulées de néphélinites et de tufs 'carbonatitiques' sont inter-stratifiés sur le flanc nord-ouest du volcan, proche du lac Balangida (Dawson 2008). Ce volcan a été actif au quaternaire entre 1,5 ± 0,3 Ma et 0,9 ± 0,2 Ma (Bagdasaryan et al. 1973, datation par la méthode K-Ar). Des études préliminaires basées sur l'analyse des éléments majeurs des laves suggèrent que: (1) le Hanang fait partie des volcans les plus récents avec l'Oldoinyo Lengai et le Kerimasi et que

ces 3 volcans résultent d'un magmatisme riche en éléments volatils (Dawson 2012) (2) l'existence d'une interaction entre des laves silicatées et carbonatées (Nonnotte 2007).

Le volcan Labait (4°34'12", 35°26'04") est un cône volcanique constitué de mélilitites à olivine (Dawson et al. 1997) qui se situe à 10 km au sud du Hanang. On note la présence de nombreux types de xénolithes mantelliques : des harzburgites à phlogopite-spinelle, des lherzolites et harzburgites à grenat, et des dunites (Lee and Rudnick 1999, Koornneef et al. 2009). Les péridotites ont de faibles teneurs en eau (< 40 ppm H_2O), une vitesse de remontée rapide ($4 – 28$ m·s^{-1}) et sont inclus dans des mélilitites pauvres en eau (Hui et al. 2015). L'activité volcanique du Labait a été datée indirectement par la méthode U-Pb sur zircon métasomatique ($0,4 \pm 0,2$ Ma, Rudnick et al. 1999) dans une péridotite. Les mélilitites du Labait ont des signatures isotopiques proches de celles des cratons (Aulbach et al. 2008, MacDonald et al. 2001).

Le volcan Kwaraha (4°13'45", 35°48'53") est constitué de laves, de tufs et d'agglomérats de composition néphélinitiques (Dawson et al. 1997, Paslick et al. 1996). Une coulée de lave de calciocarbonatite a été trouvée sur le flanc du volcan (Dawson 2008). De petits cônes volcaniques et des cratères explosifs se sont mis en place tout autour de l'édifice principal. Les petits cônes volcaniques ont des compositions néphélinitiques (i.e. Sora hill, Haindadonga; Dawson et al. 1997). Comme le Hanang et le Labait, le volcan Kwaraha était actif lors du quaternaire (1,5 – 0,7 Ma, Bagdasaryan et al. 1973).

I.IV Problématique

Le rifting et le volcanisme dans le REA sont liés à la présence d'un point chaud qui aurait une origine profonde associé au superpanache de l'Afrique du Sud. Dans la divergence nord-tanzanienne, où la rupture continentale est à son stade le plus précoce, deux zones distantes de seulement ~ 150 km (Natron et Manyara) présentent des styles de déformation et de volcanisme différents. Le bassin de Manyara est caractérisé par la présence de 2 centres volcaniques hyperalcalins (Hanang et Kwaraha) (< 1,5 Ma) et d'un essaim sismique dans la croûte inférieure (20 – 40 km) qui pourrait être liée à la circulation de fluide en profondeur (Albaric et al. 2010, 2014). La déformation de la croûte et la propagation de la rupture continentale pourraient être facilitées par la percolation de magmas et de fluide. La caractérisation chimique des magmas qui percolent dans la zone d'initiation du rift est nécessaire pour comprendre le mode de déformation et le fonctionnement de la rupture continentale. Cette thèse se focalise sur la signature géochimique des laves du bassin de Manyara, leurs conditions pré-éruptives (éléments volatils, état oxydation) et sur les conditions de fusion partielle. La caractérisation géochimique des laves de Manyara a été réalisée afin de contraindre les processus magmatiques liés à la genèse des magmas alcalins et des carbonatites associées dans une zone d'initiation de rift. Par ailleurs, cette thèse s'inscrit dans le projet CoLiBrEA qui a pour but d'identifier les interactions entre le magmatisme, les structures héritées et la sismicité actuelle afin de mieux comprendre les processus à l'origine de la rupture continentale.

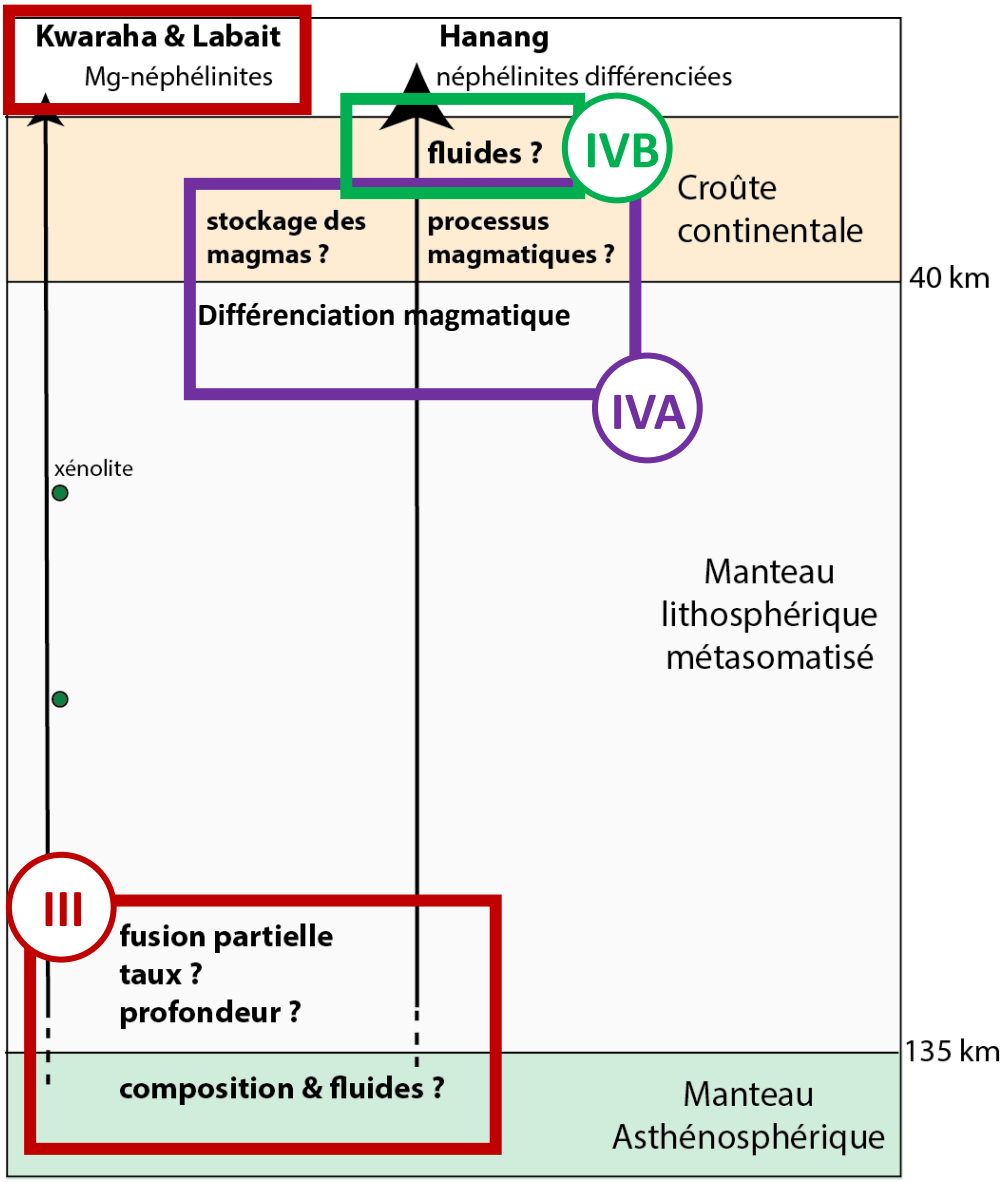

Le ***chapitre II*** présente l'échantillonnage réalisé lors de 2 missions de terrain ainsi que les différentes méthodes utilisées pour les analyses des laves en roche totale, des minéraux et des inclusions vitreuses.

Le ***chapitre III*** aborde la composition des laves primaires de la zone méridionale de la divergence nord-tanzanienne (bassin de Manyara) afin de pouvoir caractériser la source et l'environnement de cristallisation des laves alcalines en zone d'initiation de rift.

Le ***chapitre IV*** correspond à l'étude des laves du volcan Hanang. Une **première** étude (***IVA***), publié dans *Contributions to Mineralogy and Petrology*, se focalise sur les caractéristiques minéralogiques, pétrologiques et géochimiques afin de contraindre les processus magmatiques à l'origine de la formation de ces laves. Une **deuxième** étude (***IVB***) se focalise sur l'étude des inclusions vitreuses et a pour but de déterminer les concentrations en volatils, les conditions pré-éruptives et de discuter du processus d'immiscibilité au sein des magmas alcalins.

Le ***chapitre V*** présente l'étude préliminaire réalisée sur l'état d'oxydation des laves du Hanang et de la zone d'initiation du rift. Pour contraindre les conditions redox, une approche multi-méthodes a été utilisée, avec des analyses XANES sur les inclusions vitreuses et les minéraux (Hanang & Kwaraha) et des analyses Mössbauer sur les roches totales et minéraux séparés.

La divergence nord-tanzanienne (DNT) est la zone d'initiation de la rupture continentale du rift est-africain (REA). Elle est constituée de 2 axes volcano-tectoniques: l'axe est-ouest composé de laves alcalines et l'axe nord-sud, de laves hyperalcalines. Le ***chapitre VI*** présente les caractéristiques volcaniques de la DNT, par types, âges et localisation géographique. Afin d'avoir une meilleure compréhension de l'initiation de la rupture continentale, il est important de lier le volcanisme aux contraintes structurales (e.g. données tectoniques et géophysiques). La relation temporelle entre les activités tectoniques et magmatiques est un enjeu majeur pour comprendre le fonctionnement de la rupture continentale.

La dernière partie de cette thèse résume les principales ***conclusions*** et perspectives.

Chapitre II. Échantillonnage et méthodes analytiques

Ce chapitre présente l'échantillonnage réalisé lors de 2 missions de terrain ainsi que les différentes méthodes utilisées pour les analyses des laves en roche totale, des minéraux et des inclusions vitreuses.

II.I Échantillonnage

Les échantillons ont été collectés lors de deux campagnes de terrain (décembre 2013 et février 2015). L'objectif de ces deux campagnes était d'échantillonner les différents types de laves qui se trouvent dans le bassin de Manyara. Contrairement aux laves du nord de la divergence nord tanzanienne (i.e. bassin du Natron, Oldoinyo Lengai, Kilimandjaro), les laves du bassin de Manyara ont été peu étudiées (voir section I.III.3). L'échantillonnage s'est fait en priorité dans le bassin de Manyara (axe N-S), et pour quelques volcans du nord de la divergence nord-tanzanienne (axe E-O, voir Fig.II.1) (résultats en annexe B), afin de pouvoir comparer les laves en fonction de leur types et de leur localisation géographique. Un repérage des affleurements a été effectué à partir des cartes géologiques 1:125000 fournies par '*Tanzania Mineral Resources Division*' afin que l'échantillonnage soit bien représentatif des différents types de laves présents sur la zone. L'échantillonnage de certaines parties des volcans (e.g. sommet du Kwaraha) a été impossible à cause de la végétation abondante (zone tropicale), du terrain accidenté et de la faune locale (e.g. lions, hyènes). En bilan de ces deux missions, 67 échantillons (>150 kg) ont été collectés, incluant des laves silicatées, des carbonatites, des tufs et des xénolites mantelliques (Fig.II.1, coordonnées GPS des échantillons dans l'annexe B). Les volcans échantillonnés de l'axe N-S sont le Kwaraha, le Hanang et le Labait (bassin de Manyara) et le volcan Oldoinyo Lengai (bassin de Natron) (Fig.II.1). Les volcans échantillonnés de l'axe E-O sont le Ngorongoro, l'Essimingor, le Burko, le Monduli et l'Olmani (Fig.II.1).

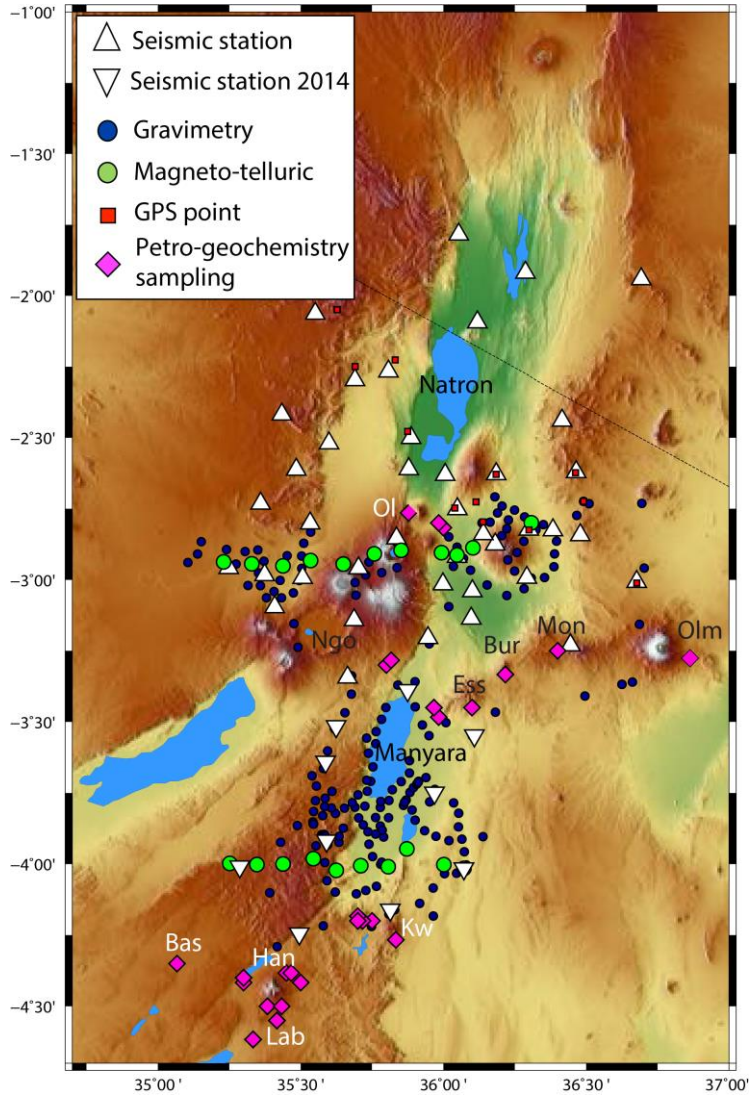

***Fig.II.1** : Carte du nord de la Tanzanie avec la localisation des stations sismiques, magnéto-telluriques, GPS et gravimétriques de l'AnR CoLiBrEA et des stations sismiques NSF CRAFTI. Les échantillons de laves sont symbolisés par des losanges roses. Volcans de l'axe* N-S *: Ol Oldoinyo Lengai, Kw Kwaraha, Han Hanang, Lab Labait, Bas Basotu. Volcans de l'axe E-O : Ngo Ngorongoro, Ess Essimingor, Bur Burko, Mon Monduli, Olm Olmani.*

Une étude au microscope optique sur 50 lames minces a été réalisée afin de sélectionner les échantillons pour les analyses des minéraux *in situ*, et déterminer la texture, l'assemblage minéralogique et les proportions modales des laves (annexe B). Le microscope a également été utilisé pour repérer les sulfures (en lumière réfléchie) (annexe B) et les inclusions vitreuses.

II.I.1 Volcans de l'axe nord-sud

II.I.1.1 Le Volcan Kwaraha

Les échantillons du Kwaraha (Kw2 à Kw12) proviennent chacun d'un petit cône volcanique autour de l'édifice principal (Fig.II.2) L'échantillon Kw1, provient quant à lui, d'une coulée de carbonatite de l'édifice principal (Fig.II.3).

Une carte géologique simplifiée au 1:125000 (Fig.II.2) permet de localiser l'échantillonnage réalisé autour du volcan Kwaraha (sommet à 2225 m) et de la ville de Babati. La Fig.II.4 met en évidence le type d'affleurement (e.g. cône parasitique Kw3) que l'on peut trouver autour du volcan Kwaraha.

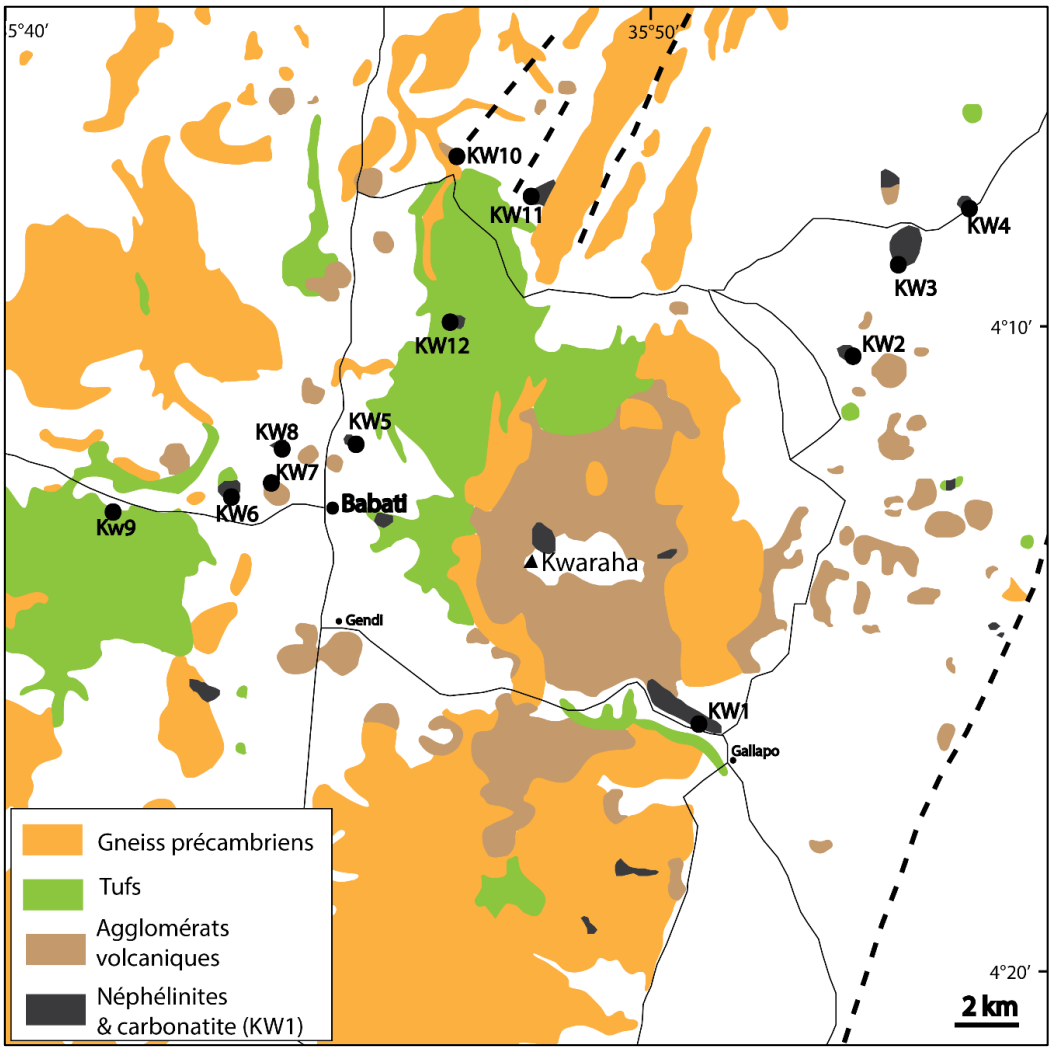

***Fig.II.2** : Carte géologique simplifiée du volcan Kwaraha (Modifiée d'après Mudd et Orridge 1966)*

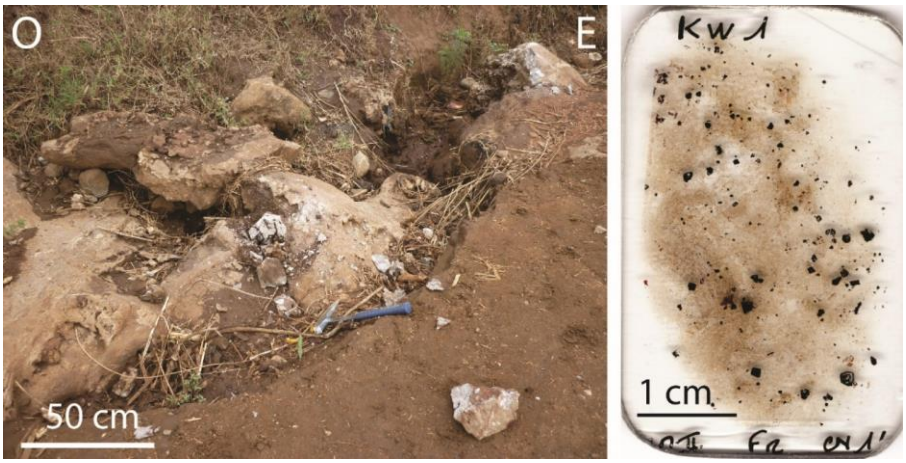

***Fig. II.3** : Photo d'affleurement de l'échantillon Kw1. L'échantillon est une carbonatite qui affleure sous la forme d'une coulée près de l'école de Gallapo (S4°16.55, E35°50.75).*

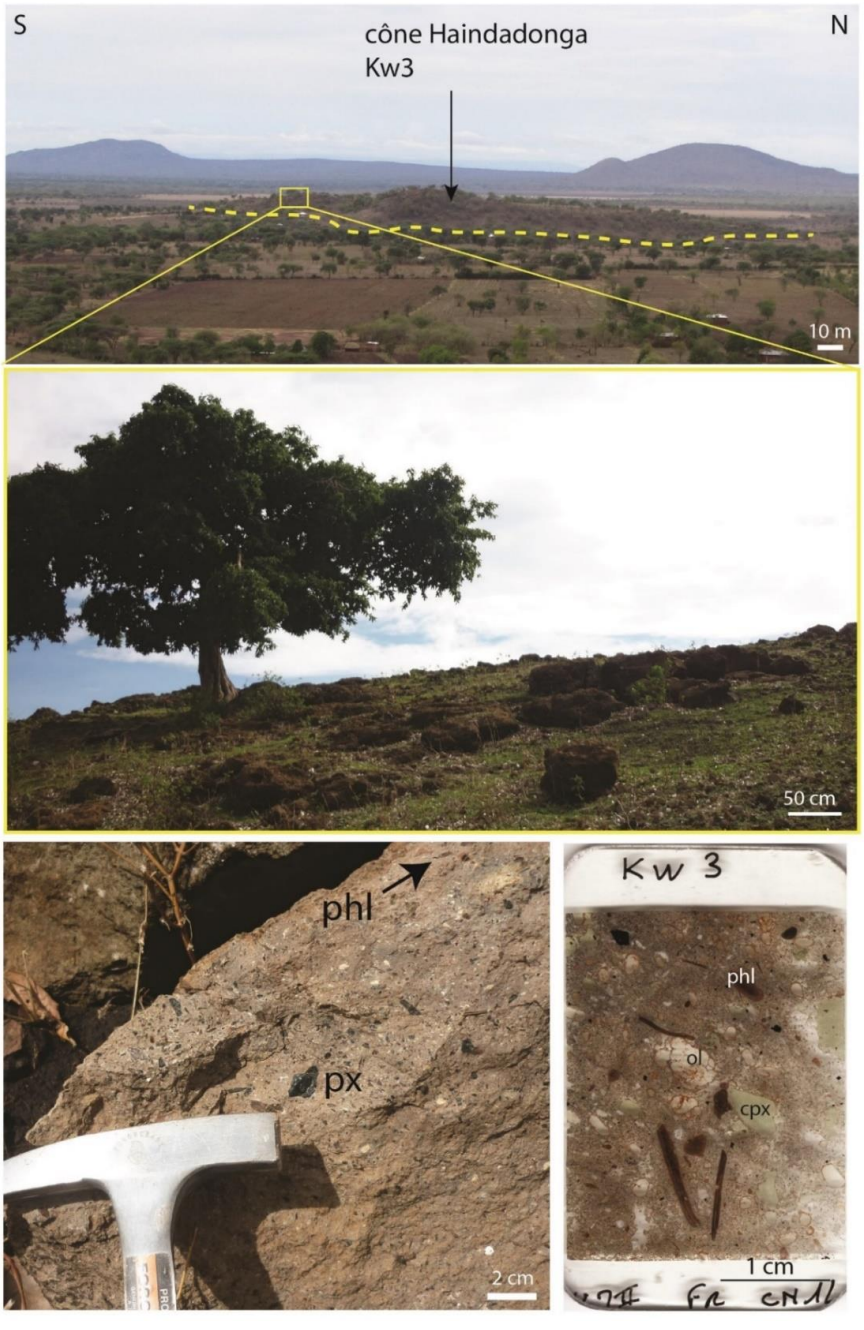

***Fig. II.4**: Photo à plusieurs échelles d'affleurement de Kw3 (22 vol % de phénocristaux).*

II.I.1.2 Le Volcan Hanang

Le volcan Hanang (sommet à 3420 m) est composé de coulées de laves néphélinitiques ainsi que de tufs (Fig.II.5). Ce volcan se situe à 10 km à l'est de l'escarpement principal du rift (200 m de dénivelé), au niveau de la faille normale du lac Balangida (N63°).

Les échantillons ont été collectés sur les pentes du volcan (Fig.II.6 et II.7) dans des coulées de laves (e.g. Han11 et Han13) ou sous forme de blocs basculés (e.g. Han7). Les tufs (Han10 et Han12) ont été collectés entre les coulées.

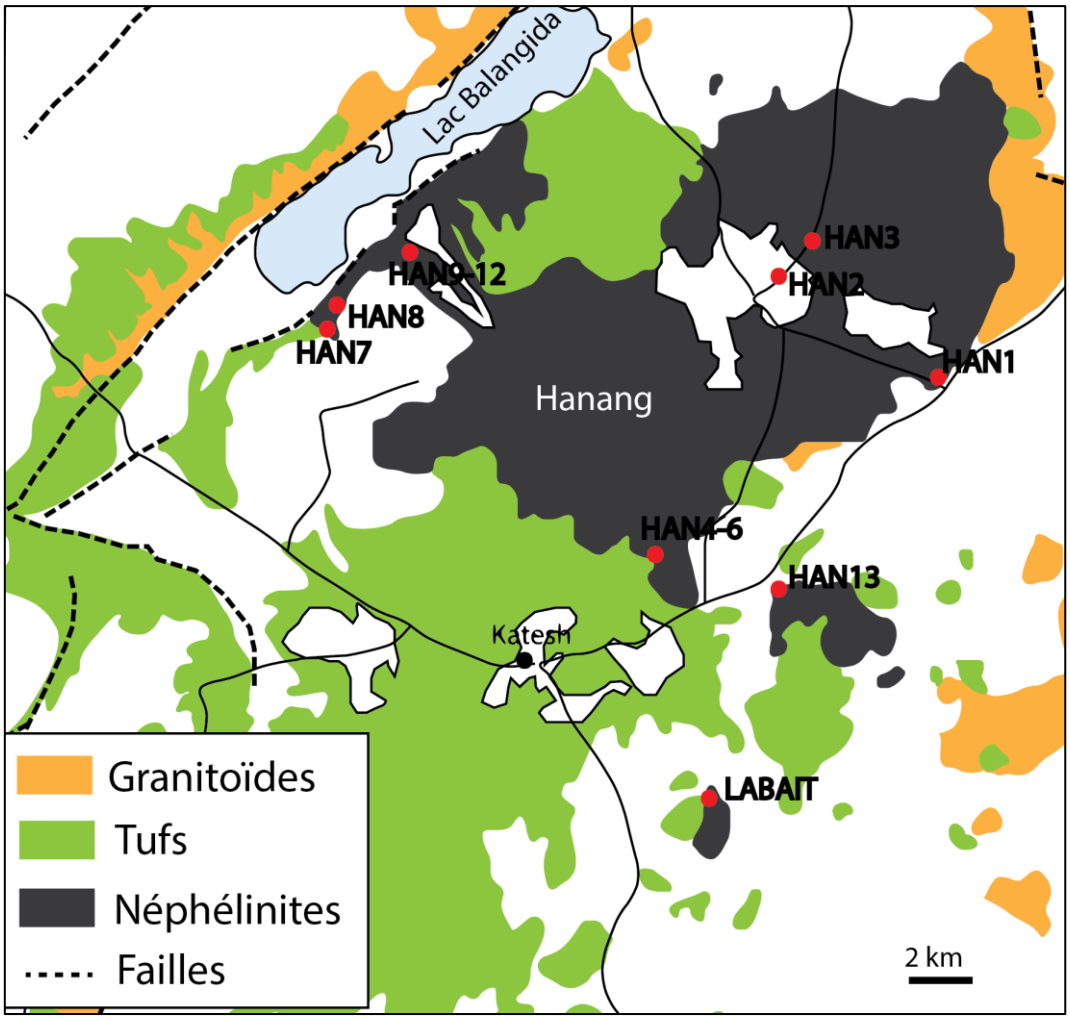

***Fig.II.5** : Carte géologique simplifiée du volcan Hanang (Modifiée d'après Thomas 1966)*

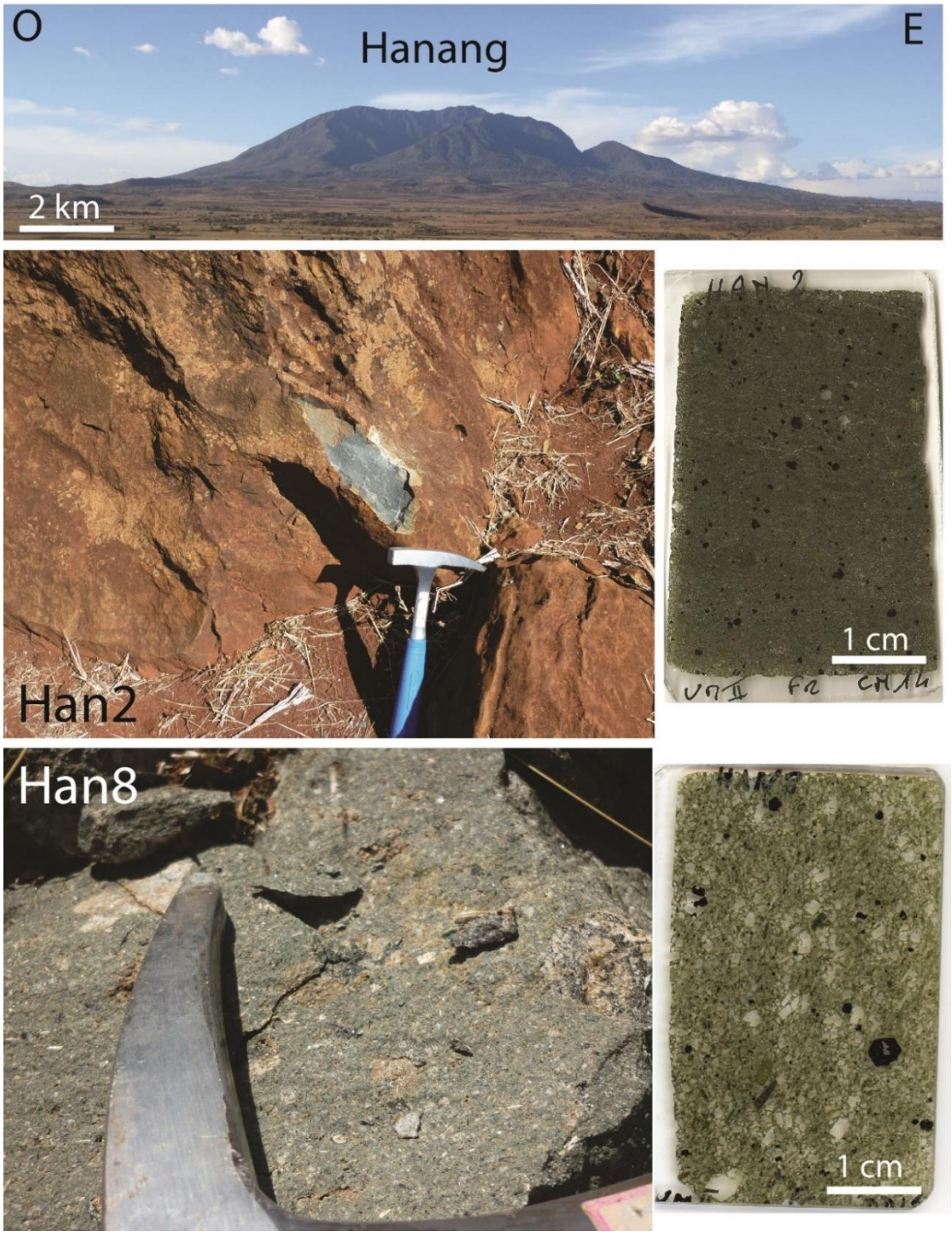

***Fig.II.6** : Photos du volcan Hanang et des affleurements et laves Han2 (11 vol % de phénocristaux) et Han8 (30 vol % de phénocristaux).*

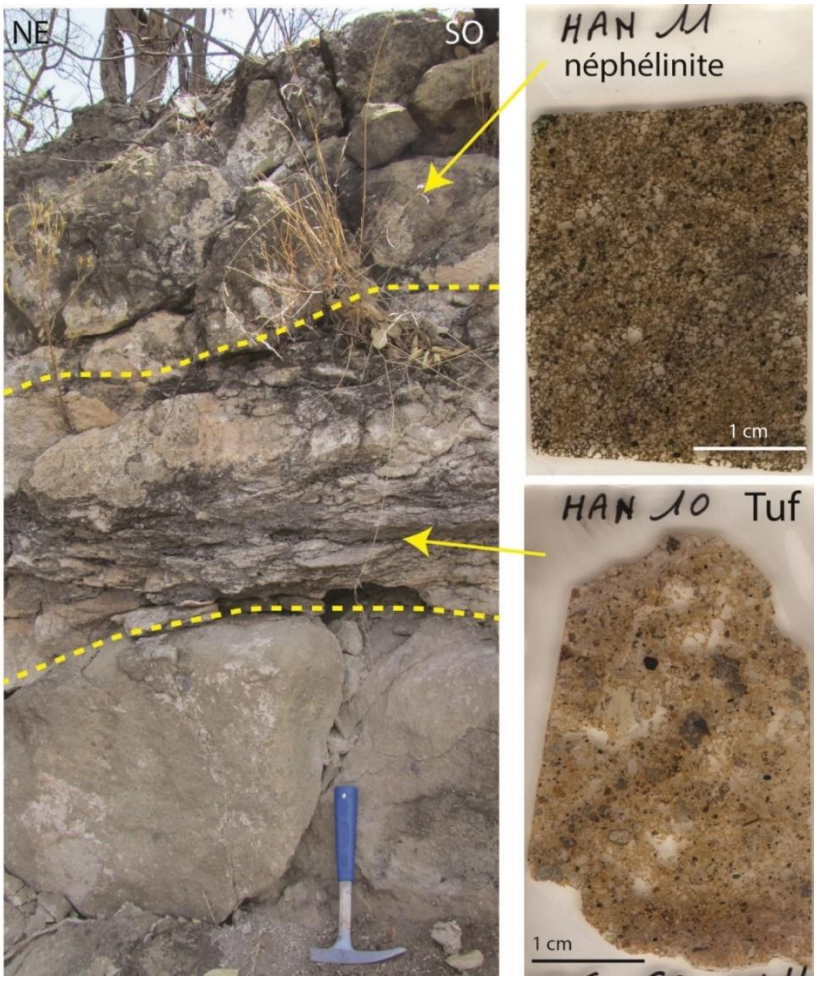

Fig. II.7*: Photos montrant la relation stratigraphique entre un tuf carbonatitique (Han10) et une néphélinite (Han11, 35 vol % de phénocristaux).*

II.I.1.3 Le Volcan Labait

Le Labait est un cône parasitique au sud du volcan Hanang (10 km au sud, Fig.II.5). Les échantillons (laves et xénolites) ont été collectés sur les pentes du volcan.

Fig.II.8 *: Photo du cône volcanique Labait (250 m de haut)*

II.I.1.4 Le Maar de Basotu

L'échantillon 'Basotu' (Bas1) est un tuf qui provient de l'ensemble 'maar de Basotu' sur le plateau de Mbulu (voir Fig.II.1 pour la localisation de Basotu). Les maars sont alignés selon un axe N30°, et sont parallèles aux failles normales de la zone (Fig.II.9). Les tufs contiennent des blocs pyroclastiques (Fig.II.10) de granitoïde et de quartzite archéens qui constituent le craton Tanzanien. Les roches des maars de Basotu sont des tufs à matrice calcaire (Fig.II.10) et constitués de clastes de clinopyroxènes et de phlogopites.

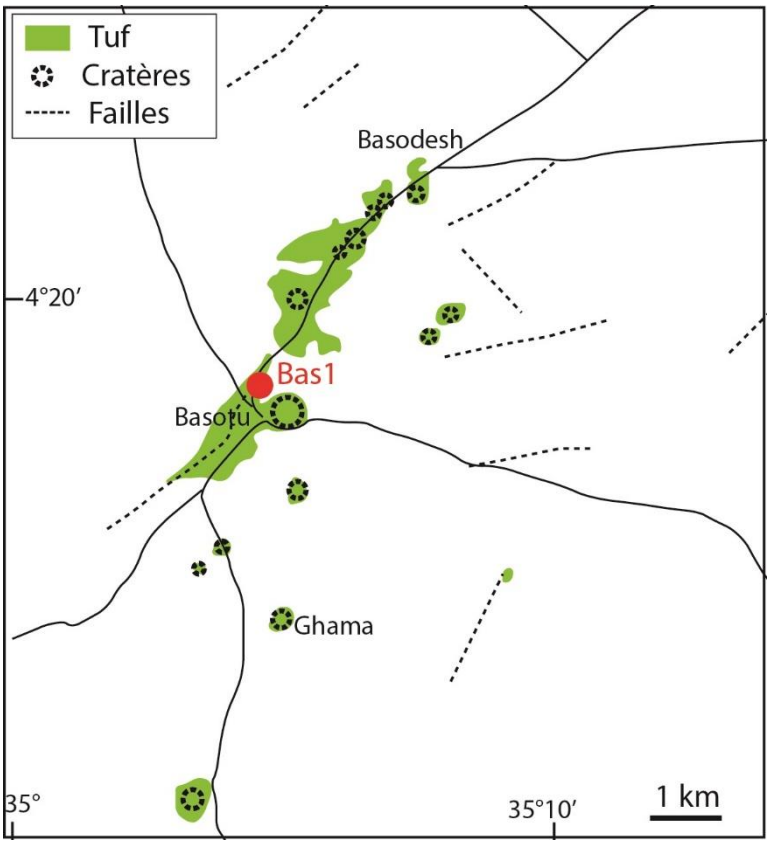

***Fig.II.9** : Carte simplifiée de Basotu (Modifiée d'après Tomas 1966)*

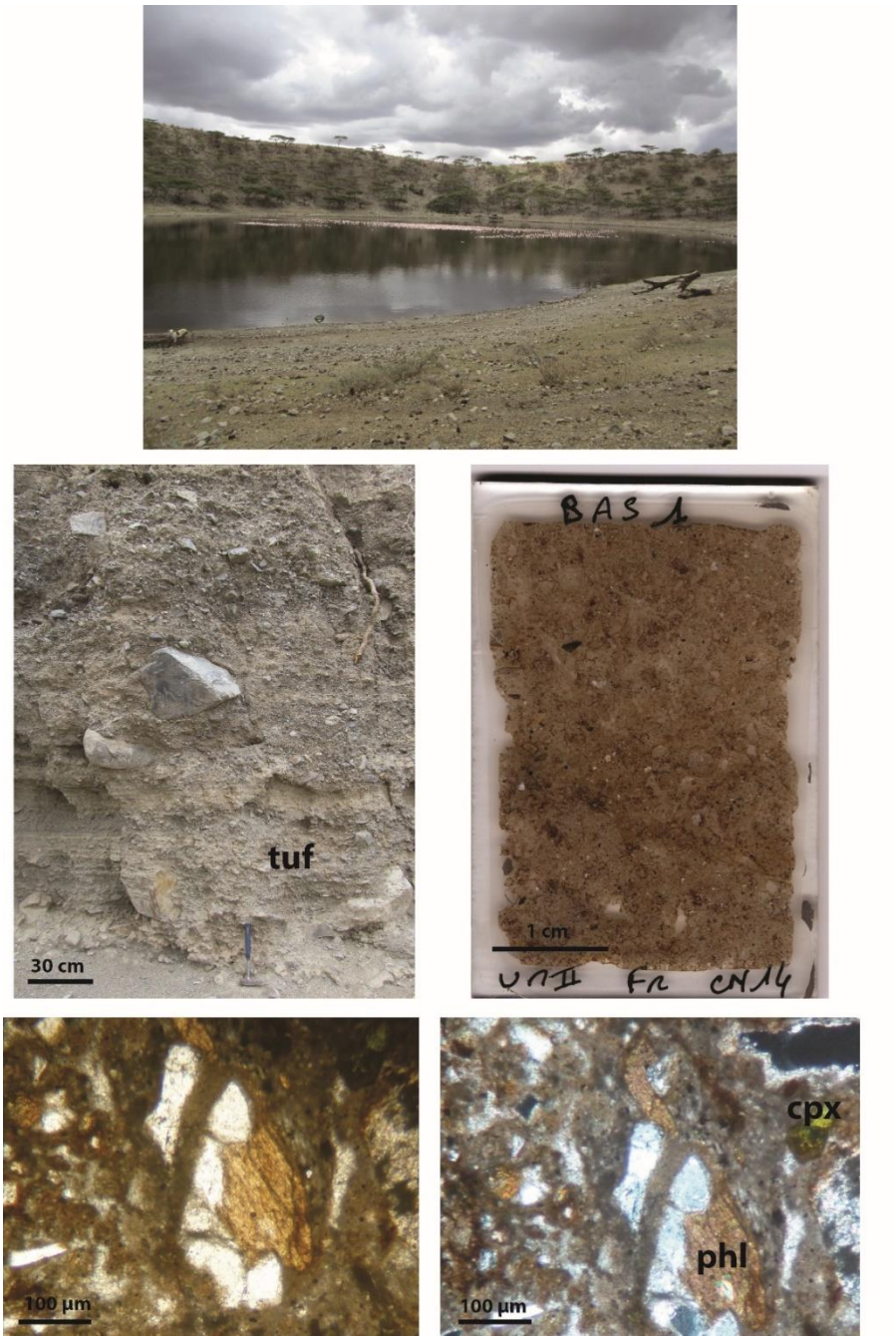

***Fig. II.10** : Photo du maar de Basotu et de l'affleurement Bas1 constitué de tuf et de blocs pyroclastiques cratoniques, ainsi que des photos de lame mince.*

II.I.1.5 L'Oldoinyo Lengai et le bassin de Natron

Les échantillons collectés à quelques km du lac Natron sont un échantillon de tuf (OL1, cratère de Kisete) et de lave (OL2, cône au nord de Loolmurwak) provenant de cônes et cratères parasitiques autour de l'Oldoinyo Lengai. Les échantillons OL3 (natrocarbonatite), et OL3x, OL4 (xénolites) proviennent de la coulée carbonatitique de 2007 sur le flanc SW de l'Oldoinyo Lengai (pétrographie et géochimie des échantillons en annexe C).

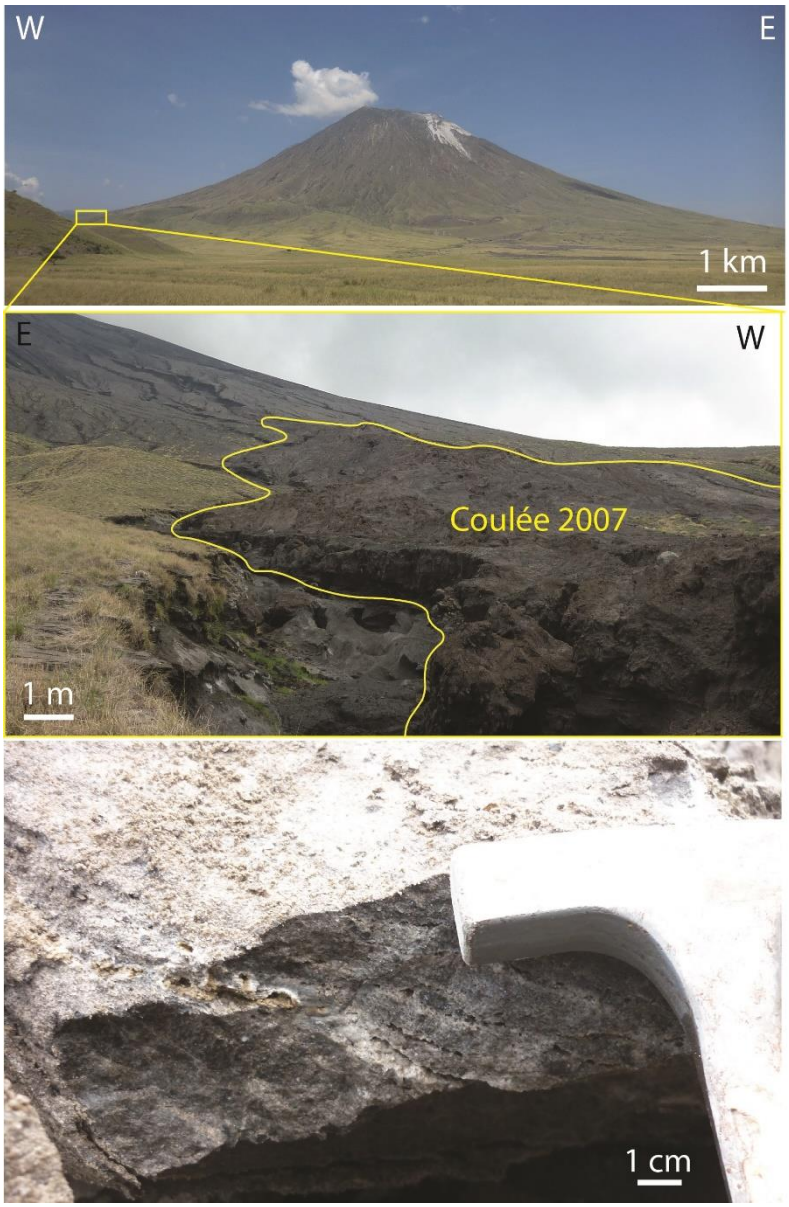

Fig. II.11 *: Photos de l'Oldoinyo Lengai, et de l'affleurement de natrocarbonatite OL3.*

II.I.2 Les volcans de l'axe est-ouest

Des échantillons provenant de 4 volcans de l'alignement E-O de la divergence nord-tanzanienne ont été collectés (Fig.II.1) (pétrographie et géochimie des échantillons en annexe C). Le volcan le plus à l'ouest est le Ngorongoro, les échantillons proviennent du flanc sud-est de la caldera (Ngo1 et Ngo2) (Fig.II.12). Les laves du stratovolcan Essimingor (Ess1 à Ess4) sur le flanc sud du volcan (coordonnées GPS en annexe B). Les laves de Burko (Bur1, Bur2) et de Monduli (Mon1) ont été échantillonnées à partir de blocs basculés dû à l'absence d'affleurement (végétation et altération importante).

Le volcan le plus à l'est qui ait été échantillonné est le volcan Olmani. Olmani est un cône parasitique au sud du volcan Mt Meru (Fig. II.1). Les échantillons (laves et xénolites) ont été collectés sur les pentes du volcan.

***Fig. II.12** : Photos de l'affleurement Ngo1 (Ngorongoro) et des laves d'Essimingor (Ess1, Ess2, Ess3) et de Burko (Bur2).*

II.II Analyses des roches totales

II.II.1 Spectroscopie de masse couplée à un plasma inductif (ICP-MS)

Pour préparer la solution à analyser, 100 mg de poudre d'échantillon sont pesés à l'aide d'une balance de précision (± 1 mg). Deux échantillons blancs et 2 standards externes (UB-N et BEN) sont également préparés. Une série d'attaques-acide ($HF + HNO_3 + HClO_4$) est effectuée afin de casser les liaisons atomiques et ainsi permettre leurs analyses quantitatives par spectromètre de masse. Chaque attaque est suivie d'une évaporation à une température de 150 °C pendant 24 h. Les solutions sont réduites à l'état solide par évaporation, puis de l'eau milliQ© et de l'HNO_3 sont ajoutés afin d'obtenir une solution. Ces solutions sont ensuite

diluées à 1:4000 pour éviter la saturation en éléments traces lors de l'analyse au spectromètre de masse. Les blancs permettent de détecter d'éventuelles traces de contamination au cours de la série d'attaques ou des analyses et les standards externes valident l'exactitude des analyses. Les teneurs des éléments en trace sur roche totale sont mesurées (en fonction des solutions étalons A2 et A4) avec le spectromètre de masse Agilent 7700x (Laboratoire Géosciences Montpellier) dont la sensibilité est de l'ordre de 200 millions de coups par ppm sur ^{115}In. Les standards internes choisis sont ^{115}In et ^{209}Bi. L'ICP-MS est affecté par différentes interférences (e.g. ^{138}Ba + ^{16}O = ^{154}Gd) qui sont corrigées en utilisant les standards externes et les valeurs de référence Zr et Hf.

II.II.2 XRF et analyseur élémentaire

Les éléments majeurs en roche totale ont été analysés au Laboratoire 'Instituto Andaluz de Ciencias de la Tierra' (Grenade, Espagne) par fluorescence à rayon-X avec un spectromètre Bruker S4 Pioneer. Les conditions d'analyses pour le tube à rayon-X en Rh étaient de 160 kV et 159 mA. L'intensité des rayons-X des échantillons a été comparée à 9 standards. Lors de ces analyses, l'état d'oxydation du fer a été ignoré. La perte au feu est calculée par le déficit de masse d'un gramme de poudre qui a été chauffé pendant 1 h à 900 °C. La perte au feu correspond à la perte massique des éléments volatils (OH, S, Cl, F). Des analyses complémentaires ont été réalisées par ICP-OES (iCap 6500 ThermoFisher) au service analytique du CRPG (France). L'analyse des éléments volatils des roches totales (C, S, Cl, F) ont été réalisées par service analytique du CRPG-SARM (France) (Carignan et al. 2001). Les concentrations en fluor et en chlore ont été déterminées par spectrophotométrie (Varian Cary 50) (Vernet et al. 1987) et les concentrations en soufre et carbone ont été déterminées avec un analyseur élémentaire.

II.III Analyses des minéraux

II.III.1 Microsonde électronique (EPMA)

Les éléments majeurs et volatils (S, Cl, F) des minéraux ont été analysés sur des lames minces polies avec la microsonde électronique CAMECA SX100 à l'Université Montpellier (service Microsonde Sud). Les conditions d'analyses sont de 20 keV (15 keV pour les apatites) de tension pour un courant de 10 nA. Les standards utilisés pour calibrer les éléments sont la wollastonite pour Si et Ca, Al_2O_3 pour Al, TiO_2 pour Ti, la forstérite pour Mg, l'hématite pour Fe, l' orthose pour K, l'albite pour Na, l'apatite pour P, du métal pour Ni, Mn, Cu, de la barytine pour S et Ba, de la fluorite pour F et de la chloroapatite pour Cl. Le faisceau est focalisé (1 μm) et le temps d'analyse pour chaque élément est de 20 s. L'erreur sur les mesures est toujours inférieure à 0,5 pds % (Table 1) pour les éléments majeurs les plus abondants. La calibration est adaptée selon les phases analysées notamment pour la mesure de S et Cl (40 s).

Table 1 : Écarts types et des limites de détection (pds %) des éléments majeurs

	Std deviation			limite de détection
	Olivine (n = 80)	Cpx (n = 120)	inclusions vitreuses (n = 30)	minéraux & inclusions
SiO_2	0.48	0.55	0.72	0.004
Al_2O_3	0.03	0.09	0.15	0.004
TiO_2	0.04	0.09	0.19	0.005
FeO	0.27	0.16	0.38	0.005
MgO	0.66	0.29	0.1	0.04
CaO	0.03	0.61	0.32	0.047
MnO	0.05	0.04	0.1	0.005
Na_2O	0.04	0.08	0.37	0.003
Cr_2O_3	0.05	0.07	0.11	0.058
NiO	0.05	0.05	0.09	0.005
K_2O	-	-	0.09	0.002
P_2O_5	-	-	0.1	0.01
F	-	-	0.46	0.29
Cl	-	-	0.04	0.013
S	-	-	0.06	0.014

II.III.2 ICP-MS par ablation laser

L'abondance des éléments en trace dans les minéraux silicatés, l'apatite et les sulfures des laves est déterminée en utilisant un système d'ablation laser (Plateforme GeoLas Q+ dotée d'un laser Excimer CompEx102) couplé avec un spectromètre de masse à source plasma (ThermoFinnigan Element XR). Les minéraux ont été analysés sur des lames épaisses (150 µm) et des minéraux séparés montés sur epoxy. La taille du faisceau est ajustée en fonction du minéral et de sa taille, 26 µm, 51 µm, 77 µm ou 102 µm avec une fluence de 10-12 $J.cm^{-2}$ et une fréquence de 7 à 10 Hz a été utilisée.
Les standards internes sont Nist612 50 ppm pour les minéraux silicatés et l'apatite et PGE-A, JK-37 et une bille Re-Os (Standard O. Alard) pour les sulfures. Les concentrations en CaO et SiO_2 pds % pour les minéraux silicatés et S pds% pour les sulfures (à partir des analyses de la microsonde électronique) sont utilisées pour calculer les concentrations des éléments en trace. Les données sont ensuite traitées à l'aide du logiciel GLITTER (Griffin et al. 2008). Le logiciel GLITTER permet de convertir le signal (coup/seconde) en concentration à partir des concentrations connues d'un standard.

II.III.3 Spectroscopie infrarouge à transformée de Fourrier (IRTF)

Les concentrations en hydrogène des clinopyroxènes et des olivines ont été mesurées en transmission par spectroscopie IRTF. Les spectres d'absorption ont été acquis à l'aide d'un spectromètre Bruker IFS 66v (laboratoire des colloïdes, verres et nanomatériaux, université de Montpellier), équipé d'un détecteur MCT (Mercure Cadmium Tellure) et couplé à un

microscope Hyperion. Pour les analyses IRTF, les grains séparés de clinopyroxène et d'olivine ont été doubles polis (70 – 325 µm). La concentration d'hydrogène a été calculée par intégration du spectre entre 3770 et 3000 cm^{-1} pour le clinopyroxène et entre 3610 and 3000 cm^{-1} pour l'olivine (méthode complète dans Demouchy et Bolfan-Casanova 2016). L'erreur induit par la calibration (Paterson, 1982), la mesure d'épaisseur des grains et du bruit de fond est de ± 15 %.

II.III.4 titrage de Karl Fischer

Les analyses des concentrations en H_2O des phlogopites (KW3) ont été réalisées par Pr. Harald Behrens au laboratoire de minéralogie à Hanovre (Allemagne) suivant la méthode de titrage de Karl Fisher décrite dans Behrens et al. (1996).

II.IV Analyses des inclusions vitreuses

Afin d'analyser les inclusions de verre, il est nécessaire qu'elles soient à affleurement. Pour conserver la phase carbonatée incluse dans le verre, le liquide de polissage doit être anhydre (éthanol ou Kerdane©). Un polissage à la main est réalisé avec une observation à la lumière réfléchie entre chaque phase de polissage. Divers tests ont été réalisés avec des tapis SiC, des films diamantés entre 30 µm et 1 µm et l'utilisation de la pâte diamantée à 6 µm et 1 µm afin de préserver les phases microcristallines. Le seul protocole qui a permis de préserver la phase carbonaté est l'utilisation du plateau 2400 et 1200 (taille des grains 9 µm) avec de l'éthanol, sans affiner le polissage avec de la pâte diamantée. La pâte s'incruste dans les cavités à l'intérieur des micro-phases carbonatées et arrache les microcristaux. Au final, la phase carbonatée a pu être conservée mais avec un aspect poreux. Les micro-phases observées au MEB sont inférieures à 0,25 µm.

II.IV.1 Eléments majeurs et en trace

Les éléments majeurs et volatils (S, Cl, F) des inclusions vitreuses ont été analysés sur des lames minces avec la microsonde électronique CAMECA SX100 à l'Université Montpellier (service Microsonde Sud). Les conditions d'analyses sont de 15 keV de tension pour un courant de 10 nA. La validité des analyses des inclusions vitreuses ont été vérifiées avec des standards externes (verres synthétiques). La taille importante des inclusions (10 – 30 µm) permet la détermination des concentrations sans contamination du minéral hôte.

Les abondances des éléments en trace des inclusions vitreuses ont été déterminées avec l'ICPMS par ablation laser. Les inclusions les plus larges (20 µm) ont été choisies pour être analysées avec un faisceau de 15 µm, avec une fluence de 1 mJ (10 J/cm^{-2}) et une fréquence de 7 Hz. Le standard interne était NIST610 500 ppm et la concentration en silice (SiO_2) analysée à la microsonde électronique a été utilisée pour déterminer les concentrations

des éléments en trace. Le signal des inclusions vitreuses est facilement identifiable par rapport à celui de la néphéline qui est très pauvre en éléments en trace (Fig.II.13).

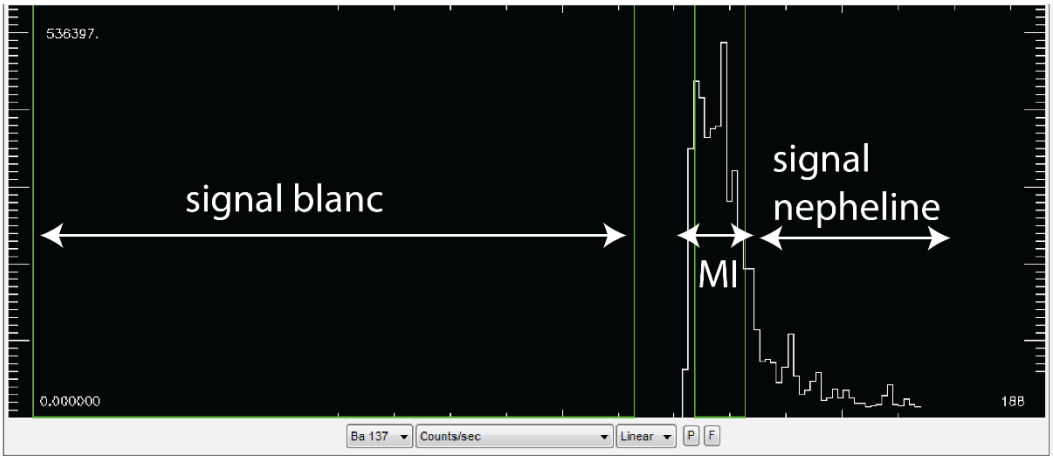

***Fig. II.13** : Signal des coups/seconde du Ba pour l'inclusion Han8 MI-5.*

II.IV.2 Spectroscopie raman

La spectroscopie raman consiste à envoyer une lumière (laser) sur l'échantillon. L'échantillon analysé va légèrement modifier la fréquence de la lumière en fonction des molécules (différents modes vibrationnels) présentes dans le milieu. La spectrométrie Raman peut se faire *in situ*, de manière non destructive sur des échantillons de petites dimensions (1 – 2 µm). C'est une méthode adéquate à l'étude des inclusions présentes dans les minéraux (i.e. inclusions vitreuses) puisque il n'est pas nécessaire que les inclusions soient à la surface. Les analyses par spectroscopie raman ont été acquises à l'aide d'un spectromètre Renishaw Invia (laboratoire Charles Coulomb, université de Montpellier, collaboration Thierry Michel) avec un laser opérant à 633 et 532 nm et une puissance de 15 nW. Les analyses ont été effectuées en utilisant un objectif x100 (Leica N Plan), ce qui permet d'avoir un volume d'analyse de quelques micromètres cubes. La gamme spectrale couverte était entre 50 et 4550 cm^{-1}.

II.IV.3 Spectroscopie de masse à ionisation secondaire (SIMS)

La concentration en carbone des inclusions vitreuses a été déterminée avec un spectromètre CAMECA IMS4f à l'université de Montpellier (microsonde sud). Les analyses en ^{12}C et ^{28}Si ont été réalisées avec une source d'ion primaire au Cs^+ (courant 1 nA, taille du faisceau 20 µm). La tension du canon à électron était de -4,5 kV. L'estimation de l'erreur (σ) pour le CO_2 calculée à partir du standard est environ de 10 %. Le standard de verre avec la même composition en élément majeur que les inclusions a été réalisé à 200 MPa et 1200 °C (ES : élément dans le standard, ici le carbone, C_{ES} = 2200 ppm CO_2, ELTRA CS 800). La fusion de la poudre de départ et la synthèse des verres trachytiques contenant du carbone a été mené dans un autoclave à chauffage interne (IHPV) à l'Institut de minéralogie d'Hanovre (Allemagne).

La concentration C_E (carbone) dans un échantillon est proportionnelle à l'intensité ionique secondaire I_E mesurée en c/s. Pour tenir compte des fluctuations d'origines diverses en cours d'analyse, on normalise I_E à l'intensité d'un signal de référence interne I_R (Si) dont la concentration est constante dans le volume analysé. Le facteur de proportionnalité (RSF_E) est égal à : $RSF_E = C_{ES}*(I_{RS}/I_{ES})$ (E : élément (C), S : standard, I : intensité, R : élément de référence (Si)). Connaissant le facteur de proportionnalité (RSF_E), il est ensuite possible de déterminer la concentration en carbone des inclusions vitreuses : $C_E = RSF_E * (I_E/I_R) * (C_R/C_{RS})$.

II.V Etat d'oxydation

II.V.1 XANES - Spectroscopie de structure près du front d'absorption de rayons X

La méthode de spectroscopie d'absorption X consiste à suivre l'évolution du coefficient d'absorption d'un échantillon en fonction de l'énergie du faisceau incident (rayon X). Un spectre d'absorption classique se détaille en 3 parties : le pré-seuil, le seuil et les oscillations lointaines (Fig.II.14). Le balayage en énergie (énergie du photon incident) est effectué au voisinage d'un seuil d'absorption de l'atome dont on souhaite étudier l'état d'oxydation. Les variations de l'absorption dans la zone du préseuil sont liées à la structure électronique de l'atome (i.e. Fer, 7111 – 7115 eV). Dans le cas du Soufre, il y a un décalage important en énergie (~ 13 eV) du seuil d'absorption *K* entre S^{2-} (2468 eV) et S^{6+} (2482 eV) (Wilke et al. 2011).

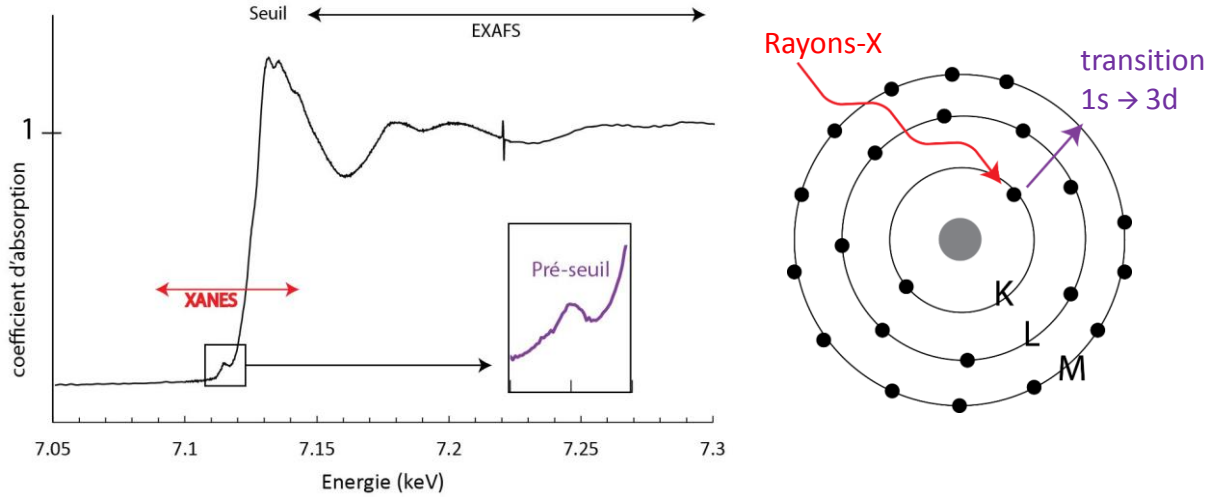

***Fig. II.14** : Exemple de spectre d'absorption pour le seuil K du Fer.*

Les spectres XANES pour le pré-seuil du Fe et le seuil *K* du S ont été acquis à l'European Synchroton Radiation Facility (ESRF, Grenoble, collaboration : post-doc Bernhard Hesse) avec un microscope à rayon X (SXM) sur la ligne ID21. La ligne ID21 est équipée d'un monochomateur Si(111) à double cristal qui permet de mesurer l'énergie incidente et de 2 miroirs parallèles avec des angles ajustables. Pour l'analyse des inclusions vitreuses et des minéraux, la zone analysée correspond à 1×1.5 µm. Des matériaux de référence ont été analysés : « *Fe foil* » (7,1127 keV), et les standards de sidérite, andradite,

sanidine, et le staurotide. Les analyses entre 7,05 – 7,35 keV ont été réalisées avec un pas de 0,33eV et un duel time de 0,1 s pour le fer. Les spectres XANES ont été normalisés en absorbance en ajustant la région spectrale avant le pré-pic et en utilisant une fonction polynomiale pour soustraire le bruit de fond. L'information du pré-pic a été dérivée en calculant la zone intégrée et la position du centroïde.

Les matériaux de référence pour le soufre sont des sulfates (haüyne, gypse, barytine, anhydrite) et des sulfures (pyrite, pyrrhotite, pentlandite). Les analyses entre 2,4 – 2,55 keV ont été réalisées avec un pas de 0,19 eV pour 2,4 – 2,45 keV, de 0.18 eV pour 2.45 – 2.51 keV et de 0.25eV pour 2.51 – 2.55 keV. Pour obtenir un signal avec un ratio signal/bruit satisfaisant, 20 scans ont été accumulés. La détermination de la spéciation du soufre est basée sur la méthode de Jugo et al. (2010) en utilisant l'intensité du signal aux positions d'énergie du sulfure et du sulfate dans le verre ou le minéral. L'intensité du sulfure I (S^{2-}) a été intégrée entre 2475,7 et 2480 eV et l'intensité du sulfate I (S^{6+}) a été intégrée entre 2481,5 et 2484 eV. $S^{6+}/\Sigma S$ a été calculé en utilisant l'équation empirique de Jugo et al. (2010):

$S^{6+}/\Sigma S = -C * \ln((I(S6+)/I\Sigma S - A)/B)$ avec A=1.2427, B=-0.94911, and C=0.81354.

Les inclusions vitreuses ont été analysées par spectroscopie XANES en mode réflexion sans la contribution du minéral hôte.

Les calibrations pour corréler les données des centroïdes (7113 – 7115 eV) déterminées au XANES et les rapports $Fe^{3+}/\Sigma Fe$ ont des différences non négligeables (e.g. Cottrell et al. 2009 et Wilke et al. 2005). Les calibrations utilisent des standards analysés en chimie humide et/ou par spectroscopie Mössbauer. Il est important de noter que les données Mössbauer ont tendance à surestimer Fe^{3+} par rapport aux données chimiques (Ottonello et al. 2001) et peuvent être une source d'erreur. Il est nécessaire de comparer les différentes calibrations et d'utiliser des standards ayant été analysés par différentes méthodes afin de limiter les erreurs. Des analyses complémentaires ont été réalisées par spectroscopie Mössbauer pour proposer une nouvelle calibration.

II.V.2 Spectroscopie Mössbauer

La spectroscopie Mössbauer est basée sur l'absorption de rayons gamma par les noyaux atomiques, cette méthode a été utilisée pour déterminer le rapport $Fe^{3+}/\Sigma Fe$ des roches et minéraux afin de servir de calibration externe pour les données XANES. Le rapport $Fe^{3+}/\Sigma Fe$ a été déterminé au service 'réseau de rayons X et gamma' de l'Université de Montpellier en collaboration avec Pr. Lorenzo Stievano et Dr. Moulay Tahar Sougrati (réseau de rayons x et γ, UM). Les échantillons (200 mg pour les verres et 30 mg pour les minéraux) ont été broyés dans un bol en agate et préparés sous forme de pastille. Les spectres du ^{57}Fe ont été acquis pendant 2 jours à partir d'un spectromètre Mössbauer à source ^{57}Co. La spectroscopie Mössbauer permet de différencier les sites dans lequel se situe le fer ferreux (Fe^{2+}) et ferrique (Fe^{3+}) dans les minéraux. Dans les clinopyroxènes, les deux sites octaédriques M1 et M2 incorporent du fer (McCammon et al. 1998, Hao et Li 2013). Les sites M2 étant liés avec les tétraèdres de silice qui incorporent de gros cations tels Ca^{2+}, Na^{+} et préférentiellement Fe^{2+} par rapport à Fe^{3+}. Les sites M1 incorporent des cations de tailles moyennes comme Mg^{2+}, Fe^{3+}, Mn^{2+}, Al^{3+} et également Fe^{2+}. Dans les grenats, le fer est

incorporé dans les sites dodécaèdres X, octaédriques Y et tétraédriques Z (McCammon et al. 1998).

Les données du Mössbauer sont distribuées selon des doublets de gaussienne (intensité en fonction de la vitesse ($mm \cdot s^{-1}$)). Les différentes gammes de vitesse permettent de distinguer le fer présent dans les minéraux et les verres et les oxydes de type magnétite.

Une source importante d'erreur (absente des analyses in situ XANES), est la séparation des minéraux qui peut être problématique entre les pyroxènes et grenats de petites tailles (< 500 µm), et les verres qui peuvent être altérés en surface.

Chapitre III. Les néphélinites magnésiennes du bassin de Manyara et leur source mantellique

Ce chapitre aborde la composition des laves primaires de la zone méridionale de la divergence nord-tanzanienne (bassin de Manyara) afin de pouvoir caractériser la source et l'environnement de cristallisation des laves alcalines en zone d'initiation de rift.

Petrogenesis of melilite nephelinites in early-stage rifting, north Tanzania

III.I Introduction

Silica-undersaturated magmas are abundant in continental rift including hyper-alkaline lavas as melilitite, nephelinite, basanite and phonolite. Low silica lavas are commonly CO_2-rich and described as the product of CO_2-bearing mantle (e.g. Brey 1978, Dasgupta et al. 2007) associated with carbonatite suggesting a cogenetic origin (Woolley and Kjarsgaard 2008). The oldest volcanism of the EAR (~ 45 Ma) occurred in Ethiopia associated with the propagation of the rift toward the South (Ebinger et al., 2000) and contains abundant hyper-alkaline rocks and carbonatites (e.g. Dawson 1992, Foley et al. 2012, Pouclet et al., 1981). Melilitites and nephelinites are located at the propagating tip and around the Tanzanian craton (i.e. Tanzania, Uganda) (Foley et al. 2012). At the North of Tanzania, primitive rocks erupted generally as monogenetic volcanic field (e.g. Engaruka-Natron monogenetic volcanic field) where they are characterized by small-volume magmatism, low fractional crystallization during ascent, relatively high ascent rates and xenolith-bearing lavas. Different type of lavas have been erupted including primitive lavas as Mg-rich nephelinites (Mattsson et al. 2013, Mana et al. 2012, Keller et al. 2006), Mg-poor nephelinites and carbonatites (e.g. Dawson 2008) suggesting differentiation at different levels (Klaudius and Keller 2006, Zaitsev et al. 2012, Baudouin et al. 2016).

In this paper, we investigated a mineralogical and geochemical study of Mg-rich nephelinite lavas from Manyara basin (Kwaraha, Labait) and Olmani to constrain the genesis of silica-undersaturated magma of the first stage of continental break-up. Our study is focus on the more primitive lavas in order to constrain mantle source and partial melting process. Comparison with Tanzanian and African volcanism allows us to discuss the genesis of carbonate-rich silicate volcanism during rift initiation and the characteristics of Tanzanian upper mantle.

III.II Geological background

The EAR is divided into 2 branches (around the Tanzanian craton) with different stages of plate boundary extension, from the initiation of the rift (Tanzania, Manyara-Balangida basin) to oceanic accretion (Afar Triple Junction). In the East branch, volcanism began at 30 Ma in the North Kenya, 15 Ma in Central Kenya and 6 Ma in the Northern Tanzania (Mana et al. 2012, 2015). The north Tanzanian rift expands over 200 km, forming the North Tanzanian Divergence (NTD), which contains many volcanic complexes (e.g. Ngorongoro, Meru, and Kilimanjaro) and small volcanic cones (e.g. Lashaine, Olmani) (Dawson et al. 1970, 1997; Jones et al. 1983). Olmani cone is composed by one of the most primitive lavas of NTD (Jones et al. 1983). In the southern part of NTD, the rift is divided into 3 areas: Eyasi, Manyara-Balangida, and Pangani (from West to East, respectively, Le Gall et al. 2008) (Fig.III.1). Eyasi and Pangani fault systems are amagmatic and represent rift propagation at west and east of the NTD, while Manyara-Balangida basin represents

propagation toward the south. The Manyara-Balangida basin is located along the rift escarpment with 2 main volcanic centers, Hanang and Kwaraha volcanoes surrounded by small volcanic cones: Labait and Sora hill, respectively (Dawson 2008). Volcanic cones erupted the most primitive lavas of Manyara basin. In this study, we samples the primitive lavas from Olmani (north part of NTD), Labait and Kwaraha (Manyara basin) small volcanic cones (Fig.III.1).

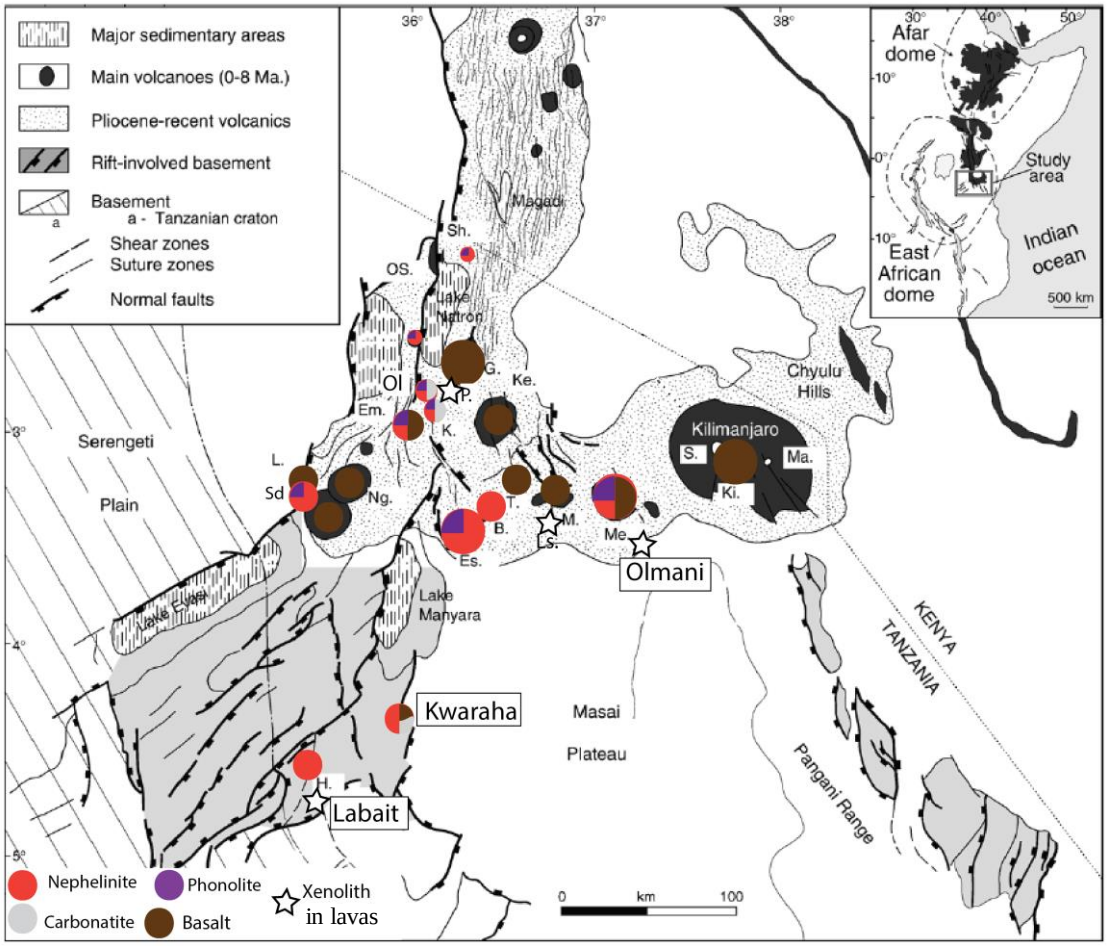

Fig.III.1 *Main structural and magmatic features of the North Tanzania Rift and the location of Labait, Kwaraha and Olmani volcanoes. Volcanoes: B. Burko, Em. Embagai, Es. Essimingor, G. Gelai, H. Hanang, K. Kerimasi, Ke. Ketumbeine, Ki. Kibo, L. Lemagrut, M. Monduli, Ma. Mawenzi, Me. Meru, Ng. Ngorongoro, Ol. Oldoinyo Lengai, OS. Ol Donyo Sambu, P. Pello hill, Sd. Sadiman, S. Shira, Sh. Shombole, T. Tarosero. Modified after Le Gall et al. (2008).*

Labait volcano (4°34'12", 35°26'04", near Hanang volcano) is a small olivine melilitite cone (Dawson et al. 1997) (Fig.III.1). Labait volcanic activity occurred at 0.4 ± 0.2 Ma (Rudnick et al. 1999). Labait lava carries abundant mantle xenoliths including spinel phlogopite harzburgites, garnet lherzolite-harzburgites, dunites and phlogopite xenoliths (Lee and Rudnick 1999; Koornneef et al. 2009). Xenoliths have a high ascent rate ($4 – 28\ m{\cdot}s^{-1}$) and low water content (<50 ppm wt H_2O) (Hui et al. 2015). Isotopic data of Labait olivine melilitite indicate that a craton or craton margin is present beneath Labait with

slightly different signature compare to lithospheric mantle (Aulbach et al. 2008, MacDonald et al. 2001).

Olmani small cone, in the Meru volcanic field, erupted between 0.06 and 2.5 Ma (Wilkinson et al. 1986). Olmani volcano (3°23'56", 36°44'54"; 15 km south of Meru) is an olivine nephelinite scoria cone (Dawson 2008). Olmani lavas carry weakly hydrated dunite and harzburgite (Baptiste et al. 2015) which can contain interstitial glasses indicating melt-rock interaction occurred in the lithospheric mantle and that refractory peridotites are metasomatized by a carbonate liquid (~ 2 %) (Nonnotte 2007, Rudnick et al. 1993, Jones et al. 1983).

Kwaraha volcano (4°13'45", 35°48'53") consists of Mg-rich nephelinite agglomerates, tuffs and lavas (James 1966, Dawson et al. 1997). Kwaraha has a quaternary eruptive history from 1.5 to 0.7 Ma (Bagdasaryan et al. 1973). A lava flow of calciocarbonatite, tuffs cones and craters are present around the main edifice (Dawson 2008). Isotopic data for Kwaraha lavas indicate an orogenic belt source (low $^{87}Sr/^{86}Sr$; Paslick et al. 1996, MacDonald et al. 2001). Kwaraha district contains also small parasitic cones with melilitite to nephelinite composition (Dawson et al. 1997). Lavas from these small volcanic cones are more mafic than the main edifice and may represent the parental melt (Dawson et al. 1997, Dawson 2008). We studied these cones including Sora hill (Kw2) and Haindadonga cones (Kw3) (Dawson et al. 1997) (Fig.III.1).

III.III Analytical Methods

III.1 Major and volatile elements

Whole-rock major elements were measured by ICP-OES (iCap 6500 ThermoFisher) at the analytical services (SARM) of the CRPG (Nancy, France) following the protocol established by Carignan et al. (2001). One gram of whole rock powder is dissolved with HNO_3 and the sample the mixture (with $LiBO_2$) is fused. Standard reference were SLRS-5 and the errors (1σ) were estimated < 2 %.Whole rock sulfur and carbon contents were determined for each sample by element analyzer at the SARM. Whole rock F and Cl contents were determined by wet precipitation-ferrithiocyanate spectrophotometry using Varian Cary 50 spectrophotometer. Standard solutions were used to check the accuracy of the analyses. Standard deviations are less than 5 %.

The concentrations of major and volatile elements in minerals were determined using electron microprobe (Cameca XS100 at the "Microsonde sud" facility, University of Montpellier, France). Operating conditions comprised an accelerating voltage of 20 keV for minerals, a 10 nA beam current and a beam focalized (1 µm). The counting time was fixed at 20 s for each element analysis and 40 s for volatile element (S, Cl). The standards used for major and volatile element analyses are: wollastonite for Si and Ca, Al_2O_3 for Al, TiO_2 for Ti, forsterite for Mg, hematite for Fe, orthose for K, albite for Na, apatite for P, native metal for Ni, Mn, Cu, baryte for S and Ba, fluorite for F and chloroapatite for Cl.

III.2 Trace elements

Trace element analyses of Kwaraha and related small volcanic cones (Kw1-Kw8), Labait and Olmani samples were performed by ICP-Mass Spectrometry (ICP-MS) after HNO_3 and HF digestion of 0.1 g of sample powder in a Teflon-lined vessel at 180 °C and 200 psi for 30 min, evaporation to dryness, and subsequent dissolution in 100 mL of 4 vol % HNO_3. Instrument measurements were carried out in triplicate with a NexION 300d (Perkin Elmer) ICP-MS spectrometer (at Instituto Andaluz de Ciencias de la Tierra, university of Grenada) using Rh as internal standard, and by external calibration using multi-elemental calibration solutions. The precision was better than ± 5 % for concentrations over 10 ppm. Analyses of Kw10, Kw11, Kw12 samples were carried out at the AETE facility (University of Montpellier, France). Whole-rock analyses were performed using a quadrupole 7700x inductively coupled plasma-mass spectrometry (ICP-MS) at the University of Montpellier (AETE platform) where 0.1 g of whole-rock powder was dissolved with acid (HF-HNO3). Blanks were prepared with samples spiked with In and Bi to monitor internal drift. Solutions were analyzed at a final dilution factor of 4000. ICP-MS sensitivity in this configuration was 200 ×106 cps/ppm ^{115}In. Analytical accuracy was estimated from measurements of international rock standards UBN and G1.

Trace element concentrations in minerals were determined by a laser ablation ICP-MS system at the University of Montpellier (AETE platform), using GeoLas Q + Excimer CompEx102. A 26 and 56 µm diameter laser beam were used for apatite and silicate minerals with a laser repetition rate of 6 - 10 Hz and laser power of 0.5 mJ (5 J·cm^{-2}). The spot size was chosen as a compromise between signal intensity and the size of the minerals of interest in the samples. The concentrations are calibrated with NIST612 glass and the concentrations of SiO_2 and CaO previously determined by electron microprobe for individual minerals. BIR-1 standard is used as external standard. Glitter Software (Griffin et al. 2008) was used to process the raw data files containing the signal intensity versus time toward element concentrations. This allows precise selection of blanks and signals, and rapid visualization of the intensity data. The drift is compensated by the internal standard calculations using the Glitter software; no other drift corrections are performed.

III.3 Water content analyses

Water content of clinopyroxene (cpx) and olivine (ol) has been determined using FTIR (Fourier Transform Infrared) spectroscopy. Handpicked minerals were prepared as doubly polished section thickness between 140 and 325 µm. The hydrogen concentration was measured in transmission mode by FTIR spectroscopy at the Laboratoire Charles Coulomb (University of Montpellier, France). The unpolarized infrared spectra were acquired using a Bruker IFS 66v coupled with an optical microscope Hyperion. A Globar light source and a Ge-KBr beam splitter are used to generate unpolarized mid-infrared radiation (between 4000–400 cm^{-1}). Water contents were calculated by integration of the spectrum between 3770 and

3000 cm^{-1} for cpx and 3610 and 3000 cm^{-1} for olivine (for complete method see Denis et al. 2015). Water concentration is calculated using the calibration of Paterson (1982), considering the water concentration as a function of density of the cpx (χ_{cpx}(Kw3) = 2707 ppm wt H_2O, χ_{cpx}(Kw5) = 2737 wt H_2O) and olivine (χ_{ol}(Kw) = 2605 - 2612 ppm wt H_2O; χ_{ol}(Lab) = 2587 ppm wt H_2O). The errors on water content due to calibration (Paterson, 1982), uncertainties on the sample thickness and background correction are ± 15 % (Denis et al. 2015). The integrated unpolarized absorbance normalized to 1 cm of thickness values is also reported in order to use alternative mineral specific FTIR calibrations.

The water content of phlogopite from sample Kw3 was measured on separated minerals by Karl-Fischer titration (KFT) using air as transporting gas and muscovite as standard (σ=0.1 wt% H_2O) (Behrens et al. 1996).

III.IV Results

Lava (Kwaraha) and scoria samples (i.e. Labait and Olmani) have microlitic porphyric texture with large phenocrysts olivine and cpx (> 1 mm) (Fig.III.2). Although Kwaraha lavas are in melilitite area and Olmani and Labait lavas are in nephelinite area (Le Bas 1986) (Fig.III.3a), following the nomenclature for silica-undersaturated alkaline lavas from Woolley et al. (1996), all the samples are named melilite nephelinites (Fig.III. 3b).

IV.1 Labait volcano

IV.1.1 Petrography and whole rock geochemistry

The melilite nephelinites from Labait contain olivine (15 - 30 vol %, 0.5 - 4 mm) phenocrysts set in a groundmass of cpx, magnetite (magnesioferrite, Ti-magnetite) (< 1 vol %), altered melilite (trace), and pyrrhotite. Olivine is in many cases transformed into iddingsite. Rare and altered phlogopite phenocrysts (0.5 - 1 vol %, 1 mm) are present in Lab1 (Fig.III.2a) and Lab2 samples. One sample (Lab3) contains altered plagioclase phenocrysts (5 vol %, 0.2 - 2 mm) (Fig.III.2b).

These melilite nephelinites have very high Mg# (Mg# = Mg/(Mg+Fe)*100) values ranging from 76.5 to 79.3 (MgO = 21.9 - 24.4 wt %) (Fig.III.3a). These lavas have variable peralkaline index (Na+K/Al = 0.7 - 1.2) and K_2O/Na_2O ratio (0.7 - 1.1), high CaO content (7.97 - 10.98 wt % CaO) and moderately Al_2O_3 content (4.6 - 5.8 wt % Al_2O_3) (Fig.III.4, Table 1). Lavas have variable whole rock concentrations in volatile elements: 0.7 - 4.6 wt % CO_2, 200 - 360 ppm S, 1100 - 1700 ppm F, and 44 - 71 ppm Cl.

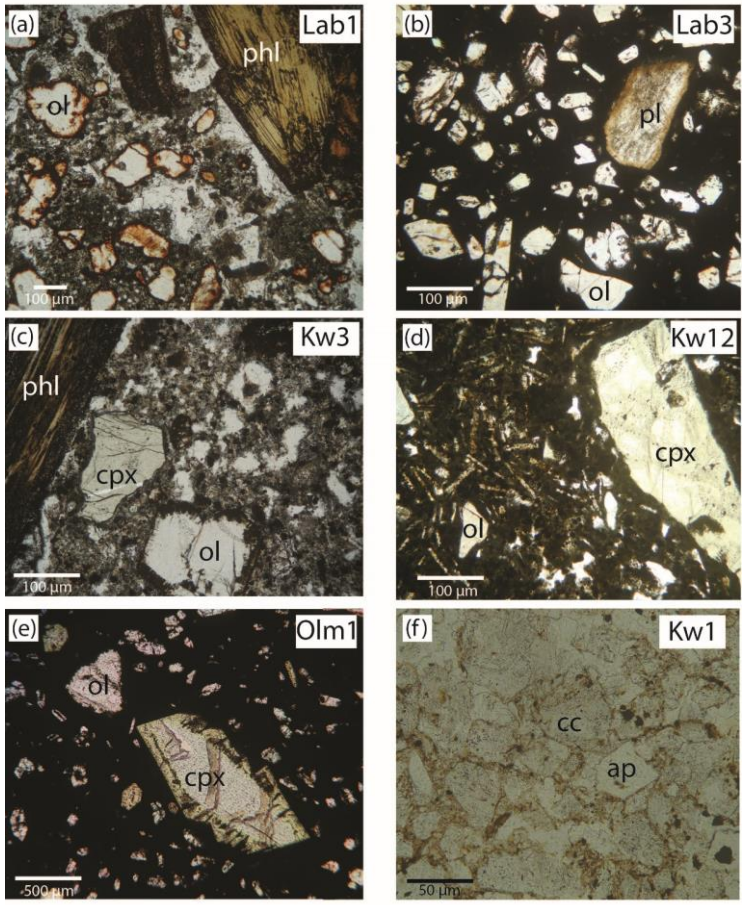

Fig.III.2 *Microphotographs of nephelinitic lavas: (a) (b) Labait, (c)(d) Kwaraha, (e) Olmani and (f) carbonatite from Kwaraha. ol olivine phl phlogopite cpx clinopyroxene pl plagioclase cc calcite ap apatite*

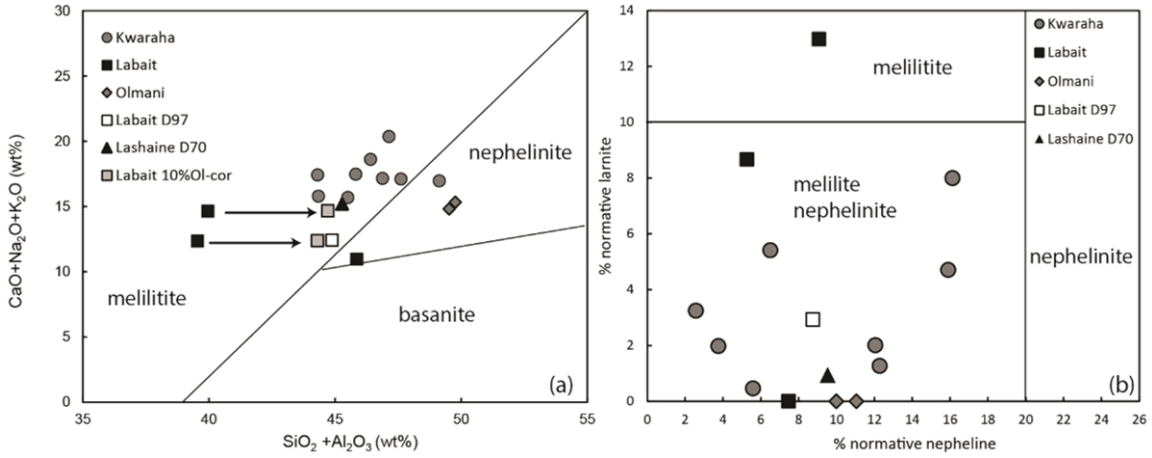

Fig.III.3 *(a) Melilitite-nephelinite-basanite classification Le Bas et al. (1986) and (b) melilitite-melilite nephelinite-nephelinite discrimination diagram (Wooley et al. 1996) of the Kwaraha, Labait, Olmani samples (this study) and Lashaine and Labait lavas (Dawson et al. 1997, 1970).*

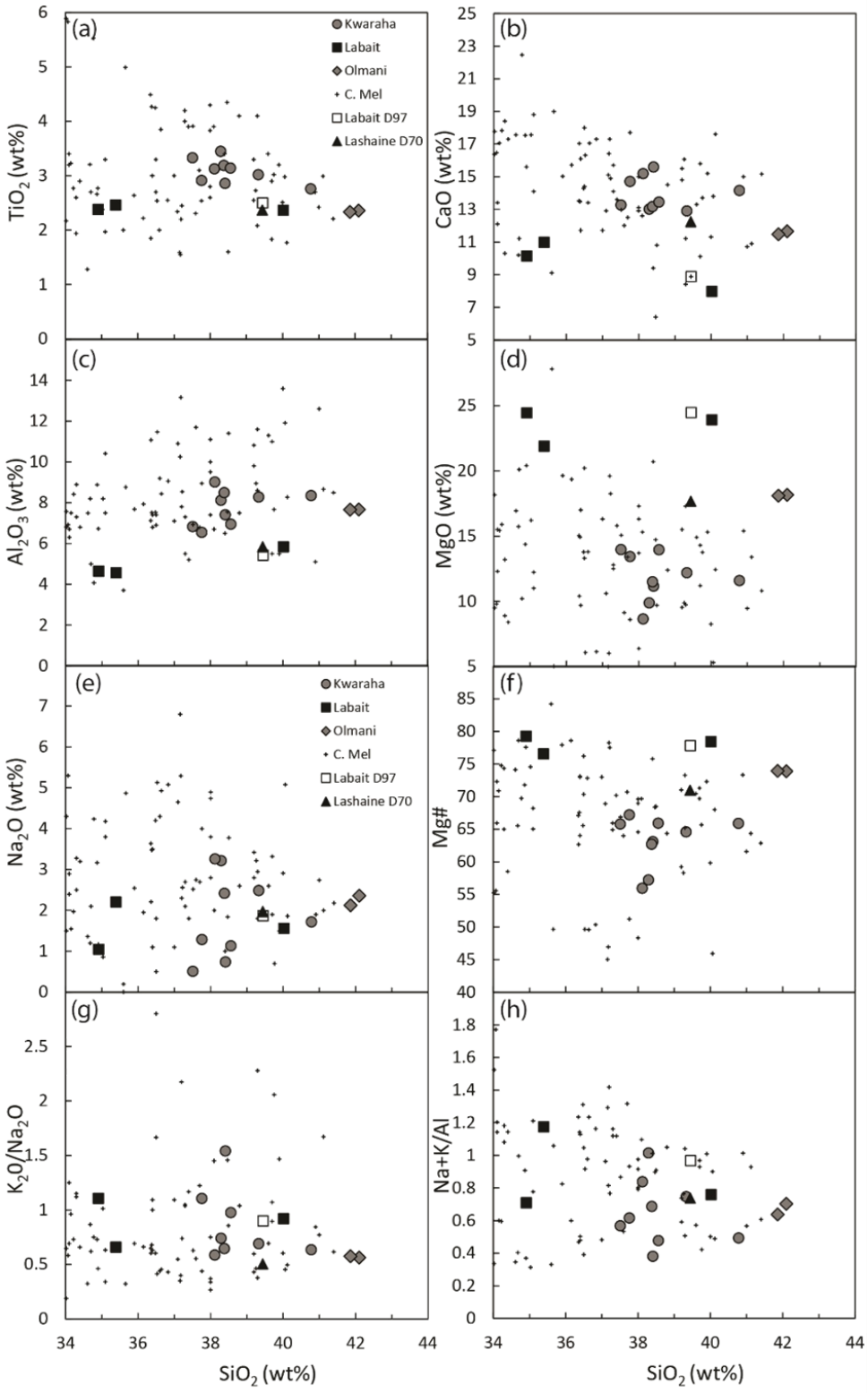

Fig.III.4 *(a) TiO_2 content, (b) CaO content, (c) Al_2O_3 and (d) MgO (e) Na_2O (f) Mg# (g) K_2O/Na_2O and (h) Na+K/Al vs SiO_2 content of Kwaraha, Labait, Olmani samples (this study), Labait and Lashaine lavas (Dawson et al. 1997, 1970) and continental melilitite (Georoc database).*

Table 1: Major, volatile and trace element concentrations of melilite nephelinitic lavas

Sample	Kw1	Kw2	Kw3	Kw4	Kw5	Kw6	Kw8	Kw10	Kw11	Kw12	Lab1	Lab2	Lab3	Olm1a	Olm1b
SiO_2 (wt%)	bdl	38.41	37.51	40.78	38.29	38.12	39.33	38.38	38.56	37.76	34.91	35.39	40.02	42.10	41.86
TiO_2	bdl	2.86	3.33	2.76	3.45	3.13	3.02	3.19	3.14	2.92	2.38	2.46	2.37	2.36	2.33
Al_2O_3	bdl	7.41	6.83	8.35	8.12	9.02	8.28	8.50	6.95	6.55	4.64	4.57	5.84	7.67	7.66
Fe_2O_3	2.59	12.94	14.38	11.88	14.63	13.49	13.24	13.55	14.29	12.98	12.66	13.29	13.03	12.73	12.63
MnO	0.41	0.20	0.20	0.18	0.23	0.22	0.21	0.21	0.20	0.19	0.19	0.19	0.18	0.19	0.19
MgO	0.51	11.17	13.97	11.59	9.88	8.65	12.19	11.50	13.95	13.43	24.43	21.89	23.90	18.17	18.09
CaO	62.06	15.59	13.26	14.15	13.01	15.19	12.90	13.17	13.45	14.70	10.14	10.98	7.97	11.65	11.47
Na_2O	0.26	0.74	0.51	1.72	3.22	3.26	2.49	2.42	1.13	1.29	1.05	2.21	1.56	2.36	2.12
K_2O	0.15	1.14	2.02	1.09	2.38	1.91	1.72	1.56	1.11	1.42	1.16	1.45	1.43	1.33	1.22
P_2O_5	1.16	0.57	0.58	0.22	0.55	0.44	0.60	0.60	0.56	0.51	0.64	0.51	0.46	0.46	0.46
LOI	33.00	9.65	7.88	7.89	6.49	6.96	6.29	6.73	5.21	7.27	8.21	5.85	3.25	0.94	1.49
Total	100.14	100.67	100.45	100.62	100.25	100.37	100.27	99.81	98.54	99.02	100.41	98.78	100.01	99.94	99.53
Mg#	28.06	63.10	65.81	65.90	57.22	55.95	64.59	62.70	65.91	67.21	79.26	76.54	78.42	73.87	73.94
CO_2	41.15	2.85	1.67	0.73	2.57	3.07	0.15	1.17	0.51	2.76	4.58	3.70	0.71	0.07	0.01
F (ppm)	880	-	1900	1600	1400	2100	-	2000	2200	2600	1500	1700	1100	1300	1500
Cl	47	-	33	660	1150	550	-	99	89	72	44	71	49	295	490
S	70.0	270	222	148	140	220	300	100	100	100	260	200	200	200	300
Cr	4.54	294	366	246	141	110	334	247	368	335	756	495	1126	672	970
Ni	52.3	125	143	102	60.0	64.6	90.4	74.9	145	121	827	1000	890	505	647
Cu	12.5	171	168	150	262	219	173	182	198	193	117	118	115	108	135
Cs	0.19	0.26	0.28	0.27	0.44	0.36	0.34	0.27	0.24	0.11	0.21	0.15	2.62	0.36	0.51
Rb	11.3	48.4	74.3	36.1	58.5	45.4	61.3	41.9	48.0	67.2	44.9	51.0	64.7	32.8	40.7
Ba	852	775	801	1225	673	1166	812	854	750	689	595	621	551	570	793
Th	11.49	7.83	8.06	8.51	9.70	9.79	10.70	9.73	9.89	8.99	7.34	8.37	7.99	7.67	9.87
U	0.79	1.70	1.72	1.68	2.01	2.05	2.02	2.22	4.59	1.89	1.48	1.73	1.45	1.34	1.79
Nb	190	86.0	82.4	81.0	104	107	101	102	87.3	95.7	78.9	90.4	78.3	85.4	107
Ta	2.17	5.96	5.70	5.49	7.45	7.73	6.94	5.41	5.42	6.02	5.40	5.13	4.80	5.20	6.66
La	266	68.2	68.2	69.2	76.6	76.8	82.2	75.7	80.8	77.9	64.9	68.3	62.7	62.8	81.1
Ce	507	128.6	130.2	130.5	144.8	142.8	152.0	130.2	132.5	128	123	120	111	104	133
Pb	33.2	3.06	4.16	4.50	8.09	6.22	8.31	9.80	5.35	0.64	2.99	3.85	7.04	3.77	4.89
Pr	59.1	14.4	14.9	14.8	16.3	15.8	16.7	14.6	14.1	13.8	13.7	13.4	12.5	10.8	14.0
Sr	3081	1009	643	1108	811	931	989	934	937	867	840	754	853	523	577
Nd	221	53.7	55.9	54.9	59.9	58.9	60.9	54.1	51.6	50.6	49.7	49.6	46.3	38.7	50.3
Zr	26.3	180	207	226	255	259	220	255	168	190	178	183	168	126	168
Hf	0.44	4.47	4.97	5.28	6.52	6.43	5.34	5.68	4.14	4.63	4.16	3.97	3.94	3.01	4.16
Sm	36.4	9.13	9.76	9.57	10.65	10.27	10.47	8.96	8.35	8.33	7.91	7.73	7.34	6.11	7.96
Eu	9.42	2.53	2.64	2.71	2.84	2.91	2.86	2.75	2.51	2.45	2.14	2.27	2.10	1.84	2.40
Gd	27.2	7.15	7.48	7.45	8.37	8.08	7.96	9.49	8.83	8.81	6.07	7.81	7.37	6.47	8.35
Tb	3.54	0.941	0.990	1.012	1.120	1.103	1.077	1.041	0.936	0.953	0.787	0.799	0.770	0.683	0.894
Dy	15.6	4.34	4.51	4.62	5.25	5.19	5.22	4.91	4.41	4.52	3.34	3.54	3.47	3.21	4.18
Y	69.5	19.8	19.8	20.3	23.3	23.6	23.4	21.2	17.6	19.3	14.2	14.3	13.1	12.6	16.3
Ho	2.70	0.78	0.79	0.81	0.91	0.93	0.93	0.84	0.75	0.78	0.55	0.58	0.57	0.55	0.72
Er	5.85	1.81	1.71	1.90	2.06	2.08	2.01	1.94	1.71	1.80	1.26	1.31	1.25	1.26	1.65
Tm	0.80	0.25	0.22	0.26	0.28	0.30	0.29	0.25	0.22	0.23	0.16	0.16	0.15	0.17	0.21
Yb	4.52	1.47	1.35	1.50	1.66	1.62	1.68	1.50	1.29	1.42	0.91	0.96	0.91	0.99	1.30
Lu	0.57	0.20	0.19	0.22	0.24	0.24	0.24	0.21	0.18	0.20	0.14	0.13	0.12	0.14	0.18

Mg# = Mg/(Mg+Fe)*100; bdl: below detection limit

Labait lavas have high incompatible element concentration up to 300 times chondrite for rare earth elements (REE). REE patterns show an enrichment in light REE (LREE) compared to heavy REE (HREE) (63 – 68 ppm La, 0.12 - 0.14 ppm Lu, La/Sm = 8.2 - 8.8, La/Yb = 69.1 - 71.7) (Fig.III.5a). Lavas have high content in large ion lithophiles elements (LILE) (e.g. 551 – 621 ppm Ba), and relatively low content in high field strength elements (HFSE) (e.g. 168 - 178 ppm Zr) (Fig.III.5b). Trace element concentrations have a negative anomaly in K and Zr-Hf (Fig.III.5b) and Zr/Hf (42.6 - 46), Ce/Y (8.4 - 8.7), Nb/U (52.2 - 53.9), Rb/Sr (0.05 - 0.08) and low trace elements ratios as Zr/Nb (2 - 2.3), Ba/Rb (8.5 - 13.3) ratios. Labait lavas are characterized by high contents in Cr (490 - 1125 ppm) and Ni (826 - 1000 ppm).

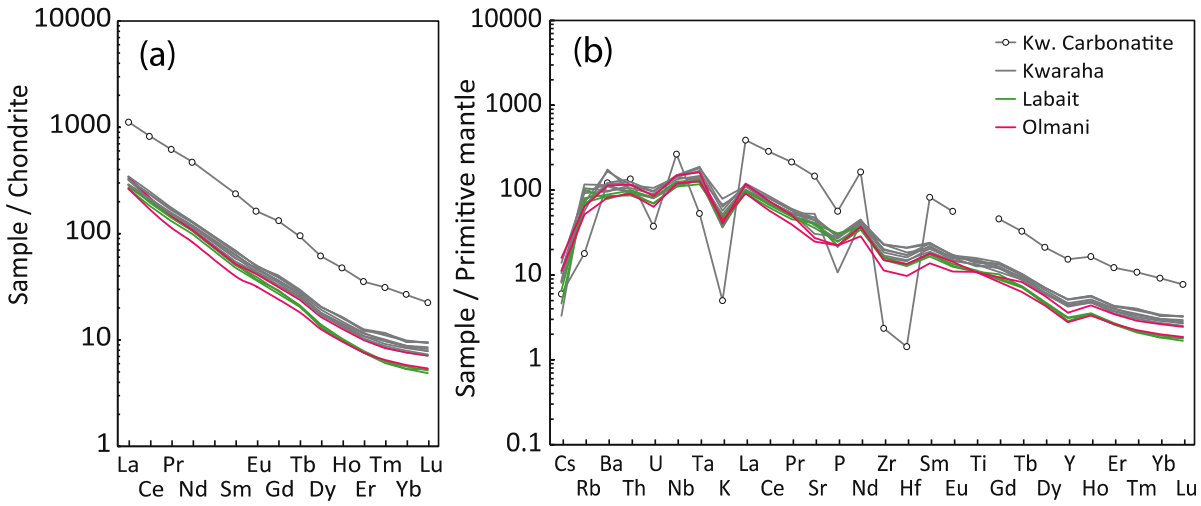

Fig.III.5 *(a) Normalized REE content and (b) Normalized trace element composition of Kwaraha, Labait, Olmani nephelinites. Primitive mantle and chondrite values from Sun and McDonough (1989)*

IV.1.2 Mineral chemistry

Olivine from Labait lavas has different forsterite (Fo) and NiO content for Lab1 (Fo_{91} to Fo_{81}, 0.37 - 0.18 wt % NiO) and Lab3 (Fo_{89} to Fo_{87}, 0.45 - 0.24 wt % NiO) (Fig.III.6) (Table 2). Phenocrysts from Lab3 and Lab1 are zoned with decreasing MgO and NiO content from core to rim and increasing CaO content (0.04 - 0.61 wt %). Olivine from Lab1 with the lower Fo has reverse zoning with increasing Fo content toward the rim (Fo_{83} to Fo_{88}). The water content of olivine (Lab1) ranges from 2.5 to 5.4 ppm wt H_2O (Fig.III.7).

Groundmass cpx (< 30 µm) has diopsidic composition ($En_{40}Wo_{49}Fs_{11}$) with relative low Mg# (Mg# 78 - 79) (Fig.III.8), high TiO_2 content (2.5 - 3 wt %), low Na_2O (0.7 - 0.9 wt %) and Al_2O_3 (1.4 - 2 wt %) contents, and very low Cr_2O_3 content (< 0.01 wt %) (Fig.III.8).

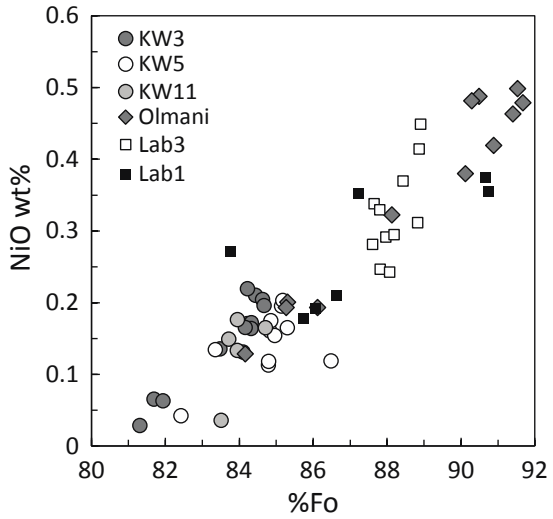

Fig.III.6 *NiO vs Fo content of olivine from Kwaraha (Kw3, Kw5, Kw11), Labait (Lab1, Lab3) and Olmani lavas.*

Table 2: Major element compositions of minerals

Sample	Kw3	Lab1	Olm1b	Olm1b	Olm1b	Kw3	Kw3	Kw5	Kw11	Kw11	Lab1	Kw3	Lab3
Mineral	ol	ol	ol	cpx	cpx	cpx	cpx	cpx	cpx	cpx	phl	phl	pl
Type	core	core	core	core	rim	core	core	core	core	core	core	core	core
SiO_2	40.96	40.71	40.60	52.02	45.86	52.12	50.55	52.97	53.50	50.15	39.97	38.30	61.76
TiO_2	0.06	0.03	0.00	0.84	3.55	0.85	0.85	0.58	0.55	1.50	3.26	3.61	0.02
Al_2O_3	0.03	0.06	0.02	2.32	6.28	2.03	2.34	1.33	1.37	2.39	12.43	14.03	24.01
FeO	11.35	8.89	14.24	3.77	6.82	5.49	11.17	4.34	3.96	9.09	8.89	7.69	0.04
MnO	0.19	0.12	0.22	0.07	0.09	0.11	0.22	0.07	0.06	0.20	0.04	0.04	0.00
MgO	46.69	49.61	44.28	15.56	12.35	15.04	10.88	16.22	15.85	11.68	19.77	20.02	0.00
CaO	0.29	0.12	0.21	23.67	23.62	23.53	22.83	23.31	22.32	23.03	0.01	0.05	5.41
Na_2O	0.00	0.03	0.04	0.44	0.41	0.84	1.48	0.66	0.88	0.94	0.76	0.08	8.06
K_2O	0.01	0.00	0.00	0.00	0.01	0.00	0.00	0.01	0.00	0.01	9.89	10.68	0.45
Cr_2O_3	0.07	0.10	0.03	0.91	0.11	0.03	0.03	0.49	1.11	0.00	n.a.	n.a.	0.00
NiO	0.25	0.36	0.16	0.02	0.03	0.01	0.03	0.01	0.05	0.00	n.a.	n.a.	0.00
F	n.a.	n.a.	n.a.	n.a.	n.a.	n.a.	n.a.	n.a.	n.a.	n.a.	0.78	0.42	
Total	99.90	100.02	99.81	99.62	99.20	100.05	100.30	99.97	99.64	99.01	95.84	94.92	99.76
Mg#	87.8	90.7	84.5	88.0	73.4	82.9	63.3	86.9	87.7	69.6	79.8	82.2	
Numbers of ions on the basis of													
	4O			***6O***							***24O***		***8O***
Si	1.01	1.02	1.02	1.91	1.73	1.91	1.89	1.94	1.96	1.90	5.68	5.50	2.76
Al^{IV}	-	-	-	0.09	0.27	0.09	0.10	0.06	0.04	0.10	2.08	2.38	-
Al^{VI}	-	-	-	0.01	0.00	0.00	0.00	0.00	0.02	0.00	0.00	0.00	-
Al tot	0.00	0.00	0.00	-	-	-	-	-	-	-	-	-	1.26
Ti	0.00	0.00	0.00	0.02	0.10	0.02	0.02	0.02	0.02	0.04	0.35	0.39	0.00
Fe^{2+}	-	-	-	0.09	0.12	0.07	0.17	0.06	0.11	0.20	-	-	0.00
Fe^{3+}	-	-	-	0.03	0.10	0.10	0.18	0.07	0.01	0.08	-	-	0.00
Fe tot	0.23	0.18	0.30	-	-	-	-	-	-	-	1.06	0.92	-
Mn	0.00	0.00	0.00	0.00	0.00	0.00	0.01	0.00	0.00	0.01	0.00	0.00	0.00
Mg	1.72	1.78	1.65	0.85	0.69	0.82	0.61	0.88	0.87	0.66	4.19	4.29	0.00
Ca	0.01	0.00	0.01	0.93	0.95	0.92	0.91	0.91	0.88	0.93	-	-	0.26
Na	-	-	-	0.03	0.03	0.06	0.11	0.05	0.06	0.07	0.21	0.02	0.70
K	-	-	-	0.00	-	-	0.00	-	-	-	1.79	1.96	0.03
Ni	0.00	0.01	0.00	-	-	-	-	-	-	-	-	-	-
Cr	-	-	-	0.03	0.00	0.00	0.00	0.01	0.03	0.00	-	-	-
OH	-	-	-	-	-	-	-	-	-	-	3.65	3.81	-
F	-	-	-	-	-	-	-	-	-	-	0.35	0.19	-
Total	3	3	3	4	4	4	4	4	4	4	19.36	19.43	5

Mg# = Mg/(Mg+Fe)*100; n.a.: not analyzed; ol: olivne; cpx: clinopyroxene; phl: phlogopite; pl: plagioclase.

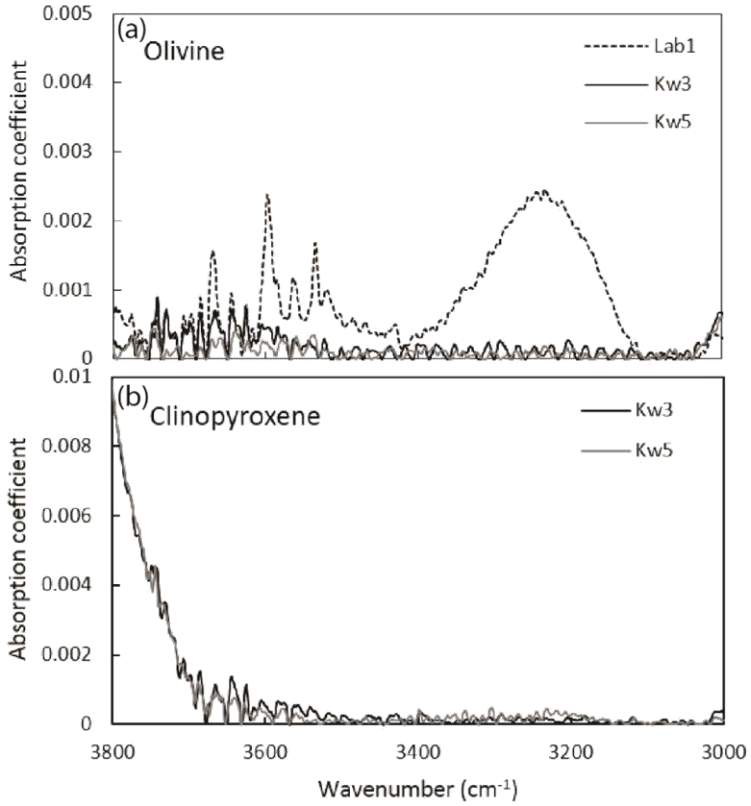

Fig.III.7 *Representative FTIR spectra of unoriented (a) olivine and (b) cpx from Labait and Kwaraha lavas. All spectra are normalized to 1 cm of thickness.*

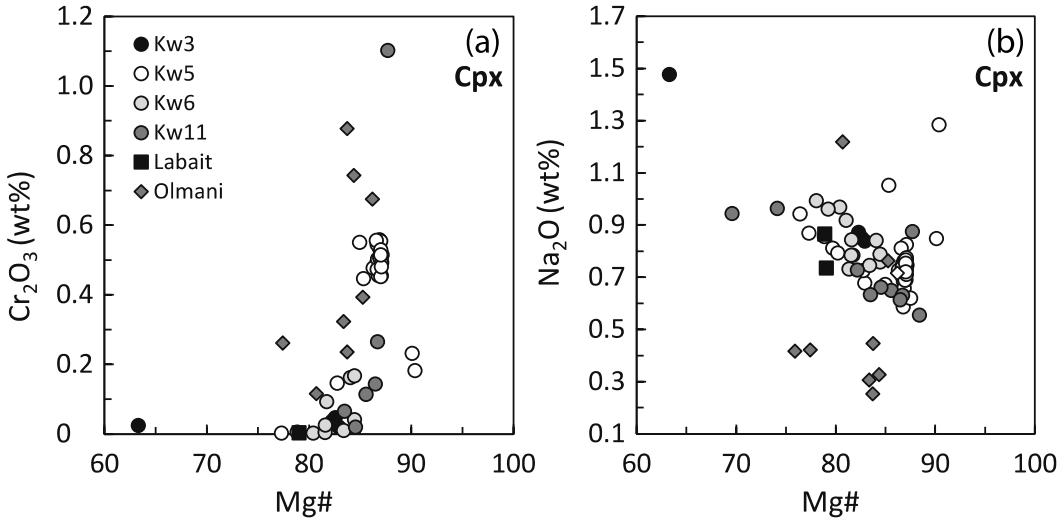

Fig.III.8 *(a) Cr_2O_3 and (b) Na_2O vs Mg# of clinopyroxene from Kwaraha, Labait and Olmani lavas.*

Phlogopite phenocryst (Mg# = 80) has relatively low F (0.8 ± 0.2 wt% F), Ti (3.2 wt % TiO_2) and Al contents (12.4 wt % Al_2O_3). Phlogopite is extremely enriched in trace elements with REE concentrations up to 200 times chondritic values (Fig.III.9). Trace element concentrations are 49 - 137 ppm La and 418 - 1188 ppm Sr (Table 3). Phlogopite from Labait has a negative anomaly in HFSE (Fig.III.9).

Nepheline is present as groundmass Fe-rich microcrystals (10-20 µm) (2.3 - 3.4 wt % FeO). Plagioclase within Labait lavas (Lab3) are oligoclase with low An content (An_{25} to An_{27}) and high LILE contents (943 - 1112 ppm Sr, 371 - 1249 ppm Ba and 2093 - 2245 ppm Rb) (Fig.III.A1, sup material).

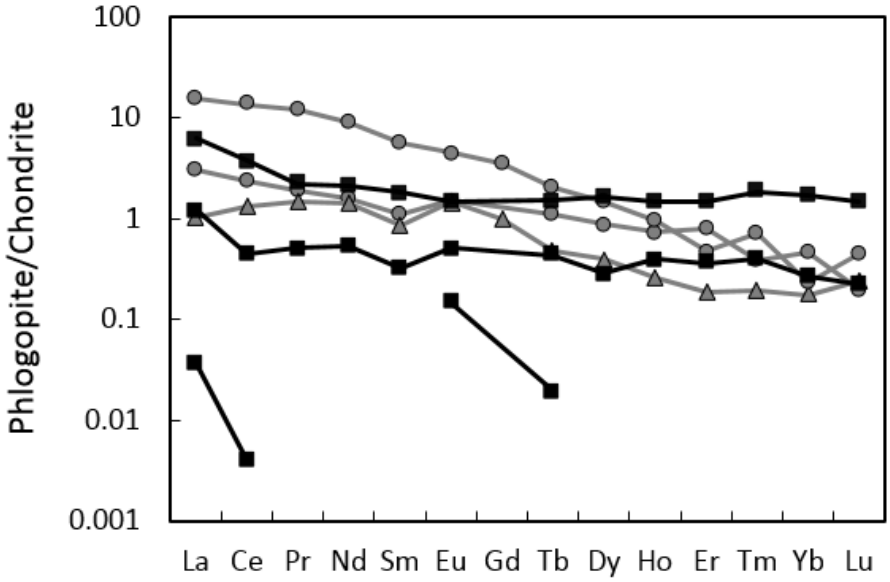

Fig.III.9 *(a) Normalized REE from Kwaraha (circle) and Labait (square). Chondrite values from Sun and McDonough (1989).*

Labait lavas have oxide phases including magnetite (7.3 - 8.6 wt % TiO_2, 0.8 - 1.2 wt % MgO), Cr-magnetite (30 - 50 wt % Cr_2O_3, 3.5 - 7.5 wt % TiO_2), Mg-magnetite (8.9 - 9.4 wt % TiO_2, 15 - 17.4 wt % MgO), and perovskite (55.2 wt % TiO_2) (Table 4).

Apatite from Labait is fluorapatite (3 - 4 wt % F) with low Cl (< 0.02 wt %) and SO_3 (0.02 - 0.09 wt %) content. Sulfides are Ni-rich pyrrhotites (5.7 wt % Ni, 0.06 wt % Cu, 37.6 - 38.8 wt % S, Pd/Ir = 2 - 41) with a rim of chalcopyrite (0.2 wt % Ni, 31.5 wt % Cu, 34.7 wt % S).

Table 3: Trace element concentrations of minerals

Sample	Kw3	Lab1	Olm1b	Olm1b	Kw3	Kw5	Kw5	Kw11	Kw11	Lab1	Kw3	Lab3
Mineral	ol	ol	cpx	cpx	cpx	cpx	cpx	cpx	cpx	phl	phl	pl
Type	core	core	core	rim	core	core	core	core	core	core	core	core
Cs (ppm)	0.01	0.01	0.01	0.01	0.18	0.01	0.01	< 0.01	< 0.01	3.32	1.94	135
Rb	0.09	0.06	0.01	0.34	0.50	0.03	0.03	< 0.01	< 0.01	558	314	2245
Ba	0.11	0.14	0.04	26.1	3.45	0.11	0.10	0.06	0.05	2383	2014	1250
Th	0.00	0.00	0.03	0.46	0.21	0.01	0.04	0.02	0.02	0.01	-	0.47
U	-	0.02	< 0.01	0.08	< 0.01	-	-	-	< 0.01	1.50	0.09	0.55
Nb	0.05	0.36	0.27	5.17	2.62	0.92	0.4	0.19	0.28	15.8	6.67	19.4
Ta	0.00	0.02	0.05	0.67	0.34	0.13	0.14	0.04	0.02	1.42	0.47	0.53
La	0.01	0.01	3.48	13.6	49.8	4.57	4.75	3.29	8.12	48.6	0.62	6.67
Ce	0.01	0.09	11.51	36.5	148	16.0	15.5	11.0	17.5	29.3	0.11	11.9
Pr	0.00	0.00	1.83	4.8	24.3	2.69	2.6	1.87	2.33	5.61	0.04	0.93
Sr	0.02	0.08	105	138	790	216	155	124	303	418	142	1282
Nd	0.04	0.03	9.24	22.0	127	12.7	12.6	9.33	10.1	26.5	0.22	3.09
Zr	0.73	0.55	29.3	113	419	320	110	49.2	110	49.2	8.72	68.6
Hf	0.01	0.01	1.50	5.74	23.9	9.62	5.65	2.41	4.13	0.9	0.12	1.00
Sm	0.02	0.01	2.43	4.64	32.2	2.72	3.07	2.49	1.94	6.00	0.05	0.53
Eu	0.01	0.01	0.76	1.31	10.7	0.86	0.91	0.72	0.60	2.66	0.04	0.46
Gd	0.08	0.07	2.04	3.88	23.2	2.34	2.65	2.02	1.63	10.8	0.23	0.68
Tb	0.00	0.01	0.27	0.51	3.66	0.29	0.33	0.26	0.23	2.21	0.04	0.08
Dy	0.05	0.01	1.44	2.59	16.1	1.71	1.91	1.32	1.10	13.9	0.31	0.49
Y	0.45	0.13	6.17	10.4	58.4	6.26	6.08	4.62	4.09	141	3.76	2.80
Ho	0.02	0.01	0.28	0.42	2.66	0.29	0.28	0.20	0.17	3.75	0.09	0.10
Er	0.05	0.01	0.58	0.92	6.04	0.73	0.63	0.42	0.43	12.7	0.30	0.28
Tm	0.02	0.00	0.06	0.10	0.76	0.12	0.08	0.05	0.06	2.11	0.05	0.04
Yb	0.13	0.04	0.42	0.69	2.56	1.27	0.47	0.32	0.43	10.9	0.31	0.23
Lu	0.04	0.01	0.04	0.11	0.49	0.28	0.07	0.05	0.09	1.63	0.04	0.03

ol: olivne; cpx: clinopyroxene; phl: phlogopite; pl: plagioclase.

Table 4: Major element compositions of oxides

Sample	Kw5	Kw5	Kw1	Olmb	Lab3	Lab3	Lab1
Mineral	mag	chr	mag	chr	chr	mag	prv
SiO_2 (wt%)	0.08	0.11	0.07	0.20	0.82	0.20	0.09
TiO_2	18.17	4.23	0.02	4.75	7.59	13.47	55.19
Al_2O_3	1.87	7.53	0.00	10.24	5.26	1.29	0.14
FeO	71.29	34.14	90.78	40.62	49.98	71.76	1.00
MnO	0.67	0.34	0.37	0.54	0.82	0.80	0.00
MgO	4.48	9.74	0.07	7.28	5.60	4.16	0.00
CaO	0.03	0.01	0.07	0.27	0.38	0.28	36.97
Na_2O	0.05	0.02	0.00	0.01	0.23	0.03	0.00
K_2O	0.01	0.00	0.00	0.04	0.16	0.03	0.05
Cr_2O_3	0.01	42.55	0.03	31.69	23.38	0.98	0.02
NiO	0.03	0.06	0.00	0.11	0.09	0.10	0.00
Total	96.69	98.75	90.78	95.75	94.32	93.11	94.57

mag: magnetite; chr: chromite; prv: perovskite.

IV.2 Olmani volcano

IV.2.1 Petrography and whole rock geochemistry

The melilite nephelinitic lavas from Olmani have olivine (13 - 18 vol %, 1 - 2 mm), euhedral zoned cpx (5 - 10 vol%, 1 - 2 mm), magnetite (< 0.5 vol %, 100 - 200 µm) phenocrysts and microcrystals of nepheline, cpx and magnetite in the groundmass.

Olmani lavas have high Mg# values (Mg# ~ 74, MgO = 18.1-18.2 wt %), low peralkaline index (Na+K/Al = 0.64 - 0.7) and K_2O/Na_2O ratio (0.56 - 0.57). These lavas have also high content in CaO (11.5 - 11.6 wt % CaO) and in Al_2O_3 (~ 7.7 wt % Al_2O_3). They have low whole rock concentrations in volatile elements with 0.01 - 0.07 wt % CO_2, 200 - 300 ppm S, 1300 - 1500 ppm F, and 295 - 490 ppm Cl.

Olmani lavas have high incompatible element concentrations up to 340 times chondrite for REE. REE patterns show an enrichment in LREE compared to HREE (62.8 - 81.1 ppm La, 0.14 - 0.18 ppm Lu, La/Sm = 10.1 - 10.3, La/Yb = 62.2 - 63.5) (Fig.III.5a). Trace element concentrations show a negative anomaly in K and Zr-Hf (Fig.III.5b). Lavas have high content in LILE (e.g. 570 - 793 ppm Ba) and relatively low content in HFSE (e.g. 126 -168 ppm Zr) (Fig.III.5b). Olmani lavas display high trace element ratios in Zr/Hf (40.3 - 42), Ce/Y (8.1 - 8.2), Nb/U (59.4 - 63.8), Rb/Sr (0.06 - 0.07) and low ratios in Zr/Nb (1.5 - 1.6) and Ba/Rb (17.4 - 19.5). Olmani lavas are characterized by high content in Cr (672 - 970 ppm) and Ni (505 - 647 ppm).

IV.2.2 Mineral chemistry

Olivine from Olmani lavas has a high Fo (Fo_{91} to Fo_{84}) and NiO content (0.55 - 0.14 wt % NiO) (Fig.III.6). Olivine phenocrysts are normally zoned with decreasing MgO and NiO content from core to rim and increasing CaO content (0.05 - 1.3 wt %).

Cpx phenocryst has MgO content ranging from 15.7 wt % to 11.4 wt % (Mg# 88.2 - 62) and diopsidic composition ($En_{36-45}Wo_{46-56}Fs_{6-22}$) with high Al^{VI}/Al^{IV} (0.28 - 1.9) ratio. Cpx are zoned, with Ti-poor (0.84 - 1.33 wt % TiO_2), Al-poor (2.18 - 3.7 wt % Al_2O_3) and Cr-rich core (0.1 - 0.9 wt % Cr_2O_3) relative to the rim (1.05 - 3.55 wt % TiO_2, 3.84 - 6.50 wt % Al_2O_3, 0.05 - 0.24 wt % Cr_2O_3) (Table 2). REE patterns show a convex shape enriched in LREE compared to HREE (3.5 - 5.6 ppm La, 0.05 - 0.2 ppm Lu, La/Yb = 3 - 13) (Table 3). The rims are enriched in LREE relative to the core (Fig.III.10). Cpx has relatively low content of Zr (26 – 112 ppm), and Sr (101 – 141 ppm) (Fig.III.11).

Nepheline is present as groundmass microcrystals and has a small variation in major elements as 42.6 - 43.3 wt % SiO_2, 12.8 - 13.5 wt % Na_2O and 1.3 - 2.9 wt % FeO.

Olmani lavas contain magnetite (7.3 - 16.2 wt % TiO_2, 0.8 - 1.2 wt % MgO) with ilmenite lamella (33.4 - 45.35 wt % TiO_2), and Cr-magnetite (48.4 - 48.7 wt % Cr_2O_3). Magnetite has high content in HFSE (10 - 144 ppm Nb, 11 - 40 ppm Zr) (Table 4) (Fig.III.A2, sup material).

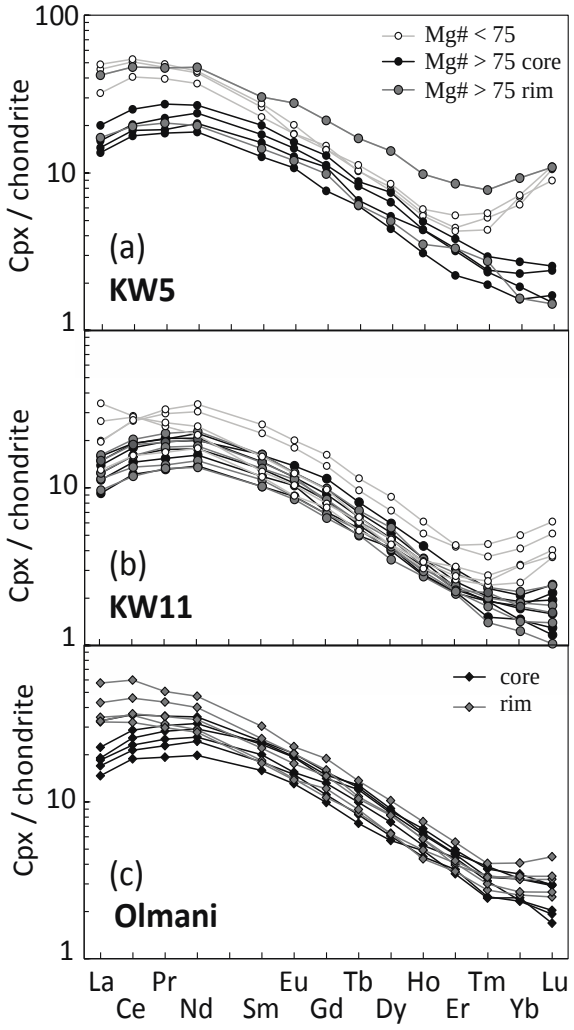

Fig.III.10 *Normalized REE content of clinopyroxene from (a)(b) Kwaraha and (c) Olmani. Chondrite values from Sun and McDonough (1989).*

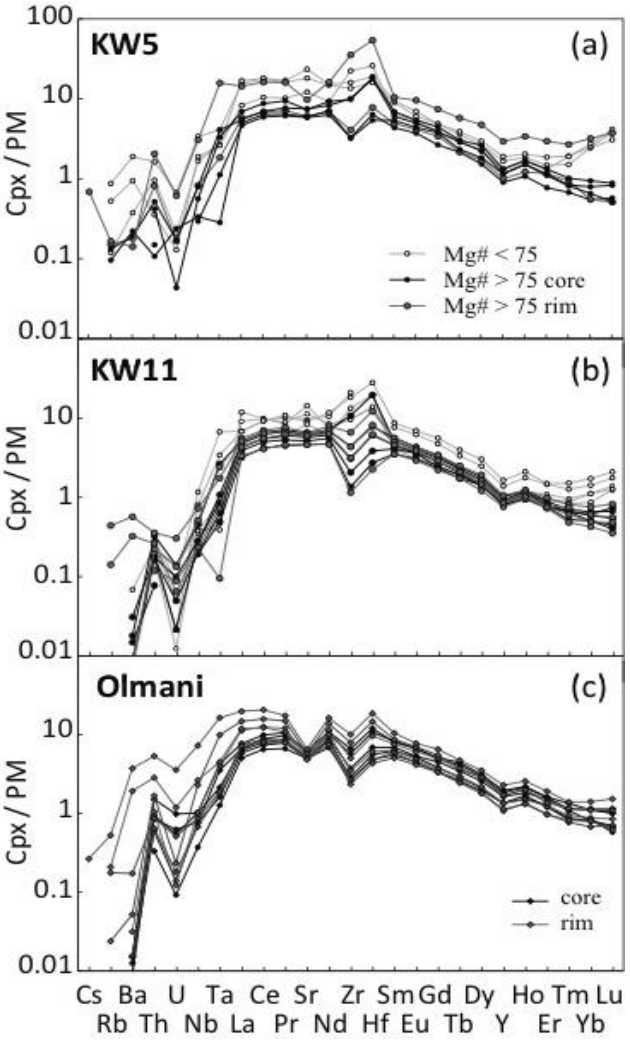

Fig.III.11 *Normalized trace element content of clinopyroxene from (a)(b) Kwaraha and (c) Olmani. Primitive mantle values from Sun and McDonough (1989).*

IV.3 Kwaraha volcano

IV.3.1 Petrography and whole rock geochemistry

The 10 samples of Kwaraha volcano are melilite nephelinites (n = 9) from the small volcanic cones and one carbonatite (Kw1) from the main volcanic center (Fig.III.3).

The melilite nephelinitic rocks contain phenocrysts of olivine (2 - 13 vol %, 0.2 - 7 mm), clinopyroxene (4 - 12 vol %, 0.2 - 8 mm), phlogopite (0 - 4 vol %, 0.2 - 10 mm), and magnetite (1 - 5 vol %, 0.5 mm). Olivine, cpx, nepheline and rare apatite occurred as microcrystals in the groundmass. Kwaraha silicate lavas have relatively high Mg# values, ranging from 67 to 56 (MgO = 13.9 - 8.65 wt %). These lavas have variable peralkaline index (Na+K/Al = 0.4 - 1), alkali content (Na_2O+K_2O = 1.9 - 5.6 wt %), K_2O/Na_2O ratio (0.6 - 1.5)

(Fig.III.4) and very high CaO (12.9 - 15.6 wt % CaO) and moderate Al_2O_3 (6.55 - 9.02 wt % Al_2O_3) content. They have variable whole rock concentrations in volatile elements with 0.1 - 3.1 wt % CO_2, 100 - 300 ppm S, 1400 - 2600 ppm F, and 33 - 1150 ppm Cl.

Kwaraha lavas have high incompatible element concentrations up to 350 times chondrite for REE. REE patterns show an enrichment in LREE compared to HREE (68.2 - 82.2 ppm La, 0.18 - 0.24 ppm Lu, La/Sm = 6.9 - 9.7, La/Yb = 46.1 - 62.4) (Fig.III.5a). These lavas have high content in LILE (673 - 1225 ppm Ba, 643 - 1009 ppm Sr) and relatively low content in HFSE (168 - 259 ppm Zr) (Fig.III.5b). Trace element concentrations show a negative anomaly in K and Zr-Hf (Fig.III.5b) and high trace element ratios in Zr/Hf (39.2 - 45), Ce/Y (6.05 - 7.53), Nb/U (45.8 - 52), Rb/Sr (0.04 - 0.12) and low ratios: Zr/Nb (1.9 - 2.8), Ba/Rb (10.3 - 33.9). Kwaraha parasitic cones (Kw2 to Kw12) are characterized by relatively low content in Cr (110 - 367 ppm) and Ni (60 - 145 ppm).

The carbonatite from Kwaraha volcano (Kw1) has calcite (200 µm, 92 vol %), euhedral apatite (50 µm, 3 vol %) and magnetite (40 - 800 µm, 5 vol %). The carbonatite is a calciocarbonatite with 62.1 wt % CaO and 33 wt % CO_2 and low content in MgO (0.51 wt %) and alkali elements (0.26 wt % Na_2O, 0.15 wt % K_2O). Calciocarbonatite has low content in sulfur (70 ppm S), fluorine (880 ppm F) and chlorine (47 ppm Cl). Calciocarbonatite (Kw1) is enriched in Sr (3080 ppm Sr), and LREE (266 ppm La, La/Yb = 58.8) (Fig.III.5a), very depleted in HFSE (e.g. Zr = 26.3 ppm) and shows a Zr-Hf and Nb-Ta fractionation (Zr/Hf = 59.5, Nb/Ta = 87.2) (Fig.III.5b).

IV.3.1 Mineral chemistry

Olivine from Kwaraha lavas has a high Fo (Fo_{86} to Fo_{81}) and NiO (0.23 -0.04 wt% NiO) content (Fig 6). Olivine phenocrysts are zoned with decreasing MgO and NiO contents from core to rim and increasing CaO (0.17 - 0.83 wt %) content. Olivine from Kwaraha have a very low water content (< 2 ppm wt H_2O) (Fig.III.7; Table 5).

There is 2 types of cpx phenocrysts, high Mg# cpx (Mg# 90 - 77) and rare low Mg# cpx (Mg# = 63 - 74), both have a diopsidic compositions ($En_{35-48}Wo_{47-52}Fs_{2-16}$). High Mg# cpx phenocrysts have 16.4-13.44 wt % MgO, 3.5- 0.3 wt % Al_2O_3 (Al^{VI}/Al^{IV} = 0.89 - 0.56) and up to 1.1 wt % Cr_2O_3 (Fig.III.8). REE patterns show a concave shape enriched in LREE compared to HREE (2 - 60 ppm La, 0.02 - 0.5 ppm Lu, La/Yb = 4 - 19) (Fig.III.10). Trace element analyses display relatively low content of Zr (12 - 480 ppm), and Sr (100 - 870 ppm) (Fig.III.10; Table 3). Low Mg# cpx (Mg# = 63 - 74) have very low Cr_2O_3 content (< 0.01 wt %), high Na_2O (0.94 - 0.96 wt % Na_2O) and are enriched in REE content compared to high Mg# cpx (Fig.III.10). Cpx from Kwaraha (Kw3, Kw5) are dry with < 2 ppm wt H_2O (Fig.III.7; Table 5).

Table 5: Water content in olivine and cpx and calculated parental melt

Sample	Mineral	ppm wt H_2O	$H/10^6Si$	Area[a]	Melt[b]
Lab1	olivine	5.3	86.5	44.8	0.41
Lab1	olivine	2.5	41.1	18.4	0.19
Lab1	olivine	5.5	89.2	47.2	0.42
Lab1	olivine	4.3	70.7	32.4	0.33
Lab1	olivine	4.9	80.4	39.6	0.38
Lab1	olivine	6.6	108.1	67.2	0.51
Lab1	olivine	5.9	96.5	54.4	0.45
Kw3	olivine	1.2	19.3	6.7	0.09
Kw3	olivine	1.7	27.9	9.3	0.13
Kw5	olivine	0.7	11.6	4.6	0.05
Kw5	olivine	0.6	10.4	4.3	0.05
Kw3	cpx	0.5	7.9	3.7	0.004
Kw3	cpx	1.7	27.0	10.3	0.013
Kw3	cpx	1.5	25.0	9.6	0.012
Kw5	cpx	0.4	7.0	3.3	0.004
Kw5	cpx	0.4	6.4	3.1	0.004
Kw5	cpx	0.3	5.7	2.8	0.003

[a] Integrated unpolarized absorbance normalised to 1 cm of thickness
[b] Melt composition calculated using $Kd^{olivine/melt}$ and $Kd^{cpx/melt}$ from Hauri et al. (2006) and Audaud et al. (2004)

Phlogopite is present in almost all samples with F-poor content (0.2 - 0.7 ± 0.2 wt % F). Phlogopite from Kw3 contains 1.57 - 2.12 wt % H_2O (KFT analyses). Phlogopites as inclusions in cpx and phenocrysts have the same composition (Mg# = 79 - 83, 3.1 - 3.6 wt % TiO_2, 13.5 - 14 wt % Al_2O_3) than interstitial phlogopite. Phlogopite has variable trace element concentrations in REE (0.03 - 32.8 ppm La), in HFSE (5 - 426 ppm Zr) and LILE (42 - 2261 ppm Sr) (Fig.III.9; Table 3).

Nepheline is present in all samples as groundmass microcrystals. Nepheline has a small variation in major elements with 39.5 - 40.5 wt % SiO_2, 10.75 - 11 wt % Na_2O and 1.6 - 1.7 wt % FeO.

Kwaraha lavas have different types of opaque phases as Ti-magnetite (18.1-18.6 wt % TiO_2, 4.5 - 5.6 wt % MgO), magnetite (0.03 wt % TiO_2, 0.1 - 0.2 wt % MgO), and rare Cr-magnetite (42.55 wt % Cr_2O_3). Magnetites contain low content in HFSE (7 - 75 ppm Nb, 16 - 39 ppm Zr). Apatite in the nephelinite is F-rich (3 - 4 wt % F), Cl-poor (< 0.02 wt %) and SO_3-poor (0.01 - 0.07 wt %).

Calciocarbonatite (Kw1) has calcite with 50.3 - 55.6 wt % CaO, 0.12 - 0.53 wt % Na_2O, 0.06 - 0.68 wt % MgO and 0.03 - 0.13 wt % FeO and high content in trace elements (i.e. 94 - 112 ppm La and 934 - 4225 ppm Sr). Oxide from Kw1 is magnetite with 0.08 - 0.82 wt % TiO_2, and 0.07 - 0.25 wt % MgO and < 0.02 wt % Cr_2O_3 (Table 4). Apatite is F-rich (3.5 - 4.5 wt % F), Cl-poor (< 0.01 wt %) and SO_3-poor (0.01 - 0.03 wt %) with REE concentrations up to 10000 times chondritic values (Table 6) (Fig.III.A3, sup material).

Table 6: Major and trace element compositions of apatite and calcite

	Kw1 ap	Kw1 ap	Kw1 cc	Kw1 cc	Kw3 ap	Kw3 ap	Lab1 ap	Lab1 ap
SiO_2 (wt %)	0.03	0.02	0.01	0.01	0.30	0.27	0.77	0.41
FeO	0.04	0.04	0.13	0.13	bdl	bdl	bdl	bdl
MnO	0.04	0.05	0.24	0.24	bdl	bdl	bdl	bdl
CaO	52.60	53.26	53.79	54.07	56.88	56.99	53.86	54.73
Na_2O	0.14	0.13	0.53	0.20	bdl	bdl	0.01	0.06
K_2O	bdl	bdl	0.01	0.01	0.17	0.02	bdl	bdl
P_2O_5	43.46	44.12	0.20	n.a.	41.92	40.71	39.96	40.16
SO_2	bdl	0.01	bdl	bdl	0.01	0.06	0.05	0.07
Cl	0.00	bdl	bdl	bdl	0.00	0.00	bdl	bdl
F	4.87	4.13	bdl	bdl	2.58	3.40	5.07	4.31
Total	101.04	101.69	54.91	54.66	101.82	101.35	99.73	99.75
Cs (ppm)	0.57	0.55	0.21	0.02				
Rb	6.11	22.5	17.9	2.01				
Ba	302	1235	254	104				
Th	50.2	52.1	7.64	4.97				
U	1.14	1.13	2.88	0.28				
Nb	6.67	9.04	2.66	0.34				
Ta	< 0.02	0.55	0.42	0.03				
La	3268	5935	113	94.0				
Ce	10565	20145	293	246				
Pr	983	654	26.7	26.9				
Sr	13568	32382	934	4224.7				
Nd	932	1515	95.3	117				
Zr	51.3	25.7	174	19.5				
Hf	0.62	0.70	3.91	0.53				
Sm	182	176	13.5	20.7				
Eu	68.8	63.3	3.44	5.57				
Gd	318	255	9.90	15.4				
Tb	9.12	12.0	1.17	1.66				
Dy	33.7	77.7	5.70	7.52				
Y	98.1	170	34.5	24.4				
Ho	5.59	9.78	1.13	1.02				
Er	9.50	15.2	2.79	2.09				
Tm	1.72	2.21	0.44	0.20				
Yb	9.97	11.5	2.05	1.13				
Lu	1.13	1.62	0.39	0.11				

bdl: below detection limite; n.a.: not analyzed; ap: a patite; cc: calcite.

III.V Discussion

V.1 Origin of the nephelinites

Alkaline mafic lavas such as melilitites and nephelinites represent the more primitive magma erupted in intracontinental setting. High incompatible element content and strong fractionation of LREE and HREE (Dautria et al. 1992, Ivanikov et al. 1998, Platz et al. 2004, Keller et al. 2006) have been proposed as the result of very low degree of partial melting of

CO_2-bearing lherzolite (Green and Falloon 1998, Herzberg and O'Hara 1998, Foley et al. 2009, 2012).

Melilite nephelinites have high Mg# and Cr, Ni content (Table 1). The chemical features is characteristics of primary lavas (e.g. Baasner et al. 2016). Although Labait lavas show accumulation of olivine (high Mg# = 76 - 79, Fig.III.A4) and Kwaraha lavas with Mg# < 60 and low Ni content show small fractional crystallization of olivine (2 %) and cpx (2.5 %). Accumulation and fractional crystallization have only a minor effect on trace element and all melilite nephelinites are considered as primary magmas.

The deep mantle source of Labait, Kwaraha and Olmani lavas is unknown. Lithospheric mantle (spinel facies) beneath Olmani volcano has been sampled (Rudnick et al. 1993). Tanzanian mantle sampled by xenoliths is heterogeneous with garnet or spinel peridotite including occasionally amphibole and phlogopite (Gibson et al. 2013, Dawson and Smith 1988). Xenoliths carried out by lavas represent mantle at different depth. Assuming garnet peridotite theoretical chemical composition (Sun and McDonough 1989), partial melting of garnet peridotite give high Ce/Y ~ 3, low Rb/Sr (< 0.04) and Zr/Hf ratios and cannot lead to melilite nephelinite composition (Ce/Y > 5, Rb/Sr >0.04, Zr/Hf = 39.2 -46). Trace elements such as Y and Sr are compatible in garnet and phlogopite, respectively and can account for the high Ce/Y and Rb/Sr in the melt (MacDonald et al. 2001; Foley and Jenner 2004; Platz et al. 2004, Rogers et al. 1992). Garnet-rich and phlogopite-bearing mantle source melting led to low Zr/Nb, high Ce/Y fractionations and Zr/Hf fractionation indicating a carbonated mantle source (Rudnick et al. 1993).

Garnet-rich and phlogopite-bearing peridotite source (62 % olivine, 16 % opx, 10 % cpx, 10 % garnet, 2 % phlogopite) with no modal fractional melting (degree of partial melting < 5 %) are necessary to model melilite nephelinite compositions. In addition, the presence of small amount of carbonate in the source can reproduced high Zr/Hf fractionation observed for Labait (Zr/Hf = 42.6 - 46). We model partial melting of carbonated mantle with 0.3% and 1% of carbonatitic component (Fig.III.12). The best fit for partial melting suggest that melilite nephelinites result from a very low degree of partial melting (< 1 %) of peridotite (Fig.III.12), similar to those observed for nephelinites from Engaruka-Natron basin (Mattsson et al. 2013) and Essimingor (Mana et al. 2012) in north Tanzania (Fig.III.12). The variation of trace elements among the different volcanoes (Olmani, Labait and Kwaraha) suggest that different degree of partial melting (0.2 - 1 %) and heterogeneous deep mantle source with carbonatitic rich component (0.2 - 0.5 %, Labait) (Fig.III.12).

The presence of garnet and phlogopite in the mantle source of nephelinite suggests that partial melting occur at depth > 80 km (McKenzie and O'Nions 1991, Foley, 1993, Sato et al., 1997). The occurrence of mantle xenoliths in Labait nephelinites with equilibrium conditions between 100 to 147 km (3.2 to 4.9 GPa), suggesting that partial melting of nephelinite occurred at ≥ 150 km (Lee and Rudnick 1999). The high CaO/Al_2O_3 ratio of Olmani and Kwaraha Lavas (1.5 - 1.52, 1.7 - 2.2, respectively) corroborate a high pressure melting at > 90 km (Baker and Stolper 1994). This is also constrained by empirical equation from Albarède 1992, calibrated for partial melting conditions and basalt products, and based on SiO_2 (SiO_2/Al_2O_3 = 5.46 - 5.49, 4.9 - 5.76) and MgO (MgO/CaO = 1.56 - 1.58, 0.81 - 1.05)

content of primary melt indicating that melting pressure was at ~ 120 km (4 GPa) for Olmani and 110 to 130 km (3.7 - 4.3 GPa) for Kwaraha lavas, below or close to the lithosphere-asthenosphere boundary (Craig et al. 2011).

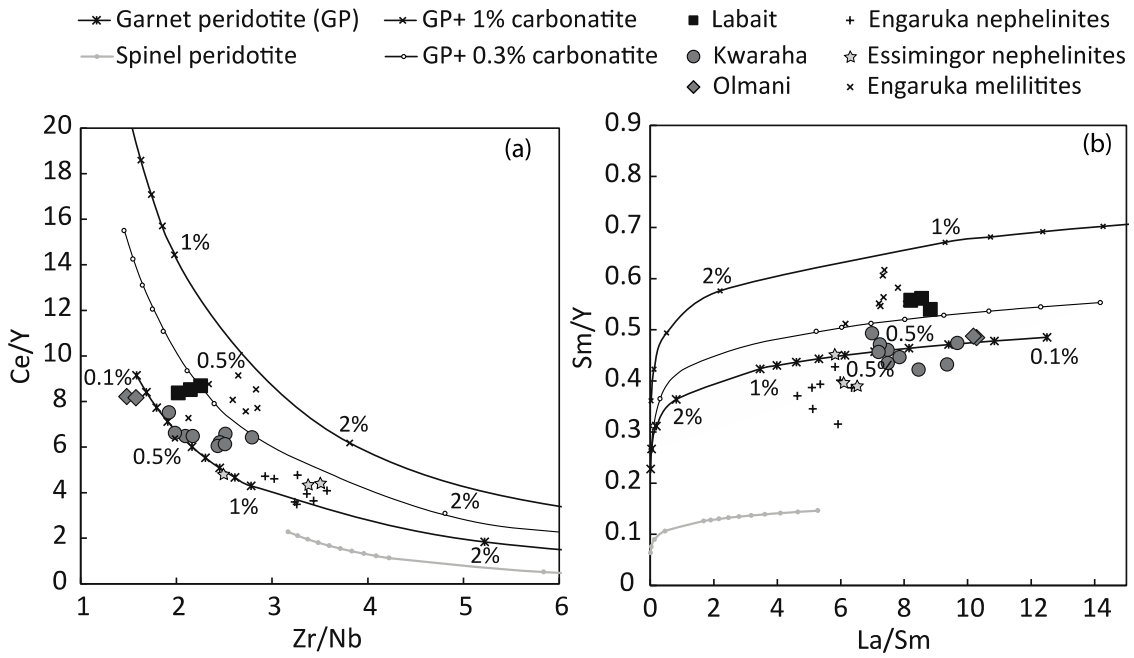

Fig.III.12 *Modelling of primary mantle melting for Kwaraha and Labait lavas using (a) Ce/Y vs Zr/Nb ratios and (b) Sm/Y vs La/Sm ratios. The partial melting was modelled with no modal fractional melting from a garnet peridotite with olivine 62%, orthopyroxene 16%, clinopyroxene 10%, garnet 10% and phlogopite 2% and from a garnet peridotite with the addition of 0.3% and 1% of carbonatite (Kw1 composition). Nephelinites and melilitites from Engaruka-Natron basin (Mattsson et al. 2013) and nephelinites from Essimingor (Mana et al. 2012) are also reported.*

V.2 Crystallization environment and volatile concentrations

Temperature, pressure and volatile contents are key parameters which control phase equilibria and minerals, melt and gas compositions and further magmatic evolution including fractional crystallization and immiscibility, and degassing processes (Carmichael and Ghiorso 1990, Toplis and Caroll 1995, Mavrogenes and O'neill 1999, Berndt et al. 2005).

Pressure and temperature have a major role in phase equilibrium and magmatic differentiation. The composition of cpx in mafic magmas is strongly dependent of melt composition, pressure and temperature conditions of crystallization. Cpx of melilite nephelinite have Kd(Fe^{2+}/Mg) ranging from 0.2 to 0.41 for Kwaraha and 0.39 and 0.44 for Olmani suggesting that cpx are close to equilibrium with silicate liquid and are suitable for calculation of the pressure and temperature conditions of nephelinite crystallization.

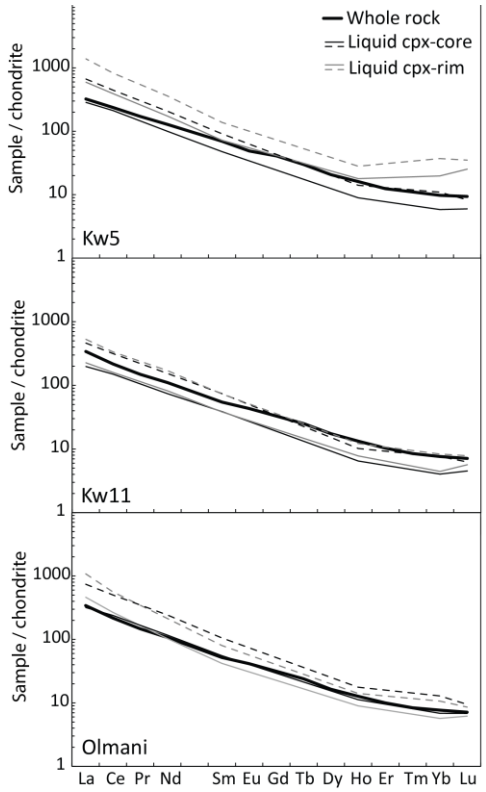

Fig.III.13 *Recalculated melt in equilibrium with cpx used to determine P–T conditions (minimal and maximal partition coefficient from Adam and Green 2006) and whole-rock composition (WR)*

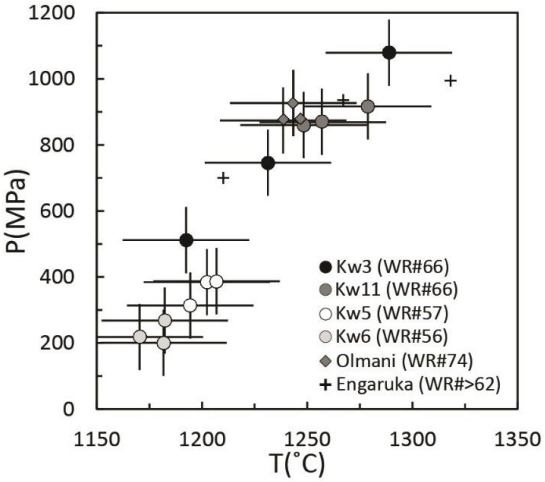

Fig.III.14 *P–T conditions calculated from cpx-liquid thermobarometer (Putirka 2008) for Kwaraha, Olmani and Engaruka-Natron (Mattsson et al. 2013) nephelinites.*

This is corroborated by the concentration of trace elements of cpx, that reflected equilibrium with whole rock using partition coefficients determined by Adam and Green (2006) (Fig.III.13). Assuming cpx-melt equilibria and using the thermobarometer defined by Putirka (2008) (σ = 50 ℃, 150 MPa), the temperature and pressure of crystallization can be estimated between 1170 – 1290 ℃ and 200 – 1080 MPa for Kwaraha lavas and for Olmani lavas at 1240 ℃ and 880 – 930 MPa (Fig.III.14). The high pressure of cpx crystallization is well correlated with the pressure of 1000 MPa estimated by Simonetti et al. (1996), for high Al^{VI}/Al^{IV} ratio in cpx (0.89 - 0.56).

Volatiles as CO_2 and H_2O plays a fundamental role in magmatic evolution during ascent and controlling the chemical evolution and eruptive style (e.g. Berndt et al. 2005, Oppenheimer 2003). The presence of H_2O in silicate melt is recorded by hydrous minerals (amphibole, phlogopite) and Nominally Anhydrous Minerals (NAMs; olivine, pyroxene) (e.g. Wade et al. 2008). Hydrous minerals as phlogopite phenocrysts are present in Kwaraha and Labait and suggest that melt was H2O-bearing at the time of phlogopite crystallization (1.57-2.12 wt% H2O in phlogopite, KFT method). Calculated liquid in equilibrium (kd: Adam and Green 2006) with phlogopite from Kwaraha and Labait have similar REE (Fig.A5) and trace element (Ba, Sr) concentration than melilite nephelinite (whole rock) suggesting a crystallization at the liquidus with cpx and olivine. However, olivine and cpx (NAMs) may incorporate trace concentration of hydrogen allowing determination of the H2O content in silicate melt during crystallization. The water content in cpx (< 1 ppm wt H2O) and olivine (< 1 ppm wt H2O) (Fig.7) from Kwaraha and 3 - 6 ppm wt H2O for the olivine from Labait. Hydrogen is very incompatible in cpx and olivine (Kdcpx/melt = 0.01 –0.013, Kdolivine/melt = 0.0013, Hauri et al. 2006, Audaud et al. 2004) and these minerals co-crystallize with phlogopite. Consequently, the low water content recorded by cpx and olivine for Kwaraha lavas is not representative of the water content within the melt. Phlogopite is rare in Labait lavas (few phenocrysts) and the presence of water in olivine from Labait (3 - 6 ppm wt H2O) suggests hydrous conditions with 0.2 to 0.5 wt % H2O in the nephelinitic melt (table 5), corroborated by the study of hydrogen diffusion from Labait xenoliths (Hui et al. 2015). Considering that the solubility of H2O in alkali-rich silicate melts is 6 - 7 wt% at 200 - 300 MPa in CO2-free system (Lesne et al. 2011) and CO2-bearing system (Behrens et al. 2009), nephelinitic magmas in Manyara basin are probably H2O-undersaturated . Although, nephelinitic magmas have relatively low water content, the presence of phlogopite in Kwaraha and Labait lavas indicates that the asthenospheric mantle source is hydrated (400 ppm wt H2O with 1% of phlogopite) and considerably decrease the solidus temperature (e.g. Green et al. 2014).

CO_2 content in the silicate melt is generally investigate through melt inclusion studies. The lack of melt inclusions in Labait, Olmani and Kwaraha lavas prevents to precisely constrain the CO_2 content. However, North Tanzania is one of the most concentrated areas of carbonatite magmatism on Earth (e.g. Dawson 2012) and CO_2 abundance in silicate melt must be considered. Carbon content of whole rock are high for Labait lavas (0.7 - 4.6 wt % CO_2), intermediate for Kwaraha lavas (0.15 - 3.1 wt % CO_2) and very low for Olmani lavas (0.01-0.07 wt % CO_2). These carbon concentrations are minimal values due to degassing during ascent. The CO_2 solubility was calibrated experimentally for several magma compositions (e.g. melilitite, phonolite) at 1.5 - 2 GPa and depends of the non-bridging oxygen (NBO/T) of the melt (Brooker et al. 2001). Considering the compositions of nephelinitic lavas, the CO_2 solubility, which represents the maximum CO_2 dissolved in magmas, ranges from 7.5 to 15.8 wt % CO_2 (Labait (NBO/T = 1.4 - 1.67), Olmani (NBO/T = 1.04 - 1.34) and Kwaraha (NBO/T=0.93-1.26)). At Kwaraha volcano, nephelinitic lavas are associated with a calciocarbonatite (Kw1) suggesting CO_2 -rich magmatism. Carbonatite can be primary mantle melts or resulting from CO_2-silcate melt by magmatic differentiation and immiscibility

process (review in Jones et al. 2013). The calciocarbonatite (MgO = 0.51 wt %) composition was not experimentally reproduced by partial melting of peridotite (Stagno and Frost 2010, Keshav and Gudfinnsson 2013, Dasgupta et al. 2006), suggesting the presence of CO_2-rich silicate melt at depth in the Manyara basin, in agreement with the natrocarbonatite and calciocarbonatite in Natron basin, as products of immiscibility process and fractional crystallization from CO_2-rich silicate melt (Dawson 1998, Keller et al. 2006, Harmer et al. 1998).

Tanzanian lithospheric mantle records deep fluid-rock interaction with a large amount of Ca-carbonatitic fluid (2 % of carbonatitic fluid, Jones et al. 1983; Rudnick et al. 1993) and minor H_2O-rich fluid (< 50 ppm wt H_2O whole rock peridotite; Baptiste et al. 2015; Hui et al. 2015). The low H_2O and high CO_2 melilite nephelinite of Manyara may represent the interstitial glass and melt inclusion with K-alkaline and CaO-H_2O-poor silicate composition observed in xenoliths (Koornneef et al. 2009). Asthenospheric magma can metazomatized the lithospheric mantle during magma ascent, generating fluid-rock interaction.

V.3 Alkaline rocks from early stage rifting of East African Rift

Highly alkaline and silica-undersaturated lavas are common in the West (W-EAR) and East (E-EAR) branches of East African Rift (EAR). Rift propagation occurred from South (Kivu, 8 – 12 Ma) to North (Toro-Ankole) at W-EAR and inverse propagation from North (north and central Kenya, 30 – 15 Ma) to South (North Tanzania, < 6 Ma) at E-EAR (Ebinger et al., 2000, Mana et al. 2015, Furman et al. 2016).

At E-EAR, lava compositions change along the rift axis from alkali basalt to more mafic magmas (e.g. nephelinite and melilitite). Mafic magmas (i.e. melilite nephelinite) occurred preferentially in North Tanzania among Manyara basin (this study) which represent the early stage of rifting. They result from a deep (> 120 km) phlogopite-bearing source with low degree of partial melting (< 1 to 4 %) (this study, Mana et al. 2012, Mattsson et al. 2013). The central Kenya represents a more mature rifting (e.g. Ebinger et al. 2000) with alkali-basalt and basanites suggesting a higher degree (2 – 8 %) of partial melting from a lower amphibole-bearing source (MacDonald 2012, Roex et al. 2001). Similar variations of lavas have been also observed in the W-EAR with basanite at the Kivu (South) and K-nephelinite at the early stage rifting (North) (Rosenthal et al. 2009, Pouclet et al. 1981, Pouclet et al. 2016, Chakrabarti et al 2009, Maravyeva et al. 2014).

Lava composition variations in E-EAR and W-EAR result from different propagation of continental break-up involving different rate and depth of partial melting. Early-stage rifting magmatism (Manyara and Toro-Ankole) is associated with a phlogopite and CO_2-rich asthenospheric source and low degree of partial melting (this study, Rosenthal et al. 2009). This low volume volcanism is related with abundant normal faults and deep earthquake swarms (depth > 20 km) (e.g. Lindenfeld et al. 2012, Albaric et al. 2014). The occurrence of such seismic activity may triggered by fluid migration (CO_2 vapor exsolution) of CO_2-rich silicate melt (i.e. melilite nephelinite) in the lower crust (20 – 40 km) (Keir et al. 2009; Lee et

al. 2016). CO_2-rich magmatism may localize deformation in the lower crust and facilitate the rift propagation.

Supplementary material

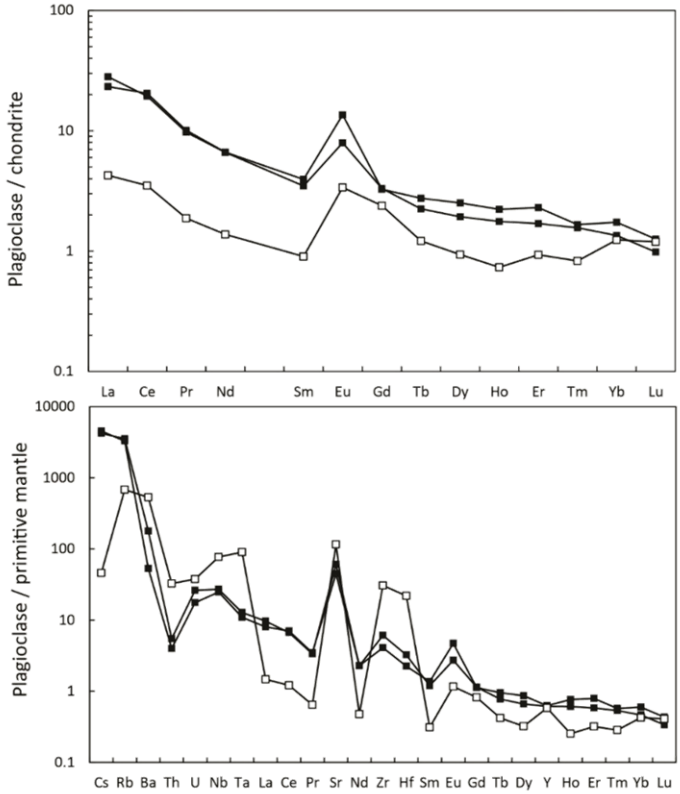

Fig.III.A1 *Normalized REE and trace element content of plagioclase (black square) and altered plagioclase (open square) from Labait (Lab3). Chondrite and primitive mantle values from Sun and McDonough (1989)*

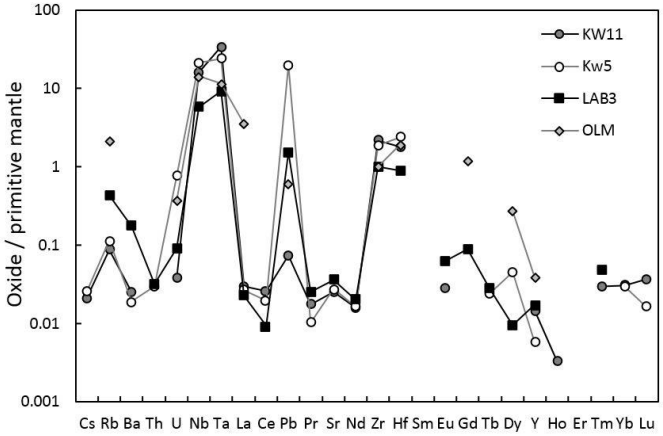

Fig.III.A2 *Normalized trace element content of oxide from Kwaraha, Labait and Olmani lavas.*

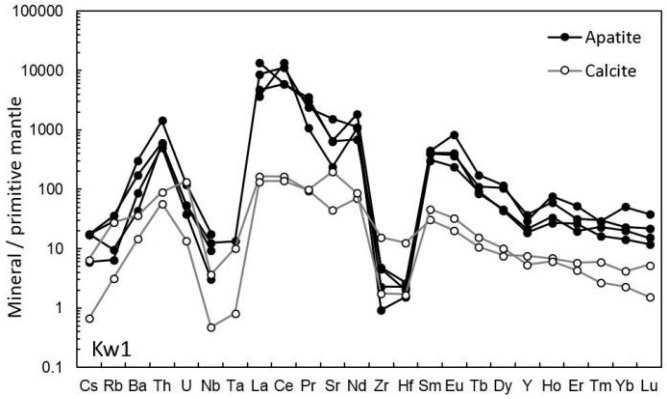

Fig.III.A3 *Normalized trace element content of apatite and calcite from Kwaraha carbonatite (Kw1). Primitive mantle values from Sun and McDonough (1989)*

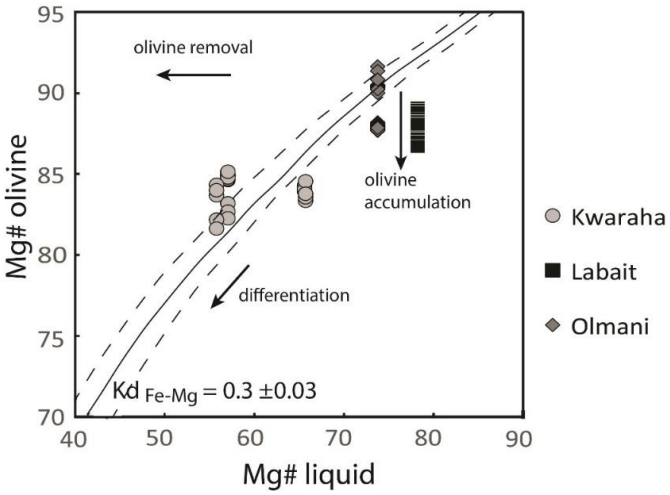

Fig.III.A4 *Mg# of olivine vs Mg# of whole rock from Kwaraha, Labait and Olmani lavas.*

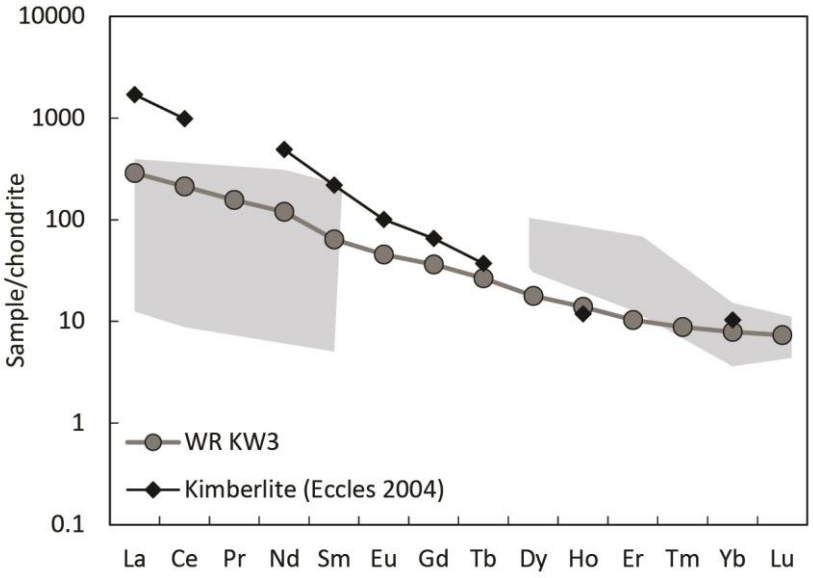

Fig.III.A5 *Recalculated melt in equilibrium with phlogopite and cpx (partition coefficient from Adam and Green 2006) and whole-rock composition of Kw3.*

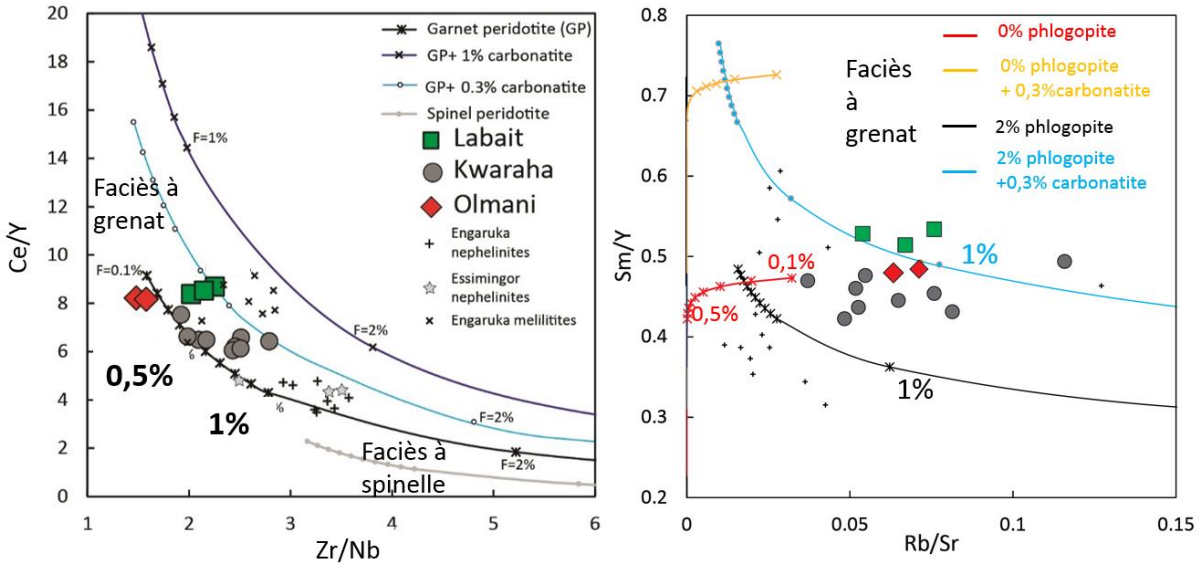

Modèle de fusion partielle et rapport de concentration des éléments en trace pour les laves du Labait, Kwaraha et Olmani

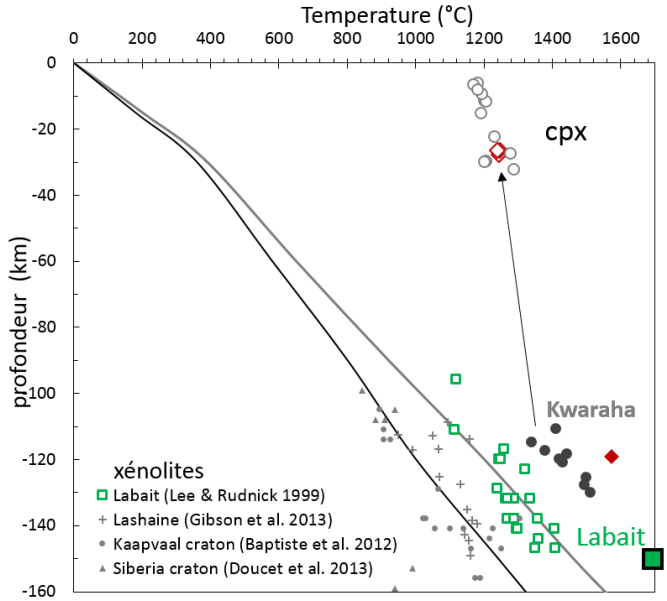

Conditions d'équilibre des xénolites (péridotites) de Tanzanie (Labait, Lashaine), ainsi que les géothermes associés. Conditions de genèse des laves primaires : Labait (carré vert), Kwaraha (point noir) et de cristallisation des clinopyroxènes.

Conclusions chapitre III

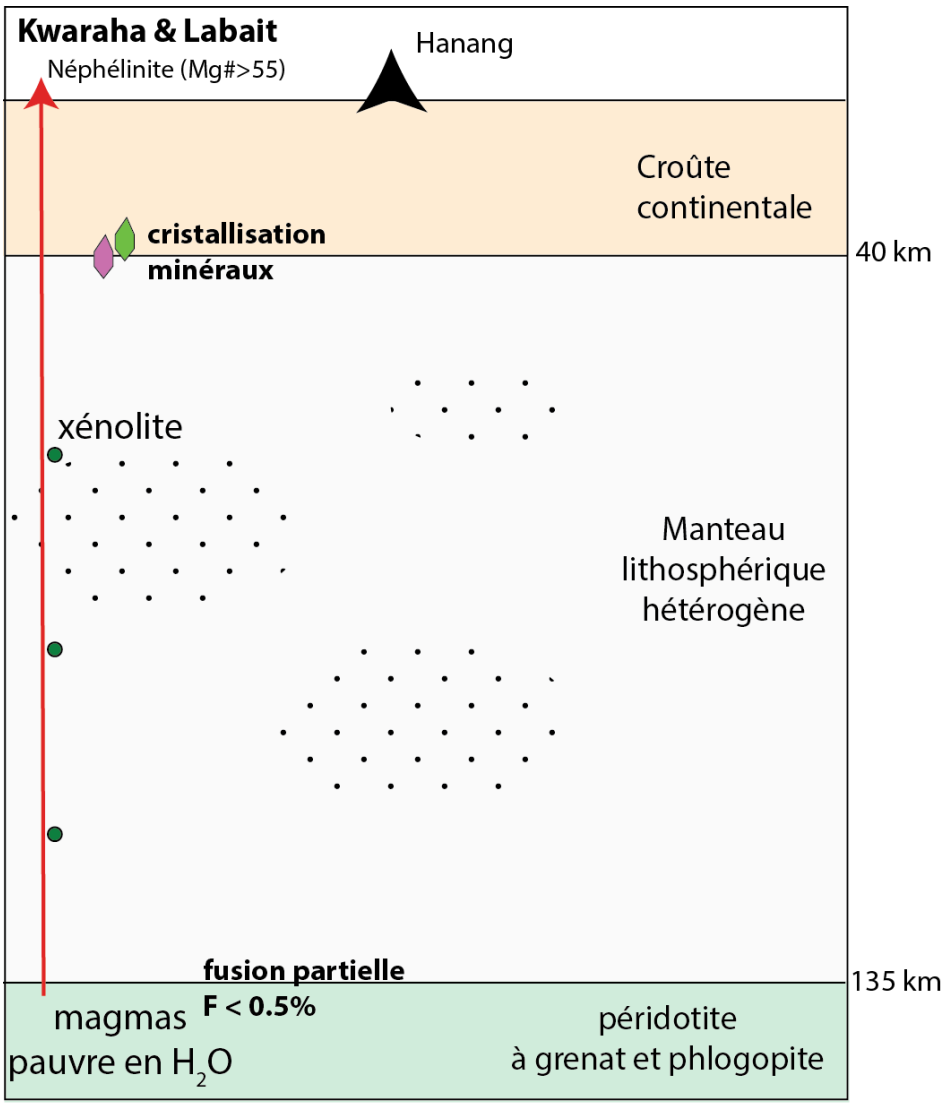

Chapitre IV. Néphélinites au premier stade de la rupture continentale : le volcan Hanang

*Le **chapitre IV** correspond à l'étude des laves du volcan Hanang. Une **première** étude, publié dans Contributions to Mineralogy and Petrology, se focalise sur les caractéristiques minéralogiques, pétrologiques et géochimiques afin de contraindre les processus magmatiques à l'origine de la formation de ces laves. Une **deuxième** étude se focalise sur l'étude des inclusions vitreuses (soumis à Lithos) et a pour but de déterminer les concentrations en volatils, les conditions pré-éruptives et de discuter du processus d'immiscibilité au sein des magmas alcalins.*

Contrib Mineral Petrol (2016) 171:64
DOI 10.1007/s00410-016-1273-5

ORIGINAL PAPER

Nephelinite lavas at early stage of rift initiation (Hanang volcano, North Tanzanian Divergence)

Céline Baudouin[1] · Fleurice Parat[1] · Carole M. M. Denis[1] · Fredrik Mangasini[2]

Received: 28 February 2016 / Accepted: 7 June 2016

Abstract North Tanzanian Divergence is the first stage of continental break-up of East African Rift (<6 Ma) and is one of the most concentrated areas of carbonatite magmatism on Earth, with singular Oldoinyo Lengai and Kerimasi volcanoes. Hanang volcano is the southernmost volcano in the North Tanzanian Divergence and the earliest stage of rift initiation. Hanang volcano erupted silica-undersaturated alkaline lavas with zoned clinopyroxene, nepheline, andradite-schorlomite, titanite, apatite, and pyrrhotite. Lavas are low MgO-nephelinite with low Mg# and high silica content (Mg# = 22.4–35.2, SiO_2 = 44.2–46.7 wt%, respectively), high incompatible element concentrations (e.g. REE, Ba, Sr) and display Nb–Ta fractionation (Nb/Ta = 36–61). Major elements of whole rock are consistent with magmatic differentiation by fractional crystallization from a parental melt with melilititic composition. Although fractional crystallization occurred at 9–12 km and can be considered as an important process leading to nephelinite magma, the complex zonation of cpx (e.g. abrupt change of Mg#, Nb/Ta, and H_2O) and trace element patterns of nephelinites recorded magmatic differentiation involving open system with carbonate–silicate immiscibility and primary melilititic melt replenishment. The low water content of clinopyroxene (3–25 ppm wt. H_2O) indicates that at least 0.3 wt% H_2O was present at depth during carbonate-rich nephelinite crystallization at 340–640 MPa and 1050–1100 °C. Mg-poor nephelinites from Hanang represent an early stage of the evolution path towards carbonatitic magmatism as observed in Oldoinyo Lengai. Paragenesis and geochemistry of Hanang nephelinites require the presence of CO_2-rich melilititic liquid in the southern part of North Tanzanian Divergence and carbonate-rich melt percolations after deep partial melting of CO_2-rich oxidized mantle source.

Keywords Nephelinite · Carbonatite · Liquid immiscibility · Rift initiation · Hanang · Tanzania · East African Rift

Introduction

The East African Rift (EAR) initiated in the North Ethiopia and evolved to oceanic accretion (Afar, 45 Ma to present, review in Furman 2007). The dynamics of the EAR has been related to one or two mantle plumes (Ebinger and Sleep 1998; Nyblade et al. 2000; Pik et al. 2006; Hansen et al. 2012; Mulibo and Nyblade 2013). In mature stages of rifting, continental break-up observed in Ethiopian rift regions is mainly regulated by magmatic processes, with the occurrence of dyking events (e.g. Dumont et al. 2016; Rubin and Pollard 1988; Wright et al. 2006). In early stages of rifting, both dyking events and fluid percolation may have contributed to rift initiation (Calais et al. 2008; Lee et al. 2016).

Communicated by Jochen Hoefs.

Electronic supplementary material The online version of this article (doi:10.1007/s00410-016-1273-5) contains supplementary material, which is available to authorized users.

✉ Céline Baudouin
baudouin@gm.univ-montp2.fr

[1] Géosciences Montpellier, UMR 5243 - CC 60, Université de Montpellier, Place Eugène Bataillon, 34095 Montpellier Cedex 5, France

[2] Department of Mining and Mineral Processing Engineering, University of Dar Es Salaam, Dar Es Salaam, Tanzania

Published online: 23 June 2016

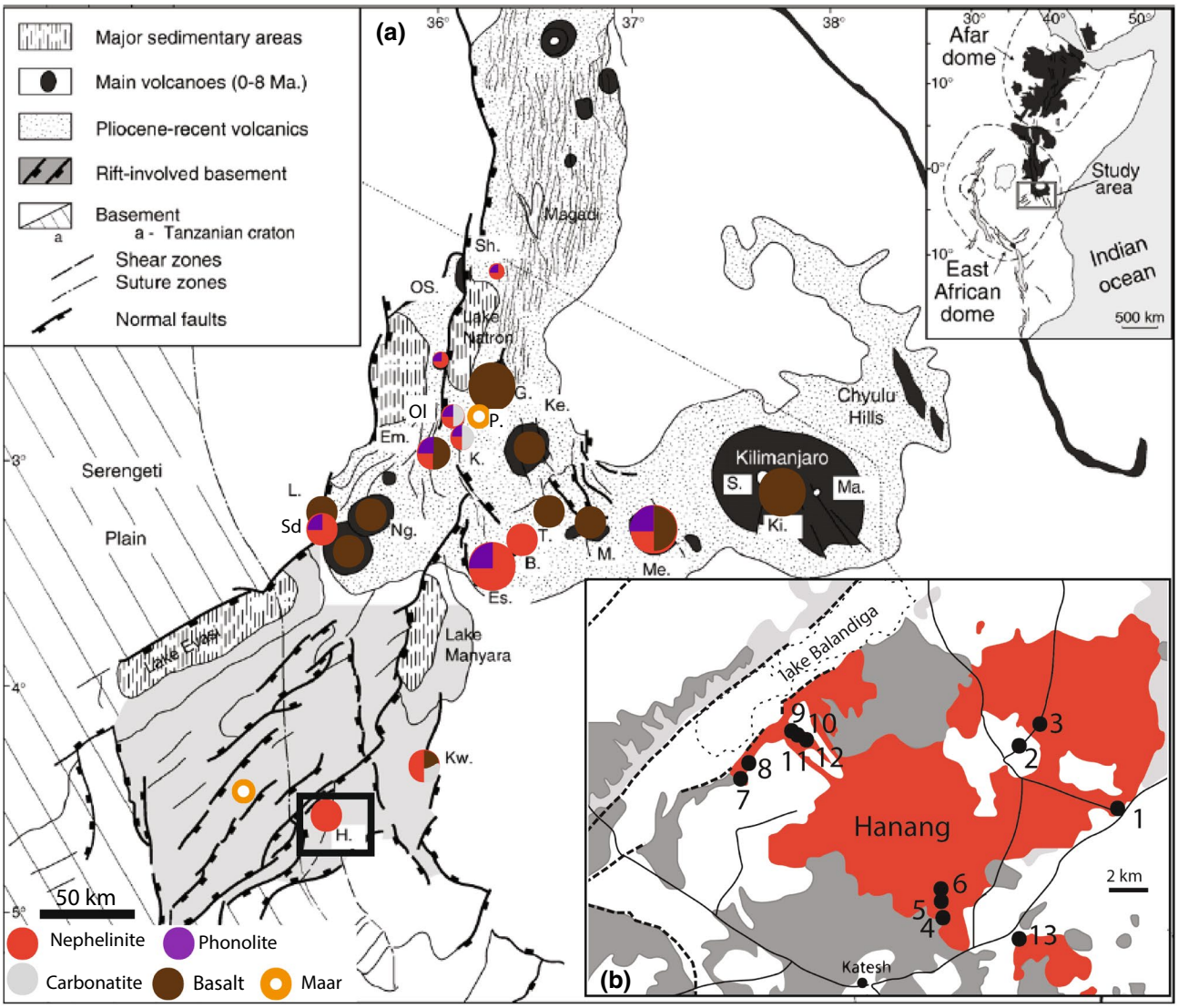

Fig. 1 **a** Main structural and magmatic features of the North Tanzania Rift. Volcanoes: *B*. Burko, *Em*. Embagai, *Es*. Essimingor, *G*. Gelai, *H*. Hanang, *K*. Kerimasi, *Ke*. Ketumbeine, *Ki*. Kibo, *Kw*. Kwaraha, *L*. Lemagrut, *M*. Monduli, *Ma*. Mawenzi, *Me*. Meru, *Ng*. Ngorongoro, *Ol*. Oldoinyo Lengai, *OS*. Ol Donyo Sambu, *P*. Pello hill, *Sd*. Sadiman, *S*. Shira, *Sh*. Shombole, *T*. Tarosero. Modified after Le Gall et al. (2008). **b** Map of Hanang volcano. *Light grey* Precambrian cataclastic granitic rock, *medium grey* Pleistocene calcareous tuffs, *dark grey* Pleistocene nephelinite lavas. *Full circle* samples of this study (Han1–Han13). Modified after Thomas (1966)

The EAR propagated to the South at the border of the East African Craton along the North Tanzanian Divergence (NTD), representing continental break-up initiation (<6 Ma) (Le Gall et al. 2008; Fig. 1). Volcanism attests of rift-related magmatic activities from 6 Ma to present (e.g. Bagdasaryan et al. 1973; Mana et al. 2015). The youngest extrusive volcanoes of the North Tanzanian Divergence are Oldoinyo Lengai (natrocarbonatite-phonolite-nephelinite, 0.15 Ma-present), Kerimasi (calciocarbonatite-phonolite-nephelinite, 1.1 Ma) and Hanang (0.9 Ma) volcanoes (Fig. 1). Most of previous studies have focused on the particular natrocarbonatite-calciocarbonatite- nephelinite association at Oldoinyo Lengai and several small scoria cones of olivine melilitite and olivine nephelinite in the restricted area of the Natron basin in the North part of the NTD (e.g. Oldoinyo Lengai, Dawson 1989; Klaudius and Keller 2006; Keller et al. 2006, 2010; Mitchell and Dawson 2012, and Kerimasi volcano, Church 1996; Guzmics et al. 2012, 2015; Mariano and Roeder 1983). This area represents one of the most abundant carbonatite magmatism on Earth. The magmatic processes involved evolution from melilitite-nephelinite magma to carbonatite at crustal depth (Dawson 1998; Lee and Wyllie 1998), while carbonatite magmas represent a late component after multistage

magmatic differentiation, including fractional crystallization and liquid immiscibility (e.g. Dawson 1998; Freestone and Hamilton 1980; Kjarsgaard 1998).

In the southern part of the NTD, the Manyara basin represents the earlier stage of rift initiation. It is characterized by NE-SW normal faults and deep seismic swarm (Albaric et al. 2010, 2014) with low-volume volcanism (Kwaraha, Hanang, Labait volcanoes, Fig. 1). The Hanang volcano, located in the South part of the Manyara basin, erupted Mg-poor nephelinite lavas allowing study of magma genesis and evolution at early stage of East African rift opening.

We investigated a detailed petrological, mineralogical and geochemical study of nephelinite lavas from Hanang volcano to constrain the pre-eruptive conditions of silica-undersaturated liquid and their magmatic evolution during ascent to the surface. Comparison with the Natron Basin volcanism and more primitive lava cones in the Manyara basin (e.g. melilitites) allows us to discuss the genesis of carbonate-rich silicate magmatism at different stages of differentiation during rift initiation and to characterize deep mantle beneath the East African Craton.

Geological setting

The East African Rift exposes different stages of plate boundary extension, from the initiation of the rift (Tanzania, Manyara basin) to oceanic accretion (Afar Triple Junction). EAR is divided into two branches (West branch and East branch) located mainly in the Proterozoic orogenic belt accreted around the Tanzanian craton (>2.5 Ga) (Fig. 1).

In the East branch, volcanism began at 30 Ma in the North Kenya, at 15 Ma in Central Kenya and at 6 Ma in the Northern Tanzania (Essimingor volcano; Mana et al. 2012, 2015). The axial valley is narrow (50 km) in the central Kenyan rift and expands over 200 km to the South, forming the NTD, with many volcanic complexes (e.g. Ngorongoro, Kilimanjaro). In the south part of NTD, the rift propagated via three fault systems: Eyasi, Manyara and Pangani (Le Gall et al. 2008). The NTD has an intense seismic activity, with deep crustal earthquakes in the North part of the Manyara basin and few deep earthquakes around Hanang volcano in the South part (Albaric et al. 2010, 2014) (Fig. 1).

Hanang volcano (4°27′S 35°24′E) is the main volcano of the Manyara basin (with Kwaraha volcano, Fig. 1). Hanang is the southern volcano of northern Tanzania volcanic area (200 km South to Oldoinyo Lengai), at the edge of the rift scarp and Tanzanian craton (Fig. 1). Hanang volcano was active during the Quaternary between 1.5 ± 0.3 and 0.9 ± 0.2 Ma (K–Ar ages by Bagdasaryan et al. 1973). Small tuff cones are present in the surrounding of Hanang volcano including the Labait hill (10 km SE to Hanang), an olivine melilitite cone with numerous mantle xenoliths which document multiple metasomatic events in the sub-lithospheric mantle (e.g. spinel phlogopite harzburgites, garnet lherzolite-harzburgite, wehrlite, dunite; Aulbach et al. 2008; Koornneef et al. 2009; Lee and Rudnick 1999; Selby and Thomas 1966; Vauchez et al. 2005). The lithospheric thickness beneath Hanang and Labait volcanoes is estimated around 140 km based on surface wave tomography and geothermal gradient (Craig et al. 2011).

Hanang lavas erupted on Precambrian cataclastic granitic rocks (Thomas 1966). The volcano is composed of nephelinitic tuffs and agglomerates, carbonatitic tuffs and nephelinite lavas (Thomas 1966). Nephelinitic and carbonatitic tuffs are highly altered and interbedded on the north-western slope near the lake Balangida (Dawson 2008). Lava flows are present in the north-western, north-eastern and southern parts of Hanang volcano, and each lava flow has been sampled for this study (Fig. 1).

Few geochemical studies of Hanang nephelinite (Dawson 2012; Nonnotte 2007; Paslick et al. 1996; Wood 1968) suggested that Hanang volcano is part of the youngest extrusive volcanoes of North Tanzania with Oldoinyo Lengai and Kerimasi. These stratovolcanoes are volumetrically smaller than the older extrusive centres (e.g. Essimingor, Ngorongoro, Fig. 1), resulting from highly explosive volatile-rich magmatism (Dawson 2012). Nonnotte (2007) interpreted trace element compositions of two samples from Hanang as complex petrogenetic processes during magmas genesis which can be related to interaction/demixion processes of silicate/carbonate between the parental magma and a carbonatite-type magma.

Analytical method

Major elements

Whole-rock major elements were measured by wide-angle X-ray fluorescence using sequential spectrometer Bruker S4 Pioneer at the analytical services of the Instituto Andaluz de Ciencias de la Tierra (IACT, University of Granada, Spain) using Rh X-ray tube (160 kV, 159 mA). Rock powders (1 g) are weighed with di-lithium tetraborate flux, and then the mixture is fused at 1000 °C for 15 min. The concentrations of major elements in the samples are measured by comparing the X-ray intensity for each element with nine reference geological standard samples.

The concentrations of major and volatile elements in minerals were determined using electron microprobe (Cameca XS100 at the “microsonde sud” facility, University of Montpellier, France). Operating conditions comprised an accelerating voltage of 20 keV for silicate minerals and oxides, and 15 keV for apatite, a beam current

of 10 nA and a focused beam (1 μm). The counting time was fixed at 20 s for all elements except for volatile elements (40 s; S, Cl, F). The standards used for major and volatile element analyses were: wollastonite for Si and Ca, Al_2O_3 for Al, TiO_2 for Ti, forsterite for Mg, hematite for Fe, orthose for K, albite for Na, apatite for P, native metal for Ni, Mn, Cu, baryte for S and Ba, fluorite for F and chloroapatite for Cl.

Trace elements

Trace element analyses were performed by ICP-Mass Spectrometry (ICP-MS) after HNO_3 and HF digestion of 0.1 g of sample powder in a Teflon-lined vessel at 180 °C and 200 psi for 30 min, evaporation to dryness, and subsequent dissolution in 100 mL of 4 vol% HNO_3. Instrument measurements were carried out in triplicate with a NexION 300d (PerkinElmer) ICP-MS spectrometer (at IACT) using Rh as internal standard, and by external calibration using multielemental calibration solutions. The precision was better than ±5 % for analysed concentrations of 10 ppm.

Trace element concentrations in minerals were determined by a laser ablation ICP-MS system (at the University of Montpellier, AETE platform), using GeoLas Q + Excimer CompEx102. A 26-μm and 56-μm diameter laser beams were used for apatite and silicate minerals, respectively, with a laser repetition rate of 6–10 Hz and a laser power of 0.5 mJ (5 J cm^{-2}). The spot size was chosen as a compromise between signal intensity and the size of the minerals of interest in the samples. The concentrations are calibrated with NIST612 glass and the concentrations of SiO_2 and CaO previously determined by electron microprobe for individual mineral. BIR-1 standard is used as external standard.

For data processing and calculation of concentrations, Glitter Software (Griffin et al. 2008) was used to process the raw data files containing the signal intensity versus time. This allows precise selection of blanks and signals, and rapid visualization of the intensity data. The drift is compensated by the internal standard calculations using the Glitter software; no other drift corrections are performed.

Volatile elements

Whole-rock sulphur and carbon contents were determined for each sample by element analyser at the IACT. Total inorganic carbon (TIC) or carbonate carbon was removed by reaction with dilute 3N HCl, followed by washing in distilled H_2O. To minimize adsorption of atmospheric CO_2, powders were degassed at 100 °C and stored under vacuum in a desiccator. Standard deviations were between 10 and 60 ppm for sulphur and 10–100 ppm for carbon. Whole-rock fluorine and chlorine contents were determined by wet precipitation-ferrithiocyanate spectrophotometry (Varian Cary 50 spectrophotometer) at the Service d' Analyse des Roches et des Minéraux (Nancy, France). Standard solution was used to check the accuracy of the analyses. Standard deviation is less than 5 % (Vernet et al. 1987).

FTIR spectroscopy

Water content of clinopyroxene (cpx) and nepheline (nph) has been determined using FTIR (Fourier transform infrared) spectroscopy. Hand-picked minerals were prepared as doubly polished section thickness between 70 and 130 μm. The hydrogen concentration was measured in transmission mode by FTIR spectroscopy at the Laboratoire Charles Coulomb (University of Montpellier, France). The unpolarized infrared spectra were acquired using a Bruker IFS 66v coupled with an optical microscope Hyperion. A Globar light source and a Ge-KBr beam splitter are used to generate unpolarised mid-infrared radiation (between 4000 and 400 cm^{-1}). The concentration of hydrogen was calculated by integration of the spectrum between 3770 and 3000 cm^{-1} (for complete method see Denis et al. 2015). Water concentration is calculated using the calibration of Paterson (1982), where the water concentration is a function of density of the mineral distinguished below (χcpx-I = 2557 ppm wt H_2O; χcpx-II = 2642 ppm wt H_2O; χcpx-III = 2550 ppm wt H_2O, χnph = 3462 ppm wt H_2O). The errors on water content due to calibration (Paterson 1982), uncertainties on the sample thickness and background correction are ±15 %. The integrated unpolarized absorbance normalised to 1 cm of thickness values is also reported in order to use alternative mineral specific FTIR calibrations (e.g. Bell et al. 1995).

Results

Lavas from Hanang volcano have porphyritic texture with 10–37 vol% of nepheline (nph) (3.5–31 vol%), clinopyroxene (4.5–7.5 vol%, diopside), garnet (0–3 vol%, andradite-schorlomite$_{ss}$) phenocrysts and accessory minerals, titanite (0–0.5 vol%), apatite (0–1.5 vol%) and rare pyrrhotite set in a groundmass of nepheline microliths (Fig. 2, Table 1). The matrix of nephelinites did not contain any accessory minerals as observed in Sadiman nephelinites (e.g. götzenite, barytolamprophyllite, delhayelite; Zaitsev et al. 2012).The lavas are normative nph >20 % (CIPWnph = 24–31 %), and can be defined as nephelinites *sensus lato* (i.e. Le Bas et al. 1986).

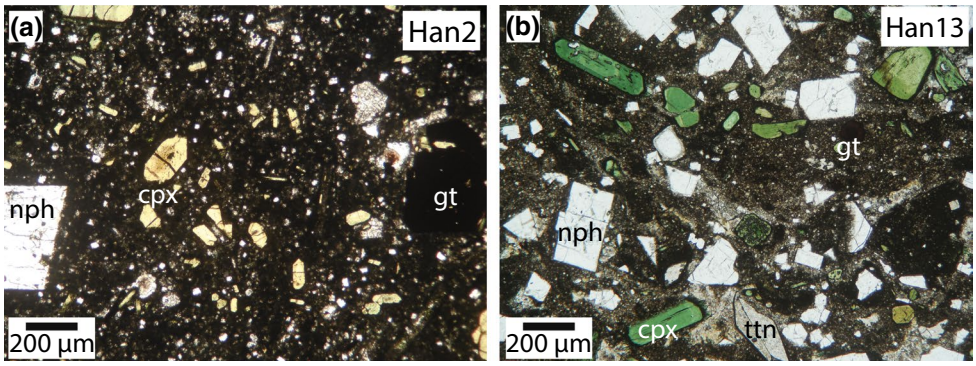

Fig. 2 Microphotographs of Hanang lavas. **a** Crystal-poor sample (11 vol% phenocrysts, Han2) and **b** crystal-rich sample (25 vol% phenocrysts, Han13). *Cpx* clinopyroxene, *ttn* titanite, *nph* nepheline, *gt* garnet (andradite-schorlomite$_{ss}$)

Table 1 Modal proportion of minerals in Hanang lavas

	Han1	Han2	Han4	Han7	Han8	Han11	Han13
% phenocryst	30.1	10.8	15.6	23.5	30.5	37.2	25.4
Nepheline	24.5	3.5	9.1	14.8	18.5	31	17.3
Clinopyroxene	5	4.5	4.5	5.9	7.5	4.7	5.7
Garnet	0.4	2.8	0.5	1.6	2.5	0	0.9
Apatite	0	0	1	1	1.5	1	1
Titanite	0.2	0	0.5	0.2	0.5	0.5	0.5
Pyrrhotite	0	0.001	0	0	0.002	0	0.001

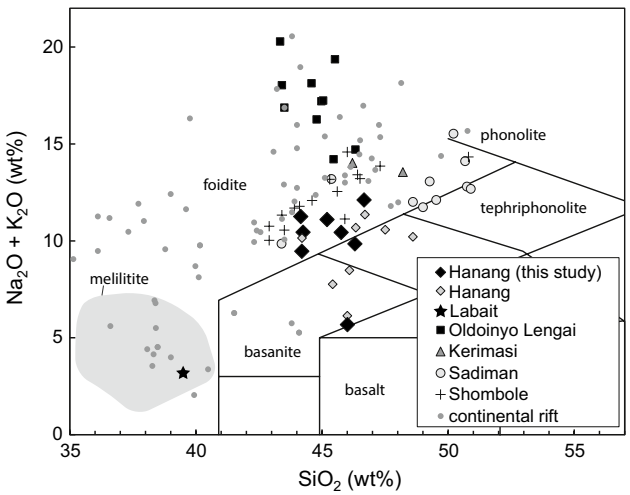

Fig. 3 Alkali versus silica composition of the Hanang nephelinites (*black diamond*, this study; and *grey diamond*, Wood 1968; Nonnotte 2007), Oldoinyo Lengai CWN nephelinites (*black square*, Klaudius and Keller 2006), Kerimasi nephelinites (*triangle*, Church 1996), Sadiman nephelinites (*grey circle*, Zaitsev et al. 2012), Shombole nephelinites (*black plus*, Peterson 1989), melilitite from Labait (*black star*, Dawson et al. 1997), melilitite (*grey field*) and nephelinite from continental rift (*small circle*, Georoc database, http://georoc.mpch-mainz.gwdg.de/georoc/). Modified after Le Bas et al. (1986)

Whole-rock nephelinite composition

Hanang nephelinites have high silica and alkaline content (44.2–46.7 wt% SiO_2, 9.5–12.1 wt% $Na_2O + K_2O$, respectively) and a composition within the foidite field defined in TAS diagram (Fig. 3; Table 2, Le Bas et al. 1986). Nephelinites have very low Mg# (molar Mg/(Mg + Fe_t)*100 = 22.4–35.2), high content in Al_2O_3 (12.7–15.3 wt%) and CaO (7.1–11.2 wt%) (Fig. 4) and an alkalinity index ranging from 0.93 to 1.29 (molar Na + K/Al). Nephelinites are volatile rich (whole-rock composition) with 750–8700 ppm C, 1200–4200 ppm F, 150–1060 ppm S and 63–680 ppm Cl (Table 2).

Hanang nephelinites have high contents in trace elements (Fig. 5). REE patterns are enriched in light rare earth elements (LREE) relative to middle rare earth elements (MREE, 20–50*chondrite, La/Sm = 11–14.7) and heavy rare earth elements (HREE, 10–20*chondrite, La/Yb = 38.2–56) (Fig. 5a). Relative to primitive mantle (PM), all lavas have high large ion lithophile elements (LILE, 100*PM) and high field strength elements (HFSE, 50–100*PM) and Pb (16.1–29 ppm) concentrations (Fig. 5b) with Sr and Zr positive anomalies, and Zr–Hf and Nb–Ta fractionation (Zr/Hf = 45–56.6 and Nb/Ta = 36-61, respectively; Fig. 5b).

Mineral chemistry

Nepheline occurs in all samples as phenocrysts (100–1200 µm) and microcrysts. Nepheline crystals contain inclusions of clinopyroxene microcrysts and rare melt inclusions. Nepheline has a small range in K_2O (7.3–8.3 wt%), Na_2O (15.1–15.9 wt%) and minor element

Table 2 Major, volatile and trace element concentrations of Hanang lavas

Sample	HAN1	HAN2	HAN4	HAN7	HAN8	Han10*	HAN11	HAN13
SiO_2 (wt%)	44.19	44.15	46.30	44.24	45.75	46.13	45.19	46.66
TiO_2	1.17	2.09	1.70	1.27	1.21	1.90	1.23	1.11
Al_2O_3	13.40	12.69	15.33	13.96	13.73	11.64	14.78	14.75
Fe_2O_3	8.21	11.11	9.51	8.98	8.87	9.28	8.93	8.52
MnO	0.26	0.25	0.26	0.25	0.22	0.20	0.28	0.27
MgO	1.76	2.94	2.61	2.30	2.01	3.39	1.30	1.97
CaO	11.24	11.18	7.47	10.47	9.96	9.37	7.99	7.15
Na_2O	6.82	7.32	6.99	7.15	7.20	0.74	7.39	8.40
K_2O	2.64	3.93	2.85	3.29	3.23	4.58	3.71	3.71
P_2O_5	0.62	0.79	0.59	0.61	0.58	0.45	0.43	0.38
LOI	10.51	3.55	6.95	8.07	7.59	12.63	9.53	7.46
Total	100.8	99.99	100.55	100.59	100.35	100.31	100.77	100.37
Mg#	29.80	34.4	35.2	33.7	31.0	42.00	22.4	31.4
CO_2	4.31	0.27	0.49	3.13	2.91	1.58	2.92	0.94
F (ppm)	–	1700	–	2000	2300	–	1200	4200
Cl (ppm)	–	105	–	63	120	–	250	680
S (ppm)	500	750	410	150	1060	210	430	540
Cr (ppm)	9.67	5.45	7.15	10.4	11.6	48.7	7.73	7.07
Ni	14.9	13.0	10.0	14.4	13.9	28.2	10.3	9.24
Cu	51.4	137	72.5	59.4	64.1	68.1	36.7	26.4
Cs	3.94	1.37	2.29	2.67	2.02	1.10	5.79	3.12
Rb	83.2	91.1	84.7	59.3	50.4	120	104	113
Ba	6730	1602	2199	2330	2664	1198	2159	1751
Th	14.0	6.93	10.1	9.21	8.80	12.1	10.9	10.4
U	5.83	4.16	3.16	1.28	2.17	2.20	2.96	5.68
Nb	185	142	173	151	145	123	194	179
Ta	3.52	3.92	3.92	2.91	2.68	4.71	3.37	2.91
La	143	85.1	125	86.7	85.9	95.9	119	111
Ce	206	123	173	126	124	161	166	154
Pb	29.1	16.1	26.3	23.5	23.2	18.8	28.4	29.8
Pr	20.3	12.2	16.7	12.3	12.1	16.7	15.7	14.4
Sr	1315	2212	1917	1827	3001	3267	2901	3628
Nd	66.7	41.2	55.5	41.2	39.5	56.6	50.6	45.9
Zr	569	493	563	498	486	323	643	561
Hf	10.1	10.4	11.2	9.69	9.29	7.01	11.7	10.4
Sm	11.1	7.76	9.80	7.12	6.91	9.23	8.33	7.53
Eu	3.88	2.43	3.08	2.26	2.24	2.45	2.48	2.23
Gd	9.06	6.91	8.78	6.28	6.04	7.07	7.15	6.41
Tb	1.27	1.01	1.25	0.88	0.85	0.97	1.01	0.92
Dy	6.41	5.66	6.88	4.73	4.62	4.52	5.35	4.75
Y	36.4	31.3	39.1	27.4	26.7	22.9	31.4	28.8
Ho	1.18	1.06	1.32	0.91	0.89	0.81	1.02	0.91
Er	3.04	2.65	3.34	2.29	2.20	1.97	2.51	2.32
Tm	0.44	0.40	0.50	0.35	0.33	0.29	0.39	0.36
Yb	2.47	2.23	2.78	1.99	1.95	1.69	2.30	1.98
Lu	0.36	0.32	0.40	0.31	0.29	0.24	0.34	0.31

$Mg\# = Mg/(Mg + Fe_{tot}) \times 100$, * Tuff

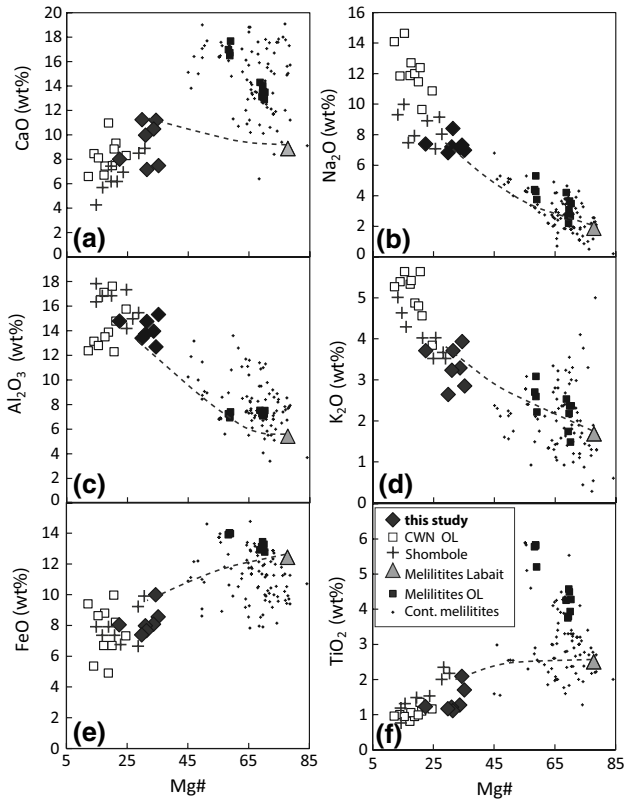

Fig. 4 Mg# versus **a** CaO content, **b** Na_2O content, **c** Al_2O_3 content **d** K_2O content, **e** FeO content and **f** TiO_2 content of nephelinites from Hanang (*black diamond*), Combeite Wollastonite Nephelinite (CWN) from Oldoinyo Lengai (*black square*, Keller et al. 2006) and Shombole (*plus*, Peterson 1989), melilitites from Labait (*triangle*, Dawson et al. 1997) and continental setting (small black plus, Georoc database, http://georoc.mpch-mainz.gwdg.de/georoc/). Fractional crystallisation curves from melilitite (47 % olivine, 8.5 % melilite, 10.6 % cpx, 10.9 % phlogopite and 1 % magnetite, 4 % titanite, and 0.9 % apatite) are also reported

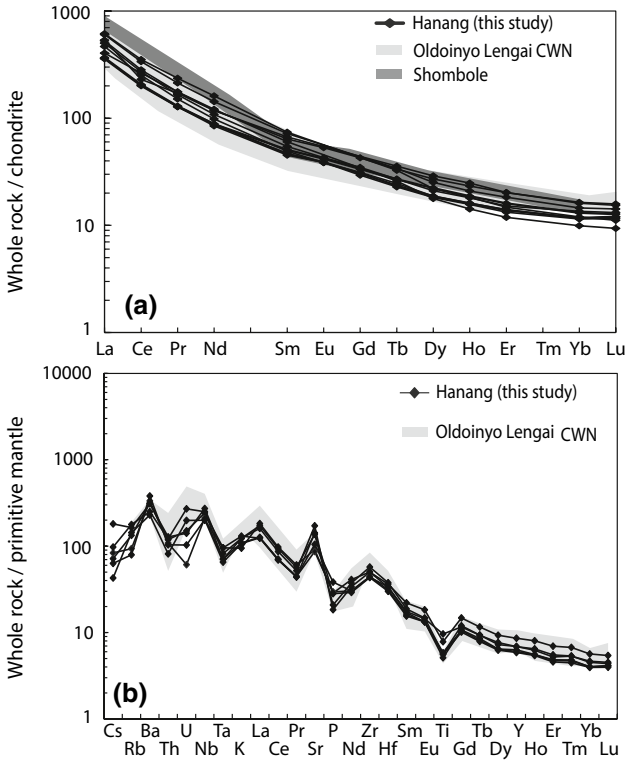

Fig. 5 **a** Normalized REE content of Hanang nephelinites (this study), Combeite Wollastonite Nephelinite (CWN) from Oldoinyo Lengai (Klaudius and Keller 2006), and Shombole nephelinites (Peterson 1989). Chondrite values from Sun and McDonough (1989). **b** Normalized trace element composition of Hanang nephelinites (this study), and Combeite Wollastonite Nephelinite (CWN) from Oldoinyo Lengai (Klaudius and Keller 2006). Primitive mantle values from Sun and McDonough (1989)

concentrations (e.g. 1–2.17 wt% Fe_2O_3; 0.05–0.23 wt% CaO) (Table 3). Trace element concentrations are below the detection limit (<0.03 ppm) except for LILE (45–180 ppm Rb, 18–88 ppm Sr, 4–12 ppm Ba) and LREE (0.3–0.6 ppm La, La/Sm = 0.34–1) (Table 4). Nepheline is an anhydrous mineral but can contain up to 5500 ppm wt H_2O (Johnson 2006). In Hanang nepheline, the water concentration was determined by FTIR and ranges from 240 to 550 ppm wt H_2O (Table 5).

Clinopyroxene is the more complex mineral in Hanang nephelinites. Three types of clinopyroxene phenocrysts (100–800 μm) are present (Figs. 6, 7; Table 3): (1) zoned cpx with green core (cpx-I, $En_{25-31}Fs_{21-28}Wo_{46-48}$,), yellow middle zone (cpx-II, $En_{30-35}Fs_{16-22}Wo_{48-49}$) and green rim (cpx-III, $En_{20-31}Fs_{21-33}Wo_{45-49}$), (2) unzoned yellow cpx (cpx-II, $En_{32-36}Fs_{17-22}Wo_{48-49}$) and (3) unzoned green cpx (cpx-III, $En_{18-32}Fs_{20-39}Wo_{42-49}$). All clinopyroxene have diopside compositions according to the classification of Morimoto (1988).

Zoned clinopyroxene phenocrysts represent 5–7 % of total clinopyroxene. They have low Mg# core (Mg# = 48–59), yellow middle zone with the highest Mg# (61–70, 200 μm) and green rim with very low Mg# (30–40). The different parts of the cpx have, however, similar REE concentrations with concave pattern and trace element concentrations except for Ta (Figs. 8, 9). The green cpx core and green rim (cpx-I and III, respectively) have low content in Ta relative to Nb, whereas the yellow middle cpx does not have Nb–Ta fractionation (Fig. 9). Zoned cpx have higher H_2O content in the middle-yellow zone (14–21 ppm wt. H_2O) compared to the green core (6–10 ppm wt H_2O) and rim (8–12 ppm wt H_2O) (Fig. 10, Table 5). Minor element concentrations for green cpx core (cpx-I) are 1.47-2.18 wt% Na_2O, 0.36–0.52 % TiO_2 and 0.62–1.04 wt% Al_2O_3 (Table 3; Fig. 7). Minor element concentrations for cpx-II are lower than cpx-I and III with: 0.82–1.3 wt% Na_2O, and 0.14–0.9 wt% Al_2O_3 (Table 3; Fig. 7).

Table 3 Major element composition of minerals

Sample	Han8	Han8	Han8	Han8	Han8	Han13	Han8	Han8	Han8	Han13	Han8	Han8
Mineral	Nph	Cpx-I	Cpx-II	Cpx-III	Cpx-II	Cpx-III	Garnet	Garnet	Titanite	Titanite	Apatite	Apatite
Type	Core	Core	Middle	Rim	Core	Core	Core	Rim	Core	Core	Core	Rim
SiO_2	41.35	51.43	52.16	50.27	52.59	51.52	29.60	29.87	30.28	30.14	0.73	0.80
TiO_2	0.02	0.60	0.61	0.64	0.44	0.35	13.17	12.82	37.22	36.29	–	–
Al_2O_3	32.95	1.15	1.03	0.86	0.48	0.57	0.72	0.78	0.51	0.60	0.01	0.01
FeO^t	1.64	11.06	8.96	17.01	10.13	15.33	21.01	20.99	1.88	2.21	–	0.31
MnO	–	0.29	0.27	0.52	0.29	0.41	0.24	0.29	0.02	0.03	0.05	0.06
MgO	0.03	10.96	12.37	7.34	11.56	8.29	0.62	0.55	–	–	–	–
CaO	0.08	23.16	23.49	20.76	23.02	20.75	32.75	31.85	28.98	28.91	56.07	56.00
Na_2O	15.73	1.25	0.93	2.35	1.20	2.14	0.38	0.33	0.15	0.11	–	–
K_2O	8.09	–	0.01	–	–	–	–	–	–	–	–	–
P_2O_5	0.02	–	–	–	–	–	–	–	–	–	40.86	40.81
Cr_2O_3	–	0.02	–	–	–	–	0.03	–	–	–	–	–
SO_3	–	–	–	–	–	–	–	–	–	–	0.07	0.07
F	–	–	–	–	–	–	–	–	–	–	3.19	3.12
Cl	–	–	–	–	–	–	–	–	–	–	0.01	–
$-O \equiv F$	–	–	–	–	–	–	–	–	–	–	1.34	1.31
Total	99.91	99.92	99.84	99.75	99.71	99.36	98.52	97.48	99.04	98.29	99.65	99.93
Mg#	–	63.7	71.1	43.3	67.0	49.1	–	–	–	–	–	–
Numbers of ions on the basis of	32O	6O					12O		5O		26O	
Si	8.12	1.94	1.95	1.93	1.98	1.98	2.52	2.57	0.99	0.99	0.12	0.13
Al^{IV}	–	0.05	0.05	0.04	0.02	0.03	–	–	–	–	–	–
Al^{VI}	–	–	–	–	–	–	–	–	–	–	–	–
Al tot	7.63	–	–	–	–	–	0.07	0.08	–	–	–	–
Ti	–	0.02	0.02	0.02	0.012	0.01	0.84	0.83	0.91	0.90	–	–
Fe^{2+}	–	0.21	0.19	0.31	0.23	0.33	0.28	0.37	–	–	–	0.04
Fe^{3+}	0.27	0.14	0.09	0.24	0.09	0.16	1.21	1.13	0.05	0.06	–	–
Mn	–	0.01	0.01	0.02	0.01	0.01	0.02	0.02	–	–	–	–
Mg	0.01	0.61	0.69	0.42	0.65	0.47	0.08	0.07	–	–	–	–
Ca	0.02	0.93	0.94	0.85	0.93	0.85	2.98	2.93	1.01	1.02	10.19	10.17
Na	5.99	0.09	0.07	0.17	0.09	0.16	–	–	0.01	0.01	–	–
K	2.03	–	–	–	–	–	–	–	–	–	–	–
P	–	–	–	–	–	–	–	–	–	–	5.87	5.86
S	–	–	–	–	–	–	–	–	–	–	0.01	0.01
Cl	–	–	–	–	–	–	–	–	–	–	–	–
OH	–	–	–	–	–	–	–	–	–	–	1.08	1.1
F	–	–	–	–	–	–	–	–	–	–	0.91	0.89
Total	24.00	4.00	4.00	4.00	4.00	4.00	8.00	8.00	3.00	3.00	18.18	18.23

$Mg\# = Mg/(Mg + Fe_{tot}) \times 100$; *Nph* nepheline, *Cpx* clinopyroxene

Unzoned yellow cpx phenocrysts (10–13 % of total cpx) have identical major and trace element compositions compare to the middle-yellow zone of zoned cpx (cpx-II) (e.g. high Mg# = 58–69, no Ta anomaly, Figs. 8, 9), and high H_2O content (38–120 ppm wt H_2O, Table 5).

Unzoned green cpx phenocrysts represent 80–85 % of total cpx population. They have low Mg# (Mg# = 50–60) similar to the rim of zoned cpx (cpx-III). Minor element concentrations are: 1.12–3.5 wt% Na_2O, 0.1–1.83 wt% TiO_2, and 0.3–3.22 wt% Al_2O_3 (mean = 1.01 wt%)

Table 4 Trace element composition of minerals

Sample	Han8	Han8	Han8	Han8	Han8	Han13	Han8	Han8	Han8	Han13	Han8	Han8
Mineral	Nph	Cpx-I	Cpx-II	Cpx-III	Cpx-II	Cpx-III	Garnet	Garnet	Titanite	Titanite	Apatite	Apatite
Type	Core	Core	Middle	Rim	Core	Core	Core	Rim	Core	Core	Core	Rim
Ni	2.56	2.88	3.74	4.35	30.2	3.58	0.57	0.59	1.57	0.85	0.32	0.66
Cu	0.57	0.38	0.48	0.46	0.12	9.95	2.65	2.48	5.21	4.96	0.24	0.19
Rb	69.3	<0.01	0.01	<0.01	<0.01	2.37	0.08	0.05	0.70	0.17	0.04	0.02
Ba	11.6	0.09	0.06	1.11	0.15	40.9	0.05	0.06	12.4	1.21	64.9	70.2
Th	<0.01	<0.01	<0.01	<0.01	<0.01	0.39	3.20	2.80	3.83	28.4	12.2	16.1
U	<0.01	<0.01	<0.01	<0.01	<0.01	0.18	3.45	3.18	2.42	21.9	1.10	1.30
Nb	0.02	0.25	0.51	0.24	0.67	11.7	229	213	2396	8940	0.12	0.15
Ta	0.01	<0.01	0.05	<0.01	0.05	0.09	11.7	10.2	92.5	152	<0.01	<0.01
Pb	0.04	0.05	0.02	0.12	0.13	3.15	0.05	0.01	0.55	1.17	0.32	0.40
Sr	71.2	490	454	555	711	1031	83.8	77.0	1147	774	11761	11516
Zr	0.16	203	273	186	223	381	1987	1680	2244	4316	0.83	0.99
Hf	0.10	6.11	9.80	5.46	6.53	10.1	48.6	39.2	58.7	81.6	<0.01	<0.01
Y	0.01	2.51	4.44	5.75	2.58	3.79	239	230	127	274	76.3	81.1
La	0.02	1.83	3.84	3.75	3.62	3.84	17.2	17.1	241	425	856	1006
Ce	0.03	3.35	7.98	7.23	7.93	7.85	86.3	90.6	584	1279	1168	1400
Pr	0.01	0.45	1.12	0.91	1.02	0.89	17.6	18.1	74.6	181	112	132
Nd	0.04	1.85	4.73	4.21	4.11	3.58	108	111	297	759	376	449
Sm	<0.01	0.35	1.03	0.83	0.77	0.66	38.9	40.8	62.5	158	50.7	59.9
Eu	0.03	0.09	0.29	0.21	0.23	0.18	13.8	14.8	18.8	45.6	12.8	14.7
Gd	0.16	0.27	0.93	0.92	0.7	0.59	45.5	48.0	53.4	125	41.4	45.3
Tb	0.01	0.06	0.11	0.08	0.08	0.09	7.28	7.52	7.25	17.4	3.86	4.28
Dy	0.02	0.24	0.62	0.69	0.44	0.48	46.2	47.6	38.7	91.0	17.2	18.8
Ho	<0.01	0.04	0.12	0.14	0.08	0.14	9.03	8.89	5.91	13.9	2.57	2.75
Er	0.02	0.21	0.33	0.67	0.30	0.52	24.2	23.3	12.0	27.8	5.00	5.55
Tm	0.01	0.05	0.08	0.15	0.07	0.14	3.12	2.93	1.17	2.67	0.49	0.53
Yb	0.04	0.74	0.63	1.61	0.79	1.59	18.8	16.1	4.8	10.6	2.25	2.41
Lu	0.01	0.21	0.17	0.38	0.18	0.41	2.30	1.85	0.32	0.64	0.22	0.23

(Table 3). Cpx-III have a concave REE pattern enriched in LREE (2–10 ppm La, La/Sm = 2.7–8.6) and HREE (0.55–4.7 ppm Yb, La/Yb = 1.4–8.7) relative to MREE (0.65–1.7 ppm Sm; 0.2–1.2 ppm Dy) (Figs. 8, 9, Table 4). As observed for the rim of zoned cpx (cpx-III), they have low content in Ta relative to Nb (Figs. 7, 8). The water content ranges from 2.5 to 25 ppm wt H_2O (σ = 15 %) (Fig. 10; Table 5).

Garnet crystallized as dark brown euhedral phenocrysts (100–2000 µm) and microcrysts. They are normally zoned (Mg#) and have inclusions of cpx and nepheline. Garnet has andradite-schorlomite$_{ss}$ composition with Fe^{3+}>Ti (Grew et al. 2013) and variable content in TiO_2 (8.9–15.8 wt%), FeO (20.4–22.9 wt%), and MgO (0.17–0.62 wt%) (Table 3). The REE concentrations (>100* chondrite) are high with convex REE pattern (low LREE (16–20 ppm La, La/Sm = 0.35–0.44, Table 4), high MREE (107–129 ppm Nd) and HREE (16–25 ppm Yb, La/Yb = 0.71–1.06; Fig. 8). Garnet is also rich in HFSE (e.g. 1700–2700 ppm Zr, 161–389 ppm Nb) and does not have Nb–Ta fractionation (Fig. 9).

The accessory minerals are euhedral titanite (100–400 µm), apatite (50–100 µm) and pyrrhotite (10–40 µm). Titanite has variable content in trace elements: 2060–13,000 ppm Nb, 1300–8080 ppm Zr, 228–530 ppm La (La/Sm = 2.07–5.64), 240–1070 ppm Nd (Figs. 8, 9; Tables 3, 4). Apatite is fluorapatite with 3.01–3.19 wt% F and low content in other volatile elements: 40–100 ppm Cl and 370–740 ppm SO_3 and very high concentrations in trace elements (5500–11,700 ppm Sr; 750–2060 ppm La, La/Sm = 12.1–16.9, Figs. 8, 9). Pyrrhotite (N_{FeS} (molar fraction of FeS) = 0.98, 0.05–0.6 wt% Cu, 0.01–0.16 wt% Ni, Pd/Ir = 15–260, Table S1) occurs as inclusions in cpx (rarely in garnet, titanite and nepheline) and in the matrix.

Table 5 Water content in cpx, and nepheline and calculated parental melt

Sample	Type	ppm wt.	Melt[a]	Calc. Area[b]
Han8	cpx-I C	8	1205	41.4
Han8	cpx-I C	6	854	29.8
Han8	cpx-II M	21	2982	101.1
Han8	cpx-II M	17	2402	87.6
Han8	cpx-III R	9	1248	42.2
Han8	cpx-III R	8	1197	41.4
Han8	cpx-II	119	16972	735.6
Han8	cpx-II	17	2454	129.4
Han8	cpx-II	101	16750	692.8
Han8	cpx-II	38	4800	345.1
Han8	cpx-III	9	1313	42.5
Han8	cpx-III	25	3640	145.0
Han8	cpx-III	6	917	29.8
Han11	cpx-III	3	360	19.9
Han13	cpx-III	8	1094	54.1
Han8	nph	240	–	317.8
Han8	nph	550	–	716.6

cpx-I core zoned cpx, *cpx-II* yellow cpx, *cpx-III* green cpx, *C* core, *M* middle, *R* rim, *nph* nepheline

[a] Melt composition calculated using $Kd^{cpx/melt}$ from Wade et al. (2008)

[b] Integrated unpolarized absorbance normalised to 1 cm of thickness

Discussion

Petrogenesis of Hanang nephelinites

The rock type erupted at Hanang volcano is the silicic nephelinite. Hanang nephelinites are silica-undersaturated with low magnesium and high alkaline content (1.3–2.9 wt% MgO and 10–12 wt% $Na_2O + K_2O$, respectively; Table 2) promoting the crystallization of nepheline and the absence of olivine. Lavas are porphyric (10–37 vol% phenocrysts, Table 1; Fig. 2) with mineral phase assemblage consisting of nepheline, cpx, garnet, titanite, apatite and pyrrhotite. The variations in mineral proportion are well correlated with the whole-rock major element concentrations (e.g. Mg#, Al_2O_3), whereas very restricted trace element variations are observed (Fig. 5). The small variation of cpx proportion, the inverse proportion of nepheline and garnet, and the absence of garnet in the more porphyritic and nepheline-rich sample (e.g. Han11, 37 vol% phenocrysts, Table 1) all suggest earlier crystallization of garnet and late crystallization of nepheline, whereas cpx crystallized over a large range of temperature (see below). Among the few experimental studies performed to constrain phase assemblage of nephelinite magmas, phase equilibria of Shombole nephelinite (Peterson 1989), with whole-rock composition and mineral assemblage close to the Hanang nephelinite (Fig. 3), corroborate that cpx and garnet are liquidus phases at low pressure (100–500 MPa) and nepheline is a sub-liquidus phase co-precipitating with cpx, garnet, titanite, Fe-spinel and calcite at 950 °C (Kjarsgaard 1998). The low-pressure carbonate precipitation reported in experimental run products occurred at low temperature (<950 °C) in Si-poor and Ca-rich melt composition (e.g. Kjarsgaard 1998; Lee and Wyllie 1998). The absence of calcite and perovskite as well as the presence of titanite in Hanang nephelinite indicate a crystallization environment at high pressure from Si-rich and Ca-poor silicate melt (>500 MPa, Kjarsgaard 1998). The high Fe^{2+}+Mn and low Na content of cpx as well as the low Al content of garnet all suggest crystallization at high pressure and high temperature (Kjarsgaard 1998) (Fig. 6). In addition, the low Al^{VI}/Al^{IV} ratio (0.09–0.2) of cpx ($Al^{VI} \sim 0$; Table 3) constrains the crystallization at pressure <1000 MPa (Bultitude and Green 1971; Simonetti et al. 1996).

Experimental study clearly showed that the composition of cpx is a function of the whole-rock composition, the pressure and the temperature of crystallization (e.g. Bultitude and Green 1971; Putirka 1999). The cpx and whole-rock nephelinite compositions have Kd (Fe^{2+}/Mg) ranging from 0.18 to 0.4 suggesting that cpx are close to equilibrium with silicate liquid (equilibrium with Kd = 0.3; e.g. Rhodes et al. 1979; Roeder and Emslie 1970; Putirka 1999) and are suitable for calculation of the pressure and temperature conditions of nephelinite crystallization. In addition, the concentration of trace elements of cpx and the partition coefficients determined by Fujimaki et al. (1984) for peralkaline basalt can be used to determine the composition of silicate liquid in equilibrium with cpx and corroborate that cpx crystallized from silicate melt with composition close to the whole-rock composition. The best fit (calculated silicate liquid/whole rock) for trace element composition was obtained for Kd close to 0.3 from cpx-I and less evolved lavas (Mg# = 35–30) (Fig. 11), suggesting that cpx crystallized from silicate melt with nephelinite composition. Using cpx-melt equilibria and the thermobarometer defined by Putirka (2008) (σ = 50 °C, 150 MPa), we estimate the temperature and pressure of crystallization between 1050–1100 °C and 340–640 MPa in agreement with experimental stability field of cpx in nephelinite magma (Fig. 6a) and the temperature of crystallization of garnet calibrated experimentally using TiO_2 content (8.9–15.8 wt% TiO_2 for T = 910–960 °C, Kjarsgaard 1998) (Table 2; Fig. 6c). The final crystallization temperature is recorded by nepheline phenocrysts and yields at $T < 800$ °C following the method of Hamilton (1961) (Fig. 6b).

The presence of interbedded carbonated tuffs with nephelinite lavas and the occurrence of volatile-bearing minerals in nephelinite (e.g. pyrrhotite, apatite) attest of

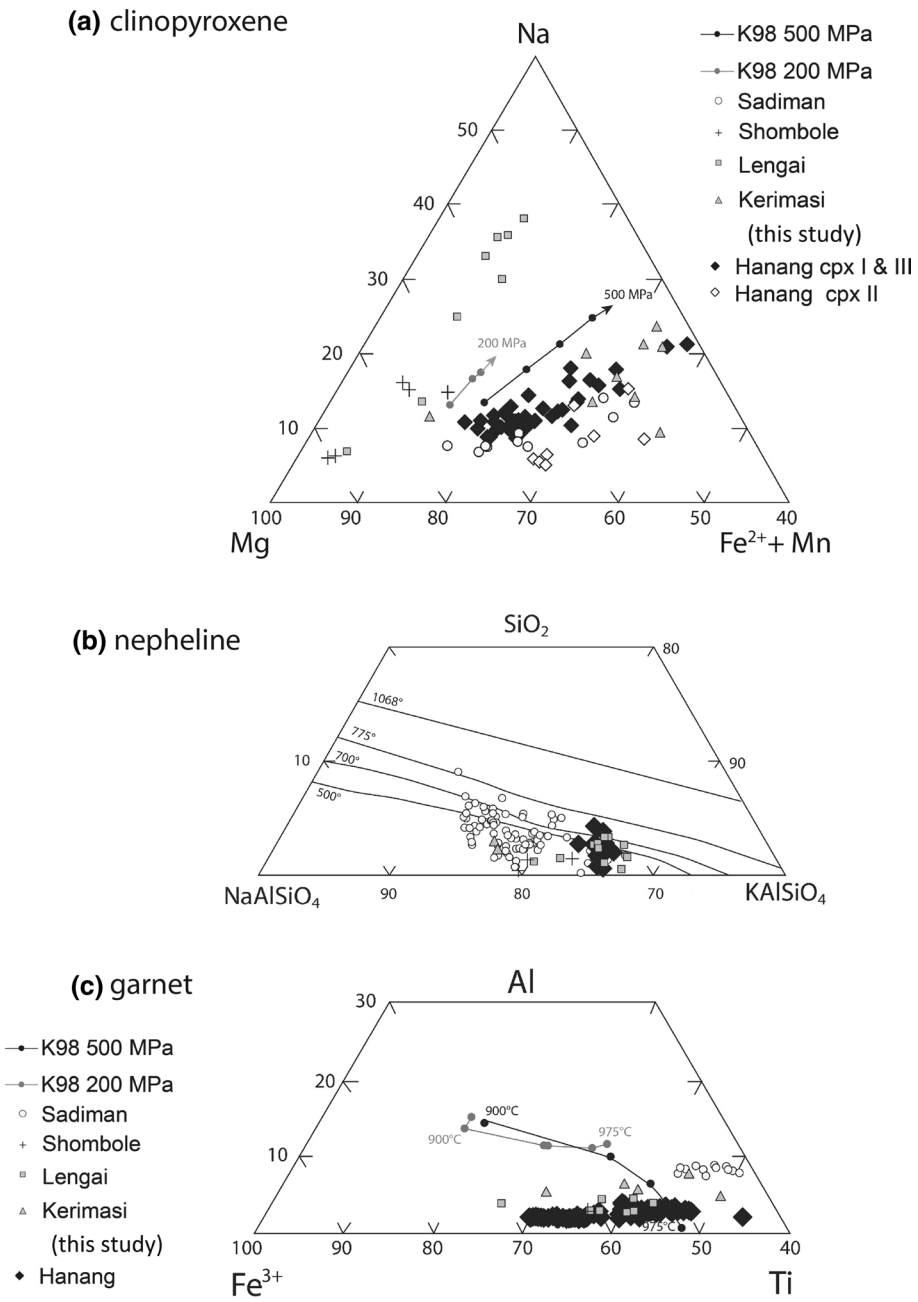

Fig. 6 **a** Clinopyroxene compositions represented an aegirine (Na)-diopside(Mg)-hedenbergite (Fe^{2+}+Mn) triangular (atom %) plot. Cpx from Hanang (diamond, this study), Sadiman (*open circle*, Zaitsev et al. 2012), Shombole (*black plus*, Peterson 1989), Oldoinyo Lengai (*square*, Peterson 1989) and Kerimasi (*triangle*, Church 1996) and from experiments (K98, at 500 and 200 MPa, *black* and *grey circle*, respectively, Kjarsgaard 1998); **b** Nepheline compositions. The isotherms are from Hamilton (1961), **c** Compositions of garnet represented on an Al-Fe^{3+}-Ti triangular (atom %) plot and isotherms from Kjarsgaard (1998)

the presence of complex volatile association at depth (CO_2, S, Cl, F). The bulk volatile content of Hanang nephelinites, which represents the volatile content after eruption (i.e. after degassing), also indicates that CO_2, S, Cl and F were present during magma evolution (0.3–4.3 wt% CO_2, 150–1060 ppm S, 63–680 ppm Cl and 1200–4200 ppm F; Table 2). The presence of pyrrhotite and S-bearing apatite in nephelinite indicates that sulphur was present as sulphide (S^{2-}) and sulphate species (S^{6+}), respectively, and moderated oxidized condition above the fayalite-magnetite-quartz buffer (FMQ) prevailed during crystallization (Jugo et al. 2010). This redox state agrees with thermodynamic equilibrium between titanite, andradite and wollastonite and crystallization of titanite and andradite at high oxidation state (ΔFMQ = −0.5 to +2) for silica activity between 0.1 and 0.25, whereas wollastonite is stable at more reduced conditions (Marks et al. 2008; Zaitsev et al. 2012).

Water may be present with CO_2 in alkaline undersaturated magmas and various proportions have been reported in the literature from 0.1 to 8.4 wt% H_2O (e.g. Brey and Green 1977; de Moor et al. 2013). Since water degassed at the early stages during magma evolution, hydrous melt inclusions and hydrous minerals are the only reliable

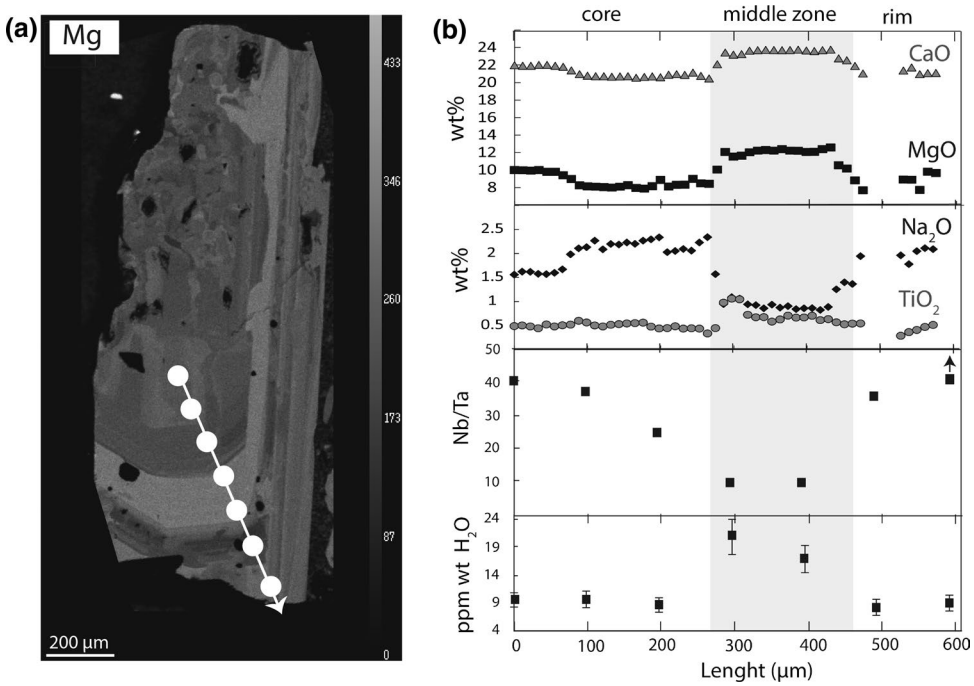

Fig. 7 **a** Mg chemical map of zoned cpx from Han8, **b** Clinopyroxene zoning profile showing heterogeneous chemical compositions: MgO and Na_2O, TiO_2, CaO content, Nb/Ta ratio and water content (ppm wt H_2O) along the transect shown in (**a**)

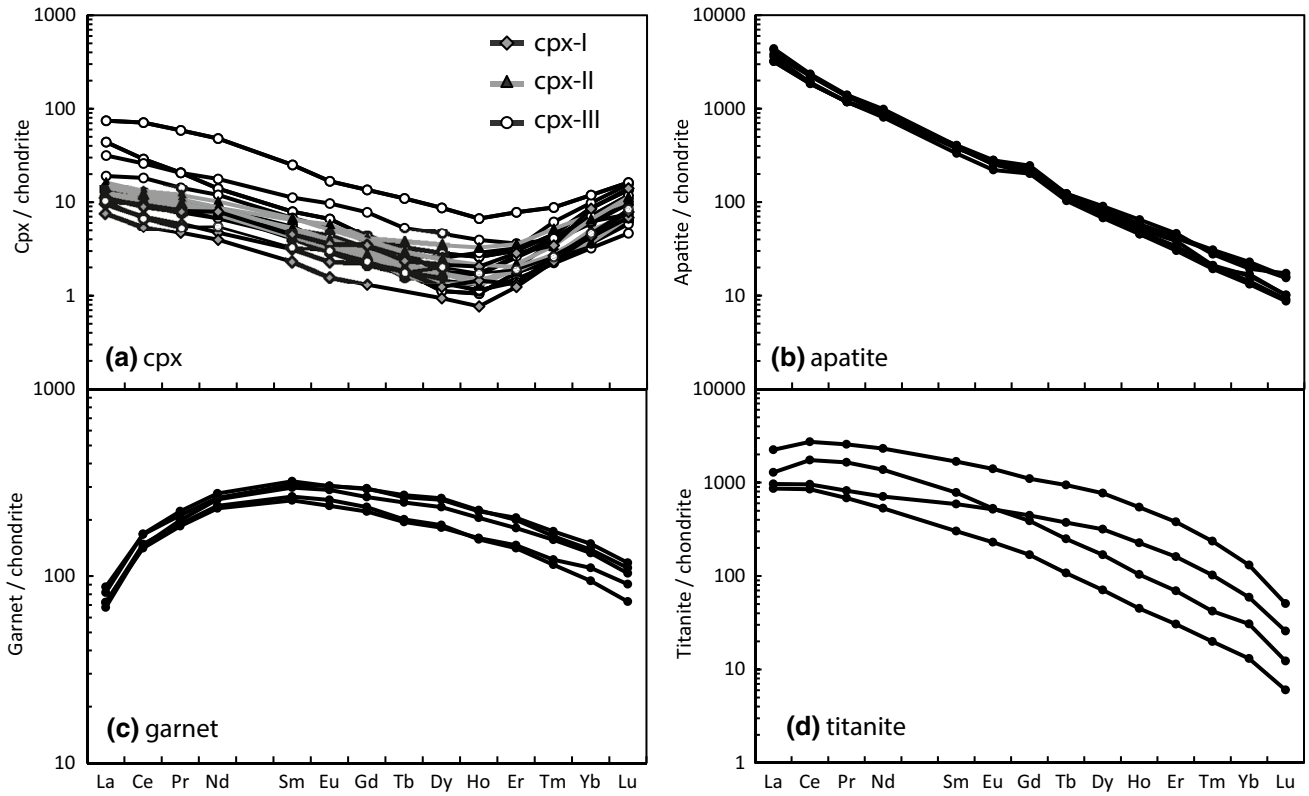

Fig. 8 Normalized REE content of **a** cpx, **b** apatite, **c** garnet and **d** titanite from Hanang nephelinites. Chondrite values from Sun and McDonough (1989)

indicators of the presence of water at depth (Moore 2008; Oppenheimer et al. 2003). In Hanang nephelinite, rare melt inclusions in nepheline and the absence of hydrous minerals (e.g. amphibole, biotite) do not allow us to determine directly the amount of water during nephelinite differentiation. However, among nominally anhydrous

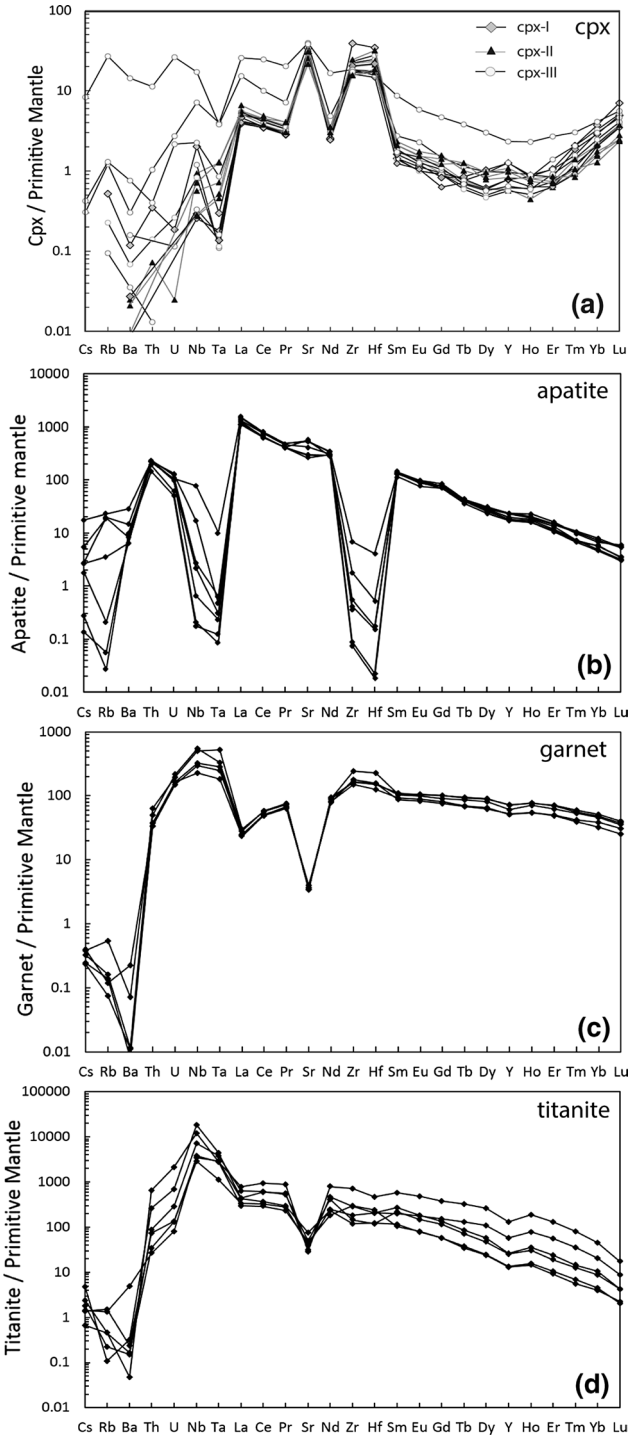

Fig. 9 Normalized trace element composition of Hanang minerals: **a** cpx-I (*diamond*), cpx-II (*triangle*) and cpx-III (*circle*), **b** apatite, **c** garnet and **d** titanite. Primitive mantle values from Sun and McDonough (1989)

minerals, cpx and nepheline may incorporate trace concentration of hydrogen (Chen et al. 2015; Hauri et al. 2006; Johnson 2006) and can attest of the presence of water at depth and allow determination of the water content in silicate melt during crystallization. The partitioning of H_2O between silicate liquid and cpx ($Kd^{cpx/melt}$) has been calibrated experimentally (e.g. Hauri et al. 2006, Wade et al. 2008). The partition coefficient is a function of $Al^{IV}/[IV]_{total}$ in cpx, and the resulting partition coefficient is 0.005–0.008 for $Al^{IV}/[IV]_{total} = 0.015–0.023$. The water content of green core and rim pyroxenes (cpx-I and III) indicates crystallization from silicate melt with low H_2O content from 0.036 to 0.36 wt% H_2O, whereas yellow cpx (cpx-II) crystallized from more hydrous silicate melt with 0.2–1.7 wt% H_2O (Table 5). The presence of water in nepheline (240–550 ppm wt H_2O) also suggests crystallization from H_2O-bearing silicate melt. Unfortunately, the partitioning of water between nepheline and silicate melt has not been calibrated experimentally. However, the water content in nepheline from nephelinite is low compared to the amount of water content measured in natural nepheline in tephritic-phonolite (500–5500 ppm H_2O, see review by Johnson 2006), suggesting low water content during magmatic differentiation. Considering that the solubility of H_2O in alkali-rich silicate melts is 10 wt% at 500 MPa and 7 wt% at 200 MPa (Behrens et al. 2009; Vetere et al. 2014), the low water content estimated from cpx compositions (<3600 ppm wt H_2O) indicates that nephelinite magmas from Hanang are H_2O-poor and H_2O-undersaturated.

The amount of other volatile elements such as S, Cl and F in nephelinite magmas can be estimated using the composition of apatite. Using S, Cl and F partition coefficient determined experimentally (Mathez and Webster 2005; Parat and Holtz 2005; Parat et al. 2011), we estimated that apatites crystallized from silicate melt with 24–31 ppm S^{6+}_{melt}, 26–125 ppm Cl_{melt} and 0.89–0.94 wt% F_{melt}. These values are low compared to the solubility of these elements in mafic magmas (Jugo et al. 2010; Webster et al. 1999), suggesting that nephelinite magmas are S–Cl–F-poor magmas or that apatite is a late crystallizing phase after early in situ degassing.

Fractional crystallization from melilitite

Alkaline and highly alkaline intraplate lavas range in composition from slightly undersaturated alkali basalts to strongly undersaturated olivine nephelinites and olivine melilitites (Foley et al. 2012; Green and Ringwood 1967). Experimental partial melting of carbonated mantle peridotite reproduced the composition of MgO-rich nephelinite (>12 wt % MgO) but failed to reproduce Mg-poor nephelinite composition, suggesting that MgO-poor magmas are not primary magmas (e.g. Dasgupta et al. 2007; Hirose 1997). Early fractional crystallization of olivine in more primitive magmas may have led to the very low Mg# (22.4–35.2) and very low MgO and Ni content (<3 wt% and 9.2–14.4 ppm, respectively) as observed for Hanang nephelinite.

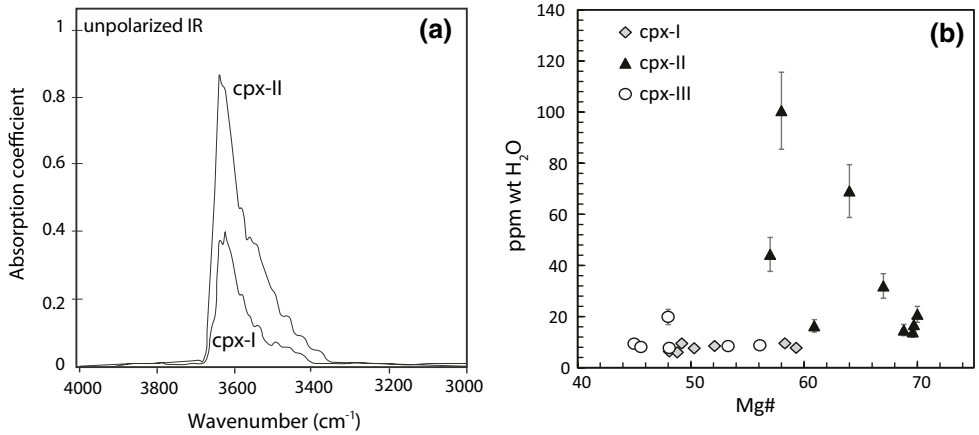

Fig. 10 **a** Representative FTIR spectra of unoriented cpx from Hanang nephelinites. All spectra are normalized to 1 cm of thickness. **b** Water content as a function of Mg# versus in different types of cpx

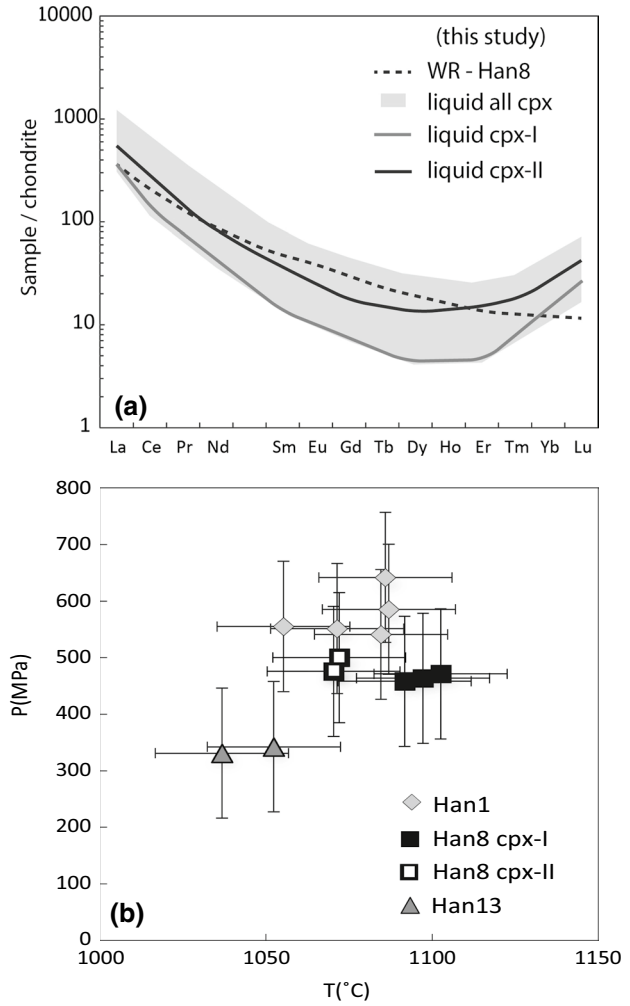

Fig. 11 **a** Recalculated melt in equilibrium with cpx used to determine P–T conditions (partition coefficient from Fujimaki et al. 1984) and whole-rock composition (WR) of Han8, **b** P–T conditions calculated from cpx-liquid thermobarometer (Putirka 2008) for Hanang nephelinites

Among the Si-undersaturated magma series, only melilitite magmas have more mafic compositions than nephelinite and can be considered as potential parental magmas of nephelinites (melilitites: 29.8–40.8 wt% SiO_2, 4.75–27.8 wt% MgO as reported by Dasgupta et al. 2007; Ivanikov et al. 1998 and Georoc database (http://georoc.mpch-mainz.gwdg.de/georoc), Figs. 3, 4). Using whole-rock and mineral major element compositions of nephelinite and Mg-rich olivine melilitite from Labait (Dawson et al. 1997), the composition of nephelinite can be modelled by high fractional crystallization (80 wt%, $r^2 = 0.27$; Fig. 4) of 47 % olivine, 8.5 % melilite, 10.6 % cpx, 10.9 % phlogopite and 1 % magnetite, 4 % titanite, and 0.9 % apatite. The high fractional crystallization of melilitite is coherent with petrographic observations of olivine melilitite from Labait (South Hanang) containing 25–35 % phenocrysts of olivine with tabular and altered melilite and minor phlogopite, cpx, magnetite and apatite (Dawson et al. 1997).

Although fractional crystallization can be considered as an important process leading to nephelinite major element composition, the complex zonation of cpx and the trace element signature of nephelinite (e.g. high LILE and HFSE content, low concentration of Ta and Nb–Ta fractionation, Table 4, Figs. 5, 8, 9) cannot result from fractional crystallization of melilitite magma (Fig. 12). Melilitites have no Ta anomaly and Nb/Ta ratio <25 (Chakhmouradian 2006; Mattsson et al. 2013) and fractional crystallisation of olivine, cpx and garnet does not fractionate Nb–Ta ($D_{Nb/Ta}$ olivine = 0.17–0.35, $D_{Nb/Ta}$ cpx = 0.23–0.54; $D_{Nb/Ta}$ garnet = 0.58–0.90; Adam and Green 2006; Wood and Trigila 2001). Among mineral phase assemblages of Hanang nephelinites, only titanite ($CaTiSiO_5$) preferentially incorporates Ta over Nb (D_{Ta} = 9.9–88 and D_{Nb} = 2.8–7.2, Foley 2008; Marks et al. 2008; Prowatke and Klemme 2005) increasing the Nb/Ta ratio in the silicate melt. Using

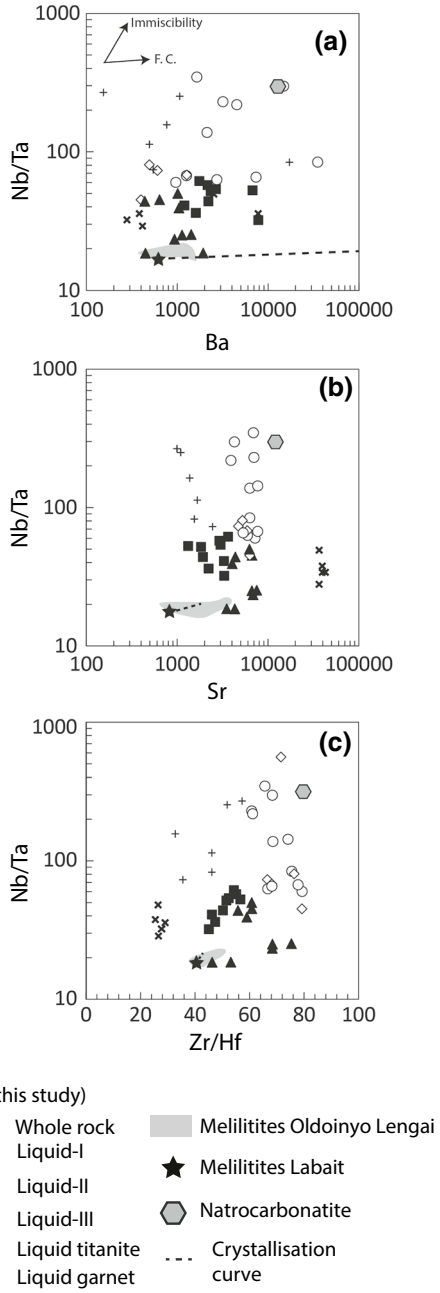

Fig. 12 Nb/Ta versus **a** Ba content, **b** Sr content and **c** Zr/Hf for melt recalculated from cpx composition (liquid I: *diamond*, liquid II: *triangle* and liquid III: *circle*) (partition coefficient from Adam and Green 2006). Whole-rock nephelinite (*black square*, this study); melilitites from Oldoinyo Lengai (*grey field*, Mattsson et al. 2013) and Labait (*black star*, Dawson et al. 1997), natrocarbonatite (*hexagon*, Keller et al. 2010) and fractional crystallization curves from melilitite (47 % olivine, 8.5 % melilite, 10.6 % cpx, 10.9 % phlogopite and 1 % magnetite, 4 % titanite, and 0.9 % apatite)

melilitite composition, we estimated that 8–9 % of titanite crystallization is necessary to fractionate Nb–Ta and reproduced the Nb/Ta ratio measured in cpx-I and cpx-III (Figs. 9, 12).

Experimental studies involving silicate liquid and carbonatitic liquid have demonstrated that carbonate immiscibility process may lead to the close association of carbonatite and Mg-rich nephelinite in North Tanzania (e.g. Oldoinyo Lengai, Brooker and Kjarsgaard 2011; Freestone and Hamilton 1980; Lee and Wyllie 1997). Among trace elements, LILE (e.g. Ba, Sr) are compatible in carbonatitic liquid (Martin et al. 2013; Veksler et al. 1998; 2012), whereas other elements as HFSE, Sc, Al, Ti are highly incompatible in carbonate liquid. More specifically, these studies showed that Ta and Nb, and in a less extent Zr and Hf, (Hamilton et al. 1989) have different behaviours during immiscibility of silicate and carbonate liquid with $D_{Ta} \ll D_{Nb}$ in carbonate liquid, resulting in Nb–Ta fractionation (Martin et al. 2013; Veksler et al. 1998, 2012). In Hanang nephelinites, major and trace element whole-rock concentrations (Figs. 4, 12) strongly suggest a carbonate affinity (Table 4, Fig. 5), and fractional crystallization and immiscibility processes have occurred during nephelinite differentiation.

Cyclicity of silicate and carbonate liquid

Although most of phenocrysts recorded simple fractional crystallization (e.g. decreasing Mg# from core to rim of garnet, minor zonation of nepheline phenocrysts), cpx has more complex compositions recording different crystallization environments at high temperature (Nakagawa et al. 2002; Streck et al. 2005). The presence of abrupt changes in composition in cpx suggests at least three different crystallization events (Fig. 7). Early silicate liquid, from which the core of cpx crystallized, is a relatively evolved magma with low Mg#, Nb–Ta fractionation and low water content (cpx-I, Fig. 7). This first liquid has a strong carbonatitic affinity characterized by Nb/Ta fractionation, low HFSE and high LILE content, suggesting that immiscibility process has occurred before cpx crystallization (i.e. during melilitite to nephelinite evolution) leading to a carbonated-rich and H_2O-poor silicate liquid and a carbonated-poor, H_2O-rich silicate liquid not observed at Hanang volcano.

A second environment of crystallization is recorded by the mantle of cpx and yellow cpx as well as garnet compositions and differs from the first environment with more mafic composition (e.g. high Mg#), no Nb–Ta fractionation and high H_2O content (Figs. 9, 12). The composition of this second liquid is very close to the composition of melilitite (Fig. 12), suggesting that replenishment with melilitite-like magma has occurred during fractional crystallization. The third and late silicate liquid in equilibrium with the rim of cpx and apatite (interstitial crystal, Fig. 9b) has a composition very close to the early silicate liquid from which the core of cpx crystallized with low Mg#, Nb–Ta fractionation and low H_2O content, suggesting that immiscibility process

also occurred during fractional crystallization leading to the presence of late carbonate-rich liquid.

The abrupt change in composition recorded by cpx and the absence of zonation in the mantle part of cpx (as wells as in yellow cpx) and garnet suggest that crystallization, carbonate saturation and immiscibility processes occurred over a small range of crystallization and temperature (1100–1060 °C) corresponding to the crystallization of the core of the green cpx. Furthermore, the melilitite-like silicate liquid (liquid II) needs to be close to carbonate saturation to allow new immiscibility process leading to carbonated-rich silicate liquid III.

The close composition of carbonated-rich silicate liquid I and III recorded by cpx phenocrysts implies that cyclicity of silicate-rich melt and carbonate-rich melt may have been an important process involved in the genesis of nephelinite over a small range of temperature similar to those proposed for the genesis of the complex carbonatite and nephelinite association at Lengai volcano (Keller et al. 2010). The carbonatite affinity recorded by cpx core and rim, as well as the whole-rock compositions, suggest that immiscibility is a dominant process. The magma evolution can be described by several steps as follows:

1. Fractional crystallization and carbonate saturation of melilitite magma
2. Liquid immiscibility leading to carbonated-rich silicate liquid (liquid I) and potentially to another liquid, H_2O-bearing silicate liquid (not observed at Hanang)
3. Replenishment with H_2O-bearing melilitite-like magmas (liquid II)
4. Fractional crystallization and carbonate saturation (liquid I + II)
5. Liquid immiscibility leading to carbonated-rich silicate liquid (liquid III) and potentially to another liquid, H_2O-bearing silicate liquid (not observed at Hanang)

Sparse melt inclusions (with silicate glass and carbonate phase) in nepheline crystals also suggest that late carbonatite immiscibility occurred during ascent. This late process leading to evolved magma will be considered in a companion paper (in prep).

Carbonatite-nephelinite association in North Tanzanian Divergence (NTD)

Hanang volcano is part of the southern part of the NTD, and its specific location allows evaluation of magma genesis at the earliest stage of EAR opening, South to the Natron basin (Fig. 1). The Natron basin is characterized by the presence of closely associated natrocarbonatite, calciocarbonatite and carbonate-nephelinite lavas (e.g. Lengai and Shombole volcanoes, Dawson 2012). Although Hanang volcano did not erupt *sensus stricto* carbonatite lavas, nephelinite lavas have bulk-rock composition and isotopic signature close to the Natron carbonatite-nephelinite (e.g. Bell and Tilton 2001; Harmer and Gittins 1998) and mineral crystallization records magmatic differentiation of carbonated-rich silicate liquid. Melilitite magmas evolved to nephelinite magmas at 9–12 km through fractional crystallization, carbonate–silicate immiscibility and replenishment.

Multistage model involving carbonate-rich silicate liquid and silicate-rich liquid has been proposed to explain the variety of nephelinitic lavas and the presence of natrocarbonatite at Oldoinyo Lengai (Dawson 1998) including (1) olivine-pyroxene-phlogopite fractionation from carbonated olivine nephelinite, followed by (2) crystallization of pyroxene-perovskite-garnet-apatite and (3) at least three events of immiscibility process linked to carbonate saturation. The carbonated-rich silicate liquid identified at Hanang is coherent with the first stages of Oldoinyo Lengai evolution involving immiscibility and formation of combeite wollastonite nephelinite (CWN) after crystallization of olivine nephelinite (Figs. 3, 4, 5). The absence of wollastonite and perovskite in Hanang nephelinite compared to Oldoinyo Lengai nephelinites may suggest crystallization under slightly more oxidized conditions (Marks et al. 2008; Zaitsev et al. 2012).

The very close bulk-rock composition of carbonate-free nephelinite at Hanang and carbonate-bearing nephelinite at Shombole (Figs. 3, 4, 5a) suggest slightly different carbonate saturation leading to the formation of *sensus stricto* carbonate liquid. The carbonate/silicate melt ratio in Shombole nephelinite is estimated at 9 vol% (9–22 % for Oldoinyo Lengai; Pyle et al. 1991). For Shombole lavas, immiscibility and crystallization occurred at 950 °C and 200 MPa (experiments from Kjarsgaard and Peterson 1991; Peterson 1989 and low-pressure cpx crystallization; Fig. 6), whereas carbonate-rich silicate liquids in Hanang evolved at higher pressure (P = 400–600 MPa, Figs. 6, 11). The higher pressure at Hanang would be related to its position at the leading edge of rifting, as the rifting is abutting against the Tanzanian craton. The difference in carbonate saturation and the formation of carbonatite and carbonated-nephelinite may then be the result of the different pressure of differentiation observed between the North and the South parts of the NTD, although lower CO_2 component in mantle source hindering "true" carbonate saturation cannot be excluded. The presence of high CO_2 concentrations in melt inclusions in nepheline phenocrysts from CWN lavas of Oldoinyo Lengai in the Natron area (2.76–8.75 wt%, de Moor et al. 2013) and variable H_2O concentrations have been reported depending on Oldoinyo Lengai eruptions [eruption 2007: 0.7–10.1 wt% H_2O (de Moor et al. 2013); eruption 1917: 0.1–0.7 wt% H_2O (Sharygin et al.

2012)]. Hanang nephelinites contain very low water content (~0.3 wt% H_2O) and carbonate affinity, similar to those reported for the CWN lavas of Oldoinyo Lengai erupted in 1917, indicating that high CO_2 activity and solubility prevailed during magma differentiation (e.g. Mysen and Boettcher 1975; Papale 1999).

The Tanzanian upper mantle sampled by small Pello hill-Eledoi and Labait cone volcanoes in North and South part of the NTD, respectively (peridotite xenoliths in melilitites, Fig. 1) are harzburgite, wherlite and dunite, with garnet, hydrous minerals (e.g. phlogopite, amphibole) and primary calcite related to the presence of complex mantle metasomatism events (Dawson and Smith 1988; Koornneef et al. 2009; Lee et al. 2000; Rudnick et al. 1993). The refractory mantle beneath the East African Craton records deep fluid–rock interaction at >90 km with a large amount of Ca-carbonatitic fluid (2 % of carbonatitic fluid, Jones et al. 1983; Rudnick et al. 1993) and minor H_2O-rich fluid (<50 ppm wt H_2O whole-rock peridotite; Baptiste et al. 2015; Hui et al. 2015) and Fe-rich, Ca-rich and Si-rich metasomatic events leading to a heterogeneous lithospheric mantle (Dawson 2012; Gibson et al. 2013). The silicic nephelinite from Hanang corroborates the presence of CO_2-rich H_2O-poor melilititic liquid in the southern part of the NTD and melt percolations after deep partial melting of CO_2-rich oxidized mantle source. The nature of the melt produced, i.e. melilitite, is strongly dependent of the degree of partial melting and the pressure of carbon-assisted melting with silicate melt formed after higher degree of partial melting (temperature) or lower pressure (<4 GPa) compared to carbonatite (>4 GPa) (Foley et al. 2009; Gudfinnsson and Presnall 2005; White and Wyllie 1992). The close association of carbonatite and melilitite-nephelinite is then the result of immiscibility at low pressure (400–600 MPa) as liquid immiscibility at pressures greater than 2–3 GPa has not been observed experimentally (Hammouda and Keshav 2015).

Carbonatite-melilitite-nephelinite magmatism in the NTD must be caused by thermal perturbation possibly by the presence of mantle plumes in this area, which were subject to prior metasomatism by carbonated melts. Melt percolation from an asthenosphere thermal anomaly would facilitate faulting and creeping on inherited structures of the Precambrian lower crust leading to deep seismic swarm observed in Manyara Basin (20–40 km, Albaric et al. 2014) and Magadi-Natron basin (15–30 km, Lee et al. 2016). Deep earthquakes can be triggered by fluids movement and gas release from melilitite magmas in the lower crust (CO_2 as free phase between 1 and 0.5 GPa; Keir et al. 2009; Lee et al. 2016; Lindenfeld et al. 2012).

Acknowledgments This research was financially supported by the ANR project CoLiBrEA CTN°LS 104568. We thank Tanzania COSTECH and the French Embassy for help for Research Permits, and University of Dar es Salaam and Nelson Mandela African Institute of Science and Technology in Arusha for their help during field sampling. We would like to thank C. Nevado, C. Garrido and Microsonde Sud for their valuable technical assistance, and S. Demouchy and J.M. Dautria for informative discussions. Constructive reviews by A. Zaitsev and an anonymous reviewer are gratefully acknowledged. We thank J. Hoefs for editorial handling of the manuscript.

References

Adam J, Green T (2006) Trace element partitioning between mica—and amphibole-bearing garnet lherzolite and hydrous basanitic melt: 1. Experimental results and the investigation of controls on partitioning behaviour. Contrib Mineral Petrol 152(1):1–17. doi:10.1007/s00410-006-0085-4

Albaric J, Perrot J, Déverchère J, Deschamps A, Le Gall B, Ferdinand RW, Petit C, Tiberi C, Sue C, Songo M (2010) Contrasted seismogenic and rheological behaviours from shallow and deep earthquake sequences in the North Tanzanian Divergence, East Africa. J Afr Earth Sci 58(5):799–811. doi:10.1016/j.jafrearsci.2009.09.005

Albaric J, Déverchère J, Perrot J, Jakovlev A, Deschamps A (2014) Deep crustal earthquakes in North Tanzania, East Africa: interplay between tectonic and magmatic processes in an incipient rift. Geochem Geophys Geosyst 15(2):374–394. doi:10.1002/2013GC005027

Aulbach S, Rudnick RL, McDonough WF (2008) Li-Sr-Nd isotope signatures of the plume and cratonic lithospheric mantle beneath the margin of the rifted Tanzanian craton (Labait). Contrib Mineral Petrol 155(1):79–92. doi:10.1007/s00410-007-0226-4

Bagdasaryan GP, Gerasimovskiy VI, Polyakov AI, Gukasyan RK, Vernadskiy VI (1973) Age of volcanic rocks in the rift zones of East Africa. Geochem Int 10(1):66–71

Baptiste V, Tommasi A, Vauchez A, Demouchy S, Rudnick RL (2015) Deformation, hydration, and anisotropy of the lithospheric mantle in an active rift: constraints from mantle xenoliths from the North Tanzanian Divergence of the East African Rift. Tectonophysics 639:34–55. doi:10.1016/j.tecto.2014.11.011

Behrens H, Misiti V, Freda C, Vetere F (2009) Solubility of H2O and CO2 in ultrapotassic melts at 1200 and 1250 C and pressure from 50 to 500 MPa. Am Mineral 94(1):105–120. doi:10.2138/am.2009.2796

Bell K, Tilton GR (2001) Nd, Pb and Sr isotopic compositions of East African carbonatites: evidence for mantle mixing and plume inhomogeneity. J Petrol 42(10):1927–1945

Bell D, Ihinger P, Rossman G (1995) Quantitative and analysis of trace OH in garnet and pyroxenes. Am Mineral 80:465–474

Brey G, Green DH (1977) Systematic study of liquidus phase relations in olivine melilitite + H_2O + CO_2 at high pressures and petrogenesis of an olivine melilitite magma. Contrib Mineral Petrol 61(2):141–162

Brooker RA, Kjarsgaard BA (2011) Silicate–carbonate liquid immiscibility and phase relations in the system SiO_2–Na_2O–Al_2O_3–CaO–CO_2 at 0.1–2.5 GPa with applications to carbonatite genesis. J Petrol 52(7–8):1281–1305. doi:10.1093/petrology/egq081

Bultitude RJ, Green DH (1971) Experimental study of crystal-liquid relationships at high pressures in olivine nephelinite and basanite compositions. J Pet 12(1):121–147

Calais E, d'Oreye N, Albaric J, Deschamps A, Delvaux D, Déverchere J, Ebinger C, Ferdinand RW, Kervyn F, Macheyeki AS, Oyen A, Perrot J, Saria E, Smets B, Stamps DS, Wauthier C (2008) Strain accommodation by slow slip and dyking in a youthful continental rift, East Africa. Nature 456(7223):783–787. doi:10.1038/nature07478

Chakhmouradian AR (2006) High-field-strength elements in carbonatitic rocks: geochemistry, crystal chemistry and significance for constraining the sources of carbonatites. Chem Geol 235(1):138–160. doi:10.1016/j.chemgeo.2006.06.008

Chen H, Xia QK, Ingrin J, Jia ZB, Feng M (2015) Changing recycled oceanic components in the mantle source of the Shuangliao Cenozoic basalts, NE China: new constraints from water content. Tectonophysics 650:113–123. doi:10.1016/j.tecto.2014.07.022

Church A (1996) The petrology of the Kerimasi carbonatite volcano and the carbonatites of Oldoinyo Lengai with a review of other occurrences of extrusive carbonatites. Ph.D. Thesis, University College of London

Craig TJ, Jackson JA, Priestley K, McKenzie D (2011) Earthquake distribution patterns in Africa: their relationship to variations in lithospheric and geological structure, and their rheological implications. Geophys J Int 185(1):403–434. doi:10.1111/j.1365-246X.2011.04950.x

Dasgupta R, Hirschmann MM, Smith ND (2007) Partial melting experiments of peridotite + CO_2 at 3 GPa and genesis of alkalic ocean island basalts. J Petrol 48(11):2093–2124. doi:10.1093/petrology/egm053

Dawson JB (1989) Sodium carbonatite extrusions from Oldoinyo Lengai, Tanzania: implications for carbonatite complex genesis. In: Carbonatites: genesis and evolution. Unwin Hyman London, pp 255–277

Dawson JB (1998) Peralkaline nephelinite–natrocarbonatite relationships at Oldoinyo Lengai, Tanzania. J Petrol 39(11–12):2077–2094

Dawson JB (2008) The Gregory rift valley and Neogene-recent volcanoes of northern Tanzania. Geological Society, London **33**

Dawson JB (2012) Nephelinite–melilitite–carbonatite relationships: evidence from Pleistocene-recent volcanism in northern Tanzania. Lithos 152:3–10. doi:10.1016/j.lithos.2012.01.008

Dawson JB, Smith JV (1988) Metasomatised and veined upper–mantle xenoliths from Pello Hill, Tanzania: evidence for anomalously-light mantle beneath the Tanzanian sector of the East African Rift Valley. Contrib Mineral Petrol 100(4):510–527

Dawson JB, James D, Paslick C, Halliday AM (1997) Ultrabasic potassic low-volume magmatism and continental rifting in north-central Tanzania: association with enhanced heat flow. Russ Geol Geophys 38:69–81

de Moor JM, Fischer TP, King PL, Botcharnikov RE, Hervig RL, Hilton DR, Barry PH, Mangasini F, Ramirez C (2013) Volatile-rich silicate melts from Oldoinyo Lengai volcano (Tanzania): implications for carbonatite genesis and eruptive behavior. Earth Planet Sci Lett 361:379–390. doi:10.1016/j.epsl.2012.11.006

Denis CM, Alard O, Demouchy S (2015) Water content and hydrogen behaviour during metasomatism in the uppermost mantle beneath Ray Pic volcano (Massif Central, France). Lithos 236:256–274. doi:10.1016/j.lithos.2015.08.013

Dumont S, Socquet A, Grandin R, Doubre C, Klinger Y (2016) Surface displacements on faults triggered by slow magma transfers between dyke injections in the 2005–2010 rifting episode at Dabbahu–Manda–Hararo rift (Afar, Ethiopia). Geophys J Int 204(1):399–417. doi:10.1093/gji/ggv449

Ebinger CJ, Sleep NH (1998) Cenozoic magmatism throughout east Africa resulting from impact of a single plume. Nature 395(6704):788–791

Foley SF (2008) A trace element perspective on Archean crust formation and on the presence or absence of Archean subduction. Geol Soc Am Spec Pap 440:31–50

Foley SF, Yaxley GM, Rosenthal A, Buhre S, Kiseeva ES, Rapp RP, Jacob DE (2009) The composition of near-solidus melts of peridotite in the presence of CO_2 and H_2O between 40 and 60 kbar. Lithos 112:274–283. doi:10.1016/j.lithos.2009.03.020

Foley SF, Link K, Tiberindwa JV, Barifaijo E (2012) Patterns and origin of igneous activity around the Tanzanian craton. J Afr Earth Sci 62(1):1–18. doi:10.1016/j.jafrearsci.2011.10.001

Freestone IC, Hamilton DL (1980) The role of liquid immiscibility in the genesis of carbonatites: an experimental study. Contrib Mineral Petrol 73(2):105–117

Fujimaki H, Tatsumoto M, Aoki KI (1984) Partition coefficients of Hf, Zr, and REE between phenocrysts and groundmasses. J Geophys Res Solid Earth 89(Suppl):662–672

Furman T (2007) Geochemistry of East African Rift basalts: an overview. J Afr Earth Sci 48:147–160. doi:10.1016/j.jafrearsci.2006.06.009

Gibson SA, McMahon SC, Day JA, Dawson JB (2013) Highly refractory lithospheric mantle beneath the Tanzanian craton: evidence from Lashaine pre-metasomatic garnet-bearing peridotites. J Petrol 54(8):1503–1546. doi:10.1093/petrology/egt020

Green DH, Ringwood AE (1967) The genesis of basaltic magmas. Contrib Mineral Petrol 15(2):103–190

Grew ES, Locock AJ, Mills SJ, Galuskina IO, Galuskin EV, Hålenius U (2013) Nomenclature of the garnet supergroup. Am Mineral 98(4):785–811. doi:10.2138/am.2013.4201

Griffin WL, Powell W, Pearson NJ, O'Reilly SY (2008) GLITTER: data reduction software for laser ablation ICP-MS. Laser ablation-ICP-MS in the earth sciences vol 40. Mineralogical Association of Canada Short Course Series, pp 204–207

Gudfinnsson GH, Presnall DC (2005) Continuous gradations among primary carbonatitic, kimberlitic, melilititic, basaltic, picritic, and komatiitic melts in equilibrium with garnet lherzolite at 3–8 GPa. J Pet 46(8):1645–1659. doi:10.1093/petrology/egi029

Guzmics T, Mitchell RH, Szabó C, Berkesi M, Milke R, Ratter K (2012) Liquid immiscibility between silicate, carbonate and sulfide melts in melt inclusions hosted in co–precipitated minerals from Kerimasi volcano (Tanzania): evolution of carbonated nephelinitic magma. Contrib Mineral Petrol 164(1):101–122. doi:10.1007/s00410-012-0728-6

Guzmics T, Zajacz Z, Mitchell RH, Szabó C, Wälle M (2015) The role of liquid–liquid immiscibility and crystal fractionation in the genesis of carbonatite magmas: insights from Kerimasi melt inclusions. Contrib Mineral Petrol 169(2):1–18. doi:10.1007/s00410-014-1093-4

Hamilton DL (1961) Nephelines as crystallization temperature indicators. J Geol 69(3):321–329

Hamilton DL, Bedson P, Esson J (1989) The behaviour of trace elements in the evolution of carbonatites. In: Bell K (ed) Carbonatites: genesis and evolution. Unwin Hyman, London, pp 405–427

Hammouda T, Keshav S (2015) Melting in the mantle in the presence of carbon: review of experiments and discussion on the origin of carbonatites. Chem Geol 418:171–188. doi:10.1016/j.chemgeo.2015.05.018

Hansen SE, Nyblade AA, Benoit MH (2012) Mantle structure beneath Africa and Arabia from adaptively parameterized P-wave tomography: implications for the origin of Cenozoic Afro-Arabian tectonism. Earth Planet Sci Lett 319:23–34. doi:10.1016/j.epsl.2011.12.023

Harmer RE, Gittins J (1998) The case for primary, mantle-derived carbonatite magma. J Petrol 39(11–12):1895–1903

Hauri EH, Gaetani GA, Green TH (2006) Partitioning of water during melting of the Earth's upper mantle at H_2O-undersaturated conditions. Earth Planet Sci Lett 248(3):715–734. doi:10.1016/j.epsl.2006.06.014

Hirose K (1997) Partial melt compositions of carbonated peridotite at 3 GPa and role of CO_2 in alkali-basalt magma generation. Geophys Res Lett 24(22):2837–2840

Hui H, Peslier AH, Rudnick RL, Simonetti A, Neal CR (2015) Plume-cratonic lithosphere interaction recorded by water and other

trace elements in peridotite xenoliths from the Labait volcano, Tanzania. Geochem Geophys Geosyst. doi:10.1002/2015GC005779

Ivanikov VV, Rukhlov AS, Bell K (1998) Magmatic evolution of the melilitite–carbonatite–nephelinite dyke series of the Turiy Peninsula (Kandalaksha Bay, White Sea, Russia). J Petrol 39(11–12):2043–2059

Johnson EA (2006) Water in nominally anhydrous crustal minerals: speciation, concentration, and geologic significance. Rev Mineral Geochem 62(1):117–154. doi:10.2138/rmg.2006.62.6

Jones AP, Smith JV, Dawson JB (1983) Glasses in mantle xenoliths from Olmani, Tanzania. J Geol 91(2):167–178

Jugo PJ, Wilke M, Botcharnikov RE (2010) Sulfur K-edge XANES analysis of natural and synthetic basaltic glasses: implications for S speciation and S content as function of oxygen fugacity. Geochim Cosmochim Acta 74(20):5926–5938. doi:10.1016/j.gca.2010.07.022

Keir D, Bastow ID, Whaler KA, Daly E, Cornwell DG, Hautot S (2009) Lower crustal earthquakes near the Ethiopian rift induced by magmatic processes. Geochem Geophys Geosyst. doi:10.1029/2009GC002382

Keller J, Zaitsev AN, Wiedenmann D (2006) Primary magmas at Oldoinyo Lengai: the role of olivine melilitites. Lithos 91(1):150–172. doi:10.1016/j.lithos.2006.03.014

Keller J, Klaudius J, Kervyn M, Ernst GG, Mattsson HB (2010) Fundamental changes in the activity of the natrocarbonatite volcano Oldoinyo Lengai, Tanzania. Bull Volcanol 72(8):893–912. doi:10.1007/s00445-010-0371-x

Kjarsgaard BA (1998) Phase relations of a carbonated high-CaO nephelinite at 0.2 and 0.5 GPa. J Petrol 39(11–12):2061–2075

Kjarsgaard B, Peterson T (1991) Nephelinite-carbonatite liquid immiscibility at Shombole volcano, East Africa: petrographic and experimental evidence. Miner Petrol 43(4):293–314

Klaudius J, Keller J (2006) Peralkaline silicate lavas at Oldoinyo Lengai, Tanzania. Lithos 91(1):173–190. doi:10.1016/j.lithos.2006.03.017

Koornneef JM, Davies GR, Döpp SP, Vukmanovic Z, Nikogosian IK, Mason PR (2009) Nature and timing of multiple metasomatic events in the sub-cratonic lithosphere beneath Labait, Tanzania. Lithos 112:896–912. doi:10.1016/j.lithos.2009.04.039

Le Bas MJ, Le Maitre RW, Streckeisen A, Zanettin B (1986) A chemical classification of volcanic rocks based on total alkali-silica diagram. J Petrol 27(3):745–750

Le Gall B, Nonnotte P, Rolet J, Benoit M, Guillou H, Mousseau-Nonnotte M, Albaric J, Deverchère J (2008) Rift propagation at craton margin: distribution of faulting and volcanism in the North Tanzanian Divergence (East Africa) during Neogene times. Tectonophysics 448(1):1–19. doi:10.1016/j.tecto.2007.11.005

Lee CT, Rudnick RL (1999) Compositionally stratified cratonic lithosphere: petrology and geochemistry of peridotite xenoliths from the Labait volcano, Tanzania. In: Proceedings of the VIIth international kimberlite conference, vol 1. pp 503–521

Lee WJ, Wyllie PJ (1997) Liquid immiscibility between nephelinite and carbonatite from 1.0 to 2.5 GPa compared with mantle melt compositions. Contrib Mineral Petrol 127(1–2):1–16

Lee WJ, Wyllie PJ (1998) Processes of crustal carbonatite formation by liquid immiscibility and differentiation, elucidated by model systems. J Petrol 39(11–12):2005–2013

Lee CT, Rudnick RL, McDonough WF, Horn I (2000) Petrologic and geochemical investigation of carbonates in peridotite xenoliths from northeastern Tanzania. Contrib Mineral Petrol 139(4):470–484

Lee H, Muirhead JD, Fischer TP, Ebinger CJ, Kattenhorn SA, Sharp ZD, Kianji G (2016) Massive and prolonged deep carbon emissions associated with continental rifting. Nat Geosci 9:145–149. doi:10.1038/NGEO2622

Lindenfeld M, Rümpker G, Link K, Koehn D, Batte A (2012) Fluid-triggered earthquake swarms in the Rwenzori region, East African Rift: evidence for rift initiation. Tectonophysics 566:95–104. doi:10.1016/j.tecto.2012.07.010

Mana S, Furman T, Carr MJ, Mollel GF, Mortlock RA, Feigenson MD, Turrin BD, Swisher CC (2012) Geochronology and geochemistry of the Essimingor volcano: melting of metasomatized lithospheric mantle beneath the North Tanzanian Divergence zone (East African Rift). Lithos 155:310–325. doi:10.1016/j.lithos.2012.09.009

Mana S, Furman T, Turrin BD, Feigenson MD, Swisher CC (2015) Magmatic activity across the East African North Tanzanian Divergence zone. J Geol Soc Lond. doi:10.1144/jgs2014-072

Mariano AN, Roeder PL (1983) Kerimasi: a neglected carbonatite volcano. J Geol 91:449–455

Marks MA, Schilling J, Coulson IM, Wenzel T, Markl G (2008) The alkaline–peralkaline Tamazeght complex, High Atlas Mountains, Morocco: mineral chemistry and petrological constraints for derivation from a compositionally heterogeneous mantle source. J Petrol 49(6):1097–1131. doi:10.1093/petrology/egn019

Martin LH, Schmidt MW, Mattsson HB, Guenther D (2013) Element partitioning between immiscible carbonatite and silicate melts for dry and H_2O-bearing systems at 1–3 GPa. J Petrol 54:2301–2338. doi:10.1093/petrology/egt048

Mathez EA, Webster JD (2005) Partitioning behavior of chlorine and fluorine in the system apatite-silicate melt-fluid. Geochim Cosmochim Acta 69(5):1275–1286. doi:10.1016/j.gca.2004.08.035

Mattsson HB, Nandedkar RH, Ulmer P (2013) Petrogenesis of the melilititic and nephelinitic rock suites in the Lake Natron–Engaruka monogenetic volcanic field, northern Tanzania. Lithos 179:175–192. doi:10.1016/j.lithos.2013.07.012

Mitchell RH, Dawson JB (2012) Carbonate–silicate immiscibility and extremely peralkaline silicate glasses from Nasira cone and recent Eruptions at Oldoinyo Lengai Volcano, Tanzania. Lithos 152:40–46. doi:10.1016/j.lithos.2012.01.006

Moore G (2008) Interpreting H_2O and CO_2 contents in melt inclusions: constraints from solubility experiments and modeling. Rev Mineral Geochem 69(1):333–362. doi:10.2138/rmg.2008.69.9

Morimoto N (1988) Nomenclature of pyroxenes. Miner Petrol 39(1):55–76

Mulibo GD, Nyblade AA (2013) Mantle transition zone thinning beneath eastern Africa: evidence for a whole-mantle superplume structure. Geophys Res Lett 40(14):3562–3566. doi:10.1002/grl.50694

Mysen BO, Boettcher AL (1975) Melting of a hydrous mantle: I. Phase relations of natural peridotite at high pressures and temperatures with controlled activities of water, carbon dioxide, and hydrogen. J Petrol 16(1):520–548

Nakagawa M, Wada K, Wood CP (2002) Mixed magmas, mush chambers and eruption triggers: evidence from zoned clinopyroxene phenocrysts in andesitic scoria from the 1995 eruptions of Ruapehu volcano, New Zealand. J Petrol 43(12):2279–2303

Nonnotte P (2007) Etude Volcano-tectonique de La Zone de Divergence Nord Tanzanienne (Terminaison Sud Du Rift Kenyan). Caractérisation Pétrologique et Géochimique Du Volcanisme Récent (8 Ma–Actuel) et Du Manteau Source. Contraintes de Mise En Place. Université de Bretagne Occidentale

Nyblade AA, Owens TJ, Gurrola H, Ritsema J, Langston CA (2000) Seismic evidence for a deep upper mantle thermal anomaly beneath east Africa. Geology 28(7):599–602

Oppenheimer C, Pyle DM, Barclay J (eds) (2003) Volcanic degassing. Geological Society of London 213

Papale P (1999) Modeling of the solubility of a two-component $H_2O + CO_2$ fluid in silicate liquids. Am Mineral 84(4):477–492

Parat F, Holtz F (2005) Sulfur partition coefficient between apatite and rhyolite: the role of bulk S content. Contrib Mineral Petrol 150(6):643–651

Parat F, Holtz F, Klügel A (2011) S-rich apatite-hosted glass inclusions in xenoliths from La Palma: constraints on the volatile partitioning in evolved alkaline magmas. Contrib Mineral Petrol 162(3):463–478. doi:10.1007/s00410-011-0606-7

Paslick CR, Halliday AN, Lange RA, James D, Dawson JB (1996) Indirect crustal contamination: evidence from isotopic and chemical disequilibria in minerals from alkali basalts and nephelinites from northern Tanzania. Contrib Mineral Petrol 125(4):277–292

Paterson MS (1982) The determination of hydroxyl by infrared absorption in quartz, silicate glasses, and similar materials. Bull Soc Fr Minéral Crist 105:20–29

Peterson TD (1989) Peralkaline nephelinites. I. Comparative petrology of Shombole and Oldoinyo L'engai, East Africa. Contrib Mineral Petrol 101(4):458–478

Pik R, Marty B, Hilton DR (2006) How many mantle plumes in Africa? The geochemical point of view. Chem Geol 226(3):100–114. doi:10.1016/j.chemgeo.2005.09.016

Prowatke S, Klemme S (2005) Effect of melt composition on the partitioning of trace elements between titanite and silicate melt. Geochim Cosmochim Acta 69(3):695–709. doi:10.1016/j.gca.2004.06.037

Putirka K (1999) Clinopyroxene + liquid equilibria to 100 kbar and 2450 K. Contrib Mineral Petrol 135(2–3):151–163

Putirka KD (2008) Thermometers and barometers for volcanic systems. Rev Mineral Geochem 69(1):61–120. doi:10.2138/rmg.2008.69.3

Pyle DM, Dawson JB, Ivanovich M (1991) Short-lived decay series disequilibria in the natrocarbonatites lavas of Oldoinyo Lengai, Tanzania: constraints on the timing of magma genesis. Earth Planet Sci Lett 105:378–398

Rhodes JM, Dungan MA, Blanchard DP, Long PE (1979) Magma mixing at mid-ocean ridges: evidence from basalts drilled near 22 N on the Mid-Atlantic Ridge. Tectonophysics 55(1):35–61

Roeder PL, Emslie R (1970) Olivine-liquid equilibrium. Contrib Mineral Petrol 29(4):275–289

Rubin AM, Pollard DD (1988) Dike-induced faulting in rift zones of Iceland and Afar. Geology 16(5):413–417

Rudnick RL, McDonough WF, Chappell BW (1993) Carbonatite metasomatism in the northern Tanzanian mantle: petrographic and geochemical characteristics. Earth Planet Sci Lett 114(4):463–475

Selby J, Thomas C (1966) Balangida Lelu, Quarter Degree Sheet 103. Tanzania Mineral Resources Division

Sharygin VV, Kamenetsky VS, Zaitsev AN, Kamenetsky MB (2012) Silicate–natrocarbonatite liquid immiscibility in 1917 eruption combeite–wollastonite nephelinite, Oldoinyo Lengai Volcano, Tanzania: melt inclusion study. Lithos 152:23–39. doi:10.1016/j.lithos.2012.01.021

Simonetti A, Shore M, Bell K (1996) Diopside phenocrysts from nephelinite lavas, Napak Volcano, eastern Uganda; evidence for magma mixing. Can Mineral 34(2):411–421

Streck MJ, Dungan MA, Bussy F, Malavassi E (2005) Mineral inventory of continuously erupting basaltic andesites at Arenal volcano, Costa Rica: implications for interpreting monotonous, crystal-rich, mafic arc stratigraphies. J Volcanol Geotherm Res 140(1):133–155. doi:10.1016/j.jvolgeores.2004.07.018

Sun SS, McDonough WF (1989) Chemical and isotopic systematics of oceanic basalts: implications for mantle composition and processes. Geol Soc Lond Spec Publ 42(1):313–345

Thomas C (1966) Hanang, quarter degree sheet 84. 1:125000 Geol. Surv. Tanganyika, Tanzania Mineral Resources Division

Vauchez A, Dineur F, Rudnick R (2005) Microstructure, texture and seismic anisotropy of the lithospheric mantle above a mantle plume: insights from the Labait volcano xenoliths (Tanzania). Earth Planet Sci Lett 232(3):295–314. doi:10.1016/j.epsl.2005.01.024

Veksler IV, Nielsen TFD, Sokolov SV (1998) Mineralogy of crystallized melt inclusions from Gardiner and Kovdor ultramafic alkaline complexes: implications for carbonatite genesis. J Petrol 39(11–12):2015–2031

Veksler IV, Dorfman AM, Dulski P, Kamenetsky VS, Danyushevsky LV, Jeffries T, Dingwell DB (2012) Partitioning of elements between silicate melt and immiscible fluoride, chloride, carbonate, phosphate and sulfate melts, with implications to the origin of natrocarbonatite. Geochim Cosmochim Acta 79:20–40. doi:10.1016/j.gca.2011.11.035

Vernet M, Marin L, Boulmier S, Lhomme J, Demange JC (1987) Dosage du fluor et du chlore dans les matériaux géologiques y compris les échantillons hyperalumineux. Analusis 15(9):490–498

Vetere F, Holtz F, Behrens H, Botcharnikov RE, Fanara S (2014) The effect of alkalis and polymerization on the solubility of H_2O and CO_2 in alkali–rich silicate melts. Contrib Mineral Petrol 167(5):1–17. doi:10.1007/s00410-014-1014-6

Wade JA, Plank T, Hauri EH, Kelley KA, Roggensack K, Zimmer M (2008) Prediction of magmatic water contents via measurement of H_2O in clinopyroxene phenocrysts. Geology 36(10):799–802. doi:10.1130/G24964A.1

Webster JD, Kinzler RJ, Mathez EA (1999) Chloride and water solubility in basalt and andesite melts and implications for magmatic degassing. Geochim Cosmochim Acta 63(5):729–738

White BS, Wyllie PJ (1992) Solidus reactions in synthetic lherzolite-H_2O-CO_2 from 20–30 kbar, with applications to melting and metasomatism. J Volcanol Geotherm Res 50(1):117–130

Wood CP (1968) A geochemical study of East African Alkaline Lavas and its Relevance to the Petrogenesis of Nephelinites. Ph.D. thesis, University of Leeds

Wood BJ, Trigila R (2001) Experimental determination of aluminous clinopyroxene–melt partition coefficients for potassic liquids, with application to the evolution of the Roman province potassic magmas. Chem Geol 172(3):213–223

Wright TJ, Ebinger C, Biggs J, Ayele A, Yirgu G, Keir D, Stork A (2006) Magma-maintained rift segmentation at continental rupture in the 2005 Afar dyking episode. Nature 442(7100):291–294. doi:10.1038/nature04978

Zaitsev AN, Marks MAW, Wenzel T, Spratt J, Sharygin VV, Strekopytov S, Markl G (2012) Mineralogy, geochemistry and petrology of the phonolitic to nephelinitic Sadiman volcano, Crater Highlands, Tanzania. Lithos 152:66–83. doi:10.1016/j.lithos.2012.03.001

Conclusions du chapitre IVA

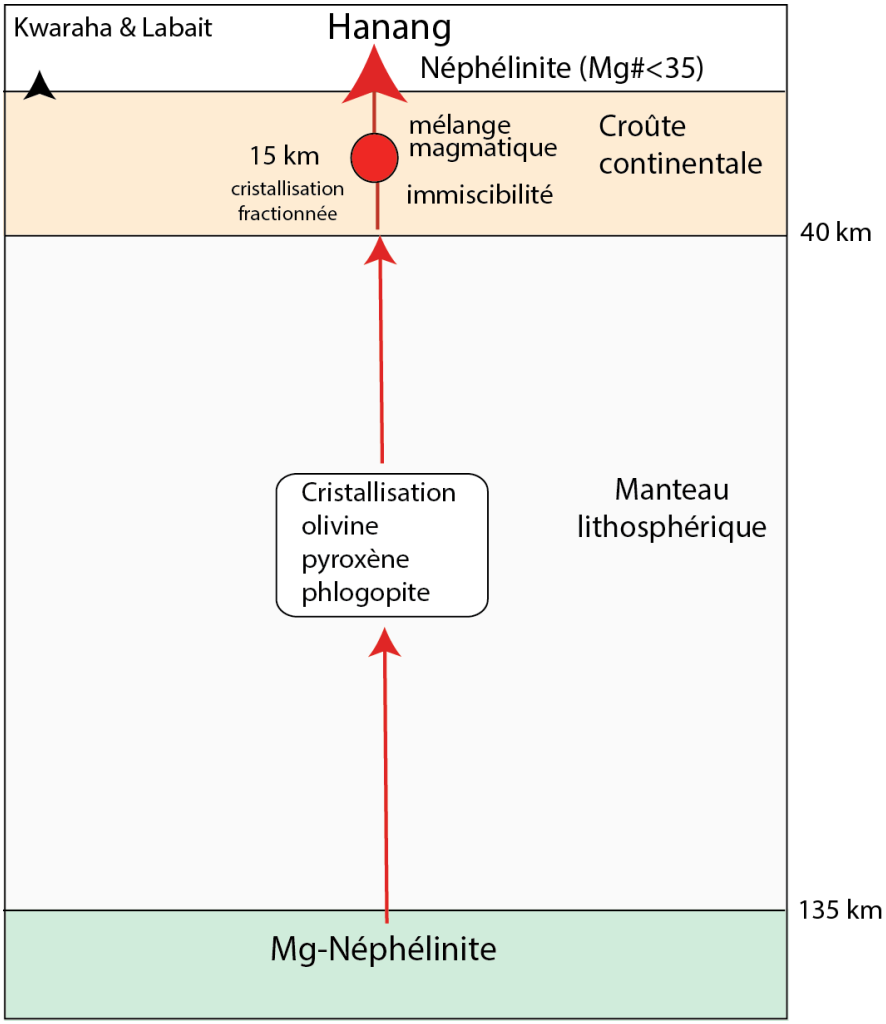

IV.B CO_2- rich silicate melt and carbonatite immiscibility in early stage rifting: melt inclusions from Hanang volcano

Abstract

North Tanzanian Divergence is the first stage of continental break-up of East African Rift (<6 Ma) and is one of the most concentrated areas of carbonatite magmatism on Earth, with singular Oldoinyo Lengai and Kerimasi volcanoes. Hanang is the southern volcano of the North Tanzanian Divergence and represents volcanic activity at early stage rifting. In this study, we investigate glassy melt inclusions in nepheline phenocrysts to constrain the late stage of Mg-poor nephelinite evolution and the behaviour of volatiles (CO2, H2O, S, F, Cl) during magma storage and ascent. The melt inclusions have a green silicate glass, a microcrystalline carbonate phase and a shrinkage bubble free of gas phase indicating that carbonatite:silicate (18:82) liquid immiscibility occurred during nephelinite magmatic evolution. The silicate glasses have trachytic composition (Na+K/Al = 1.6 - 7.2, SiO2 = 54 - 65.5 wt%) with high CO2 (0.43 wt% CO2), sulfur (0.21-0.92 wt% S) and halogens (0.28 - 0.84 wt% Cl; 0.35-2.54 wt% F) contents and very low H2O content (<0.1wt%). The carbonate phase is an anhydrous Ca-Na-K-S carbonate with 33 wt% CaO, 20 wt% Na2O, 3 wt% K2O, and 3 wt% S. The entrapped melt in nepheline corresponds to evolved interstitial silicate melt after crystallisation of cpx (17%), nepheline (40%) garnet (6.5%) and apatite (1.7%) from a Mg-rich nephelinite magma. The pre-immiscible silicate liquid has a CO2 -rich phonolitic composition (Na+K/Al = 6.2 - 6.9) with 6 ± 1.5 wt% CO2 at pressure of 800 ± 200 MPa. The immiscibility process leading to glassy silicate melt and microcrystalline carbonatitic melt occurred in closed system during rapid ascent at crustal level ~500 MPa. The Ca-Na carbonatitic liquid in Hanang nephelinite recorded immiscible process with intermediate compositions between Na-carbonatite at Oldoinyo Lengai and Ca-carbonatite at Kerimasi. The absence of carbonatite lava flows at Hanang volcano suggest that Hanang magma did not reach carbonate saturation and evolved through open system differentiation.

IV.B.I. Introduction

North Tanzanian Divergence (NTD) at the southern part of the East branch of East African Rift is one of the most concentrated areas of carbonatite magmatism on Earth. Carbonatites are associated with alkaline lavas (nephelinite, phonolite, afrikandite) and are described as the result of immiscibility process at crustal level (e.g. Lee and Wyllie 1998, Kjarsgaard et al. 1995). Immiscible process lead to different type of carbonatite: Ca ± Na carbonatite (Kerimasi) and natrocarbonatite (Oldoinyo Lengai) suggesting different source and/or conditions of crystallisation (de Moor et al. 2013, Guzmics et al. 2011, Sharygin et al. 2012). Melt inclusions are present in alkaline lavas from the North Tanzanian Divergence (East African Rift) at Kerimasi (Guzmics et al. 2011, 2012, 2015; Káldos et al. 2015), Sadiman

(Zaitsev et al. 2012) and Hanang (this study). Melt inclusions trapped in phenocrysts are potential tracer of intermediate and/or late processes leading to the formation of carbonatite magmas during alkaline magma evolution (e.g. Mitchell and Dawson 2012, Sharygin et al. 2012). At Oldoinyo Lengai, melt inclusions in nephelinite attest of the presence of Na-H2O-CO2-rich magmas at depth (2.7 - 8.7 wt% CO2 and 0.7 - 10.1 wt% H2O; de Moor et al. 2013) and immiscibility between carbonate and silicate liquid at very low pressure (Kjarsgaard et al. 1995). At Oldoinyo Lengai and Kerimasi, melt inclusion studies constrain that immiscibility process lead to the formation of carbonatite at crustal pressure (from 100 to 1000 MPa) from a CO2-rich parental melt. At Sadiman, Alkaline lavas are not directly associated with carbonatite lavas but mineral and whole rock chemistry suggest a pre-stage on the evolutionary path towards carbonatitic magmatism (Zaitsev et al. 2012).

Hanang volcano is located at the southern part of NTD and represents early stage rifting and complex early magmatic differentiation involving fractional crystallisation from melilitite parental melt and carbonate-silicate immiscibility and melilitite replenishment at ~ 600 MPa (Baudouin et al. 2016). The presence of melt inclusions in nephelinite phenocrysts (Fig.IV.1) allows us to determine the composition of the interstitial melt and the behaviour of volatiles that controls late magmatic evolution with decreasing depth and temperature during magma ascent and degassing.

IV.B.II. Analytical Methods

Sample preparation

Nephelinite samples have been crushed to a fraction of 100 - 200 µm and large nepheline crystals have been selected by hand picking. Nepheline crystals were placed in epoxy and polished to expose the melt inclusions. Polish was realized with ethanol instead of water to prevent loss of soluble phase, in particular for the carbonate part of the inclusions. The polishing was carried out with an abrasive paper of silica carbide with a particle size of 9 µm and 6 µm.

Preparation of reference material for major and volatile element analyses

CO2-bearing synthetic glass with the mean composition of Hanang silicate glass (n=30, standard composition in supplementary data) has been synthetized at the Institut of Mineralogy, Leibniz University Hannover, Germany for calibration of volatile and major element analyses. The synthetic glass was prepared with powders of $NaCO_3$, K_2CO_3, FeO, MgO, MnO, Al_2O_3, P_2O_5 and SiO_2 and two cycles of melting at 1600 °C and 1 atm. The synthesis of volatile-bearing trachytic glass (synthetic glass + silver oxalate $Ag_2C_2O_4$) was conducted at 1200°C and 200 MPa in Internally Heated Pressure Vessel (IHPV) (for details of the IHPV design see Berndt et al., 2002). The experiment was carried at anhydrous conditions. Temperature was controlled with four thermocouples and the variations were less than ±5°C. The variation of pressure during the experiments was less than 5 MPa. The intrinsic redox conditions in the IHPV (log fO_2 intrinsic) were close to ΔNNO+3. The capsule was rapidly (~150°C/s) and isobarically quenched after the run. After experiment, the CO_2 content of synthetic glass was determined using ELTRA CS 800 analyzer (Institut of Mineralogy, University of Hanover). The carbon

solubility of trachytic melt at 200 MPa and 1200°C is 0.22 wt% CO_2 (standard composition in supplementary material).

Microprobe analyses

The concentration of major and volatile elements in melt inclusions were determined using electron microprobe (EMPA) (Cameca XS100 at "Microsonde Sud", University of Montpellier, France). Operating conditions for silicate glass analyses comprised an accelerating voltage of 15 keV, a 10 nA beam current and a beam at 5 µm. The counting time was fixed at 20 s for each element analysis and 40 s for volatile elements (S, Cl, F). Melt inclusion analyses were validated with external glass standards with andesitic and trachytic (i.e. reference material) composition. The standards used for major and volatile element analyses are: wollastonite for Si and Ca, Al_2O_3 for Al, TiO_2 for Ti, forsterite for Mg, hematite for Fe, orthose for K, albite for Na, apatite for P, native metal for Ni, Mn, Cu, baryte for S and Ba, fluorite for F and chloroapatite for Cl.

The total of silicate glass analyses range between 96 and 100 suggesting the presence of volatiles (CO_2 or H_2O) or alkalis losses in glassy melt inclusion during analyses (e.g. Sekisova et al. 2015).

Laser Ablation Inductively Coupled Plasma Mass Spectrometry (LA-ICPMS)

Trace element concentration of the largest melt inclusions (> 20µm) in nepheline phenocrysts (e.g. melt inclusions in Fig.IV.2) were determined by a LA-ICP-MS system using GeoLas Q + Excimer CompEx102 (AETE platform, University of Montpellier). Analyses were realized with a 15 µm diameter laser beam; a laser repetition rate of 7 Hz and laser power of 1 mJ (10 $J.cm^{-2}$). For the quantification of trace elements, we used the internal standard Nist610 500 ppm and the SiO_2 content of the silicate glass of melt inclusions previously determined by electron microprobe.

The instrumental drift is compensated by the internal standard calculations in the Glitter software (Griffin et al. 2008); no other drift corrections are used. For data processing and calculation of concentrations, Glitter Software was used to process the raw data files containing the signal intensity versus time. This allows precise selection of blanks and signals, and rapid visualization of the intensity data.

Raman spectroscopy

The micro-Raman scattering measurements were performed on a Renishaw Invia spectrometer equipped with a Peltier-cooled silicon CCD detector using a 532 nm laser excitation wavelength (laser power 30 mW). The scattered light was collected through a 100× Leica N Plan objective (N.A. = 0.85) in backscattering configuration (laser spot lateral size of about 0.8 µm).

Raman point-by-point mapping (Fig.IV.2d) was performed over approx. ~50x50 $µm^2$ areas with a step of 1 µm. Raman maps analysis was performed using the Direct Classical Least Squares (DCLS) algorithm from Wire software (Renishaw ©).

Synthetic glass standards with known H_2O concentrations (0.8 and 3.3 wt% H_2O determined by Karl Fisher Titration, University of Hanover) were used to ascertain the presence of low water content.

Secondary electron microscopy (SEM)

We used a scanning electron microscope (FEI Quanta FEG 200, University of Montpellier) to characterize the microcrystalline phases present in the melt inclusions and determine semi-quantitatively the composition of microcrystals. The analyses were performed using a silicon drift detector X-Max 50 mm^2 and a voltage at 15 kV.

Secondary ion mass spectrometry (SIMS)

CO_2 concentrations of silicate glasses was measured using the CAMECA IMS4f at the 'Microsonde Sud' at the University of Montpellier. The analyses (^{12}C and ^{28}Si) were performed with a Cs^+ primary beam (beam current = 1 nA, beam size = 20 µm) and the electron gun is operated at -4.5 kV. The raw data were monitored continually for fluctuation of signal intensity during 3 min of acquisition. We estimated an σ analysis error for CO_2 around 10% (σ = 10% for standard mean error).

The carbon content of the sample is proportional to the ionic intensity (c/s). The signal C/Si and the silica content determined by EPMA is used to determine the CO_2 content of melt inclusions. The CO_2-bearing synthetic glass is used to establish a relative sensitive factor (RSF) between the ratio C/Si and the CO_2 content. We compare the Si signal of sample with the reference material to define the validity of the analyses (possible contamination with carbonate) (Carbon and Silica signal in supplementary material).

IV.B.III. Results

III.1. Petrography of nephelinite and melt inclusions

Lavas from Hanang volcano are nephelinites with porphyritic texture and 10-37 vol.% of nepheline (3.5-31%), clinopyroxene (4.5-7.5%, diopside), and garnet (0-3%) phenocrysts, and titanite (0-0.5 %) and apatite (0-1.5%) microcrysts (Fig.IV.1). Hanang nephelinites are silica- and alkaline-rich (44.15-46.66 wt% SiO_2, 9.46-12.11 wt% Na_2O+K_2O) with very low Mg# (molar Mg/(Mg+Fet)*100 = 22.4 - 35.2). The chemistry and mineralogy of Hanang lavas are described in details in Baudouin et al. (2016).

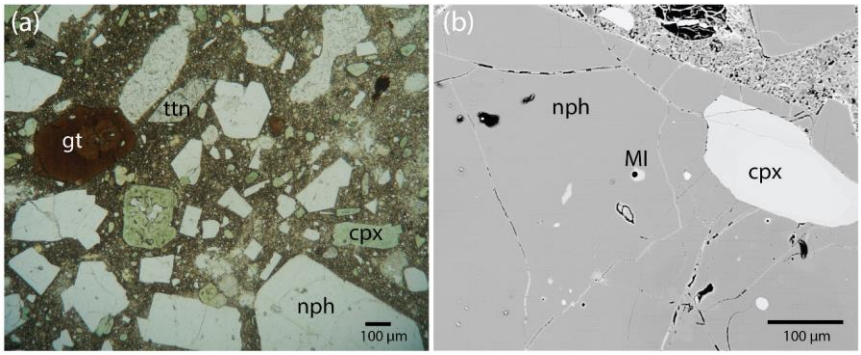

Fig.IV.1 *Microphotographs of Hanang lavas. (a) Han8, (b) nepheline from Han8 (Backscattered electron (BSE) photo). Cpx clinopyroxene, ttn titanite, nph nepheline, gt garnet (andradite-schorlomite), MI melt inclusion*

Melt inclusions are present in nepheline phenocrysts in phenocrysts-rich (> 30 vol %) and nepheline-rich samples (nepheline phenocrysts > 18%, i.e. Han8 and Han11) (Fig.IV.1b). They occur in 65% of nepheline phenocrysts and 1 to 12 melt inclusions are present in individual crystal. All melt inclusions have a green silicate glass, a finely crystalline phase, and a shrinkage bubble (Fig.IV.2).

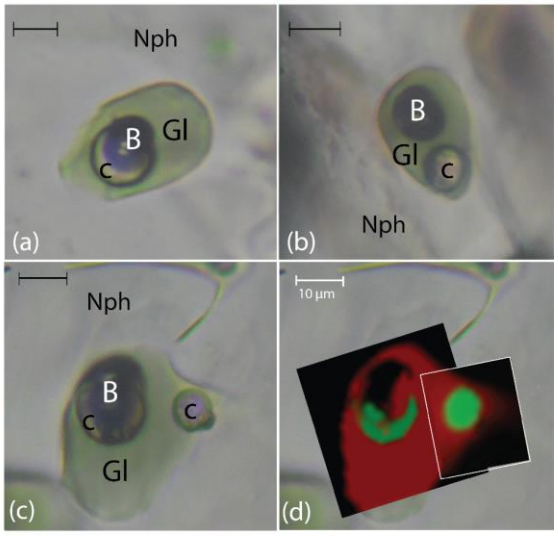

Fig.IV.2 *(a)(b)(c) Microphotography of silicate melt inclusions in nepheline phenocrysts, sample Han8. (d) Raman cartography of melt inclusions. Nph nepheline, Gl silicate glass, C carbonate phase,and B shrinkage bubble.*

The melt inclusions occur at the middle (63%) or at the rim (25%) and rarely at the core (12%) of nepheline phenocrysts. They are 10 to 30 µm in size, oval or rounded, and free of daughter minerals (Fig.IV. 2). A finely crystalline phase is always present as globule (1 to 10 µm) in the silicate glass or around the shrinkage bubble (Figs. 2 and 3). Using 2D imaging analyses, we estimate that the crystalline rim or globule represent 9 to 30 % of the melt inclusions (n = 15, mean = 18%, 80% of MI have a carbonate volume between 13 and 23%). The crystalline globule is colourless in plane-polarized light and we observed microcrystalline phases (< 0.5 µm) with high birefringence in cross-polarized light.

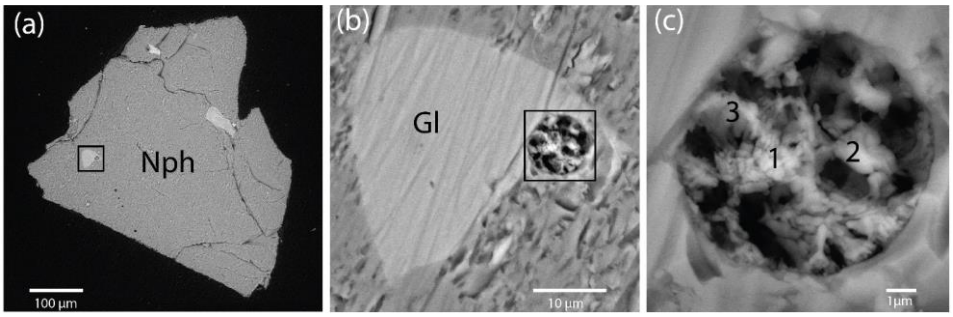

Fig.IV.3 *SEM photos of (a) nepheline crystal, (b) melt inclusions and (c) carbonate phase. SEM analyses (1, 2, 3) of carbonate are reported in Table 2.*

III.2. Silicate glass composition in melt inclusions

Silicate glasses in melt inclusions are silica- and alkali rich with 54.0 - 65.5 wt% SiO_2 and 6.9- 12.9 wt% $Na_2O + K_2O$ (Fig.IV. 4) and have peralkaline index (Na+K/Al ratio) ranging from 1.6 to 7.2. They have phono-tephritic to trachytic compositions with low MgO content (0.13 to 1.2 wt% MgO; Mg# = 0.94 - 7.56; Mg# = $Mg/(Mg+Fe^{tot})*100$), and high FeO and CaO content (8.8-15.3 wt% and 2.6-8.84 wt%, respectively) (Figs. 4 and 5 and Table 1). The different parts of some melt inclusions show small variations in composition with Ca-enriched silicate glass around the shrinkage bubble (see details in Chapter V). The concentrations of MgO, FeO and CaO decrease with increasing silica content (Fig.IV.5). The Al_2O_3 content increases with increasing silica content indicating no contamination by the host mineral (nepheline) during microprobe analyses (Fig.IV.5c). Silicate glass did not display correlations between major element compositions and the position of melt inclusions in one single crystal (e.g. core position = 62.4 wt% SiO_2, middle position = 62 wt% SiO_2, rim position = 64 wt% SiO_2).

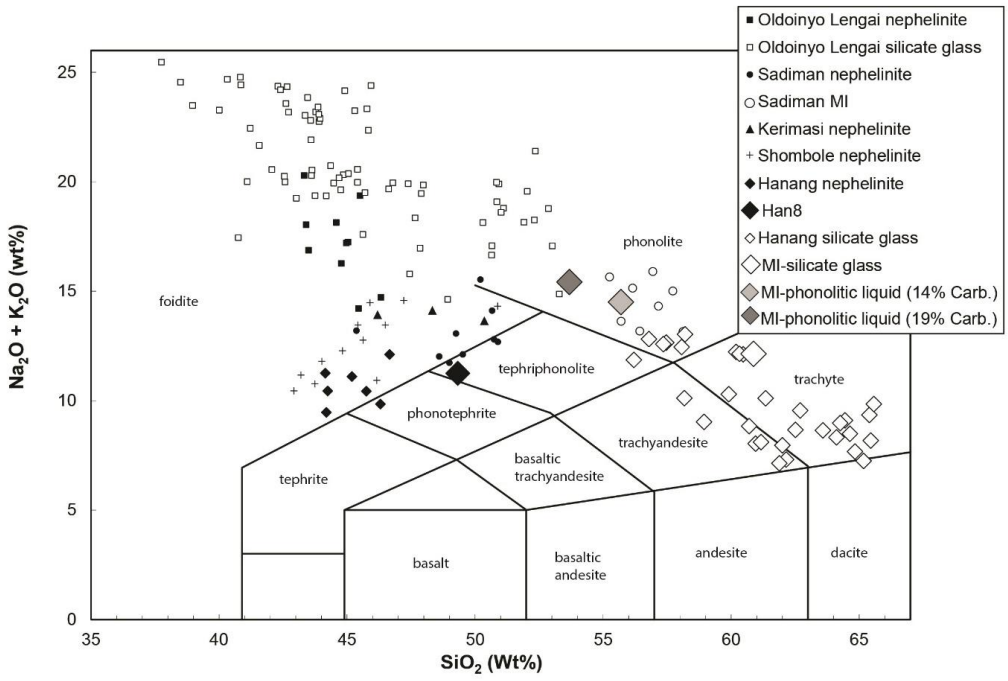

Fig.IV.4 *Alkali vs. silica composition of Hanang silicate glasses (open diamond) and calculated phonolitic composition of melt inclusions (grey diamond) and nephelinite (black diamond, Baudouin et al. 2016). Literature data are also represented: Oldoinyo Lengai (OL) nephelinite (black and grey square, Klaudius and Keller 2006), OL melt inclusions (open square, Mitchell and Dawson 2012, Sharygin et al. 2012, deMoor et al. 2013), Sadiman nephelinites (black circle, Zaitsev et al. 2012), Sadiman melt inclusions (open circle, Zaitsev et al. 2012), Kerimasi nephelinites (Church 1996) and Shombole nephelinites (Peterson 1989). Modified after Le Bas (1986).*

Silicate glasses have high Rare Earth Element (REE) content (e.g. 70-340 ppm La (300-1000*chondrite) and are enriched in Light REE (LREE) compared to Heavy REE (HREE) ratio (La/Yb = 51-89) (Fig.IV.6). The concentration in incompatible elements are enriched compared to the primitive mantle (e.g. Large ion lithophile elements (LILE): 1270-5510 ppm Ba, 940-14300 ppm Sr, and High strength field elements (HFSE): 6.4-16.8 ppm U, 165-390 ppm Nb, 420-1350 ppm Zr) with a strong fractionation in Ta relative to Nb (Nb/Ta = 65-206) and Zr relative to Hf (Zr/Hf = 41.4-75.2) (Fig.IV.6, Table 1). The concentrations of LILE (i.e. Rb) increase with increasing SiO_2, whereas the concentrations of HFSE, Ta and REE (i.e. La, Ce) decrease.

The volatile content in silicate glass is high with 0.35-2.79 wt% F, 0.28-0.84 wt% Cl, and 0.21-0.92 wt% S. Sulfur contents slightly decrease with increasing SiO_2 and decrease with decreasing FeO and MgO content (Fig.IV. 5). Raman analyses have been performed at different depth (+/- 20 µm from the focal plane with a step =1 µm) in the melt inclusion and show very similar spectra with Raman peaks at 1066 cm-1 (Fig.IV.7) corresponding to CO_2 dissolved as carbonate CO_3^{2-} (Frezzotti et al. 2012). It is worth mentioning that no large band between 3500 and 3600 cm^{-1}, characteristic of the presence of H_2O, (Behrens et al. 2006) has been observed suggesting that the silicate glass is H_2O-free or with water content lower than 1000 ppm (Di Muro et al. 2006). The glass/bubble and glass/crystal boundaries have been carefully analysed for the presence of volatile elements (CO_2, H_2O) and no H_2O nor CO_2 shift has been observed.

Table 1: Major and trace element compositions of nepheline-hosted melt inclusions

Sample	Han8c	Han8c	Han8c	Han8c	Han8c	Han8c	Han11	Han8a	Han8a	Han8a
SiO_2	62.07	64.81	62.92	62.92	59.87	59.97	58.17	62.48	59.20	59.77
TiO_2	1.45	0.80	1.59	1.59	2.04	1.89	1.92	1.35	1.73	2.01
Al_2O_3	5.18	6.79	6.25	6.25	3.37	3.75	3.60	6.40	3.31	3.63
FeO	10.93	10.19	10.31	10.31	11.32	12.11	12.44	10.80	10.83	12.10
MnO	0.50	0.36	0.42	0.42	0.44	0.43	0.55	0.34	0.51	0.51
MgO	0.65	0.54	0.58	0.58	0.67	0.81	0.90	0.57	0.58	0.75
CaO	5.32	4.24	4.31	4.31	7.15	6.36	6.66	5.02	8.16	7.34
Na_2O	6.34	6.76	6.17	6.17	5.78	5.80	5.49	3.28	4.77	4.27
K_2O	2.10	2.50	2.71	2.71	1.64	1.90	1.85	2.73	3.24	2.75
P_2O_5	0.20	0.16	0.18	0.18	0.20	0.22	0.30	0.10	0.17	0.23
SO_2	0.88	0.67	0.98	0.98	1.36	1.43	1.08	0.96	1.54	0.90
F	1.58	0.91	0.92	0.92	1.42	1.51	2.22	1.11	1.43	1.40
Cl	0.42	0.35	0.28	0.28	0.87	0.50	0.63	0.30	0.33	0.50
Total	97.62	99.10	97.63	97.63	96.12	96.72	95.85	95.44	95.89	96.15
CO_2	-	-	-	-	-	-	-	0.43	2.03*	3.73*
Mg#	4.4	3.9	4.2	4.2	4.4	4.9	5.3	3.8	3.8	4.4
Na+K/Al	2.35	1.97	2.06	2.06	3.17	2.96	2.94	1.4	3.6	2.8
Cs	4.65	6.12	7.45	5.92	6.25	2.68	6.72			
Rb	172	230	171	145	180	95.8	305			
Ba	2150	3312	4462	3441	5511	1919	5428			
Th	12.9	19.9	10.7	23.3	20.5	9.72	35.4			
U	8.32	11.3	8.18	12.8	10.3	6.43	16.6			
Nb	235	350	164	334	211	173	456			
Ta	2.16	1.70	2.12	3.35	1.17	2.66	6.16			
La	123	152	339	190	151	90.7	286			
Ce	155	196	246	234	178	125	344			
Pb	46.4	55.2	35.5	72.5	46.3	45.2	97.3			
Pr	13.3	18.6	21.5	21.1	14.6	11.8	33.5			
Sr	3241	2755	14294	4337	2826	2326	6436			
Nd	39.3	58.4	54.8	73.7	43.7	37.1	105			
Zr	578	1348	422	1096	873	519	1536			
Hf	9.28	29.2	7.01	19.2	14.9	6.90	30.7			
Sm	5.49	8.03	7.67	11.7	7.88	2.66	16.5			
Eu	1.14	2.38	1.91	3.36	3.08	2.01	4.55			
Gd	7.10	10.1	7.89	9.14	7.50	3.98	12.3			
Tb	0.51	1.12	0.80	1.42	1.08	0.60	2.40			
Dy	2.80	7.54	3.02	7.98	7.66	4.96	11.5			
Y	22.1	39.5	21.4	48.7	46.3	21.3	65.3			
Ho	0.61	1.38	0.42	1.51	1.50	0.53	2.23			
Er	1.88	2.82	1.01	3.82	3.92	2.57	5.83			
Tm	0.22	0.56	0.12	0.76	0.41	0.57	0.94			
Yb	1.37	2.94	-	3.96	2.93	1.32	5.43			
Lu	0.23	0.40	0.08	0.52	0.42	0.15	1.03			

* Carbonate phase comtamination (~2-4%) during SIMS analyses

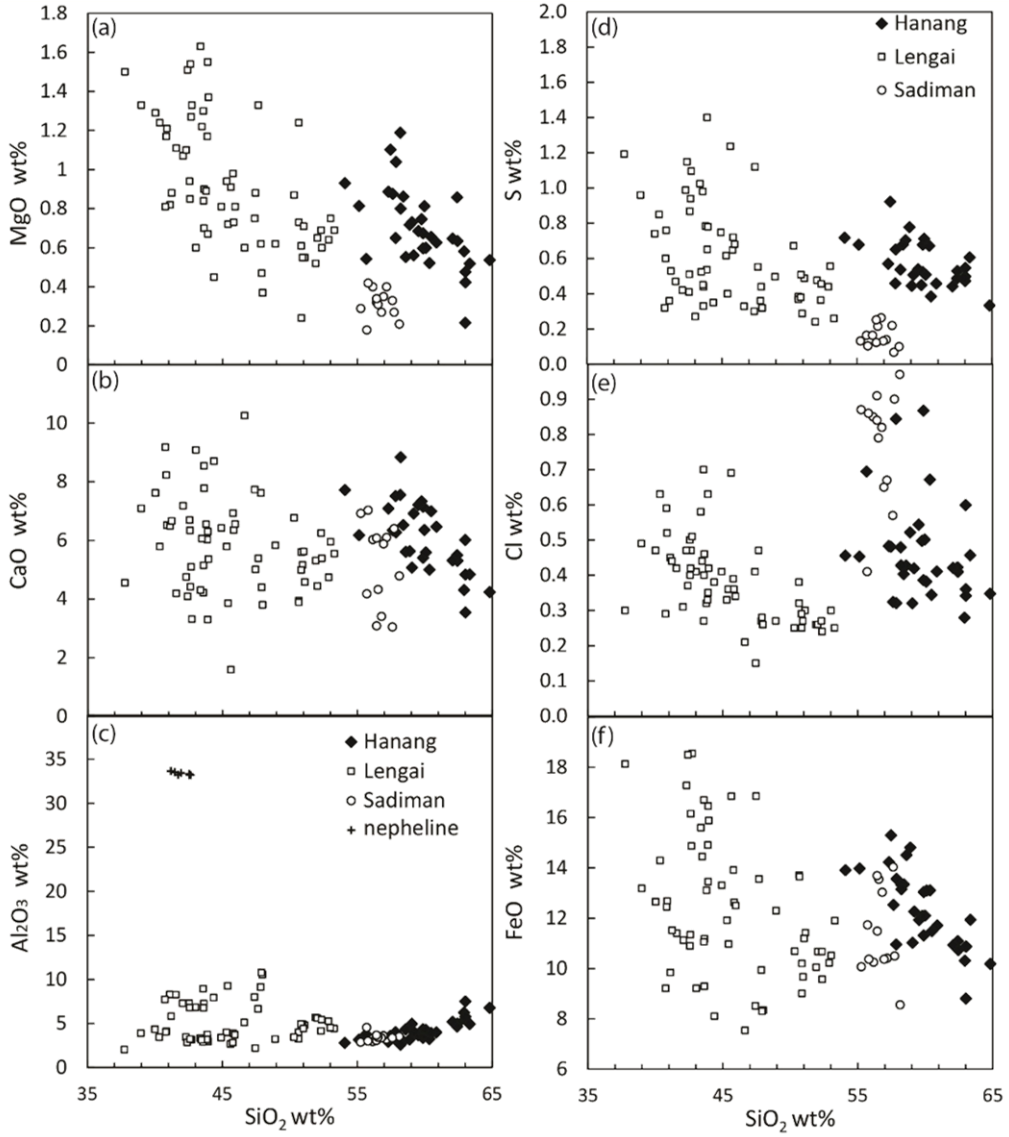

Fig.IV.5 *(a) MgO, (b) CaO, (c) Al_2O_3, (d) Sulfur, (e) Chlorine, and (f) FeO content vs silica content of melt inclusions from Hanang (grey diamond, this study), Oldoinyo Lengai (open square, Mitchell and Dawson 2012, Sharygin et al. 2012, deMoor et al. 2013) and Sadiman (open circle, Zaitsev et al. 2012).*

The CO_2 content of silicate glass was precisely determined for 10 large melt inclusions (>20 µm) using SIMS (Table 1). The CO_2 concentration of silicate glass in the larger melt inclusion (e.g. Si signal equivalent to reference standard without carbonate contamination) is 0.43 wt% (Table 1) (Figure in supplementary material). For small melt inclusions, the beam size (20 µm) does not allow ablation of the silicate glass only and analyses represent mixing between glass and carbonatite phase (CO_2 = 2.03-3.73 wt%, Table 1).

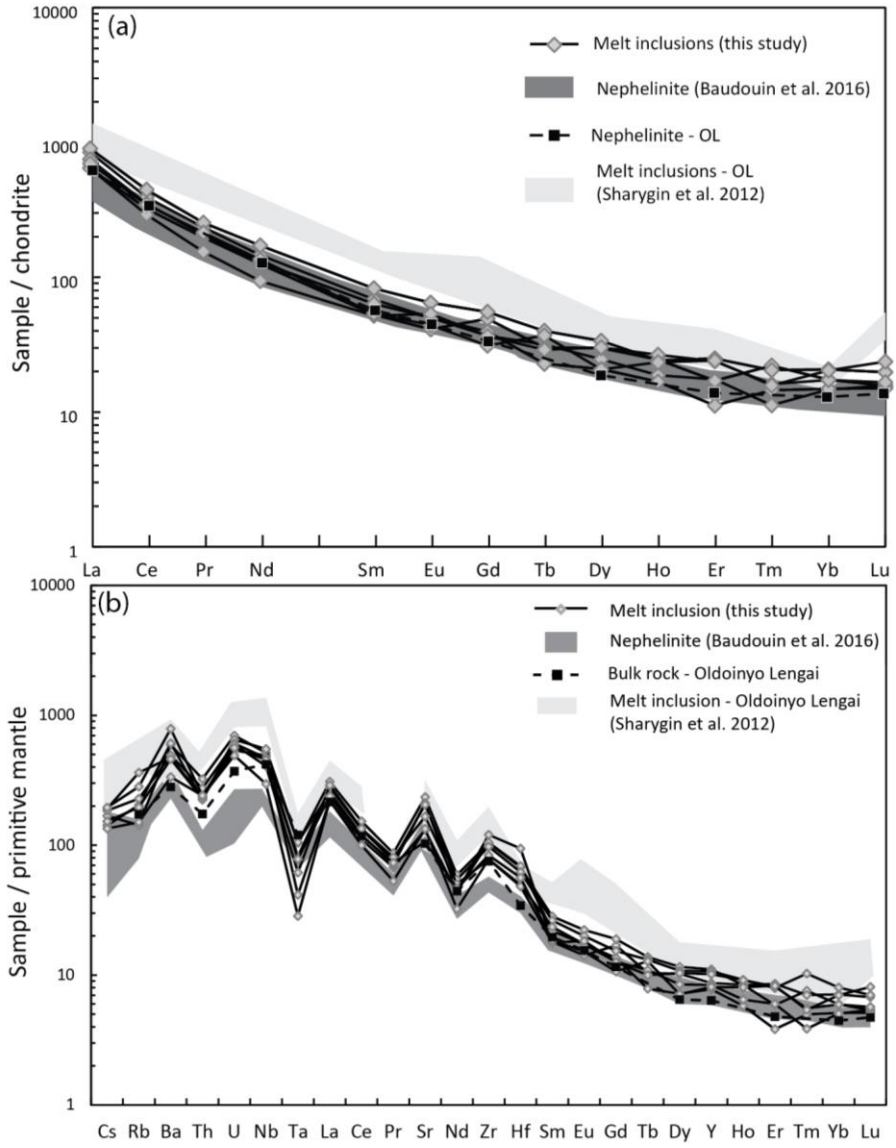

Fig.IV.6 *(a) Chondrite normalized rare earth elements and (b) Primitive mantle normalized trace element compositions of Hanang melt inclusions (this study) and nephelinite (Baudouin et al. 2016) and Oldoinyo Lengai nephelinites and MI (Sharygin et al. 2012). Normalization values from McDonough and Sun (1995).*

III.3. Composition of carbonate phase in melt inclusions

Carbonate globules and carbonate rim around shrinkage bubble have been characterized using Raman spectroscopy and SEM. The microcrystalline phases have four distinct peaks at 1072 cm^{-1}, 1005 cm^{-1}, 703 cm^{-1}, 631 cm^{-1} compared to silicate glasses (Fig.IV. 7). The very strong (vs: 1072 cm^{-1}) and weak (w: 703 cm^{-1}) peaks correspond to vibrational regions of alkali-rich carbonates (Frezzotti et al. 2012). However, the peaks are shifted to lower value with respect to that of calcite (1085 cm^{-1}, Bühn et al. 1999, Frezzotti et al. 2012) suggesting the presence of Na, K, Sr, and Ba in the carbonate phase (e.g. Mernagh et al. 2011, Káldos et al. 2015). The presence of the peaks at 1005 and 631 cm^{-1} also indicates the presence of sulfur as SO_4^{2-} in the carbonate phases (e.g. Zaitsev et al. 2009, Sekisova et al. 2015). Raman spectra of

carbonate do not display peak at 3500 cm^{-1} for H_2O suggesting that carbonates do not contain water (Fig.IV.7). The spectra analyses for the shrinkage bubbles are very similar to those of nepheline crystals suggesting that the bubbles do not contain any volatile species.

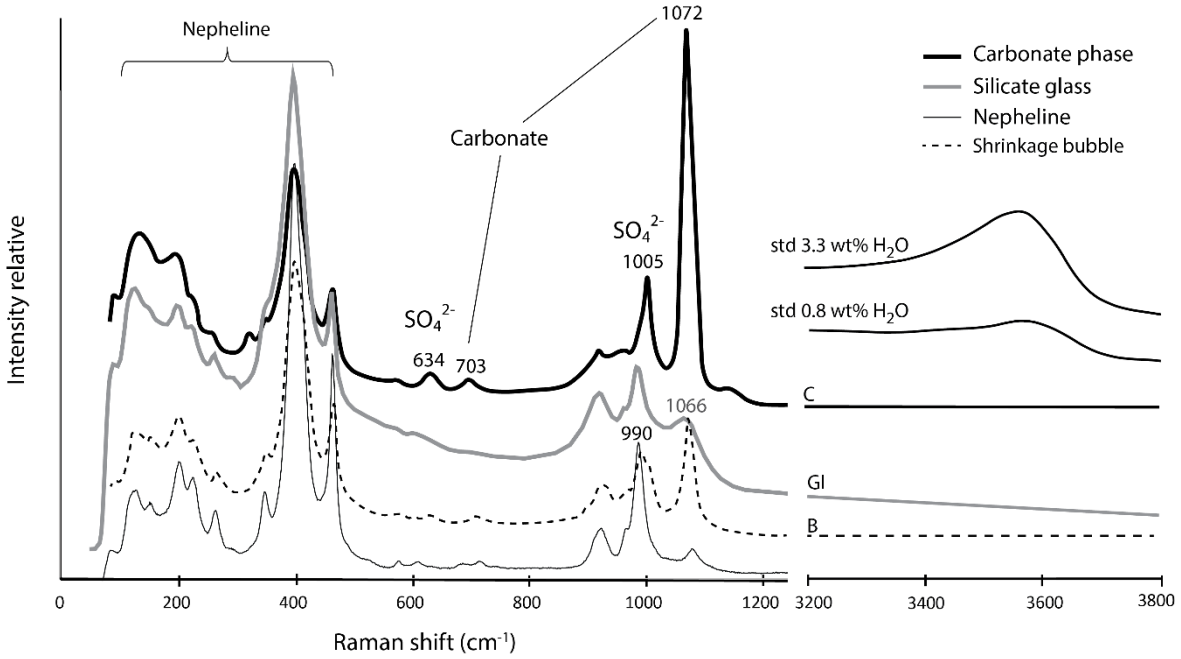

Fig.IV.7 *Raman spectra of nepheline (923, 990, 1081 cm^{-1}), silicate glass (Gl) (1066 cm^{-1}), carbonate phase (c) (703, 1005, 1072 cm^{-1}) and shrinkage bubble (B) from melt inclusion reported in Fig.2d. Raman spectra of the reference glasses with 3.3 wt% H_2O and 0.8 wt% H_2O are also reported in the high frequency range.*

The carbonate phase was analysed by SEM for semi-quantitative analyses. Carbonate globules (~5 µm) are composed of fine-grained aggregate (<0.2 µm) of fluorite and carbonate phase (Fig.IV.3, Table 2). Semi-quantitative analyses characterized the microcrystalline carbonate phase as Ca-Na carbonate with 33 wt% CaO, 20 wt% Na_2O and 3 wt% K_2O and significant amount of sulfur (~3 wt%) (standard deviation : CaO ±8 wt%, Na_2O ± 2.5 wt%, K_2O ±1.2 wt%, S ± 1 wt%) (Table 2). The carbonate composition can be defined as shortite ($Na_2K_{0.2}Ca_{1.8}(CO_3)_3$). The microcrystalline texture of the carbonate does not allow us to analyse precisely the composition of individual microliths with electron microprobe.

Table 2: Major element compositions of the carbonate phase, trachytic glass and calculated pre-immiscible phonolitic liquid

Sample	C phase 1	C phase 2	C phase 3	C phase 4	Melt inclusion 1 (MI-1) trachytic glass 1	Melt inclusion 1 (MI-1) phonolitic liquid[a]	Melt inclusion 1 (MI-1) phonolitic liquid[b]	Mean melt inclusion (MI mean) trachytic glass*	Mean melt inclusion (MI mean) phonolitic liquid[c]	Mean melt inclusion (MI mean) phonolitic liquid**
SiO_2					57.63	53.68	55.69	60.04	54.71	54.73
TiO_2					1.66	1.54	1.6	1.61	1.56	1.15
Al_2O_3					3.43	3.2	3.32	4.35	3.68	3.84
FeO					12.53	11.96	12.32	12.22	11.68	11.93
MnO					0.48	0.45	0.47	0.49	0.46	0.47
MgO					0.88	0.82	0.85	0.69	0.71	0.64
CaO	28.91	40.95	28.69	27.70	6.35	12.72	11.03	5.9	13.7	13.86
Na_2O	23.48	12.90	22.95	6.80	9.11	12.58	11.75	6.88	9.99	10.06
K_2O	3.81	1.96	3.33	1.90	2.39	2.84	2.75	2.75	3.36	3.22
P_2O_5					0.22	0.21	0.22	0.16	0.16	0.1
S	2.85	2.36	3.06	0.30	0.42			0.54		
F		1.27		28.4	1.07			1.21		
Cl					0.32			0.44		
Total	59.04	59.45	58.03	65.10	96.49	100	100	97.28	100	100
NBO/T					0.79	1.1	1.01	0.69	1.04	1.05
Na+K/Al					4.82	6.90	6.26	3.21	5.24	4.99

C phase 1,2, 3 : SEM quantitative analyses of carbonate (Fig.3)

C phase 4 : SEM analyses of carbonate and fluorite microcrystals

a 81% trachytic liquid 1 + 19% carbonate (33% CaO, 20%Na_2O, 3%K_2O)

b 86% trachytic liquid 1 + 14 % carbonate

c 80% mean trachytic liquid + 20 % carbonate

* mean melt inclusions (n=30)

**Calculated for fractional crystallisation of 17% cpx, 40% nepheline, 7% garnet, 1.7% apatite from whole rock nephelinite (Baudouin et al. 2016)

IV.B.IV. Discussion

In Hanang lavas, fractional crystallisation of cpx in carbonated-rich nephelinite liquid occurred at 1060-1100°C and 500-600 MPa followed by the crystallisation of nepheline, titanite and apatite (Baudouin et al. 2016), suggesting that melt inclusions entrapment occurred during nepheline crystallisation at lower pressure. To account for the presence of silicate glass and carbonate phases in melt inclusions, two hypotheses can be considered: (i) a silicate liquid and a carbonate liquid were present in magma chamber during the crystallization of nepheline (i.e. early immiscibility at ≤ 500 MPa) or (ii) Melt inclusion entrapment occurred before immiscibility and immiscibility process proceed during magma ascent (≤ 500 MPa).

The absence of carbonatite globules in nephelinite lavas and the absence of carbonatite lava flows at Hanang volcano, as reported at Shombole (Peterson 1989), Kerimasi and Oldoinyo Lengai volcanoes (e.g. Dawson 1962, 2008; Guzmics et al. 2011), both argue for late immiscibility after melt inclusions entrapment. The immiscibility processes in Hanang nephelinitic lavas have been recorded in zoned cpx (e.g. zonation in Mg# and H2O) (Baudouin et al. 2016). The carbonatite affinity (e.g. Nb/Ta) recorded by cpx as well as the whole rock composition suggest that immiscibility is a dominant process during nephelinite differentiation (Baudouin et al. 2016). However, Hanang cpx core and rim crystallised from a carbonate-rich silicate melt rather than to a 'true" carbonatite composition (Baudouin et al. 2016). The carbonate-rich silicate liquid at Hanang is coherent with the first stages observed during Oldoinyo Lengai nephelinites differentiation, whereas 'true' carbonatite occurred in a late stage of magma evolution (Dawson 1998).

IV.1. Interstitial phonolitic melt during differentiation of nephelinite magma

Nephelinite magma results from fractional crystallisation and liquid immiscibility of melilitite magma at pressure of 500-600 MPa (Baudouin et al. 2016). During ascent, fractional crystallisation leads to interstitial melt that evolves to more differentiated composition resulting in more viscous and volatile-rich magma controlling magma ascent and eruption style at the surface (Neuville and Richet 1991, Whittington et al. 2000, Oppenheimer 2003). The melt inclusions trapped in nepheline phenocrysts represent interstitial melt during fractional crystallisation and the composition of the melt inclusions corresponds to the interstitial liquid in equilibrium with nepheline before immiscibility of the silicate glass and the carbonate phase. The bulk composition of the melt inclusions can be considered as pre-immiscible silicate liquid and can be determined considering the volume and the composition of the carbonate phase and silicate glass.

The silicate glass has a trachytic composition (Fig.IV. 4) and the carbonate phases have microliths with 33 wt% CaO, 20 wt% Na_2O, and 3 wt% K_2O (mean of analyses C phase 1, 2, 3; table 2). The absence of correlation in major element compositions between nepheline-host mineral and melt inclusion (i.e. decreasing Al_2O_3 and SiO_2, Fig.IV.5) suggest that post-entrapment nepheline crystallisation did not occur during cooling (Fig.IV.5c). The variations of major element concentration of the silicate glasses, i.e. increasing SiO_2 and Al_2O_3 and decreasing Na_2O, S and CaO, are then related to the immiscibility process and the presence of the carbonate phases that modified the chemistry of silicate liquid (Fig.IV.5).

The proportion of silicate glass and carbonate in melt inclusions estimated using SEM and raman images range from 13 to 23% with an average volume of 18% (MeanMI, Fig.IV.8) indicating that the pre-immiscible liquid composition, i.e. silicate glass + carbonate, has phonolitic compositions with relatively high CaO and Na_2O contents (11-13.7 wt % and 10-12.6 wt%, respectively, Table 2) and very low Mg# (~5).

Considering the mineral assemblage of the nephelinite lavas, i.e. nepheline, cpx, garnet with minor apatite, titanite and pyrrhotite, the composition of phonolite melt can be modelled in term of fractional crystallisation. Crystallisation of 17% cpx, 40% nepheline, 6.5% garnet and 1.7% apatite from Mg-poor nephelinite composition ($r^2 = 0.28$, mineral composition from Baudouin et al. 2016, Fig.IV.8) led to the formation of the interstitial liquid with high Na+K/Al ratio (Na+K/Al = 5-6.9) (Fig.IV.8) close to the phonolitic composition determined from melt inclusion compositions. During fractional crystallisation, the residual interstitial liquid (phonolite) is enriched silica and alkali content (Fig.IV.8) and volatile elements (i.e. CO_2).

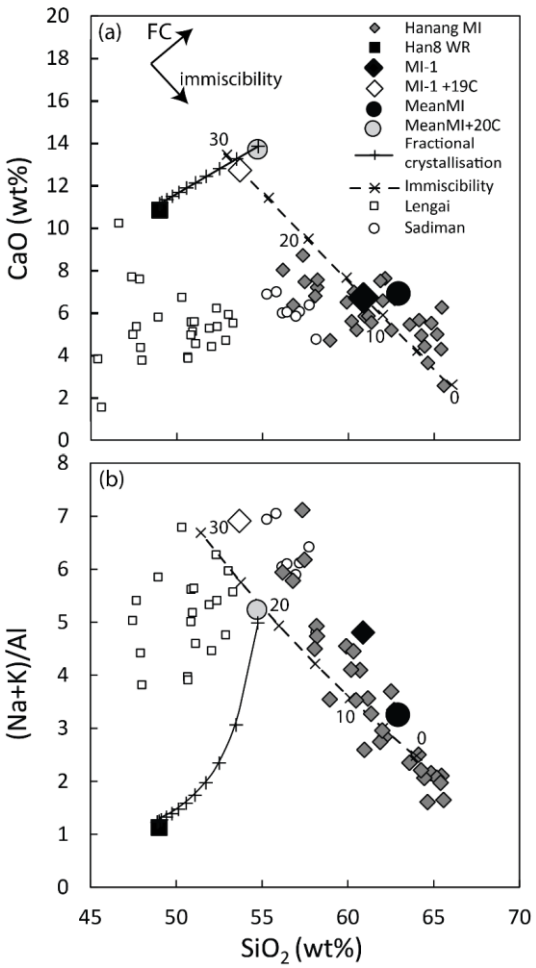

Fig.IV.8 *(a) (a) CaO vs SiO_2 and (b) Na+K/Al vs SiO_2 content of melt inclusions and calculated pre-immiscible phonolitic liquid (open symbols). Curve of fractional crystallisation (FC) (17% cpx, 40% nepheline, 6.5% garnet and 1.7% apatite) from nephelinite (black square) to pre-immiscible liquid and curve with different % of immiscibility with a carbonate liquid (33% CaO, 20% Na_2O, 3% K_2O) are represented. MI-1 corresponds to 'trachytic glass 1' and MI-1+19C corresponds to the calculated 'phonolitic liquid[a]' in Table 2. Mean-MI (n=30) corresponds to 'trachytic glass 2' and Mean-MI +20C corresponds to the calculated 'phonolitic liquid[c]' in Table 2. References for Oldoinyo Lengai and Sadiman data are in Fig.IV.4.*

The CO_2 content of the pre-immiscible phonolite melt trapped in melt inclusions [C_{CO2} phonolite = [C] trachyte glass (0.43 wt% CO_2, table 1)* V (volume) trachyte glass (85 ± 4%) + [C] carbonate 41 ± 1 wt% CO_2 * V carbonate (15 ± 4%)] ranges from 4.5 to 7.5 wt% CO_2 with a mean value at 6 wt%. This concentration corresponds to the CO_2 solubility in the interstitial melt at the depth of melt entrapment. The solubility of CO_2 is strongly dependant of the pressure and the melt composition (i.e. NBO/T, Brooker et al. 2001, Fig.IV.9) and the CO_2 concentration estimated from melt inclusions (i.e. for phonolitic composition: NBO/T = 1.04, Table 2) correspond to experimentally determined CO_2 saturation (i.e. presence of CO_2 gas phases, e.g. Dixon et al. 1995, Behrens et al. 2009) at 800 MPa +/- 200 MPa (Fig.IV.9) suggesting that nephelinite magma was CO_2 saturated at the time of nepheline and cpx crystallisation (500-600 MPa, Baudouin et al. 2016).

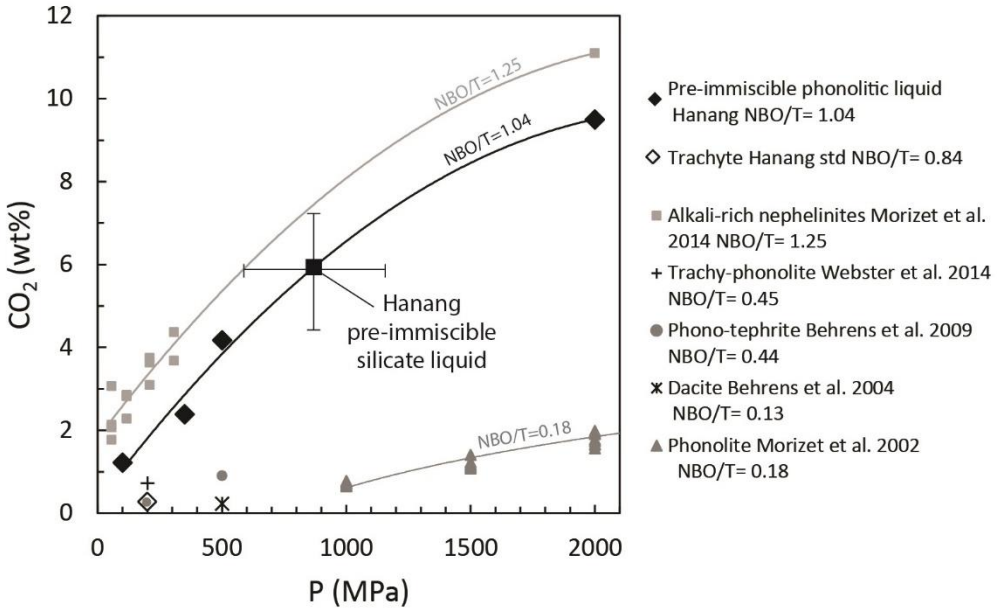

Fig.IV.9 *CO_2 solubility vs pressure for silicate melt with different compositions. CO_2 curves were calculated using experimental data at 100-350 MPa (Moussallam et al. 2015), 500 MPa (Vetere et al. 2014) and 2000 MPa (Brooker et al. 2001). The CO2 solubility of alkali-rich nephelinites (Morizet et al. 2014), trachy-phonolite (Webster et al. 2014), phono-tephrite (Behrens et al. 2009), dacite (Behrens et al. 2004), phonolite (Morizet et al. 2002) and with Hanang trachytic composition and 200 MPa (open diamond, this study) are also reported.*

IV.2. Immiscibility of trachytic silicate liquid and calciocarbonatite during magma ascent

The presence of carbonatite has been reported in several alkaline volcanoes of the NDT (Keller and Krafft 1990, Dawson 2008, Guzmics et al. 2011) at different scales from carbonatite and silicate lava flows at Kerimasi and Oldoinyo Lengai (e.g. Dawson 1962, 2008; Guzmics et al. 2011) to carbonatite globules in the matrix of nephelinites at Shombole (Peterson 1989) and carbonate phases in melt inclusions (e.g. Mitchell and Dawson 2012, deMoor et al. 2013, Sharygin et al. 2012, Guzmics et al. 2012) and has been observed in experimental products as immiscible liquid at crustal and mantle pressure (Kjarsgaard et al. 1995, 1998; Lee and Wyllie 1998).

The late immiscibility process observed in phonolitic melt inclusions in Hanang lavas led to the formation of trachytic and calciocarbonatite magmas. Reported in Hamilton diagram (Hamilton et al. 1979), the silicate melt and the carbonatite phases compositions have composition close to the experimental solvus determined at 500 MPa for CO_2-saturated nephelinite composition (Fig.IV.10) (Kjarsgaard et al. 1995, Kjarsgaard 1998, Brooker and Kjarsgaard 2011). However, the absence of CO_2 (or H_2O) fluid in the shrinkage bubble may suggest that carbonatite immiscibility occurred under vapor-undersaturated conditions.

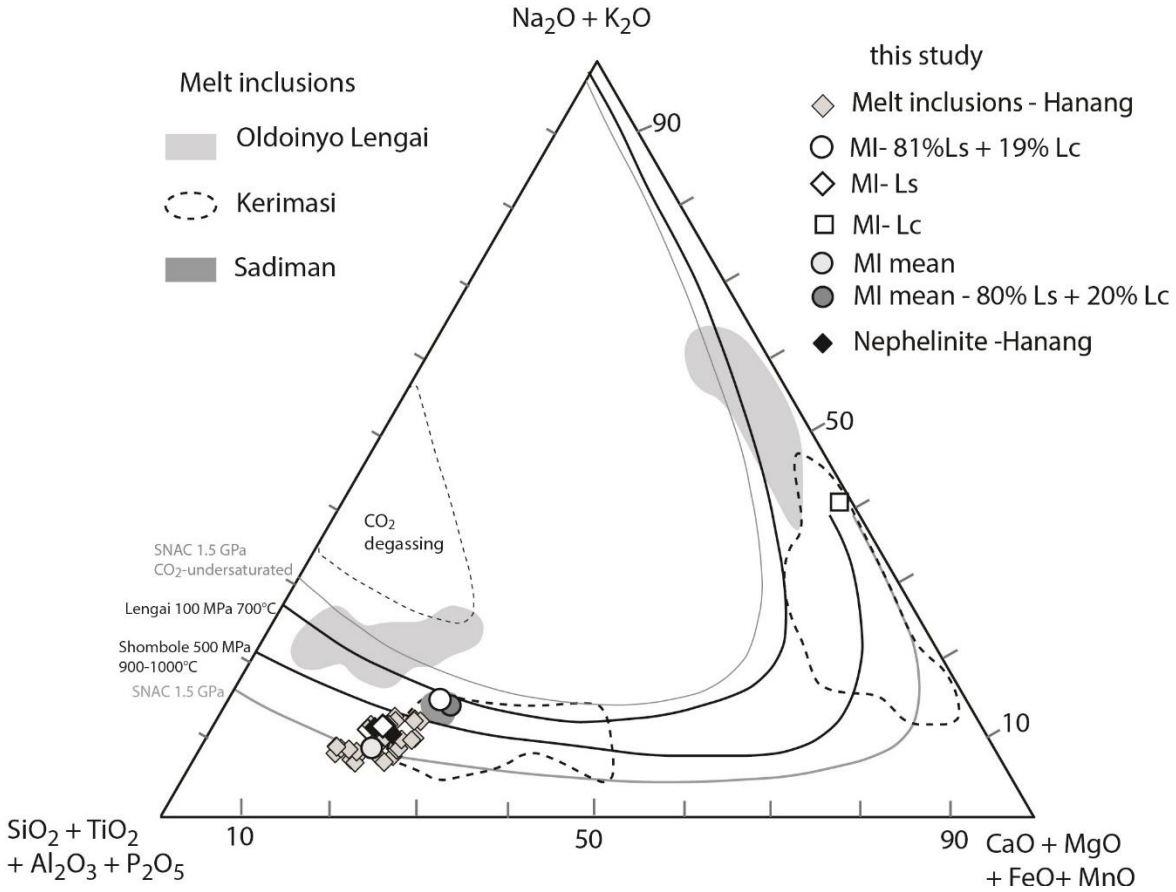

Fig.IV.10 *Hamilton projection (Hamilton et al. 1979) for silicate and carbonate melts in melt inclusions (MI) from Hanang. The solvus curves are from Kjarsgaard et al. (1995), Kjarsgaard 1998, Brooker and Kjarsgaard (2011). Melt inclusions from Oldoinyo Lengai (Mitchell and Dawson 2012, Sharygin et al. 2012, deMoor et al. 2013), Kerimasi (Guzmics et al. 2011, 2012, 2015) and Sadiman (Zaitsev et al. 2012) are also reported. SNAC= SiO_2-Na_2O-Al_2O_3-CaO (+CO_2) system. MI-Ls=trachytic glass 1 from table 2, MI-Lc= 33% CaO, 20% Na_2O, 3% K_2O and MI mean -81%Ls + 19 %Lc= phonolitic liquid[a] (table 2). Mean-MI (n=30) correspond to the data 'trachytic glass*' and MI mean -80% Ls + 20 % Lc correspond to 'phonolitic liquid[c]' include in table 2.*

Koster van Groos and Wyllie (1968) and Lee and Wyllie (1998) suggested that the presence of H_2O increases the pressure of immiscibility of carbonatite melt: addition of large amount of water (5-20 wt% H_2O) decreases the partial pressure of CO_2 (P_{CO2}) and prevent the formation of an immiscible carbonate melt at a given pressure (Kjarsgaard & Hamilton, 1989). In Hanang nephelinite, the melt inclusions have very low H_2O content (raman spectra below detection, <0.1 wt% H_2O). Although H content in melt inclusions can be modified by diffusion after entrapment (e.g. Bucholz et al. 2013, Chen et al. 2011), the low water content measured in nepheline phenocrysts (240-550 ppm wt H_2O, Baudouin et al. 2016) suggest that diffusion of H has not been significant after entrapment and the very low H_2O content is representative of the water content in the phonolitic melt.

However, the presence of fluorine and sulfur (S^{6+}) in carbonate globule (Table 2) strongly suggests very high concentrations of other volatile elements in primitive magmas that may have lowered the partial pressure of CO_2 and influence carbonatite immiscibility. If sulphur and

fluorine have an important effect on immiscibility, and this should be experimentally tested, the pressure of immiscibility should be considered as a minimum pressure.

IV.3. Calciocarbonatite / natrocarbonatite and alkaline lavas association

North Tanzania is one of the most concentrated areas of carbonatite magmatism on Earth, with calciocarbonatite (Shombole and Kerimasi) and natrocarbonatite (Oldoinyo Lengai) associated with alkaline lavas (e.g. Dawson 2008). The presence of CO_2-rich nephelinite lavas with carbonatite-trachytic melt inclusions and the absence of carbonatite lavas at Hanang volcano is unique and allow discussions of calciocarbonatite–nephelinite and natrocarbonatite–nephelinite genesis and evolution.

The absence of carbonatite lava flows in carbonatitic–nephelinite system as observed Hanang and Sadiman volcanoes suggest that nephelinite magma evolved to the surface did not reach carbonate saturation. Carbonate solubility of CO_2-rich silicate magma can only be lowered if open system differentiation with primary melt replenishment occurred at depth, as recorded in both systems by abrupt zoning in clinopyroxene (Baudouin et al. 2016, Zaitsev et al. 2012). The presence of Ca-carbonatite globules in the matrix of nephelinites at Shombole volcanoes (Peterson 1989) may represent higher carbonate component in primary magmas related to heterogeneous CO_2-bearing mantle source or an intermediate stage related to a late closed system differentiation.

The carbonatites erupted in NTD ranges in compositions from natrocarbonatite to calciocarbonatite (Keller and Krafft 1990, Church 1996), whereas the melt inclusions have Na-carbonatite in equilibrium with Na-rich silicate liquid (Oldoinyo Lengai; Mitchell and Dawson 2012, Sharygin et al. 2012, deMoor et al. 2013) and Ca-carbonatite in equilibrium with Na-poor silicate liquid (Kerimasi; Guzmics et al. 2011, 2012) (Fig.IV.10). The immiscibility processes leading to the formation of Na-carbonatite at Oldoinyo Lengai have been studied for the combeite–wollastonite nephelinite 1917 eruption (Sharygin et al. 2012) and suggested that water-poor complex multistage differentiation occurred in intermediate magma chamber, whereas the last 2007 eruption constrained the immiscibility at low pressure (~100-200 MPa) in a hydrous system (0.7-10.1 wt% H_2O) (deMoor et al. 2013). On the other hand, the study of melt inclusions in phenocrysts of Ca-rich carbonatite at Kerimasi volcano strongly suggest high temperature (~1050°C) and high pressure (500-1000 MPa) of calciocarbonatite immiscibility (Guzmics et al. 2012, Káldos et al. 2015). The Ca-Na carbonatite liquid in Hanang nephelinite recorded immiscibility process at ~500 MPa with intermediate pressure between Na-carbonatite at Oldoinyo Lengai (100-200 MPa) and Ca-carbonatite at Kerimasi (500-1000 MPa) (Fig.IV.10).

Although all eruptive lavas associated to carbonatites in the NTD are Mg-poor and alkaline nephelinites (Fig.IV.4), the studies of MI indicate that the evolution of the interstitial melt occurred by fractional crystallisation and immiscibility process at different P, T and H_2O content. Silicate alkaline melt evolved from nephelinitic to phonolitic composition by fractional crystallisation of nepheline–dominated assemblage at high pressure and anhydrous conditions

at Hanang, Sadiman volcanoes (Fig.IV.8), whereas Na-rich silicate liquid from Oldoinyo Lengai record late magmatic evolution controlled by fractional crystallisation of cpx, wollastonite and combeite, which decrease silica content of residual liquid at low pressure and hydrous conditions (Dawson 1998, deMoor et al. 2013).

The different conditions of crystallisation of Mg-poor nephelinites leading to the eruptions of various carbonatite/nephelinite association are then related to the parental magmas consisting of Na-Ca-H_2O-poor and Mg-rich melilitites (e.g. Dawson et al. 1997, Hui et al. 2015) and Na-Ca-H_2O-rich and Mg-poor melilitites (e.g. natrocarbonatite Keller et al. 2006). The variability of the primary melt composition and further evolution is the result of partial melting of heterogeneous mantle source affected by fluid–rich metasomatic events (Dawson and Smith 1988, Koornneef et al. 2009, Lee et al. 2000, Rudnick et al. 1993).

Conclusion

North Tanzanian Divergence is characterized by highly alkaline and carbonatite volcanism at early stage of rifting (i.e. Oldoinyo Lengai and Kerimasi, Shombole volcanoes). Erupted carbonatite lavas are calciocarbonatite (Kerimasi) and natrocarbonatite (Oldoinyo Lengai) associated with nephelinite magmas. In Hanang volcano, melt inclusions in nephelinite crystals attest of the presence of intermediate Ca-Na carbonatite with trachytic melt. The Ca-Na carbonatite results from immiscibility process of H_2O-poor and CO_2-rich phonolitic melts (6 ± 1.5 wt% CO_2) at the late stage of nephelinitic differentiation. The variability in carbonatite composition is related to fractional crystallisation and immiscibility processes of nephelinitic magmas at different P, T and volatile contents (e.g. H_2O-rich and H_2O-poor nephelinite in Oldoinyo Lengai and Hanang, respectively) conditions. The absence of carbonatite lavas at Hanang volcano is then explained by open system with primary nephelinitic magma replenishment preventing alkaline enrichment and carbonatite-silicate immiscibility at depth.

Supplementary data

Secondary ion mass spectrometry (SIMS)

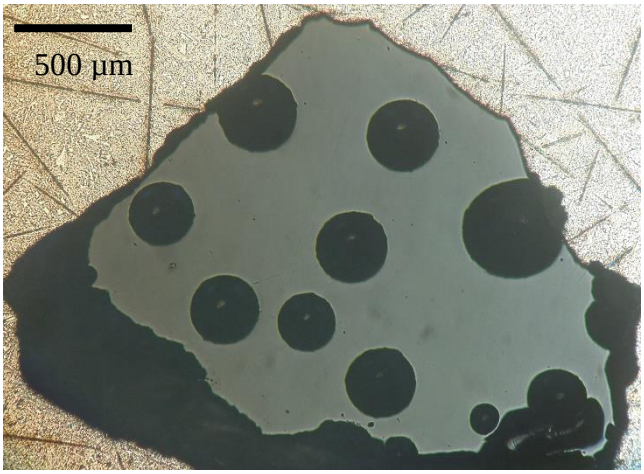

SiO_2	59.41
TiO_2	1.82
Al_2O_3	3.64
FeO	14.71
MnO	0.55
MgO	0.97
CaO	7.02
Na_2O	7.07
K_2O	4.31
P_2O_5	0.28
CO_2	0.22

Photography and composition of the trachytic standard.

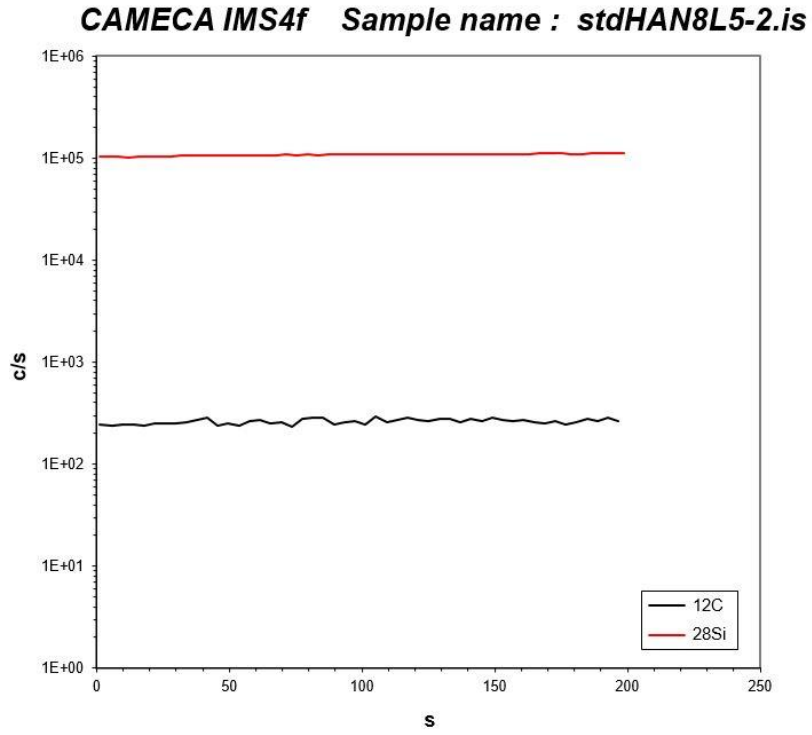

Intensity of the Carbon and Silicium signal for the standard

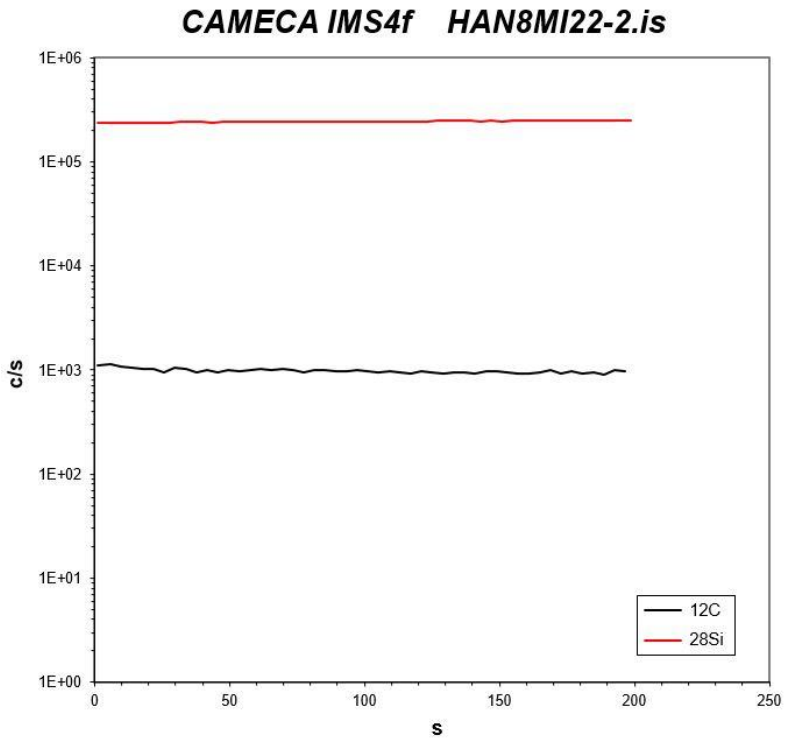

Intensity of the Carbon and Silicium signal for the silicate glass of melt inclusion without contamination by the carbonate phase.

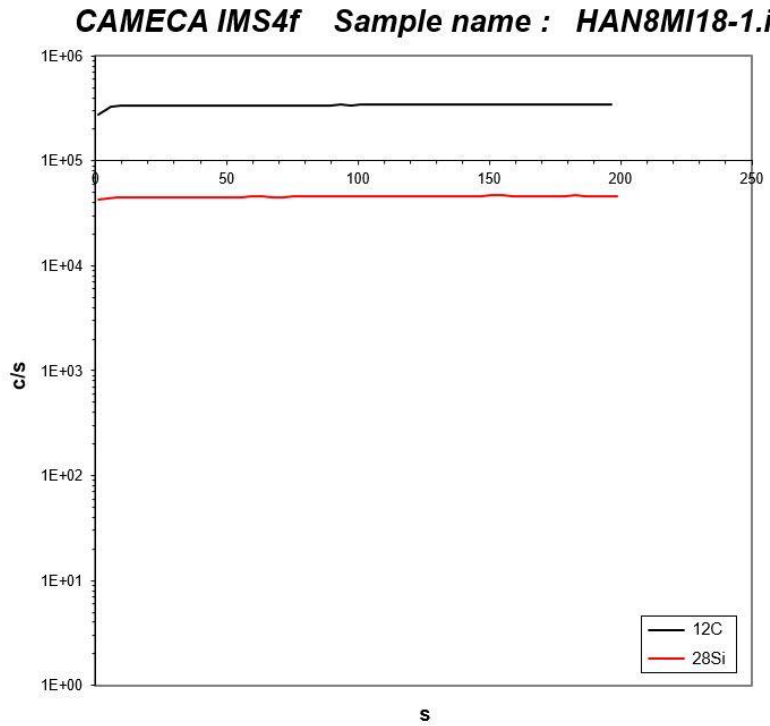

Intensity of the Carbon and Silicium signal for the silicate glass of melt inclusion with contamination by the carbonate phase.

SIMS analyses

type	name	C/Si (IE/IR)	Si (wt%)	CO_2 (wt%)
standard	Std Han8L5-2	0.0026	27.8	0.22
standard	Std Han8L5-3	0.0019	27.8	0.22
standard	Std Han8L5-4	0.0021	27.8	0.22
standard	Std Han8L5-5	0.0023	27.8	0.22
standard	Std Han8U5-1	0.0024	27.8	0.22
standard	Std Han8U5-2	0.0021	27.8	0.22
MI	MI22-1	0.0041	29.21	0.43
MI	MI23-2	0.0212	27.12	*2.07**
MI	MI27-1	0.0401	26.26	*3.96**
MI	MI26-1	0.5641	12.52	-
MI	MI21-1	0.7323	10.75	-
MI	MI20-1	1.0025	8.55	-
MI	MI15-1	0.2374	17.63	-
MI	MI19-1	0.0536	23.97	-
MI	MI25-1	2.6476	-	-
MI	MI18-1	5.8763	-	-
nepheline	nepheline	0.00026	19.329	7 ppm

* C/Si ratio variation due to carbonate contamination

Conclusions chapitre IVB

Hanang

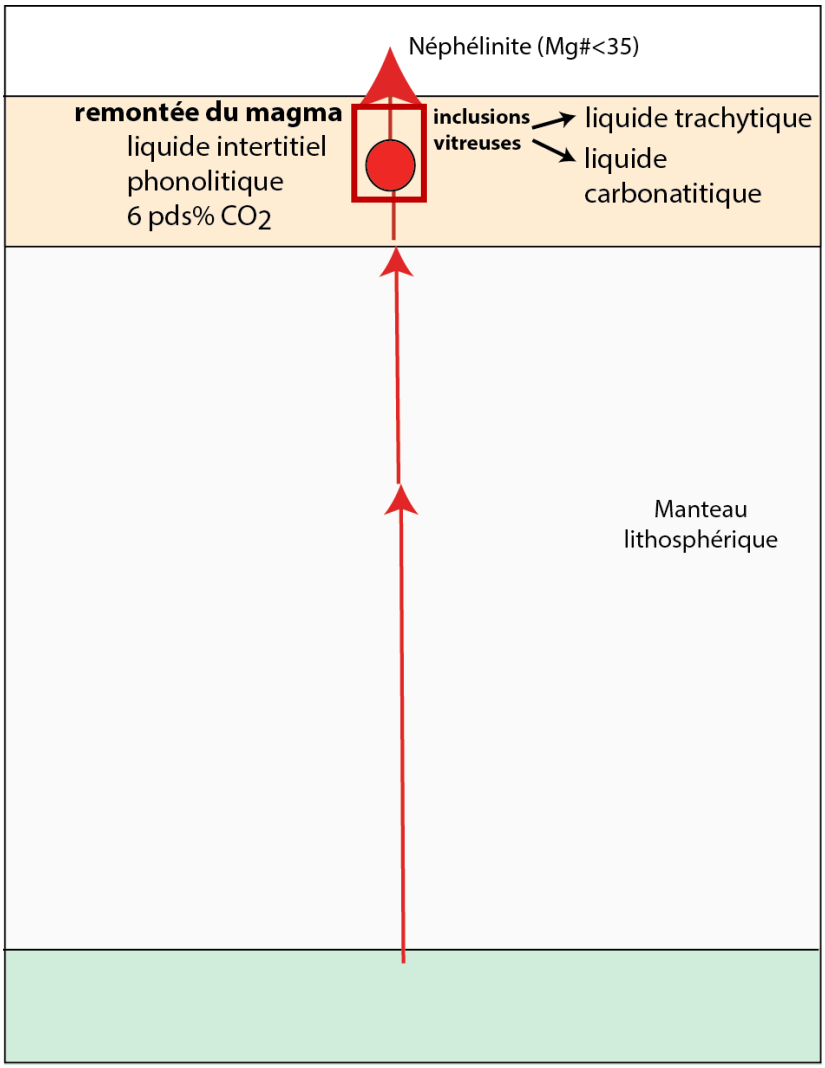

- Liquides silicatés évoluent jusqu'à des phonolites riches en CO_2
- Immiscibilité dans les inclusions (système fermé) lors de la remontée
- Absence de carbonatite induite par une évolution en système ouvert (mélange magmatique, dégazage)

Chapitre V. Conditions redox à l'initiation du rift

Pour contraindre les conditions redox, une approche multi-méthode a été utilisée, avec des analyses XANES (soufre et fer) sur les inclusions vitreuses et les minéraux (Hanang & Kwaraha) et des analyses Mössbauer sur les roches totales et minéraux séparés.

Redox of early stage rifting (Tanzania): a XANES and Mossbauer study

V.I Introduction

Oxygen fugacity (fO_2, expressed relative to fayalite magnetite quartz buffer, ΔFMQ) with temperature and pressure are important parameters which controls phase equilibria and the composition of minerals, melt and gas (Carmichael and Ghiorso 1990, Toplis and Carroll 1995, Mavrogenes and O'Neill 1999, Berndt et al. 2005). Oxygen fugacity varies in magmas according to their geological setting from relatively reduced condition in mid-oceanic basalt (MORB: ΔFMQ -1 to ΔFMQ +1) to more oxidized condition in oceanic island basalt (OIB: ΔFMQ to ΔFMQ +2) and island-arc basalt (ΔFMQ +1 to ΔFMQ +3) (Frost and McCammon 2008, Ballhaus 1993, Parkinson and Arculus 1999, Jugo et al. 2010). Fractional crystallization has a moderate effect on oxidation state of silicate melt consequently the oxidation state of magmas may reflect the oxidation state of their source region (Kelley and Cottrell 2009, Crabtree and Lange 2012, Dauphas et al. 2014).

The East African Rift (EAR) exposes different stage of rifting associated with different magmatic series. In Ethiopia (mature stage rifting, 30 Ma), lavas belong to the sub-alkaline series at reduced condition close to ~ ΔFMQ (deMoor et al. 2013). Southward at the east branch of EAR, Kenya volcanism (intermediate stage of rifting, 15 Ma) is characterized by alkaline lavas with variable fO_2 from ΔFMQ -1 to ΔFMQ +0.7 (Scaillet and Macdonald 2006, Ren et al. 2006). In Tanzania (early stage of rifting, < 8 Ma), the alkaline to hyper-alkaline lavas crystallized under relatively oxidizing conditions (> ΔFMQ, Sadiman volcano, Zaitsev et al. 2012). Potassic nephelinites at Toro-Ankole volcanic field (Uganda, <50 ka), which correspond to the early stage rifting at west branch of EAR, have the more oxidizing conditions of the EAR (~ ΔFMQ +1.5) (Murav'eva and Senin 2009).

The Manyara basin, south Tanzania, is the earliest stage rifting of the East branch of EAR (volcanism < 1 Ma). Lavas are hyper-alkaline Mg-poor nephelinites (Hanang volcano) and Mg-rich nephelinites (Labait volcano, Kwaraha volcano). Volcanism in Manyara basin erupted hyperalkaline and alkaline CO_2-rich and H_2O-poor mafic magmas from at least 120 km below the rift escarpment (Baudouin et al. in prep, chapter III) indicating that the early-stage rifting volcanism resulted from low degree of partial melting and deep phlogopite and CO_2-rich mantle source (Baudouin et al. in prep, Rosenthal et al. 2009). The goal of the present study is to determine the redox conditions of Manyara lava evolution and constrain the redox conditions of early stage rifting volcanism. The redox conditions of Manyara lavas have been determined from the speciation of iron (Fe^{2+}/Fe^{3+}) and sulfur (S^{2-}/S^{6+}) of lavas and minerals using a multi-method approach consisting of XANES analyses for melt inclusions (Hanang) and minerals (Hanang & Kwaraha) and Mössbauer analyses for whole rock (Hanang, Labait, Kwaraha) and minerals (Hanang & Kwaraha).

V.II Samples and Analytical Methods

II.1 Samples

In this study, 4 samples (Han8, Kw8, Kw1, Lab3) from the Manyara basin (north Tanzania) have been analyzed by XANES and/or Mössbauer spectroscopy. Samples from Manyara basin represent different stage of differentiation at early stage rifting, with primitive lavas (melilite nephelinite; Kw8, Lab3), evolved lavas (e.g. Mg-poor nephelinite; Han8) and carbonatite (Kw1). Nephelinite from Hanang volcano (Han8) is the only lava from Manyara basin that contains melt inclusions allowing the determination of the oxidation state of interstitial melt (chapter IV). Melt inclusions (MI) and minerals were analyzed during the same XANES session at the ID21 beamline ESRF facilities (Grenoble, France). In addition, 8 reference samples and a set of 40 MORB glasses have been investigated with the same technique (Alard et al., in prep). Although the discussion will be focused on the Tanzanian samples, it is necessary to consider reference samples and MORB glasses analyzed during the session for the purpose of calibration and assessing analytical reproducibility and accuracy.

II.1.1 Natural samples from the Manyara basin (Tanzania)

Samples from Manyara basin are lavas from Labait and Kwaraha (chapter III) and Hanang (chapter IV) volcanoes, representing an evolution from primary to more evolved silicate melt.

Labait melilite nephelinite (Lab3) is a Mg-rich, silica- and alkaline-poor lava (40.02 wt% SiO_2, 2.99 wt% $Na_2O + K_2O$, respectively) and has high Mg# (Mg#= 78.4) and contains olivine (30%vol) and minor magnetite (magnesioferrite, Ti-magnetite), plagioclase and pyrrhotite. Labait lavas are considered as the parent melt of Hanang Mg-poor nephelinites (Baudouin et al. 2016, Dawson et al. 1997).

Kwaraha melilite nephelinite is a Mg-rich, silica- and alkaline-poor lava (39.33 wt% SiO_2, 4.21 wt% $Na_2O + K_2O$, respectively) and has high Mg# (Mg# = 64.6). Kwaraha sample (Kw8) has porphyritic texture with 16% phenocrysts of olivine (3 %), cpx (12 %, diopside), phlogopite (0.9 %) and magnetite (0.2 %).

Carbonatite lava erupted from a nearby cone of the Kwaraha volcano. The carbonatite sample (Kw1) is a calciocarbonatite (Kw1) with 62 wt% CaO and 33 wt% CO_2, with low content in MgO (0.51 wt%) and alkali elements (0.26 wt% Na_2O, 0.15 wt% K_2O) and contains calcite (95 vol%), euhedral apatite (2 vol%) and magnetite (3 vol%). Petrological and geochemical details for Labait and Kwaraha lavas are presented in chapter III.

Hanang sample (Han8) is a Mg-poor nephelinite with porphyritic texture with 30.5 vol.% of phenocryts including nepheline (18.5 %), clinopyroxene (7.5 %, diopside), Ti-rich garnet (2.5 %, melanite) phenocrysts along with titanite (0.5 %), apatite (1.5 %) and rare pyrrhotite set in a groundmass of nepheline microliths. Hanang nephelinite is a silica- and

alkaline-rich lava (45.75 wt% SiO_2, 10.43 wt% Na_2O+K_2O, respectively), and has a very low Mg# (molar Mg/(Mg+ΣFe)*100 = 31.2). Melt inclusions hosted by nepheline crystals are composed by a trachytic silicate glass, a carbonate phase and a shrinkage bubble (chapter IV). The carbonate phase was unfortunately lost when melt inclusions were exposed at the surface. Petrological and geochemical study for Hanang lavas and MI are presented in chapter IV.

II.1.2 Reference samples

We selected four natural MORB and four experimental glasses as reference samples. MORB samples have been analyzed by Mossbauer spectroscopy and are used for Fe and S calibrations (Table 1). MORB samples are PH33, CH98-DR12, CLIP-Raie08, and GN0207. The geochemistry of these samples have been previously investigated by Labidi et al. (2012), Bézos and Humler (2005), and Hékinian et al. (1995), and the $Fe^{3+}/\sum Fe$ of samples CH98-DR12 and GN0207 were determined by wet chemistry (Bézos and Humler 2005). We also used experimental glasses synthetized in IHPV fitted with a Shaw-type membrane for the control of oxygen fugacity (Berndt et al. 2002): one andesite DA4#01 at NNO+1.12 (59 wt% SiO_2, 3.32 wt% FeO_{tot}, 1150 ppm S, Parat et al. 2008), one S-free basalt MJS05#2 at NNO+2.35 (51 wt% SiO_2, 7.96 wt% FeO_{tot}, Parat et al. 2014) and one S-bearing and Fe-free rhyolitic glass, apa#53, at NNO+2 (72.14 wt% SiO_2, 637 ppm S, Parat and Holtz 2004) (Table 1). This set of glasses was completed by a rhyolite glass from the Ben Lomond volcano named OARGOU (NZ, Alard et al. in prep), which have been used as an in-house standard for XRF and LA-ICPMS analyses (76.98 wt% SiO_2, 1.36 wt% FeO_{tot}) and the basaltic experimental glass 'Nath3' at ΔFMQ-1 (Pers. Com. N. Bolfan-Casanova).

II.2 Analytical methods

II.2.1 Mössbauer spectroscopy

Mössbauer spectroscopy analyses were obtained at the 'Réseau de rayons x et γ' facility at the University of Montpellier (France). Approximately 300 mg of sample were grounded to powder in an agate motar and pressed into 10 mm diameter pellets. ^{57}Fe spectra were collected at room temperature in constant acceleration transmission mode on a ^{57}Co source. The Mössbauer drive was calibrated with Fe foil. Spectra were collected for 1-2 days and 5 days for Fe-poor samples Kw1 and OARGOU. $Fe^{3+}/\Sigma Fe$ was calculated from the ratio of the area of the fitted Fe^{3+} doublet relative to the entire absorption envelope. Doublets are characterized by a Quadripole Splitting (QS), an Isomer Shift (IS) and a linewidth (LW) (Table 1). $Fe^{3+}/\Sigma Fe$ ratios were determined for four MORB reference samples (PH33, CLIP Raie 08, CH98 DR12, GN0207) and 1 rhyolite (OARGOU) (Table 1) (Fig.V. A1, supplementary material). The $Fe^{3+}/\Sigma Fe$ varies between 0.125 and 0.140 for MORB samples and is 0.323 for OARGOU. $Fe^{3+}/\Sigma Fe$ is 0.110 for sample 'Nath3' which was analyzed by C.

McCammon at the Bayerisches Geoinstitut (BGI). Mossbauer results for lava samples (Han8, Lab3, Kw1, Kw8) and minerals (Han8, Kw8) are reported in section III.1 (Table 2).

Table 1: Sulfur and iron speciation, and fO_2 of reference samples

	XANES $I_{S^{6+}}/I_{\Sigma S}$	XANES $S^{6+}/\Sigma S$	XANES Fe Centroid	Mossbauer $Fe^{3+}/\Sigma Fe$	Calculated* $Fe^{3+}/\Sigma Fe$	exp. fO_2 (ΔFMQ)	Calculated* fO_2 (ΔFMQ)
Experimental glasses							
DA4#01a	0.701	0.457	7112.85	-	0.32	1.7	-
DA4#01b	0.730	0.501	-	-	0.32	1.7	-
DA4#01c	0.758	0.547	-	-	0.32	1.7	-
apa53	0.873	0.767	-	-	-	2.7	-
MJS05#2	-	-	7112.88	-	0.44	3	-
Nath3	-	-	7112.26	0.110	-	-1	-
Natural glasses							
PH33-G2	0.379	0.077	7112.40	0.1355	-	-	-0.39
PH33-2G1	0.373	0.071	7112.36	0.1355	-	-	-0.39
PH33-2G1	0.376	0.074	-	0.1355	-	-	-0.39
CLIPRAIE08	0.394	0.091	7112.35	0.1450	-	-	-0.22
CLIPRAIE08bis	0.390	0.087	-	0.1450	-	-	-0.22
CH98DR12	0.381	0.079	7112.35	0.1250	-	-	-0.49
GN0207	0.394	0.091	7112.34	0.1401	-	-	-0.30
GN0207bis	0.394	0.091	-	0.1401	-	-	-0.30
Oargou	-	-	7112.90	0.3234	-	-	0.747

exp. fO_2: experimental fO_2; *Kress and Carmichael 1991

II.2.2 XANES spectroscopy at the Fe and S K-edges

Pre-edge and XANES spectra at the Fe and S K-edge were collected at the European Synchrotron Radiation Facility (ESRF, Grenoble, France) on the beamline ID21. The beam size at the sample position was 1*1.5 µm. A Si(111) double-crystal monochromator was used for these experiments. Normalized spectra were obtained with the ATHENA software (Ravel and Newville 2005).

Iron spectra acquisition between 7050-7350 eV were performed with a step of 0.33 eV and a dwell time of 0.1 s. For all experiments, a reference Fe foil (7112.7 eV) was used to provide an accurate internal energy calibration of the monochromator. Reference materials for Fe^{2+} and Fe^{3+} were also analyzed ([4]Fe^{2+}(staurotide), [6]Fe^{2+}(siderite), [4]Fe^{3+} (sanidine), and [6]Fe^{3+} (andradite). The XANES spectra were normalized in absorbance by fitting the spectral region before the pre-edge using a polynomial function and subtracting it as background absorption. The pre-edge information was derived by calculating the integrated area and the centroid position of the background subtracted pre-edge.

$Fe^{3+}/\Sigma Fe$ of reference samples were obtained by Mössbauer spectroscopy and by experimental glasses with known fO_2 which allow to calculate $Fe^{3+}/\Sigma Fe$ as a function of temperature and glass composition from empirical equation from Kress and Carmichael (1991) (Table 1). $Fe^{3+}/\Sigma Fe$ and centroid position determined by XANES for the reference samples are used to define a $Fe^{3+}/\Sigma Fe$ ratio versus centroid correlation. This correlation can be used to deduce $Fe^{3+}/\Sigma Fe$ of the studied samples (e.g. melt inclusions) from XANES analyses. Two different

$Fe^{3+}/\Sigma Fe$ ratio versus centroid position of the Fe pre-edge XANES spectra are used to determine iron redox state in glasses (e.g. Cottrell et al. 2009, Dauphas et al. 2014), a basalt calibration with SiO_2 < 58 wt% and a Si-rich glass calibration with SiO_2 > 58 wt% (Fig.V.1). Using our reference samples, we derived our basalt calibration (r^2 = 0.985) (Fig.V.1a) which yield intermediate values between Wilke et al. (2005) (erratum Wilke et al. 2006) and Cottrell et al. (2009) calibrations. Si-rich glass calibration used OARGOU, DA4#01 samples (Fig.V.1b)(Table 1) and Si-rich samples from Wilke et al. (2005), Cottrell et al. (2009) and Dauphas et al. (2014) (r^2 = 0.996).

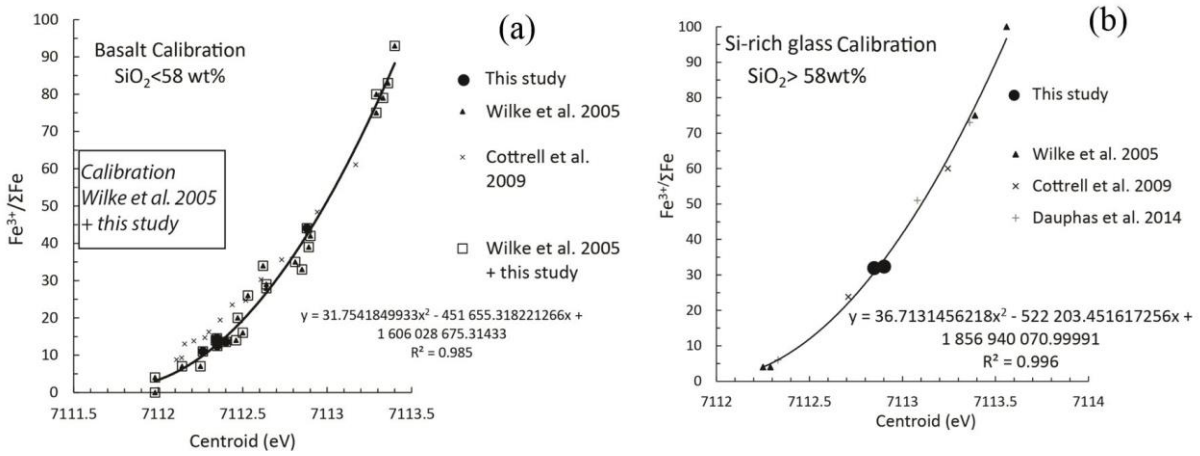

Fig.V.1 *$Fe^{3+}/\Sigma Fe$ versus centroid and calibrations for (a) basalt and (b) Si-rich glass from this study, Wilke et al. (2005), Cottrell et al. (2009) and Dauphas et al. (2014).*

Sulfur spectra acquisitions were performed between 2400 and 2550 keV with a step of 0.19 eV for 2400-2450 eV, 0.18 eV for 2450-2510 eV and 0.25 eV for 2510-2550 eV. The energy of the monochromator was calibrated on the white line of the spectrum of gypsum (2482.5 eV). Reference materials for sulfur were sulfates (haüyne, gypsum, baryte, anhydrite) and sulfides (pyrite, pyrrhotite, pentlandite). The samples were typically scanned quickly from 2400 to 2550 eV (dwell time of 0.2 s) and the quick-scans were stacked until an appropriate signal-to-noise ratio was achieved (typically in groups of 20 scans). Spectra were normalized by fitting the energy region before the edge with a polynomial function and subtracting this function to the spectra to eliminate the background. The determination of the sulfur speciation is based on the method of Jugo et al. (2010) using the signal intensity at the energy positions of sulfide and sulfate in glass or mineral. The intensity for sulfide $I(S^{2-})$ was integrated between 2475.7 and 2480 eV and the intensity of sulfate $I(S^{6+})$ was integrated between 2481.5 and 2484 eV. $S^{6+}/\Sigma S$ ratio was calculated using the empirical equation from Jugo et al. (2010):

$$S^{6+}/\Sigma S = -C * \ln((I(S^{6+})/I\Sigma S - A)/B) \quad (1)$$

where A=1.2427, B=-0.94911, and C=0.81354.

V.III Iron and Sulfur Speciation results

III.1 Mössbauer analyses

Iron speciation from the $Fe^{3+}/\Sigma Fe$ of whole rock varies as a function of lava compositions. In mafic lavas, melilite nephelinite from Labait volcano (Lab3) has a low $Fe^{3+}/\Sigma Fe$ ratio of 0.24 (Table 2, Fig.V.2) and melilite nephelinite lavas from Kwaraha has a relatively higher $Fe^{3+}/\Sigma Fe$ ratios of 0.51. The $Fe^{3+}/\Sigma Fe$ ratio of the carbonatite associated with the Mg-rich nephelinite is the highest ratio determined in Manyara lava with $Fe^{3+}/\Sigma Fe$ ratio=0.90 (Kw1) (Table 2, Fig.V.2). Mössbauer spectra of melilite nephelinite and carbonatite (Kw8 and Kw1, respectively) have signature of magnetic phase (Fig.V.2). The clinopyroxenes from melilite nephelinite have more Fe^{2+} compare to Fe^{3+} with $Fe^{3+}/\Sigma Fe$=0.37. Cpx doublet has a half width at half maximum of 0.42 together with a QS of 1.16 and a IS of 1.96 is coherent with all the Fe^{2+} assigned is one site, probably M2 site while doublet with a QS of 0.63 and IS of 0.35 was assigned to Fe^{3+} in the M1 site (Woodland et al. 2006, Hao et al. 2013).

Mg-poor nephelinite from Hanang volcano (Han8) has a high $Fe^{3+}/\Sigma Fe$ ratio of 0.69. Clinopyroxenes have higher Fe^{3+} than Fe^{2+} concentration with $Fe^{3+}/\Sigma Fe$=0.59 (Table 2) and Fe^{2+} is assigned in 2 different crystallographic sites (M1 and M2). On the basis of previous studies (Woodland et al. 2006, Hao et al. 2013), doublet with QS of 2.51 and IS of 1.05 was assigned to Fe^{2+} in the M1 site, doublet with QS of 2.04 and IS of 1.12 was assigned Fe^{2+} to M2 site and doublet with QS of 0.54 and IS of 0.43 was assigned to Fe^{3+} in the M1 site.

Table 2: Mössbauer spectroscopy parameters for natural samples from Tanzania

Sample	Type	Fe^{2+}			Fe^{2+}			Fe^{3+}			Fe^{3+}			$Fe^{3+}/\Sigma Fe$	χ^2
		IS	QS	LW	IS	QS	LW	IS	QS	LW	IS	QS	LW		
Han8	cpx	1.05	2.51	0.61	1.12	2.04	0.31	0.43	0.54	0.41				0.593	0.66
Han8	gt	1.05	2.72	0.55	1.13	1.97	0.36	0.44	0.65	0.42				0.654	0.80
Han8	WR	1.09	2.69	0.39	1.16	1.92	0.39	0.39	0.51	0.53				0.694	0.53
Kw8	cpx	1.16	1.96	0.42				0.35	0.80	0.63				0.366	0.12
Kw8	WR	1.14	2.98	0.31	1.14	1.99	0.64	0.38	0.58	0.70				0.507	0.69
Kw1	WR	0.84	2.25	0.53				0.40	0.58	0.53				0.899	0.40
Lab3	WR	1.14	2.98	0.31	0.91	2.26	0.81	0.36	0.34	0.55	0.46	0.68	0.55	0.243	0.78

IS: isomer shift (mm/s); QS: quadrupole splitting (mm/s); LW; linewidth = half width at half maximum.
cpx: clinopyroxene; gt: garnet; WR: whole rock.

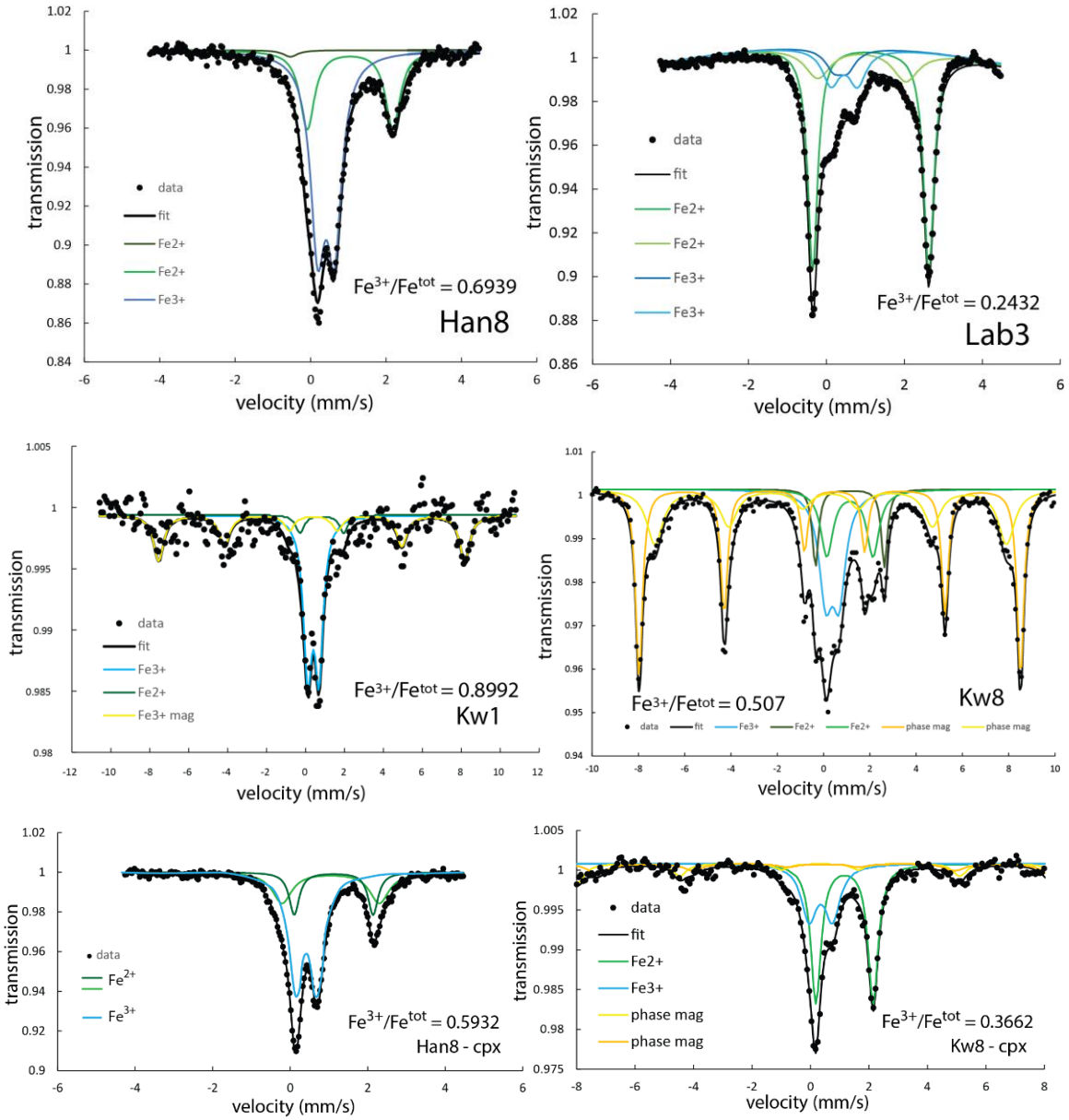

Fig.V.2 *Mossbauer spectra of melilite nephelinite (Lab3 and Kw8), Mg-poor nephelinite (Han8), and carbonatite (Kw1) and Mossbauer spectra of clinopyroxenes (Han8 and Kw8).*

III.2 XANES results

III.2.1 Iron speciation

Reference samples

The centroid positions of MORB samples have small variations between 7112.34 and 7112.40 eV (Table 1). Centroid position of the basaltic glass MJ05#2 is 7112.88 eV and 7112.26 eV for the basaltic glass 'nath3'. For Si-rich reference samples, the centroid positions are 7112.85 eV for DA4#01 and 7112.90 eV for OARGOU (Table 1).

Melt inclusions from Mg-poor nephelinites

We analyzed 9 melt inclusions from Mg-poor nephelinites (Han8). Melt inclusions are formed by a trachytic silicate glass and a carbonate phase. All carbonate phases consist of very fined microliths and have been removed during polishing of the sample and were not analyzed (Figs.3 and 4, Chapter IV). The size of the melt inclusions (20 µm) allows us to analyze different part of silicate glass with XANES and electron microprobe (beam size 1 µm) (Fig.V.3). The different parts of three melt inclusions (MI-1, MI-5 and MI-6) show small variations in composition with Ca-enriched silicate glass around the shrinkage bubble (i.e. MI1-g2'Ca, MI5-g3'Ca, Fig 3 and Table 3). We selected the position for the analyses from Ca map performed using XANES acquisitions before Fe and S analyses. All XANES spectra have Fe K-edges with characteristic shapes of silicate glasses (e.g. Wilke et al. 2001, 2005).

Silicate glasses have a centroid position between 7112.67 and 7112.96 eV (Fig.V.4, Table 1). We observed a variation of the centroid position within silicate glass. MI-5 have a Si-rich glass ('Si-glass' g1 and g2, Fig.V.3) with a centroid at 7112.67 eV and a Ca-enriched silicate glass ('Ca-silicate glass' g3'Ca, Fig.V.3) with a centroid at 7113 eV (Fig.V.4). Silicate glasses are Si-rich with ~ 60 wt% SiO_2, and using the Si-rich calibration (Fig.V.1b), we determined that the centroid positions correspond to $Fe^{3+}/\Sigma Fe$ ratio ranging from 0.15 to 0.42 (Table 3) with $Fe^{3+}/\Sigma Fe$ = 0.15 to 0.37 for 'Si-glass' and $Fe^{3+}/\Sigma Fe$ =0.29 to 0.42 for 'Ca-silicate glass' (MI-1, MI-5, MI-6) (Table 3).

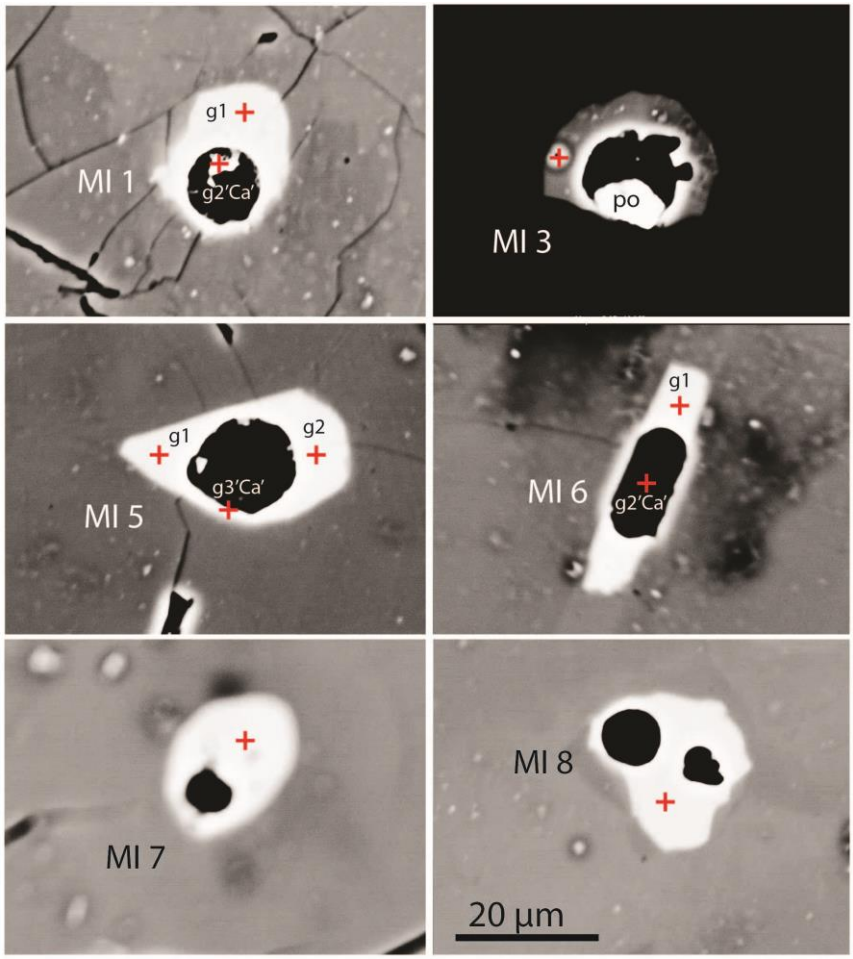

Fig.V.3 *Backscattered electron (BSE) images of melt inclusions from Hanang nephelinites.*

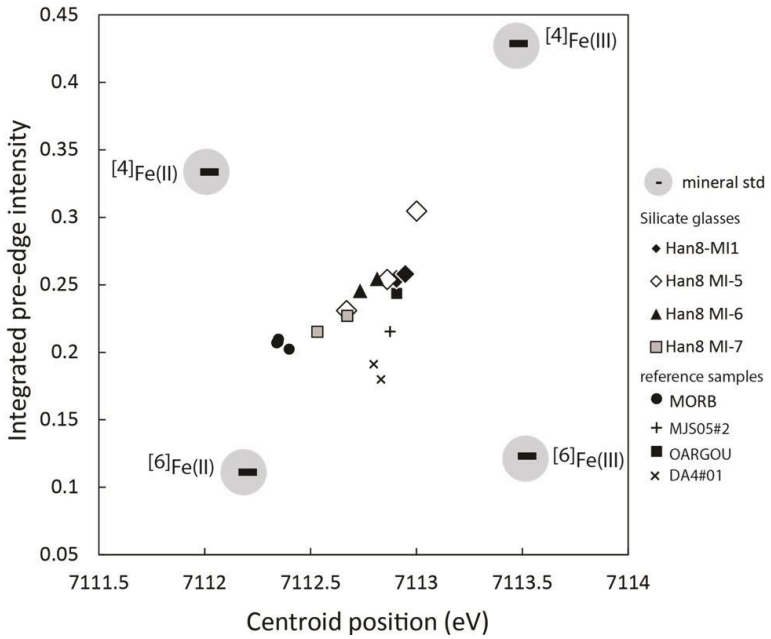

Fig.V.4 *Pre-edge characteristics (centroid position and integrated pre-edge intensity) for trachytic silicate glasses (Han8), reference samples (MORB, OARGOU, MJS05#02, DA4#01) and iron standards, i.e. [4]Fe^{2+}(staurotide), [6]Fe^{2+}(siderite), [4]Fe^{3+} (sanidine), and [6]Fe^{3+} (andradite).*

Table 3: Major element compositions and iron and sulfur speciation of melt inclusions from Hanang nephelinites (Han8)

n° MI	1-g	1-g2'Ca'	2-g	3-g	5-g1	5-g2	5-g3'Ca'	6-g	6-g2'Ca'	7-g	8-g	9-g
wt.%												
SiO_2	60.48		58.22	58.19	59.18	59.87		57.86		56.21	58.78	59.33
TiO_2	1.67		1.67	1.96	1.38	1.53		2.04		2.56	1.54	1.81
Al_2O_3	3.92		2.58	2.97	4.07	4.35		3.15		2.06	3.27	4.04
FeO	11.49		13.16	13.34	12.27	13.04		13.56		9.73	11.17	11.26
MnO	0.43		0.50	0.52	0.52	0.54		0.56		0.36	0.49	0.51
MgO	0.66		0.80	1.19	0.56	0.60		1.04		0.99	1.01	0.49
CaO	6.99		8.84	7.55	6.92	5.41		6.28		14.35	6.99	6.10
Na_2O	9.68		10.23	10.61	9.42	7.51		7.68		0.18	6.86	6.70
K_2O	2.49		2.54	2.20	3.27	2.36		2.26		1.29	2.07	2.12
P_2O_5	0.11		0.21	0.33	0.18	0.10		0.18		0.39	0.34	0.17
SO_2	0.77		1.07	0.42	1.02	1.05		1.30		0.63	0.82	0.84
F	1.23		0.26	0.51	0.72	0.86		0.35		7.51	1.42	1.19
Cl	0.34		0.43	0.48	0.42	0.39		0.32		1.54	0.66	0.40
Total	100.25		100.51	100.27	99.91	97.60		96.58		97.81	95.42	94.95
Na+K/Al	4.45		7.12	6.18	4.50	3.27		4.55		1.10	3.93	3.15
Mg#	4.2		4.5	6.5	3.4	3.4		5.6		7.3	6.6	3.2
$IS^{6+}/I\sum S$	0.42	0.434	0.32	0.30	0.32	0.32	0.420	0.32	0.368	0.328	-	-
$S^{6+}/\sum S$	0.11	0.130	0.03	0.01	0.02	0.02	0.116	0.02	0.067	0.03	-	-
Fe centroid (eV)	7112.90	7112.95	7112.96	7112.78	7112.67	7112.86	7113.00	7112.73	7112.81	7112.67	7112.77	7112.76
$Fe^{3+}/\sum Fe$	0.322	0.377	0.367	0.234	0.150	0.290	0.418	0.197	0.285	0.152	0.224	0.218
fO_2 (relative to ΔFMQ) determined for trachytic silicate glasses with different calibrations												
Sulfur (calibration from this study)	0.13	0.29	-1.24	-2.5	-1.4	-1.49	0.178	-1.36	-0.345	-1.08	-	-
Sulfur (Jugo et al. 2010)	0.60	0.64	0.26	-0.04	0.22	0.2	0.61	0.23	0.48	0.3	-	-
Iron (T=1200°C)	2.14	2.44	2.57	1.26	0.08	1.83	2.84	0.82	1.49	0.12	1.15	1.08
Iron (T=1000°C)	0.87	1.43	1.33	-0.02	-0.88	0.55	1.84	-0.40	0.49	-0.86	-0.12	-0.19

Iron speciation in minerals from Mg-poor and melilite nephelinites (Hanang and Kwaraha)

Several XANES analyses were performed for minerals to attenuate the anisotropy effect. The variations of the centroid positions are important for cpx (n=8, σ=10-15 %) and minor for garnet (n=8, σ=3-7 %,) and nepheline (n=3, σ=1-2 %,). $Fe^{3+}/\Sigma Fe$ ratios of minerals can be determined from the centroid position using calibration from mineral standards (staurotide, siderite, sanidine, and andradite) (see Wilke et al. 2001 for details).

For melilite nephelinite from Kwaraha lava (Kw8), cpx have a centroid position between 7112.72 and 7113.05 eV and $Fe^{3+}/\Sigma Fe = 0.52$ (Table 4). For Mg-poor nephelinites (Han8), cpx has a centroid position between 7112.47 and 7112.96 eV, garnet has a centroid position between 7113.28 and 7113.4 eV for garnet and nepheline has a centroid position between 7113.35 and 7113.39 eV (Fig.V.5). The $Fe^{3+}/\Sigma Fe$ ratio is 0.37 for cpx, 0.89 for garnet and 0.93 for nepheline (Table 4).

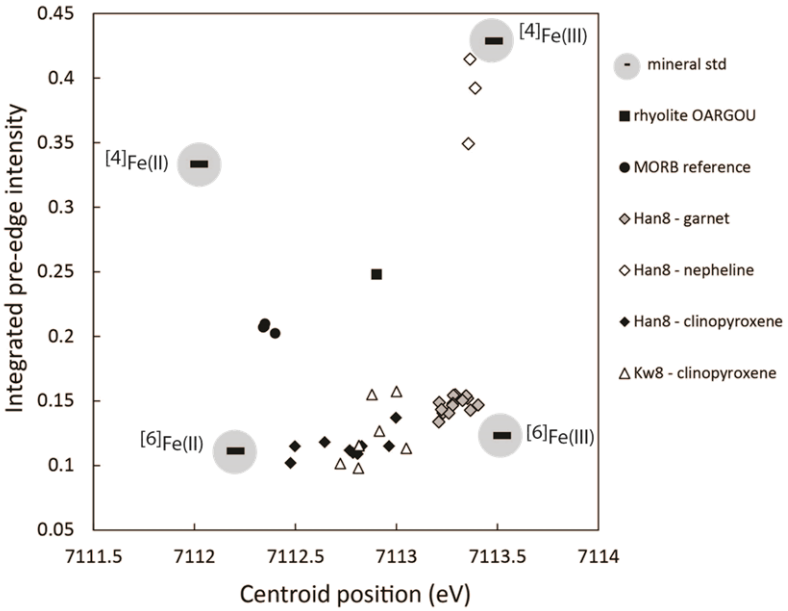

Fig.V.5 *Pre-edge characteristics (centroid position and integrated pre-edge intensity) for cpx, garnet and nepheline from Hanang (Han8) and cpx from Kwaraha (Kw8).*

Table 4: Representative major element compositions and $Fe^{3+}/\Sigma Fe$ of minerals (XANES)

Sample	Han8	Han8	Han8	Kw8
Mineral	nph (n=3)	cpx (n=5)	gt (n=8)	cpx (n=8)
SiO_2	41.35	51.43	29.60	53.50
TiO_2	0.02	0.60	13.17	0.55
Al_2O_3	32.95	1.15	0.72	1.37
FeO	1.64	11.06	21.01	3.96
MnO	bdl	0.29	0.24	0.06
MgO	0.03	10.96	0.62	15.85
CaO	0.08	23.16	32.75	22.32
Na_2O	15.73	1.25	0.38	0.88
K_2O	8.09	bdl	bdl	0.00
P_2O_5	0.02	bdl	bdl	bdl
Cr_2O_3	bdl	0.02	0.03	1.11
Total	99.91	99.92	98.52	99.64
$Fe^{3+}/\Sigma Fe$	0.93	0.37	0.90	0.52

bdl: below detection limit; nph: nepheline; cpx: clinopyroxene; gt: garnet

III.2.2 Sulfur speciation

Reference samples

XANES analysis of the reference material (pyrrhotite and haüyne) are used to determine the position of the S^{2-} and S^{6+} species. S^{2+} (pyrrhotite) has a sharp peak at 2470 eV and a broad peak at ~ 2477 eV. A single peak at 2482.5 eV characterize the S^{6+} of haüyne spectrum. Sulfide-dominated samples (MORB reference samples) spectra are characterized by the dominance of the broad peak related to the presence of S^{2-} (Fig.V. A2, supplementary

material). I(S^{6+})/IΣS and S^{6+}/ΣS ratios was determined as function of the signal intensity at the energy positions of sulfide and sulfate in glass (see section II.2.2 for details).

MORB reference samples have I(S^{6+})/IΣS ratio between 0.373 and 0.394 (Table.1) and S^{6+}/ΣS ranging from 0.07 to 0.09 (Table.1). The experimental glass DA4#01 (NNO+1.12) and apa#53 (NNO+2) are sulfate-dominated and oxidized samples (Fig.V. A4, supplementary material). We observed a small peak at 2470 eV (i.e. S^{2-}) for DA4#01, absent for apa#53 which is more oxidized glass. DA4#01 and apa#53 have a I(S^{6+})/IΣS ratio of 0.7-0.76 and 0.87 and S^{6+}/ΣS ratio of DA4#01 ranging from 0.46 to 0.55 and of 0.767 for apa#53 (Table 1).

Melt inclusions from Mg-poor nephelinites

All XANES spectra of melt inclusions display well-resolved peaks at ~ 2470 eV and 2477 eV typical of the presence of S^{2-} in the glass and small peak at the S^{6+} position (Fig.V. A4, supplementary material), indicating a small proportion of S^{6+} relative to S^{2-}. Using the method of Jugo et al. (2010) based on signal intensity at the energy positions of sulfide and sulfate in glass, the I(S^{6+})/IΣS ratio was calculated between 0.30 to 0.43 that correspond to S^{6+}/ΣS ratio between 0.01 to 0.13 (Table 3).

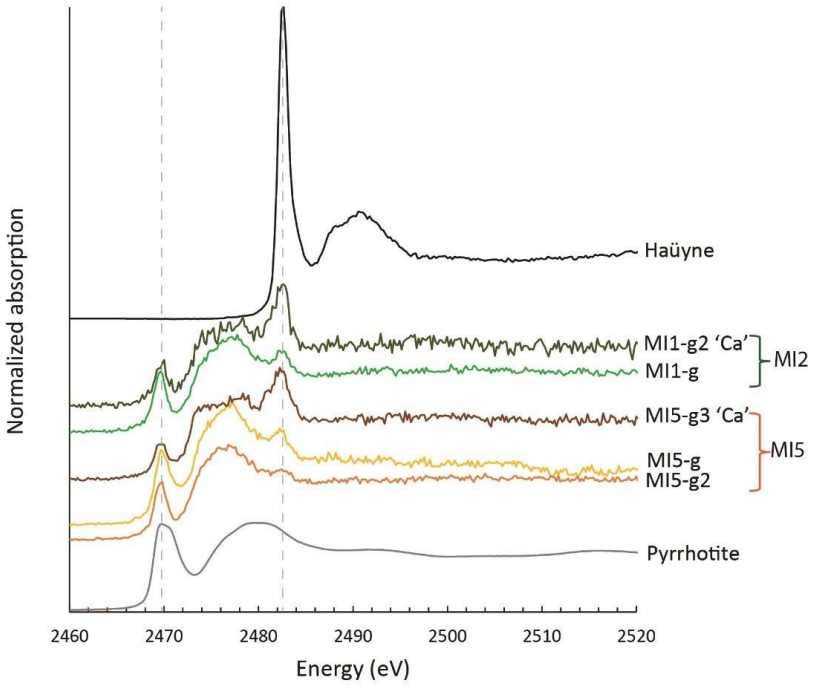

Fig.V.6 *XANES spectra of trachytic silicate glasses from Hanang Mg-poor nephelinite (MI1 and MI5) and reference material (haüyne and pyrrhotite).*

We observe different peak shapes for 'Si-glasses' (i.e. MI-1g, MI-5g spectra) and 'Ca-glasses' with more pronounced peak for S^{6+} in Ca-rich glasses (i.e.MI-1g2Ca, MI-5g3Ca spectra) (Fig.V.6) with S^{6+}/ΣS=0.07-0.13 for 'Ca-glasses' and S^{6+}/ΣS=0.01-0.11 for Si-glasses

(Fig.V.7a, Table 3). A slight correlation is observed between $S^{6+}/\Sigma S$ and sulfur content of melt inclusions, except for MI-3 that contains a small pyrrhotite crystal lowering the S content of the silicate glass (Fig.V.7b).

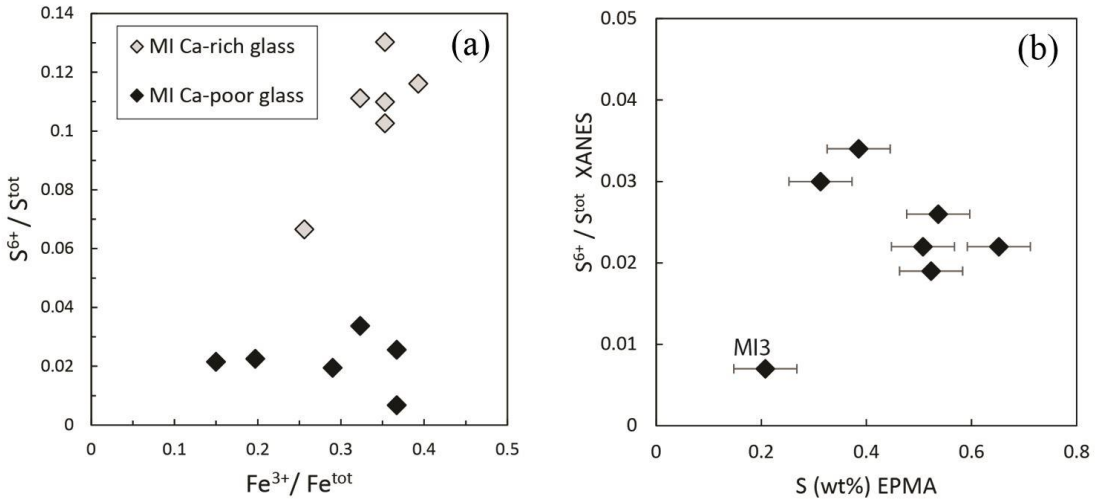

Fig.V.7 (a) *$S^{6+}/\Sigma S$ vs $Fe^{3+}/\Sigma Fe$ of Ca-enriched silicate glass and Ca-poor silicate glass.* ***(b)*** *$S^{6+}/\Sigma S$ of silicate glass vs sulfur content (Table 3).*

V.IV Oxygen Fugacity calculations

IV.1 Oxygen Fugacity derived from Iron redox

The oxygen fugacity has been defined as a function of temperature and silicate melt composition, especially the Fe_2O_3/FeO ratio, following the empirical equation of Kress and Carmichael (1991):

$$\ln X_{Fe2O3}/X_{FeO} = a*\ln fO_2 + b/T + c + \sum d_i x_i \quad (2)$$

where a = 0.196, b = 11492, c = -6.675, d_{Al2O3} = -2.243, d_{FeO} = -1.828, d_{Na2O} = 5.854, d_{K2O} = 6.215 and d_{CaO} = 3.201.

Considering the MORB composition (microprobe analyses), the Fe_2O_3/FeO ratio from XANES acquisition and the temperature for MORB genesis (1200°C), we determined that MORB reference samples have an oxygen fugacity at ΔFMQ-0.33 (log fO_2 =- 8) (Fig.V.8). These results are coherent with the redox conditions determined be wet chemistry by Bézos and Humler (2005) at ΔFMQ -0.4±0.4.

Silicate glasses have trachytic compositions (SiO_2 = 60 wt%) with $Fe^{3+}/\Sigma Fe$ = 0.15 - 0.36 for 'Ca-poor' silicate glasses and 0.29-0.42 for Ca-rich silicate glass (Table 3). The temperature of crystallization of Mg-poor nephelinite is ~1050 ±50°C (chapter IV). At 1000°C, the fO_2 of silicate glasses ranges from log fO_2 = -11 to log fO_2~ -9 (ΔFMQ=-0.9 to ΔFMQ +1.8) with slightly more oxidizing conditions (ΔFMQ = + 0.5 to +1.8) for 'Ca-glass' than 'Si-glass' (ΔFMQ=-0.9 to 1.4).

IV.2 Oxygen Fugacity derived from sulfur speciation

The oxygen fugacity of experimental glasses (apa#53, DA4#01) and natural reference glasses from Mössbauer analyses and the $S^{6+}/\Sigma S$ from XANES acquisitions are used as calibration to determine the sulfur speciation as a function of fO_2. Our data are in good agreement with data from the literature on basaltic and andesitic compositions (Jugo et al. (2005), Wallace and Carmichael (1992), Matthews et al. (1999), Nilsson and Peach (1993) (Fig.V.8a). We observed however for MORB data at low $S^{6+}/\Sigma S$ a discrepancy with experimental calibration from Jugo et al. (2010) (0.6 log unit) that may result from poorly constrain $S^{6+}/\Sigma S$ ratio between 0.05 and 0.2 or a small amount of S^{6+} in silicate glasses resulting from electron exchange between sulfur and iron during of cooling and overestimating the $S^{6+}/\Sigma S$ in natural basalts for a fixed fO_2 (Métrich et al. 2009).

Our andesitic and rhyolitic experimental glasses at high $S^{6+}/\Sigma S$ and fO_2 agree with andesitic calibration from Matthew et al (1999). The differences observed between andesite-rhyolite and basalt experimental glasses may result from effect of silicate liquid composition.

The best fit for calibration (r=0.99) was obtained for a polynomial equation including data from natural samples from Wallace and Carmichael (1992) (Fig.V.8). For trachytic silicate glasses in melt inclusions, the $S^{6+}/\Sigma S$ ratio determined from Xanes acquisitions ($S^{6+}/\Sigma S$ = 0.01 to 0.13, Table 3) correspond to an oxygen fugacity ranging from ΔFMQ = -3 to ΔFMQ =+0.3 (Fig.VI. 8b, Fig.VI.9).

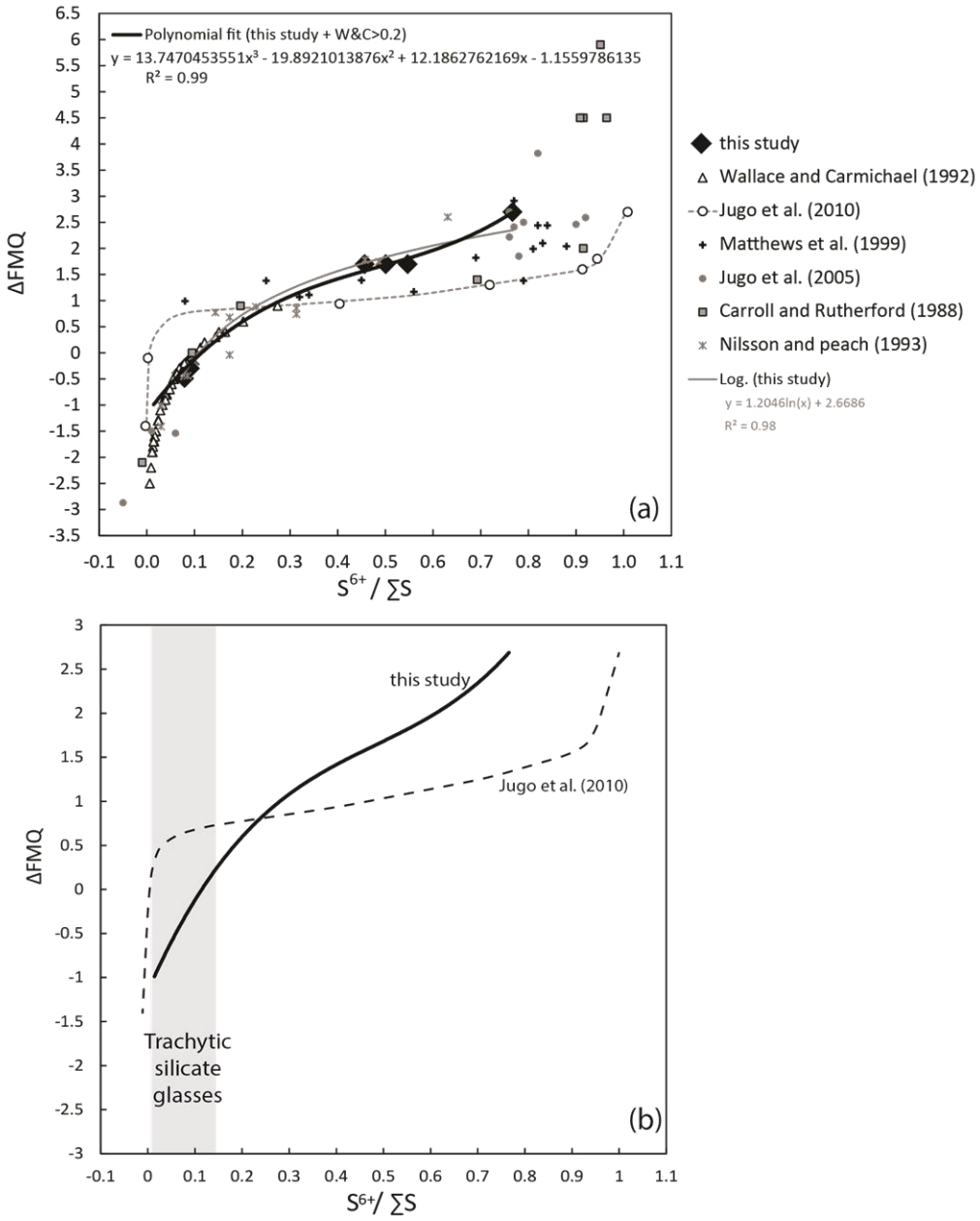

Fig.V.8 *fO_2 relative to FMQ vs $S^{6+}/\Sigma S$* ***(a)*** *Reference samples are represented with data from literature (Jugo et al. 2005, Jugo et al. 2010, Wallace and Carmichael 1992, Matthews et al. 1999, Nilsson et Peach 1993, Carroll and Rutherford 1988).* ***(b)*** *fO_2 relative to FMQ vs $S^{6+}/\Sigma S$ The distribution of $S^{6+}/\Sigma S$ (*0.01 to 0.13*) for trachytic silicate glasses are also reported (grey box).*

V.V Discussion

The oxygen fugacity determined by iron (ΔFMQ -0.3) is well correlated with S (ΔFMQ -0.21) for MORB samples (Fig.V.10a). Unlike the MORB, fO_2 of silicate glasses (MI) calculated from Fe and S are not correlated (e.g. MI-2, ΔFMQ =1.33 from Fe, and ΔFMQ = -1.24 from S) (Fig.V.9). This erroneous relationship can be due to (1) inaccurate estimated temperature (±100°C), (2) Kress and Carmichael (1991) calibration applied for basaltic glasses and not for trachytic glasses, and (3) post-entrapment processes. However, calculated fO_2 of silicate glasses at 1000°C and Kress and Carmichael calibration yields coherent values with previous data from EAR (e.g. de Moor et al. 2013, Scaillet and Macdonald 2006, Ren et al. 2006). The large variation of fO_2 may be explained by post-entrapment process.

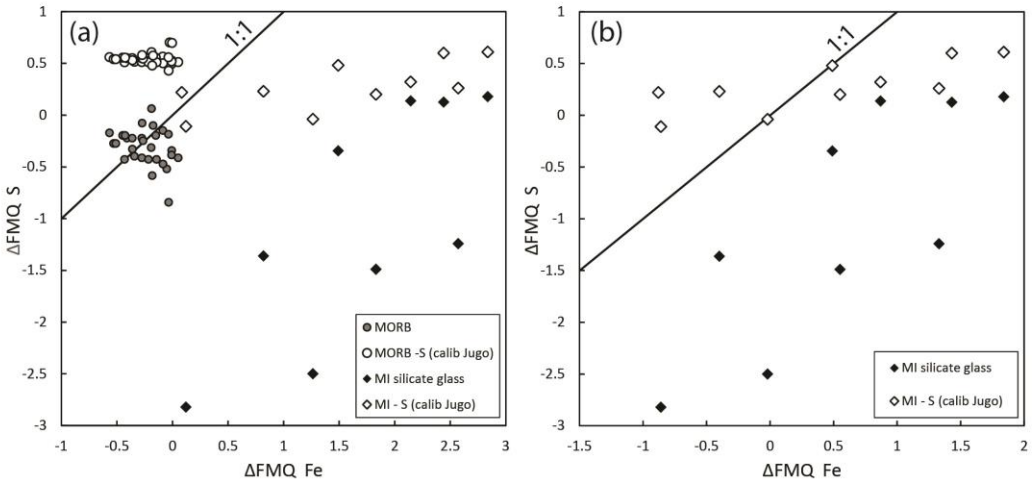

***Fig.V.9**. fO_2 (ΔFMQ) from $S^{6+}/\Sigma S$ calibrated from reference samples (this study) vs fO_2 deduced from $Fe^{3+}/\Sigma Fe$ (Kress and Carmichael 1991) **(a)** at 1200°C and **(b)** at 1000°C.*

V.1. Post-entrapment modification of oxygen fugacity in nepheline-hosted melt inclusions

This work is the first study conducted to constrain the redox magmatic conditions of nepheline-hosted melt inclusions with silicate liquid and carbonate phases. The melt inclusions from Hanang volcano are formed by a silicate glass with trachytic composition, a Ca-Na-K-S^{6+}-rich carbonate phase and a shrinkage bubble and allow characterization of redox conditions of interstitial melt during late nepheline crystallization and the role of immiscibility process during ascent (chapter IV).

Raman spectra of MI indicate the presence of SO_4^{2-} (S^{6+}) in carbonate phase and SEM analyses show that carbonate phases contain ~ 3 wt% S. In comparison, trachytic silicate glasses contain ~ 0.5 wt% S (microprobe analyses) indicating a partitioning of sulfur between carbonate and silicate liquid ($D_S^{carb/liq}$ >1) (see chapter IV). At high oxidation state, S^{6+} and S^{2-} present in the interstitial phonolitic liquid before immiscibility are then distributed between carbonate (S^{6+}) and trachytic silicate glass (S^{2-} >> S^{6+} , $S^{6+}/\Sigma S$ = 0.05). Recent studies of trace

element partitioning have suggested that sulfate is highly compatible in carbonate liquid (e.g. Guzmics et al. 2015) and immiscibility may strongly modify the $S^{6+}/\Sigma S$ ratio. The sulfate and sulfide content of pre-immiscible phonolitic liquid in Hanang lavas can be approximate considering the sum of S^{6+} and S^{2-} within carbonate (3 wt% S as S^{6+}) and trachytic glass (0.5 wt% S, $S^{6+}/\Sigma S = 0.05$). Although the S content of carbonate phase is semi-quantitative, the volume proportion of carbonate phase/silicate glass (18:82, Chapter IV) and the concentration of sulfur of both phases indicate that sulfate dominates in the pre-immiscible phonolite liquid with 0.54 wt% S^{6+} and 0.41 wt% S^{2-} ($S^{6+}/\Sigma S_{calculated}$ = 0.56) and phonolite liquid entrapment occurred under oxidized condition at ΔFMQ +1.65 (calculated from sulfur calibration) (Fig.V.10).

Silicate glasses have small variations of major element concentrations within single MI (e.g. MI5) (Table 3) suggesting that chemical re-equilibration may have occurred after entrapment as well re-equilibration of $S^{6+}/\Sigma S$ and $Fe^{3+}/\Sigma Fe$ during cooling through electron exchange (Métrich et al. 2009).

Carbonate phase in melt inclusions has low Fe concentration, (0.53 - 1.33 ± 1.2 wt% FeO, semi-quantitative SEM analyses, chapter IV) relative to the trachytic glass (9.73 - 13.56 wt% FeO) (Table 3) indicating that iron is more compatible in silicate glass than in carbonatite as experimentally observed by Veskler et al. (2012) ($D^{Fe}_{carb/sil}$= 0.04 in dry system, $D^{Fe}_{carb/sil}$= 0.34 with 11 wt% H_2O) and within natural melt inclusions by Guzmics et al. (2015) ($D^{Fe}_{carb/sil}$= 0.20-0.61, hydrous system). The partitioning of iron (FeO_t) between silicate and carbonate phase may imply, as observed for sulfur, a partitioning of Fe^{3+} and Fe^{2+} consequently influencing the redox state during immiscibility. However the very low concentration of iron in carbonate strongly suggest that immiscibility was not a dominant process affecting the redox state of the system

The large variations of $Fe^{3+}/\Sigma Fe$ (0.15 to 0.42) determined for the trachytic silicate glasses can result from post-entrapment processes including daughter sulfide crystallization or re-equilibration through H diffusion (Bucholz et al. 2013). One melt inclusions in nepheline, has sulfide daughter crystal (Figs.3 and 7b) with $Fe^{3+}/\Sigma Fe$ (0.23) within the range of sulfide-free MI suggesting that pyrrhotite has little effect on $Fe^{3+}/\Sigma Fe$.

Re-equilibration between host-mineral and MI may induced decrease of $Fe^{3+}/\Sigma Fe$ through H diffusion by proton-vacancy mechanism (Bucholz et al. 2013). In nephelinite lavas, MI glass has low H_2O content (< 0.1 wt% H_2O, chapter IV) and are entrapped in nepheline that contain very low water content (240 to 550 ppm wt H_2O, Baudouin et al. 2016) suggesting that hydrogen diffusion was not an effective process. However, in nepheline lattice, Fe^{3+} and Fe^{2+} ($Fe^{3+}/\Sigma Fe$ = 0.93 in Hanang nepheline) is assumed to be in Al site (e.g. McCloy et al. 2015) and the crystallographic lattice of nepheline and olivine may result in different diffusion mechanism and need to be experimentally constrained.

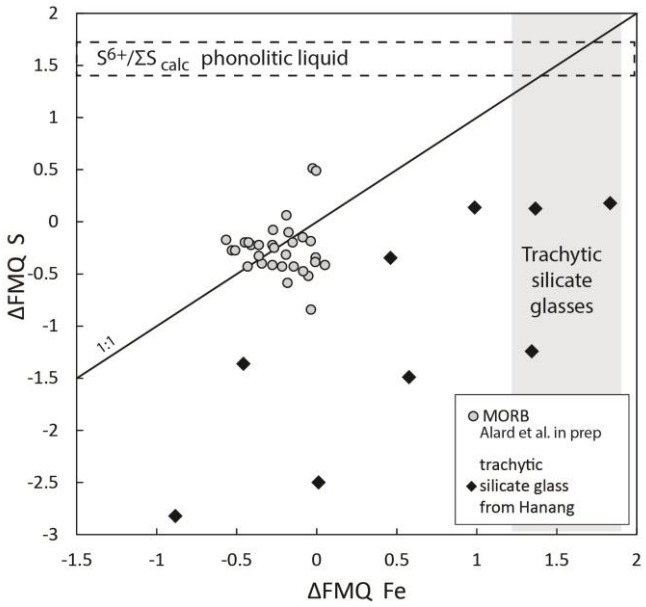

Fig.V.10 *fO_2 (ΔFMQ) deduced from $S^{6+}/\Sigma S$ vs fO_2 deduced from $Fe^{3+}/\Sigma Fe$ for MORB and silicate glasses. Grey box represents silicate glass with the higher fO_2 at ΔFMQ+1.3 to ΔFMQ+1.8 (trachytic glass) and dashed box represents fO_2 from $S^{6+}/\Sigma S_{calculated}$ (pre-immiscible phonolitic liquid = S^{6+} + S^{2-} from trachytic glass and carbonate) at ΔFMQ +1.65.*

The effect of post-entrapment processes (immiscibility process, hydrogen diffusion, post-entrapment re-equilibration) is then difficult to determine. However, all these processes would result in a decrease of $Fe^{3+}/\Sigma Fe$ in silicate glass and silicate glasses. The trachytic glass in melt inclusions with the higher $Fe^{3+}/\Sigma Fe$ may represent the silicate glass less modified by post-entrapment processes. The redox conditions of the interstitial phonolitic glass before entrapment is then close to ΔFMQ+1 to ΔFMQ+1.7. This is in agreement by the oxidation state estimated for phonolitic liquid (i.e. trachytic + carbonate phase) with $S^{6+}/\Sigma S_{calculated}$ at ΔFMQ +1.65 (Fig.V.10).

V.2. Redox state of early-stage rifting volcanism

The Manyara basin represents the early stage rifting of the East branch of EAR and comprises 2 main volcanic centers, Hanang and Kwaraha volcanoes surrounded by small volcanic cones with primitive magmas (i.e. melilite nephelinite) and more evolved lavas Mg-poor and Mg-rich melilite nephelinite. The redox conditions determined from XANES analyses of melt inclusions in Mg-poor nephelinite (i.e. Hanang lava) strongly suggest that the oxidation state was oxidized at ΔFMQ +1.65 during magmatic differentiation.

The redox conditions of more primitive lavas can be determined from the $Fe^{3+}/\Sigma Fe$ ratio of the whole-rock and phenocrysts in Mg-rich melilite nephelinitic lavas. Among phenocrysts present in alkaline magmas, cpx and garnet can contain both Fe^{2+} and Fe^{3+} (e.g. McCammon et al. 1998, Hao and Li 2013) while nepheline is assumed to be a Fe^{2+}-poor mineral (McCloy et al. 2015). The iron redox state of minerals is controlled by crystallographic lattice and $Fe^{3+}/\Sigma Fe$ of minerals only indicate a qualitative redox conditions.

For Mg-poor nephelinites, the high oxidized condition determined from melt inclusion study is corroborated by XANES and Mössbauer acquisition of Fe^{3+}-rich cpx ($Fe^{3+}/\Sigma Fe$ = 0.37-0.59), Fe^{3+}-rich garnet ($Fe^{3+}/\Sigma Fe$ = 0.90), and Fe^{3+}-rich nepheline ($Fe^{3+}/\Sigma Fe$ = 0.93)) (Table 4) and mineral assemblage stable at high oxidizing condition (>>FMQ) (Marks et al. 2008, Gustafson 1974). Although no correlation between $Fe^{3+}/\Sigma Fe$ of whole-rock and oxidation state has been calibrated, the high whole-rock $Fe^{3+}/\Sigma Fe$ of Mg-poor nephelinite argues for high oxidation state as observed for minerals and melt inclusions.
For melilite nephelinite, olivine-rich lava from Labait has very low $Fe^{3+}/\Sigma Fe$ (0.24, Table 2) whereas, cpx-rich lava from Kwaraha has intermediate $Fe^{3+}/\Sigma Fe$ ratio ($Fe^{3+}/\Sigma Fe$=0.51 for the whole-rock and 0.37-0.52 for cpx, Tables 2 and 4) suggesting more reduced conditions.

In carbonatite lava, the extremely high $Fe^{3+}/\Sigma Fe$ whole-rock (Table 2) strongly suggests very high oxidation state. The role of immiscibility process on fO_2 has been observed at small scale within melt inclusions composed by a silicate glass enriched in S^{2-} and Fe^{2+} and a carbonate phase enriched in S^{6+} and Fe^{3+}. At larger scale involving eruption of alkaline and carbonatite magmas as observed in Kwaraha lavas, the calciocarbonatite are most commonly considered as derived from a CO_2- rich melilite nephelinite through fractional crystallisation and immiscibility process (Dawson 1998, Keller et al. 2006, Harmer et al. 1998). Melilite nephelinite contains significantly less Fe^{3+} content ($Fe^{3+}/\Sigma Fe$ = 0.51) than calciocarbonatite ($Fe^{3+}/\Sigma Fe$ = 0.90) and confirm that as observed in S in MI, immiscibility process lead to very high Fe^{3+} content and consequently high fO_2 in carbonatitic liquid.

The magmatic differentiation of the Labait Mg-rich nephelinites to Hanang Mg-poor nephelinites involves fractional crystallization with carbonate-rich silicate liquid immiscibility and primary melt replenishment process (Baudouin et al. 2016). The increase of oxidation state from melilite nephelinite to nephelinite can be relative to immiscibility increasing the fO_2 during magma evolution. However, other additional process increasing of fO_2 have been proposed and may have participated to the change of redox conditions. Magma degassing involving mixed H-C-O-S-Cl fluid reactions may lead to high Fe^{3+} in the degassed melt controlling the oxidation state (Mathez 1984, Carmichael and Ghiorso 1986, Burgisser and Scaillet 2007, Bell and Simon 2011). Magmas from Manyara Basin are CO_2-rich and H_2O-poor and the presence of large amount of CO_2 degassing would influence the redox conditions. The presence of sulfur may lead to redox reactions involving sulfur and iron between silicate liquid and gas phase and change in oxidation state (Carmichael and Ghiorso 1986, Métrich et al. 2009, Moussallam et al. 2014) following the reactions:

$$SO_4^{2-}{}_{(melt)} + 2Fe^{2+}O_{(melt)} = SO_{2\,(gas)} + Fe_2^{3+}O_{3\,(melt)} + O^{2-}{}_{(melt)} \quad (3)$$

$$S^{2-}{}_{(melt)} + 3Fe_2^{3+}O_{3\,(melt)} = SO_{2\,(gas)} + 6Fe^{2+}O_{(melt)} + O^{2-}{}_{(melt)} \quad (4)$$

In Mg-poor nephelinite, the high sulfur content and the presence of both S^{6+} and S^{2-} ($S^{6+}/\Sigma S$ = 0.56) suggest that both reducing and oxidizing reaction may have occurred, limiting the effect of sulfur degassing on the redox conditions. Therefore, immiscibility and CO_2 degassing are the dominant processes increasing the oxidation state during magmas differentiation and ascent.

Conclusions

Manyara lavas have the more oxidizing conditions of the East branch of EAR (deMoor et al. 2013, Scaillet and Macdonald 2006, Ren et al. 2006, Zaitsev et al. 2012), with increasing oxidation state during differentiation through immiscibility and degassing processes until a fO_2 around ΔFMQ +1.65 in phonolitic liquid. West branch of EAR have potassic nephelinites in the Toro-Ankole volcanic field (Uganda, <50 ka) with similar fO_2 at ΔFMQ +1.5 (Murav'eva and Senin 2009). Although, West branch lavas are potassic suggesting slightly different mantle source (chapter III), lavas from Manyara (East branch) and Toro-Ankole (West branch) represent early stage rifting CO_2-rich volcanism in relatively oxidizing conditions.

Supplementary material

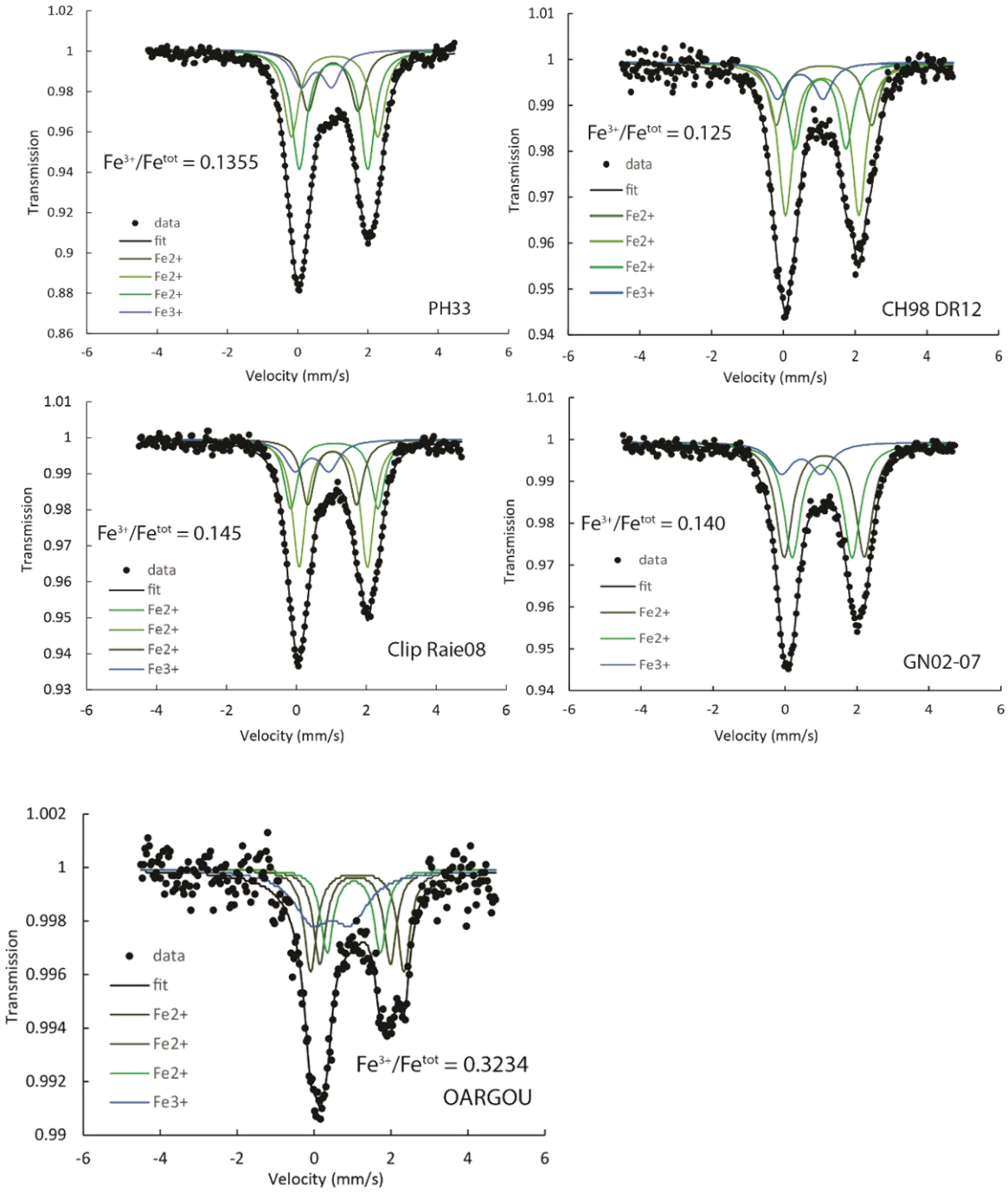

Fig.V. A1 Mossbauer spectra of the reference samples

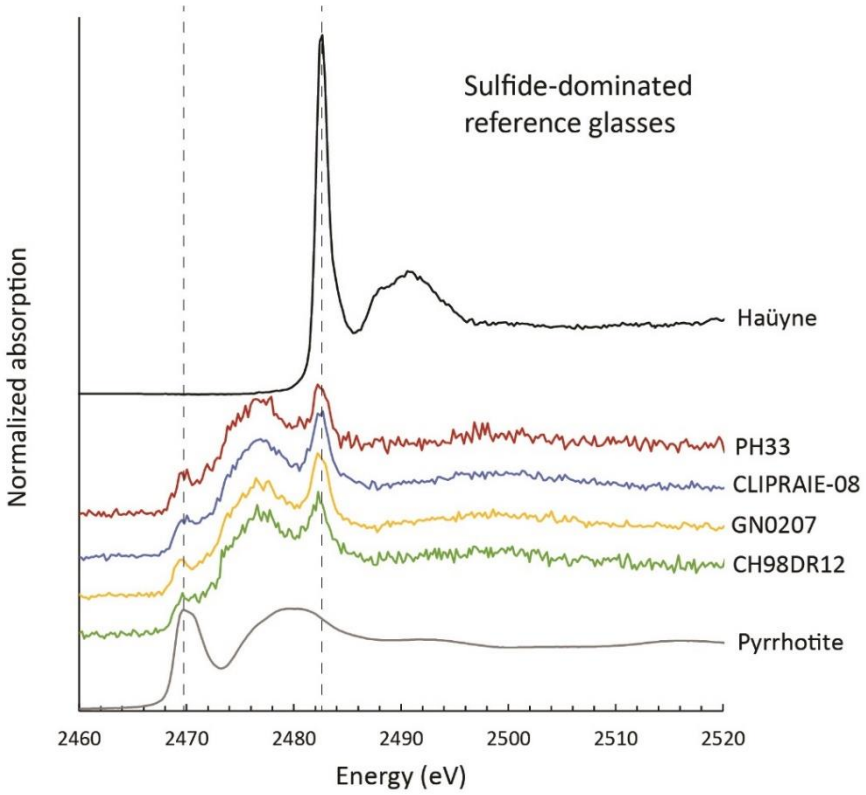

Fig.V.A2 XANES spectra of sulfide-dominated reference samples (MORB) and reference material (Haüyne and pyrrhotite)

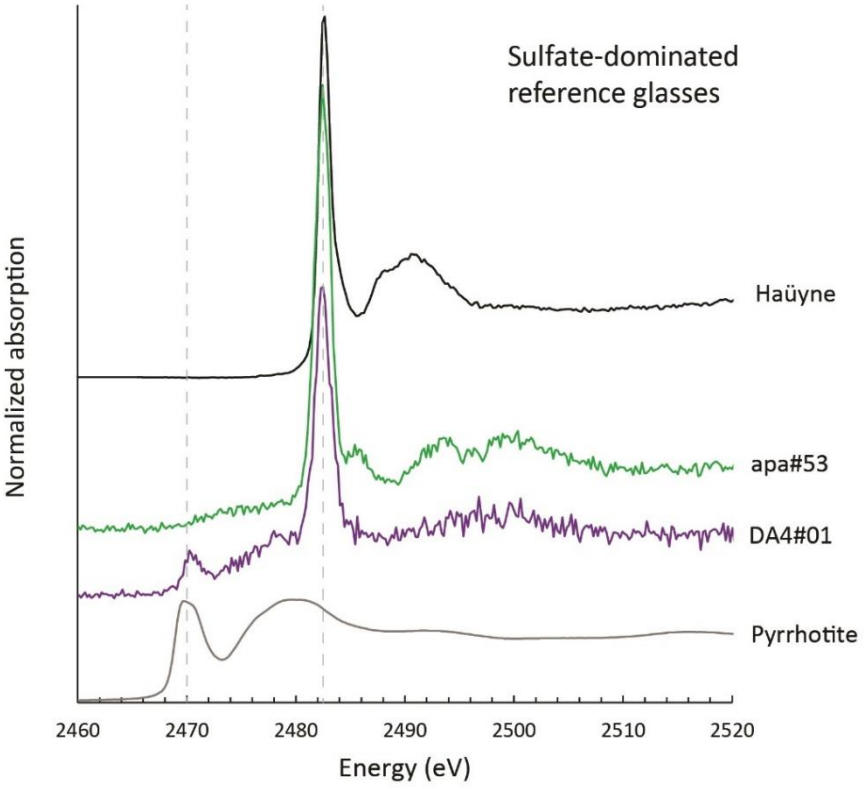

Fig.V.A3 XANES spectra of sulfate-dominated reference samples (apa#53 and Da4#01) and reference material (Haüyne and pyrrhotite).

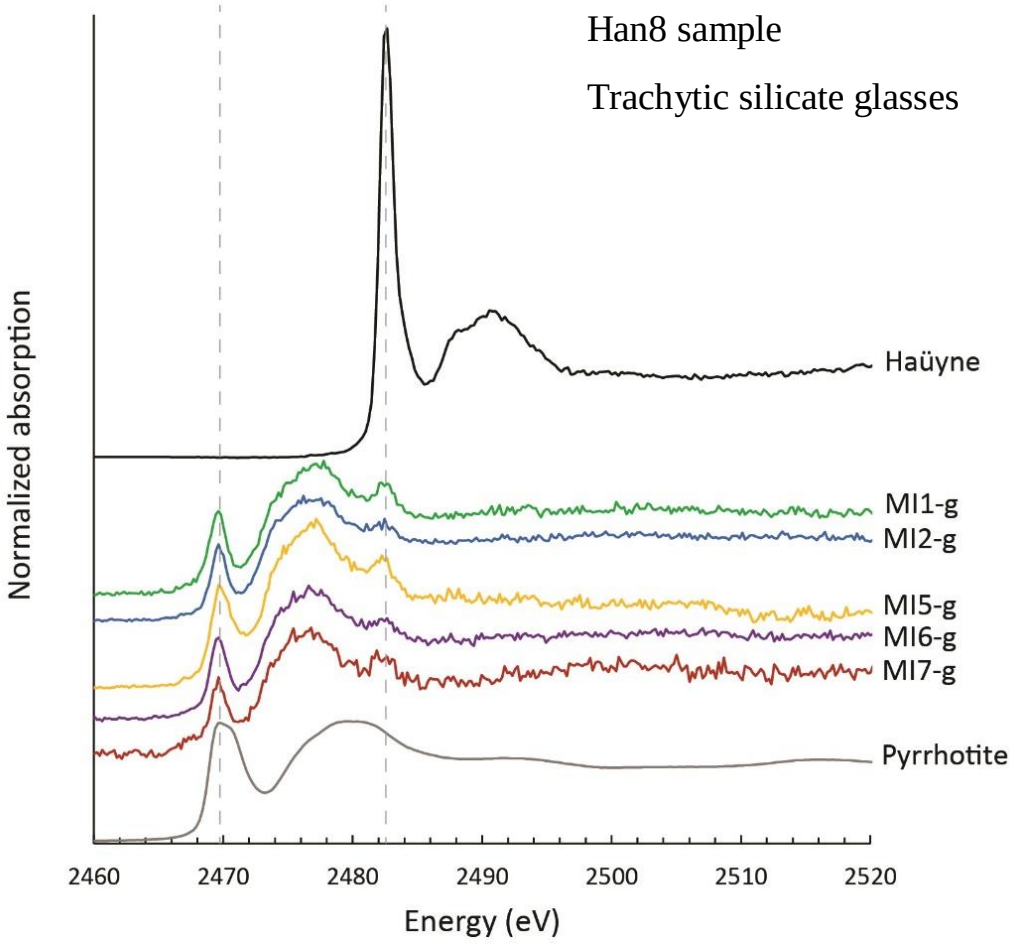

Fig.V.A4 XANES spectra of trachytic silicate glasses (from melt inclusions) from Hanang (Han8) and reference material (Haüyne and pyrrhotite)

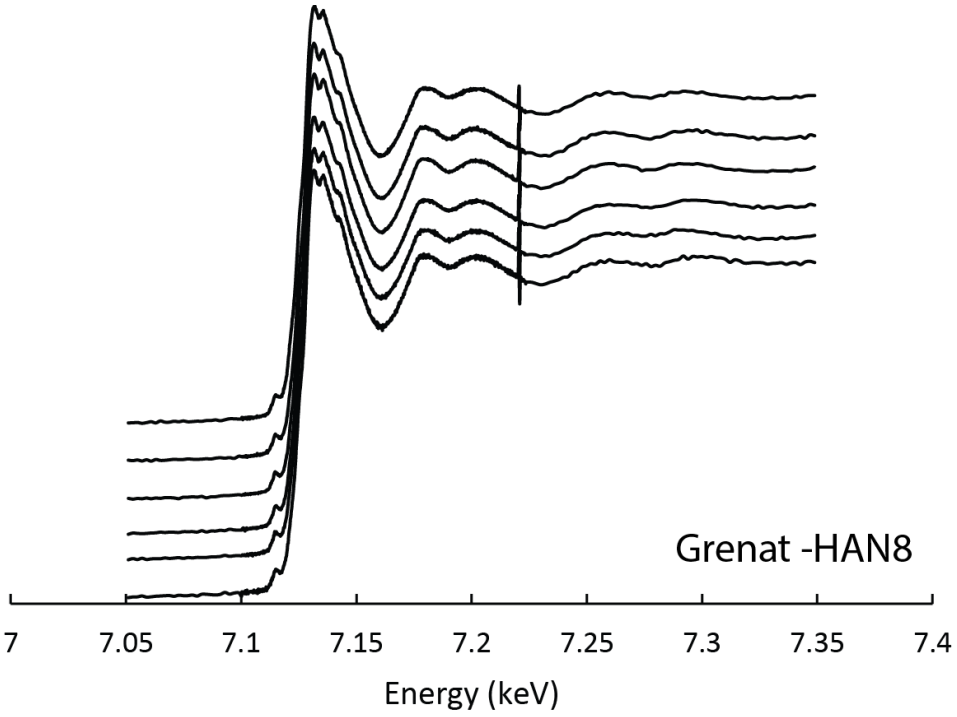

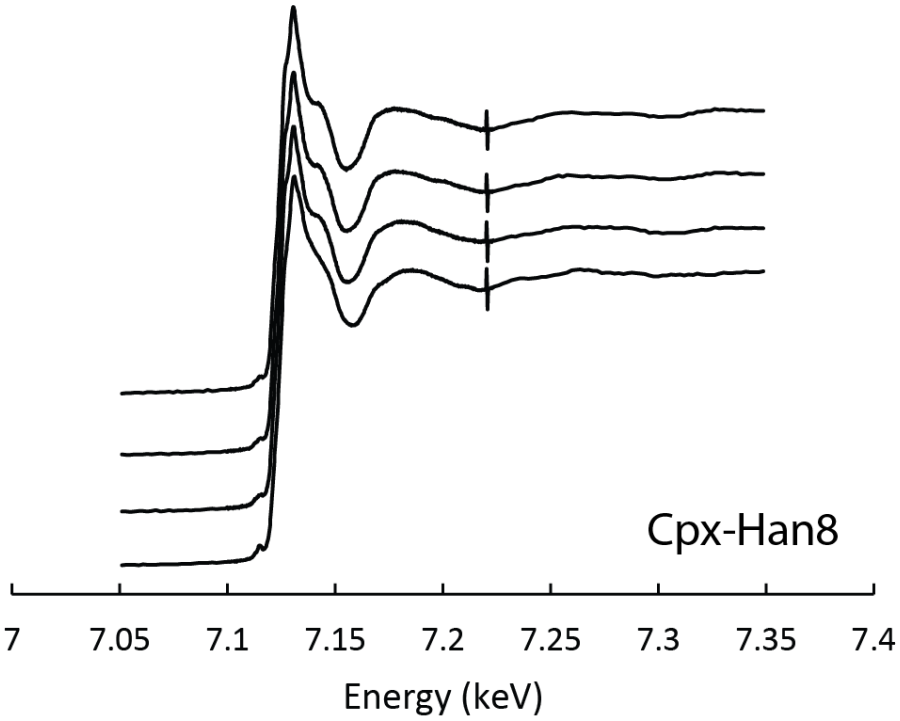

XANES spectra of garnet and cpx (iron K-edge)

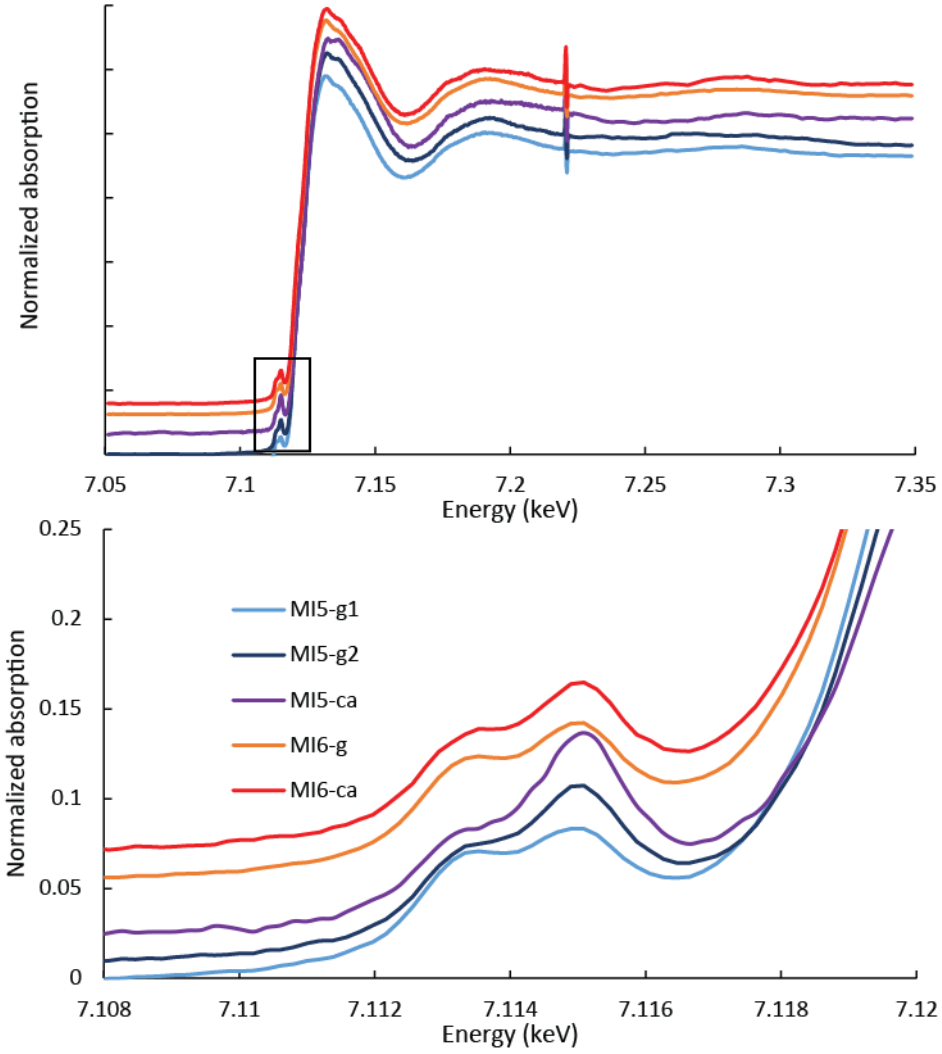

XANES spectra of silicate glasses from melt inclusions (iron K-edge)- Han8 sample

Chapitre VI. La divergence nord tanzanienne

Le rifting et le volcanisme dans le Rift Est Africain sont liés à la présence d'un point chaud qui aurait une origine profonde associé au superpanache de l'Afrique du Sud (Ebinger et Sleep 1998, Nyblabe et al. 2000, Pik et al. 2006). La divergence nord-tanzanienne (DNT) est la zone d'initiation de la rupture continentale du rift est-africain (REA). Elle est constituée de 2 axes volcano-tectoniques: l'axe est-ouest composé de laves alcalines et l'axe nord-sud, de laves hyperalcalines. L'axe E-O a été échantillonné pour 4 volcans, afin de comparer les laves de la DNT par types, âges et localisation géographique. Ces laves seront présentées succinctement avant d'être comparées à celles de l'axe N-S, et de faire une synthèse de la mise en place du volcanisme associé à l'initiation de la rupture continentale au sein de la DNT. Afin d'avoir une meilleure compréhension de l'initiation de la rupture continentale, il est important de lier le volcanisme aux contraintes structurales (e.g. données tectoniques et géophysiques). La relation temporelle entre les activités tectoniques et magmatiques est un enjeu majeur pour comprendre le fonctionnement de la rupture continentale (e.g. Huisman et al. 2001).

La divergence nord tanzanienne (DNT) est constituée de 2 axes volcano-tectoniques : l'axe E-O et l'axe N-S (Fig.VI.1). Les volcans Hanang, Labait et Kwaraha (chapitre III, IV, V) se situent dans la partie méridionale de l'axe N-S. Les volcans de l'axe E-O qui ont été étudiés sont Monduli (est), Burko (centre), Essimingor (centre), et Ngorongoro (ouest), (Fig.VI.1).

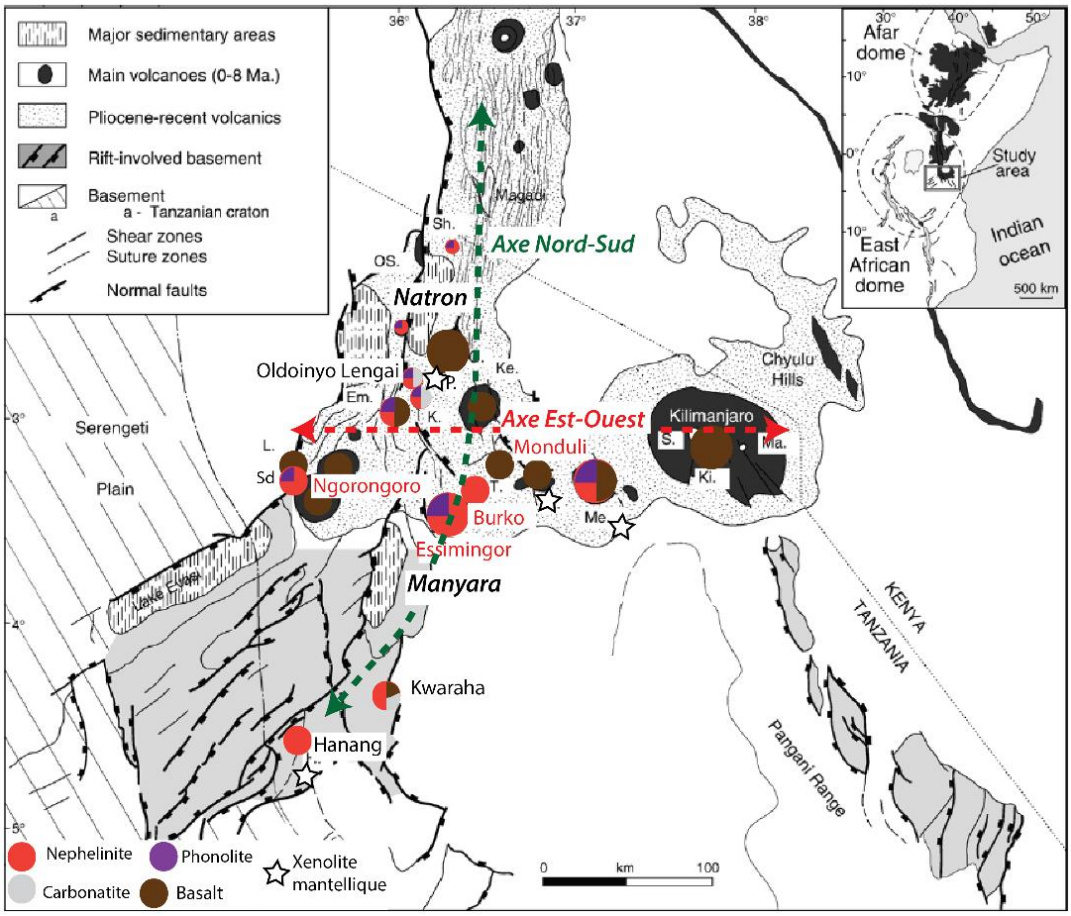

Fig.VI.1 *: Schéma structural de la DNT (Modifié d'après Le Gall et al. 2008). Les différents types de laves émises à la surface sont indiqués (néphélinites, phonolites, carbonatites et basaltes). Les volcans étudiés se situent sur l'axe N-S dans le bassin de Manyara (Kwaraha, Hanang), et le bassin de Natron (annexe C) et sur l'axe E-O (Monduli, Burko, Essimingor, et Ngorongoro). Em. Empakai, K. Kerimasi, Ke. Ketumbeine, Ki. Kibo, L. Lemagrut, Ma. Mawenzi, Me. Meru, OS. OlDonyo Sambu, S. Shira, Sh. Shombole.*

VI.I Volcanisme de l'axe nord-sud

Le bassin de Manyara est composé de plusieurs types de laves hyperalcalines comprenant les néphélinites à melilite (Mg# > 55) (Labait, Kwaraha), les néphélinites différenciées (Mg# < 35) (Hanang) et une calciocarbonatite (Kwaraha).

Les néphélinites à mélilite des volcans Kwaraha et Labait proviennent des cônes volcaniques adjacents à l'édifice principal. Ces néphélinites sont des laves primaires, avec des Mg# > 55 et des concentrations en silice < 40 % SiO_2 (chapitre III), qui sont issues d'un faible taux de fusion partielle d'une source profonde (≥ 120 km) riche en CO_2 et pauvre en H_2O. Les

néphélinites de Hanang (Mg# < 35) sont issues des néphélinites à mélilite proche de celle du Labait par cristallisation fractionnée (chapitre IV). La genèse de ces laves est complexe puisque le magma initialement riche en CO_2 en profondeur devient saturé en carbonate et forme 2 liquides (processus d'immiscibilité) qui résulte en un liquide néphélinitique enrichi en carbonate et un second liquide silicaté enrichi en H_2O (lave non émise à la surface) (Baudouin et al. 2016). Les néphélinites enrichies en carbonate d'Hanang évoluent vers des compositions phonolitiques riches en CO_2 par cristallisation fractionnée dans des conditions oxydées à relativement faible profondeur à environ 20 km (700 MPa).

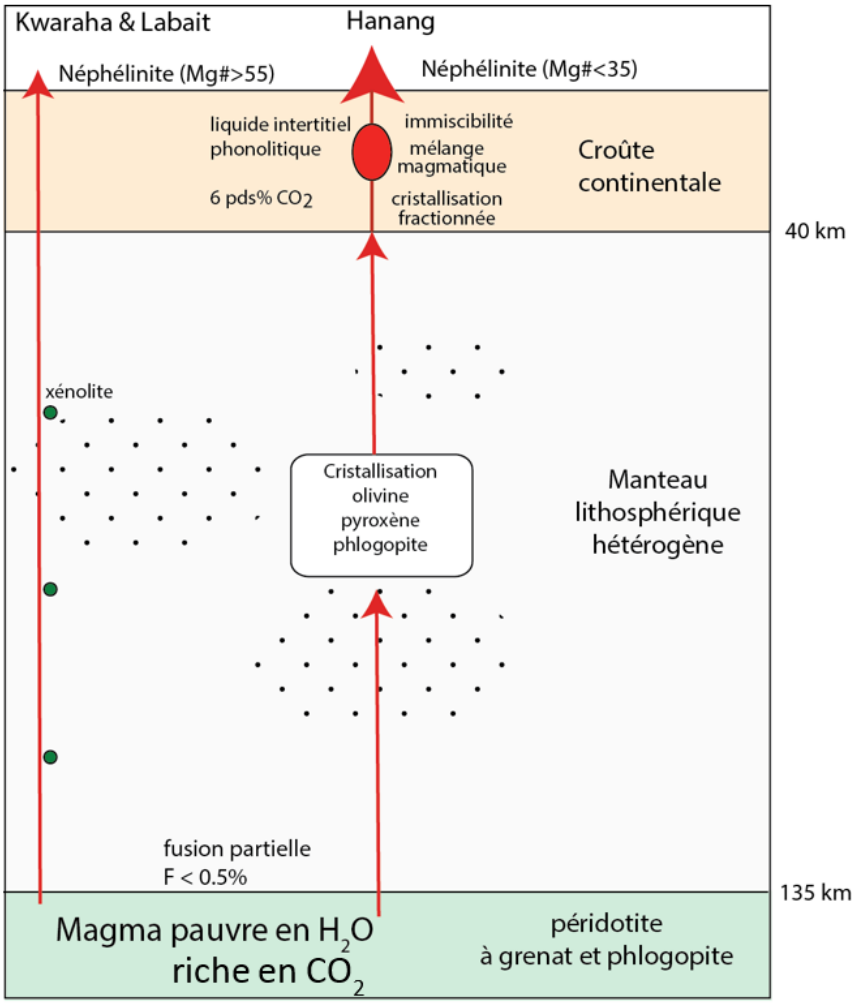

Fig.VI.2 *Associations néphélinites-mélilitites-carbonatites en Tanzanie (modifiée d'après Dawson 2012). Le manteau lithosphérique tanzanien a été caractérisé par l'étude de xénolites (e.g. Koornneef el al. 2009, Dawson et Smith 1988, Gibson et al. 2013).*

Les carbonatites, associées aux laves alcalines, sont omniprésentes sur l'axe NS : Oldoinyo Lengai, Kerimasi, Shombole (Keller and Krafft 1990, Dawson 2008, Guzmics et al. 2011). L'absence des carbonatites associées aux laves du Hanang et de Sadiman (10 km à l'ouest du Ngorongoro) peut être liée à une différenciation magmatique qui se produit en système ouvert, avec des mélanges magmatiques entre magma différencié et magma primaire (i.e. remplissage de chambre magmatique) empêchant le magma d'atteindre la saturation en

carbonate et la formation de lave carbonatitique (chapitre IV, Zaitsev et al. 2012). Les associations néphélinites-mélilitites-carbonatites observées dans le bassin de Manyara sont proches de celles du bassin de Natron (Engaruka, Oldoinyo Lengai). Dawson (1998) et Klaudius et Keller (2006) ont montré que les mélilitites et les néphélinites mafiques sont à l'origine des néphélinites différenciées et des carbonatites via des processus de cristallisation fractionnée et d'immiscibilité (Dawson 1998, Klaudius et Keller 2006) (Fig.VI.2). Le bassin de Natron est caractérisé par l'abondance de lave carbonatitique (i.e. Oldoinyo Lengai, Kerimasi) ce qui suggère une différenciation en système fermé.

VI.II Volcanisme de l'axe est-ouest

L'axe E-O est formé par un volcanisme alcalin à subalcalin comprenant des trachy-basaltes, téphrites, et des néphélinites (Fig.VI.3). Parmi les volcans échantillonnés, le Monduli est le plus à l'est de la DNT et est composé de téphrite (MON1) et de trachy-basaltes (Mana et al. 2015). Les volcans Burko et Essimingor se situent à l'intersection des axes E-O et N-S (Fig.VI.1). Le volcan Burko est composé de néphélinites alcalines (BUR1), et le volcan Essimingor est composé de néphélinites (Ess4) et de laves plus différenciées, i.e basanite (Ess2), phonotéphrite (Ess1) et phonolites (Mana et al. 2012). Le Ngorongoro, situé le plus à l'ouest de la DNT, est formé de trachy-basaltes, picro-basaltes (NGO1 et NGO2) et de trachyte (Nonnotte 2007, Mollel et al. 2008).

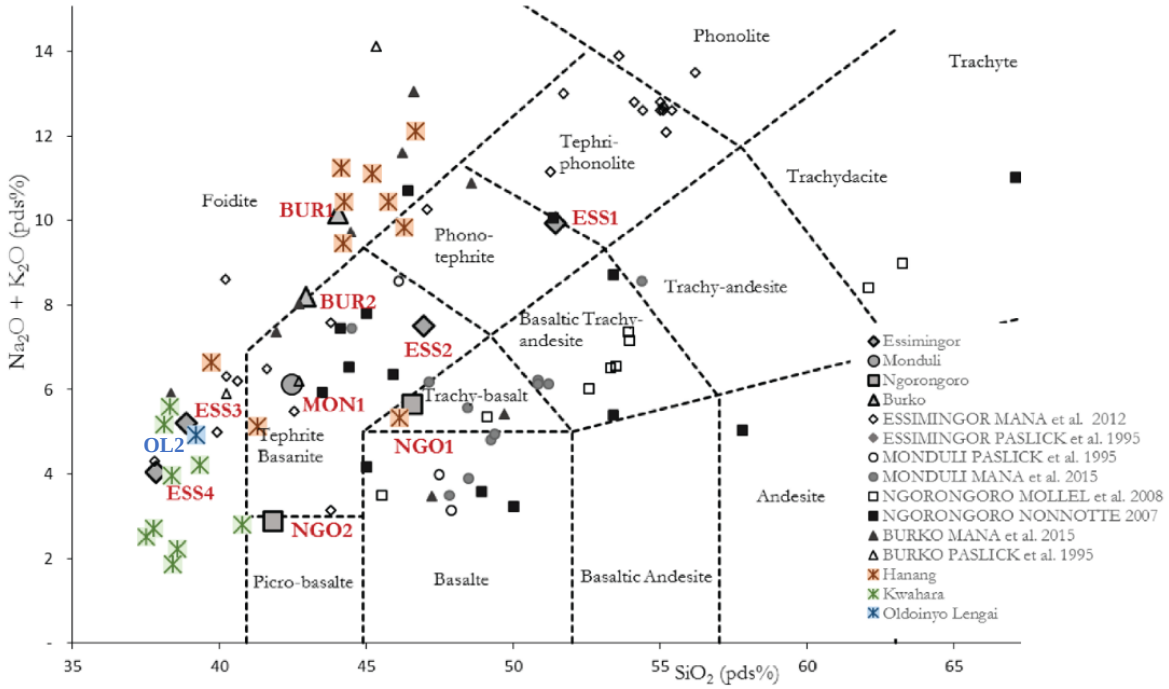

Fig.VI.3 : *TAS avec les laves du bassin de Manyara et les laves de l'axe E-O (Monduli, Burko, Essimingor, et Ngorongoro).*

Les concentrations en éléments incompatibles des laves du Ngorongoro, Essimingor et Monduli sont assez similaires, présentant les mêmes anomalies négatives par rapport au manteau primitif (e.g. K, Zr, Hf) (Fig.VI.4). Les spectres de terres rares ont des variations entre 1000 fois les chondrites pour les laves de Burko et 20 fois les chondrites pour les laves du Ngorongoro avec un rapport La/Yb allant de 71 (Burko) à 32 (Essimingor, Ess3) (Fig.VI.4). Les néphélinites du volcan Burko se dégagent des autres laves par leurs fortes teneurs en éléments incompatibles tels que Th, U, Nb, Zr et les LREE (Fig.VI.4).

Les laves de l'axe E-O ont les mêmes compositions que celles étudiées par Nonnotte (2007) et Mana et al. (2015). L'annexe C est composée d'une description détaillée de l'assemblage minéralogique, de la chimie des minéraux et des tables de données des éléments majeurs et en trace (roches totales et minéraux).

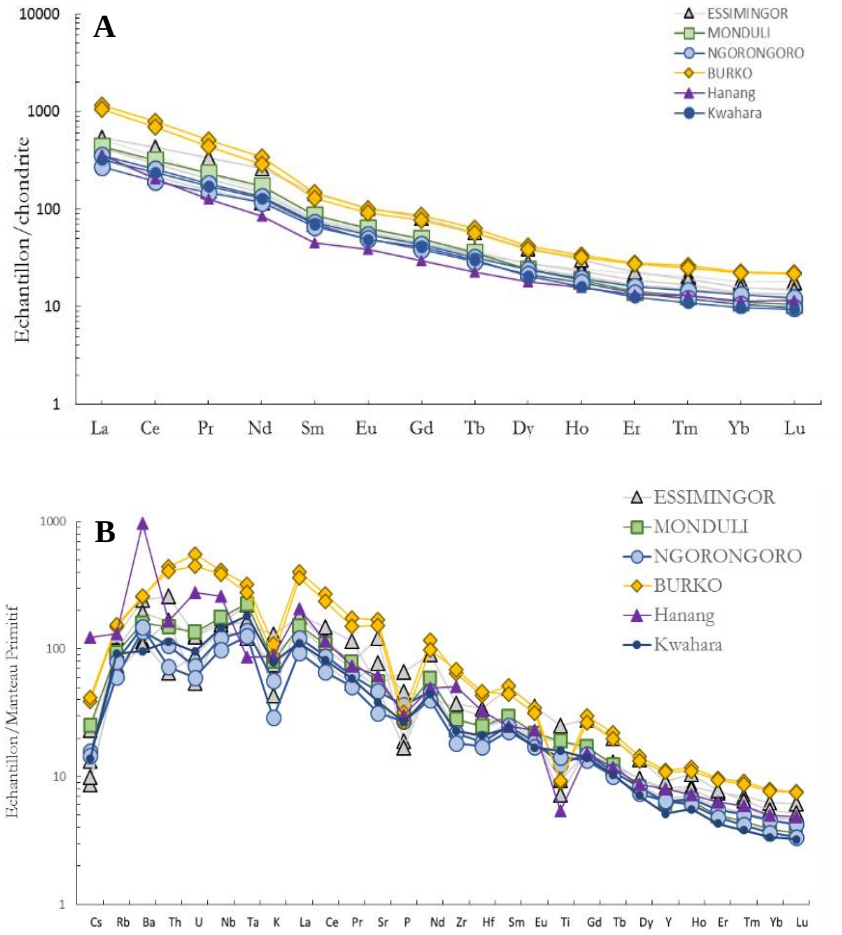

Fig. VI.4 : ***A*** *Spectres des REE,* ***B*** *Spectres élargis pour les laves de la DNT (axe E-O) ainsi que de Kwaraha et de Hanang.*

VI.III Synthèse du volcanisme de la DNT

Le volcanisme de la DNT est composé de laves hyperalcalines dans l'axe N-S, et de laves alcalines à subalcalines dans l'axe E-O (Fig.VI.5).

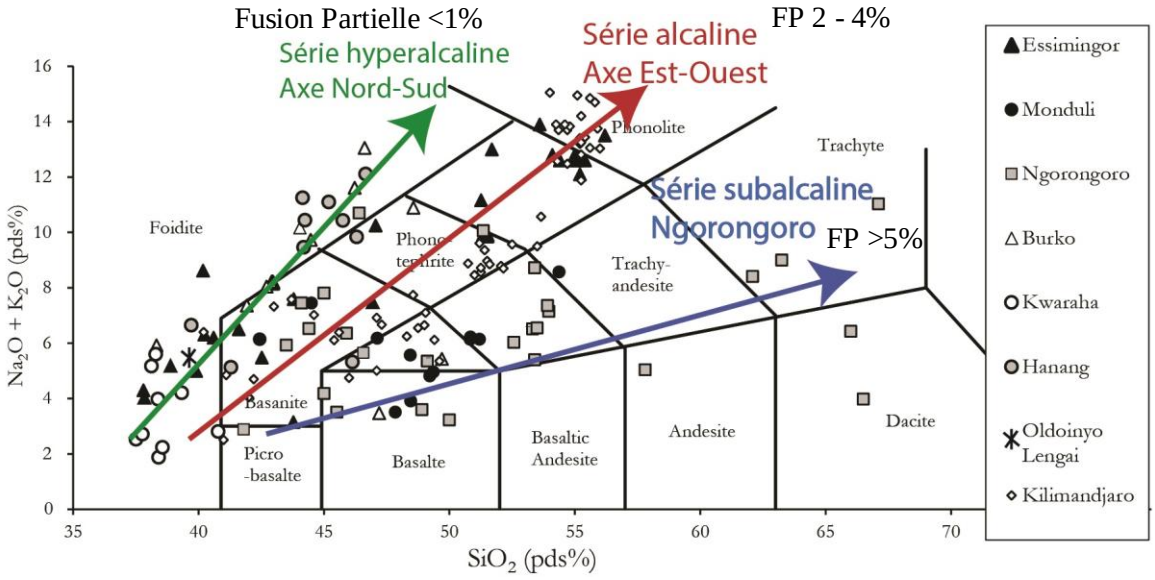

Fig.VI.5 Composition en alcalin versus silice **(***TAS) des laves de la divergence nord-tanzanienne (Le Bas 1989).*

Les laves hyperalcalines de l'axe N-S représentent un volcanisme récent (< 1,5 Ma) avec les plus faibles taux de fusion partielle de la DNT (≤ 1 %, Chapitre III) (Fig.VI.6). Les cpx des laves de Manyara (zone méridionale de l'axe N-S) ont cristallisés à haute température 1290 – 1170 °C et à des profondeurs variant de 6 à 33 km (200 – 1100 MPa) pour les laves primitives (Kwaraha) et 1050 – 1100 °C et 12 – 19 km (400 – 600 MPa) pour les laves différentiées (Hanang) (Fig.VI.7).

À l'intersection des 2 axes, le volcanisme est alcalin (Essimingor) à affinité hyperalcaline (Burko) (Fig.VI.5). Comme pour l'axe N-S, les laves sont issues d'un taux de fusion relativement faible ~ 2 – 3 % (Mana et al. 2012). Les laves d'Essimingor et de Burko sont plus anciennes que celles de l'axe N-S et ont été émises entre 6 et 1 Ma (Fig.VI.6). Les conditions de cristallisation des laves différenciées (i.e. phonotéphrite) sont identiques à celles du Hanang (Fig. VI.7) suggérant une évolution magmatique dans des conditions très proches des laves du Burko, d'Essimingor et du bassin de Manyara.

Le volcanisme le plus éloigné de l'intersection des 2 axes est alcalin à subalcalin, au Ngorongoro à l'ouest (4 – 2 Ma) et au Monduli à l'est (2,5 – 2 Ma) (Fig.VI.5 et VI.6). Le volcanisme subalcalin est lié aux taux de fusion les plus élevés de la DNT, à environ 6 % (Mana et al. 2015). Les cpx ont cristallisés à haute température (1200 – 1250 °C) et haute pression (800 – 1100 MPa) (Fig.VI .7), ce qui peut suggérer la présence d'une zone de stockage de magma assez profonde (24 – 33 km). La zone de stockage profonde du Ngorongoro à environ

30 –33 km, peut indiquer que l'emplacement excentré du volcan ainsi que sa proximité avec le craton ne favorisent pas la mise en place de la zone de stockage dans la croûte moyenne (15 km).

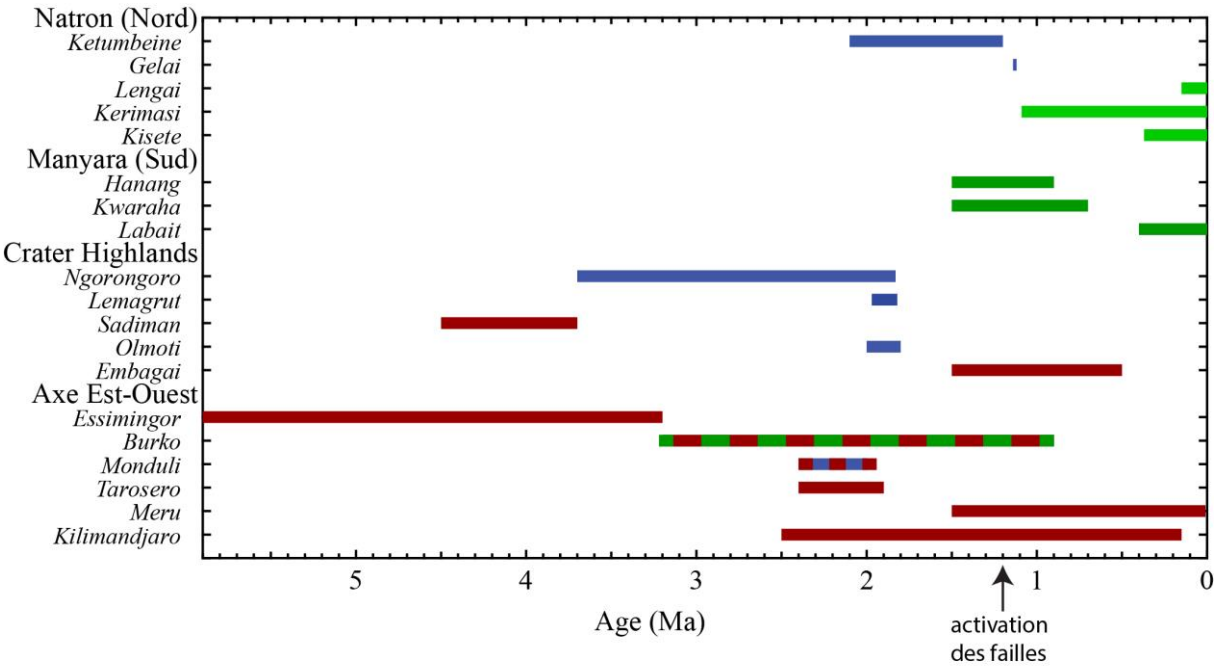

Fig.VI.6 *Datation des laves de la DNT (Mana et al. 2015 ; Bagdasaryan et al. 1973 ; Macintyre 1974 ; Manega 1993 ; Gromme et al. 1970 ; Hay 1976 ; Drake et Curtis 1987 ; Mollel 2009, Mana et al. 2012 Wilkinson et al. 1986 ; Nonnotte 2007 ; Rudnick et al. 1999). Les différentes séries magmatiques sont représentées : alcaline (trait rouge), sub-alcaline (trait bleu) et hyperalcaline (trait vert).*

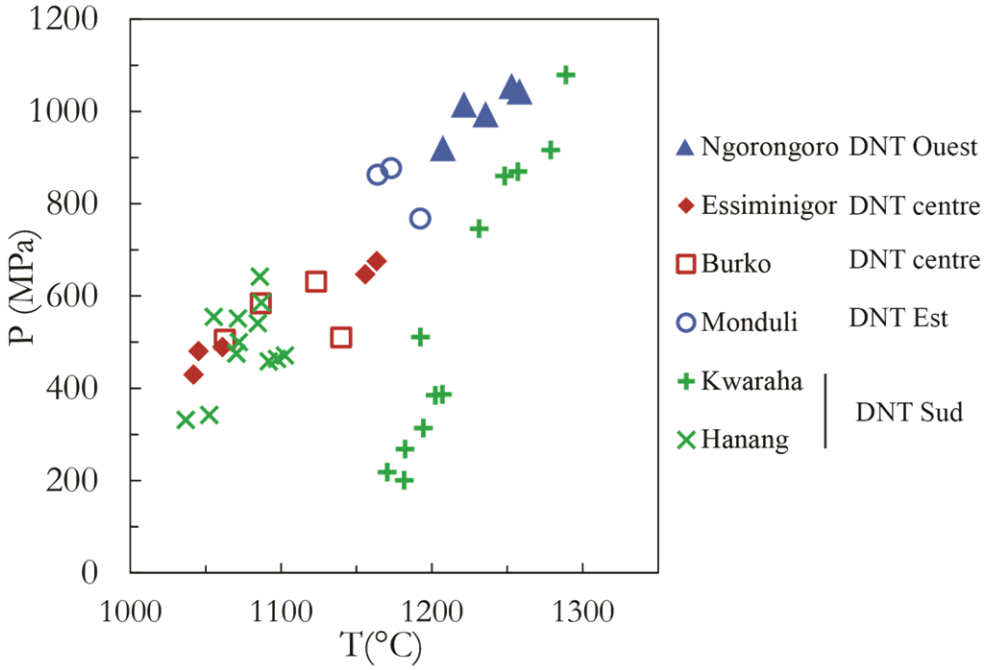

Fig.VI.7 *Conditions pression-température (*P-T*) de cristallisation des clinopyroxènes des laves de la DNT (Putirka 2008). Les différentes séries magmatiques sont représentées : alcaline (symboles rouges), sub-alcaline (symboles bleus) et hyperalcaline (symboles verts).*

On observe une variation spacio-temporelle des séries magmatiques avec tout d'abord l'éruption de laves alcalines (Essimingor, 6 – 3 Ma), puis subalcalines dans l'axe E-O (i.e. Ngorongoro, 4 – 2 Ma) et enfin des laves alcalines dans l'axe E-O (< 2 Ma) et hyperalcalines dans l'axe N-S (≤ 1,5 Ma) (Fig.VI.5 et 6). L'épisode majeur de tectonique active de la DNT s'est produit il y 1,2 Ma et entre 1,4 et 1 Ma pour l'escarpement de Manyara, suggérant que dans la DNT, le magmatisme précède l'activation des failles (Fig.VI.6) (Le Gall et al. 2008). La présence de magma en profondeur a pu ainsi conduire à l'affaiblissement thermique de la croûte inférieure et permettre la localisation de la déformation (Albaric et al. 2010, 2014). Après l'éruption des laves du volcan Essimingor à 3 Ma, le rift s'est propagé dans l'axe E-O alors que la propagation du REA se produit du nord vers le sud dans la branche E (Ebinger et al. 1997, Chorowicz 2005). La présence de bloc plus rigide dans l'axe N-S (i.e. craton tanzanien, bloc Masai) et/ou la présence de zone de faible résistance dans l'axe E-O (i.e. zone de cisaillement, écaille de l'orogène panafricain) a eu un rôle prépondérant dans la propagation du rift de la DNT (Le Gall et al. 2008). La propagation du rift dans la DNT est contrôlée par le magmatisme et par l'héritage structural.

Les variations chimiques des laves alcalines à subalcalines dans l'axe E-O peuvent être liées à des degrés variables de fertilisation de la lithosphère par le panache ou par une lithosphère hétérogène affétées par d'anciens épisodes métasomatiques, induisant des taux variables de fusion partielle (Mana et al. 2015). Le prolongement récent du volcanisme vers l'est (Meru-Kilimandjaro, < 2 Ma) est lié à l'héritage structural (zone de cisaillement d'Assoua) et du métasomatisme induit par la percolation des magmas pendant le plio-quaternaire (Nonnotte 2007). La propagation du rift dans l'axe N-S (< 1,5 Ma) est probablement induite par le changement de contrainte tectonique guidé par des structures héritées (Le Gall et al. 2008). Le volcanisme hyperalcalin lié à de faible taux de fusion dans le bassin de Manyara pourrait donc être guidée par des structures crustales et/ou lithosphériques.

VI.IV Lien entre le volcanisme et les structures lithosphériques

Le projet CoLiBrEA (AnR) est pluridisciplinaire (géochimie, géophysique, tectonique) et a pour but d'identifier les interactions entre le magmatisme, les structures héritées et la sismicité actuelle afin de mieux comprendre les processus à l'origine de la rupture continentale. Néanmoins, il est nécessaire de prendre en compte que les modèles géophysiques représentent la lithosphère actuelle, alors que les laves ont été émises à partir de 6 Ma (Fig.VI.6). Les stations sismiques et les 2 profils magnétotelluriques sont localisés sur la Fig.VI.8. Les méthodes géophysiques, telles que les méthodes sismiques (tomographie, fonctions récepteurs) et magnétotelluriques, permettent d'imager les structures crustales et mantelliques, et de mettre en évidence les variations brutales de température et/ou de composition à partir de l'analyse des vitesses des ondes sismiques et de la résistivité du milieu. Par exemple, un fort rapport Vp/Vs est souvent interprété comme la présence de magmas/fluides dans les régions soumises à l'extension (Daly et al. 2008; Stuart et al. 2006). La résistivité ($\rho = \Omega/m$) et donc la conductivité électrique (σ, grandeur inverse de la résistivité) de la croûte et du manteau peut varier en fonction de la présence de magma, de la circulation de fluide (H_2O et CO_2) et de structures tectoniques en profondeur (failles) (e.g. Hautot et Tarits 2000, Gaillard 2004).

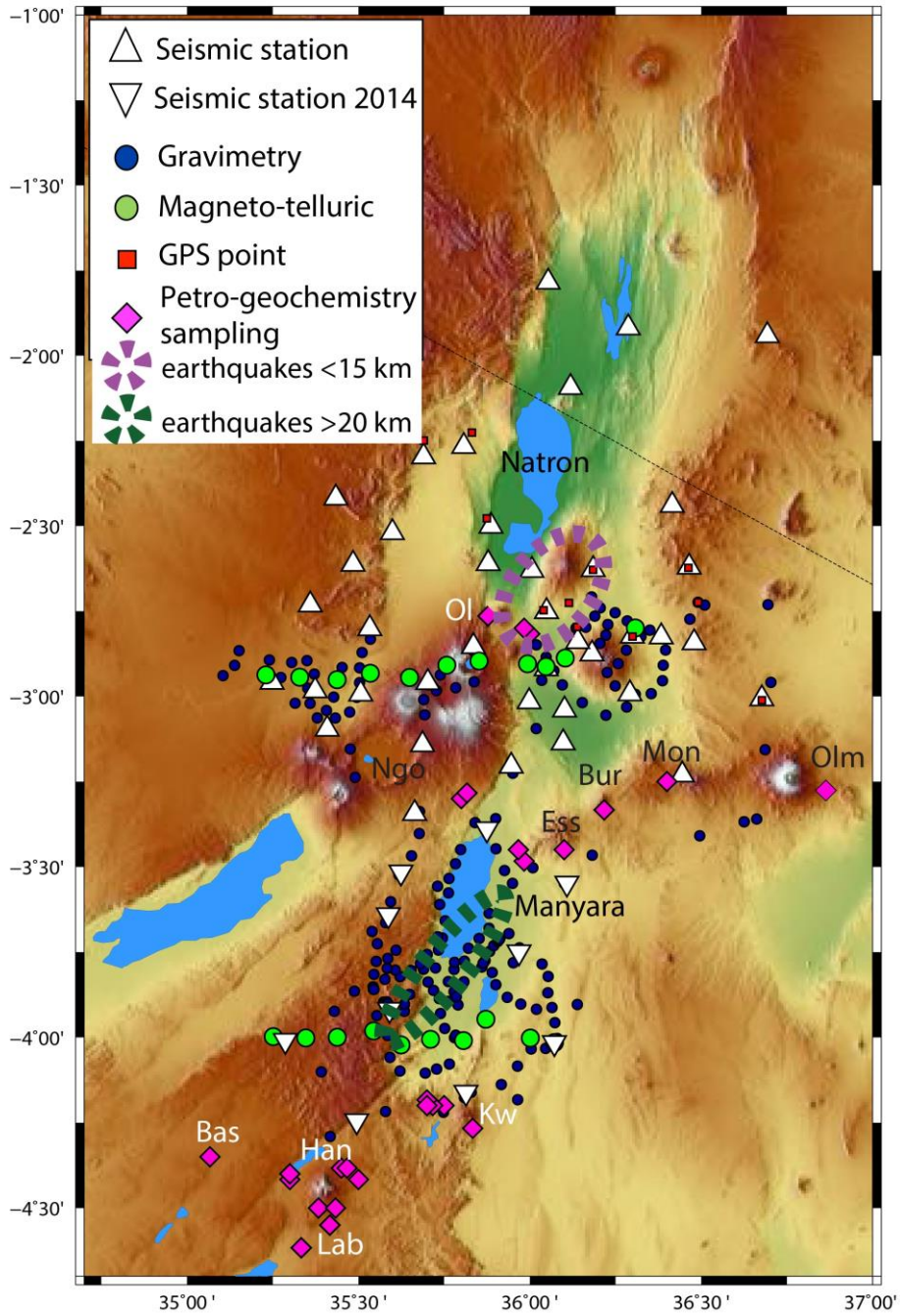

Fig.VI.8 *Carte du nord de la Tanzanie avec la localisation des stations sismiques, magnétotelluriques, GPS et gravimétriques de l'AnR CoLiBrEA et des stations sismiques NSF CRAFTI. Les échantillons de laves sont symbolisés par des losanges roses. Volcans de l'axe* N-S *: Ol Oldoinyo Lengai, Kw Kwaraha, Han Hanang, Lab Labait, Bas Basotu. Volcans de l'axe E-O : Ngo Ngorongoro, Ess Essimingor, Bur Burko, Mon Monduli, Olm Olmani. Localisation des 2 essaims sismiques d'après Albaric et al. (2010).*

Dans la DNT, l'interface du Moho se situe entre 33 et 41 km suggérant que l'amincissement crustal dans cette zone est extrêmement faible alors que l'expression du rift en surface est bien marquée (faisceau de failles normales, Fig.VI.1). Les profondeurs les plus élevées (> 37 km) au sud-ouest correspondent à la bordure du craton tanzanien. Plusieurs structures crustales ont pu être remarquées sur les modèles géophysiques. Par exemple, sous le

volcan Oldoinyo Lengai (profil magnétotellurique Nord, Fig .VI.8), il y a une zone conductrice de 10 km d'épaisseur (~ 150 Ω/m) associée à l'essaim sismique (<15 km) (Fig .VI.8), potentiellement liée à la propagation d'un dyke en profondeur (Calais et al. 2008).

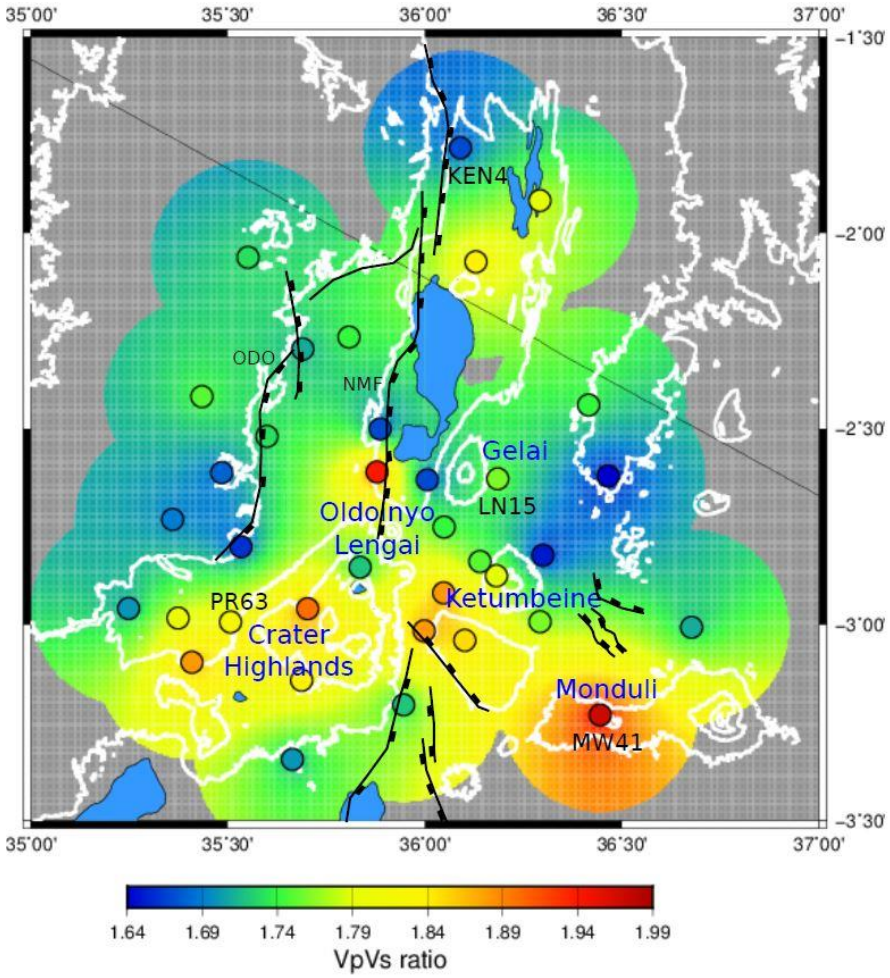

Fig.VI.9 *Modèle crustal des rapports Vp/Vs. Les cercles représentent les stations sismiques du réseau CRAFTI- CoLiBrEA, les lignes blanches sont les contours topographiques (Plasman et al. en préparation).*

Dans l'axe E-O (Ngorongoro-Monduli), les rapports Vp/Vs sont très élevés (> 1,8) (Fig.VI.9). Ces rapports Vp/Vs élevés (intégration sur toute la croûte) sont corrélés avec la présence des édifices volcaniques ce qui suggère la présence de magmas dans la croûte. Les fonctions récepteurs indiquent la présence d'une interface à ~ 15 km avec une zone de vitesse plus lente dans la croute inférieure (Vp = 6.5 km·s^{-1}) (Fig.VI.10), suggérant la présence d'un matériel anormalement chaud entre 15 et 30 km. Ces anomalies de vitesses négatives peuvent correspondre à des zones plus chaudes et sont interprétées comme des zones de stockage de magma dans la croute inférieure (e.g. Daly et al. 2008). Sous le volcan Ngorongoro, une zone d'anomalie de vitesse négative (- 8 % pour Vp) est présente vers 30 – 40 km sur les profils de fonctions récepteurs ainsi qu'en tomographie, ce qui correspond à la profondeur estimée de cristallisation des clinopyroxènes (Fig.VI.6). Cette zone pourrait correspondre à une zone de stockage de magma, et aux vues des données géophysiques, elle serait volumineuse et assez

profonde (> 30 km). Le volcanisme de la zone du Ngorongoro pourrait être associé à de forts taux de fusion avec du magma bloqué à grande profondeur.

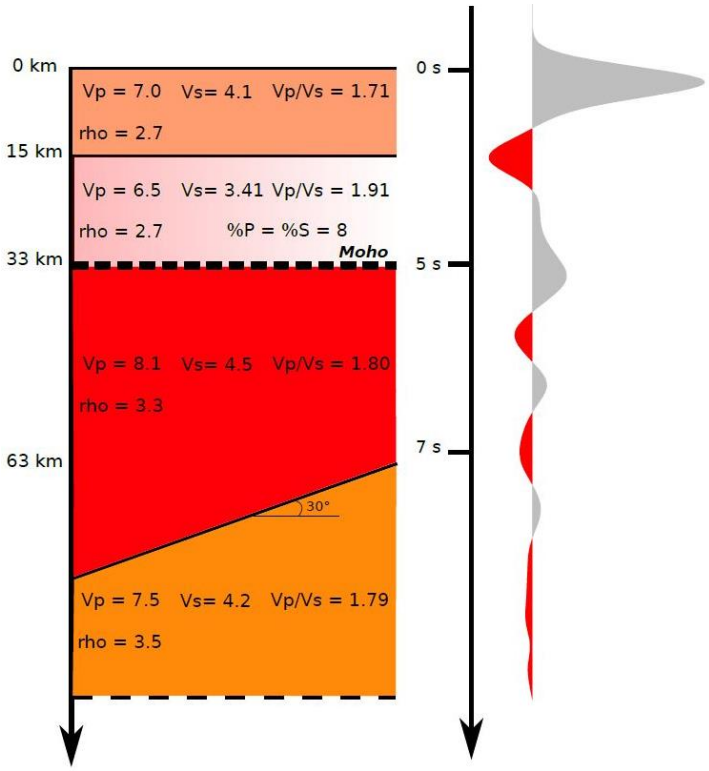

Fig.VI.10 *Modèle de la lithosphère déduite des fonctions récepteur (e.g. station sismisque KEN4) (Plasman et al. en préparation).*

On peut également observer des structures crustales au sud du lac de Manyara (Fig.VI.11). L'interface à ~ 15 km avec une zone de vitesse plus lente observée au nord pourrait être prolongée au sud et correspondre à la zone conductrice A sur la Fig.VI.11. La zone A (30-150 Ω/m) se trouve sous une zone plus résistante (~1000 Ω/m), le plateau de Mbulu (entre la zone A et B), constitué de blocs basculés de roches précambriennes (LeGall et al. 2008). Le bloc Masai à l'est est également très résistant (~1000 Ω/m). La croûte sous l'escarpement du rift (zone B) et dans l'axe du rift (zone C) est très conductrice (30-150 Ω/m) ce qui peut être interpréter comme une remontée de matériel mantellique plus chaud. L'essaim sismique se situant sous l'escarpement du rift entre 20 et 35 km (Fig.VI.8) pourrait se trouver à la limite entre une zone résistante et conductrice (Fig.VI.11).

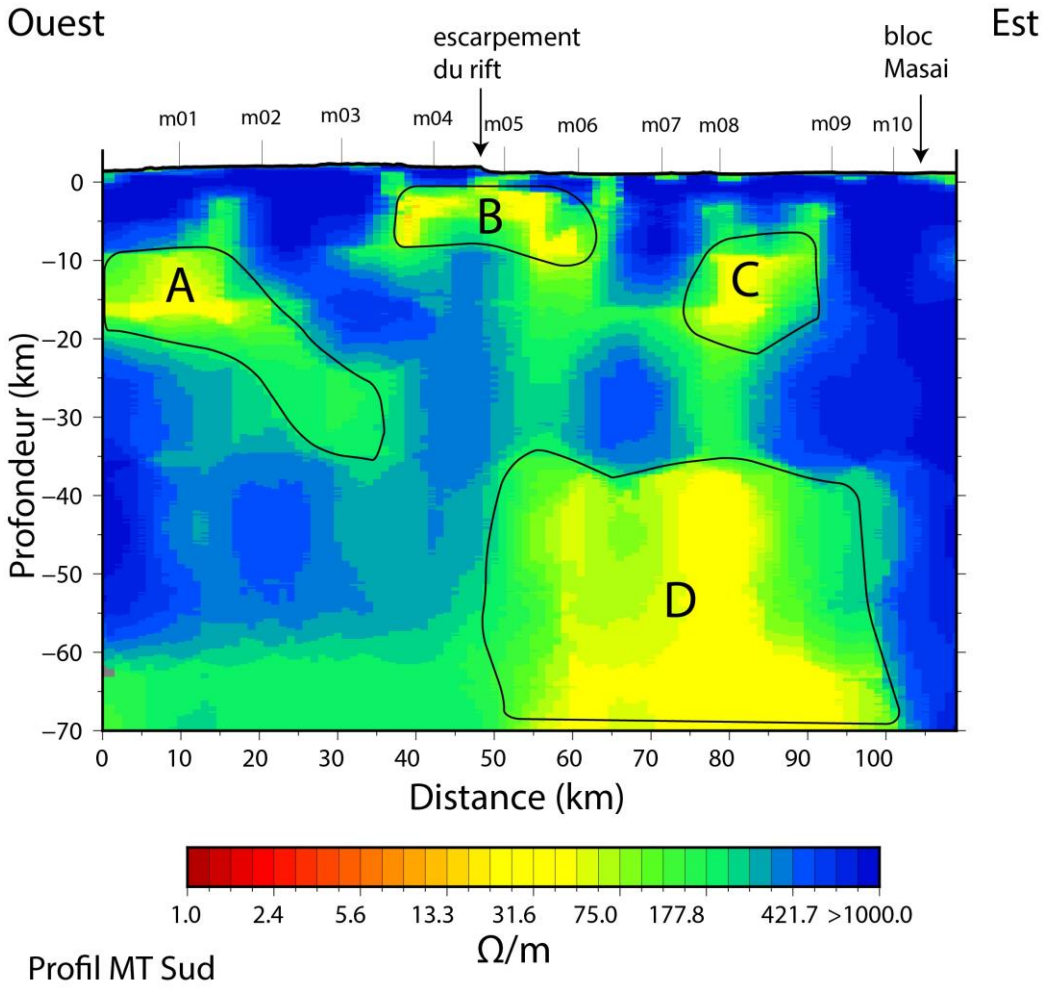

Fig.VI.11 *Modèle de résistivité de la lithosphère au sud du lac Manyara. (La localisation du profil des stations magnétotelluriques voir Fig.VI.8). (Plasman et al. en préparation). Les zones conductrices sont notées des lettres A, B, C et D.*

Les modèles géophysiques ont mis en évidence des structures mantelliques. Dans la partie nord de la DNT (i.e. de la frontière Kenyane jusqu'au lac Manyara), une interface est mise en évidence à 60 ± 10 km avec des anomalies négatives de vitesse (- 9 % pour Vp) présente sur tout le profil et avec un pendage de 30 ° vers les bords (Fig.VI.10). Un analogue à cette interface est localisé dans la branche ouest (Uganda) vers 60 km et pourrait être la signature d'un manteau métasomatisé par des magmas riches en CO_2 (Lindenfeld et al. 2012; Wölbern et al. 2012). L'interface à 60 km pourrait aussi être le toit d'une lithosphère contenant ~ 2 % de magma, guidée par des structures lithosphériques préexistantes (Plasman et al. en préparation, Takei 2002). La présence de verre silicaté dans des xénolites du faciès à spinelle (e.g. Jones et al. 1983) consolide cette hypothèse.

Dans la partie sud de la DNT (entre le lac Manyara et le volcan Kwaraha), le manteau lithosphérique (40- 70km) au niveau de l'axe du rift (Fig.VI.11, zone D) est très conducteur (30 – 70 Ω/m), et pourrait être liée à une remontée de matériel d'origine mantellique plus conducteur, i.e. plus chaud et/ou présence de fluide et de magma (Fig.VI.10). On peut calculer l'effet de la présence de liquide silicaté dans la lithosphère sur la conductivité électrique du

milieu (Sifre et al. 2014, Pommier et Le-Trong 2011). Les magmas hyperalcalins du volcan Hanang ont environ 7 % CO_2 et 0,5 % H_2O à 45 km (1,5 GPa). Une lithosphère avec une fraction de liquide de 0,5 %, et un magma de la composition observé au Hanang à une conductivité électrique de 0,01 $S \cdot m^{-1}$ (= 100 Ω/m en résistivité) (Pr. Tarits, communication personnelle) ce qui est la même conductivité que celui du modèle magnétotellurique du profil sud.

Au cours du projet CoLiBrEA, nous avons pu mettre en évidence des interactions entre le magmatisme, les structures héritées et la sismicité actuelle. Les profondeurs de stockage de magma et les différents taux de fusion ont pu être corrélés avec des modèles de vitesses sismiques et les données géochimiques, notamment pour le volcan Ngorongoro. Les zones sismogènes de Tanzanie sont associées aux zones plus conductrices et/ou aux zones de contrastes de résistivité, suggérant l'implication de la dynamique de mise en place des magmas dans la croûte. Par ailleurs, les modèles géophysiques (sismiques et magnétotelluriques) de la lithosphère de la zone de Manyara sont toujours en cours d'analyse et les prochains résultats pourraient donner de nouvelles contraintes sur les différences de sismicité active entre le bassin de Manyara (20-35 km) et le bassin de Natron (<15 km) ainsi que sur leurs modes de déformation associés.

Conclusions et perspectives

Le rift Est africain (REA) est une frontière de plaque en extension qui présente plusieurs stades d'extension, de l'initiation du rift dans la lithosphère cratonique (Tanzanie) jusqu'à l'accrétion océanique en Afar. Dans la divergence nord-tanzanienne (DNT), le magmatisme et des processus tectoniques sont impliqués dans la rupture continentale. De par sa localisation au sein de la DNT, le bassin de Manyara offre l'opportunité d'étudier le volcanisme associé au premier stade de l'initiation de la rupture continentale. Le bassin de Manyara a un volcanisme hyperalcalin associé à un essaim sismique dans la croûte inférieure (20 – 40 km). Cette thèse se focalise sur la signature géochimique des laves du bassin de Manyara, leurs conditions pré-éruptives (concentration en éléments volatils, état oxydation) et sur les conditions de fusion partielle. Une approche pétro-géochimique multi-échelle a été adoptée. Le volcanisme de Manyara a été étudié, d'une part, par localités (Labait, Kwaraha, Hanang), et d'autre part, à différentes échelles depuis la roche totale, les minéraux, jusqu'aux des inclusions vitreuses. La caractérisation géochimique des laves de Manyara a été réalisée afin de contraindre les processus magmatiques liés à la genèse des magmas alcalins et des carbonatites associées dans une zone d'initiation de rift. Par ailleurs, la caractérisation géochimique des magmas, notamment en éléments volatils, est nécessaire pour comprendre les interactions entre le magmatisme, les structures héritées et la sismicité actuelle afin de déterminer le mode de déformation et le fonctionnement de la rupture continentale.

La zone d'initiation de la rupture continentale (i.e. Manyara) est composée de plusieurs types de laves hyperalcalines, de néphélinites à mélilite (Mg# > 55) (Labait, Kwaraha), d'une calciocarbonatite (Kwaraha) et de néphélinites différenciées (Mg# < 35) (Hanang). Les néphélinites à mélilite (Mg# > 55) sont des laves primaires qui résultent de la fusion d'une péridotite à grenat et phlogopite à des profondeurs > 120 km avec un taux de fusion ≤ 1 %. La percolation de ces magmas asthénosphériques induit un métasomatisme riche en CO_2 et pauvre en H_2O dans le manteau lithosphérique tanzanien. Les néphélinites de Hanang (Mg# < 35) sont issues des néphélinites à mélilite du Labait par cristallisation fractionnée, et d'autres processus impliqués dans la genèse de ces laves (immiscibilité et le remplissage magmatique). Au Hanang, l'absence de carbonatite associée aux néphélinites peut être attribuée à la différenciation en système ouvert, avec un remplissage de liquide mafique empêchant le magma d'atteindre la saturation en carbonate. Les néphélinites enrichies en carbonate évoluent jusqu'à des liquides phonolitiques par cristallisation fractionnée à des conditions crustales (~ 600 MPa, 1050°C) et relativement oxydées (~ ΔQFM +1,5). Le liquide phonolitique piégé dans les inclusions vitreuses forme 2 liquides, un liquide trachytique et une carbonatite, pendant l'ascension rapide du magma à ~ 500 MPa.

Par ailleurs, l'étude des laves du bassin de Manyara a mis en évidence les perspectives à suivre pour approfondir notre connaissance sur les magmas alcalins et leurs concentrations en éléments volatils.

Dans cette thèse, il a été montré que les magmas du bassin de Manyara sont riches en CO_2. L'origine du CO_2 dans le manteau tanzanien n'a pas été abordé lors de cette thèse ni par les études précédentes sur les xénolites mantelliques. Le carbone provient probablement du

panneau plongeant liée à la subduction Panafricaine (600 Ma), une analyse isotopique du carbone pourrait apporter des contraintes à cette hypothèse.

Dans les roches les plus mafiques, l'absence d'inclusions vitreuses ne permet pas de quantifier la concentration en CO_2. Dans les roches différenciées, des problèmes de quantification du CO_2 dans les inclusions vitreuses ont également été observés. La taille des inclusions vitreuses est similaire à la taille du faisceau de la SIMS (~ 20 µm), ce qui rend difficile l'interprétation des données entre le CO_2 du verre silicaté et de la phase carbonatée. Afin de minimiser les incertitudes, il serait pertinent d'analyser ces inclusions avec une SIMS ou nanoSIMS ayant une taille de faisceau ~ 5 µm. Une autre solution serait l'utilisation des spectres raman des verres trachytiques expérimentaux (à 0 pds % CO_2 et 0,22 pds % CO_2) afin de calibrer le CO_2 pour les spectres raman des inclusions. Cependant la taille des inclusions ne permet pas d'obtenir un signal non contaminé par celui de la néphéline (minéral hôte), par conséquent un travail minutieux de déconvolution du signal est nécessaire. Les conclusions sur les inclusions vitreuses sont dépendantes du nombre d'inclusions analysées et notamment de la phase carbonatée analysée avec le MEB. L'avantage des analyses raman est une analyse facile du carbonate sans qu'il ne soit nécessaire d'avoir les inclusions vitreuses à la surface. Il a été montré que l'incorporation de Na dans le carbonate diminue la position du shift raman dans les carbonates. Une solution alternative pour quantifier le rapport Ca:Na des carbonates serait de calibrer expérimentalement la proportion Ca:Na dans des liquides carbonatés et d'utiliser ces expériences comme standards au raman. Afin d'obtenir des résultats plus robustes, des analyses complémentaires au MEB et EPMA de la phase carbonatée sont nécessaires. Pour analyser le carbonate (à la surface), un protocole précis de polissage doit être réalisé. Les contrastes importants de dureté entre les différentes phases (néphéline, verre et carbonate), la taille du carbonate (~ 5 µm) et sa dissipation sous l'effet du solvant (eau et/ou éthanol) rendent très difficile la mise à l'affleurement d'une inclusion tout en conservant le carbonate.

Une étude plus approfondie des inclusions vitreuses pourraient aussi apporter de nouvelles données sur les conditions de température de l'immiscibilité (réhomogénéisation avec une platine chauffante) ou de définir les coefficients de partage des éléments en trace entre un liquide silicaté trachytique et un liquide carbonaté (laser-ICPMS avec un faisceau à 5 µm). Le processus d'immiscibilité a un effet important sur le fractionnement de S^{6+}- S^{2-} et Fe^{3+}- Fe^{2+}. Le comportement des espèces du fer et du soufre en présence d'un liquide silicaté et carbonaté doit être déterminé expérimentalement. Les laves alcalines sont souvent composées de phénocristaux de néphéline qui incorporent de l'hydrogène lors de sa cristallisation (500 – 3500 ppm H_2O) à partir d'un magma hydraté. Cependant aucun coefficient de partage ($Kd^{H}_{nph/liq}$) entre néphéline et magmas alcalins pour l'H_2O n'a encore été calibré expérimentalement. L'établissement de ce coefficient permettrait de quantifier les concentrations en eau dans les laves alcalines dépourvues d'inclusions vitreuses.

Cette thèse a permis de montrer que la composition des laves et les associations néphélinites, (Mg# > 55)-néphélinites, (Mg# < 35)-carbonatites, observées dans le bassin de Manyara, sont proches de celles du bassin de Natron (e.g Oldoinyo Lengai).

Les concentrations élevées du carbone et du soufre dans les magmas peut avoir un rôle important sur la viscosité et la vitesse d'ascension des magmas ainsi que sur le style éruptif.

Cette thèse a permis de mettre en évidence des résultats préliminaires sur le comportement et la spéciation des éléments volatils pendant la différentiation et le processus d'immiscibilité. Néanmoins, l'occurrence de l'immiscibilité entre des liquides silicatés et carbonatitiques empêche la détermination de l'état rédox ainsi que l'effet du dégazage associé aux magmas alcalins riches en CO_2. Pour pouvoir contraindre l'origine et les propriétés (redox) des carbonatites et des magmas alcalins, ainsi que les processus d'immiscibilité et de dégazage, une étude combinant la pétrologie expérimentale et les isotopes du soufre est nécessaire. Ces 2 méthodes pourraient apporter des contraintes sur (1) les équilibres de phase et les conditions P-T associées aux systèmes néphélinitiques en présence ce CO_2, S +/- H_2O, (2) la distribution des isotopes du soufre entre 2 liquides co-existants (nephelinite et carbonatite) et (3) le rôle respectif de l'immiscibilité et du dégazage sur le fractionnement des isotopes du soufre dans les systèmes alcalins.

Le bassin de Manyara et de Natron forment l'axe N-S de la DNT caractérisé par un volcanisme hyperalcalin récent (< 1,5 Ma) et qui s'est formé après le volcanisme E-O de la DNT entre 6 Ma et 2,5 Ma. La propagation du rift dans l'axe N-S est probablement induite par le changement de contrainte tectonique guidé par des structures crustales et/ou lithosphériques, ainsi qu'une variation importante du géotherme (effet du panache). Avec l'association de données structurales, géophysiques, et géochimiques, il a été possible de mettre en évidence des interactions entre le magmatisme, les structures héritées et la sismicité actuelle dans la DNT, notamment pour le volcan Ngorongoro et le bassin de Natron. Toutefois, l'interprétation des modèles géophysiques pour le bassin de Manyara est encore préliminaire, et pourrait à terme permettre de comprendre les différences de profondeur de la sismicité entre le bassin de Manyara (20-35 km) et le bassin de Natron (<15 km) et leurs modes de déformation respectifs ainsi que sur le rôle de l'exsolution du CO_2 en profondeur.

Mes travaux ont porté sur le volcanisme effusif du bassin de Manyara (laves hyperalcalines). Des évidences de volcanisme explosif sont également présentes dans cette zone (maar de Basotu et ceux présents autour de Hanang). L'étude des tufs carbonatés des maars permettrait de compléter nos conclusions sur le rôle des éléments volatils lors du volcanisme de l'initiation de la rupture continentale.

Références bibliographiques

A

Adam, J., Green, T. (2006). Trace element partitioning between mica-and amphibole-bearing garnet lherzolite and hydrous basanitic melt: 1. Experimental results and the investigation of controls on partitioning behaviour. Contributions to Mineralogy and Petrology, 152(1), 1-17.

Adams, A., Nyblade, A., & Weeraratne, D. (2012). Upper mantle shear wave velocity structure beneath the East African plateau: evidence for a deep, plateauwide low velocity anomaly. Geophysical Journal International, 189(1), 123-142.

Albarede, F. (1992). How deep do common basaltic magmas form and differentiate? Journal of Geophysical Research: Solid Earth, 97(B7), 10997-11009.

Albaric, J., Perrot, J., Déverchère, J., Deschamps, A., Le Gall, B., Ferdinand, RW., Petit, C., Tiberi, C., Sue, C., Songo, M. (2010). Contrasted seismogenic and rheological behaviours from shallow and deep earthquake sequences in the North Tanzanian Divergence, East Africa. Journal of African Earth Sciences, 58(5), 799-811.

Albaric, J., Déverchère, J., Perrot, J., Jakovlev, A., Deschamps, A. (2014). Deep crustal earthquakes in North Tanzania, East Africa: Interplay between tectonic and magmatic processes in an incipient rift. Geochemistry, Geophysics, Geosystems, 15(2), 374-394.

Anderson, A. T., Brown, G. G. (1993). CO_2 contents and formation pressures of some Kilauean melt inclusions. American Mineralogist, 78(7-8), 794-803.

Aubaud, C., Hauri, E. H., Hirschmann, M. M. (2004). Hydrogen partition coefficients between nominally anhydrous minerals and basaltic melts. Geophysical Research Letters, 31(20).

Aubaud, C., Pineau, F., Hékinian, R., Javoy, M. (2005). Degassing of CO_2 and H_2O in submarine lavas from the Society hotspot. Earth and Planetary Science Letters, 235(3), 511-527.

Aulbach, S., Rudnick, R. L., McDonough, W. F. (2008). Li-Sr-Nd isotope signatures of the plume and cratonic Lithospheric mantle beneath the margin of the rifted Tanzanian craton (Labait). Contributions to Mineralogy and Petrology, 155(1), 79-92

B

Baasner, A., Médard, E., Laporte, D., Hoffer, G. (2016). Partial melting of garnet lherzolite with water and carbon dioxide at 3 GPa using a new melt extraction technique: implications for intraplate magmatism. Contributions to Mineralogy and Petrology, 171(5), 1-23.

Bagdasaryan, G. P., Gerasimovskiy, V. I., Polyakov, A. I., Gukasyan, R. K., Vernadskiy, V. I. (1973). Age of volcanic rocks in the rift zones of East Africa. Geochemistry International, 10(1), 66-71.

Ballhaus, C. (1993). Redox states of Lithospheric and asthenospheric upper mantle. Contributions to Mineralogy and Petrology, 114(3), 331-348.

Baker, D. R., Alletti, M. (2012). Fluid saturation and volatile partitioning between melts and hydrous fluids in crustal magmatic systems: The contribution of experimental measurements and solubility models. Earth-Science Reviews, 114(3), 298-324.

Baker, M. B., Wyllie, P. J. (1990). Liquid immiscibility in a nephelinite-carbonate system at 25 kbar and implications for carbonatite origin. Nature, 346, 168-170.

Baker, M. B., Stolper, E. M. (1994). Determining the composition of high-pressure mantle melts using diamond aggregates. Geochimica et Cosmochimica Acta, 58(13), 2811–2827.

Ballhaus, C. (1993). Redox states of Lithospheric and asthenospheric upper mantle. Contributions to Mineralogy and Petrology, 114(3), 331-348.

Baptiste, V., Tommasi, A., Vauchez, A., Demouchy, S., Rudnick, RL. (2015). Deformation, hydration, and anisotropy of the Lithospheric mantle in an active rift: Constraints from mantle xenoliths from the North Tanzanian Divergence of the East African Rift. Tectonophysics, 639, 34-55.

Baudouin, C., Parat, F. (2015). Role of volatiles (S, Cl, H_2O) and silica activity on the crystallization of haüyne and nosean in phonolitic magmas (Eifel, Germany and Saghro, Morocco). American Mineralogist, 100(10), 2308-2322.

Baudouin, C., Parat, F., Denis, C.M.M., Mangasini, F. (2016). Nephelinite lavas at early stage of rift initiation (Hanang volcano, North Tanzanian Divergence). Contributions to Mineralogy and Petrology, 171(7), 1-20.

Behrens, H., Misiti, V., Freda, C., Vetere, F. (2009). Solubility of H_2O and CO_2 in ultrapotassic melts at 1200 and 1250 °C and pressure from 50 to 500 MPa. American Mineralogist, 94(1), 105-120

Behrens, H, Ohlhorst, S, Holtz, F, Champenois, M (2004). CO_2 solubility in dacitic melts equilibrated with H_2O-CO_2 fluids: Implications for modeling the solubility of CO_2 in silicic melts. Geochimica et Cosmochimica Acta, 68(22):4687–4703

Behrens, H., Roux, J., Neuville, D.R., Siemann, M. (2006). Quantification of dissolved H_2O in silicate glasses using confocal microRaman spectroscopy. Chemical Geology, 229(1), 96-112

Behrens, H., Meyer, M., Holtz, F., Benne, D., Nowak, M. (2001). The effect of alkali ionic radius, temperature, and pressure on the solubility of water in $MAlSi_3O_8$ melts (M= Li, Na, K, Rb). Chemical Geology, 174(1), 275-289.

Behrens, H., Romano, C., Nowak, M., Holtz, F., Dingwell, D. B. (1996). Near-infrared spectroscopic determination of water species in glasses of the system $MAlSi_3O_8$ (M= Li, Na, K): an interlaboratory study. Chemical Geology, 128(1), 41-63.

Bell D, Ihinger P, Rossman G (1995) Quantitative and analysis of trace OH in garnet and pyroxenes. American Mineralogist, 80:465-474

Bell, K., Tilton, G.R. (2001). Nd, Pb and Sr isotopic compositions of East African carbonatites: evidence for mantle mixing and plume inhomogeneity. Journal of Petrology, 42(10), 1927-1945.

Bell, K. (1998). Radiogenic isotope constraints on relationships between carbonatites and associated silicate rocks-a brief review. Journal of Petrology, 39(11-12), 1987-1996.

Bell, A. S., Simon, A. (2011). Experimental evidence for the alteration of the $Fe^{3+}/\Sigma Fe$ of silicate melt caused by the degassing of chlorine-bearing aqueous volatiles. Geology, 39(5), 499-502.

Berndt, J., Liebske, C., Holtz, F., Freise, M., Nowak, M., Ziegenbein, D., Koepke, J. (2002). A combined rapid-quench and H_2-membrane setup for internally heated pressure vessels: description and application for water solubility in basaltic melts. American Mineralogist, 87(11-12), 1717-1726

Berndt, J., Koepke, J., Holtz, F. (2005). An experimental investigation of the influence of water and oxygen fugacity on differentiation of MORB at 200 MPa. Journal of Petrology, 46(1), 135-167.

Bézos, A., Humler, E. (2005). The $Fe^{3+}/\Sigma Fe$ ratios of MORB glasses and their implications for mantle melting. Geochimica et Cosmochimica Acta, 69(3), 711-725.

Botcharnikov, R. E., Holtz, F., Behrens, H. (2007). The effect of CO_2 on the solubility of H_2O-Cl fluids in andesitic melt. European Journal of Mineralogy, 19(5), 671-680.

Brey, G. (1978). Origin of olivine melilitites–chemical and experimental constraints. Journal of Volcanology and Geothermal Research, 3(1-2), 61-88.

Brey, G. P., Green, D. H. (1976). Solubility of CO_2 in olivine melilitite at high pressures and role of CO_2 in the Earth's upper mantle. Contributions to Mineralogy and Petrology, 55(2), 217-230.

Brey, G., Green, D. H. (1977). Systematic study of liquidus phase relations in olivine melilitite+ H_2O+ CO_2 at high pressures and petrogenesis of an olivine melilitite magma. Contributions to Mineralogy and Petrology, 61(2), 141-162.

Brooker, R.A., Kjarsgaard, B.A. (2011). Silicate–carbonate liquid immiscibility and phase relations in the system SiO_2–Na_2O–Al_2O_3–CaO–CO_2 at 0.1–2.5 GPa with applications to carbonatite genesis. Journal of Petrology, 52(7-8), 1281–1305

Brooker, R.A., Kohn, S.C., Holloway, J.R., McMillan, P.F. (2001). Structural controls on the solubility of CO_2 in silicate melts: part II: IR characteristics of carbonate groups in silicate glasses. Chemical Geology, 174(1), 241-254

Bucholz, C. E., Gaetani, G. A., Behn, M. D., Shimizu, N. (2013). Post-entrapment modification of volatiles and oxygen fugacity in olivine-hosted melt inclusions. Earth and Planetary Science Letters, 374, 145-155.

Buck, W.R. (2006). The role of magma in the development of the Afro-Arabian Rift System. Geological Society, London, Special Publications, 259(1), 43-54.

Bühn, B., Rankin, A. H., Radtke, M., Haller, M., Knöchel, A. (1999). Burbankite, a (Sr, REE, Na, Ca)-carbonate in fluid inclusions from carbonatite-derived fluids: Identification and characterization using Laser Raman spectroscopy, SEM-EDX, and synchrotron micro-XRF analysis. American Mineralogist, 84(7-8), 1117-1125.

Bultitude, R. J., Green, D. H. (1971). Experimental study of crystal-liquid relationships at high pressures in olivine nephelinite and basanite compositions. Journal of Petrology, 12(1), 121-147.

Burgisser, A., Scaillet, B. (2007). Redox evolution of a degassing magma rising to the surface. Nature, 445(7124), 194-197.

C

Calais, E., d'Oreye, N., Albaric, J., Deschamps, A., Delvaux, D., Déverchere, J., Ebinger C., Ferdinand RW, Kervyn, F., Macheyeki, AS, Oyen, A., Perrot, J., Saria, E., Smets, B., Sarah Stamps, D., Wauthier C. (2008). Strain accommodation by slow slip and dyking in a youthful continental rift, East Africa. Nature, 456(7223), 783-787.

Canil, D., O'Neill, H. S. C. (1996). Distribution of ferric iron in some upper-mantle assemblages. Journal of Petrology, 37(3), 609-635.

Carignan, J., Hild, P., Mevelle, G., Morel, J., Yeghicheyan, D. (2001). Routine analyses of trace elements in geological samples using flow injection and low pressure on-line liquid chromatography coupled to ICP-MS: a study of geochemical reference materials BR, DR-N, UB-N, AN-G and GH. Geostandards Newsletter, 25(2-3), 187-198.

Carmichael, I. S. (1991). The redox states of basic and silicic magmas: a reflection of their source regions? Contributions to Mineralogy and Petrology, 106(2), 129-141.

Carmichael, I. S., Ghiorso, M. S. (1986). Oxidation-reduction relations in basic magma: a case for homogeneous equilibria. Earth and Planetary Science Letters, 78(2), 200-210.

Carmichael, I. S., Ghiorso, M. S. (1990). The effect of oxygen fugacity on the redox state of natural liquids and their crystallizing phases. Reviews in mineralogy and geochemistry, 24(1), 191-212.

Carroll, M. R., Blank, J. G. (1997). The solubility of H_2O in phonolitic melts. American Mineralogist, 82(5-6), 549-556.

Carroll, M.R., Rutherford, M. J. (1988). Sulfur speciation in hydrous experimental glasses of varying oxidation state--results from measured wavelength shifts of sulfur X-rays. American Mineralogist, 73(7), 845-9.

Cartigny, P., Pineau, F., Aubaud, C., Javoy, M. (2008). Towards a consistent mantle carbon flux estimate: Insights from volatile systematics (H_2O/Ce, δD, CO_2/Nb) in the North Atlantic mantle (14° N and 34° N). Earth and Planetary Science Letters, 265(3), 672-685.

Chakhmouradian, A. R. (2006). High-field-strength elements in carbonatitic rocks: geochemistry, crystal chemistry and significance for constraining the sources of carbonatites. Chemical Geology, 235(1), 138-160.

Chakrabarti, R., Basu, A. R., Santo, A. P., Tedesco, D., Vaselli, O. (2009). Isotopic and geochemical evidence for a heterogeneous mantle plume origin of the Virunga volcanics, Western rift, East African Rift system. Chemical Geology, 259(3), 273-289.

Chen, H., Xia, Q. K., Ingrin, J., Jia, Z. B., Feng, M. (2015). Changing recycled oceanic components in the mantle source of the Shuangliao Cenozoic basalts, NE China: New constraints from water content. Tectonophysics, 650, 113-123.

Chen, Y., Provost, A., Schiano, P., Cluzel, N. (2011). The rate of water loss from olivine-hosted melt inclusions. Contributions to Mineralogy and Petrology, 162(3), 625-636.

Chorowicz, J. (2005). The east African rift system. Journal of African Earth Sciences, 43(1), 379-410.

Church, A. A. (1996). The petrology of the Kerimasi carbonatite volcano and the carbonatites of Oldoinyo Lengai with a review of other occurrences of extrusive carbonatites (Doctoral dissertation, University of London).

Church, A. A., Jones, A. P. (1995). Silicate-Carbonate Immiscibility at Oldoinyo Lengai. Journal of Petrology, 36(4), 869-889.

Cottrell, E., Kelley, K. A. (2011). The oxidation state of Fe in MORB glasses and the oxygen fugacity of the upper mantle. Earth and Planetary Science Letters, 305(3), 270-282.

Cottrell, E., Kelley, K. A., Lanzirotti, A., Fischer, R. A. (2009). High-precision determination of iron oxidation state in silicate glasses using XANES. Chemical Geology, 268(3), 167-179.

Crabtree, S. M., Lange, R. A. (2012). An evaluation of the effect of degassing on the oxidation state of hydrous andesite and dacite magmas: a comparison of pre-and post-eruptive Fe^{2+} concentrations. Contributions to Mineralogy and Petrology, 163(2), 209-224.

Craig, T. J., Jackson, J. A., Priestley, K., McKenzie, D. (2011). Earthquake distribution patterns in Africa: their relationship to variations in lithospheric and geological structure, and their rheological implications. Geophysical Journal International, 185(1), 403-434.

D

Daly, E., Keir, D., Ebinger, C. J., Stuart, G. W., Bastow, I. D., Ayele, A. (2008). Crustal tomographic imaging of a transitional continental rift: the Ethiopian rift. Geophysical Journal International, 172(3), 1033-1048.

Dasgupta, R., Hirschmann, M. M., Smith, N. D. (2007). Partial melting experiments of peridotite + CO_2 at 3 GPa and genesis of alkalic ocean island basalts. Journal of Petrology, 48(11), 2093-2124.

Dasgupta, R., Hirschmann, M. M. (2010). The deep carbon cycle and melting in Earth's interior. Earth and Planetary Science Letters, 298(1), 1-13.

Dasgupta, R., Chi, H., Shimizu, N., Buono, A. S., Walker, D. (2013). Carbon solution and partitioning between metallic and silicate melts in a shallow magma ocean: implications for the origin and distribution of terrestrial carbon. Geochimica et Cosmochimica Acta, 102, 191-212.

Dautria, J. M., Dupuy, C., Takherist, D., Dostal, J. (1992). Carbonate metasomatism in the Lithospheric mantle: peridotitic xenoliths from a melilititic district of the Sahara basin. Contributions to Mineralogy and Petrology, 111(1), 37-52.

Dauphas, N., Roskosz, M., Alp, E. E., Neuville, D. R., Hu, M. Y., Sio, C. K., Cordier, C. (2014). Magma redox and structural controls on iron isotope variations in Earth's mantle and crust. Earth and Planetary Science Letters, 398, 127-140.

Dawson, J. B. (1989). Sodium carbonatite extrusions from Oldoinyo Lengai, Tanzania: implications for carbonatite complex genesis. Carbonatites: Genesis and evolution, 255-277.

Dawson, J. B. (1998). Peralkaline nephelinite–natrocarbonatite relationships at Oldoinyo Lengai, Tanzania. Journal of Petrology, 39(11-12), 2077-2094.

Dawson, J.B. (2008). The Gregory Rift Valley and Neogene–Recent Volcanoes of Northern Tanzania. Geological Society, London, Memoirs, 33.

Dawson, J.B. (2012). Nephelinite–melilitite–carbonatite relationships: Evidence from Pleistocene–recent volcanism in northern Tanzania. Lithos, 152, 3-10.

Dawson, J. B., James, D., Paslick, C., Halliday, A. M. (1997). Ultrabasic potassic low-volume magmatism and continental rifting in north-central Tanzania: association with enhanced heat flow. Russian geology and geophysics, 38, 69-81

Dawson, J. B., Smith, J. V. (1988). Metasomatised and veined upper-mantle xenoliths from Pello Hill, Tanzania: evidence for anomalously-light mantle beneath the Tanzanian sector of the East African Rift Valley. Contributions to Mineralogy and Petrology, 100(4), 510-527.

Dawson, J. B. (1962). Sodium carbonate lavas from Oldoinyo Lengai, Tanganyika. Nature, 195, 1075-1076.

Dawson, J. B. (1992). Neogene tectonics and volcanicity in the North Tanzania sector of the Gregory Rift Valley: contrasts with the Kenya sector. Tectonophysics, 204(1-2), 8187-8392.

Dawson, J. B. (1998). Peralkaline nephelinite–natrocarbonatite relationships at Oldoinyo Lengai, Tanzania. Journal of Petrology, 39(11-12), 2077-2094.

Dawson, J. B., Powell, D. G., Reid, A. M. (1970). Ultrabasic xenoliths and lava from the Lashaine volcano, northern Tanzania. Journal of Petrology, 11(3), 519–548.

de Moor, JM., Fischer, TP., King, PL., Botcharnikov, RE., Hervig, RL., Hilton, DR., Barry, PH., Mangasini F., Ramirez, C. (2013) Volatile–rich silicate melts from Oldoinyo Lengai volcano (Tanzania): Implications for carbonatite genesis and eruptive behavior. Earth and Planetary Sciences Letters, 361, 379-390.

de Moor, J. M., Fischer, T. P., Sharp, Z. D., King, P. L., Wilke, M., Botcharnikov, R. E., Rivard, C. (2013). Sulfur degassing at Erta Ale (Ethiopia) and Masaya (Nicaragua) volcanoes: Implications for degassing processes and oxygen fugacities of basaltic systems. Geochemistry, Geophysics, Geosystems, 14(10), 4076-4108.

Demouchy, S., Bolfan-Casanova, N. (2016). Distribution and transport of hydrogen in the Lithospheric mantle: A review. Lithos, 240, 402-425.

Denis, C. M., Alard, O., Demouchy, S. (2015). Water content and hydrogen behaviour during metasomatism in the uppermost mantle beneath Ray Pic volcano (Massif Central, France). Lithos, 236, 256-274.

Di Muro, A., Villemant, B., Montagnac, G., Scaillet, B., Reynard, B. (2006). Quantification of water content and speciation in natural silicic glasses (phonolite, dacite, rhyolite) by confocal microRaman spectrometry. Geochimica et Cosmochimica Acta, 70(11), 2868-2884.

Dixon, J. E., Stolper, E. M., Holloway, J. R. (1995). An experimental study of water and carbon dioxide solubilities in mid-ocean ridge basaltic liquids. Part I: calibration and solubility models. Journal of Petrology, 36(6), 1607-1631.

Dixon, J. E., Stolper, E. M. (1995). An experimental study of water and carbon dioxide solubilities in mid-ocean ridge basaltic liquids. Part II: applications to degassing. Journal of Petrology, 36(6), 1633-1646.

Downie, C., Wilkinson, P. (1962). The explosion craters of Basotu, Tanganyika Territory. Bulletin of Volcanology, 24(1), 389-420.

Drake, R., Curtis, G. H. (1987). K-Ar geochronology of the Laetoli fossil localities. Laetoli: A Pliocene site in northern Tanzania, 48-52.

Dumont, S., Socquet, A., Grandin, R., Doubre, C., Klinger, Y. (2016). Surface displacements on faults triggered by slow magma transfers between dyke injections in the 2005–2010 rifting episode at Dabbahu–Manda–Hararo rift (Afar, Ethiopia). Geophysical Journal International, 204(1), 399-417.

E

Ebinger, C. J., Sleep, N. H. (1998). Cenozoic magmatism throughout east Africa resulting from impact of a single plume. Nature, 395(6704), 788-791.

Ebinger, C., Djomani, Y. P., Mbede, E., Foster, A., Dawson, J. B. (1997). Rifting Archaean Lithosphere: the Eyasi-Manyara-Natron rifts, East Africa. Journal of the Geological Society, 154(6), 947-960.

Ebinger, C. J., Yemane, T., Harding, D. J., Tesfaye, S., Kelley, S., Rex, D. C. (2000). Rift deflection, migration, and propagation: Linkage of the Ethiopian and Eastern rifts, Africa. Geological Society of America Bulletin, 112(2), 163–176.

Edgar, A. D. (1987). The genesis of alkaline magmas with emphasis on their source regions: inferences from experimental studies. Geological Society, London, Special Publications, 30(1), 29-52.

Eggler, D. H., Mysen, B. O., Brey, G. P., Green, D. H. (1976). The role of CO_2 in the genesis of olivine melilitite: discussion. Contributions to Mineralogy and Petrology, 55(2), 231-239.

Eggler, D. H., Holloway, J. R. (1977). Partial melting of peridotite in the presence of H_2O and CO_2: Principles and review. Magma Genesis. Bulletin, State of Oregon, Department of Geology and Mineral Resources, 96, 15-36.

F

Faure, F., Schiano, P. (2005). Experimental investigation of equilibration conditions during forsterite growth and melt inclusion formation. Earth and Planetary Science Letters, 236(3), 882-898.

Fleet, M. E., Crocket, J. H., Stone, W. E. (1996). Partitioning of platinum-group elements (Os, Ir, Ru, Pt, Pd) and gold between sulfide liquid and basalt melt. Geochimica et Cosmochimica Acta, 60(13), 2397-2412.

Foley, S. F. (1993). An experimental study of olivine lamproite: first results from the diamond stability field. Geochimica et Cosmochimica Acta, 57(2), 483-489.

Foley, S. (2008). A trace element perspective on Archean crust formation and on the presence or absence of Archean subduction. Geological Society of America Special Papers, 440, 31-50.

Foley, S. F., Link, K., Tiberindwa, J. V., Barifaijo, E. (2012). Patterns and origin of igneous activity around the Tanzanian craton. Journal of African Earth Sciences, 62(1), 1-18.

Foley, S. F., Yaxley, G. M., Rosenthal, A., Buhre, S., Kiseeva, E. S., Rapp, R. P., Jacob, D. E. (2009). The composition of near-solidus melts of peridotite in the presence of CO_2 and H_2O between 40 and 60 kbar. Lithos, 112, 274-283.

Foley, S.F., Jenner, G.A., (2004). Trace element partitioning in lamproitic magmas - the Gaussberg olivine leucitite. Lithos, 75:19-38.

Fontijn, K., Elburg, M. A., Nikogosian, I. K., van Bergen, M. J., Ernst, G. G. (2013). Petrology and geochemistry of Late Holocene felsic magmas from Rungwe volcano (Tanzania), with implications for trachytic Rungwe Pumice eruption dynamics. Lithos, 177, 34-53.

Foster, A., Ebinger, C., Mbede, E., Rex, D. (1997). Tectonic development of the northern Tanzanian sector of the East African Rift System. Journal of the Geological Society, 154(4), 689-700.

Freestone IC, Hamilton DL (1980) The role of liquid immiscibility in the genesis of carbonatites—an experimental study. Contributions to Mineralogy and Petrology, 73(2):105–117

Frost, D. J., McCammon, C. A. (2008). The redox state of Earth's mantle. Annual Review of Earth Planetary Sciences, 36, 389-420.

Frezzotti, M. L., Tecce, F., Casagli, A. (2012). Raman spectroscopy for fluid inclusion analysis. Journal of Geochemical Exploration, 112, 1-20.

Fujimaki, H., Tatsumoto, M., Aoki, KI. (1984) Partition coefficients of Hf, Zr, and REE between phenocrysts and groundmasses. Journal Geophysical Research: Solid Earth, (1978–2012) 89(S02):B662–B672

Furman, T. (2007). Geochemistry of East African Rift basalts: an overview. Journal of African Earth Sciences, 48(2), 147-160.

Furman, T. (1995). Melting of metasomatized subcontinental Lithosphere: undersaturated mafic lavas from Rungwe, Tanzania. Contributions to Mineralogy and Petrology, 122(1-2), 97–115.

Furman, T., Graham, D. (1999). Erosion of Lithospheric mantle beneath the East African Rift system: geochemical evidence from the Kivu volcanic province. Lithos, 48(1), 237-262.

Furman, T., Nelson, W. R., Elkins-Tanton, L. T. (2016). Evolution of the East African rift: Drip magmatism, Lithospheric thinning and mafic volcanism. Geochimica et Cosmochimica Acta, 185, 418-434.

G

Gaillard, F. (2004). Laboratory measurements of electrical conductivity of hydrous and dry silicic melts under pressure. Earth and Planetary Science Letters, 218(1), 215-228.

Ghiorso, M. S., Sack, O. (1991). Fe-Ti oxide geothermometry: thermodynamic formulation and the estimation of intensive variables in silicic magmas. Contributions to Mineralogy and Petrology, 108(4), 485-510.

Gibson, S. A., McMahon, S. C., Day, J. A., Dawson, J. B. (2013). Highly refractory lithospheric mantle beneath the Tanzanian craton: evidence from Lashaine pre-metasomatic garnet-bearing peridotites. Journal of Petrology, 54(8), 1503-1546.

Giggenbach, W. F. (1996). Chemical composition of volcanic gases. In Monitoring and mitigation of volcano hazards (pp. 221-256). Springer Berlin Heidelberg.

Giordano, D., Mangiacapra, A., Potuzak, M., Russell, J. K., Romano, C., Dingwell, D. B., Di Muro, A. (2006). An expanded non-Arrhenian model for silicate melt viscosity: A treatment for metaluminous, peraluminous and peralkaline liquids. Chemical Geology, 229(1), 42-56.

Gittins, J., Jago, B. C. (1998). Differentiation of natrocarbonatite magma at Oldoinyo Lengai volcano, Tanzania. Mineralogical Magazine, 62(6), 759-768.

Giuli, G., Paris, E., Hess, K. U., Dingwell, D. B., Cicconi, M. R., Eeckhout, S. G., Valenti, P. (2011). XAS determination of the Fe local environment and oxidation state in phonolite glasses. American Mineralogist, 96(4), 631-636.

Green, D. H., Ringwood, A. E. (1967). The genesis of basaltic magmas. Contributions to Mineralogy and Petrology, 15(2), 103-190.

Green, D. H. (1970). A review of experimental evidence on the origin of basaltic and nephelinitic magmas. Physics of the Earth and Planetary Interiors, 3, 221-235.

Green, D. H. (1973). Conditions of melting of basanite magma from garnet peridotite. Earth and Planetary Science Letters, 17(2), 456-465.

Green, D. H. (2015). Experimental petrology of peridotites, including effects of water and carbon on melting in the Earth's upper mantle. Physics and Chemistry of Minerals, 42(2), 95-122.

Green, D. H., Falloon, T. J. (1998). Pyrolite: a Ringwood concept and its current expression. The Earth's mantle: composition, structure, and evolution, 311-378.

Green, T. H., Ringwood, A. E. (1968). Genesis of the calc-alkaline igneous rock suite. Contributions to Mineralogy and Petrology, 18(2), 105-162.

Grégoire, M., Bell, D. R., Le Roex, A. P. (2002). Trace element geochemistry of glimmerite and MARID mantle xenoliths: their relationship to kimberlite and to phlogopite-bearing peridotite revisited. Contributions to Mineralogy and Petrology, 142, 603-625.

Grew, E. S., Locock, A. J., Mills, S. J., Galuskina, I. O., Galuskin, E. V., Hålenius, U. (2013). Nomenclature of the garnet supergroup. American Mineralogist, 98(4), 785-811.

Griffin, WL., Powell, W., Pearson, NJ., O'Reilly, SY. (2008). GLITTER: data reduction software for laser ablation ICP–MS. Laser Ablation–ICP–MS in the Earth Sciences vol. 40. Mineralogical Association of Canada Short Course Series, pp. 204-207

Grocke, S. B., Cottrell, E., de Silva, S., Kelley, K. A. (2016). The role of crustal and eruptive processes versus source variations in controlling the oxidation state of iron in Central Andean magmas. Earth and Planetary Science Letters, 440, 92-104.

Gromme, C. S., Reilly, T. A., Mussett, A. E. Hay, R. L. 1970. Palaeomagnetism and potassium-argon ages of volcanic rocks of Ngorongoro caldera, Tanzania. Geophysical Journal of the Royal Astronomical Society, 22, 101–115.

Grove, T. L., Elkins-Tanton, L. T., Parman, S. W., Chatterjee, N., Müntener, O., Gaetani, G. A. (2003). Fractional crystallization and mantle-melting controls on calc-alkaline differentiation trends. Contributions to Mineralogy and Petrology, 145(5), 515-533.

Gudfinnsson, G. H., Presnall, D. C. (2005). Continuous gradations among primary carbonatitic, kimberlitic, melilititic, basaltic, picritic, and komatiitic melts in equilibrium with garnet lherzolite at 3–8 GPa. Journal of Petrology, 46(8), 1645-1659.

Gustafson, W. I. (1974). The Stability of Andradite, Hedenbergite, and Related Minerals in the System Ca-Fe-Si-O-H. Journal of Petrology, 15(3), 455-496.

Guzmics, T., Mitchell, R. H., Szabó, C., Berkesi, M., Milke, R., Abart, R. (2011). Carbonatite melt inclusions in coexisting magnetite, apatite and monticellite in Kerimasi calciocarbonatite, Tanzania: melt evolution and petrogenesis. Contributions to Mineralogy and Petrology, 161(2), 177-196.

Guzmics, T., Mitchell, R. H., Szabó, C., Berkesi, M., Milke, R., Ratter, K. (2012). Liquid immiscibility between silicate, carbonate and sulfide melts in melt inclusions hosted in co-precipitated minerals from Kerimasi volcano (Tanzania): evolution of carbonated nephelinitic magma. Contributions to Mineralogy and Petrology, 164(1), 101-122.

Guzmics, T., Zajacz, Z., Mitchell, R. H., Szabó, C., Wälle, M. (2015). The role of liquid–liquid immiscibility and crystal fractionation in the genesis of carbonatite magmas: insights from Kerimasi melt inclusions. Contributions to Mineralogy and Petrology, 169(2), 1-18.

H

Halliday, A. N., Lee, D. C., Tommasini, S., Davies, G. R., Paslick, C. R., Fitton, J. G., James, D. E. (1995). Incompatible trace elements in OIB and MORB and source enrichment in the sub-oceanic mantle. Earth and Planetary Science Letters, 133(3), 379-395.

Hamilton, D. L. (1961). Nephelines as crystallization temperature indicators. The Journal of Geology, 321-329.

Hamilton, DL., Bedson, P., Esson, J. (1989). The behaviour of trace elements in the evolution of carbonatites. In: K. Bell (Editor), Carbonatites – Genesis and Evolution. Unwin Hyman, London, pp 405-427

Hamilton, DL., Freestone, IC., Dawson, JB., Donaldson, CH. (1979). Origin of carbonatites by liquid immiscibility. Nature, 279, 52–54

Hammouda, T., Keshav, S. (2015). Melting in the mantle in the presence of carbon: Review of experiments and discussion on the origin of carbonatites. Chemical Geology, 418, 171-188.

Hammouda, T. (2003). High-pressure melting of carbonated eclogite and experimental constraints on carbon recycling and storage in the mantle. Earth and Planetary Science Letters, 214(1), 357-368.

Hansen SE, Nyblade AA, Benoit MH (2012). Mantle structure beneath Africa and Arabia from adaptively parameterized P–wave tomography: Implications for the origin of Cenozoic Afro–Arabian tectonism. Earth and Planetary Science Letters, 319:23–34.

Hao, X. L., Li, Y. L. (2013). ^{57}Fe Mössbauer spectroscopy of mineral assemblages in mantle spinel lherzolites from Cenozoic alkali basalt, eastern China: Petrological applications. Lithos, 156, 112-119.

Harmer, R. E., Gittins, J. (1998). The case for primary, mantle-derived carbonatite magma. Journal of Petrology, 39(11-12), 1895-1903.

Hauri, E. H., Gaetani, G. A., Green, T. H. (2006). Partitioning of water during melting of the Earth's upper mantle at H 2 O-undersaturated conditions. Earth and Planetary Science Letters, 248(3), 715-734.

Hautot, S., Tarits, P., Whaler, K., Le Gall, B., Tiercelin, J. J., Le Turdu, C. (2000). Deep structure of the Baringo Rift Basin (central Kenya) from three-dimensional magnetotelluric imaging: Implications for rift evolution. Journal of Geophysical Research: Solid Earth, 105(B10), 23493-23518.

Hay, RL. (1976). Geology of the Olduvai Gorge. PhD thesis, University of California Press, Berkeley.

Hazen, R. M., Downs, R. T., Jones, A. P., Kah, L. (2013). Carbon mineralogy and crystal chemistry. Reviews in mineralogy and geochemistry, 75, 7-46.

Head, E. M., Shaw, A. M., Wallace, P. J., Sims, K. W., Carn, S. A. (2011). Insight into volatile behavior at Nyamuragira volcano (DR Congo, Africa) through olivine-hosted melt inclusions. Geochemistry, Geophysics, Geosystems, 12(10).

Helmy, H. M., Ballhaus, C., Wohlgemuth-Ueberwasser, C., Fonseca, R. O., Laurenz, V. (2010). Partitioning of Se, As, Sb, Te and Bi between monosulfide solid solution and sulfide melt–application to magmatic sulfide deposits. Geochimica et Cosmochimica Acta, 74(21), 6174-6179.

Hékinian, R., Bideau, D., Hébert, R., Niu, Y. (1995). Magmatism in the Garrett transform fault (East Pacific Rise near 13 27′ S). Journal of Geophysical Research: Solid Earth, 100(B6), 10163-10185.

Herzberg, C., O'Hara, M. J. (1998). Phase equilibrium constraints on the origin of basalts, picrites, and komatiites. Earth-Science Reviews, 44(1), 39-79.

Hirose, K. (1997). Partial melt compositions of carbonated peridotite at 3 GPa and role of CO_2 in alkali-basalt magma generation. Geophysical Research Letters, 24, 2837-2840.

Hofmann, A. W. (1986). Nb in Hawaiian magmas: constraints on source composition and evolution. Chemical Geology, 57(1), 17-30.

Hofmann, A. W. (1988). Chemical differentiation of the Earth: the relationship between mantle, continental crust, and oceanic crust. Earth and Planetary Science Letters, 90(3), 297-314.

Holloway, J. R., Blank, J. G. (1994). Application of experimental results to C-O-H species in natural melts. Reviews in mineralogy and geochemistry, 30,187-230.

Hudgins, T. R., Mukasa, S. B., Simon, A. C., Moore, G., Barifaijo, E. (2015). Melt inclusion evidence for CO_2-rich melts beneath the western branch of the East African Rift: implications for long-term storage of volatiles in the deep Lithospheric mantle. Contributions to Mineralogy and Petrology, 169(5), 1-18.

Hui, H., Peslier, A. H., Rudnick, R. L., Simonetti, A., Neal, C. R. (2015). Plume-cratonic lithosphere interaction recorded by water and other trace elements in peridotite xenoliths from the Labait volcano, Tanzania. Geochemistry, Geophysics, Geosystems, 16(6), 1687-1710.

Huismans, R. S., Podladchikov, Y. Y., Cloetingh, S. (2001). Transition from passive to active rifting: Relative importance of asthenospheric doming and passive extension of the Lithosphere. Journal of Geophysical Research: Solid Earth, 106(B6), 11271-11291.

I – J

Ionov, D. A., Griffin, W. L., O'Reilly, S. Y. (1997). Volatile-bearing minerals and lithophile trace elements in the upper mantle. Chemical Geology, 141(3), 153-184.

Ivanikov, V. V., Rukhlov, A. S., Bell, K. (1998). Magmatic evolution of the melilitite–carbonatite–nephelinite dyke series of the Turiy Peninsula (Kandalaksha Bay, White Sea, Russia). Journal of Petrology, 39(11-12), 2043-2059.

James, T. C. (1966). The Carbonatites of Tanganyika: a Phase of Continental-type Volcanism. DIC thesis, Imperial College, London

Johnson, E. A. (2006). Water in nominally anhydrous crustal minerals: speciation, concentration, and geologic significance. Reviews in mineralogy and geochemistry, 62(1), 117-154.

Jones, A. P., Smith, J. V., Dawson, J. B. (1983). Glasses in mantle xenoliths from Olmani, Tanzania. The Journal of Geology, 167-178.

Jones, A. P., Genge, M., Carmody, L. (2013). Carbonate melts and carbonatites. Reviews in mineralogy and geochemistry, 75(1), 289-322.

Jugo, PJ., Wilke, M., Botcharnikov, RE. (2010). Sulfur K–edge XANES analysis of natural and synthetic basaltic glasses: Implications for S speciation and S content as function of oxygen fugacity. Geochimica et Cosmochimica Acta, 74(20), 5926-5938.

Jugo, P. J. (2009). Sulfur content at sulfide saturation in oxidized magmas. Geology, 37(5), 415-418.

K

Káldos, R., Guzmics, T., Mitchell, R. H., Dawson, J. B., Milke, R., Szabó, C. (2015). A melt evolution model for Kerimasi volcano, Tanzania: Evidence from carbonate melt inclusions in jacupirangite. Lithos, 238, 101-119.

Keir, D., Bastow, I. D., Whaler, K. A., Daly, E., Cornwell, D. G., Hautot, S. (2009). Lower crustal earthquakes near the Ethiopian rift induced by magmatic processes. Geochemistry, Geophysics, Geosystems, 10(6).

Keller, J., Klaudius J., Kervyn, M., Ernst, GG., Mattsson, HB. (2010). Fundamental changes in the activity of the natrocarbonatite volcano Oldoinyo Lengai, Tanzania. Bulletin of Volcanology, 72(8), 893-912.

Keller J, Krafft M (1990) Effusive natrocarbonatite activity of Oldoinyo Lengai, June 1988. Bulletin of Volcanology, 52(8): 629-645.

Keller, J., Zaitsev, AN., Wiedenmann, D. (2006). Primary magmas at Oldoinyo Lengai: the role of olivine melilitites. Lithos, 91(1), 150-172.

Keller, J., Zaitsev, A. N. (2012). Reprint of "Geochemistry and petrogenetic significance of natrocarbonatites at Oldoinyo Lengai, Tanzania: Composition of lavas from 1988 to 2007". Lithos, 152, 47-55.

Kelley, K. A., Cottrell, E. (2009). Water and the oxidation state of subduction zone magmas. Science, 325(5940), 605-607.

Keshav, S., Gudfinnsson, G. H. (2013). Silicate liquid-carbonatite liquid transition along the melting curve of model, vapor-saturated peridotite in the system CaO-MgO-Al_2O_3-SiO_2-CO_2 from 1.1 to 2 GPa. Journal of Geophysical Research: Solid Earth, 118(7), 3341-3353.

Kessel, R., Pettke, T., Fumagalli, P. (2015). Melting of metasomatized peridotite at 4–6 GPa and up to 1200°C: an experimental approach. Contributions to Mineralogy and Petrology, 169(4), 1-19.

Kjarsgaard B, Peterson T (1991). Nephelinite–carbonatite liquid immiscibility at Shombole volcano, East Africa: Petrographic and experimental evidence. Mineralogy and Petrology, 43(4):293–314

Kjarsgaard, BA. (1998). Phase relations of a carbonated high–CaO nephelinite at 0.2 and 0.5 GPa. Journal of Petrology, 39(11–12), 2061-2075.

Kjarsgaard, BA., Hamilton, DL., Peterson, TD. (1995). Peralkaline nephelinite/carbonatite liquid immiscibility: comparison of phase compositions in experiments and natural lavas from Oldoinyo Lengai. In Carbonatite Volcanism (pp. 163-190). Springer Berlin Heidelberg

Klaudius, J., Keller, J. (2006). Peralkaline silicate lavas at Oldoinyo Lengai, Tanzania. Lithos, 91(1), 173-190.

Knipping, J. L., Behrens, H., Wilke, M., Goettlicher, J., Stabile, P. (2015). Effect of oxygen fugacity on the coordination and oxidation state of iron in alkali bearing silicate melts. Chemical Geology, 411, 143-154.

Koornneef, JM., Davies, GR., Döpp, SP., Vukmanovic, Z., Nikogosian, IK., Mason, PR. (2009). Nature and timing of multiple metasomatic events in the sub–cratonic Lithosphere beneath Labait, Tanzania. Lithos, 112, 896-912.

Koptev, A., Calais, E., Burov, E., Leroy, S., Gerya, T. (2015). Dual continental rift systems generated by plume-Lithosphere interaction. Nature Geoscience, 8(5), 388-392.

Koster van Groos, A. F. Wyllie, P. J. (1968). Liquid immiscibility in the join $NaAlSi_3O_8$–Na_2CO_3–H_2O. American Journal of Science, 266:932–967

Kress, V. C., Carmichael, I. S. (1991). The compressibility of silicate liquids containing Fe_2O_3 and the effect of composition, temperature, oxygen fugacity and pressure on their redox states. Contributions to Mineralogy and Petrology, 108(1-2), 82-92.

Kushiro, I. (1968). Compositions of magmas formed by partial zone melting of the earth's upper mantle. Journal of Geophysical Research, 73(2), 619-634.

L

Labidi, J., Cartigny, P., Birck, J. L., Assayag, N., Bourrand, J. J. (2012). Determination of multiple sulfur isotopes in glasses: A reappraisal of the MORB δ 34 S. Chemical Geology, 334, 189-198.

LaTourrette, T., Hervig, R. L., Holloway, J. R. (1995). Trace element partitioning between amphibole, phlogopite, and basanite melt. Earth and Planetary Science Letters, 135(1), 13-30.

Le Bas, MJ., Le Maitre, RW., Streckeisen, A., Zanettin, B. (1986). A chemical classification of volcanic rocks based on the total alkali-silica diagram. Journal of Petrology, 27(3), 745-750.

Le Bas, M. J. (1987). Nephelinites and carbonatites. Geological Society, London, Special Publications, 30(1), 53-83.

Le Bas, M. J. (1989). Nephelinitic and basanitic rocks. Journal of Petrology, 30(5), 1299–1312.

Le Gall, B., Nonnotte, P., Rolet, J., Benoit, M., Guillou, H., Mousseau–Nonnotte, M., Albaric, J., Deverchère, J. (2008) Rift propagation at craton margin: Distribution of faulting and volcanism in the North Tanzanian Divergence (East Africa) during Neogene times. Tectonophysics, 448(1), 1-19.

Le Maitre, R. W., Streckeisen, A., Zanettin, B., Le Bas, M. J., Bonin, B., Bateman, P., Lameyre, J. (2002). Igneous rocks. A classification and glossary of terms. Recommendations of the IUGS Subcomission on the Systematics of Igneous Rocks.

Lee, CT., Rudnick, RL, (1999). Compositionally stratified cratonic Lithosphere: petrology and geochemistry of peridotite xenoliths from the Labait volcano, Tanzania. In Proceedings of the VIIth International Kimberlite Conference (Vol. 1, pp. 503–521)

Lee, CT., Rudnick, RL., McDonough, WF., Horn, I. (2000). Petrologic and geochemical investigation of carbonates in peridotite xenoliths from northeastern Tanzania. Contributions to Mineralogy and Petrology, 139(4), 470-484.

Lee, H., Muirhead, J. D., Fischer, T. P., Ebinger, C. J., Kattenhorn, S. A., Sharp, Z. D., Kianji, G. (2016). Massive and prolonged deep carbon emissions associated with continental rifting. Nature Geoscience.

Lee, W. J., Wyllie, P. J. (1997). Liquid immiscibility between nephelinite and carbonatite from 1.0 to 2.5 GPa compared with mantle melt compositions. Contributions to Mineralogy and Petrology, 127(1-2), 1-16.

Lee, W. J., Wyllie, P. J. (1998). Processes of crustal carbonatite formation by liquid immiscibility and differentiation, elucidated by model systems. Journal of Petrology, 39(11-12), 2005-2013.

Lee, H., Muirhead, J. D., Fischer, T. P., Ebinger, C. J., Kattenhorn, S. A., Sharp, Z. D., Kianji, G. (2016). Massive and prolonged deep carbon emissions associated with continental rifting. Nature Geoscience.

Lesne, P., Scaillet, B., Pichavant, M., Iacono-Marziano, G., Beny, J. M. (2011). The H_2O solubility of alkali basaltic melts: an experimental study. Contributions to Mineralogy and Petrology, 162(1), 133-151.

Levesque, S. (1999). Rhéologie de silicates fondus et de laves partiellement cristallisés (Doctoral dissertation).

Lindenfeld, M., Rümpker, G., Link, K., Koehn, D., Batte, A. (2012). Fluid-triggered earthquake swarms in the Rwenzori region, East African Rift—Evidence for rift initiation. Tectonophysics, 566, 95-10.

M

Macdonald, R. (2012). Evolution of peralkaline silicic complexes: lessons from the extrusive rocks. Lithos, 152, 11–22.

MacDonald, R., Rogers, N. W., Fitton, J. G., Black, S., Smith, M. (2001). Plume–Lithosphere interactions in the generation of the basalts of the Kenya Rift, East Africa. Journal of Petrology, 42(5), 877-900.

MacIntyre, R. M. (1974). Age of fault movements in Tanzanian sector of East African Rift System. Nature, 247, 354-356.

MacKenzie, D. A. N., O'nions, R. K. (1991). Partial melt distributions from inversion of rare earth element concentrations. Journal of Petrology, 32(5), 1021-1091.

Mana, S., Furman, T., Carr, M. J., Mollel, G. F., Mortlock, R. A., Feigenson, M. D., Swisher, C. C. (2012). Geochronology and geochemistry of the Essimingor volcano: melting of metasomatized lithospheric mantle beneath the North Tanzanian Divergence zone (East African Rift). Lithos, 155, 310-325.

Mana, S., Furman, T., Turrin, B. D., Feigenson, M. D., Swisher, C. C. (2015). Magmatic activity across the East African North Tanzanian Divergence Zone. Journal of the Geological Society, 2014-072.

Manega, P. C. (1993). Geochronology, geochemistry and isotopic study of the Plio-Pleistocene hominid sites and the Ngorongoro volcanic highland in northern Tanzania. PhD thesis, Univerty of Colorado.

Mariano, A. N., Roeder, P. L. (1983). Kerimasi: a neglected carbonatite volcano. The Journal of Geology, 449-455.

Marks, M. A., Schilling, J., Coulson, I. M., Wenzel, T., Markl, G. (2008). The alkaline–peralkaline Tamazeght complex, High Atlas Mountains, Morocco: mineral chemistry and petrological constraints for derivation from a compositionally heterogeneous mantle source. Journal of Petrology, 49(6), 1097-1131.

Martin, L. H., Schmidt, M. W., Mattsson, H. B., Guenther, D. (2013). Element partitioning between immiscible carbonatite and silicate melts for dry and H_2O-bearing systems at 1–3 GPa. Journal of Petrology, 54, 2301-2338.

Mathez, E. A. (1984). Influence of degassing on oxidation states of basaltic magmas. Nature, 310(5976), 371-375.

Mathez, E. A., Webster, J. D. (2005). Partitioning behavior of chlorine and fluorine in the system apatite-silicate melt-fluid. Geochimica et Cosmochimica Acta, 69(5), 1275-1286.

Matthews, S. J., Moncrieff, D. H. S., Carroll, M. R. (1999). Empirical calibration of the sulphur valence oxygen barometer from natural and experimental glasses: method and applications. Mineralogical Magazine, 63(3), 421-431.

Mattsson, H. B., Nandedkar, R. H., Ulmer, P. (2013). Petrogenesis of the melilititic and nephelinitic rock suites in the Lake Natron–Engaruka monogenetic volcanic field, northern Tanzania. Lithos, 179, 175-192.

Mavrogenes, J. A., O'Neill, H. S. C. (1999). The relative effects of pressure, temperature and oxygen fugacity on the solubility of sulfide in mafic magmas. Geochimica et Cosmochimica Acta, 63(7), 1173-1180.

McCammon, C. A., Chinn, I. L., Gurney, J. J., McCallum, M. E. (1998). Ferric iron content of mineral inclusions in diamonds from George Creek, Colorado determined using Mössbauer spectroscopy. Contributions to Mineralogy and Petrology, 133(1-2), 30-37.

McCloy, J., Washton, N., Gassman, P., Marcial, J., Weaver, J., Kukkadapu, R. (2015). Nepheline crystallization in boron-rich alumino-silicate glasses as investigated by multi-nuclear NMR, Raman, Mössbauer spectroscopies. Journal of Non-Crystalline Solids, 409, 149-165.

McDonough, W. F., Sun, S. S. (1995). The composition of the Earth. Chemical geology, 120(3), 223-253.

McKenzie, D. (1978). Some remarks on the development of sedimentary basins, Earth and Planetary Science Letters, 25-32.

Mernagh, T. P., Kamenetsky, V. S., Kamenetsky, M. B. (2011). A Raman microprobe study of melt inclusions in kimberlites from Siberia, Canada, SW Greenland and South Africa. Spectrochimica Acta Part A: Molecular and Biomolecular Spectroscopy, 80(1), 82-87.

Métrich, N., Berry, A. J., O'Neill, H. S. C., Susini, J. (2009). The oxidation state of sulfur in synthetic and natural glasses determined by X-ray absorption spectroscopy. Geochimica et Cosmochimica Acta, 73(8), 2382-2399.

Métrich, N., Wallace, P. J. (2008). Volatile abundances in basaltic magmas and their degassing paths tracked by melt inclusions. Reviews in mineralogy and geochemistry, 69(1), 363-402.

Métrich, N., Allard, P., Spilliaert, N., Andronico, D., Burton, M. (2004). 2001 flank eruption of the alkali- and volatile-rich primitive basalt responsible for Mount Etna's evolution in the last three decades. Earth and Planetary Science Letters, 228(1), 1-17.

Métrich, N., Susini, J., Foy, E., Farges, F., Massare, D., Sylla, L., Bonnin-Mosbah, M. (2006). Redox state of iron in peralkaline rhyolitic glass/melt: X-ray absorption micro-spectroscopy experiments at high temperature. Chemical Geology, 231(4), 350-363.

Mitchell, R. H., Dawson, J. B. (2012). Carbonate–silicate immiscibility and extremely peralkaline silicate glasses from Nasira cone and recent eruptions at Oldoinyo Lengai Volcano, Tanzania. Lithos, 152, 40-46.

Mollel, G. F., Swisher, C. C., Feigenson, M. D., Carr, M. J. (2008). Geochemical evolution of Ngorongoro Caldera, Northern Tanzania: Implications for crust–magma interaction. Earth and Planetary Science Letters, 271(1), 337-347.

Mollel, G. F., Swisher, C. C., McHenry, L. J., Feigenson, M. D., Carr, M. J. (2009). Petrogenesis of basalt–trachyte lavas from Olmoti Crater, Tanzania. Journal of African Earth Sciences, 54(5), 127-143.

Moore, G. (2008). Interpreting H_2O and CO_2 contents in melt inclusions: constraints from solubility experiments and modeling. Reviews in Mineralogy and Geochemistry, 69(1), 333-362.

Morimoto, N. (1988). Nomenclature of pyroxenes. Mineralogy and Petrology, 39(1), 55-76.

Morizet, Y., Brooker, R. A., Kohn, S. C. (2002). CO 2 in haplo-phonolite melt: solubility, speciation and carbonate complexation. Geochimica et Cosmochimica Acta, 66(10), 1809-1820.

Morizet, Y., Paris, M., Gaillard, F., Scaillet, B. (2014). Carbon dioxide in silica-undersaturated melt. Part I: the effect of mixed alkalis (K and Na) on CO_2 solubility and speciation. Geochimica et Cosmochimica Acta, 141, 45-61.

Moune, S., Holtz, F., Botcharnikov, R. E. (2009). Sulphur solubility in andesitic to basaltic melts: implications for Hekla volcano. Contributions to Mineralogy and Petrology, 157(6), 691-707.

Moussallam, Y., Morizet, Y., Massuyeau, M., Laumonier, M., Gaillard, F. (2015). CO_2 solubility in kimberlite melts. Chemical Geology, 418, 198-205.

Moussallam, Y., Morizet, Y., Gaillard, F. (2016). H_2O–CO_2 solubility in low SiO_2-melts and the unique mode of kimberlite degassing and emplacement. Earth and Planetary Science Letters, 447, 151-160.

Moussallam, Y., Oppenheimer, C., Scaillet, B., Gaillard, F., Kyle, P., Peters, N., Donovan, A. (2014). Tracking the changing oxidation state of Erebus magmas, from mantle to surface, driven by magma ascent and degassing. Earth and Planetary Science Letters, 393, 200-209.

Mudd, G.C., Orridge, G.R. (1966). Babati. Tanzania Mineral Resources Division, Quarter Degree Sheet 85.

Mulibo, G. D., Nyblade, A. A. (2013). Mantle transition zone thinning beneath eastern Africa: Evidence for a whole-mantle superplume structure. Geophysical Research Letters, 40(14), 3562-3566.

Muravyeva, N. S., Senin, V. G. (2009). Carbonate-silicate equilibria in the high-magnesia ultrapotassic volcanics of the Toro-Ankole Province (Eastern African rift zone). Geochemistry International, 47(9), 882-900.

Muravyeva, N. S., Belyatsky, B. V., Senin, V. G., Ivanov, A. V. (2014). Sr–Nd–Pb isotope systematics and clinopyroxene-host disequilibrium in ultra-potassic magmas from Toro-Ankole and Virunga, East-African Rift: Implications for magma mixing and source heterogeneity. Lithos, 210, 260-277.

Mysen, B. O., Boettcher, A. L. (1975). Melting of a hydrous mantle: I. Phase relations of natural peridotite at high pressures and temperatures with controlled activities of water, carbon dioxide, and hydrogen. Journal of Petrology, 16(1), 520-548.

Mysen, B. O., Carmichael, I. S. E., Virgo, D. (1985). A comparison of iron redox ratios in silicate glasses determined by wet-chemical and 57Fe Mössbauer resonant absorption methods. Contributions to Mineralogy and Petrology, 90(2-3), 101-106.

Mysen, B. O., Eggler, D. H., Seitz, M. G., Holloway, J. R. (1976). Carbon dioxide in silicate melts and crystals; Part I, Solubility measurements. American Journal of Science, 276(4), 455-479.

N

Nakagawa, M., Wada, K., Wood, CP. (2002). Mixed magmas, mush chambers and eruption triggers: evidence from zoned clinopyroxene phenocrysts in andesitic scoria from the 1995 eruptions of Ruapehu volcano, New Zealand. Journal of Petrology, 43(12), 2279-2303.

Neuville, D. R., Richet, P. (1991). Viscosity and mixing in molten (Ca, Mg) pyroxenes and garnets. Geochimica et Cosmochimica Acta, 55(4), 1011-1019.

Nilsson, K., Peach, C. L. (1993). Sulfur speciation, oxidation state, and sulfur concentration in backarc magmas. Geochimica et Cosmochimica Acta, 57(15), 3807-3813.

Nonnotte, P. (2007). Etude Volcano–tectonique de La Zone de Divergence Nord Tanzanienne (Terminaison Sud Du Rift Kenyan). Caractérisation Pétrologique et Géochimique Du Volcanisme Récent (8 Ma – Actuel) et Du Manteau Source. Contraintes de Mise En Place. PhD thesis. Université de Bretagne Occidentale.

Nonnotte, P., Benoit, M., Le Gall, B., Hémond, C., Rolet, J., Cotten, J. Makoba, E. (2011). Petrology and geochemistry of alkaline lava series, Kilimanjaro, Tanzania: New constraints on petrogenetic processes. Geological Society of America Special Papers, 478, 127–158.

Nyblade, A. A., Owens, T. J., Gurrola, H., Ritsema, J., Langston, C. A. (2000). Seismic evidence for a deep upper mantle thermal anomaly beneath east Africa. Geology, 28(7), 599-602.

Nyblade, A. A., Langston, C. A. (1995). East African earthquakes below 20 km depth and their implications for crustal structure. Geophysical Journal International, 121(1), 49-62.

O – P

Oppenheimer, C., Pyle, D. M., Barclay, J. (Eds.). (2003). Volcanic degassing. Geological Society of London.

Ottonello, G., Moretti, R., Marini, L., Zuccolini, M. V. (2001). Oxidation state of iron in silicate glasses and melts: a thermochemical model. Chemical Geology, 174(1), 157-179.

Papale, P. (1999). Modeling of the solubility of a two-component H_2O+ CO_2 fluid in silicate liquids. American Mineralogist, 84(4), 477-492.

Papale, P. (1997). Modeling of the solubility of a one-component H_2O or CO_2 fluid in silicate liquids. Contributions to Mineralogy and Petrology, 126(3), 237-251.

Parat, F., Holtz, F., Feig, S. (2008). Pre-eruptive conditions of the Huerto andesite (Fish canyon system, San Juan volcanic field, Colorado): influence of volatiles (C–O–H–S) on phase equilibria and mineral composition. Journal of Petrology, 49(5), 911-935.

Parat, F., Streck, M. J., Holtz, F., Almeev, R. (2014). Experimental study into the petrogenesis of crystal-rich basaltic to andesitic magmas at Arenal volcano. Contributions to Mineralogy and Petrology, 168(2), 1-18.

Parat, F., Holtz, F. (2004). Sulfur partitioning between apatite and melt and effect of sulfur on apatite solubility at oxidizing conditions. Contributions to Mineralogy and Petrology, 147(2), 201-212.

Parat, F., Holtz, F., Klügel, A. (2011). S-rich apatite-hosted glass inclusions in xenoliths from La Palma: constraints on the volatile partitioning in evolved alkaline magmas. Contributions to Mineralogy and Petrology, 162(3), 463-478.

Paris, E., Giuli, G., Carroll, M. R., Davoli, I. (2001). The valence and speciation of sulfur in glasses by X-ray absorption spectroscopy. The Canadian Mineralogist, 39(2), 331-339.

Parkinson, I. J., Arculus, R. J. (1999). The redox state of subduction zones: insights from arc-peridotites. Chemical Geology, 160(4), 409-423.

Paslick, C. R., Halliday, A. N., Lange, R. A., James, D., Dawson, J. B. (1996). Indirect crustal contamination: evidence from isotopic and chemical disequilibria in minerals from alkali basalts and nephelinites from northern Tanzania. Contributions to Mineralogy and Petrology, 125(4), 277-292.

Paslick, C., Halliday, A., James, D., Dawson, J. B. (1995). Enrichment of the continental Lithosphere by OIB melts: isotopic evidence from the volcanic province of northern Tanzania. Earth and Planetary Science Letters, 130(1), 109-126.

Paterson, MS. (1982). The determination of hydroxyl by infrared absorption in quartz, silicate glasses, and similar materials. Bulletin de la Société Francaise de Minéralogie et Cristallographie, 105, 20–29.

Peterson, T. D. (1989). Peralkaline nephelinites. I. Comparative petrology of Shombole and Oldoinyo L'engai, East Africa. Contributions to Mineralogy and Petrology, 101(4), 458-478.

Pik, R., Marty, B., Hilton, D. R. (2006). How many mantle plumes in Africa? The geochemical point of view. Chemical Geology, 226(3), 100-114.

Plasman, M., Tiberi, C., Ebinger, C., and coworkers (in prep) Lithospheric structure of the North Tanzanian Divergence, East African rift, estimated from Receiver Functions.

Platz, T., Foley, S. F., André, L. (2004). Low-pressure fractionation of the Nyiragongo volcanic rocks, Virunga Province, DR Congo. Journal of Volcanology and Geothermal research, 136(3), 269-295.

Pommier, A., Le-Trong, E. (2011). "SIGMELTS": A web portal for electrical conductivity calculations in geosciences. Computers Geosciences, 37(9), 1450-1459.

Pouclet, A., Bellon, H., Bram, K. (2016). The Cenozoic volcanism in the Kivu rift: Assessment of the tectonic setting, geochemistry, and geochronology of the volcanic activity in the South-Kivu and Virunga regions. Journal of African Earth Sciences.

Pouclet, A., Menot, R. P., Piboule, M. (1981). Discriminant factor-analysis applied to central africa rift lavas (Zaire, Rwanda, Uganda). Comptes Rendus De L Academie Des Sciences Serie II, 292(8), 679.

Prowatke, S., Klemme, S. (2005). Effect of melt composition on the partitioning of trace elements between titanite and silicate melt. Geochimica et Cosmochimica Acta, 69(3), 695-709.

Putirka, K. (1999). Clinopyroxene+ liquid equilibria to 100 kbar and 2450 K. Contributions to Mineralogy and Petrology, 135(2-3), 151-163.

Putirka KD (2008). Thermometers and barometers for volcanic systems. Reviews in mineralogy and geochemistry, 69(1):61–120.

Putirka, K. D., Perfit, M., Ryerson, F. J., Jackson, M. G. (2007). Ambient and excess mantle temperatures, olivine thermometry, and active vs. passive upwelling. Chemical Geology, 241(3), 177–206.

Pyle, D. M., Dawson, J. B., Ivanovich, M. (1991). Short-lived decay series disequilibria in the natrocarbonatite lavas of Oldoinyo Lengai, Tanzania: constraints on the timing of magma genesis. Earth and Planetary Science Letters, 105(4), 378-396.

R

Ravel, B., Newville, M. (2005). ATHENA, ARTEMIS, HEPHAESTUS: data analysis for X-ray absorption spectroscopy using IFEFFIT. Journal of synchrotron radiation, 12(4), 537-541.

Ren, M., Omenda, P. A., Anthony, E. Y., White, J. C., Macdonald, R., Bailey, D. K. (2006). Application of the QUILF thermobarometer to the peralkaline trachytes and pantellerites of the Eburru volcanic complex, East African Rift, Kenya. Lithos, 91(1), 109-124.

Rhodes, J. M., Dungan, M. A., Blanchard, D. P., Long, P. E. (1979). Magma mixing at mid-ocean ridges: evidence from basalts drilled near 22 N on the Mid-Atlantic Ridge. Tectonophysics, 55(1-2), 35-61.

Roeder, P. L., Emslie, R. (1970). Olivine-liquid equilibrium. Contributions to mineralogy and petrology, 29(4), 275-289.

Roex, A. P., Späth, A., Zartman, R. E. (2001). Lithospheric thickness beneath the southern Kenya Rift: implications from basalt geochemistry. Contributions to Mineralogy and Petrology, 142(1), 89–106.

Rogers, N. W., Hawkesworth, C. J., Palacz, Z. A. (1992). Phlogopite in the generation of olivine-melilitites from Namaqualand, South Africa and implications for element fractionation processes in the upper mantle. Lithos, 28(3), 347-365.

Rosenthal, A., Foley, S. F., Pearson, D. G., Nowell, G. M., Tappe, S. (2009). Petrogenesis of strongly alkaline primitive volcanic rocks at the propagating tip of the western branch of the East African Rift. Earth and Planetary Science Letters, 284(1), 236-248.

Rosenthal, A., Hauri, E. H., Hirschmann, M. M. (2015). Experimental determination of C, F, and H partitioning between mantle minerals and carbonated basalt, CO_2/Ba and CO_2/Nb systematics of partial melting, and the CO_2 contents of basaltic source regions. Earth and Planetary Science Letters, 412, 77-87.

Rubin, A. M., Pollard, D. D. (1988). Dike-induced faulting in rift zones of Iceland and Afar. Geology, 16(5), 413-417.

Rudnick, R. L., McDonough, W. F., Chappell, B. W. (1993). Carbonatite metasomatism in the northern Tanzanian mantle: petrographic and geochemical characteristics. Earth and Planetary Science Letters, 114(4), 463-475.

Rudnick, R. L., Ireland, T. R., Gehrels, G., Irving, A. J., Chesley, J. T., Hanchar, J. M. (1999). Dating mantle metasomatism: U–Pb geochronology of zircons in cratonic mantle xenoliths from Montana and Tanzania. In Proceedings of the 7th International Kimberlite Conference (Vol. 2, pp. 728–735).

S

Sack, R. O., Carmichael, I. S. E., Rivers, M. L., Ghiorso, M. S. (1980). Ferric-ferrous equilibria in natural silicate liquids at 1 bar. Contributions to Mineralogy and Petrology, 75(4), 369-376.

Sato, K., Katsura, T., Ito, E. (1997). Phase relations of natural phlogopite with and without enstatite up to 8 GPa: implication for mantle metasomatism. Earth and Planetary Science Letters, 146(3), 511-526.

Scaillet, B., Macdonald, R. (2006). Experimental and thermodynamic constraints on the sulphur yield of peralkaline and metaluminous silicic flood eruptions. Journal of Petrology, 47(7), 1413-1437.

Schiano, P. (2003). Primitive mantle magmas recorded as silicate melt inclusions in igneous minerals. Earth-Science Reviews, 63(1), 121-144.

Sekisova, V. S., Sharygin, V. V., Zaitsev, A. N., Strekopytov, S. (2015). Liquid immiscibility during crystallization of forsterite-phlogopite ijolites at Oldoinyo Lengai Volcano, Tanzania: study of melt inclusions. Russian Geology and Geophysics, 56(12), 1717-1737.

Selby. J., Thomas, C. (1966). Balangida Lelu, Quarter Degree Sheet 103. Tanzania Mineral Resources Division

Selway, K., Yi, J., Karato, S. I. (2014). Water content of the Tanzanian Lithosphere from magnetotelluric data: implications for cratonic growth and stability. Earth and Planetary Science Letters, 388, 175–186.

Sharygin, V. V., Kamenetsky, V. S., Zaitsev, A. N., Kamenetsky, M. B. (2012). Silicate–natrocarbonatite liquid immiscibility in 1917 eruption combeite–wollastonite nephelinite, Oldoinyo Lengai Volcano, Tanzania: Melt inclusion study. Lithos, 152, 23-39.

Shaw, D. M. (1970). Trace element fractionation during anatexis. Geochimica et Cosmochimica Acta, 34(2), 237-243.

Shelly, D. R., Beroza, G. C., Ide, S., Nakamula, S. (2006). Low-frequency earthquakes in Shikoku, Japan, and their relationship to episodic tremor and slip. Nature, 442(7099), 188-191.

Shishkina, T. A., Botcharnikov, R. E., Holtz, F., Almeev, R. R., Jazwa, A. M., & Jakubiak, A. A. (2014). Compositional and pressure effects on the solubility of H 2 O and CO 2 in mafic melts. Chemical Geology, 388, 112-129.

Sifré, D., Gardés, E., Massuyeau, M., Hashim, L., Hier-Majumder, S., Gaillard, F. (2014). Electrical conductivity during incipient melting in the oceanic low-velocity zone. Nature, 509(7498), 81-85.

Signorelli, S., Carroll, M. R. (2000). Solubility and fluid-melt partitioning of Cl in hydrous phonolitic melts. Geochimica et Cosmochimica Acta, 64(16), 2851-2862.

Simonetti, A., Shore, M., Bell, K. (1996). Diopside phenocrysts from nephelinite lavas, Napak Volcano, eastern Uganda; evidence for magma mixing. The Canadian Mineralogist, 34(2), 411-421.

Spilliaert, N., Allard, P., Métrich, N., Sobolev, A. V. (2006). Melt inclusion record of the conditions of ascent, degassing, and extrusion of volatile-rich alkali basalt during the powerful 2002 flank eruption of Mount Etna (Italy). Journal of Geophysical Research: Solid Earth, 111(B4).

Stagno, V., Frost, D. J. (2010). Carbon speciation in the asthenosphere: Experimental measurements of the redox conditions at which carbonate-bearing melts coexist with graphite or diamond in peridotite assemblages. Earth and Planetary Science Letters, 300(1), 72-84.

Stamps, D. S., Calais, E., Saria, E., Hartnady, C., Nocquet, J. M., Ebinger, C. J., Fernandes, R. M. (2008). A kinematic model for the East African Rift. Geophysical Research Letters, 35(5).

Streck, M. J., Dungan, M. A., Bussy, F., Malavassi, E. (2005). Mineral inventory of continuously erupting basaltic andesites at Arenal volcano, Costa Rica: implications for interpreting monotonous, crystal-rich, mafic arc stratigraphies. Journal of Volcanology and Geothermal Research, 140(1), 133-155.

Stuart, G. W., Bastow, I. D., Ebinger, C. J. (2006). Crustal structure of the northern Main Ethiopian Rift from receiver function studies. Geological Society, London, Special Publications, 259(1), 253-267.

Sun SS, McDonough WF (1989) Chemical and isotopic systematics of oceanic basalts: implications for mantle composition and processes. Geological Society, London, Special Publications, 42(1):313–345

T

Takei, Y. (2002). Effect of pore geometry on Vp/Vs: From equilibrium geometry to crack. Journal of Geophysical Research: Solid Earth, 107(B2).

Tenner, T. J., Hirschmann, M. M., Humayun, M. (2012). The effect of H_2O on partial melting of garnet peridotite at 3.5 GPa. Geochemistry, Geophysics, Geosystems, 13(3), Q03016.

Thomas, C. (1966) Hanang, Quarter Degree Sheet 84. Tanzania Mineral Resources Division.

Thompson, G., Smith, I., Malpas, J. (2001). Origin of oceanic phonolites by crystal fractionation and the problem of the Daly gap: an example from Rarotonga. Contributions to Mineralogy and Petrology, 142(3), 336-346.

Tommasi, A., Vauchez, A. (2001). Continental rifting parallel to ancient collisional belts: an effect of the mechanical anisotropy of the Lithospheric mantle. Earth and Planetary Science Letters, 185(1), 199-210.

Toplis, M. J., Carroll, M. R. (1995). An experimental study of the influence of oxygen fugacity on Fe-Ti oxide stability, phase relations, and mineral-melt equilibria in ferro-basaltic systems. Journal of Petrology, 36(5), 1137-1170.

V

Vauchez, A., Dineur, F., Rudnick, R. (2005). Microstructure, texture and seismic anisotropy of the lithospheric mantle above a mantle plume: insights from the Labait volcano xenoliths (Tanzania). Earth and Planetary Science Letters, 232(3), 295-314.

Veksler, I. V., Dorfman, A. M., Dulski, P., Kamenetsky, V. S., Danyushevsky, L. V., Jeffries, T., Dingwell, D. B. (2012). Partitioning of elements between silicate melt and immiscible fluoride, chloride, carbonate, phosphate and sulfate melts, with implications to the origin of natrocarbonatite. Geochimica et Cosmochimica Acta, 79, 20-40.

Veksler, I. V., Nielsen, T. F. D., Sokolov, S. V. (1998). Mineralogy of crystallized melt inclusions from Gardiner and Kovdor ultramafic alkaline complexes: implications for carbonatite genesis. Journal of Petrology, 39(11-12), 2015-2031.

Vernet, M., Marin, L., Boulmier, S., Lhomme, J., Demange, J. C. (1987). Dosage du fluor et du chlore dans les matériaux géologiques y compris les échantillons hyperalumineux. Analusis, 15(9), 490-498.

Vetere, F., Holtz, F., Behrens, H., Botcharnikov, R. E., Fanara, S. (2014). The effect of alkalis and polymerization on the solubility of H_2O and CO_2 in alkali-rich silicate melts. Contributions to Mineralogy and Petrology, 167(5), 1-17.

W

Wade, J. A., Plank, T., Hauri, E. H., Kelley, K. A., Roggensack, K., Zimmer, M. (2008). Prediction of magmatic water contents via measurement of H_2O in clinopyroxene phenocrysts. Geology, 36(10), 799-802.

Wallace, P., Carmichael, I. S. (1992). Sulfur in basaltic magmas. Geochimica et Cosmochimica Acta, 56(5), 1863-1874.

Wallace, P. J., Edmonds, M. (2011). The sulfur budget in magmas: evidence from melt inclusions, submarine glasses, and volcanic gas emissions. Reviews in mineralogy and geochemistry, 73(1), 215-246.

Webster, J. D., Goldoff, B., Sintoni, M. F., Shimizu, N., De Vivo, B. (2014). C–O–H–Cl–S–F volatile solubilities, partitioning, and mixing in phonolitic–trachytic melts and aqueous–carbonic vapor±saline liquid at 200 MPa. Journal of Petrology, 55, 2217-2248.

Webster, J. D., Holloway, J. R. (1990). Partitioning of F and Cl between magmatic hydrothermal fluids and highly evolved granitic magmas. Geological Society of America Special Papers, 246, 21-34.

Webster, J. D., Kinzler, R. J., Mathez, E. A. (1999). Chloride and water solubility in basalt and andesite melts and implications for magmatic degassing. Geochimica et Cosmochimica Acta, 63(5), 729-738.

White, B. S., Wyllie, P. J. (1992). Solidus reactions in synthetic lherzolite-H_2O-CO_2 from 20–30 kbar, with applications to melting and metasomatism. Journal of Volcanology and Geothermal Research, 50(1-2), 117-130.

Whittington, A., Richet, P., Holtz, F. (2000). Water and the viscosity of depolymerized aluminosilicate melts. Geochimica et Cosmochimica Acta, 64(21), 3725-3736.

Wilke, M., Farges, F., Petit, P. E., Brown, G. E., Martin, F. (2001). Oxidation state and coordination of Fe in minerals: An Fe K-XANES spectroscopic study. American Mineralogist, 86(5-6), 714-730.

Wilke, M., Partzsch, G. M., Bernhardt, R., Lattard, D. (2005). Determination of the iron oxidation state in basaltic glasses using XANES at the K-edge. Chemical Geology, 220(1), 143-161.

Wilke, M., Klimm, K., Kohn, S. C. (2011). Spectroscopic studies on sulfur speciation in synthetic and natural glasses. Reviews in mineralogy and geochemistry, 73(1), 41-78.

Wilkinson, P., Mitchell, J. G., Cattermole, P. J., Downie, C. (1986). Volcanic chronology of the Men–Kilimanjaro region, Northern Tanzania. Journal of the Geological Society, 143(4), 601–605.

Wölbern, I., Rümpker, G., Link, K., Sodoudi, F. (2012). Melt infiltration of the lower Lithosphere beneath the Tanzania craton and the Albertine rift inferred from S receiver functions. Geochemistry, Geophysics, Geosystems, 13(8).

Wood, B. J., Trigila, R. (2001). Experimental determination of aluminous clinopyroxene–melt partition coefficients for potassic liquids, with application to the evolution of the Roman province potassic magmas. Chemical Geology, 172(3), 213-223.

Wood, CP. (1968). A Geochemical Study of East African Alkaline Lavas and its Relevance to the Petrogenesis of Nephelinites. PhD thesis, University of Leeds.

Woodland, A. B., Kornprobst, J., Tabit, A. (2006). Ferric iron in orogenic lherzolite massifs and controls of oxygen fugacity in the upper mantle. Lithos, 89(1), 222-241.

Woolley, A. R., Kjarsgaard, B. A. (2008). Paragenetic types of carbonatite as indicated by the diversity and relative abundances of associated silicate rocks: evidence from a global database. The Canadian Mineralogist, 46(4), 741-752.

Woolley, A. R., Bergman, S. C., Edgar, A. D., Le Bas, M. J., Mitchell, R. H., Rock, N. M., Scott Smith, B. H. (1996). Classification of lamprophyres, lamproites, kimberlites, and the kalsilitic, melilitic, and leucitic rocks. The Canadian Mineralogist, 34, 175–186.

Wörner, G., Schmincke, H. U. (1984). Mineralogical and chemical zonation of the Laacher See tephra sequence (East Eifel, W. Germany). Journal of Petrology, 25(4), 805-835.

Wright, T. J., Ebinger, C., Biggs, J., Ayele, A., Yirgu, G., Keir, D., Stork, A. (2006). Magma-maintained rift segmentation at continental rupture in the 2005 Afar dyking episode. Nature, 442(7100), 291-294.

Z

Zaitsev, A. N., Keller, J., Spratt, J., Jeffries, T. E., Sharygin, V. V. (2009). Chemical composition of nyerereite and gregoryite from natrocarbonatites of Oldoinyo Lengai volcano, Tanzania. Geology of Ore Deposits, 51(7), 608-616.

Zaitsev, A. N., Marks, M. A. W., Wenzel, T., Spratt, J., Sharygin, V. V., Strekopytov, S., Markl, G. (2012). Mineralogy, geochemistry and petrology of the phonolitic to nephelinitic Sadiman volcano, Crater Highlands, Tanzania. Lithos, 152, 66-83.

Annexes

Annexe A - Minéraux riches en volatils dans les phonolites
Annexe B - Liste des échantillons et données complémentaires
Annexe C - Données géochimiques des laves de la divergence nord tanzanienne

Annexe A

A.I Résumé de l'étude et spéciation du soufre des haüynes et des noséanes

A.I.1 Résumé de l'étude (Baudouin et Parat 2015)

Les éléments volatils jouent un rôle clé dans la genèse des magmas alcalins et dans les processus magmatiques. L'étude des éléments volatils présents dans les laves alcalines a été approfondie dans le chapitre 3. Il y a plusieurs méthodes pour déterminer la concentration des éléments volatils dans les laves. L'étude des éléments volatils en roche totale est insuffisante dû au dégazage important qui affecte le magma lors de la remontée. Les inclusions vitreuses, qui sont sans aucun doute des outils très puissants pour contraindre les conditions éruptives sont néanmoins rares, et donc leur faible abondance implique que tous les systèmes volcaniques ne peuvent pas être caractérisés. Les éléments volatils (F, S, Cl) peuvent également être étudiés à travers les minéraux accessoires (apatite, sodalite) afin de contraindre leurs rôles lors de la genèse et la différenciation des magmas ainsi que leurs conditions éruptives.

Dans les roches volcaniques alcalines et sous saturées en silice, la présence des minéraux du groupe des sodalites implique que les magmas sont riches en éléments volatils dans le volcanisme intracontinental (Holm et al. 2006, Bryan 2006, Brousse et al. 1969; Wörner et Schmincke 1984a; De Fino et al. 1986). Les minéraux du groupe de la sodalite (i.e. haüyne, nosean, lazurite) incorporent du soufre et du chlore dans leur structure cristalline. Les sodalites sont des minéraux clés pour caractériser les concentrations, la spéciation des éléments volatils et les conditions pré-éruptives ainsi qu'étudier le comportement des éléments volatils pendant la différenciation magmatique et le dégazage.

Les sodalites ont été observées dans de nombreuses roches volcaniques mafiques à felsiques, mais sont majoritairement présentes dans les phonolites (review dans Parat et al. 2011). Une compilation des phonolites à « sodalites » a permis de mettre en évidence 2 groupes : (1) les phonolites riches en silice avec des haüynes (Wörner et Schmincke 1984a; Holm et al. 2006; Bryan 2006) et (2) les phonolites pauvres en silice avec des noséanes (Berger et al. 2009, Brousse et al. 1969). L'étude de ces 2 groupes de phonolites (haüynes et noséanes) est une opportunité d'une part, de contraindre les conditions de cristallisation des minéraux du groupe des sodalites, et d'autre part d'apporter de nouvelles contraintes sur les conditions prééruptives des magmas phonolitiques en contexte intracontinental.

Les environnements de cristallisation des 2 types de phonolites (phonolites à haüyne : Eifel, Allemagne ; phonolites à noséane: Saghro, Maroc) sont très différents.

Dans le cas des phonolites à haüyne (55-59 pds% SiO_2, K > Na), la faible activité de la silice et du sodium permet la cristallisation précoce de l' haüyne riche en soufre (13 pds% SO_3) et de l'apatite (0,8 pds% SO_3) suivit par la cristallisation du clinopyroxene et des feldspaths. Cette cristallisation survint à faible pression et température (250 MPa, 850 °C) et dans des conditions oxydantes (ΔNNO). La cristallisation de l'haüyne se produit dans un

environnement sous saturé en fluide (6 pds% H_2O, 0,2 pds% Cl, 0,11-0,4 pds% S et 0,1 pds% F).

Les phonolites à noséane (52-54 pds% SiO_2, K < Na) cristallisent à plus haute pression et température (300 MPa, 950 °C) et dans des conditions légèrement moins oxydantes. La réaction, qui permet de former des noséanes, requière des activités en silice et sodium élevées. L'assemblage minéralogique suggère une cristallisation précoce de la néphéline suivie par la noséane (8 pds% SO_3, 1 pds% Cl). La séquence de cristallisation est la suivante : cpx, néphéline avec des apatites pauvres en S (< 0,04 pds% S) et des pyrrhotites suivies par la cristallisation des noséanes et des titanites. La cristallisation de la noséane se produit dans un environnement sous saturé en fluide (4 pds% H_2O, < 0,25 pds% Cl, < 0,05 pds% S et 0,1 pds% F, de plus, Cl peut s'être exsolvé pendant la remontée du magma et formé une phase riche en NaCl).

L'haüyne et la noséane cristallisent dans des conditions pré-éruptives oxydantes et riches en éléments volatils. Ces minéraux enregistrent les concentrations des éléments volatils en profondeur et peuvent être utilisés comme oxybaromètre. La concentration initiale en éléments volatils des magmas néphélinitiques (magmas primaires) ou directement lors de la fusion partielle d'une roche mantellique riche en volatils et en potassium (Laporte et al. 2014), est un des principaux facteurs favorisant la cristallisation d'une phonolite à haüyne (riche en Si et K) ou d'une phonolite à noséane (pauvre en Si) dans les contextes de volcanisme intraplaque.

En conclusion, les minéraux accessoires comme la sodalite permettent d'apporter des contraintes sur l'évolution magmatique des laves alcalines et sur les conditions pré-éruptives. Ce type d'étude (Baudouin et Parat 2015) est primordial pour étudier les éléments volatils dans des laves alcalines dépourvues d'inclusions vitreuses.

A.I.2 Spéciation du soufre dans les haüynes et les noséanes

Les analyses WDS (Fig.A.1) permettent d'établir que l'haüyne d'Eifel et la noséane contiennent majoritairement du soufre sous sa forme oxydée (S^{6+}). Le décalage du pic WDS pour les noséanes (S^{6+}/S^{tot} = 0,87 ± 0,04) indiquent qu'au moins 10 % du soufre est sous sa forme réduite et que le S^{2-} est davantage présent dans la noséane que dans l'haüyne (S^{6+}/S^{tot} = 0,91 ± 0,04). Il est néanmoins difficile de contraindre la spéciation du Soufre avec cette méthode. En effet, le décalage du pic ne permet pas de spécifier sous quelle forme se trouve le Soufre (S^-, S^{2-}, S^0). Pour vérifier la présence de soufre réduit dans les minéraux de type 'sodalite', ces minéraux ont été analysés par la méthode XANES (ESRF, ID21). Cette méthode est la plus précise pour la détermination de la spéciation du soufre (voir chapitre V pour la méthodologie).

Dans les spectres XANES (Fig.A.2), l'haüyne d'Eifel possède seulement le pic caractéristique du S^{6+} (2,4825 keV). La noséane possède 2 pics, le plus important est celui du S^{6+}, le pic mineur a une énergie de 2,4718 keV. Ce pic peut correspondre au S^{2-} (2,4702 keV) mais il est plus proche de celui du S^- (2,4721 keV). A partir des analyses des spectres

XANES, on peut établir le rapport des intensités des aires de S^{2-} (2,4577-2 ,480 keV) et S^{6+} (2.4815-2.484 keV). Le rapport S^{6+}/S^{tot} est de 0,93 pour l' haüyne et le rapport de S^{6+}/S^{tot} pour les 5 grains de noséanes varient de 0,75 à 0,88. Des études récentes ont montré que les minéraux du groupe de la sodalite (i.e. lazurite) peuvent contenir du soufre S_2^- ou S_3^- (e.g. [1] Finch et al. 206, [2] Gambardella et al. 2016, [3] Tauson et al. 2005).

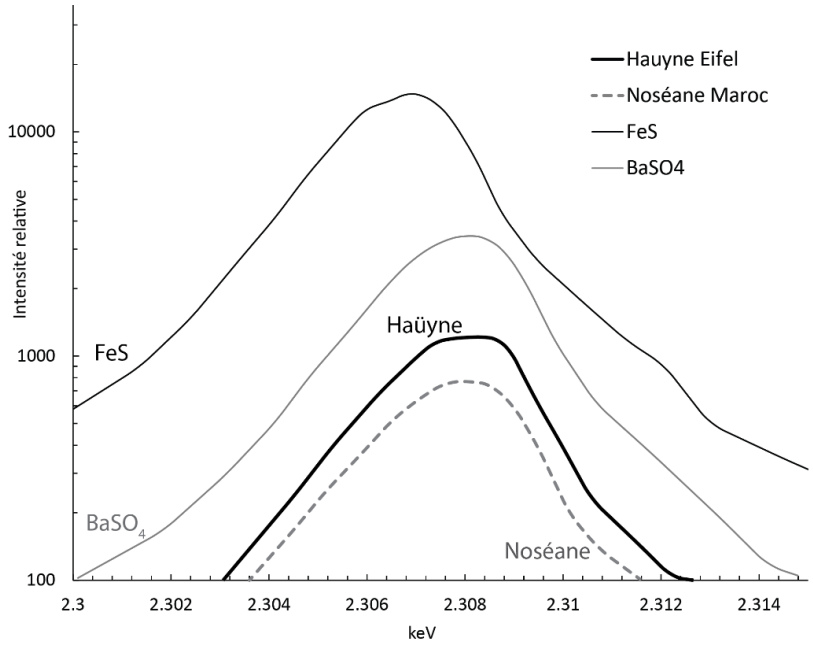

Fig.A.1 : Spectre WDS représentatif de l'haüyne d'Eifel et de la noséane du Saghro avec les spectres des standards FeS et $BaSO_4$

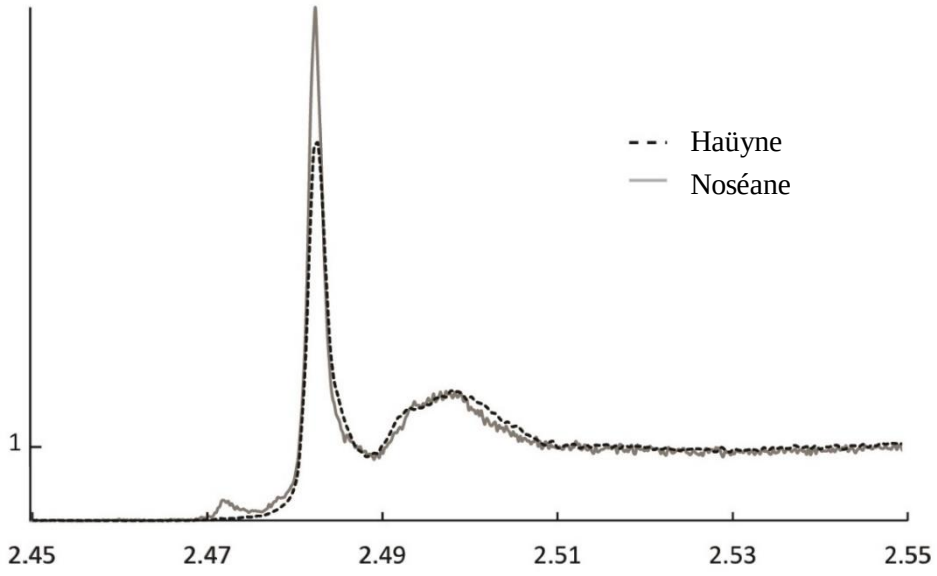

Fig.A.2 : Spectre Xanes représentatif de l' haüyne d'Eifel et de la noséane du Saghro. Le pic du S^{6+} est à 2,4825 keV. La noséane a un second pic autour de 2,4718 keV.

Références : [1] Finch, A. A., Friis, H., & Maghrabi, M. (2016). Defects in sodalite-group minerals determined from X-ray-induced luminescence. Physics and Chemistry of Minerals, 1-11. [2] Gambardella, A. A., Patterson, C. M. S., Webb, S. M., & Walton, M. S. (2016). Sulfur K-edge XANES of lazurite: Toward determining the provenance of lapis lazuli. Microchemical Journal, 125, 299-307. [3] Tauson, V. L., Goettlicher, J., Sapozhnikov, A. N., Mangold, S., & Lustenberg, E. E. (2012). Sulphur speciation in lazurite-type minerals (Na, Ca) 8 [Al6Si6O24](SO4, S) 2 and their annealing products: a comparative XPS and XAS study. European Journal of Mineralogy, 24(1), 133-152.

American Mineralogist, Volume 100, pages 2308–2322, 2015

SPECIAL COLLECTION: GLASSES, MELTS, AND FLUIDS, AS TOOLS FOR UNDERSTANDING VOLCANIC PROCESSES AND HAZARDS

Role of volatiles (S, Cl, H_2O) and silica activity on the crystallization of haüyne and nosean in phonolitic magmas (Eifel, Germany and Saghro, Morocco)†

CÉLINE BAUDOUIN[1,*] AND FLEURICE PARAT[1]

[1]Géosciences Montpellier, UMR 5243, CC 60, Université Montpellier, Place Eugène Bataillon, 34095 Montpellier cedex 5, France

ABSTRACT

To constrain the crystallization of alkaline and volatile-rich lavas present in intraplate settings, we studied the petrological features and the geochemical composition of major, trace, and volatile elements of mineral and bulk-rock of two sodalite-bearing phonolites: (1) haüyne-plagioclase-bearing Si-K-rich phonolite from Laacher See (Germany) and (2) nosean-nepheline-bearing Si-poor phonolite from Saghro (Morocco). In haüyne-bearing phonolites (55–59 wt% SiO_2, K > Na, Na+K/Al = 0.96–1.08), we found that the low silica and low sodium activity promoted the early crystallization of S-rich haüyne (13.7–13.9 wt% SO_3, 0.4 wt% Cl) + S-rich apatite (0.7–0.9 wt% SO_3), titanite, and rare pyrrhotite followed by clinopyroxene-plagioclase-sanidine at relatively low pressure and temperature (P = 250 MPa and T = 850 °C) and oxidized condition (ΔNNO-NNO+1, where NNO is nickel-nickel oxide buffer). The crystallization of haüyne occurred at fluid-undersaturated conditions from a silicate melt with 6 wt% H_2O, 0.17–0.23 wt% Cl, 0.11–0.4 wt% S, and 0.07–0.14 wt% F. Nosean-bearing phonolites from Saghro are silica-poor and peralkaline (52–54 wt% SiO_2, Na > K, Na+K/Al = 1.2) and crystallized at higher P and T (300 MPa and 950 °C) and more reduced conditions (NNO) compared to haüyne-bearing phonolites. The incongruent reaction to form nosean requires high silica and Na_2O activity. The mineral assemblage and composition suggest early crystallization of nepheline followed by nosean (7.8–8.8 wt% SO_3; 1–1.1 wt% Cl). The sequence of crystallization is: clinopyroxene + nepheline + S-poor apatite (<0.04 wt% SO_3) + pyrrhotite followed by nosean and titanite. Nosean-bearing magmas are fluid-undersaturated with relatively low volatile content (4 wt% H_2O, <0.25 wt% Cl, <0.056 wt% S, 0.08–0.1 wt% F), although Cl may have exsolved during ascent and formed a fluid phase (NaCl-bearing).

Both haüyne- and nosean-bearing phonolites are last equilibrated at relatively low pressure and high temperature. Haüyne and nosean crystallized at oxidized and volatile-rich pre-eruptive conditions. They record the volatile concentrations at depth and may be used as oxybarometer. The incongruent reactions involved to form haüyne and nosean suggest that phonolitic magmas became more oxidized during crystallization. The initial volatile concentrations in basanite/nephelinite magmas, from partial melting of volatile-bearing K_2O-rich mantle rock, should have been one important factor influencing the crystallization of haüyne-bearing Si-K-rich phonolite and nosean-bearing Si-poor phonolite in intracontinental setting.

Keywords: Phonolite, sodalite, haüyne, nosean, volatile elements, pre-eruptive conditions

INTRODUCTION

In alkaline- and silica-undersaturated volcanic rocks, the presence of minerals of the sodalite group [volatile-bearing feldspathoid mineral $Na_8(AlSiO_4)_6(Cl_2,SO_4)$] attests to the presence of volatile in magmas and possible deep magmatic fluids in both oceanic (e.g., Cape Verde: Holm et al. 2006, Canary island: Bryan 2006) and continental intraplate setting (Brousse et al. 1969; Wörner and Schmincke 1984a; De Fino et al. 1986). Sodalite minerals are phenocrysts and incorporate volatile elements such as Cl and S. Therefore they are key minerals to characterize volatile concentrations and speciation at pre-eruptive conditions, constrain the behavior of volatile elements during magma differentiation and ascent (e.g., crystallization and degassing), and address the question of the role and origin of volatile elements in alkaline magma genesis.

Sodalite minerals have been reported in mafic and felsic alkaline magmatic rock compositions from tephrite to phonolite, but are predominantly present in phonolite (review in Parat et al. 2011b). Phonolites are alkali-rich and silica-rich magmas and the processes involved for their genesis are still under debated including (1) fractionational crystallization from low-silica melts, with nephelinite, basanite, and melilitite primary compositions (Edgar 1987; Thompson et al. 2001; Wedepohl et al. 1994; Wörner and Schmincke 1984b), (2) direct melting or fractionating of the mantle (Price and Green 1972; Bailey 1987; Laporte

* E-mail: baudouin@gm.univ-montp2.fr

† Special collection papers can be found on GSW at http://ammin.geoscienceworld.org/site/misc/specialissuelist.xhtml.

0003-004X/15/0010–2308$05.00/DOI: http://dx.doi.org/10.2138/am-2015-5318

et al. 2014), or (3) remelting of basanite (Legendre et al. 2005).

Phonolites can erupt explosively or form extrusive dome as a result of variable volatile concentration at depth. However, published data on volatile concentrations and speciations are scarce. Interestingly, among sodalite-bearing phonolites, we identified two groups: (1) Si-rich phonolite with haüyne (Wörner and Schmincke 1984a; Holm et al. 2006; Bryan 2006) and (2) Si-poor phonolite with nosean (Brousse et al. 1969; Berger et al. 2009) or only sodalite (Klaudius and Keller 2006; Zaitsev et al. 2012) (Fig. 1).

These two groups of phonolites with haüyne or nosean represent a unique opportunity to constrain the condition of crystallization of sodalite minerals in natural environments. We selected two samples, one with haüyne and one with nosean, and investigated in detail the mineralogy and geochemistry: (1) haüyne-bearing Si-rich phonolite, a tephra from Laacher See (Eifel, Germany) and (2) nosean-bearing Si-poor phonolite, a lava dome from Saghro volcanic field, Morocco (Fig. 1). We combine an extensive multi-method geochemical study of major, minor, and trace elements including volatile elements in sodalite, silicate minerals, apatite, titanite, pyrrhotite, and bulk rock. We determined the phase assemblage, mineral-melt equilibrium, and volatile concentration and speciation in phonolite at depth and constrained the pre-eruptive conditions and the crystallization environment of phonolitic magmas in intracontinental settings.

SODALITE GROUP MINERALS IN MAGMATIC ROCKS

Sodalite (cubic, $P43n$) is a high-temperature, low-pressure mineral, crystallizing well above the solidus in sodic silica-undersaturated magmas enriched in NaCl, and its presence constrains NaCl activities in magmas (Sharp et al. 1989). Sodalite group minerals are alkali- and volatile-bearing mineral with solid solutions evolving between 4 end-members: Na-Ca(-K) end-members and Cl-S end-members $Na_8(AlSiO_4)_6(Cl_2,SO_4)$-$(Na,Ca)_{4-8}(AlSiO_4)_6(SO_4,S)$ (Tomisaka and Eugster 1968): sodalite (Na-Cl sodalite), nosean (Na-S-Cl sodalite), and haüyne (Na-Ca-S sodalite). Only few experimental and thermodynamic studies have been performed to constrain the stability of sodalite group minerals at high pressure and high temperature (Tomisaka and Eugster 1968; Stormer and Carmichael 1971). They showed that a complete solid solution exists between nosean and haüyne at 600 °C and 100 MPa, whereas the solid solution sodalite-nosean and sodalite-haüyne is limited, as Cl^- and SO_4^{2-} substitute with much more difficulty than Ca^{2+} and Na^+ (Van Peteghem and Burley 1963). The presence of volatile elements such as S and Cl as well as H_2O and CO_2 in haüyne (up to 1 and 0.75 wt%, respectively, Bellatreccia et al. 2009) in the structural cavities of the mineral is directly linked to the composition of magmatic silicate liquid from which they crystallized. Thus, determining the composition of sodalite constraints the composition of magma from which they crystallized and the concentration of volatile at depth.

The stability of sodalite $Na_8(AlSiO_4)_6(Cl_2,SO_4)$ has been examined using thermodynamic equilibrium (Stormer and Carmichael 1971). The sodalite crystallization is related to the crystallization of nepheline or plagioclase and is strongly dependent of silica activity and Cl and SO_4 fugacities in the silicate liquid (liq) with the following incongruent reactions (Stormer and Carmichael 1971):

$$\underset{\text{sodalite}}{Na_4Al_3Si_3O_{12}Cl} = \underset{\text{liq}}{NaCl} + 3\underset{\text{nepheline}}{NaAlSiO_4} \quad (1)$$

$$\underset{\text{sodalite}}{Na_4Al_3Si_3O_{12}Cl} + 6\ \underset{\text{liq}}{SiO_2} = \underset{\text{liq}}{NaCl} + 3\ \underset{\text{albite}}{NaAlSi_3O_8} \quad (2)$$

$$\underset{\text{nosean}}{Na_8Al_6Si_6O_{24}(SO_4)} + 12\ \underset{\text{liq}}{SiO_2} = \underset{\text{liq}}{NaSO_4} + 6\ \underset{\text{albite}}{NaAlSi_3O_8} \quad (3)$$

XANES and electron microprobe studies from Jugo et al. (2010) and Hettmann et al. (2012), respectively, corroborated the presence of sulfur as pure sulfate (SO_4^{2-}) in haüyne from Eifel, Germany, and the high oxidation state at pre-eruptive conditions, whereas nosean in syenite has a large proportion of S^{2-} (e.g., sodalite from Ilimaussaq in Greenland and Mont Saint Hilaire in Canada) suggesting more reduced conditions. These previous studies demonstrated that the sulfate/sulfide ratio in sodalite is strongly correlated with oxidation state of the magmas (Hettmann et al. 2012) and that the determination of S^{6+}/S^{2-} ratio is a powerful tool to estimate the pre-eruptive redox state of alkaline magmas.

The phase equilibrium and conditions of crystallization have been studied experimentally in two natural phonolites (Berndt et al. 2001; Giehl et al. 2014). Haüyne from Laacher See phonolite crystallized at relatively low temperature and pressure (760–840 °C, 200–400 MPa) from water-undersaturated melt with 6 wt% H_2O at oxidized conditions at ΔNNO+2.3 ($\Delta NNO = \log f_{O_2} - \log f_{O_2}$ of the Ni-NiO buffer calculated at P and T) (Berndt et al. 2001), whereas sodalite from Ilimaussaq phonolite crystallized at 650–825 °C, 100 MPa, in water-undersaturated and reducing conditions (low H_2O content: 1.2 wt%, ΔNNO-0.5 to ΔNNO-1; Giehl et al. 2014). So far, neither the stability of nosean nor the crystallization of sodalite-group minerals in complex fluid (e.g., with CO_2, S, and Cl) has been investigated experimentally.

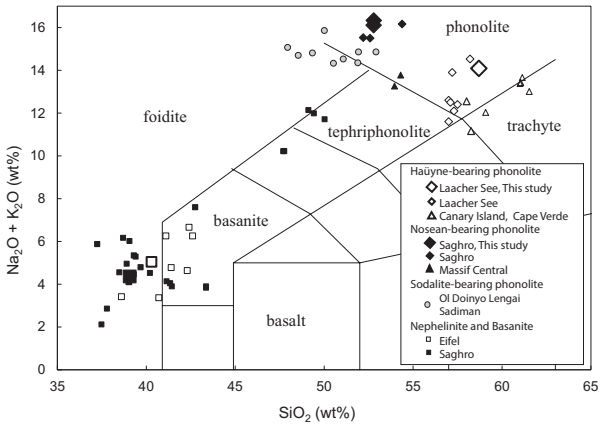

FIGURE 1. Alkali vs. silica composition (after Le Maitre 1984) of the sodalite-bearing phonolites: haüyne-bearing phonolites (white diamond and triangle = this study; Wörner and Schmincke 1984a; Holm et al. 2006; Bryan 2006); nosean-bearing phonolites (black diamond and triangle = this study; Berger et al. 2009; Brousse et al. 1969); sodalite-bearing phonolite (gray full circle = Klaudius and Keller 2006; Zaitsev et al. 2012); and nephelinite and basanite, Eifel (white square = Mertes and Schmincke 1985; Wedepohl et al. 1994), nephelinite Saghro (black square = Berger et al. 2009).

Sodalite-bearing phonolites

Haüyne-bearing phonolite, Laacher See, Eifel, Germany

Haüynes have been reported in Laacher See phonolitic pyroclastic deposits (N50°24′48″, E7°16′24″) (Wörner and Schmincke 1984a; Bogaard 1995; Schmincke et al. 1999) from the youngest (12900 ± 560 yr BP) eruptive centers of Quaternary East Eifel volcanic field (400–13 ka). East Eifel volcanic field erupted basanite, leucitite, nephelinite, and tephrite with a total magma volume of 1 km^3, whereas the Laacher See volcano erupted about 5 km^3 of phonolitic magma (Bogaard 1983) with alternately plinian and phreatomagmatic phase eruptions of ash, pumice, and pyroclastic flows that attest of large volume of dissolved magmatic fluids at depth. The Laacher See tephras (only phonolitic rocks) are divided into three units based on stratigraphic position (Wörner and Schmincke 1984a): Lower Laacher See Tephra (LLST, that corresponds to the upper part of the magma chamber), a highly vesicular and crystal-poor pumice (<5% phenocrysts of sanidine); Middle Laacher See Tephra (MLST) with 15 vol% phenocrysts of sanidine, clinopyroxene (Cpx), amphibole, and biotite; and Upper Laacher See Tephra (ULST, that corresponds to the lower part of the magma chamber) with 50–60 vol% phenocrysts of sanidine, plagioclase, and haüyne. Laacher See phonolites are silica-rich (54.4–58.7 wt% SiO_2) and Mg-poor ($Mg\# = Mg/Mg+Fe^{tot} = 0.06–0.15$) (Fig. 1). They have higher K_2O content (6.6–8.7 wt%) relative to Na_2O (4.9–7.3 wt% Na_2O; $Na_2O/K_2O = 1.2–0.6$) and are slightly peralkaline ($Na+K/Al = 0.96–1.08$). Laacher See phonolites have high concentrations in rare earth elements (REE) (80–160 ppm La; 150–200 ppm Ce; 0.5–2.4 ppm Eu; La/Yb = 36.5–47.5), Rb (88–188 ppm), Sr (798–1385 ppm), and volatile elements: F (700–1400 ppm), Cl (1200–5500 ppm), and S (300–2000 ppm) (Wörner and Schmincke 1984a). Major, trace element, and isotope studies constrained the differentiation of phonolitic magmas to fractional crystallization of olivine, Cpx, plagioclase, amphibole, FeTi-oxides, and apatite from nepheline basanite and very limited assimilation of crustal rocks (Wörner and Schmincke 1984b; Wedepohl et al. 1994). Sodalite-group minerals have been reported in all LLST, MLST, and ULST tephras (Wörner and Schmincke 1984a). They are blue minerals with 0.3 wt% Cl in LLST (rare), MLST (rare), and in ULST (abundant) and white or black (with abundant small sulfide inclusions) minerals with 1–1.5 wt% Cl in LLST and MLST.

Nosean-bearing phonolite, Saghro, Morocco

Sodalite-bearing phonolites are present in Cenozoic volcanic rocks from the Saghro volcanic field in Anti-Atlas (Morocco) on the northern edge of the West African Craton (9.6–2.9 Ma, Berrahma et al. 1993; Berger et al. 2009). The volcanic deposits are nephelinite lava flows (low volume; 6 km^3, Missenard and Cadoux 2011), phonolitic domes and pyroclastic deposits (Ibhi et al. 2002; Berger et al. 2009). According to the bulk composition and mineral assemblages, three groups of phonolites have been identified with variable silica content and Mg# (50.0–55.5 wt% and 0.04–0.31, respectively, Fig. 1): Sr-rich and alkaline phonolite, peralkaline phonolite, and Si-enriched phonolite (Berger et al. 2009, 2014). All phonolites are depleted in K_2O (5.4–7.7 wt%) relative to Na_2O (5.7–10.6 wt%; $Na_2O/K_2O = 0.74–1.87$) and are peralkaline ($Na+K/Al = 0.85–1.2$). Saghro phonolites have high content in incompatible elements with high REE content (Berger et al. 2014) and are enriched in light-REE (LREE) compared to heavy-REE (HREE) (La/Yb = 32.3–40.1). Geochemical modeling shows that Si-enriched phonolites are residual melt after fractional crystallization of olivine, Cpx, amphibole, magnetite, apatite, and alkali feldspar from nephelinitic melt, and crustal assimilation (Fig. 1, Berger et al. 2009, 2014).

Analytical methods

Major elements

Whole-rock major elements were measured by wide-angle X-ray fluorescence (WDXRF) using sequential spectrometer Bruker S4 Pioneer at the analytical services of the Instituto Andaluz de Ciencias de la Tierra (IACT, Spain) using Rh X-ray (160 kV, 159 mA). One gram of whole-rock powder is weighed with di-lithium tetraborate flux (8:1 flux:rock) and the mixture is fused at 1000 °C during 15 min. The concentrations of major elements are measured by comparing the X-ray intensity for each element with the intensity for two fused beads each of nine reference geological standard samples.

The concentrations of major elements in minerals were determined using electron microprobe (Cameca XS100 at the "Microsonde Sud" facility of the University of Montpellier, France). Operating conditions comprised an accelerating voltage of 20 keV, a 10 nA beam current, and a beam focalized (1 µm). The counting time was fixed at 20 s for each element analysis and 40 s for volatile element (S, Cl). The standards used for major and volatile element analyses are: wollastonite for Si and Ca; Al_2O_3 for Al; TiO_2 for Ti; forsterite for Mg; hematite for Fe; orthose for K; albite for Na; apatite for P; native metal for Ni, Mn, Cu; barite for S and Ba; pyrite for S; apatite for F; and chloroapatite for Cl.

The valence state of S was determined for haüyne and nosean by measuring the wavelengths of the S*K*α X-rays using electron microprobe wavelength-dispersive spectrometry (WDS) and an LPET crystal (Carroll and Rutherford 1988). We counted the S X-rays with a spectrometer sin θ range of 0.61158–0.61657 using sin θ steps of 0.00001, a dwell time of 100 ms per step, and a beam of 10 µm. The electron beam was set at 20 keV and 20 nA current, and we accumulated 5 scans for $BaSO_4$ and FeS_2 reference standard analysis, and 10 scans for haüyne and nosean analysis to improve precision.

Whole-rock volatile element analyses

Whole-rock sulfur and carbon (total carbon and total organic carbon) concentrations were determined for each sample by element analyzer (IACT, Spain, Alt et al. 2012). Total inorganic carbon (TIC) and carbonate carbon was removed by reaction with dilute (3 N) HCl, followed by washing in distilled H_2O. To minimize adsorption of atmospheric CO_2, powders were degassed at 100 °C and stored under vacuum in a dessicator. Standard deviations were between 10–40 ppm for sulfur and 10 ppm for carbon.

Whole-rock F and Cl contents were determined by wet precipitation-ferrithiocyanate spectrophotometry using Varian Cary 50 spectrophotometer at the SARM (Nancy, France). Standard solutions were used to check the accuracy of the analyses. Standard deviations are less than 5% (Vernet et al. 1987).

Trace elements

Whole-rock analyses were performed using a quadrupole 7700x inductively coupled plasma-mass spectrometry (ICP-MS) at the AETE facility (University of Montpellier, France); 0.1 g of whole-rock powder was dissolved with acid ($HF-HNO_3$). Blanks were prepared with samples spiked with In and Bi to monitor internal drift. Solutions were analyzed at a final dilution factor of 8000. ICP-MS sensitivity in this configuration was 200×10^6 cps/ppm ^{115}In. Analytical accuracy was estimated from measurements of international rock standards UBN and G1.

Trace element concentrations in minerals were determined by a laser ablation ICP-MS system at the University of Montpellier (France), using GeoLas Q + Excimer CompEx102. The diameter laser beam was 26 and 56 µm; a laser repetition rate of 6–10 Hz and a laser power of 0.5 mJ (5 J cm^{-1}) were used for this study. The NIST612 standard, USGS standard BIR-1, BHVO-1, and a NiS bead doped with platinum group elements (PGE) were used as external standard and SiO_2, CaO, and S content determined by electron microprobe were used as internal standard. The drift is compensated by the internal standard calculations in the Glitter software (Van Achterbergh et al. 2001); no other drift corrections are used. For data processing

and calculation of concentrations, Glitter Software was used to process the raw data files containing the signal intensity vs. time. This allows precise selection of blanks and signals, and rapid visualization of the intensity data.

Results

Haüyne-bearing phonolite, Laacher See, Eifel, Germany

For this study, we selected the more silica-rich tephra (ULST tephra) containing 5 vol% of sodalite. This lava is peralkaline (Na+K/Al = 1.03) with 58.7 wt% SiO_2 and 8.7 wt% K_2O and plots into the silica-rich group of phonolite in TAS diagram (Fig. 1, Table 1). Our sample has high concentrations in REE (32.3 ppm La; 56.1 ppm Ce; 0.98 ppm Eu, La/Yb = 47.5), Ba (2052 ppm), Sr (919 ppm), and volatile elements: C (391 ppm), F (440 ppm), Cl (820 ppm), and S (4000 ppm). It contains up to 60 vol% phenocrysts of Cpx (3 vol%), sanidine (37 vol%), haüyne (5 vol%), plagioclase (12.5 vol%), amphibole (1 vol%) + magnetite (1 vol%, X_{ulvo} = 0.10), titanite (0.3 vol%), apatite (0.3 vol%), and sparse pyrrhotite (Fig. 2a).

Table 1. Major (wt%) and trace element (ppm) compositions of Saghro (TAG) and Laacher See (HE2) phonolite

Sample	TAG	HE2
	wt%	
SiO_2	52.79	58.72
TiO_2	0.84	0.51
Al_2O_3	19.87	20.38
$Fe_2O_3^{tot}$	4.96	2.12
MgO	1.12	0.18
MnO	0.23	0.09
CaO	2.72	2.45
Na_2O	9.58	5.32
K_2O	6.75	8.77
P_2O_5	0.20	0.11
LOI	0.89	1.28
Total	99.95	99.93
Mg#	0.31	0.13
	Parts per million	
C	130	391
S	560	4000
F	520	440
Cl	2530	820
Cr	44.6	4.8
Ni	15.7	2.2
Cu	5.9	7.0
Rb	234	102
Sr	1146	919
Y	21.8	5.85
Zr	1014	171
Nb	278	54.3
Ba	609	2052
La	70.9	32.3
Ce	108	56.1
Pr	8.8	5.0
Nd	28.1	15.1
Sm	4.2	1.80
Eu	1.4	0.98
Gd	3.4	1.58
Tb	0.6	0.21
Dy	3.7	1.11
Ho	0.8	0.25
Er	2.4	0.70
Tm	0.4	0.11
Yb	2.7	0.68
Lu	0.5	0.10
Hf	11.9	3.39
Ta	5.3	3.04
Pb	18.2	8.06
Th	35.8	5.06
U	12.5	1.05

Note: Mg# = Mg/[Mg+Fe^{2+}].

Sodalite-group mineral occurs as phenocrysts (1 mm in size, 5 vol%, Fig. 2). They are Ca-rich (9.7–9.9 wt% CaO) and Na-poor (15.1–15.4 wt% Na_2O) (Fig. 3, Table 2). Sodalites in Laacher See tephra are haüynes according to the classification of Lessing and Grout (1971) (Fig. 3). The concentration of S is higher than Cl (5.2 to 5.6 wt% S; 0.3 to 0.5 wt% Cl) and the peak position determined by WDS is very close to the peak position of $BaSO_4$ standard indicating that sulfur in haüyne is predominantly present as S^{6+} (2.3082 and 2.3081 keV, respectively, S^{6+}/S^{tot} = 0.91 ± 0.04, see Hettmann et al. 2012 for method). The sums of oxides from microprobe analysis are close to or higher than 100, suggesting that no or minor CO_2 and H_2O are present in haüynes. Haüynes are enriched in LREE compared to HREE (La/Yb = 325–1030) with a strong Eu positive anomaly (0.2–0.28 ppm Eu, Eu/Eu* = $[2Eu_n]/([Sm_n]+[Gd_n])$ = 2.1–3.5) and have low concentrations of high field strength elements (HFSE) [e.g., 0.1 ppm Zr, Ta, and Hf < 0.1 (detection limit)] (Table 3, Fig. 4). These minerals have low content in Cu (<1 ppm), Ni (<1 ppm), Re (20–100 ppb), PGE (Pd, Ir), and chalcophile elements (Se, Te) have not been detected (Table 2).

Cpx are unzoned augite phenocrysts (200–800 μm, WoEnFs = 49:30:21; Mg# = 0.37–0.40) (Fig. 2 and Table 2). The REE concentrations display a concave pattern slightly enriched in LREE compared to HREE (La/Yb = 8.9–9.1; Fig. 4). Plagioclases are present as phenocrysts (500 μm, An_{46}) and as inclusions (An_{35}) in sanidine. Plagioclases are enriched in LREE compared to HREE (La/Yb = 3200–3400) and have a strong Eu positive anomaly (0.72–0.74 ppm Eu, Eu/Eu* = 7.49–12.15) (Fig. 4, Table 3). Sanidine phenocrysts (37 vol%) are K-rich with $An_4Ab_{28}Or_{68}$ and contain high Ba and Sr content (4200 and 1725 ppm, respectively; Table 3). Rare amphiboles are kaersutite crystals (100 μm), they are Ti-rich (4.6–4.8 wt% TiO_2) and Fe-rich (16.1–16.6 wt% FeO).

Accessory minerals are present as inclusions in Cpx and/or in the matrix. Titanites occur as inclusions in Cpx. They have very high REE concentrations (4000 ppm La; 10 ppm Lu, Fig. 4), Nb (9000 ppm), and Zr (5700 ppm) with small negative Eu anomaly (Fig. 4, Table 3). Apatites (50–100 μm) are present as inclusions in Cpx and interstitial crystals in the matrix. They are fluoro-apatites (3.26–3.67 wt% F, 0.22–0.25 wt% Cl) and contain up to 0.77–0.95 wt% SO_3. Apatites have high REE content (La/Yb = 60.1 to 93.7, Fig. 4), Eu negative anomaly, and low Sr and Ba contents (5 and 0.23 ppm, respectively) (Table 3). Sulfides are scarce and occur as inclusions in magnetite and Cpx. Two pyrrhotites (N_{FeS} = 0.96) with low Cu content (0.3 wt%) and very low Ni content (0.02 wt%) have been found as inclusions in Cpx and magnetite (Cu/Ni = 24.6 and 89.4, respectively; Table 4). The concentrations in chalcophile and siderophile elements are variable (i.e., 7–100 ppm As, 10–20 ppm Se, 1–3 ppm Te, 6–40 ppb Ir, Table 2). One single crystal of bornite in Cpx has been identified (62 wt% Cu, 25.4 wt% S, 14% wt% Fe, Table 4). Bornite is richer in chalcophile Se (500 ppm) and siderophile (Ir = 80 ppb) elements than pyrrhotite. FeTi-oxides in the matrix and as inclusions in Cpx are magnetites (X_{ulvo} = 0.10).

Nosean-bearing phonolite, Saghro, Morocco

Sodalite minerals are only present in silica-poor peralkaline phonolites [52.2–54.4 wt% SiO_2, Mg# = 0.07–0.31, Na+K/Al = 1.05–1.20 (Fig. 1)]. We selected a more silica-poor phonolite

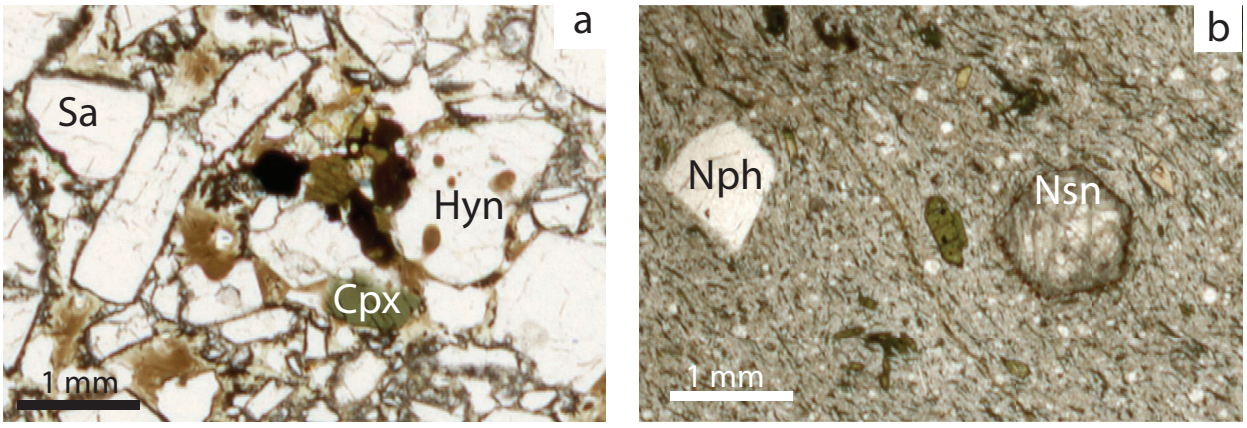

FIGURE 2. Photomicrographs of phonolite from (**a**) Laacher See and (**b**) Saghro. Sa = sanidine, Cpx = clinopyroxene, Hyn = haüyne, Nph = nepheline, Nsn = nosean. Scale bar = 1 mm. (Color online.)

with 3 vol% sodalite (Table 1, Figs. 1 and 2). This phonolite has lower K_2O content (6.75 wt%) relative to Na_2O content (9.6 wt%; Na_2O/K_2O = 1.4) and is peralkaline (Fig. 1). Our sample has high concentrations in REE (70.9 ppm La; 108 ppm Ce; 1.4 ppm Eu, La/Yb = 26.3), Ba (609 ppm), and Sr (1146 ppm). The concentrations of volatile elements are high for Cl (2530 ppm) and low for C (130 ppm), F (520 ppm), and S (560 ppm) (Table 1).

The investigated phonolite is crystal-poor (12 vol% phenocrysts) with Cpx (1.5 vol%), sanidine (3.5 vol%), nepheline (6 vol%), nosean (0.4 vol%), altered amphibole (0.1 vol%), magnetite (0.3 vol%), titanite (0.05 vol%), apatite (0.05 vol%), and pyrrhotite (<0.01 vol%). Sodalite minerals (1 mm, gray-brown color, Fig. 2) have high Na_2O and K_2O content (18–23 and 0.5–3.3 wt%, respectively; Fig. 3a), high S and low Cl content (S = 2.8–3.5 wt%; Cl = 0.75–1.27 wt%; Fig. 3b), and S > Cl, characteristic for nosean (Na-S-Cl sodalite) (Lessing and Grout 1971). $\lambda(SK\alpha)$ peak position for Saghro nosean is between S^{6+} ($BaSO_4$) and S^{2-} (FeS_2) indicating that both sulfur species, S^{6+} and S^{2-}, are present [$\lambda(SK\alpha)$ = 2.30805 keV, S^{6+}/S^{tot} = 0.87 ± 0.04; see Hettmann et al. 2012 for method]. Noseans have high LREE content (3–10 ppm La), low middle-REE (MREE) (0.2–0.3 ppm Sm), and HFSE (1.4–6 ppm Zr, <0.1 ppm Hf) contents, very low HREE content (<0.01 ppm) and a strong Eu negative anomaly (Fig. 5b). Noseans have variable Cu (6–500 ppm) and Ni (0.5–23 ppm) contents and, siderophile element contents (Pd, Ir). Although sulfide-free crystal surfaces have been analyzed, high Cu content may be due to the presence of tiny sulfide crystals at depth. Chalcophile elements (Se, Te) have not been detected (Table 4). Nosean crystals have reaction rims (150–200 µm, Fig. 2) with low Na_2O (15 wt%) and high K_2O and FeO content (10 and 3 wt%, respectively). Cl content is lower (0.06 wt%) at the rim than at the core, whereas S content is constant (3–2.5 wt% S) (Fig. 3b).

Cpx are phenocrysts (300 µm) with green core and yellow rim. The cores are rich in MgO (Mg# = 0.7–0.8), Al_2O_3 (8–10 wt%), TiO_2 (3–4.5 wt%), and Cr_2O_3 (0.15–0.3 wt%). REE patterns show a concave shape enriched in LREE compared to HREE (20–30 ppm La, 8–10 ppm Sm, 0.1–0.5 ppm Lu, Fig. 5a, Table 3). Trace element analyses display relatively high content of Zr (300–400 ppm), Rb (0.02–3.7 ppm), and Sr (60–650 ppm). There is an abrupt change in composition at the rim of Cpx crystals. The rims are 100 µm wide and have low MgO (Mg# = 0.4–0.6), and high FeO (11–13.7 wt%) and Na_2O (2.5–3 wt%) content. The rims are enriched in Zr (400–2700 ppm), LREE (30–100 ppm La), and HREE (0.25–1.6 ppm Lu) and depleted in MREE (6–7 ppm Sm) compared to the core (Fig. 5a, Table 3).

Nepheline crystals are euhedral (1 mm) with high Na_2O (11.2–13.25 wt%) and SiO_2 content (43.3–48.5 wt%) (Table 2). The concentrations of trace elements in nephelines are below the detection limit for trace elements, except for Rb, Sr, and Ba (82, 42, and 7.4 ppm, respectively). Rare sanidine crystals (<100 µm) have less than 0.01 wt% CaO and Or_{73}.

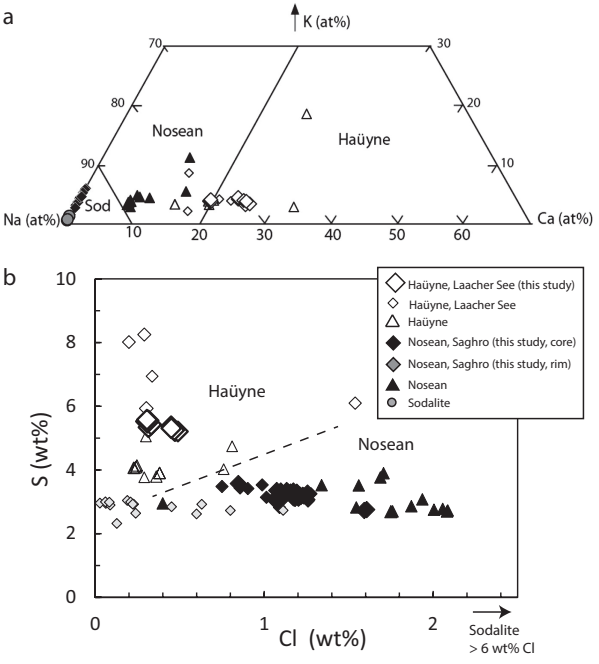

FIGURE 3. (**a**) Cl vs. S content in sodalite, (**b**) Composition of the sodalite group in phonolites recalculated to cation percentage (after Lessing and Grout 1971); symbols as in Figure 1.

TABLE 2. Representative major element compositions (wt%) of mineral in Saghro (TAG) and Laacher See (HE2) phonolite

Sample	TAG	TAG	HE2	HE2	TAG	HE2	HE2	TAG	HE2	TAG	HE2	TAG	TAG	HE2	HE2	TAG	TAG	HE2	TAG	HE2
Mineral	Cpx	Cpx	Cpx	Cpx	Ttn	Ttn	Amp	Nph	Pl	Sa	Sa	Nsn	Nsn	Hyn	Hyn	Ap	Ap	Ap	Mt	Mt
Type	core	rim	core	core	core	core	core	core	core	core	core	core	rim	core	core	in Cpx	int	int	core	core
SiO_2	44.84	51.14	46.35	45.60	29.66	29.22	38.55	45.96	57.94	63.73	63.27	38.51	35.59	33.52	33.31	0.55	0.46	0.87	0.23	0.11
TiO_2	3.4	0.94	1.73	2.04	36.04	36.60	4.79	–	0.05	0.07	0.1	–	–	–	–	–	–	–	8.34	7.56
Al_2O_3	8.66	2.13	6.21	7.13	1.13	1.26	13.04	35.58	25.98	18.47	19.86	34.43	30.51	28.95	29.21	0.01	–	–	0.14	2.36
FeO^{tot}	6.24	13.65	11.42	11.31	1.59	1.22	16.14	0.76	0.35	0.79	0.17	0.30	0.52	0.21	0.18	0.12	0.07	–	88.59	86.69
MnO	0.1	0.77	0.69	0.62	0.06	0.13	0.61	b.d.	b.d.	b.d.	b.d.	–	–	0.02	0.02	0.04	0.03	0.09	1.58	1.84
MgO	12.06	8.44	9.74	9.44	0.02	0.02	9.30	0.01	0.02	b.d.	0.01	–	–	0.03	0.04	–	–	–	0.83	1.4
CaO	23.32	19.70	22.46	22.51	27.83	28.02	11.87	0.01	7.52	0.01	0.77	0.01	0.36	9.88	9.87	53.59	54.35	52.94	0.18	0.01
Na_2O	0.56	2.81	1.27	1.18	1.05	0.01	2.17	12.23	6.31	3.30	3.16	20.49	15.01	15.09	15.2	0.1	0.03	0.05	–	–
K_2O	b.d.	0.02	b.d.	b.d.	0.01	0.01	2.47	5.26	1.61	13.15	11.91	1.42	11.15	1.17	1.12	0.01	0.01	–	–	–
P_2O_5	–	–	–	–	–	–	–	–	–	–	–	0.07	0.23	0.01	0.03	40.36	41.24	41.91	–	–
Cr_2O_3	0.34	0.02	0.01	0.02	b.d.	b.d.	0.02	b.d.	0.01	–	–	–	–	–	–	–	–	–	0.05	0.02
SO_2	–	–	–	–	–	–	–	–	–	–	–	6.52	6.01	11.08	11.14	0.08	0.04	0.78	–	–
F	–	–	–	–	–	–	–	–	–	–	–	–	–	–	–	3.05	3.75	3.62	–	–
Cl	–	–	–	–	–	–	–	–	–	–	–	1.19	0.19	0.31	0.30	0.04	0.01	0.25	–	–
Total	99.5	99.6	99.88	99.85	97.8	96.51	98.96	99.85	99.79	99.52	99.25	102.9	99.65	100.3	100.4	97.97	99.29	99.79	100	100
S^{6+}/S^{tot}	–	–	–	–	–	–	–	–	–	–	–	0.87	0.87	0.91	0.91	–	–	–	–	–
Mg#	0.60	0.32	0.40	0.39	–	–	0.50	–	–	–	–	–	–	–	–	–	–	–	–	–
								Numbers of ions on the basis of												
	6 O				5 O		23 O	32 O	8 O			4 O on Al+Si tetrahedrons				26 O				4 O
Si	1.67	1.94	1.75	1.72	1.01	0.99	5.87	8.61	2.60	2.95	2.90	5.84	5.97	5.95	5.90	0.10	0.08	0.15	0.01	0.01
^{IV}Al	0.33	0.06	0.25	0.28	–	–	2.13	–	–	–	–	–	–	–	–	–	–	–	–	–
^{VI}Al	0.05	0.03	0.02	0.04	–	–	0.21	–	–	–	–	–	–	–	–	–	–	–	–	–
Al^{tot}	–	–	–	–	0.05	0.05		7.87	1.38	1.01	1.07	6.16	6.03	6.05	6.10	–	–	–	0.01	0.12
Ti	0.10	0.03	0.05	0.06	0.92	0.94	0.55	–	–	–	–	–	–	–	–	–	–	–	0.28	0.25
Fe^{2+}	0.08	0.25	0.13	0.15	–	–	–	–	–	–	–	–	–	–	–	–	–	–	–	–
Fe^{3+}	0.11	0.18	0.23	0.21	–	–	–	–	–	–	–	–	–	–	–	–	–	–	–	–
Fe^{tot}	–	–	–	–	0.05	0.03	2.05	0.12	0.01	0.03	0.01	0.04	0.06	0.03	0.02	–	–	–	3.29	3.15
Mn	–	0.02	0.02	0.02	–	–	0.08	–	–	–	–	–	–	–	–	0.01	–	0.01	0.06	0.07
Mg	0.67	0.48	0.55	0.53	–	–	2.11	–	–	–	–	0.00	0.00	0.00	0.01	–	–	–	0.06	0.09
Ca	0.93	0.80	0.91	0.91	1.01	1.02	1.94	–	0.36	–	0.04	0.00	0.06	1.60	1.59	10.20	9.92	9.70	0.01	–
Na	0.04	0.21	0.09	0.09	0.01	–	0.64	4.46	0.55	0.3	0.28	5.78	4.16	4.42	4.43	0.05	-	0.02	–	–
K	–	–	–	–	–	–	0.48	1.26	0.09	0.78	0.7	0.26	2.03	0.23	0.22	–	–	–	–	–
P	–	–	–	–	–	–	–	–	–	–	–	–	–	–	–	5.86	5.95	5.87	–	–
SO_4^{2-}	–	–	–	–	–	–	–	–	–	–	–	1.27	1.64	1.72	1.73	0.02	0.01	0.15	–	–
S^{2-}	–	–	–	–	–	–	–	–	–	–	–	0.19	0.24	0.17	0.17	–	–	–	–	–
Cl	–	–	–	–	–	–	–	–	–	–	–	0.53	0.12	0.11	0.10	–	–	0.02	–	–
OH	–	–	–	–	–	–	–	–	–	–	–	–	–	–	–	1.03	0.91	0.92	–	–
F	–	–	–	–	–	–	–	–	–	–	–	–	–	–	–	0.96	1.09	1.06	–	–
Total	4.00	4.00	4.00	4.00	3.03	3.04	16.00	22.32	5.00	5.00	5.00	20.07	20.11	20.27	20.27	18.23	17.96	17.89	3.70	3.70

Notes: b.d.= below detection, Cpx = clinopyroxene, Ttn = titanite, Amp = amphibole, Nph = nepheline, Pl = plagioclase, Sa = sanidine, Nsn = nosean, Hyn = haüyne, Ap = apatite, int = interstitial, Mag = magnetite. Mineral abbreviations from Whitney and Evans (2010).

Titanites are euhedral crystals (300 μm) in the matrix with high LREE content (La/Sm = 6.6–7.7, La/Yb = 49–51) (Fig. 5, Table 3). Apatites are fluoro-apatite microcrystals (20–30 μm in size) with no S and Cl [up to 3 wt% F, <0.04 wt% Cl, and 0.05–0.1 wt% SO_3 (200–400 ppm S)]. Apatites as inclusion in Cpx and titanite have high REE concentrations (2800–3200 ppm La; 2.1–3.4 ppm Lu) and Sr (9800–13 000 ppm) and low Cu/Ni ratio (0.29–0.65). Interstitial apatites have higher Sr content (10 000–18 000 ppm) and Cu/Ni ratio (1.2–1.4) relative to the apatite as inclusions in Cpx (9000–12 000 ppm Sr) and titanite. Sulfides are relatively abundant and have pyrrhotite composition ($Fe_{1-x}S$) with low Cu and Ni content (<2 and <1.4 wt%, respectively; Cu/Ni = 0.05–50, Table 4). Pyrrhotites as inclusions in Cpx have N_{FeS} values from 0.90 to 0.92, whereas interstitial pyrrhotites have higher N_{FeS} values (0.92–0.98). The concentrations of chalcophile elements are variable (6–1000 ppm As, 10–150 ppm Se, 0.4–5 ppm Te) and the concentrations of siderophile elements are very low [i.e., I-PGE (Os, Ir, Ru) are often under detection limit (Table 4)]. FeTi-oxides are interstitial magnetites with X_{ulvo} = 0.15–0.16 and 0.03–0.10 wt% Ni and 0.01–0.05 wt% Cu (Cu/Ni = 0.1) (Table 2).

DISCUSSION

Crystallization of sodalite minerals

The stability of pure sodalite [$Na_8(AlSiO_4)_6(Cl_2,SO_4)$] is directly related to incongruent reaction of melt with nepheline and albite (reactions 1 and 2 above, Stormer and Carmichael 1971). However, the presence of Ca in natural sodalite and feldspar (Fig. 3, Table 2) requires both Na and Ca in the equilibrium reactions to constrain the solid solution for sodalite-group minerals and determine the stability of sodalite and feldspar in natural systems. Using mineral stoichiometry (Table 2) and phase equilibria in phonolites, we established the reaction for haüyne (Ca-bearing sodalite) and plagioclase in Laacher See phonolite and nosean (Ca-free sodalite) and nepheline in Saghro phonolite.

For Ca-bearing minerals (Laacher See phonolite), the reaction can be expressed as follows:

$$\underset{\text{haüyne}}{Na_{4.5}Ca_{1.5}Al_6Si_6O_{24}(SO_4)_2} + 4\ \underset{\text{liq}}{SiO_2} + 1.5\ \underset{\text{liq}}{Na_2O} + 0.25\ O_2 = 4\ \underset{\text{plagioclase}}{Na_{0.25}Ca_{0.4}(Al_{1.4}Si_{2.6})O_8} + 2\ \underset{\text{liq}}{Na_2SO_4} \quad (4)$$

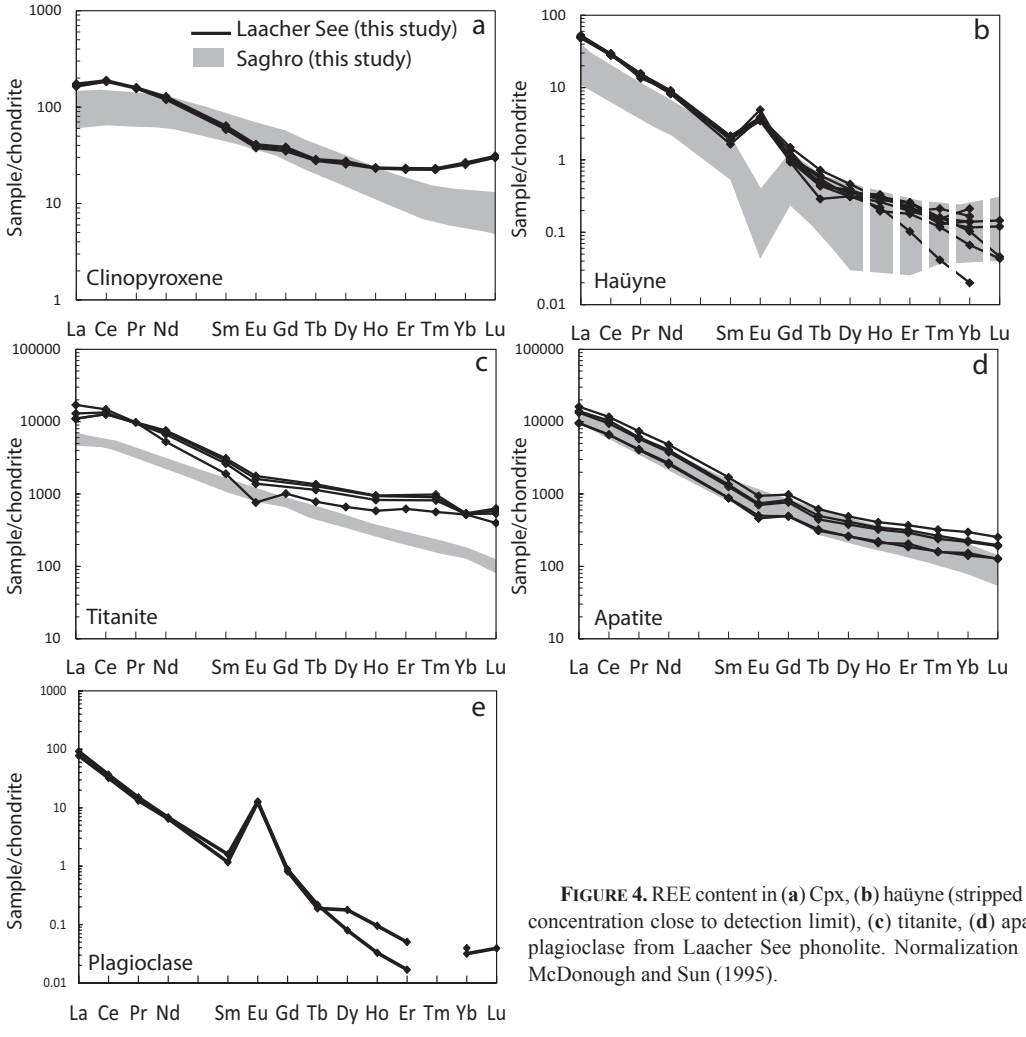

FIGURE 4. REE content in (**a**) Cpx, (**b**) haüyne (stripped zone: HREE concentration close to detection limit), (**c**) titanite, (**d**) apatite, and (**e**) plagioclase from Laacher See phonolite. Normalization values from McDonough and Sun (1995).

The presence of silica and sodium (component in the melt) on the left side of the incongruent reaction 4 indicates that low silica and low sodium activity would promote the crystallization of haüyne (feldspathoid), whereas plagioclase crystallized from silica-saturated silicate melt. Since oxygen is also present on the left side of the equation it indicates that the reaction from haüyne to plagioclase consumed oxygen, and the silicate liquid becomes more oxidized as plagioclase crystallized.

For Ca-free sodalite, in Si-undersaturated silicate liquid with low silica activity and low volatile activity, nepheline is the first phase to crystallize leading to an enrichment of silica and volatile (Cl and SO_4^{2-}) in the residual melt (Barker 1976; Sharp et al. 1989). This continues until nosean begins to crystallize. NaCl and Na_2SO_4 activity of the magma is then buffered as follows:

$$6\ \underset{\text{nepheline}}{NaAlSiO_4} + 1.5\ \underset{\text{liq}}{Na_2SO_4} + 0.75\ \underset{\text{liq}}{NaCl} + 3.4\ O_2 = \underset{\text{nosean}}{Na_8Al_6Si_6O_{24}\left[(SO_4)_{1.5},\ Cl_{0.5}\right]} + 1.5\ \underset{\text{liq}}{Na_2O} \quad (5)$$

The incongruent reaction nepheline/nosean constrains the crystallization at high Na_2O activity. Again, the reaction consumed oxygen as nosean crystallizes. Consequently, for both cases, the oxygen fugacity increases and the magma becomes more oxidized.

Haüyne and nosean have similar REE patterns, enriched in LREE compare to MREE (La/Sm = 35.4–46.4 and 20.2–36.5 for haüyne and nosean, respectively, Figs. 5 and 6). The strong positive Eu anomaly, present only in haüyne crystal (Fig. 5b), suggests that Eu substitutes to cation in the structure of haüyne [$Kd_{mineral/matrix}$ (in situ) varies from incompatible (Kd = 0.05, Francalanci et al. 1987) to moderately incompatible (Kd = 0.6, Wörner et al. 1983)]. The element distribution in haüyne is thus very similar to what is observed in plagioclase (Fig. 4) with Eu^{2+}-Ca^{2+} substitution (Schnetzler and Philpotts 1970).

In nosean (Ca-free), Eu should behave as incompatible elements with Eu^{3+} behaving like Sm and Gd (no Eu anomaly). The strong negative Eu anomaly observed in nosean (Fig. 5) is then related to prior crystallization of Eu^{2+}-rich minerals and to Eu-depleted composition of the silicate melt from which they

TABLE 3. Representative trace element compositions (ppm) of mineral for Saghro (TAG) and Laacher See (HE2) phonolite

Sample	TAG	TAG	HE2	HE2	TAG	HE2	HE2	HE2	TAG	TAG	TAG	HE2	HE2	HE2	TAG	TAG	HE2	HE2
Mineral	Cpx	Cpx	Cpx	Cpx	Ttn	Ttn	Pl	Sa	Nsn	Nsn	Nsn	Hyn	Hyn	Hyn	Ap	Ap	Ap	Ap
Type	core	rim	core	core	core	core	core	core	core	core	rim	core	core	core	in Cpx	int	int	int
Ni	3.1	–	0.6	0.5	0.3	2.7	1.94	3.6	1.6	0.6	5.43	0.8	0.7	0.8	0.9	6.1	1.9	1.9
Cu	0.2	–	0.1	0.2	2.6	1.3	0.36	2.37	31.1	6.4	59.9	0.2	0.2	2.2	0.3	3.9	0.9	0.59
Rb	b.d.	7	0.5	–	0.1	0.1	2.78	107	4.9	8.6	40.8	5.6	4.9	5.4	–	2.8	–	–
Ba	0.3	2.7	0.9	0.1	0.1	0.2	1384	4264	20.6	10.7	18.4	21.3	20.7	26.7	23.6	15.3	2.2	1.6
Th	0.3	1.3	0.2	0.1	54.2	124	0.03	0.56	0.3	0.3	3.26	b.d.	–	b.d.	85	109	107	86.9
U	b.d.	0.2	b.d.	b.d.	8.8	16	b.d.	0.03	0.1	0.1	4.21	–	–	–	6.9	13.9	8.4	7.3
Nb	3.9	13.9	4.9	3.8	5863	9128	0.07	3.6	3.5	3.3	19.4	0.6	0.6	0.5	6.7	3303	0.9	0.9
Ta	0.8	0.5	0.6	0.4	325	583	b.d.	b.d.	b.d.	b.d.	0.1	b.d.	b.d.	b.d.	–	178	–	–
Pb	0.1	0.2	0.3	0.2	0.3	1.2	3.28	7.2	16.2	3.7	75.3	1.1	1.1	1.1	2.9	7.5	1.3	1.3
Sr	570	278	66.5	39.6	1388	5	2609	1725	303	268	1153	492	461	474	10942	9880	852	872
Zr	319	137	358	318	1706	5722	0.27	10.9	5.7	1.4	22.5	0.1	0.1	0.1	4.6	1156	14.5	12.8
Hf	9.1	5.5	10.6	9.2	37.5	172	b.d.	0.11	b.d.	b.d.	0.35	b.d.	–	b.d.	–	25.9	–	–
Y	21.3	14.9	35.1	33.7	543	954	0.24	0.73	0.5	0.7	1.62	0.5	0.5	0.5	330	588	555	528
La	23.6	14.3	41.4	38.6	1505	4035	21.9	9.5	5.4	8.9	6.39	11.6	11.5	11.9	2808	3204	3320	3150
Ce	65.5	39.6	116	112	3699	9041	22.5	6.2	8.9	13.2	6.21	17.5	17.1	17.9	3939	5703	6345	5774
Pr	9.32	5.94	15.2	14.7	427	928	1.43	0.45	0.7	1.1	0.77	1.5	1.4	1.5	331	542	580	550
Nd	42.9	28.7	60	55.7	1505	2469	3.2	1.3	2.1	3.1	2.23	3.9	3.9	3.9	1045	1786	1898	1771
Sm	9.4	6.8	9.8	8.9	237	290	0.24	0.20	0.2	0.3	0.27	0.3	0.3	0.3	139	242	206	192
Eu	2.9	2.1	2.3	2.1	66	44.1	0.74	0.71	b.d.	b.d.	0.09	0.2	0.2	0.2	39.2	65.6	43	40.8
Gd	7.5	5.9	7.9	7.1	186	208	0.17	0.40	0.2	0.3	0.27	0.2	0.3	0.2	115	190	169	157
Tb	1.0	0.7	1	1	24.4	29.2	0.01	b.d.	b.d.	b.d.	0.03	b.d.	0.2	0.2	11.6	23	18.7	16.7
Dy	5.3	3.8	6.9	6.5	132	168	0.03	0.12	0.1	0.1	0.19	0.1	0.1	0.1	65	133	105	96.1
Ho	0.8	0.6	1.3	1.3	21.2	33.1	b.d.	0.15	b.d.	b.d.	0.03	b.d.	b.d.	b.d.	11.2	21.7	19.4	18.3
Er	1.9	1.3	3.8	3.7	49.5	102	b.d.	0.04	b.d.	b.d.	0.11	b.d.	b.d.	b.d.	29.1	53.1	52.4	48.4
Tm	0.2	0.2	0.6	0.5	6.1	14.4	b.d.	b.d.	b.d.	b.d.	0.02	b.d.	b.d.	b.d.	3.3	6.7	6.7	6.1
Yb	1.5	0.9	4.5	4.3	31.4	88.6	b.d.	b.d.	b.d.	b.d.	b.d.	b.d.	b.d.	b.d.	18.1	32.7	38.6	36.8
Lu	0.2	0.1	0.8	0.7	3.1	10	b.d.	b.d.	b.d.	b.d.	b.d.	b.d.	b.d.	b.d.	2.1	3.4	5.0	4.9

Notes: b.d.= below detection, Cpx = clinopyroxene, Ttn = titanite, Pl = plagioclase, Sa = sanidine, Nsn = nosean, Hyn = haüyne, Ap = apatite, int = interstitial.

crystallized. The absence of plagioclase and the absence of a negative Eu anomaly in Cpx, titanite, and apatite, however, suggest that the Eu anomaly in nosean is not related to the crystallization of Eu-bearing minerals. The negative anomaly can then be the consequence of a very low Eu^{3+}/Eu^{2+} ratio in parental silicate melt, which makes Eu more incompatible than neighboring REE. Similar negative anomalies have been previously observed in zircon and were related to the oxidation state of the magma (Trail et al. 2012). Drake (1975) estimated from Eu and Sr partitioning in plagioclase that $Eu^{3+}/Eu_{total} = 0.5$ at ΔNNO-3 and recent experimental data by Cicconi et al. (2012) suggest a strong control of the silicate melt composition on Eu speciation (Eu^{3+}-Eu^{2+}) ($Eu^{3+}/Eu_{total} = 0.5$ at ΔNNO-1 for haplogranitic melt). Considering that nosean contains sulfur as sulfide (S^{2-}) and sulfate (S^{6+}), we can, however, infer that the crystallization environment of phonolitic melt was oxidized, close to NNO (Jugo et al. 2010) and the silicate melt contains predominantly Eu^{2+}. Thus, the change of Eu speciation from Eu^{2+} to Eu^{3+} may occur at high oxygen fugacity in alkaline undersaturated silicate melt and the Eu anomalies in nosean represent a potential oxygen fugacity barometer, which could be calibrated experimentally.

Pre-eruptive conditions of sodalite-bearing phonolitic magma

The pre-eruptive conditions (T, P, fugacities of volatiles) of phonolitic magma can be constrained using the mineral assemblage present in the rock and the composition of minerals (major, minor, volatile, and trace elements). The depth and temperature of crystallization can be estimated assuming equilibrium between Cpx and silicate melt and using the composition of both phases (Masotta et al. 2013; Putirka et al. 2003; Putirka 2008; Mollo and Masotta 2014). In Laacher See and Saghro phonolites, the silicate melt in equilibrium with Cpx has been calculated using trace element concentrations in Cpx and published partition coefficient using matrix mineral compositions from stratified layer ULST (sample 1088, Wörner et al. 1983). The composition of silicate melts calculated from Cpx composition is very close to the measured bulk-rock composition (Figs. 7 and 8), suggesting that Cpx are suitable as thermobarometer. The thermobarometer defined by Masotta et al. (2013) for alkaline differentiated magmas (error: T = 15 °C and P = 115 MPa) constrains the equilibrium pressure at 220–270 MPa and 760–870 °C for Si-rich phonolite (Laacher See) and 280–330 MPa and 925–950 °C for Si-poor phonolite (Saghro) (Fig. 6). Using the method of Mollo and Masotta (2014) to minimize the error of temperature (e.g., considering the difference between predicted and observed components in Cpx, ΔDiHd = 0.02), the equilibrium temperature for Laacher See is the highest estimated temperature with T = 850 °C (P = 250 MPa) for Laacher see and T = 950 °C (P = 300 MPa) for Saghro phonolites (Fig. 6). The relatively high temperature and low pressure of Laacher See phonolite agree with previous estimates from mineral compositions and xenolith evidence (Wörner and Schmincke 1984b) and with experimentally determined pre-eruptive conditions for the ULST Unit of Laacher See, i.e., 200 MPa and 830–870 °C (Berndt et al. 2001). The higher crystallization temperature of nosean-bearing phonolite (Cl-rich) is consistent with the higher temperature of crystallization of Cl-sodalite determined experimentally relative to SO_4-sodalite (Tomisaka and Eugster 1968).

The fugacities of volatile elements (i.e., f_{O_2}, f_{S_2}) represent the redox state of the magmatic system and controlled the crystallization and the composition of minerals and the phase equilibria. The fugacity of oxygen may be estimated using phase

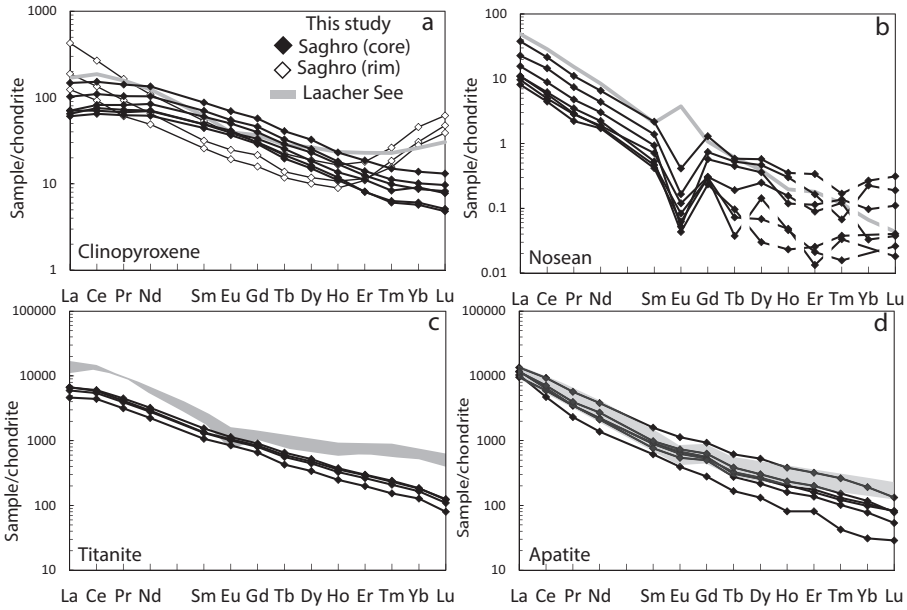

FIGURE 5. REE content in (**a**) Cpx, (**b**) nosean (stripped zone: HREE close to detection limit), (**c**) titanite, and (**d**) apatite from Saghro phonolite. Gray = Laacher See phonolite. Normalization values from McDonough and Sun (1995).

assemblage, mineral composition and element speciations in mineral and melt. The oxygen fugacity strongly controlled the speciation of iron (Fe^{3+}/Fe^{2+}) and sulfur (S^{6+}/S^{2-}) in the silicate melt and the crystallization of ferrous/ferric mineral and sulfate/sulfide mineral (i.e., Carroll and Rutherford 1988; Jugo 2009). In phonolite, the co-crystallization of sulfate-bearing sodalite (S^{6+}) and apatite (S^{6+}) as well as sulfide (S^{2-}) in both nosean- and haüyne-bearing phonolite indicates that the redox state of phonolitic magmas at pre-eruptive conditions was relatively oxidized with an oxygen fugacity close to ΔNNO-NNO+1 (Jugo 2009; Jugo et al. 2010).

Pyrrhotite is present in silicic magmas at reduced and intermediate oxidation state (i.e., ΔNNO-NNO+1) (e.g., Carroll and Rutherford 1988; Luhr 1990; Clemente et al. 2004; Parat et al. 2008) and the composition (N_{FeS}) is function of the sulfur fugacity of the silicate melt and the temperature (Toulmin and Barton 1964; Whitney 1984). In the Laacher See phonolite, rare pyrrhotites as inclusions in Cpx and magnetite indicate that they crystallized close to the liquidus and their composition (low N_{FeS}, Table 4) is representative of the liquidus environment (Whitney 1984). Assuming that both Cpx and pyrrhotite are liquidus phases and considering the temperature of crystallization of Cpx (T = 850 °C), the sulfur fugacity estimated from pyrrhotite composition (N_{FeS} = 0.92–0.93) is $\log f_{S_2}$ = 0.02 to –0.69 (1–0.2 bar). For Saghro phonolite, pyrrhotites have low S content and N_{FeS} = 0.92–0.97. For T = 950 °C, $\log f_{S_2}$ = 0.8 to –2.3 (7 to <0.1 bar). The coexistence of magnetite (X_{ulvo} = 0.08–0.17) and pyrrhotite at 850 and 950 °C indicates an oxygen fugacity close to ΔNNO-NNO+1 for Laacher See phonolite and ΔNNO-0.7-ΔNNO+1 for Saghro phonolite (Whitney 1984), in agreement with sulfate/sulfide crystallization (Jugo 2009) and high-Cl content in sodalite minerals (Stormer and Carmichael 1971).

Volatile element concentrations and speciation in phonolitic melt

The abundance of volatile elements CO_2, H_2O, S, and halogens dissolved in magmas are strongly variable because their solubility and ability to be fractionated in minerals and in the vapor phase depend on several parameters such as pressure, temperature, melt composition, and redox state. In phonolitic melts, water, CO_2, and S partition less strongly in favor of fluids, by an order of magnitude, compared to rhyolitic or dacitic melts owing to greater solubilities of these volatiles in the melt (Scaillet and Pichavant 2003; Webster et al. 2011, 2014). Also, the partitioning of Cl, H_2O, CO_2, and F varies with the molar ratio (Na_2O/Na_2O+K_2O) of the melts (Webster et al. 2014). The two phonolitic system studied here show a strong variability of volatile according to mineral assemblage and composition that may be related to their different alkalinity and/or initial volatile content in parent nephelinite (Saghro) and nepheline basanite (Laacher See).

H_2O and CO_2 content in phonolites. H_2O and CO_2 are the most abundant volatile elements in magmatic systems (e.g., Johnson et al. 1994; Métrich and Wallace 2008). In phonolitic magmas, the H_2O content are highly variable from 1 to 5 wt% H_2O and CO_2 can reach up to 3000 ppm (e.g., Signorelli et al. 1999; Scaillet et al. 2008; Oppenheimer et al. 2011). The hygrometer from Mollo et al. (2015), specific for phonolitic-trachytic melt, allows us to estimate the water content in Laacher See silicate melt in equilibrium with sanidine at 5.9 (±0.7) wt% H_2O suggesting that minerals have crystallized close to water-saturated conditions (Schmidt and Behrens 2008; Webster et al. 2014). This value corroborates data from melt inclusions (<6 wt% H_2O, Harms and Schmincke 2000) and experimental study at 200 MPa and water-saturated and CO_2-free conditions (Berndt et al. 2001). The presence of CO_2, S, and Cl lowered the water

TABLE 4. Representative major and trace element compositions of pyrrhotite

Sample	TAG	TAG	TAG	HE2	HE2	HE2
Mineral	Po	Po	Po	Bornite	Po	Po
Type	int	int	in Cpx	in Cpx	in Mag	in Cpx
			wt%			
Fe	60.06	60.05	53.03	14.46	57.93	58.86
S	37.41	37.4	38.77	25.34	38.55	38.31
Cu	1.84	1.07	<0.01	60.78	0.37	0.30
Ni	0.85	1.38	0.04	0.03	<0.01	0.01
Total	100.1	99.9	92.8	100.5	96.85	97.48
N_{FeS}	0.96	0.97	0.9	–	0.92	0.93
			Parts per million			
As	940	1162	6	100	19.4	7.9
Se	<19.6	32.6	50	541.7	19.9	15.1
Te	2.3	1.9	1.4	9.4	3.2	3.6
Pb	462.0	207.0	15.5	59.1	2.2	1.7
Bi	2.4	0.1	0.03	0.6	<0.1	<0.1
Ag	18.3	40.5	61.2	6.1	0.6	0.65
			Parts per billion			
Os	6	(7.5)	30	410	158	23.6
Ir	(2.6)	1.4	30	87	41	6.2
Ru	60	260	230	1360	150	440
Rh	230	96	80	1380	66	129
Pt	(18.0)	10	30	270	27	14
Pd	1900	300	920	n.d.	2300	1700
Au	100	60	100	1400	60	30
Re	60	50	120	50	n.d.	n.d.
Cu/Ni	2.2	0.8	0.05	55.3	89.4	24.6
Pd/Ir	711	185	30.6	933	14.8	120
S/Se	25400	15424	8000	615	18139	23857
Se/Te	8.40	16.7	35.7	57.8	6.2	4.1

Notes: N_{FeS} = fraction of FeS (Toulmin and Barton 1964), concentration under detection limit in parantheses; Po = pyrrhotite, int = interstitial, Cpx = clinopyroxene, Mag = magnetite.

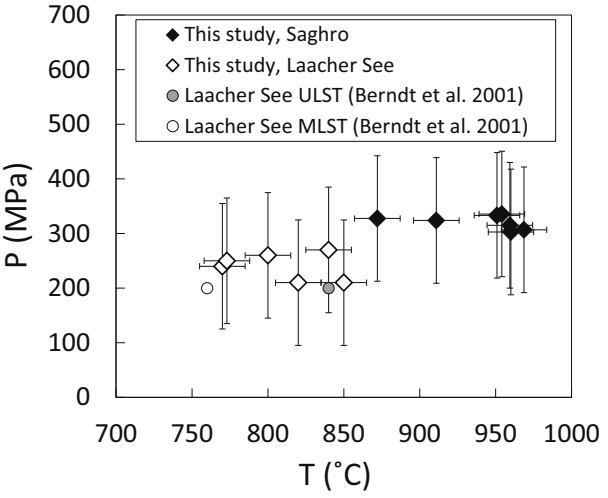

FIGURE 6. *P-T* conditions calculated from Cpx-liquid thermobarometer (Masotta et al. 2013) for Saghro and Laacher See phonolites.

solubility in phonolitic melt (at 900 °C, H_2O solubility is 6.5 and 8 wt% in Cl-bearing and CO_2-free phonolitic melt and in Cl-CO_2-free phonolitic melt, respectively, Webster et al. 2014) leading to the presence of a fluid phase at depth. However, for Laacher See, the low bulk CO_2 content in phonolite and CO_2-free melt inclusions reported by Harms and Schmincke (2000) suggest that CO_2 was not a factor that may have induced fluid saturation in the phonolitic magma.

Contrary to Laacher see phonolite, Saghro phonolite has not been studied experimentally and does not have melt inclusions in phenocrysts or glassy matrix. The bulk CO_2 content suggests a minimum value of 130 ppm C after degassing (Table 1), whereas the water content can only be estimated using K-feldspar-melt equilibrium (Mollo et al. 2015). Calculation yields water content in the melt coexisting with sanidine equals to 4.1 (±0.7) wt% H_2O. The partitioning of H_2O and CO_2 into the fluid phase increases (and Cl decreases) with increasing molar Na/Na+K in melts (Webster et al. 2014). The lower Na/Na+K ratio of Laacher See phonolite (Na/Na+K = 0.48) compared to the Saghro phonolite (Na/Na+K = 0.68) as well as the presence of other volatile species indicate water-undersaturated conditions for Laacher See at low pressure, whereas Saghro phonolite might have been closer to water-saturated conditions.

S content and speciation in phonolites. The presence of sulfur in phonolitic magmas is clearly demonstrated by the crystallization of S-bearing phases such as pyrrhotite, haüyne, nosean, and S-bearing apatite. Laacher See phonolite has abundant haüyne (5 vol%, 5.2–5.5 wt% S) and S-rich apatite (0.5 vol%, 0.7–0.9 wt% SO_3), whereas pyrrhotites are rare and the whole-rock sulfur content of the phonolite after eruption (i.e., minerals and silicate melt after volatile exsolution during ascent) is high with 4000 ppm S.

The initial sulfur content at pre-eruptive conditions can be estimated using experimentally determined partition coefficient for apatite ($Kd_S^{ap/melt}$, Parat and Holtz 2005; Parat et al. 2011a). S-rich apatites from Laacher See are in equilibrium with S-rich melt with 1100–3200 ppm S (as S^{6+}). These concentrations are higher than those measured in melt inclusions (S = 520–1490 ppm) and matrix glasses (S = 200–940 ppm) from ULST tephra (Harms and Schmincke 2000), suggesting partial degassing or crystallization of S-bearing mineral phases before melt inclusion entrapment. These values are lower than the whole-rock sulfur content suggesting that slight haüyne accumulation may have occurred in the lower part of the magma chamber.

Nosean-bearing phonolites from Saghro have 0.4 vol% nosean (2.8–3.5 wt% S), relatively abundant pyrrhotite and low whole-rock sulfur content (S = 560 ppm, Table 1, Fig. 9). Apatites are S-poor (SO_3 < 0.1 wt%) and the sulfate content (S^{6+}) in the melt in equilibrium with apatite is less than 20 ppm. Nosean-bearing phonolites from Saghro are sulfate-poor with low S^{6+}/S^{2-} ratios in the silicate melt [presence of pyrrhotite (S^{2-})].

Cl content in phonolites. Laacher See phonolite has Cl-poor haüyne (0.3–0.5 wt% Cl) and Cl-rich apatite (0.22–0.25 wt% Cl), whereas Saghro phonolite has Cl-rich nosean (1.1–1.3 wt% Cl) and Cl-poor apatite (<0.03 wt% Cl). Cl is present in large amount in Laacher See melt inclusions (1770–2600 ppm Cl) and matrix glasses (2100–5540 ppm Cl) (Harms and Schmincke 2000) relative to bulk rock (820 ppm Cl) (Fig. 9). Using experimentally determined partition coefficient, $Kd_{Cl}^{ap/melt}$ for hydrous phonolitic melts (Webster et al. 2009), the Cl concentration in the melt in equilibrium with apatite is 2000–2300 ppm Cl. This is one order of magnitude higher than the concentration estimated for Saghro phonolite, where Cl-poor apatite crystallized from a melt with Cl_{melt} < 91 ppm.

The Cl solubility in hydrous trachytic and phonolitic melts is strongly dependent of pressure and peralkaline index (Signorelli and Carroll 2002) and decreases with increasing sulfur content

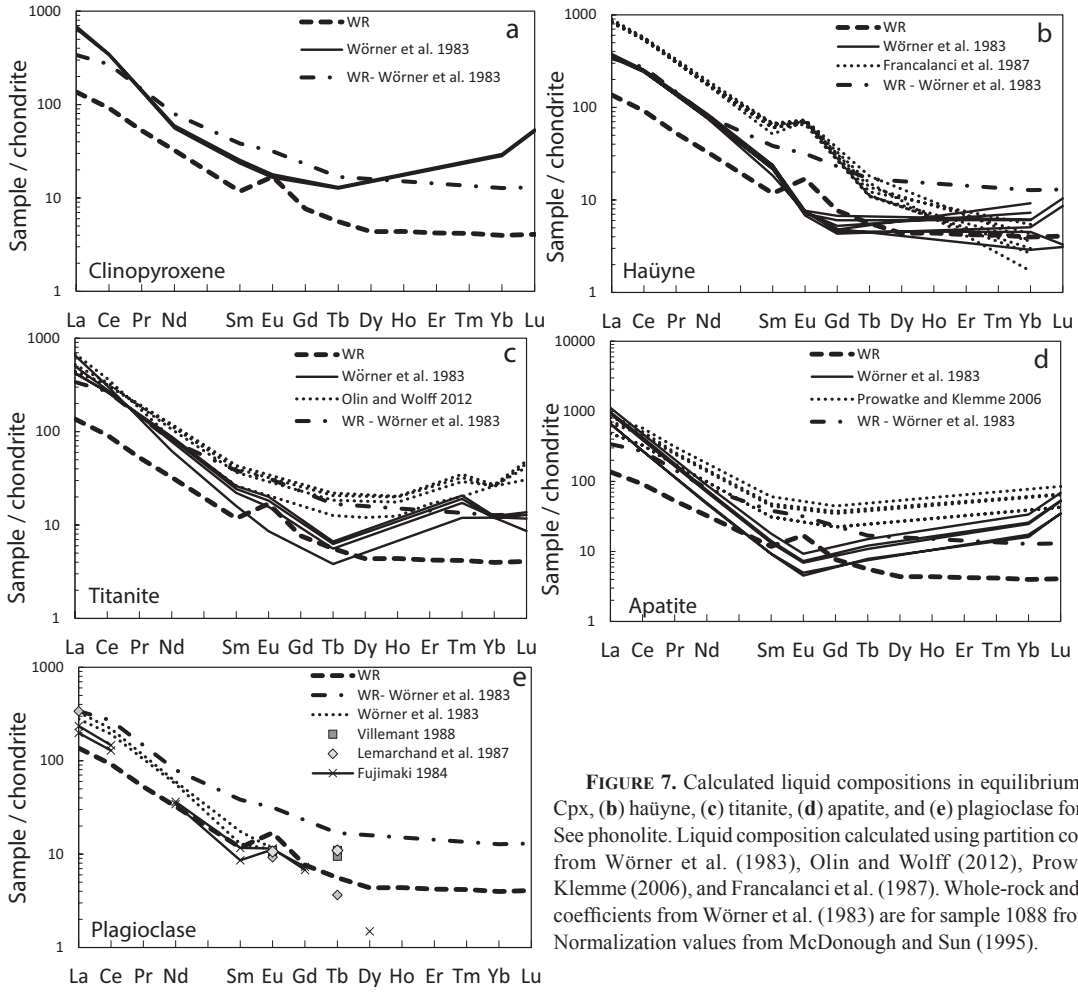

Figure 7. Calculated liquid compositions in equilibrium with (**a**) Cpx, (**b**) haüyne, (**c**) titanite, (**d**) apatite, and (**e**) plagioclase for Laacher See phonolite. Liquid composition calculated using partition coefficients from Wörner et al. (1983), Olin and Wolff (2012), Prowatke and Klemme (2006), and Francalanci et al. (1987). Whole-rock and partition coefficients from Wörner et al. (1983) are for sample 1088 from ULST. Normalization values from McDonough and Sun (1995).

(Webster et al. 2014). The two studied phonolites have very different peralkalinity and thus theoretical solubility: for Laacher See phonolite (P = 200 MPa, Na+K/Al = 1.04), Cl solubility is 5000 ppm, whereas for Saghro phonolite (P = 300 MPa, Na+K/Al = 1.2) Cl solubility is 8000 ppm (Signorelli and Carroll 2002). The maximum of Cl solubility decreases with S, from 9400 to 6700 ppm Cl in S-poor and S-bearing phonolite, respectively (Webster et al. 2014). These values are higher than those estimated from apatite compositions suggesting that the phonolitic melt was not saturated in Cl during apatite crystallization and the co-crystallization of haüyne in Laacher See phonolite occurs in the absence of an exsolved Cl-bearing fluid (before Cl saturation) (Fig. 9). The late crystallization of nosean in Saghro phonolite (Fig. 10) may suggest crystallization close to or at Cl saturation in the silicate melt.

F content in phonolites. Fluorine is the volatile element that has the lowest partition coefficient between fluid phase and silicate melt (e.g., Webster et al. 2014) and F is mainly incorporated in apatite during fractional crystallization. The partition coefficient of F between apatite and melt has been quantified experimentally and in situ for silicate melt, increasing from basalt to phonolite from 3.4 to 40, respectively (Mathez and Webster 2005; Webster et al. 2009; Parat et al. 2011a). In Laacher See and Saghro phonolites, the fluorine content in apatite ranges from 3.3 to 3.9 wt%, and using partition coefficient for phonolitic melt, F concentration in the melt in equilibrium with apatite is 800–1000 ppm. These values are lower than the concentration of F solubility determined experimentally for phonolitic melt (5000–7500 ppm, Webster et al. 2014) suggesting that at the time of apatite crystallization, the silicate melt was undersaturated in F.

Crystallization environment of sodalite-bearing phonolites

Haüyne-bearing Si-rich phonolite: Laacher See. The Laacher See phonolite represents a late stage of crystallization that evolved from nepheline basanite magmas (Wedepohl et al. 1994; Wörner and Schmincke 1984b). The phonolitic magma is Si-undersaturated and peralkaline and the crystallization of Cpx, plagioclase, amphibole, apatite, haüyne, sanidine, pyrrhotite, and magnetite occurs at depth in a shallow magma chamber (250 MPa and 850 °C). The crystallization environment is oxidized (ΔNNO-NNO+1) and the oxidation state increased with crystallization (haüyne-plagioclase crystallization). More oxidizing conditions at the top of the Laacher See magma chamber are also indicated by the speciation of sulfur in glass inclusions,

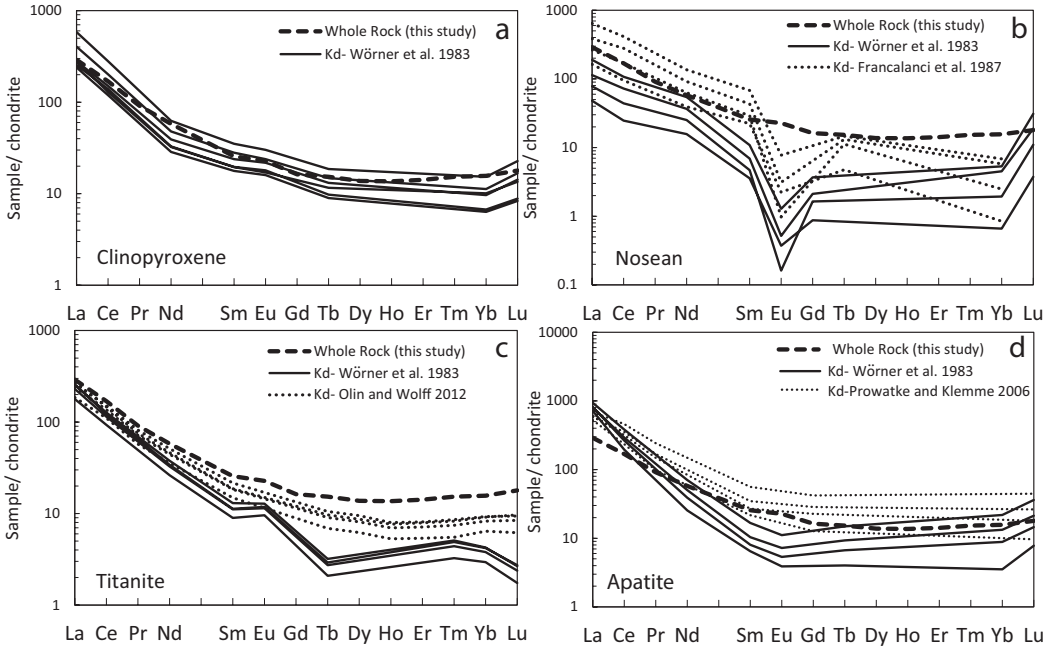

Figure 8. Calculated liquid compositions in equilibrium with (**a**) Cpx, (**b**) nosean, (**c**) titanite, and (**d**) apatite for Saghro phonolite. Liquid composition calculated using partition coefficients from Wörner et al. (1983), Olin and Wolff (2012), Prowatke and Klemme (2006), and Francalanci et al. (1987). Normalization values from McDonough and Sun (1995).

the S^{6+}/S^{tot} ratio being higher in the LLST (top of the magma chamber) than in the ULST (bottom of the magma chamber) (Harms and Schmincke 2000).

The REE compositions of the theoretical silicate melts in equilibrium with Cpx, apatite, haüyne, titanite, and plagioclase calculated from mineral composition and available empirical partition coefficient for phonolitic system (Wörner et al. 1983; Francalanci et al. 1987; Lemarchand et al. 1987; Villemant 1988; Olin and Wolff 2012; Figs. 7 and 8) suggest that minerals have crystallized from a melt with a composition close to the bulk composition. Melt calculated from Cpx shows a small discrepancy with a concave shape compare to the bulk rock with a depletion in MREE relative to LREE and HREE suggesting a slightly early crystallization of titanite before Cpx crystallization [Kd(titanite/melt) for MREE = 38–72 in titanite, Olin and Wolff 2012] in agreement with the occurrence of titanite as inclusions in Cpx. The rims of Cpx are depleted in MREE and enriched in HREE compared to the core (Fig. 5), suggesting that titanite also

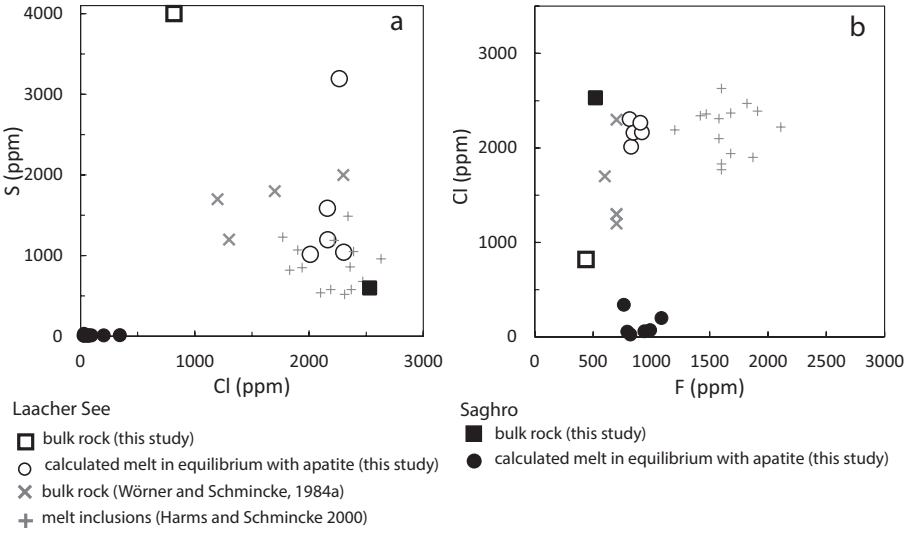

Figure 9. Sulfur and chlorine content in Saghro and Laacher See phonolites, melt inclusions and liquid in equilibrium with apatite (S^{6+}). ULST Laacher See bulk-rock data from Wörner and Schmincke (1984a) and melt inclusions data from Harms et al. (2000).

crystallized during the crystallization of Cpx rim. The trace element concentrations with different compatibility such as Cu/Ni [Cu is incompatible in silicate minerals, whereas Ni is moderately compatible; Ewart and Griffin (1994)] corroborate one crystallization environment for all minerals with similar Cu/Ni ratio (Fig. 10). The coeval crystallization of minerals in Laacher See phonolite agrees with the study of Harms and Schmincke (2000) in which melt inclusions in all minerals from the ULST have very similar composition (57–59 wt% SiO_2).

The incongruent reaction haüyne-plagioclase and the negative Eu anomaly observed in Cpx, titanite, and apatite, suggest an early crystallization of haüyne leading to an increase of the oxygen fugacity (e.g., magma becomes more oxidized) with differentiation in agreement with experimental and melt inclusion studies suggesting more oxidizing conditions at the top of the Laacher See magma chamber (more evolved magma, LLST; Berndt et al. 2001; Harms and Schmincke 2000). The sequence of crystallization may be then defined as: early crystallization of haüyne-apatite-titanite followed by Cpx-plagioclase-sanidine±amphibole. The lower trace element contents and positive Eu anomaly of the studied bulk-rock sample compared to published bulk-rock compositions of Laacher See tephra of the ULST unit and the Eu negative anomaly (Fig. 7, Wörner et al. 1983; Wörner and Schmincke 1984a) indicate, as discussed for volatile elements, that accumulation of haüyne and possibly plagioclase may have occurred in the lower part of the magma chamber.

During crystallization, the water content in the phonolitic melt (<6 wt% H_2O) indicates that at depth (250 MPa), the melt was fluid-undersaturated. However, the evolution of S, Cl, and F content in the melt in equilibrium with apatite and in the melt inclusions show an increase of F and constant S and Cl (Fig. 9), S being probably buffered by the crystallization of S-rich haüyne, whereas the melt become Cl saturated with differentiation leading to the presence of a NaCl fluid phase (Dalou et al. 2015). More likely the upper part of the magma chamber was water-saturated and the Cl partitioned into an exsolving H_2O fluid phase.

Nosean-bearing Si-poor phonolite: Saghro. The last stage of crystallization of Saghro phonolite represents a moderately peralkaline melt with low silica and low Na_2O activities and the crystallization of nepheline, Cpx, sanidine, nosean, apatite, and pyrrhotite at high-temperature (950 °C), low-pressure (300 MPa), and relatively oxidized conditions (ΔNNO) in a volatile-poor fluid-undersaturated magma (4 wt% H_2O).

The trace element ratios and the calculated melt compositions in equilibrium with Cpx (Cu/Ni = 0.1) and apatite (Cu/Ni = 0.3–1.4) suggest that both are early crystallizing mineral in equilibrium with the bulk-rock composition (Figs. 7a–7d and 10). Although the calculated melts are slightly different compared to the bulk-rock composition, the uncertainty of the partition coefficient allows us to consider that all minerals crystallized in one environment (Fig. 8). The large variability of the Cu/Ni ratio in minerals (Fig. 10) suggests however that the evolution of Saghro lava most probably involved a more fractionated differentiation compared to Laacher See. With decreasing temperature, the sequence of crystallization is Cpx-nepheline-apatite-pyrrhotite followed by nosean-titanite. The incongruent reaction nepheline-nosean consumed oxygen during nosean crystallization and consequently, the oxygen fugacity increased and the magma became more oxidized.

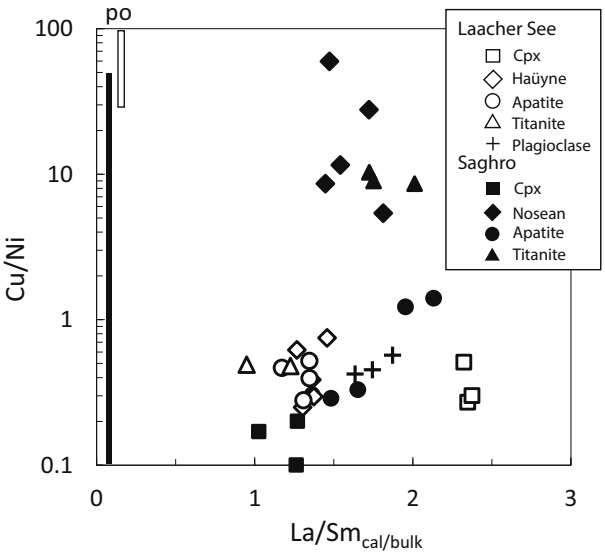

FIGURE 10. Cu/Ni in minerals vs. La/Sm ratio between bulk rock and liquid in equilibrium with minerals. Full and open symbols for Saghro and Laacher See minerals, respectively.

The volatile content in Saghro phonolitic melt is very low (Fig. 9) although it allows saturation of K-rich and Na-poor nosean (S- and Cl-bearing) in the late stage of crystallization. The rim of nosean have S content identical to the core, whereas Cl and Na strongly decreases suggesting that during ascent Cl most probably exsolved and formed a NaCl-bearing fluid phase (Fig. 3).

IMPLICATIONS

Our work shows that haüyne- and nosean-bearing phonolites are last equilibrated at low pressure and relatively high temperature with different volatile concentrations. Fractional crystallization of olivine+Cpx+amphibole+plagioclase+FeTi-oxides+apatite in Laacher See and olivine+Cpx+amphibole+magnetite+apatite+alkali feldspar in Saghro from basanite/nephelinite magmas may have led to volatile-bearing silicic peralkaline magmas. The difference in major element composition, e.g., Na, K, and Si and the concentration of volatile elements in Si-rich and Si-poor phonolites are the result of slightly different parental magma compositions and different fractional crystallization evolution involving haüyne or nosean crystallization.

Although fractional crystallization appears to be the main proposed processus for phonolite genesis (e.g., Edgar 1987; Ablay et al. 1998; Thompson et al. 2001), recent experimental study from Laporte et al. (2014) on partial melting of K_2O-bearing lherzolite reproduced the major element composition of nosean-bearing phonolite for very low partial melting. The experiments fail however to reproduce the high SiO_2 and K_2O values in haüyne-bearing phonolite, even for very low partial melting. These experiments are volatile-free and the influence of volatiles in mantle rocks on partial melting should be addressed to constrain the genesis of Si-rich and volatile-rich sodalite-

bearing phonolite and other volatile-bearing phonolites (e.g., Signorelli et al. 1999; Oppenheimer et al. 2011) and confirm the hypotheses in which volatile-rich and Si-rich phonolites are the last stage of fractional crystallization of nepheline basanite magmas, whereas volatile-bearing and Si-poor phonolites may result from partial melting of K_2O-rich mantle rocks.

ACKNOWLEDGMENTS

This research was financially supported by the "Institut National des Sciences de l'Univers" (France) (projet 772372) and the FP7-PEOPLE-2013-IRSES project MEDYNA. We thank F. Holtz for providing rock samples from Eifel, C. Nevado and D. Delmas for their valuable technical assistance, and J.-M. Dautria for informative discussions. Constructive reviews by G. Wörner and an anonymous reviewer are gratefully acknowledged. We thank C. Cannatelli for editorial handling of the manuscript.

REFERENCES CITED

Ablay, G.J., Carroll, M.R., Palmer, M.R., Marti, J., and Sparks, R.S.J. (1998) Basanite-phonolite lineages of the Teide-Pico Viejo Volcanic Complex, Tenerife, Canary Islands. Journal of Petrology, 39, 905–936.

Alt, J.C., Garrido, C.J., Shanks, W.C. III, Turchyn, A., Padrón-Navarta, J.A., Sánchez-Vizcaíno, V.L., Gómez Pugnaire, M.T., and Marchesi, C. (2012) Recycling of water, carbon, and sulfur during subduction of serpentinites: A stable isotope study of Cerro Del Almirez, Spain. Earth and Planetary Science Letters, 327-328, 50–60.

Bailey, D.K. (1987) Mantle metasomatism-perspective and prospect. Geological Society, London, Special Publications, 30, 1–13.

Barker, D.S. (1976) Phase relations in the system $NaAlSiO_4$-SiO_2-NaCl-H_2O at 400°C-800°C and 1 kilobar, and petrologic implications. The Journal of Geology, 84, 97–106.

Bellatreccia, F., Della Ventura, G., Picciniti, M., Cavallo, A., and Brilli, M. (2009) H_2O and CO_2 in minerals of the haüyne-sodalite group: an FTIR spectroscopy study. Mineralogical Magazine, 73, 399–413.

Berger, J., Ennih, N., Mercier, J.-C., Liégeois, J.-P., and Demaiffe, D. (2009) The role of fractional crystallization and late-stage peralkaline melt segregation in the mineralogical evolution of Cenozoic nephelinites/phonolites from Saghro (SE Morocco). Mineralogical Magazine, 73, 59–82.

Berger, J., Ennih, N., and Liégeois, J.-P. (2014) Extreme trace elements fractionation in Cenozoic nephelinites and phonolites from the Moroccan Anti-Atlas (Eastern Saghro). Lithos, 210-211, 69–88.

Berndt, J., Holtz, F., and Koepke, J. (2001) Experimental constraints on storage conditions in the chemically zoned phonolitic magma chamber of the Laacher See volcano. Contributions to Mineralogy and Petrology, 140, 469–486.

Berrahma, M., Delaloye, M., Faure-Muret, A., and Rachdi, H.E.N. (1993) Premières données géochronologiques sur le volcanisme alcalin du Jbel Saghro, Anti-Atlas, Maroc. Journal of African Earth Sciences, 17, 333–341.

Bogaard, V.D.P. (1983) Die Eruption Des Laacher See Vulkans. Ph.D. thesis, Ruhr-Universitat Bochum.

——— (1995) $^{40}Ar/^{39}Ar$ ages of sanidine phenocrysts from Laacher See Tephra (12,900 yr BP): Chronostratigraphic and petrological significance. Earth and Planetary Science Letters, 133, 163–174.

Brousse, R., Bizouard, H., and Varet. J. (1969) Iron in the minerals of the sodalite group. Contributions to Mineralogy and Petrology, 22, 164–184.

Bryan, S.E. (2006) Petrology and Geochemistry of the Quaternary Caldera-forming, Phonolitic Granadilla Eruption, Tenerife (Canary Islands). Journal of Petrology, 47, 1557–1589.

Carroll, M.R., and Rutherford, M.J. (1988) Sulfur speciation in hydrous experimental glasses of varying oxidation state; results from measured wavelenght shifts of sulfur X-rays. American Mineralogist, 73, 845–849.

Cicconi, M.R., Giuli, G., Paris, E., Ertel-Ingrisch, W., Ulmer, P., and Dingwell, D.B. (2012) Europium oxidation state and local structure in silicate glasses. American Mineralogist, 97, 918–929.

Clemente, B., Scaillet, B., and Pichavant, M. (2004) The solubility of sulphur in hydrous rhyolitic melts. Journal of Petrology, 45, 2171–2196.

Dalou, C., Mysen, B.O., and Foustoukos, D. (2015) In-situ measurements of fluorine and chlorine speciation and partitioning between melts and aqueous fluids in the Na_2O-Al_2O_3-SiO_2-H_2O system. American Mineralogist, 100, 47–58.

De Fino, M., La Volpe, I., Peccerillo, A., Piccarreta, G., and Poli. G. (1986) Petrogenesis of Monte Vulture Volcano (Italy): Inferences from mineral chemistry, major and trace element data. Contributions to Mineralogy and Petrology, 92, 135–145.

Drake, M.J. (1975) The oxidation state of europium as an indicator of oxygen fugacity. Geochimica et Cosmochimica Acta, 39, 55–64.

Edgar, A.D. (1987) The genesis of alkaline magmas with emphasis on their source regions: Inferences from experimental studies. Geological Society, London, Special Publications, 30, 29–52.

Ewart, A., and Griffin, W.L. (1994) Application of proton-microprobe data to trace-element portioning in volcanics rocks. Chemical Geology, 117, 251–284.

Francalanci, L., Peccerillo, A., and Poli, G. (1987) Partition coefficients for minerals potassium-alkaline rocks: Data from Roman province (Central in Italy). Geochemical Journal, 21, 1–10.

Fujimaki, H., Tatsumoto, M., and Aoki, K. (1984) Partition coefficients of Hf, Zr, REE between phenocrysts and groundmass. Journal of Geophysical Research, 89, 662–672.

Giehl, C., Marks, M., and Nowak. M. (2014) An experimental study on the influence of fluorine and chlorine on phase relations in peralkaline phonolitic melts. Contributions to Mineralogy and Petrology, 167, 977.

Harms, E., and Schmincke, H.-U. (2000) Volatile composition of the phonolitic Laacher See magma (12,900 yr BP): implications for syn-eruptive degassing of S, F, Cl and H_2O. Contributions to Mineralogy and Petrology, 138, 84–98.

Hettmann, K., Wenzel, T., Marks, M., and Markl, G. (2012) The sulfur speciation in S-bearing minerals: New constraints by a combination of electron microprobe analysis and DFT calculations with special reference to sodalite-group minerals. American Mineralogist, 97, 1653–1661.

Holm, P.M., Wilson, J.R., Christensen, B.P., Hansen, L., Hansen, S.L., Hein, K.M., Mortensen, A.K., Pedersen, R., Plesner, S., and Runge, M.K. (2006) Sampling the Cape Verde mantle plume: Evolution of melt compositions on Santo Antão, Cape Verde Islands. Journal of Petrology, 47, 145–189.

Ibhi, A., Nachit, H., Abia, E.H., and Hernandez, J. (2002) Intervention des ségrégats carbonatitiques dans la pétrogenèse des néphélinites à pyroxène de Jbel Saghro (Anti-Atlas, Maroc). Bulletin de la Societe Geologique de France, 173, 37–43.

Johnson, M.C., Anderson, A.T., and Rutherford, M.J. (1994) Pre-eruptive volatile contents of magmas. Reviews in Mineralogy and Geochemistry, 30, 281–330.

Jugo, P. (2009) Sulfur content at sulfide saturation in oxidized magmas. Geology, 37, 415–418.

Jugo, P.J., Wilke, M., and Botcharnikov, R.E. (2010) Sulfur K-edge XANES analysis of natural and synthetic basaltic glasses: Implications for S speciation and S content as function of oxygen fugacity. Geochimica et Cosmochimica Acta, 74, 5926–5938.

Klaudius, J., and Keller, J. (2006) Peralkaline silicate lavas at Oldoinyo Lengai, Tanzania. Lithos, 91, 173–190.

Laporte, D., Lambart, S., Schiano, P., and Ottolini. L. (2014) Experimental derivation of nepheline syenite and phonolite liquids by partial melting of upper mantle peridotites. Earth and Planetary Science Letters, 404, 319–331.

Le Maitre, R.W. (1984) A Proposal by the IUGS Sub-Commission on the Systematics of Igneous Rocks for a Chemical Classification of Volcanic Rocks Based on the Total Alkali Silica (TAS) Diagram. Australian Journal of Earth Sciences, 31, 243–255.

Legendre, C., Maury, R.C., Savanier, D., Cotton, J., Chauvel, C., Hemond, C., Bollinger, C., Blais, S., Guille, G., and Rossi. P. (2005) The origin of intermediate and evolved lavas in the Marquesas Archipelago: An example from Nuku Hiva Island (French Polynesia). Journal of Volcanology and Geothermal Research, 143, 293–317.

Lemarchand, F., Villemant, B., and Calas, G. (1987) Trace element distribution coefficients in alkaline series. Geochimica et Cosmochimica Acta, 51, 1071–1081.

Lessing, P., and Grout, C.H. (1971) Haüynite from Edwards, New York. American Mineralogist, 59, 1096–1100.

Luhr, J.F. (1990) Experimental Phase relations of Water- and Sulfur –Saturated Arc Magmas and the 1982 Eruptions of El Chichon Volcano. Journal of Petrology, 31, 1071–1114.

Masotta, M., Mollo, S., Freda, C., Gaeta, M., and Moore, G. (2013) Clinopyroxene-liquid thermometers and barometers specific to alkaline differentiated magmas. Contributions to Mineralogy and Petrology, 166, 1545–1561.

Mathez, E.A., and Webster, J.D. (2005) Partitioning behavior of chlorine and fluorine in the system apatite-silicate melt-fluid. Geochimica et Cosmochimica Acta, 69, 1275–1286.

McDonough, W.F., and Sun, S.-S. (1995) The composition of the Earth. Chemical Geology, 120, 223–253.

Mertes, H., and Schmincke, H.-U. (1985) Mafic potassic lavas of the Quaternary West Eifel volcanic field. Contributions to Mineralogy and Petrology, 89, 330–345.

Métrich, N., and Wallace, P. (2008) Volatile abundances in basaltic magmas and their degassing paths tracked by melt inclusions. Reviews in Mineralogy and Geochemistry, 69, 363–402.

Missenard, Y., and Cadoux, A. (2011) Can Moroccan Atlas lithospheric thinning and volcanism be induced by Edge-Driven Convection? Terra Nova, 24, 27–33.

Mollo, S., and Masotta. M. (2014) Optimizing pre-eruptive temperature estimates in thermally and chemically zoned magma chambers. Chemical Geology, 368, 97–103.

Mollo, S., Masotta. M., Forni, F., Bachmann, O., De Astis, G., Moore, G., and Scarlato, P. (2015) A K-feldspar-liquid hygrometer specific to alkaline differentiated magmas. Chemical Geology, 392, 1–8.

Olin, P.H., and Wolff, J.A. (2012) Partitioning of rare earth and high field strength elements between titanite and phonolitic liquid. Lithos, 128-131, 46–54.

Oppenheimer, C., Moretti, R., Kyle, P., Eschenbacher, A., Lowenstern, J.B., Hervig, R.L., and Dunbar, N.W. (2011) Mantle to surface degassing of alkali magmas at Erebus volcano, Antartica. Earth and Planetary Science Letters, 306, 261–271.

Parat, F., and Holtz, F. (2005) Sulfur partition coefficient between apatite and rhyolite: the role of bulk S content. Contributions to Mineralogy and Petrology, 150, 643–651.

Parat, F., Holtz, F., and Feig, S. (2008) Pre-eruptive conditions of the Huerto Andesite (Fish Canyon System, San Juan Volcanic Field, Colorado): Influence of volatiles (C-O-H-S) on phase equilibria and mineral composition. Journal of Petrology,

49, 911–935.
Parat, F., Holtz, F., and Klugel, A. (2011a) S-rich apatite-hosted glass inclusions in xenoliths from La Palma: constraints on the volatile partitioning in evolved alkaline magmas. Contributions to Mineralogy and Petrology, 162, 463–478.
Parat, F., Holtz, F., and Streck, M.J. (2011b) Sulfur-bearing magmatic accessory minerals. Reviews in Mineralogy and Geochemistry, 73, 285–314.
Price, R.C., and Green. D.H. (1972) Lherzolite nodules in a mafic phonolite from North East Otago, New Zealand. Nature, 235, 133–134.
Prowatke, S., and Klemme. S. (2006) Trace element partitioning between apatite and silicate melts. Geochimica et Cosmochimica Acta, 70, 4513–4527.
Putirka, K. (2008) Thermometers and barometers for volcanics systems. Reviews in Mineralogy and Geochemistry, 69, 61–120.
Putirka, K.D., Mikaelian, H., Ryerson, F., and Shaw, H. (2003) New clinopyroxene-liquid thermobarometers for mafic, and volatile-bearing lava composition, with applications to lavas from Tibet and the Snake River Plain, Idaho. American Mineralogist, 88, 1542–1554.
Scaillet, B., and Pichavant, M. (2003) Experimental constraints on volatile abundances in arc magmas and their implications for degassing processes. Geological Society, London, Special Publications, 213, 23–52.
Scaillet, B., Pichavant, M., and Cioni, R. (2008) Upward migration of Vesuvius magma chamber over the past 20,000 years. Nature, 455, 216–219.
Schmidt, B.C., and Behrens, H. (2008) Water solubility in phonolite melts: Influence of melt composition and temperature. Chemical Geology, 256, 259–268.
Schmincke, H.-U., Park, C., and Harms, E. (1999) Evolution and environmental impacts of the eruption of Laacher See Volcano (Germany) 12,900 a BP. Quaternary International, 61, 61–72.
Schnetzler, C.C., and Philpotts. J.A. (1970) Partition coefficients of rare-earth elements between igneous matrix material and rock-forming mineral phenocrysts—II. Geochimica et Cosmochimica Acta, 34, 331–340.
Sharp, Z.D., Helffrich, G.R., Bohlen, S.R., and Essene, E.J. (1989) The stability of sodalite in the system $NaAlSiO_4$-NaCl. Geochimica et Cosmochimica Acta, 53, 1943–1954.
Signorelli, S., and Carroll, M.R. (2002) Experimental study of Cl solubility in hydrous alkaline melts: constraints on the theoretical maximum amount of Cl in trachytic and phonolitic melts. Contributions to Mineralogy and Petrology, 143, 209–218.
Signorelli, S., Vaggelli, G., and Romano, C. (1999) Pre-eruptive volatile (H_2O, F, Cl, and S) contents of phonolitic magmas feeding the 3550-year old Avellino eruption from Vesuvius, Southern Italy. Journal of Volcanology and Geothermal Research, 93, 237–256.
Stormer, J., and Carmichael, I.S.E. (1971) The free energy of sodalite and the behavior of chloride, fluoride and sulfate in silicate magmas. American Mineralogist, 56, 292–305.
Thompson, G.M., Smith, I.E.M., and Malpas, J.G. (2001) Origin of oceanic phonolites by crystal fractionation and the problem of the Daly gap: an example from Rarotonga. Contributions to Mineralogy and Petrology, 142, 336–346.
Tomisaka, T., and Eugster. H.P. (1968) Synthesis of the sodalite group and subsolidus equilibria in the sodalite-noselite system. Journal of the Mineralogical Society of Japan, 5, 249–275.
Toulmin, P., and Barton, P. (1964) A thermodynamic study of pyrite and pyrrhotite. Geochimica et Cosmochimica Acta, 78, 641–671.
Trail, D., Watson, E.B., and Tailby, N.D. (2012) Ce and Eu anomalies in zircon as proxies for the oxidation state of magmas. Geochimica et Cosmochimica Acta, 97, 70–87.
Van Achterbergh, E., Ryan, C.G., and Griffin, W.L. (2001) GLITTER on-line interactive data reduction for the LA-ICPMS microprobe. Macquarie Research, Sydney.
Van Peteghem, J.K., and Burley. B.J. (1963) Studies on solid solution between sodalite, nosean and haüyne. Canadian Mineralogist, 7, 808–813.
Vernet, M., Marin, L., Boulmier, S., Lhomme, J., and Demange, J.C. (1987) Dosage du fluor et du chlore dans les matériaux géologiques y compris les échantillons hyperalumineux. Analusis, 15, 490–498.
Webster, J.D., Goldoff, B., Sintoni, M.F., Shimizu, N., and De Vivo. B. (2014) C-O-H-Cl-S-F volatiles solubilities, partitioning, and mixing in phonolitic-trachytic melts and aqueous-carbonic vapor and saline liquid at 200 MPa. Journal of Petrology, 55, 2217–2248.
Webster, J.D., Goldoff, B., and Shimizu, N. (2011) C-O-H-S fluids and granitic magma: how S partitions and modifies CO_2 concentrations of fluid-saturated felsic melt at 200 MPa. Contributions to Mineralogy and Petrology, 162, 849–865.
Webster, J.D., Sintoni, M.F., and De Vivo, B. (2009) The partitioning behavior of Cl, S, and H_2O in aqueous vapor- ±saline-liquid saturated phonolitic and trachytic melts at 200 MPa. Chemical Geology, 263, 19–36.
Wedepohl, K.H., Gohn, E., and Hartmann, G. (1994) Cenozoic alkali basaltic magmas of western Germany and their products of differentiation. Contributions to Mineralogy and Petrology, 115, 253–278.
Villemant, B. (1988) Trace element evolution in the Phlegrean Fields (Central Italy): fractional crystallization and selective enrichment. Contributions to Mineralogy and Petrology, 98, 169–183.
Whitney, J. (1984) Fugacities of sulfurous gases in pyrrhotite-bearing silicic magmas. American Mineralogist, 69, 69–78.
Whitney, D.L., and Evans, B.W. (2010) Abbreviations for names of rock-forming minerals. American Mineralogist, 95, 185–187.
Wörner, G., and Schmincke, H.-U. (1984a) Mineralogical and chemical zonation of the Laacher See Tephra Sequence (East Eifel, W. Germany). Journal of Petrology, 25, 805–835.
——— (1984b) Petrogenesis of the zoned Laacher See Tephra. Journal of Petrology, 25, 836–851.
Wörner, G., Beusen, J.-M., Duchateau, N., Gijbels, R., and Schmincke, H.-U. (1983) Trace element abundances and mineral/melt distribution coefficients in phonolites from the Laacher See Volcano (Germany). Contributions to Mineralogy and Petrology, 84, 152–173.
Zaitsev, A.N., Marks, M.A.W., Wenzel, T., Spratt, J., Sharygin, V.V., Strekopytov, S., and Markl, G. (2012) Mineralogy, geochemistry and petrology of the phonolitic to nephelinitic Sadiman volcano, Crater Highlands, Tanzania. Lithos, 152, 66–83.

Manuscript received February 2, 2015
Manuscript accepted May 5, 2015
Manuscript handled by Claudia Cannatelli

Annexe B

Table des échantillons avec leurs coordonnées GPS

N°	Type	GPS S	GPS E	N°	Type	GPS S	GPS E
Kwaraha				Labait			
Kw1	carbonatite	4°16,55	35°50,75	Labx9	xenolite	4°33,928'	35°25,909'
Kw2	lave	4°17593	35°88292	Labx10	xenolite	'	'
Kw3	lave	4°1531	35°8975	Labx11	xenolite	'	'
Kw4	lave	4°1396	35°9146	Labx12	xenolite	'	'
Kw5	lave	4°12,07'	35°45,421'	Labx13	xenolite	'	'
Kw6	lave	4°12,778	35°43,493'	Labx14	xenolite	'	'
Kw7	lave	4°12,507'	35°43,93'	Labx15	xenolite	'	'
Kw8	lave	4°11,932'	35°44,182'	Labx16	xenolite	'	'
Kw9	tuf	4°12,899'	35°42,867'	Labx17	xenolite	'	'
Kw10	lave	04°07'47.4''	35°46'34.7''	Basotu			
Kw11	lave	04°08'14.1''	35°48'20.5''	Bas1	tuf	4°21,835'	35°04,284'
Kw12	lave	04°10'07.63''	35°46'58.72''	Essimingor			
Hanang				Ess1	lave	3°29,051'	35°59,854'
Han1	lave	4°25,463'	35°30,157'	Ess2	lave	3°27,695'	35°58,843'
Han2	lave	4°23,639'	35°27,706'	Ess3	lave	3°27,240'	35°58,876'
Han3	lave	4°23,065'	35°28,101'	Ess4	lave	3°27,697'	36°06,460'
Han4	lave	4°30,824'	35°23,568'	Ngorongoro			
Han5	lave	4°30,232'	35°23,259'	Ngo1	lave	3°18,843'	35°48,891'
Han6	lave	4°25,728'	35°18,101'	Ngo2	lave	3°17,425'	35°49,391'
Han7	lave	4°24,363'	35°18,453'	Burko			
Han8	lave	4°24,363'	35°18,453'	Bur1	lave	3°20,667'	36°13,320'
Han9	lave	4°37'	35°20'	Bur2	lave	3°20,667'	36°13,320'
Han10	tuf	4°37'	35°20'	Monduli			
Han11	lave	4°37'	35°20'	Mon1	lave	3°15,850'	36°24,227'
Han12	tuf	4°37'	35°20'	Oldoinyo Lengai			
Han13	lave	4°30,305'	35°26,633'	Ol1	tuf	2°49,281'	36°00,36'
Labait				Ol2	lave	2°48,328'	35°59,612'
Lab1	lave	4°33,928'	35°25,909'	Ol3	carbonatite	2°44'57,34''	35°53'23,47''
Lab2	lave	'	'	OL3x	lave	2°44'57,34''	35°53'23,47''
Lab3	lave	'	'	Ol4	lave	2°44'57,34''	35°53'23,47''
LabX1	xenolite	'	'	Olmani			
LabX2	xenolite	'	'	OLMa	lave	3°23'54.81''	36°44'54.52''
LabX3	xenolite	'	'	OLMb	lave	'	'
LabX4	xenolite	'	'	olmx1	xenolite	'	'
LabX5	xenolite	'	'	olmx2	xenolite	'	'
LabX6	xenolite	'	'	olmx3	xenolite	'	'
LabX7	xenolite	'	'	olmx4	xenolite	'	'
LabX8	xenolite	'	'	olmx5	xenolite	'	'

Table des paragenèses des laves

			Texture					Paragenese												
Volcan	**n°**	nom	aph	prhy	mega	fld	ves	ol	cpx	phl	am	pl	F-K	nph	op	tit	grt	ap	sul	Cc	MI
Kwaraha	**KW1**	calcio-carbonatite	X							+					X			+		X	
	KW2	melilite néphélinite		X				X	X						X						
	KW3	melilite néphélinite		X	X			X	X	X								+			
	KW4	mélanéphélinite		X				X	X	X					X						
	KW5a	melilite néphélinite		X				X	X						X			+			
	KW5b	melilite néphélinite		X	X			X	X						X			+			
	KW6	melilite néphélinite		X				X		+					X						
	KW7	melilite néphélinite		X				+	X	X		+			+			+			
	KW8	melilite néphélinite		X			+	X	X	+					X						
	KW9	tuf					X	+	x	x		+		+	x						
	KW10	melilite néphélinite		X				x	x	x					x						
	KW11	melilite néphélinite		X				x	x	x					x						
	KW12	melilite néphélinite		X				x	x	x					x						
Hanang	**HAN1**	néphélinite	X						X					X	+	+			+		+
	HAN2	néphélinite	X						X					X	+		X				
	HAN3	néphélinite	X						X					X	+						
	HAN4	néphélinite	X						X					X		+					
	HAN5	néphélinite					X	X	X					+							
	HAN6	néphélinite	X						X					+							
	HAN7	néphélinite		X					X					X		+	X				
	HAN8	néphélinite		X					X					X		+	X	+	+		+
	HAN10	tuf							X	X					X						
	HAN11	néphélinite	X						X					X		+			+		+
	HAN12	tuf							X					+	+					X	
	HAN13	néphélinite	X						X					X				+	+		+
Basotu	**BAS1**	tuf					+	+		+				X						X	
Labait	**LAB1a**	melilite néphélinite		X				X		X					x			+			
	LAB1b	melilite néphélinite		X				X		X					+				+		
	LAB2	mélilitite		X				X		X											
	LAB3	mélanéphélinite		X				X				X							x		
Essimingor	**ESS1**	phonotéphrite	X						X	+	X				+	X		+	+		
	ESS2	basanite		X				X	X						+			+			
	ESS3	mélilite néphélinite		X	X				X						X			+			
	ESS4	mélilite néphélinite	X						X						X						
Monduli	**Mon1**	téphrite		X				X	X						X			+			
Ngorongoro	**NGO1**	trachy basalte		X				X	X						+						
	NGO2	picro basalte		X				X	X						+						
Burko	**BUR1**	néphélinite		X		X			X					X	+	X	+	+			
	BUR2	néphélinite		X		X			X					X	X	X			x		
Lengai	**OL1a**	tuf						X	X	X											
	OL1b	basalte		X				X	X						+						
	Ol2a	mélilite néphélinite	X					X	+								+				
	Ol2b	mélilite néphélinite	X					X	+								+				
	OL3	natrocabonatite	X			X	X													X	
	OL3x1	néphélinite		X			x		X				X	X							+
	OL3x2	ijolite		X				X						X							
Olmani	**OLM1a**	mélanéphélinite		X				X	X						+						
	OLM1b	mélanéphélinite		X				X	X												

Aph : aphyrique, prhy : porphyrique, mega : mégacristaux, fld : fluidale, ves : vesiculaire. Ol : olivine, cpx : clinopyroxène, phl : phlogopite, am : amphibole, pl : plagioclase, F-K : feldspath alcalin, nph : néphéline, op : opaque, tit : titanite, grt : grenat, ap : apatite, sul : sulfure, Cc : calcite, MI : inclusions vitreuses

Table des proportions modales

Proportion modale représentative des laves du Hanang

	Han1	Han2	Han4	Han7	Han8	Han11	Han13
% phénocristaux	30.1	10.8	15.6	23.5	30.5	37.2	25.4
néphéline	24.5	3.5	9.1	14.8	18.5	31	17.3
clinopyroxène	5	4.5	4.5	5.9	7.5	4.7	5.7
grenat	0.4	2.8	0.5	1.6	2.5	0	0.9
apatite	0	0	1	1	1.5	1	1
titanite	0.2	0	0.5	0.2	0.5	0.5	0.5
pyrrhotite	0	0.001	0	0	0.002	0	0.001

Proportion modale des laves du Kwaraha

	Kw2	Kw3	Kw4	Kw5	Kw6	Kw8	Kw10	Kw11	Kw12
%phénocristaux	10	21.5	20.2	22.0	13.0	16.1	8.6	19.0	19.4
olivine	5.8	10.0	1.5	10.0	2.0	3.0	1.7	12.5	11.7
cpx	3.8	6.0	11.5	7.0	9.0	12.0	5.3	5.0	4.3
magnétite	0.5	2.0	1.7	5.0	1.0	0.2	1.6	1.0	0.5
phlogopite	-	3.5	5.5	-	1.0	0.9	-	0.5	2.9

Proportion modale des laves du Labait et d'Olmani

	Lab1	Lab2	Lab3	Olm1a	Olm1b
%phénocristaux	23.0	16.5	35.0	19.0	28.0
olivine	22.0	15.0	30.0	13.0	18.0
cpx	-	-	-	5.5	10.0
magnétite	-	1.0	-	0.5	-
plagioclase	-	-	5.0	-	-
phlogopite	1.0	0.5	-	-	-

Les laves sous saturées en silice seront nommés dans cette thèse en utilisant la classification de Le Maitre et al. (2002) basé sur la minéralogie normative (C.I.P.W).

	cs	ne	ab	ol	
*** TAS F**	>10%	-	-	-	mélilitite
<41%SiO_2	<10%	<20%	-	-	mélilite néphelinite
	0	<20%	-	-	mélanéphelinite
	<10%	>20%	-	-	néphelinite
*** TAS U1**	0	<20%	<5%	>10%	mélanéphelinite
>41%SiO_2	0	<20%	>5%	>10%	basanite
	0	-	-	<10%	téphrite

d'après Le Maitre 2002

Table des calculs de norme C.I.P.W

			CIPW												
Volcan	**n°**	nom	Pl	Orth	Nph	Lc	Diop	Woll	Ol	*cs* Larn	Ac	Na_2SiO_3	Ilm	Mag	Apat
Kwaraha	**KW2**	melilite néphélinite	15.03		3.76	5.84	48.07		11.58	1.98			6.02	6.25	1.46
	KW3	melilite néphélinite	11.31		2.57	10.24	36.51		20.93	3.25			6.91	6.83	1.46
	KW4	mélanéphélinite	12.89	4.88	8.57	1.68	49.25		10.84				5.7	5.63	0.56
	KW5b	melilite néphélinite	0.74		15.91	11.91	39.89		11.57	4.71			7.07	6.86	1.37
	KW6	melilite néphélinite	4.69		16.14	9.59	38.32		9.38	8			6.42	6.35	1.11
	KW8	melilite néphélinite	6.79		12.29	8.57	42.75		14.5	1.27			6.17	6.19	1.48
	KW10	melilite néphélinite	8.39		12.06	7.83	41.29		13.95	2.01			6.57	6.39	1.51
	KW11	melilite néphélinite	11.53		5.59	5.56	44		18.28	0.46			6.46	6.73	1.41
	KW12	melilite néphélinite	8.69		6.51	7.23	40.08		18.46	5.41			6.1	6.22	1.3
Hanang	**HAN1**	néphélinite	1.43	20.22	30.34		26.17	11			5.83		2.47	1.04	1.6
	HAN2	néphélinite			24.55	19.05	34.11		0.66	3.64	10.07	1.86	4.14		1.92
	HAN3	néphélinite													
	HAN4	néphélinite	19.69	18.14	24.98		27.77		0.03	0			3.48	4.45	1.46
	HAN7	néphélinite		14.17	31.53	5.48	30.42	6.63		0	6.72		2.62	0.88	1.53
	HAN8	néphélinite	1.84	20.74	29.93		29.17	6.22		0	7.92		2.49	0.22	1.46
	HAN11	néphélinite	3.15	24.17	31.4		25.14	4.69		0	6.98		2.58	0.79	1.09
	HAN13	néphélinite	2.75	23.76	30.91		28.8	0.65		0	8.01	1.88	2.28		0.95
Basotu	**BAS1**	tuf	7.91		4.45	5.67			11.58	79.25			0.84	2.39	2.48
Labait	**LAB1a**	melilite néphélinite	4.95		5.27	5.89	13.84		48.77	8.67			4.96	6.03	1.62
	LAB1b	melilite néphélinite													
	LAB2	mélilitite			9.08	7.32	10.81		45.62	12.98	3.12		5.07	4.71	1.27
	LAB3	mélanéphélinite	4.9	6.25	7.47	2	26.23		41.42	0			4.69	5.92	1.11
Essimingor	**ESS1**	phonotéphrite	32.91	24.17	14.27		19.01		2.12				3.1	3.47	0.95
	ESS2	basanite	10.73	16.13	17.34		33.71		12.35				3.99	4.92	0.83
	ESS3	mélilite néphélinite	8.6		14.16		42.34		4	2.37			8.36	6.87	2.32
	ESS4	mélilite néphélinite	10.11		13.11	6.26	46.59		1	1.57			10.83	7.25	3.29
Monduli	**Mon1**	téphrite	11.44	14.54	16.28		36.94		4.81				8.07	6.34	1.6
Ngorongoro	**NGO1**	trachy basalte	34.05	10.34	7.17		25.24		10.8				5.26	5.38	1.78
	NGO2	picro basalte	10.4	5.32	8.38		44.71		13.64				6.08	6.13	1.34
Burko	**BUR1**	néphélinite	4.8	20.62	32.05		25.38	7.44					3.97	4.12	1.62
	BUR2	néphélinite	15.39	17.08	24.84		26.78	6.17					4.2	4.16	1.39
Lengai	**Ol2a**	mélilite néphélinite	1.34		13.8	9.45	34.73		19.77	4.56			7.63	6.51	2.22
	OL3x1	néphélinite			15.49	32.48			10	11.25	9.72	17.54	2.03		0.93
Olmani	**OLM1a**	mélanéphélinite	6.5	1.44	11.05	5.18	39.05		22.5				4.58	5.64	1.09
	OLM1b	mélanéphélinite	8.02	4.84	9.99	2.04	37.61		26.2				4.56	5.65	1.09

Pl : plagioclase, orth : orthoclase, Nph : néphéline, Lc : leucite, Diop : diopside, Woll : wollastonite, Ol : olivine, cs Larnite : larnite, Ac : acmite, Ilm : ilménite, Mag : magnétite, Apat : apatite

Table des éléments majeurs et traces dans les sulfures

Type	Han8 inc cpx	Han8 inc cpx	Han13 inc cpx	Han13 inc neph	Han13 inter	Lab1 inc ol	Lab1 inc ol	Lab1 inc ol
wt%								
Fe	59.75	58.39	59.45	59.52	57.32	54.01	51.86	30.18
S	36.68	37.65	37.77	37.31	38.20	37.61	38.79	34.72
Cu	0.18	0.17	0.23	0.60	0.40	0.06	0.06	31.49
Ni	0.01	<0.01	0.13	0.05	0.01	5.71	5.78	0.21
Total	96.62	96.67	97.58	97.48	96.93	97.38	96.49	96.60
N_{FeS}	0.98	0.99	0.98	0.99	0.98	0.91	0.90	0.52
ppm								
As	4.9	3.1	2.1	4.1	4.3	2.95	1.66	30.2
Se	39.7	24.5	29.8	45.9	15.1	34.4	83.4	273.0
Te	2.3	1.4	0.60	1.6	0.94	4.42	3.35	18.50
Pb	112	20.3	23.3	114	38.2	0.18	20.0	3.37
Bi	1.1	0.1	0.08	0.17	0.05	b.d.	0.804	3.06
Ag	7.7	5.4	0.27	0.19	0.05	0.52	4.22	7.90
Os	0.1	0.17	b.d.l	b.d.l	b.d.l	0.56	0.13	0.45
Ir	0.02	0.02	b.d.l	b.d.l	b.d.l	0.67	0.11	0.47
Ru	0.52	1.3	2.37	1.38	0.78	1.03	2.51	5.41
Rh	0.77	0.52	0.04	0.09	0.08	0.63	0.04	3.21
Pt	0.03	0.03	0.03	0.06	0.03	0.81	0.18	0.06
Pd	2.8	2.4	0.95	0.07	0.03	1.16	1.97	1.48
Au	0.09	0.03	b.d.l	0.01	0.04	0.04	0.23	0.34
Re	0.04	0.05	0.08	b.d.l	0.37	0.412	0.4	0.32
Pd/Ir	132	100	264	15	15	1.73	17.6	3.1
S/Se	9329	15127	12404	8054	24471	10768	4439	1353
Se/Te	17.4	17	49.7	28	18.1	7.77	24.9	14.8

NFeS = fraction of FeS

Composition des xénolites de Olmani (OLMx) et Labait (LABx)

	nom	ol	cpx	opx	grt	sp	phl
OLMx1	Hz	X		X		+	
OLMx2	Hz	X		X		+	
OLMx3	Hz	X		X		+	
OLMx4	Hz	X		X		+	
OLMx5	Hz	X		X		+	
LABX1	D	X					
LABX2	D	X					
LABX3	Wehrlite	X	X		+		
LABX4	Lh	X	X	X	X		
LABX5	Lh	X	X	X		+	+
LABX6	Lh	X	X	x		+	X
LABX7	xénolite						X
LABX8	Lh	X	X	X		+	
LABX10	Hz	X	X	X	+	+	
LABX11	Lh	X	X	x		+	
LABX12	D + filon cpx	X	X			+	
LABX13	Hz	X		X		+	
LABX14	Hz	X		X		+	
LABX15	Lh	X	X	X		+	
LABX16	Lh	X	X	X		+	
LABX17	Lh	X	X	X		+	

D = Dunite, Hz=Harzburgite, Lh = Lherzolite. ol=olivine, cpx=clinopyroxène, opx=orthopyroxène, gt=grenat, sp=spinelle, phl=phlogopite

Annexe C

Résultats des laves de l'axe Est-Ouest de la divergence nord tanzanienne

Les volcans échantillonnés de l'axe E-O de la divergence nord tanzanienne sont les volcans, Monduli, Burko, Essimingor, et Ngorongoro. L'axe E-O est formé par un volcanisme alcalin à subalcalin comprenant des trachy-basaltes, tephrites, et des néphélinites.

La téphrite de Monduli a une texture microlitique porphyrique avec ~ 8 % de phénocristaux, (5 % de cpx, 3 % d'olivines) (Fig.C.1) (Table C1). La matrice est composée de feldspath, de cpx, d'apatite et de magnétite avec des exsolutions d'ilménite. Les néphélinites de Burko ont une texture microlitique porphyrique avec 50 % de phénocristaux de néphéline (~ 30 %), de cpx (15 - 17 %) et de Ti-grenat (2 - 4 %) et des microlithes de néphélinites et de cpx. Les échantillons d'Essimingor ont des compositions qui varient de néphélinites (Ess3, Ess4), à des laves plus différenciées (basanite (Ess2) et phonotéphrite (Ess1)). Les laves d'Essimingor sont composées de cpx, d'apatite, de magnétites et de titanites. Seuls les échantillons Ess4 et Ess2 contiennent des olivines. Ess1 a pour minéraux accessoires la titanite, l'amphibole et la pyrrhotite. Ess3 est composée de phénocristaux de cpx, de magnétite, et de pérovskite ainsi que de microcristaux de néphéline. Les échantillons du Ngorongoro (NGO1 et NGO2) sont des trachy-basaltes et picro-basaltes. Les laves du Ngorongoro ont des phénocristaux d'olivine (5 - 7 %) et de clinopyroxène (1 - 4 %) (Fig.C.1); la matrice est composée de feldspaths, clinopyroxènes (cpx) et de Ti-magnétites.

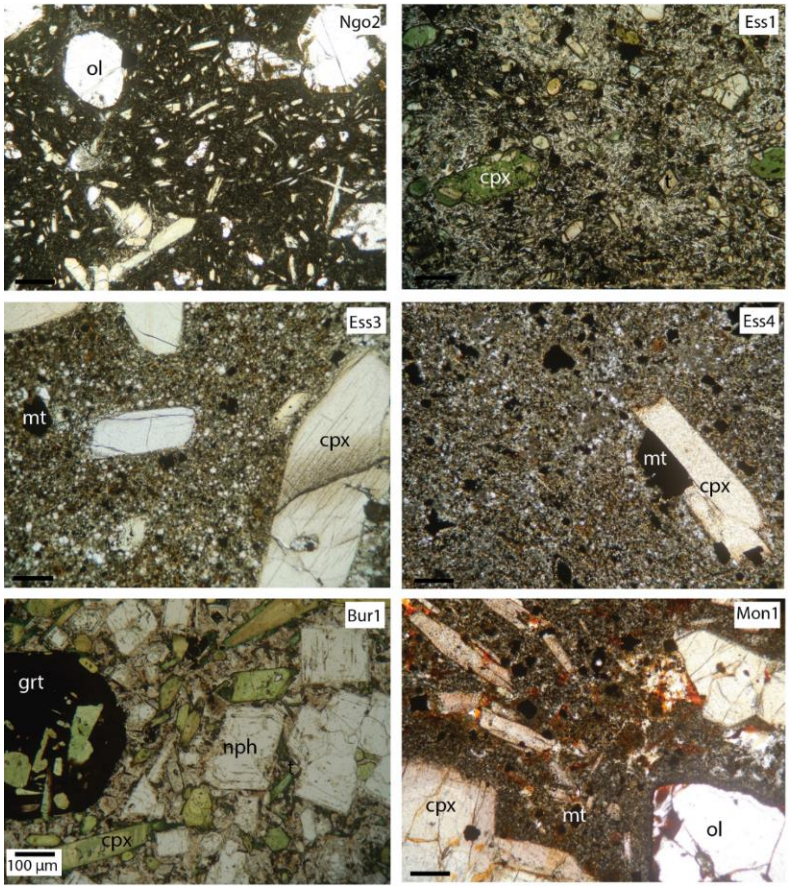

Fig.C.1*: Photographies de lames minces des volcans Ngorongoro (Ngo2), Essimingor (Ess1 Ess3, Ess4), Burko (Bur1) et Monduli (Mon1) (échelle similaire sur toutes les photographies).*

Chimie des minéraux de la divergence nord tanzanienne

- Essimingor

Les laves d'Essimingor contiennent des diopsides zonés. Les zonations sont inverses avec de plus faibles Mg# au cœur (Mg# = 38-74) par rapport aux bordures (Mg# = 78 - 84) (Fig.C.2) (Table C2). Les cpx ont des spectres enrichis en LREE par rapport au HREE (La/Yb = 5,65-36,50). Les olivines ont des teneurs en Fo entre 85 et 89 (Fig.C.3). Dans Ess1, les amphiboles sont pauvres en TiO_2 (4.6 pds %) et MgO (10 - 12 pds %) et riches en FeO (11 - 13 pds %). La titanite contient du FeO (1,5 - 2,3 pds %) et de l'Al_2O_3 (0.5 - 1,4 pds %) et présente un fractionnement LREE-HREE élevé (La/Yb = 49,3 - 66,7). Les pérovskites d'Ess3 ($CaTiO_3$) ont entre 57 et 58 pds % de TiO_2 et 39 pds % de CaO. La concentration en LREE dans les pérovskites est très élevée (10000 fois les chondrites) (Table C3).

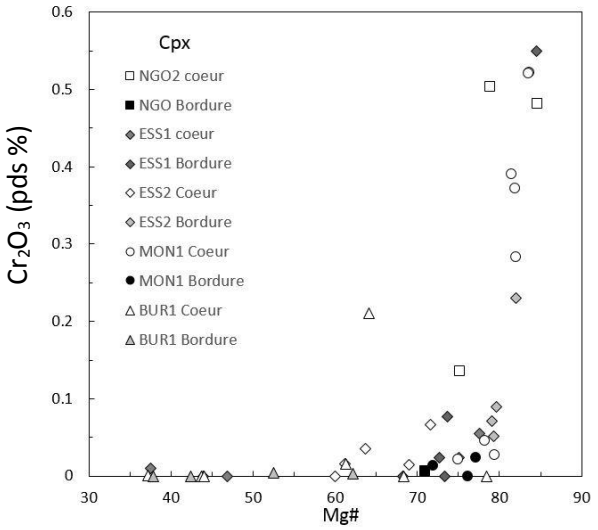

Fig. C.2 : *Cr_2O_3 vs Mg# des clinopyroxènes (cpx) des laves de la DNT.*

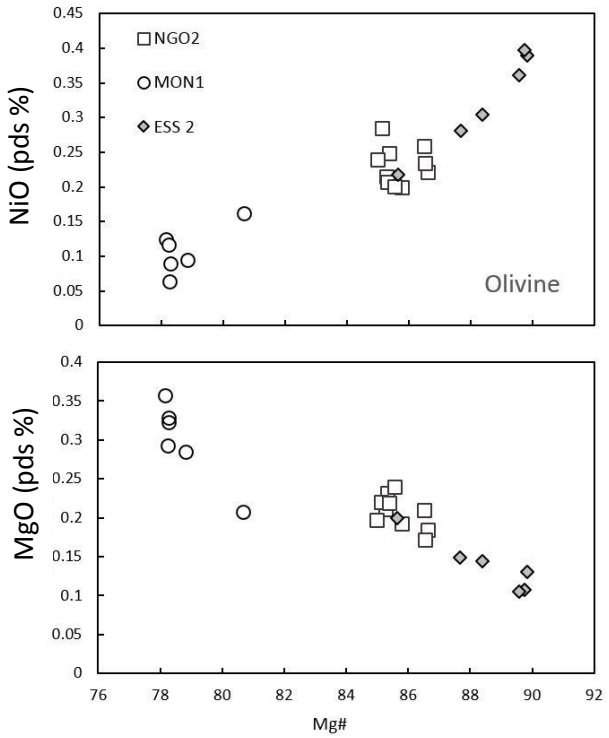

Fig. C.3 : *Concentrations en NiO, MnO et Mg# des olivines des laves de la DNT.*

- Ngorongoro

Les olivines ont des teneurs de Fo compris entre 84 et 86 (Fig.C.3). Les cpx sont des diopsides avec des zonations normales. Les cœurs sont riches en magnésium (Mg# = 83) et en Cr_2O_3 (0,62 pds %) par rapport aux bordures (Mg# = 71, Cr_2O = 0,01 pds %). Les cpx ont des spectres enrichis en LREE par rapport au HREE (La/Yb = 7,15-8,37) (Fig.C.4).

- Burko

Les néphélines ont des teneurs homogènes en SiO_2 (42 pds %) et en Al_2O_3 (31 pds %). Les néphélines contiennent très peu de REE souvent sous la limite de détection. Les grenats contiennent entre 12 et 16 pds % de TiO_2, 20 pds % de FeO, 28 pds % de SiO_2 et 31 - 32 pds % de CaO. Les spectres des REE dans les grenats sont enrichis à 1000 fois les chondrites (Fig.C.4). Les cpx sont des diopsides avec une zonation normale, présentant des cœurs riches en magnésium (Mg# = 78 - 65) par rapport aux bordures (Mg# = 40 - 60). Certains cpx montrent une zonation oscillatoire, avec des Mg# de 64 au cœur, 78 dans le manteau et de 38 en bordure.

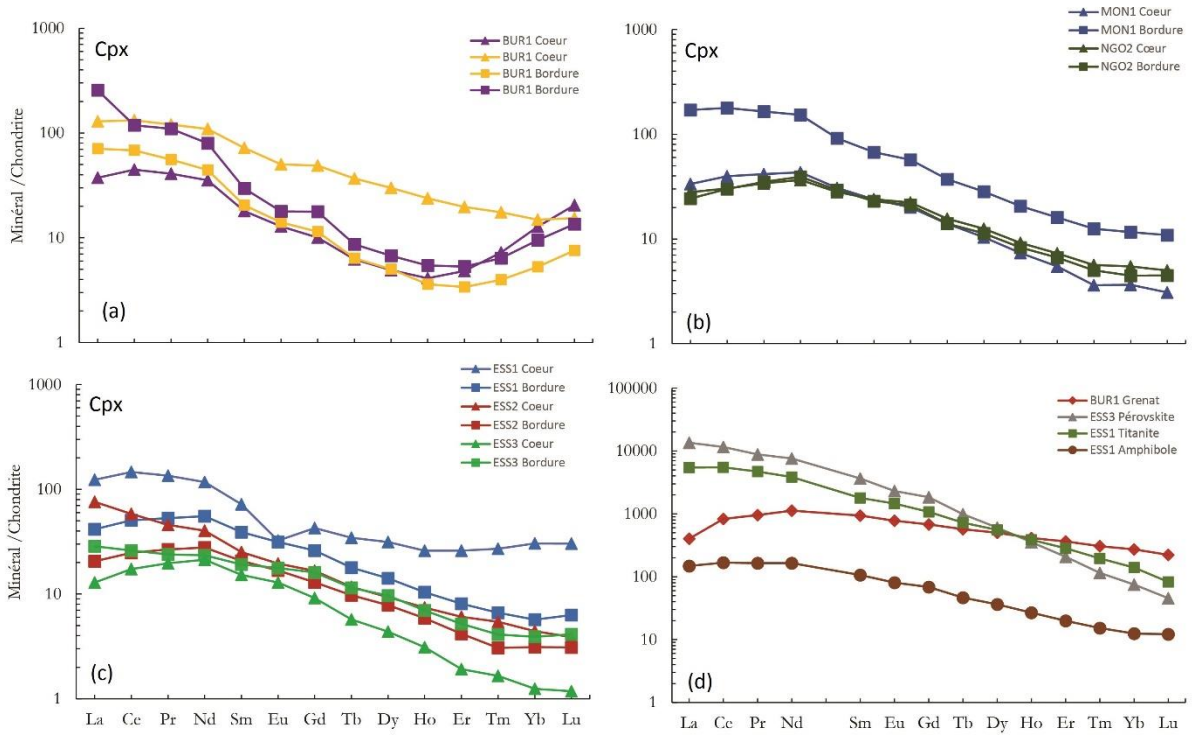

Fig. C.4 : *Spectres des REE des cpx dans les laves de (a) Burko, (b) Monduli et Ngorongoro, (c) Essimingor et (d) Spectre des REE dans un grenat (Burko), pérovskite (Ess3), titanite et amphibole (Ess1).*

- Monduli

Les clinopyroxènes sont des diopsides à zonation normale, les cœurs sont riches en magnésium (Mg# = 78 - 84) par rapport aux bordures (Mg# = 76 - 77) (Fig.C.2). Les cpx ont des spectres enrichis en LREE par rapport aux HREE (La/Yb = 9,57 - 20,43). Les olivines ont des teneurs en Fo comprises entre 77 et 80 (Fig.C.3).

Table C1 : Concentrations des éléments majeurs et en trace des laves de l'axe E-O et du Lengai

Ech.	Ngo1	Ngo2	Ess1	Ess2	Ess3	Ess4	Bur1	Bur2	Mon1	OL2	OL3	OL3x
SiO_2	46.57	41.80	51.43	46.94	38.88	37.84	44.04	42.94	42.44	39.20	0.94	44.69
TiO_2	2.71	3.08	1.57	2.05	4.19	5.48	1.96	2.02	4.14	3.93	-	1.06
Al_2O_3	13.09	8.54	16.36	11.14	10.28	9.49	15.51	15.32	11.96	7.48	0.25	13.15
Fe_2O_3	12.11	13.56	7.66	11.04	15.03	16.01	8.88	8.75	14.17	14.62	1.04	11.06
MgO	7.90	12.51	2.81	10.23	7.03	6.77	2.57	2.76	6.95	14.45	0.32	0.40
CaO	9.82	13.98	6.24	8.94	14.46	15.98	10.43	11.30	11.67	13.03	24.65	7.74
MnO	0.19	0.21	0.18	0.21	0.25	0.25	0.26	0.28	0.22	0.22	0.43	0.43
Na_2O	3.94	2.01	6.01	4.83	2.94	2.75	6.89	5.55	3.74	2.94	39.62	13.40
K_2O	1.71	0.87	3.93	2.67	2.26	1.30	3.28	2.64	2.40	1.99	10.03	7.08
P_2O_5	0.75	0.56	0.39	0.35	0.95	1.36	0.66	0.55	0.67	0.94	1.23	0.39
LOI	1.30	2.90	3.60	1.63	3.77	2.85	5.62	8.53	1.67	1.19	20.72	1.40
Total	100.1	100.0	100.2	100.0	100.0	100.1	100.1	100.7	100.0	99.99	99.23	100.8
Mg#	56.4	64.6	42.1	64.7	48.1	45.6	36.4	38.5	49.3	66.2	37.9	6.7
S (ppm)	100	143	132	60	227	894	390	260	73	90	2200	2340
CO_2 (wt%)	0.25	0.29	0.22	0.17	0.09	0.08	0.66	1.24	0.03	0.324	29.9	1.2
Cr	301	632	55.5	430	82.6	37.4	9.33	4.76	92.7	658	2.54	3.92
Ni	144	263	32.8	308	59.6	58.2	14.9	13.2	69.0	338	16.2	7.31
Cu	91.3	164	50.4	97.2	140	265	42.4	44.1	152	129	12.0	39.0
Cs	0.50	0.47	0.43	0.74	0.28	0.32	1.25	1.34	0.81	0.37	5.23	2.57
Rb	38.1	50.7	79.4	62.4	47.5	41.3	94.4	98.6	59.5	46.1	164	139
Ba	965	1032	1692	1353	809	757	1795	1823	1118	423	11715	2312
Th	9.05	6.13	22.2	13.8	5.56	14.3	37.6	34.7	12.7	9.87	5.90	18.1
U	1.54	1.25	2.70	1.14	1.89	2.62	11.6	9.39	2.85	2.17	6.84	8.33
Nb	86.4	70.5	119	107	99.0	112	294	274	126	101	60.1	347
Ta	5.73	5.19	6.35	6.84	4.97	9.24	13.2	11.3	9.31	7.37	0.21	5.87
La	84.0	64.3	123	99.3	76.1	127	277	250	105	89.2	442	165
Ce	156	117	212	180	132	264	481	420	195	178	510	249
Pb	7.22	3.33	20.0	10.9	8.31	6.13	19.8	20.1	5.57	5.05	51.5	43.6
Pr	17.3	14.0	21.6	19.3	14.9	31.8	48.1	41.3	21.9	21.0	38.8	22.3
Sr	986	666	2559	1058	1640	1114	3562	3217	1169	815	10645	2327
Nd	62.8	54.3	73.5	69.4	56.2	123	158	134	79.9	81.3	99.4	68.2
Zr	246	205	327	265	386	419	721	771	314	363	20.8	893
Hf	5.79	5.30	7.60	6.09	9.27	10.5	13.3	14.2	7.70	8.58	0.26	11.8
Sm	11.1	10.1	12.2	11.8	11.0	22.0	22.8	19.6	13.2	14.9	8.39	9.54
Eu	3.14	2.88	3.57	3.36	3.26	5.96	5.82	5.26	3.68	3.98	3.34	2.79
Gd	8.93	8.02	9.82	9.34	9.26	16.7	17.9	15.7	10.2	11.4	5.29	7.72
Tb	1.19	1.09	1.40	1.27	1.31	2.17	2.38	2.13	1.34	1.54	0.42	1.02
Dy	6.15	5.44	7.04	6.34	7.15	10.1	10.7	9.84	6.12	7.06	1.38	4.54
Y	28.8	29.5	36.8	30.6	35.0	41.8	50.7	49.5	28.3	29.8	10.0	28.9
Ho	1.10	0.99	1.38	1.16	1.32	1.71	1.94	1.82	1.06	1.20	0.22	0.87
Er	2.65	2.30	3.58	2.75	3.09	3.74	4.63	4.53	2.38	2.60	0.50	2.28
Tm	0.37	0.31	0.52	0.39	0.43	0.48	0.67	0.64	0.33	0.35	0.06	0.35
Yb	2.25	1.79	3.07	2.30	2.34	2.70	3.88	3.79	1.91	1.93	0.42	2.16
Lu	0.31	0.25	0.46	0.35	0.35	0.38	0.56	0.56	0.27	0.26	0.05	0.35

Table C.2 Concentrations en éléments majeurs des minéraux des laves de l'axe Est-Ouest

Echantillon	NGO2	NGO2	ESS2	BUR1	BUR1	MON1	MON1	NGO2	MON1	ESS2	BUR1	BUR1	ESS1	ESS3	BUR1
Mineral	CPX	CPX	CPX	CPX	CPX	CPX	CPX	Olivine	Olivine	Olivine	Neph	Grenat	Amph	Perovskite	Titanite
Type	Cœur	Cœur	Cœur	Cœur	Bordure	Cœur	Bordure	Cœur	Cœur	Cœur	Cœur	Cœur	Cœur	Cœur	Cœur
SiO_2	51.76	49.54	52.17	49.45	50.24	50.65	46.08	40.23	39.47	41.16	43.28	28.19	41.44	0.05	29.94
TiO_2	1.25	1.96	0.99	1.69	1.43	1.45	3.43	0.02	0.01	0.03	0.01	15.72	4.63	58.66	36.90
Al_2O_3	2.03	3.49	2.13	3.23	0.91	3.21	6.21	0.03	0.01	0.02	31.67	1.02	10.36	0.12	0.97
Cr_2O_3	0.48	0.62	0.78	0.00	0.00	0.37	0.01	0.04	0.00	0.06	0.02	0.02	11.69	0.00	0.00
FeO	4.97	5.53	4.65	9.49	17.53	5.76	7.91	13.82	19.43	9.62	0.98	20.31	12.99	0.84	1.94
MnO	0.09	0.07	0.05	0.24	0.47	0.10	0.16	0.22	0.28	0.13	0.00	0.32	0.17	0.02	0.03
MgO	15.38	14.08	15.10	11.48	7.25	14.67	11.37	44.37	40.61	47.74	0.00	0.79	11.43	0.00	0.00
CaO	23.83	24.12	23.99	23.37	18.97	23.13	23.30	0.35	0.34	0.18	0.34	32.08	3.04	39.69	28.07
Na_2O	0.37	0.41	0.58	1.07	3.06	0.65	0.91	0.00	0.03	0.03	15.47	0.25	1.35	0.20	0.13
K_2O	0.00	0.00	0.00	0.00	0.01	0.01	0.00	0.00	0.00	0.00	7.65	0.00	0.00	0.01	0.01
NiO	0.01	0.01	0.07	0.00	0.02	0.03	0.00	0.28	0.09	0.39	0.00	0.01	0.02	0.00	0.00
Total	100.16	99.82	100.52	100.01	99.90	100.03	99.38	99.36	100.31	99.33	99.42	98.70	97.11	99.59	97.97
Mg#	84.66	81.95	85.27	68.33	42.43	81.95	71.92	85.12	78.84	89.84	-	7	58.23	-	-
FORMULE STRUCTURALE															
Si	1.90	1.84	1.91	1.85	1.92	1.87	1.73	1.02	1.01	1.02	8.46	2.39	5.71	0.01	1.00
Al^{IV}	0.09	0.15	0.09	0.14	0.04	0.13	0.27	-	-	-	-	-	2.29	-	-
Al^{VI}	0.00	0.00	0.00	0.00	0.00	0.00	0.01	-	-	-	-	-	0.00	-	-
Al_{tot}	0.09	0.15	0.09	0.14	0.04	0.14	0.27	0.00	0.00	0.00	7.30	0.11	-	0.01	0.04
Ti	0.03	0.05	0.03	0.05	0.04	0.04	0.10	0.00	0.00	0.00	0.00	1.02	0.48	1.49	0.93
Fe^{2+}	0.10	0.09	0.09	0.16	0.30	0.09	0.12	0.29	0.42	0.20	-	0.36	0.00	-	-
Fe^{3+}	0.05	0.08	0.05	0.14	0.26	0.08	0.13	0.00	0.00	0.00	-	1.08	1.66	-	-
Fe_{tot}	-	-		-	-	-	-			-	0.16	-	-	0.03	0.05
Cr	0.01	0.02	0.02	0.00	0.00	0.01	0.00	0.00	0.00	0.00	-	0.00	-		-
Mn	0.00	0.00	0.00	0.01	0.02	0.00	0.01	0.00	0.01	0.00	0.00	0.03	0.02	0.00	0.00
Mg	0.84	0.78	0.82	0.64	0.41	0.81	0.64	1.67	1.55	1.77	0.00	0.11	2.34	0.00	0.00
Ca	0.94	0.96	0.94	0.94	0.78	0.91	0.94	0.01	0.01	0.00	0.07	2.91	0.45	1.46	1.01
Na	0.03	0.03	0.04	0.08	0.23	0.05	0.07			-	5.87	-	0.36	0.03	0.01
K	-	-	-	-	-	-	-			-	1.91	-	0.00	-	-
Total	4.00	4.00	4.00	4.00	4.00	4.00	4.00	4.02	4.01	4.02	23.77	8.00	14.91	3.03	3.05

Table C.3 Concentrations en éléments en trace des minéraux des laves de l'axe E-O

Echantillon	NGO2	NGO2	ESS2	BUR1	BUR1	MON1	MON1	NGO2	MON1	ESS2	BUR1	BUR1	ESS1	ESS3	BUR1
Mineral	CPX	CPX	CPX	CPX	CPX	CPX	CPX	Olivine	Olivine	Olivine	Neph	Grenat	Amph	perovskite	Titanite
Type	Cœur	Cœur	Cœur	Cœur	Bordure	Cœur	Bordure	Cœur	Cœur	Cœur	Cœur	Cœur	Cœur	Cœur	Cœur
Cs	0.01	<0,0031	0.11	<0,0028	0.00	<0,0030	<0,0031	0.00	<0,0014	0.10	0.08	0.01	<0,0044	<0,0038	0.05
Rb	0.21	0.04	3.19	0.07	0.33	<0,0072	0.26	0.14	0.22	3.18	83.9	10.0	7.21	0.11	0.41
Ba	39.65	7.52	174.60	0.64	4.89	0.09	1.30	1.49	2.80	1.78	25.8	15.4	582.12	1.51	2.68
Th	0.25	0.09	3.35	0.09	0.09	0.03	0.62	0.03	0.04	0.16	<0,00	35.2	0.12	660	47.4
U	0.07	0.01	2.58	0.04	0.03	0.00	0.06	0.02	0.01	0.06	<0,00	15.3	0.01	50.6	10.6
Nb	2.85	0.90	10.2	1.99	1.85	0.27	6.17	0.04	0.43	4.31	<0,0162	687	47.3	1745	7078
Ta	0.26	0.24	0.58	0.41	0.09	0.05	1.54	0.00	0.03	0.06	0.00	49.4	3.84	309	398
La	6.65	5.78	18.0	15.7	28.0	3.92	39.6	0.12	0.33	0.31	0.03	95.3	24.0	3314	884
Ce	18.6	18.4	35.7	44.3	66.8	13.0	105.8	0.20	0.64	0.39	0.04	507	71.4	7888	2644
Pb	0.17	0.07	1.19	0.23	0.49	0.06	0.17	0.41	0.06	1.20	0.12	4.65	0.41	1.66	0.53
Pr	3.23	3.33	4.36	6.51	8.12	2.20	15.6	0.03	0.07	0.04	0.01	91.1	11.1	947	369
Sr	121	112	700	390	1189	111	431	1.29	3.69	4.89	229	272	798	857	848
Nd	17.1	18.3	18.9	30.3	30.9	11.92	71.5	0.10	0.27	0.13	<0,028	527	56.4	3963	1532
Zr	70.5	83.6	36.2	469	230	32.8	343	1.20	1.18	0.79	<0,19	4013	155	101	3073
Hf	4.13	4.84	1.52	18.9	6.28	1.70	12.6	0.04	0.02	0.01	<0,0074	81.4	6.34	3.55	65.4
Sm	4.30	4.49	3.85	6.50	4.29	2.91	14.2	0.03	0.04	0.03	<0,00	143.8	12.2	622	222
Eu	1.39	1.33	1.14	1.90	1.10	0.87	3.98	0.00	0.01	0.01	0.01	45.1	3.49	150	56.4
Gd	4.57	4.33	3.42	5.68	3.23	2.46	11.73	0.02	0.03	0.04	<0,070	140.0	10.3	425	159
Tb	0.58	0.53	0.44	0.70	0.34	0.32	1.38	0.00	0.00	0.01	<0,0061	21.3	1.19	40.1	17.3
Dy	3.18	2.88	2.37	3.76	1.75	1.64	7.10	0.04	0.03	0.04	<0,0121	128	6.60	160	82.1
Y	11.1	9.48	10.6	14.1	10.5	6.14	26.8	0.24	0.20	0.34	<0,0109	592	24.4	349	286
Ho	0.52	0.47	0.42	0.65	0.39	0.27	1.15	0.01	0.01	0.01	<0,00187	23.4	1.00	19.9	12.1
Er	1.21	1.10	1.00	1.52	1.48	0.57	2.57	0.03	0.02	0.03	<0,0082	60.4	2.32	32.2	24.9
Tm	0.14	0.13	0.14	0.20	0.36	0.06	0.32	0.00	0.00	0.00	<0,00	7.81	0.26	2.73	2.65
Yb	0.93	0.76	0.75	1.59	3.82	0.39	1.95	0.03	0.04	0.03	<0,0049	46.4	1.45	11.6	13.3
Lu	0.13	0.11	0.10	0.30	0.87	0.05	0.26	0.01	0.01	0.00	<0,0022	5.66	0.21	1.06	1.20

Les laves l'Oldoinyo Lengai et du bassin de Natron

Les différentes roches ont été échantillonnées dans la région du bassin de Natron, au nord de la divergence nord tanzanienne. Les 4 échantillons ont des caractéristiques chimiques et minéralogiques différentes comprenant un tuf (OL1, clastes d'olivine, cpx et phlogopite) qui provient du cratère Kisete (10 km au S-E de l'Oldoinyo Lengai), une néphélinite (OL2, SiO_2 = 39,2 pds%, Na_2O+K_2O = 4,9 pds%) d'un cône parasitique de l'Oldoinyo Lengai, et une natrocarbonatite Oldoinyo Lengai (OL3, coulée 2007) qui est composé de phénocristaux de nyéréréite ($Na_2Ca[CO_3]_2$) et de grégoryite ($[Na_2K_2Ca]CO_3$) (Zaitsev et al. 2009). L'échantillon OL3x (coulée 2007) est une xénolite composée de néphéline, combeite, cpx et de mélanite (Ti-grenat) (Fig.C.5).

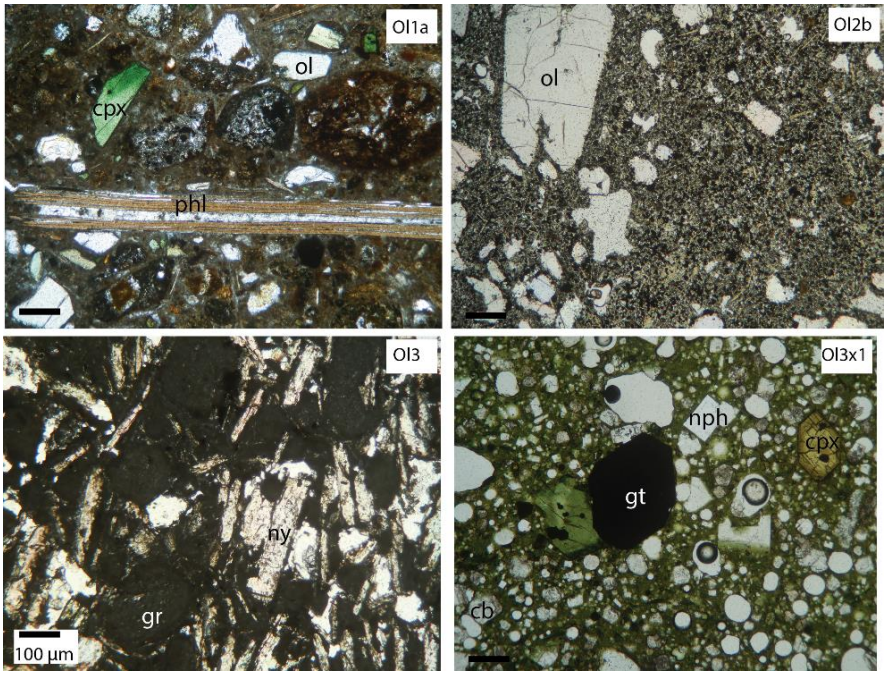

Fig.C.5: *Photographies de lames minces des échantillons provenant du Oldoinyo Lengai (cpx=clinopyroxène, ol=olivine, phl=phlogopite, gr=grégoryite, ny=nyéréréite, gt=grenat, cb=combéite, nph=néphéline).*

On observe une grande variabilité entre les échantillons. OL2 est plus pauvre en éléments incompatibles que OL3 et OL3x et a de légères anomalies négatives par rapport au manteau primitif en K, Sr, Zr et Hf. La natrocarbonatite OL3 est appauvrie en HREE comparé aux LREE (La/Yb=1050) (Fig.C.6). De plus cette lave possède des fractionnements négatifs : du Ta par rapport au Nb (Nb/Ta = 292) et du Hf par rapport au Zr (Zr/Hf = 80). OL3 a des anomalies positives par rapport au manteau primitif en Ba (1,17 pds %) et Sr (1,06 pds %). La néphélinite OL3x a un fractionnement négatif du Ta par rapport au Nb (Nb/Ta = 59) (Fig.C.6). On peut également noter que cette lave n'est pas d'appauvrie en HFSE (e.g. Zr). Les teneurs en éléments majeurs des minéraux ainsi que de la roche totale d'OL3x (néphéline, combéite, grenat, cpx) sont cohérentes avec celles publiées pour les néphélinites de l'Oldoinyo Lengai (Klaudius et Keller 2006). Les inclusions vitreuses (n=5) dans les néphélines de OL3x ont des compositions plus siliceuses (trachyandésites) que celles reportées jusqu'à présent dans la littérature (e.g. Mitchell 2009, deMoor et al. 2013)(Fig.C.7, Table C8). OL3x1 a une minéralogie et une chimie proche des néphélinites « CWN » décrites dans Klaudius et Keller (2006), mais l'absence de wollastonite et les différences de composition des inclusions vitreuses indiquent des histoires magmatiques différentes. Une étude approfondie des inclusions vitreuses de cet échantillon pourrait apporter de nouvelles informations sur l'histoire complexe et polyphasée de l'Oldoinyo Lengai.

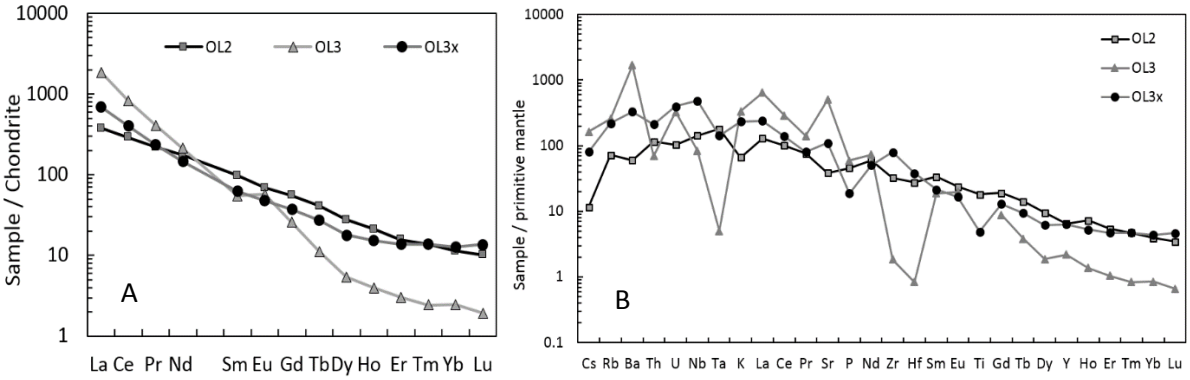

Fig.C.6 : ***A*** *Spectres des REE,* ***B*** *Spectres élargis pour les laves de l'Oldoinyo Lengai, OL2=néphélinite, OL3=natrocarbonatite, et OL3x=combéite néphélinite.*

Table C4 : Concentrations en éléments majeurs des minéraux et inclusions vitreuses de OL3x

	cpx	cpx	cpx	gt	nph	nph	comb	comb	MI	MI	MI	MI	MI
SiO_2	51.12	51.62	50.51	29.73	42.30	41.42	50.27	50.27	52.92	53.34	56.17	57.33	54.39
TiO_2	0.50	0.43	0.50	12.01	0.01	0.00	0.05	0.06	1.49	1.73	1.45	1.56	1.81
Al_2O_3	0.64	0.57	0.78	1.00	33.43	32.98	0.00	0.02	4.93	5.41	6.74	6.77	5.06
FeO	16.03	13.18	18.07	21.19	1.22	1.80	1.42	1.43	9.77	15.70	13.56	13.72	16.03
MnO	0.57	0.44	0.54	0.39	0.00	0.00	0.52	0.53	0.35	0.67	0.60	0.59	0.78
MgO	7.79	10.07	6.71	0.56	0.02	0.04	0.11	0.12	0.36	0.56	0.47	0.48	0.46
CaO	20.01	21.38	19.14	31.63	0.06	0.07	26.26	25.98	8.81	3.34	4.44	4.35	3.73
Na_2O	2.55	2.07	2.99	0.29	14.49	15.54	19.98	20.29	6.26	5.98	5.85	5.96	5.56
K_2O	0.15	0.00	0.01	0.00	8.23	8.45	0.06	0.07	4.02	2.64	2.78	2.75	2.50
P_2O_5									0.87	0.72	0.21	0.23	0.38
F									4.06	0.96	1.72	1.82	1.64
Cl									0.92	0.58	0.49	0.40	0.83
SO_2									1.07	1.11	0.95	0.97	1.39
Total	99.35	99.78	99.25	96.83	99.76	100.33	98.68	98.77	95.88	92.75	95.43	96.93	94.63

cpx clinpyroxene, gt grenat, nph nepheline, comb combéite, MI inclusions vitreuses

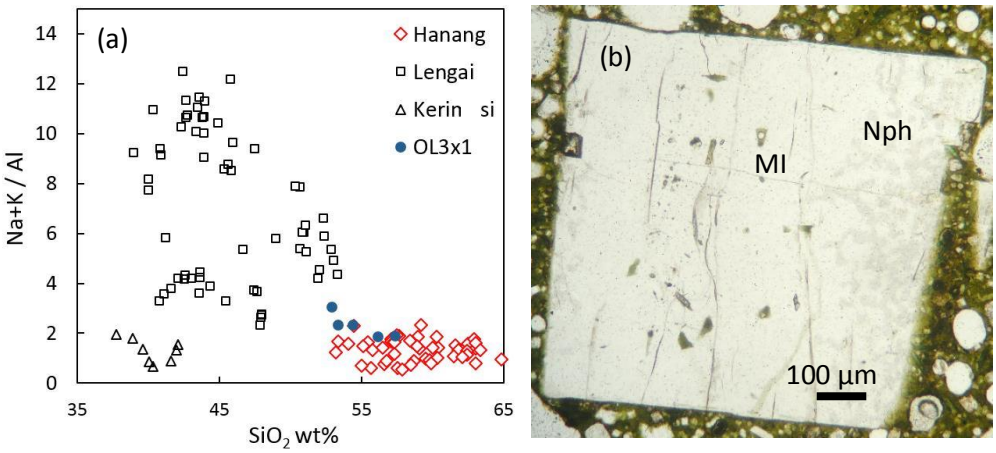

Fig.C.7 ***(a)*** *Concentration en silice vs l'index d'alcalinité (Na+K/Al) pour les inclusions vitreuses et* ***(b)*** *Photographie d'un cristal de néphéline dans la néphélinite OL3x contenant plusieurs inclusions vitreuses (inclusions entre 20 – 40 µm).*

Volcanisme alcalin à l'initiation de la rupture continentale

Exemple du Rift Est Africain : Nord Tanzanie, bassin de Manyara

Céline BAUDOUIN

Le rift Est africain (REA) est une frontière de plaque en extension qui présente plusieurs stades d'extension, de l'initiation du rift dans la lithosphère cratonique (Tanzanie) jusqu'à l'accrétion océanique en Afar. Au nord de la Tanzanie, le magmatisme et des processus tectoniques sont impliquées dans la rupture continentale. Cette étude est centrée sur le bassin de Manyara dans la partie méridionale de branche Est du REA. Le volcanisme hyperalcalin récent (< 1,5 Ma) associé à un essaim sismique dans la croûte inférieure (20 – 40 km), caractérise la zone de l'initiation de la rupture continentale.

Les néphélinites à mélilite (Labait et Kwaraha) sont des laves primaires composées d'olivines et de clinopyroxènes (cpx). La modélisation géochimique des éléments en trace suggère que ces magmas primaires résultent d'un degré de fusion partielle ≤ 1 % à partir d'une péridotite à grenat et phlogopite. Ces magmas proviennent d'une profondeur > 120 km. Les minéraux ont cristallisés à 1250°C et 1000 MPa à partir d'un magma pauvre en eau (0,1 et 0,5 pds % H_2O). La calciocarbonatite et les néphélinites différenciées sont issues des néphélinites à mélilite par cristallisation fractionnée et processus d'immiscibilité. Les néphélinites du Hanang sont riches en éléments alcalins et en silice (44,2 – 46,7 pds% SiO_2) et sont composés de cpx, grenat, néphéline, titanite et apatite. La zonation complexe dans les cpx (par exemple, changement brusque de Mg#, Nb/Ta, et H_2O) implique une différenciation magmatique en système ouvert avec immiscibilité de liquide carbonaté et silicaté ainsi qu'un remplissage de la chambre magmatique avec des liquides primaires. La faible teneur en eau des cpx (3 – 25 ppm H_2O) indique la présence d'un magma pauvre en eau (0,3 pds % H_2O) lors de la cristallisation des cpx à des conditions crustales (~600 MPa et 1050°C). L'étude des inclusions vitreuses dans les néphélines de Hanang permet de contraindre l'évolution magmatique tardive des néphélinites et le comportement des éléments volatils (CO_2, H_2O, S, F, Cl) lors du stockage et de la remontée du magma. Les inclusions vitreuses sont composées d'un verre trachytique, d'une phase carbonatée et d'une bulle de rétraction. Le verre trachytique contient du CO_2 (0,43 pds % CO_2, analyses SIMS), du soufre (0,5 pds% S), du chlore (0,28 – 0,84 pds % Cl) et très peu d'H_2O (< 0,1 pds % H_2O, analyses Raman). Le processus d'immiscibilité conduisant à la formation du carbonate se produit dans un système fermé pendant l'ascension rapide du magma à ~500 MPa. La phase carbonatée est un carbonate anhydre et riche en Ca-Na-K-S. Le liquide pré-immiscible a une composition phonolitique avec 6 ± 1,5 pds % CO_2 à une pression de 700 MPa. Une étude préliminaire des inclusions par spectroscopie XANES et des roches par spectroscopie Mössbauer a permis de déterminer que les laves de Manyara se sont formées à conditions oxydantes (~ ΔFMQ +1,5). Le volcanisme alcalin à l'initiation de la rupture continentale est caractérisé par des magmas riches en CO_2 et pauvres en H_2O issus d'une source profonde 120 km à partir de faible taux de fusion.

L'association des données géochimiques, géophysiques et tectoniques a permis de mettre en évidence des interactions entre le magmatisme, les structures héritées et la sismicité au nord de la Tanzanie. Dans le bassin de Manyara, la présence de magmas alcalins riches en CO_2 associée à de faibles volumes de lave en surface suggèreraient que le piégeage et la percolation de ces magmas en profondeur serait un déclencheur potentiel d'un essaim sismique profond.

Mots clefs : rift, néphélinite, carbonatite, éléments volatils, inclusions vitreuses, fusion partielle, immiscibilité, conditions redox